計畫編號：DOH96-TD-F-113-033-

行政院衛生署九十六年度委託科技研究計畫

非傳統性食品原料安全性評估資料之蒐集及我國審查基準之建立

研 究 報 告

執行機構：台北醫學大學 保健營養學系

計畫主持人：謝明哲

研究人員：黃士懿、陳玉華、柯佳君

全程計畫：自 96 年 3 月 1 日至 97 年 2 月 28 日止

本年度計畫：自 96 年 3 月 1 日至 97 年 2 月 28 日止

目　　錄

中文摘要

非傳統性食品及原料的使用逐年增加，但是這些食品一般皆缺乏長久食用安全的歷史，同時這一類食品的來源、結構或製造過程與國人一般食用之傳統食品或原料可能不同，因此其是否會影響食物整體之營養價值與體內之代謝方式或其是否含有害物質，以致對人體健康產生不良影響，均應進行安全性評估後，方得販賣食用。依據我國食品衛生管理法之規定：從未供於飲食且未經證明為無害人體健康的食品或食品添加物，不得使用，非傳統性食品原料亦應有相同的標準。為方便業者有依循的參考，相關衛生主管單位應制定一套相關安全性評估的審查基準。因此本計畫在蒐集一些可用於評估或已使用之各種營養毒理的文獻與資料後，彙整出可用於評估特定物質於體內吸收、分佈、代謝與排出之方法；此外，針對這些非傳統食品原料在不同族群的飲食攝取資料，包括一般消費者、極端消費者及特定族群消費者之估計攝取量及上限與建議食用或排除對象之資料，亦提出建議之計算方式。由本計畫所得之成果，可提供未來衛生主管機關建立我國針對非傳統食品或原料安全性評估之審查基準、相關管理辦法與法規的參考，並提供業者於申請新穎性食物資料提供的參考，以確保民眾可安全的食用這一類食品與原料。

關鍵詞：　非傳統性食品原料、飲食攝取、估計攝取量、營養毒理、安全性評估

Abstract

Recent years, the consumption of novel foods has become more popular. However, because of lacking of safety information, and because the sources, structures, and the production processes of these food materials may not be the same as the traditional foods that we have continued consuming, the potential risks of consumption of these foods exist. This study was aimed at collecting information on pharmacokinetics, including methods on evaluation of absorption, distribution, metabolism, excretion, and bioavailability, as well as information on dietary intake, including estimated daily intake on specific populations regarding novel foods to help vendors to understand the pharmacokinetics and to calculate estimate daily intake of various novel foods or related materials. The results obtained from this study may help government to establish a standard procedure on the safety evaluation of the novel foods and their related materials.

Key words: novel foods, dietary intake, estimated daily intake, pharmacokinetics, safety evaluation

一、前言

傳統上而言，食物主要為提供我們維持生命、修補與建造組織與調節生理機能所需之營養素與熱量，此即為我們常常所稱之食品的初級機能。然而，隨著工業的進步、經濟的改善以及科技的發展等因素，營養素攝取不足不再是國人主要的營養問題，取而代之的是營養不均衡以及衍生的一些營養相關的慢性疾病問題；所以，民眾對於食品機能的需求已漸由原來的初級機能轉變為追求食物色香味的第二機能，甚至為第三機能，亦即消費者期望透過一些特殊食物或其衍生補充品的攝取，達到預防或改善疾病、強化免疫系統甚至促進的健康作用。由於這個轉型與需求，使得一些非傳統性食品以及衍生於這一類食品之原料或活性組成等新穎性食品的使用，快速的增長當中。

依據我國食品衛生管理法第十一條第九款之規定：從未供於飲食且未經證明為無害人體健康的食品或食品添加物，不得製造、加工、調配、包裝、運送、貯存、販賣、輸入、輸出、贈與或公開陳列。於此條款內亦說明，所謂“非傳統性食品及原料”乃指對於從未供於飲食且未經證明為無害人體健康者，可稱為非傳統供食用或食用安全性未明之食品。有關這一些食品或原料僅有有限的相關資料。雖然有些民眾認為這些食品屬於天然的物質，沒有合成化合物的毒性，也可能不會像藥物一樣有副作用的產生。但是，這些觀點未必是正確的，因為

即使是一些天然的成份，或食品於生長、加工、儲存或是運送的過程皆可能受到污染或是產生一些其他的毒性物質。同時這一類食品的來源、結構或製造過程與國人一般食用之傳統食品或原料可能不同，在缺乏民眾長期食用安全歷史的情況下，民眾於攝取此類食品或原料後，其對食物整體之營養價值與體內代謝方式之影響或其是否含有害物質，以致對人體健康產生不良影響，均須進行安全性評估後，方得販賣食用。因此進口商或製造商應針對這些非傳統性食品或原料提出明確的安全性相關數據以負舉證之責，亦確保民眾可以安心的食用，並可減少民眾因誤食而導致的健康與醫療損失。

為順應此類食品或原料使用的必然趨勢，對於要求業者提供這些食品或原料安全性評估的相關資料勢必成為食品衛生管理重要的一部份。目前已有使用之非傳統性食品或新穎性食品原料的種類非常繁多，行政院衛生署所整理出的「可供食品使用原料一覽表」，便含有目前市面上所食用的各種動植物及微生物原料，包括草木本植物、藻類、微生物、海洋動物、昆蟲等十種，如中醫常用的五加皮、金線連、冬蟲夏草等，及靈芝、舞菇等。雖然多數民眾對於這些食材的食用相當熟悉，但是在食用頻率及劑量上並未統一，在食用安全上亦仍未有相關規範，所以對於人體的影響皆未被證實。因此，為方便業者有所依循及消費者的食用安全性，相關單位應先制定一套有關安全性評估

的審查基準，包括安全性評估的各種評估項目與方法，以利業者參考。有關安全性評估的項目範圍廣泛；例如，依據我國健康食品申請許可辦法第十條第一款之規定：健康產品之安全評估試驗應依中央衛生主管機關公告之「健康食品安全評估方法」進行，並檢具該方法所規定之毒性測試資料，這些安全評估方法包括基因毒性試驗、28 天餵食毒性試驗、90 天餵食毒性試驗與致畸試驗等；非傳統性食品或原料對於營養代謝之影響，過敏性及副作用的評估，以及於不同族群飲食攝取量評估方法等亦為重要的課題；因為攝取來源的多寡，影響每日攝取量之估計，若特定成份於天然食材中即可獲得一定劑量的攝取，倘若又再額外攝取高劑量萃取之濃縮錠，引起人體危害風險也會增加。

而目前行政院衛生署於健康食品申請許可上，已明確制定出食用食品的安全性評估項目。食品區分為傳統食用、非通常加工、非傳統食用及含致癌類似物等四類，不同分類間安全性評估項目亦不同，其中又指出非傳統性食品安全評估應具備人體吸收、分佈、代謝、排出等試驗報告。因此，本計劃主要蒐集資料以計算不同族群非傳統性食品原料之每日估計攝取量的算式。同時，有關這些非傳統性食品原料在人體內的毒性相關資料，包括於人體吸收、分佈、代謝、排出、生物利用率及耐受性等。利用廣泛的蒐集可用於評估或已使用之非傳統

性食品原料的各種安全性評估的文獻與資料，包括人體飲食攝取之相關資料以及於體內毒理相關資料之蒐集與彙整，期可提供一些可用於評估這一些非傳統食品原料安全性的項目與方法，及於不同族群飲食攝取量的估計方法，以提供未來衛生主管機關建立我國針對非傳統食品或原料審查基準、相關管理辦法與法規的參考，並確保民眾可安全的食用這一些食品或原料。

二、材料與方法

本計畫利用各種網路搜尋引擎以及相關的官方報告書進行資料的搜集，包括了解非傳統性食品原料之相關資訊，以及各種飲食攝取的資料，同時，亦了解這些原料於食品中的給予方式及每日給予劑量，以協助制定計算這些食品原料於飲食攝取資料方面之制定標準或建議。此外，針對一般消費者、特定消費者及極端消費者之預估攝取量及上限制定的原則，以及於特定消費者之預估攝取量及上限制定的原則，針對特定之食物或食品原料之食用對象及排除對象之篩檢原則亦將提出建議的方針。

除此之外，我們亦以 Medline 系統，針對特定物質的一些評估毒理資料的方法，包括在人體或細胞的吸收、分佈、代謝、排出、生物利用率及耐受性等資料進行相關原始文獻的搜尋，同時亦將參考已出

版之相關書籍以及有關藥物在人體毒理評估的方法，了解一些可用於評估這些非傳統性食物毒理資料的方法與資料，彙整出常用之評估方法，以提供主管機關以及業者未來送審的參考。

待資料蒐集與整理後，由這些不同途徑彙整所得之所得之結論，我們將進一步與專家學者討論，以了解該方法的可行性，同時針對業者送件時常遇到之困難，再加以補強，最後期整理出現今常用之安全性評估方法及項目，以及各族群針對特定的新穎性食品原料的估計攝取量，以提供主管機關未來制定相關法規的參考。

雖然非傳統性食品原料或新穎性食品的種類非常的繁多，但相信經由本計畫針對這些不同原料之簡單方法學的建立，對於我國非傳統性或新穎性食品原料的安全性評估將可提供一個方便且敏感的審查基準的參考。

三、結果

A. 特定食品或原料估計攝取量的計算

建議可由美國藥物食物管理局內 Guidance for Industry Estimating Dietary Intake of Substances in Food (US FDA)所建議的公式計算之：

$$EDI_x = \sum_{f=1}^{F} Freq_f \, x \, Port_f \, x \, Conc_{xf}$$

其中： x 指欲計算之特定成份；

EDI 為 Estimated Dietary Intake，即每日估計攝取量；

$Freq_f$ 指含有該成份各種食物的每日攝食頻率平均值(台灣相關的資料可自衛生署食品資訊網中"國民營養現況"及"國民營養健康狀況調查"中取得)（行政院衛生署 a, b, c）；

$Port_f$ 為含有該成份各種食物的每次攝食份量平均值(台灣相關的資料可自衛生署食品資訊網中"國民營養現況"及"國民營養健康狀況調查"中取得)（行政院衛生署 a, b, c）；

$Conc_{xf}$ 則為該成份在食物中的含量(若該成份為天然存在的形式，該數據可由不同的文獻取得；若該成份為額外添加或補充的形式，則該數據則可由該食品的食品標示取

得，或為廠商欲添加之劑量)

因此，在估算一個特定飲食成分(如非傳統性食品原料)針對特定族群每日攝取量之前，須先取得以下四個數據--

(1) 該成份在各種食物中的含量平均值；

(2) 含有該成分的各種食物；

(3) 含有該成份食物於該族群的每日攝食頻率平均值；

(4) 含有該成份食物於該族群的每次攝食份量平均值；

其中(3)及(4)兩個數據可以自行政院衛生署--食品資訊網中之"國民營養現況"及"國民營養健康狀況調查"中取得)（行政院衛生署 a, b, c）

除此之外，若該成份亦有補充劑(錠劑)的形式存在，亦應將該錠劑每日之攝取量計入。將各數據加總即為該族群每人每日特定成份之估計攝取量。

針對極端消費者（過度攝取）的估計攝取量，由於目前衛生署國民營養調查之數據中尚缺乏成人極端消費者之數據，因此本計劃建議依照相同的公式，惟攝取量平均值之數據，採用"攝取量平均值+標準差" 的數據取代計算之。

B. 範例

例一：兒茶素

若某一廠商欲推出一系列含兒茶素之產品，包括：飲品、餅乾、錠劑等提供消費者選用，產品營養標示分別如下：

飲品－ 綠茶

營養標示	
每100毫升	
熱量	16大卡
碳水化合物	4公克
蛋白質	0公克
脂肪	0公克
鈉	10.5毫克
兒茶素	25毫克

(綠茶)

烏龍茶

營養標示	
每100毫升	
熱量	10大卡
碳水化合物	2.5公克
蛋白質	0公克
脂肪	0公克
鈉	12毫克
兒茶素	25毫克

(烏龍茶)

餅乾－綠茶餅乾

營養標示	
每份	30g
本包裝共含5份	
熱量	58 大卡
碳水化合物	13 g
蛋白質	0.6 g
脂肪	0.4 g
納	37.5 mg
兒茶素	2.5 mg

錠劑－兒茶素補充劑，建議成人每日早晚飯後各一錠(2 錠/日)

營養標示	
每一份量0.7公克(一粒) 本產品含100份	
	每份
熱量	1.6大卡
碳水化合物	0.4公克
蛋白質	0公克
脂肪	0公克
鈉	0.03毫克
綠茶萃取	220毫克
EGCG	150毫克

依據市調結果，市面上宣稱含有兒茶素之產品主要包含飲品及錠劑，因而假設一般成年人主要藉由這些產品攝取而得綠茶素。欲估算一般成人消費者每日經由其推出產品攝取得兒茶素份量計算式：

步驟 1. 由衛生署食品資訊網之"1993-1996 國民營養現況"(行政院衛生署 a)查得台灣成人每日攝取飲品、餅乾之頻率以及攝取份量。(茶類飲品歸類於"冰、飲料類"；餅乾歸類於"糕點餅乾類")，數據分別為:

	男性成人		女性成人	
食物重量(g/day)	平均值	標準差	平均值	標準差
冰、飲料類	291.37	572.37	148.31	345.47
糕點餅乾類	17.42	69.63	18.76	62.25

步驟 2. 計算每人每日攝取估計量:

(a) 一般成人

由於茶類皆被歸於"冰、飲料類"，假設綠茶、烏龍茶兩者攝取量各佔 50%，且 100 ml = 100 g，所以每日由飲料攝取之兒茶素含量為：50% x 25 (mg/100 g) + 50% x 25 (25 mg/100 g) =25 (mg/100 g)。

	男性成人	女性成人
兒茶素來源	兒茶素攝取量(mg/day)	
廠商產品--綠茶以及烏龍茶	25 (mg/100 g)/100 g x 291.37 (g/day) = 72.5	25 (mg/100 g)/100 g x 148.31 (g/day) = 37
廠商產品--餅乾	2.5 (mg/30 g)/30 g x 17.42 (g/day) =1.45	2.5 (mg/30 g)/30 g x 18.76 (g/day) = 1.56
廠商產品--錠劑	150 mg x 2=300	150 mg x 2=300
EDI	72.5+1.45+300 **=375.95 (mg/day)**	37+1.56+300 **=338.56 (mg/day)**

(b) 成人極端消費者

由於目前衛生署國民營養現況之數據中缺乏成人極端消費者之數據，因此本計劃建議採用"攝取量之平均值+標準差"取代平均值計算之。

	男性成人	女性成人
兒茶素來源	兒茶素攝取量(mg/day)	
廠商產品—綠茶以及烏龍茶	25 (mg/100 g)/100 g x (291.37+572.37) g/day = 215.9	25 (mg/100 g)/100 g x (148.31+345.47) g/day = 123.45
廠商產品—餅乾	2.5 (mg/30 g)/30 g x (17.42+69.63) g/day =7.25	2.5 (mg/30 g)/30 g x (18.76+62.25) g/day =6.75
廠商產品—錠劑	150 mg x 2=300	150 mg x 2=300
EDI	215.9+7.25+300 **=523.15(mg/day)**	123.45+6.75+300 **=430.2(mg/day)**

由以上算式可知，以此廠商推出之所有產品而言，一般消費者成人男性一日可自其中攝取 375.95 mg 兒茶素，而成人女性一日可自其中攝取 338.56 mg 兒茶素；此外，極端消費者成人男性一日可自其中攝取 523.15 mg 兒茶素，成人女性一日可自其中攝取 430.2 mg 兒茶素。

取得此估計攝取量後，業者可依此數據搜尋相關文獻或資料，了解兒茶素對人體可能的影響。

例二：茄紅素

若某一廠商欲推出一系列含茄紅素之產品包括：飲品、米、錠劑等提供消費者選用，產品營養標示分別如下：

飲品—蕃茄汁；蔬果汁；蕃茄果菜汁

(蕃茄汁)　　(蔬果汁)　　(蕃茄果菜汁)

(480 ml/瓶)　　(500 ml/瓶)　　(350 ml/瓶)

營養標示	
每100毫升	
熱量	68 大卡
碳水化合物	16 g
蛋白質	1 g
脂肪	0 g
納	37.5 mg
茄紅素	3.6 mg

營養標示	
每100毫升	
熱量	50 大卡
碳水化合物	12 g
蛋白質	0.5 g
脂肪	0 g
納	45.5 mg
茄紅素	1.4 mg

營養標示	
每100毫升	
熱量	42 大卡
碳水化合物	10 g
蛋白質	0.5 g
脂肪	0 g
納	22 mg
茄紅素	2.2 mg

米—營養添加糙米

營養標示	
每100公克	
熱量	350 大卡
碳水化合物	72 g
蛋白質	7.5 g
脂肪	2.8 g
納	2 mg
茄紅素	2.6 mg

錠劑—茄紅素補充劑，建議 15 歲以上成人每日二錠，15 歲以下孩童每日一錠隨餐服用

營養標示	
每一份量0.4克(一粒) 本包裝含100份	
	每份
熱量	2大卡
碳水化合物	0.5 g
蛋白質	0 g
脂肪	0 g
納	0.1 mg
茄紅素	5 mg

依據市調結果，市面上宣稱含有茄紅素之產品主要包含飲品以及錠劑。茄紅素主要天然存在於蕃茄等產品。

(1) 估算成人消費者一日經由其推出產品攝取得茄紅素份量計算式：

步驟 1. 由衛生署食品資訊網"1993-1996 國民營養現況"（行政院衛生署 a）查得台灣成人每日攝取蔬果汁、米飯之頻率以及攝取份量。(蔬果汁歸類於"經加工處裡過的果汁"；米飯歸類於"米類及其製品類")，查得之數據分別為:

	男性成人		女性成人	
食物重量(g/day)	平均值	標準差	平均值	標準差
經加工處裡過的果汁類	35.83	138.97	13.6	67.91
米類及其製品類	209.55	146.16	129.43	111.8

步驟 2. 計算每人每日攝取估計量:

(a) 一般成人消費者:

由於蔬果汁皆被歸於"經加工處裡過的果汁"，所以蕃茄汁、蔬果汁、蕃茄果菜汁三者攝取量合併為一份計算。另外，這三種產品所含茄紅素濃度不同，因此取其平均茄紅素的濃度(mg/ml)，計算如下:

產品	攝取一瓶所得茄紅素(mg)	飲料平均茄紅素含量 (mg/ml)
蕃茄汁(480 ml/瓶)	3.6 (mg/100 ml) x 480 (ml) = 17.28 mg	(17.28+7.0+7.7)/(480+500+350) **=0.024 (mg/ml)**
蔬果汁(500 ml/瓶)	1.4 (mg/100 ml) x 500 (ml) = 7.0 mg	
蕃茄果菜汁(350 ml/瓶)	2.2 (mg/100 ml) x 350 (ml)=7.7 mg	

將平均茄紅素濃度(mg/ml)乘以衛生署食品資訊網之"1993-1996 國民營養現況"(行政院衛生署 a)選項中台灣成人每日攝取"經加工處裡過的果汁"數據，便為台灣成人每日由此廠商之飲品中獲得茄紅素估計攝取量。

	男性成人	女性成人
	茄紅素攝取量(mg/day)	
廠商產品—蕃茄汁、蔬果汁、蕃茄果菜汁	0.024 (mg/ml) x 35.83 (g/day)=0.85	0.024 (mg/ml) x 13.6 (g/day)=0.33
廠商產品—米	2.6 (mg/100 g)/ 100 (g) x 209.55 (g/day) = 5.45	2.6 (mg/100 g)/ 100 (g) x 129.43 (g/day) = 3.37
廠商產品—錠劑	5 (mg) x 2 = 10	5 (mg) x 2=10
EDI	0.85+5.45+10 **=16.3 (mg/day)**	0.33+3.37+10 **=13.7 (mg/day)**

由以上算式可知，一般消費者成人男性一日可自廠商推出之產品中攝取 16.3 mg 茄紅素，而成人女性一日可自其中攝取 13.7 mg 茄紅素。

(b) 成人極端消費者

由於目前衛生署國民營養現況之數據中缺乏成人極端消費者之數據，因此本計劃建議採用"攝取量之平均值+標準差"取代平均值計算之。

	男性成人	女性成人
	茄紅素攝取量(mg/day)	
廠商產品—蕃茄汁、蔬	0.024 (mg/ml) x	0.024 (mg/ml) x

果汁、蕃茄果菜汁	(35.83+138.97) (g/day) = 4.2	(13.6+67.91) (g/day) = 1.95
廠商產品—米	2.6 (mg/100 g)/ 100 (g) x (209.55+146.16) (g/day) = 9.25	2.6 (mg/100 g)/ 100 (g) x (129.43+111.8) (g/day) = 6.27
廠商產品—錠劑	5 (mg) x 2 = 10	5 (mg) x 2=10
EDI	4.2+9.25+10 **=23.45 (mg/day)**	1.95+6.27+10 **=18.22 (mg/day)**

由以上算式可知，極端消費者成人男性一日可自廠商推出之產品中攝取 23.45 mg 茄紅素，而成人女性一日可自其中攝取 18.22 mg 茄紅素。

(2) 老年人

由於台灣目前之"1997-2002 台灣國民營養健康狀況變遷現況調查"(行政院衛生署 b)資料中，無老年人每日各類食物攝取量的統計資料，但有老年人熱量攝取的數值，且該數值與成年人之熱量攝取量有差異，因此我們採用老年人每日各類食物提供熱量數值與成人每天各類食物提供熱量數值之比值做為"熱量-食物重量換算因子"；而後，將此換算因子乘以國民營養調查中台灣成人每日攝取各類食物之份量，間接計算出台灣地區老年人每日攝取各類食物之份量。依此原則，老年人的每日茄紅素估計攝取量，可藉由以下算式得知：

步驟 1. 由衛生署食品資訊網“1993-1996 國民營養現況”(行政院衛生署 a)選項分別查得成人與老年人每日自蔬果汁及米獲得的熱量。(蔬果汁歸類於“經加工處裡過的果汁”；米飯歸類於“米類及其製品類”)

	男性成人		女性成人	
熱量(kcal/day)	平均值	標準差	平均值	標準差
經加工處裡過的果汁類	14.96	59.26	5.51	27.51
米類及其製品類	678.1	428.69	397.3	309.83

	男性老年人		女性老年人	
熱量(kcal/day)	平均值	標準差	平均值	標準差
經加工處裡過的果汁類	1.9	0.5	4.5	1.1
米類及其製品類	571.1	28.1	500.6	24.6

步驟2. 計算“老年人攝取熱量/成人攝取熱量”的比值(即為熱量-食物重量換算因子)，乘以台灣成人每日攝取各類食物之份量，間接作為台灣老年人每日攝取各類食物之份量。

	男性老年人	女性老年人
	熱量-食物重量換算因子	
經加工處裡過 的果汁類	1.9/14.96 = **0.13**	4.5/5.51 = **0.82**
米類及其製品類	571.1/678.1 = **0.84**	500.6/397.3 = **1.26**

步驟 3. 將成人每日各類食物攝取重量乘以上述熱量-食物重量換算因子，可推算得老年人每日攝取各類食物重量，進而推算每人每日攝取估計量，計算如下:

(a) 一般老年人

每日攝取經加工處裡過的果汁類與米類及其製品類攝取份量之計算。

	男性老年人	女性老年人
	食物重量(g/day)	食物重量(g/day)
經加工處裡過 的果汁類	35.83 x **0.13=4.66**	13.6 x **0.82=11.15**
米類及其製品類	209.55 x **0.84=176.02**	129.43 x **1.26=163.08**

將數值帶入算式：

	男性老年人	女性老年人
	茄紅素攝取量(mg/day)	

廠商產品—蕃茄汁、蔬果汁、蕃茄果菜汁	0.024 (mg/ml)* x 4.66 (g/day) = 0.11	0.024 (mg/ml)* x 11.15 (g/day) = 0.27
廠商產品—米	2.6 (mg/100 g)/ 100 (g) x 176.02 (g/day) = 4.58	2.6 (mg/100 g)/ 100 (g) x 163.08 (g/day) = 4.24
廠商產品—錠劑	5 (mg) x 2 = 10	5 (mg) x 2 = 10
EDI	0.11+4.58+10 = **14.69(mg/day)**	0.27+4.24+10 = **14.51(mg/day)**
註:"*"參考本報告書 p.19。蕃茄汁、蔬果汁、蕃茄果菜汁三者攝取量合併為一份計算。取其平均茄紅素的濃度為 0.024 (mg/ml)。		

由以上算式可知，一般消費者老年人男性一日可自廠商推出之產品中攝取 14.69 mg 茄紅素，而老年人女性一日可自其中攝取 14.51 mg 茄紅素。

(b) 老年人極端消費者

極端消費者的各種食物每日攝取量以"攝取量之平均值+標準差"計算之。首先換算出老年人每日攝取經加工處裡過的果汁類與米類及其製品類攝取份量。

	男性老年人	女性老年人
	食物重量(g/day)	食物重量(g/day)
經加工處裡過	(35.83+138.97) x **0.13**	(13.6+67.91) x **0.82**

的果汁類	**=22.72**	**=66.84**
米類及其製品類	(209.55+146.16) x **0.84** **=298.8**	(129.43+111.8) x **1.26** **=303.95**

將數值帶入算式：

	男性老年人	女性老年人
	茄紅素攝取量(mg/day)	
廠商產品—蕃茄汁、蔬果汁、蕃茄果菜汁	0.024 (mg/ml)* x 22.72 (g/day) = 0.55	0.024 (mg/ml)* x 66.84 (g/day) = 1.6
廠商產品—米	2.6 (mg/100 g)/ 100 (g) x 298.8 (g/day) = 7.77	2.6 (mg/100 g)/ 100 (g) x 303.95 (g/day) = 7.9
廠商產品—錠劑	5 (mg) x 2 = 10	5 (mg) x 2 = 10
EDI	0.55+7.77+10 **=18.32 (mg/day)**	1.6+7.9+10 **=19.5 (mg/day)**
註:"*"參考本報告書 p.19。蕃茄汁、蔬果汁、蕃茄果菜汁三者攝取量合併為一份計算。取其平均茄紅素的濃度為 0.024 (mg/ml)。		

由以上算式可知，極端消費者老年人男性一日可自廠商推出之產品中攝取 18.32mg 茄紅素，而老年人女性一日可自其中攝取 19.5mg 茄紅素。

(3) 國小學童

目前之"1997-2002 台灣國民營養健康狀況變遷調查"(行政院

衛生署 c)資料內無國小學童每天各類食物攝取量的統計值，因此比照"老年人"之計算方式，將國小學童每天各類食物提供熱量數值相較於成人每天各類食物提供熱量數值之比值做為"熱量-食物重量換算因子"；將此換算因子乘以國民營養調查中台灣成人每日攝取各類食物之份量，可間接計算出台灣國小學童每日攝取各類食物之份量。

步驟 1. 衛生署食品資訊網"1993-1996 國民營養現況"（行政院衛生署 a）國民營養調查" 選項查得台灣成人與國小學童每日自蔬果汁及米獲得的熱量。(蔬果汁歸類於"經加工處裡過的果汁"；米飯歸類於"米類及其製品類")

	男性成人		女性成人	
熱量(kcal/day)	平均值	標準差	平均值	標準差
經加工處裡過的果汁類	14.96	59.26	5.51	27.51
米類及其製品類	678.1	428.69	397.3	309.83

由衛生署"1997-2002 台灣國民營養健康狀況變遷調查"（行政院衛生署 c）選項查得台灣國小學童每日自蔬果汁及米獲得的熱量。

	國小學童	
熱量(kcal/day)	平均值	標準差
經加工處裡過的果汁類	97.3	-
米類及其製品類	392.4	-
註：台灣國民營養健康狀況變遷調查中國小學童各類食物熱量攝取尚無標準差數值，因此這裡以"-"表示尚無的標準差。		

步驟 2. 計算出"國小學童攝取熱量/成人攝取熱量"的比值(即為熱量-食物重量換算因子)，乘以台灣成人每日攝取各類食物之份量，間接作為台灣國小學童每日攝取各類食物之份量。然而，由於台灣國民營養健康狀況變遷調查中國小學童尚未依性別計算食物攝取熱量，因此成人的食物攝取熱量以(男性+女性)/2 做表示。

	國小學童
	熱量-食物重量換算因子
經加工處裡過的果汁類	97.3/[(14.96+5.51)/2]=**9.51**
米類及其製品類	392.4/[(678.1+397.3)/2=**0.73**

步驟3.將成人每日各類食物攝取重量乘以上述熱量-食物重量換算因子，可以換算得老年人每日攝取各類食物重量，其中成人的食物攝取熱量以(男性+女性)/2 做表示。計算

如下:

	國小學童	
食物重量(g/day)	平均值	標準差
經加工處裡過的果汁類	(35.83+13.6)x9.51=**470.08**	-
米類及其製品類	(209.55+129.43)x0.73=**267.46**	-

步驟 4. 每人每日攝取估計量計算如下:

(a) 一般學童消費者

	國小學童
	茄紅素攝取量(mg/day)
廠商產品—蕃茄汁、蔬果汁、蕃茄果菜汁	0.024 (mg/ml)* x 470.08 (g/day) = 11.28
廠商產品—米	2.6 (mg/ml) x 267.46 (g/day) = 6.95
廠商產品—錠劑	5 mg x 1 = 5
EDI	11.28+6.95+5=**23.23 (mg/day)**
註:"*"參考本報告書 p.19。蕃茄汁、蔬果汁、蕃茄果菜汁三者攝取量合併為一份計算。取其平均茄紅素的濃度為 0.024 (mg/ml)。	

由以上算式可知，一般國小學童消費者一日可自其中攝取 23.23 mg 茄紅素。

(b) 極端學童消費者

由於"1997-2002 台灣國民營養健康狀況變遷調查"(行政院衛生署 c)中未統計國小學童攝食各類食物份量及熱量的標準差，因此目前尚無法計算國小學童極端消費攝取量。

取得上述不同族群攝取量後，業者可依不同數據蒐集相關文獻，了解茄紅素對人體可能的影響。

(4) 特定族群消費者之預估攝取量

不同的年齡族群有不同的飲食習慣，舉例而言：孩童對於糖果、糕點餅乾、冰飲料等點心零食之食物消耗量勢必較老年人高；而成年人對於各類型食物的接受度亦會高於孩童以及老年人。因此，若僅以成人攝取食物種類及攝取份數作為計算的數據代表，並不適用於代表全民的攝取量。若一個廠商預推出之產品，並無設定消費者族群，不論孩童、成人、老年人等皆可食用，必須提供依不同族群之食物消耗數據計算每日估計攝取量，得宜販售食用。此外，由於國內至今尚未有針對孕婦與哺乳婦的營養調查與食物攝取的資料，而且孕婦與哺乳婦皆為較為敏感的時期，因此不建議於此時期給予額外添加非傳統性食品原料的食品

C. 不同族群之上限攝取量

由營養的角度，謂「上限攝取量」是指營養素或食物成份的每日最大攝取量，即於長期攝取此劑量的狀況下，對最敏感族群的危害風險也極低，然而，超過此攝取上限時，不良效應的機率亦增大。「危害或不良效應」採用 WHO/FAO/IAEA 所設定的標準，包括：人體構造或功能上有明顯的改變，或重要生理功能受損，而且涵蓋營養素之間負面的交互作用(adverse nutrient-nutrient interactions)。

台灣現有國人膳食營養素參考攝取量(Dietary Reference Intakes, DRIs)中營養素的上限攝取量制定過程，是經由國民營養大調查取得國民飲食紀錄，配合長期營養不足或營養過量導致疾病歷史以及科學實驗方式結果之後，推算出不同族群以其調查來所有攝取量的第 95 個百分位作為上限攝取量(行政院衛生署 d)。然而，非傳統性食品及原料缺乏民眾長期食用的安全歷史，無法像傳統營養素一般經由全國營養大調查的方式取得大量的數據。因此，我們建議以風險評估的模式逐步建立非傳統性食品及原料攝入後對人體造成健康損害的機率，進而推算上限攝取量。

風險評估有一套既定的科學程序與目的，經由系統性的資料整理與討論，在合理的科學不確定性下鑑定出環境因子(在此可指

非傳統性食品及原料)對人體引發危害的可能性。風險評估的標準程序包括四個步驟(行政院衛生署 d)：

1. 危害評估(hazard assessment)

針對特定營養素(此指非傳統性原料或食品)，充分收集、整理、評估其毒性資料，以確認營養素造成人體毒害的證據，鑑定該營養素的毒害種類和程度，並選定危害指標。

2. 劑量效應評估(dose-response assessment)

就危害發生率與嚴重程度分析營養素攝取量與危害指標之間的關係，評定「無危害量」(NOAEL, no-observed-adverse-effect level)，即調查或實驗中，未造成危害的最高攝取量或劑量與最低危害量(LOAEL, Lowest-observed- adverse-effect level)，以及不確定因數(UF, uncertainty factor)等數值，並據以計算「上限攝取量」，此數值可分年齡層訂定。

3. 暴露評估(exposure assessment)

分析族群中目標營養素日常攝取量的分布情況，以了解其範圍與頻率。

4. 風險鑑定（risk characterization）

綜合前三步驟的結果，採用第 95 百分位的攝取量作為推測該族群風險性的基準，即「上限攝取量」(UL，upper limit)。

制定上限攝取量是需要經過許多不同的實驗模式，參考實驗結果反推出人體耐受劑量，之後再進入多重臨床階段，修正劑量後才可能得到一個適合的上限攝取量。然而這些數值會因個體變異性不同兒改變，例如：年齡、人種、性別、健康狀況、飲食習慣等等變因皆是影響因子，因此不同的國家對於相同物質訂定之上限攝取量也會有所出入。目前台灣許多物質的上限攝取量皆是參考了美洲、歐洲、日本等國家的數值後比照國人特性修正後公佈(例如飲用水中的重金屬安全含量)。

於此計畫中之非傳統性食品原料，由於缺乏民眾長期食用的歷史情況下，擬自風險評估之第一階段：危害評估(hazard assessment)著手，先廣泛的蒐集相關安全性文獻。

D. 建議食用對象及排除對象

有鑑於非傳統性食品及原料之來源、結構或是製造過程與一般食用之傳統性食品或原料可能不相同，在缺乏民眾長期食用安全歷史的情況下，不同族群在攝食之後是否會出現不同的反應，皆是有待商榷。與一般之健康食品類似，非傳統性食品亦有適合與不適合食用的對象，且對不同生理狀況的族群有不同的影響，因此，我們建議欲推出非傳統性食品及原料之廠商，應就其推出產品內特定成份，提出文獻證明對於不同族群攝食後的安全性，其中應包括族群的設定、ADME

(absorption 吸收、distribution 分佈、metabolism 代謝、excretion 排泄)、毒性測試等；若文獻資料顯示，該食品或原料對於某特定族群具有健康促進的作用，且對於該族群不會造成健康的損害或不適，則該族群則可被列為建議食用對象。然而，若該食品或原料對於某些族群曾被顯示有任何身體之不適或健康的危害，則該族群則須被列為排除對象。此外，若該食品或原料亦含有高量其他可能會影響特定族群的成份，則此特定族群亦須被列為排除對象。

舉例而言，四神湯中使用的薏苡仁，已被認為是一種在民間長期食用的安全食材，食用後會促進子宮收縮，一般女性食用或許並無大礙，但若懷孕婦女食用，則可能因此引發流產等不良影響，因此孕婦則須被列為薏苡仁的排除對象；又木耳、當歸等亦為一般人常用的食材，但因其具有抑制凝血的作用，故可能干擾術後病人的恢復，因此術後病人須被列為木耳或當歸的排除對象。又葡萄糖胺(glucosamine)對於關節退化的情況具有改善效果，然而葡萄糖胺的補充劑在製程中是與帶正電的鹽類結合的化合物型態存在，目前市面上主要有含鈉或含鉀的葡萄糖胺，在攝取其有效成分 glucosamine 的同時也會攝取入部分的鈉或鉀，故具有退化性關節炎之患者可被列為建議食用對象，但高血壓患者則可能須被列為排除對象。

E. 建議攝取之方式

非傳統性食品及原料之來源、結構或是製造過程與一般食用之傳統性食品或原料可能不相同，當人體攝取這一類的食品或原料，是否會與傳統性食品間產生交互作用，影響人體必須營養素的吸收、分佈、代謝、排泄等，目前尚未知。此外，為使非傳統性食品發揮其最大的生物利用率，這些食品原料攝取的形式、時間與劑量亦應列入考量。例如許多脂溶性的營養素在油脂的存在下有較好的吸收，而非傳統性食品原料的吸收或利用與其脂溶性或水溶性特性以及所存在的食物之間亦有密切的關連性。與藥物類似，某些非傳統性食品原料攝取的時間，於餐前、餐後亦可能影響其吸收與利用。每日給予單一較大劑量或多次較小劑量之影響以及其於體內是否會造成累積等，皆須列入考量。因此，我們建議欲推出非傳統性食品及原料之廠商，應就其推出產品提出其於攝食後的 ADME (absorption 吸收、distribution 分佈、metabolism 代謝、excretion 排泄)以及與營養素或食物交互作用的文獻證明；而後並依據該食品或原料的特性提出最佳的建議攝取方式，包括食用時間、劑量以及可能有交互作用的食物或營養素等。

舉例而言，台灣生態碳產業發展協會推出一系列竹碳產品，其中包括食用級活性竹碳粉，有日本研究指出，竹碳粉添加在食物中可以促進腸胃蠕動幫助消化，同時也可以幫助體內排除雜物。然而活性

竹碳粉在吸附雜物的同時，是否也會吸附營養素或者是影養營養素的吸收？雖然研究證實，適度食用活性竹碳粉對人體安全無虞，但若會影響營養素吸收分解途徑，亦應提出避免因此營養吸收不良的攝取方式。

F. 毒理學/藥物動力學方法相關文獻蒐集

對於一些對人體安全性尚未確定的物質(例如:新研發之藥物或是高濃度有效成分萃取物)，在進入人體臨床試驗前，通常須經由細胞、動物實驗取得之數據加以分析之後，進而取得臨床期之安全性測試劑量，並加以測試之。為了解試驗物質的安全性所進行的試驗主要分成藥物動力試驗以及毒性試驗兩個部份。在藥物動力學試驗主要包括特定物質在體內的吸收(Absorption)、分佈(Distribution)、代謝(Metabolism)及排泄(Excretion)等四各部份，又可簡稱 ADME/Tox。利用動物或細胞試驗測定及了解試驗物質在動物活體內的吸收、分佈、代謝及排泄的過程，用於預估該試驗物質在細胞、動物或是人體內的轉移過程與機轉，同時也可經由試驗物質在體內分佈、半衰期(代謝)、濃度等數據而預估發生不良反應的可能性，作為選擇安全及有效的人體使用量之依據(Ekins et al., 2005；Konishi et al., 2005)。

為協助業者於提交特定新穎性食物原料時，提供該原料已有之

ADME 之證據，因而我們針對可用於評估特定物質吸收、分佈、代謝及排泄的方法彙整於下，以使業者有一個參考的依據。

吸收 (absorption)

當物質經口攝取進入人體後，會由腸胃道消化吸收進入血液中，吸收的情況可能受物質的分子大小、腸壁細胞親和力或是腸道中其他物質競爭、螯合等因素影響。因此經由測量給予特定物質前後血液中濃度的變化，可以推算出該物質於腸胃道的吸收能力。

1. 人體或動物模式

於人體或動物試驗的方法相似。影響受測物質吸收的因素包括受測物質本身在腸胃道中的溶解度、穩定度、主要吸收的部位以及受試動物所攝食的食物、腸胃道的酸鹼值等（Kapitza et al., 2007; Eriksson et al., 2003）。

一般而言，動物經口攝入受測物質後，物質由腸道消化吸收後，經由血液進入組織、細胞中，可利用直接或間接的方式測定血液中物質的濃度以表示吸收情形。

相關實驗方法測定吸收情形簡述：於給予動物單一劑量的試驗物質前以及給予後的特定時間點採集血液，依受測物質特性的不同，可能為數分鐘至數小時甚至數十小時，直接測量動物血液中試驗物質的

濃度，藉由血液濃度與時間之曲線圖 (blood concentration v.s. time curve)，測定試驗物質及其代謝產物在血中最高濃度 (C_{max})、到達該濃度所須的時間 (T_{max})，計算出血中濃度對時間所作曲線下的面積 (area under the blood concentration curve，AUC) 等數值，可了解特定試驗物質在固定時間內的吸收速率(Konishi et al., 2005)。若欲進一步了解吸收部位，在經口給予螢光標定的試驗物質或其衍生物後，取腸道之各部位作螢光分析即可得知（Kim et al., 2007）。

舉例而言，可給予經同位素標定的物質，例如單一口服劑量[^{14}C]標定的 DJ-927(抗癌藥物 Taxane)給予大鼠、狗、猴子後 0.5、1、2、4、8、12、24、72、96、120、144、168 小時後、收集血液並分析血液中放射線含量(Chiho O et al., 2004)。

2. 體外模式

除了直接以體內動物的模式測量特定物質的吸收之外，亦可以體外的模式測定特定物質穿過細胞的能力（穿透力或滲透力)來觀察細胞對試驗物質的吸收能力。由細胞外滲透 (permeation) 至細胞內來表示此物質的吸收情形，其主要可分為穿透性(transcellular)、細胞間擴散(paracellular)及主動運輸 (active transport) 等方式。其中穿透性以及主動運輸方式指受測物質可穿透細胞膜進入細胞中，對細胞產生作用；而細胞間擴散則是受試物質間接經由對細胞膜上之受器產生刺

激，對細胞產生作用。

體外測試吸收的模式可分為：細胞型及非細胞型 (人工合成仿細胞膜) 兩種 (表一)。細胞型多選用大腸Caco-2細胞；非細胞型(van de Waterbeemd et al., 2005)。其中選用任一種方式，都可以公式推算出試驗物質的滲透能力，也就間接或直接的代表了試驗物質在細胞中的吸收情形。以下則針對此二系統分別的介紹之。

表一為體外模式偵測吸收之模式，其中包括細胞型與非細胞型。分別說明於下：

Table 1.

In vitro models for membrane permeability and oral absorption [2].

Non-cell based systems
Octanol/water distribution
Cyclohexane/water distribution, dodecane/water distribution
Phospholipid vesicles
Liposome partitioning
Immobilised artificial membranes (IAM)
Immobilised liposome chromatography (ILC)
Micellar electrokinetic chromatography (MEKC)
Biopartitioning micellar chromatography (BMC)
Impregnated (or artificial) membranes
PAMPA
Filter IAM
Hexadecane-coated polycarbonate filters
Transil^{TM} particles
SPR biosensor
Surface activity
Cell-based systems
Original cell lines Transfected cell lines
Caco-2 MDCK-MDR1
MDCK MDCK-MRP2-OATP2
TC7 LLC-PK1
HT29
2/4/A1

(1) 非細胞型模式

(a) Octanol/water distribution

待測物質在正辛醇/水系統中之分佈比，數據常轉換為對數值($log_{10}X$)表示。

(b) Cyclohexane/water distribution, dodecane/water distribution

待測物質在環己烷/水系統中之分佈比。

(c) Phospholipid vesicles

待測物質於磷脂質泡中之穿透性。

(d) Liposome partitioning

待測物質於微脂體中之穿透性(Balon K et al., 1999)。

以上(a) ~ (d)項之待測物質親脂性數據即代表對細胞膜的穿透性，穿透性越好除了代表越容易通過細胞外，其生物濃縮之潛力亦可能越好，因人體對於脂溶性物質之排泄率較水溶性物質差，累積在體內的脂溶性物質可能對人體進而造成慢性影響。

(e) Immobilised artificial membranes (IAM)

待測物質於不具流動性質的人造膜中之穿透性，可篩選出經主動滲透(非主動運輸，不消耗ATP)之物質。

(f) Immobilised liposome chromatography (ILC)

待測物質於不具流動性質的微脂體膜中之穿透性，可篩選出經被動滲透(非主動運輸，不耗費ATP)之物質。

(g) Micellar electrokinetic chromatography (MEKC)

微胞電動層析法，可以分離出中性及疏水性物質（王和謝，

2001）。

(h) Biopartitioning micellar chromatography (BMC)

生物分配膠束色譜，評斷待測物質於膜轉運情形及其活性。

(i) Impregnated (or artificial) membranes

待測物質於人造樹脂膜之穿透性。

(j) PAMPA (Parallel artificial membrane permeability assay)

使用0.45 μm並含有大範圍不相同親脂物質的PVDF膜以決定藥物的吸收。

(k) Filter IAM

一種模擬細胞膜的模型，用以測試藥物或天然物被動運輸。

(l) Hexadecane-coated polycarbonate filters

微孔聚碳酸酯過濾膜，測試試驗物質的穿透力。

(m) SPR (Surface Plasmon Resonance) biosensor

利用光學折射原理測定膜與物質(藥物或蛋白)結合的能力。

(n) Surface activity

以界面活性劑來測試待測物吸收力。

(2) 細胞型模式

可使用原始細胞株或是經基因轉殖之特定細胞株為模式。

(a) Caco-2/MDCK-MDR1

Caco-2是人類人類結腸腺癌細胞株，可用來測試人類腸道細胞對於物質　吸收的能力。MDCK-MDR1是狗的腎臟細胞帶有

人類主動運輸蛋白MDR1基因，可用以測試細胞主動運輸的能力。

(b) MDCK/MDCK-MRP2-OATP2

使用轉殖兩種主動運輸蛋白(MRP2與OATP2)的MDCK細胞，以測試細胞對試驗物質主動運輸的能力。

(c) TC7/LLC-PK1

TC-7是來自於CaCo-2的一個次株(subclone)。於腸細胞吸收的研究中，TC7是較CaCo-2更適合的細胞株。LLC-PK1是豬的腎臟上皮細胞，用來模擬腎的吸收。

(d) HT29

人類腸道腫瘤細胞株，可用來測試腸道細胞吸收能力。

(e) 2/4/A1

老鼠小腸細胞株。相較於Caco-2(二十天以上)，2/4/A1培養快速(三天)，可以較為快速得到吸收數據。

以 Caco-2 細胞為例，其可於濾膜上生長形成單層結構。利用濃度梯度原理，提供處高濃度的試驗物質擴散穿透 Caco-2 細胞單層至接收處(圖二)，測定接收處的試驗物質，或測定試驗物質穿透細胞膜所需的運輸者，可得知試驗物質的滲透係數(permeability coefficients) (Motlekar et al., 2005；Laitinen et al., 2007；Tsukura et al., 2007；Tirumalasetty., 2006)。Caco-2 細胞主要用於測量水溶性的物質。

圖二 滲透試驗模式圖

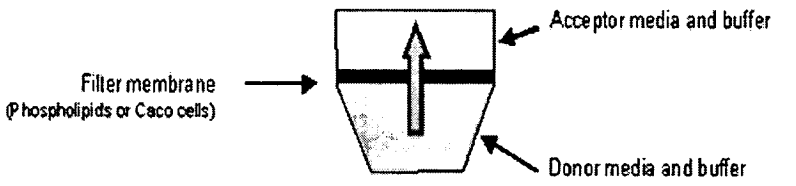

目前在進行細胞模式試驗時多會配合以EVOM epithelial voltohmmeter或是Millicell-ERS voltohmmeter等伏特-歐姆測量計測量TEER (transepithelial electrical resistance)，間接表示試驗物質的滲透性。因為細胞與細胞間為了維持相連存在有接合處(junction)，當接合越緊密，物質滲透性越差，所測得之TEER值越高。然而，影響TEER數值的因子除了細胞間的接合之外，亦包括試驗物質的濃度及試驗時間。依據流速、細胞單層面積及提供處試驗物質濃度，可計算出滲透係數(Motlekar et al., 2005；Laitinen et al., 2007；Tsukura et al., 2007；Tirumalasetty et al., 2006)。計算公式如下：

$$(P_{app})=(dQ/dt)/(AC_0)\ (\text{cm/s})$$

dQ/dt (nmol/s) 為穿透細胞的速度

A (cm^2) 為細胞單層面積

C_0 (nmol/ml) 為提供處試驗物質濃度

若待測物質為脂溶性物質，則可利用非細胞型中之磷脂質雙層構

成的脂質體 (liposomes)，或是合成的 IAM (immobilised artificial membrane) 包覆脂溶性試驗物質，再以 HPLC(高效能液相層析質譜)測定各時間點接受處的試驗物質以及衍生物的濃度，或配合其他儀器輔助測定，如 HPLC-UV-MS(高效能液相層析-UV 光-質譜儀)或 HPLC-ECD (high-performance liquid chromatography with electrochemical detection；高效能液相層析質譜-電化學檢測法)偵測之。此外亦可以有機脂質製成雙層濾膜的 PAMPA，原理與 Caco-2 細胞單層相似，但在分析上較 Caco-2 細胞單層簡易，以分光光度計測定接收處的試驗物質即可得知滲透情形(Mälkiä et al., 2004)。

於體外模式試驗中，無論是 Caco-2 細胞或 PAMPA，試驗物質必須與細胞膜結合才能滲透進入膜中，其中有許多因素會影響此過程的進行，包括試驗物質的特性、大小及電荷等。細胞膜脂質外層為氫鍵接收處，試驗物質必須為親脂性，避免與水分子產生氫鍵，試驗物質才易與脂質雙層結合，而試驗物質的大小及其結構亦會影響與脂質的結合（Mälkiä et al., 2004）。

分佈(distribution)

當特定物質吸收後進入身體循環後，經血液運送到各個不同組織。由於一些物理作用的影響，包括血流量、組織脂肪含量、局部部位之酸鹼性和細胞膜通透性等，使該物質的分佈是不規則的。特定物

質分佈的平衡取決血液中濃度與組織和細胞間液相同，血液流量是決定分佈速率之首要條件，流量少之組織，如肌肉及脂肪，其分佈速率慢，反之，流量多的組織其分佈速率快。

藥物分佈容積（volume of distribution, V_d）是指特定物質劑量與物質於血中濃度關係中之比例常數，通常不具真正生理上意義。與血漿蛋白結合力越強的物質，分佈容積越小；與組織蛋白結合力越強的物質及脂溶性物質，分佈容積越大;一般分佈容積越大的藥物其半衰期越長。

$$Vd = T / C$$

T : amount of drug in the body

C : concentration of drug in blood

測定「分佈」的受試對象大多以動物為主。因為要了解試驗物質在生物體中會停留分佈在哪些臟器，必須在實驗結束後犧牲受試對象取其臟器分析，若在細胞模式中進行，便失去了觀察「分佈」的意義。於動物口服特定劑量之經放射線標定的試驗物質後，於特定時間點犧牲動物並取其體內不同組織或器官，進行放射線含量的分析。此方法以廣泛的用於分析多種藥物於體內的分佈狀況(Yasoshima et al., 2001; Schoenig et al., 1996; Cundy et al., 1996)。

代謝(metabolism)

代謝又稱新陳代謝，是指生物體與外界環境進行物質和能量交換的過程，為發生在一個細胞或一個生物體內所有化學反應轉換的總和，這些反應是藉由一系列的酵素(酶)催化反應所產生，這些反應即稱為新陳代謝路徑。在一個新陳代謝路徑中的每一個反應都會產生代謝分子的化學改變，之後形成使用或儲存的代謝物，或是繼續引發另一個代謝途徑，最後便會轉換成最終產物(Lehninger D., 2003)。

1. 人體或動物模式

可依試驗物質是否被放射線同位素標定而有不同的方法。當經放射線同位素標定之試驗物質被使用時，將置於代謝籠中之實驗動物，口服或注射(靜脈、腹腔等)給予特定劑量的試驗物質後，於不同時間點，蒐集動物之血液、尿液以及糞便等，分析其中放射線含量，即可以算式推算出試驗物質代謝情形。若使用未經放射線標定過之試驗物質時，將置於代謝籠中之實驗動物，口服或注射(靜脈、腹腔等)給予特定劑量的試驗物質後，於不同時間點，蒐集動物之血液、尿液以及糞便等，利用分子大小的原理，以不同儀器，如液相層析儀，測定試驗物質代謝分子含量，即可以算式推算出試驗物質代謝情形。

例如將白藜蘆醇(resveratrol)利用管餵或腹腔注射方式注射入

飼養於代謝籠內之動物，在注射後 0-2 小時內收集尿液及血液，而後將所收集之檢體以 LC-UV-MS-MS 分析其代謝產物(Yu et al., 2002)。此外，將 ^{14}C 標定之三乙醇胺(trithanolamine；TEA)或[^{3}H]UCN-01(某種蛋白質抑制劑)以靜脈注射之方式投予動物，而後收集特定時間點之糞便及尿液以 MS 測定其代謝物或放射線含量(Stott et al., 2000; Yasoshima et al., 2001)

2. 體外模式

由於肝臟之微粒體為主要的代謝器官及胞器，因此肝細胞或分離之微粒體為主要的使用模式。於此二模式內，依試驗物質是否被放射線同位素標定而有不同的方法，使用經放射線標訂之試驗物質時，將單一劑量的試驗物質處理實驗細胞，而後於不同時間點，蒐集細胞培養液並分析其中之放射量，即可推算出試驗物質代謝情形。使用未經放射線標定之試驗物質時，細胞於給予單一劑量的試驗物質後，於不同時間點，蒐集細胞培養液利用分子大小之原理，使用不同的儀器，如液相層析儀，測定試驗物質代謝分子含量，即可以算式推算出試驗物質代謝情形。

例如將白藜蘆醇(trans-resveratrol)加入大鼠之初代肝臟細胞或人類肝臟微粒體(microsomes)，而後分別於培養之不同時間點收集培養液，使用 LC-UV-MS-MS (Liquid-Chromatography-UV-Mass-

Spectrometer-Mass-Spectrometer)分析相關產物(Yu et al., 2002)。此外，為測定 Eupatilin(植物異黃酮衍生物)是經由肝臟哪一個解毒系統代謝，分別將 Eupatilin 加入人類 CYP 酵素系列以及人類 UGT 酵素系列，而後蒐集培養液，利用 LC-MS 系統分析(Lee et al., 2007)。

排泄(Excretion)

排泄是指生物體(細胞)將經新陳代謝之後的廢物排出體外之過程，包括呼吸、汗液、膽汁、尿液、糞便等方式，而試驗物質的排泄作用牽涉不同的器官系統與作用機制，為了確定試驗物質及其主要代謝產物的排泄途徑、程度與速率，因此試驗須觀察各個器官的排泄速率。排泄的試驗物質可藉由分析不同時間點的排泄物(尿液、糞便)，同時依據標準曲線推算出排泄物中試驗物質的濃度。藉由試驗物質濃度與時間之曲線圖 (blood concentration v.s. time curve)，測定試驗物質及其代謝產物在排泄物內最高濃度 (C_{max})以及到達該濃度所須的時間 (T_{max})。

$$C=Ae^{-\alpha t}+Be^{-\beta t} \quad (\alpha>\beta)$$

A、B為座標截點

α、β分為分部及排泄的速率

依據此公式可再分別計算出曲線下面積 (area under the plasma concentration curve, AUC) 以及排泄半衰期 (elimination half-life, $t_{1/2\beta}$)

(Ekins et al., 2005; Puttonen et al., 2007; Suzuki et al., 2007; Hagihara et al., 2007)。若試驗物質主要是以尿液的方式排出體外，腎臟為動物主要的泌尿器官，因此可進一步以 AUC 計算出腎臟廓清率 (renal clearance, Cl_r)。公式如下：

$$AUC=A/\alpha+B/\beta$$

$$t_{1/2\beta}=0.693/\beta$$

$$Cl_r=Ae/AUC$$

Ae為尿液中試驗物質的劑量

動物的腎臟功能、尿液酸鹼值以及尿流速率等因素會影響試驗物質的排泄作用。但若試驗物質主要的排泄途徑為膽汁，則需觀察試驗物質及其代謝產物是否參與腸肝 (entro-hepatic) 循環，在收集檢體時也需收集膽汁作分析。

1. 人體與動物模式

在人體模式方面，測定排泄的實驗方法與動物模式相仿。動物模式是使用經標定的試驗物質(例如：同位素[^{14}C])，經單一劑量給與動物後，於特定時間蒐集其排泄物(尿液以及糞便)並測定放射性總量，當測定之排泄物中總含量幾乎等同於給予劑量之放射量時，實驗便停止，隨著時間點的推移，排泄物中測得之放射線含量便可推算出試驗物質在動物體中的排泄情形。但若試驗物質經身體組織代謝會產生其他衍生物，在測定時需一併測定未被代謝的試驗物質及衍生物的排

出，可先利用HPLC (High-performance Liquid Chromatography)分析試驗物質經代謝後的衍生物，再以LSC (liquid scintillation counting) 或HPLC-UV配合MS/MS (Mass Spectrophotometer)進行有標定的試驗物質的放射線分析(Ekins et al., 2005; Puttonen et al., 2007; Suzuki et al., 2007; Mangold et al., 2004; Lee et al., 2007)。

生物利用率及耐受性

生物利用率（Bioavailability，F），亦可稱生體利用度或生體可用率。生物利用率一般使用在藥物學上，是指藥品服用後藥物到達全身循環（systemic circulation）的程度（extent）與速率（rate）。一般而言，以藥物隨著時間在血中濃度變化的曲線下面積（AUC）經過劑量校正後相互的比值來表示。靜脈注射後的生體可用率視為 100%；非靜脈投藥後的生體可用率則可分絕對生體可用率（absolute bioavailability）與相對生體可用率（relative bioavailability），兩者的差別在於數值是否與靜脈注射後藥物的 AUC 比較。藥物的生體可用率主要受到吸收及首度代謝（First-Pass Effect；指肝臟代謝）的影響，可以用式子表示如下：F=（fabs）x（fG）x（fH），其中 fabs 為藥物吸收的比例，fG 與 fH 則分別為藥物未經過腸道與肝臟代謝的比例。藥物的吸收受到包括藥品特性與生理條件等多項因素影響。其中

生理條件則包括胃排空速度、胃腸酸鹼度、食物組成與腸胃蠕動速度等。試驗動物與人類在這些因素上雖然差異頗大，然而藉著從試驗動物所得到的結果，也可藉以了解腸胃道之生理因素對藥物吸收之影響，其實驗的模式基本上與上述中吸收部份的方法類似。

在藥物學方面，藥劑的生物利用率高低可以看出藥效在生物體內作用的情形，由於藥物是具療效作用的，因此作用的情形代表著藥物的療效；然而非傳統性食品原料並不是藥物，所以「生物利用率」的數值便不是用作評估效用，而是用來佐證原料的安全性，因此認為廠商也應提出相關文獻證明。

另外，由於生物體個體間具有差異性，對於外來物質刺激卻不引起個體間不良反應的容忍度也不同，因此在進行初期安全性實驗後，便會經由細胞或是動物實驗數據反推出人體耐受性劑量，這通常會是一個劑量範圍，即稱為生物耐受度(Konishi et al., 2005)。

G. 人體與動物劑量的轉換

若有廠商要推出含有非傳統性食品原料的產品，除了符合衛生署食品衛生管理法則外，必須提出產品中之非傳統性食品原料的安全證據，最好是以人體模式為主的實驗，若是尚於動物實驗階段，則可另外參考人體與動物使用劑量換算公式(何,2006)，間接證明添加之劑量

的安全性。

1. 藥品的劑量計算方式：(體表面積換算）

以70 kg成人每日劑量為1 g/kg 換算20 g 小鼠之劑量，人與小鼠換算之體表面積比值為 0.0026; 若換算200 g 大鼠之劑量，人與大鼠換算之體表面積比值為 0.018

1. 大鼠

若一個70 kg 成人的一日建議劑量1 g/kg為

→ 70kg × 1g/kg ＝ 70 g/天

→ 成人（70 kg）與大鼠（200 g）體表面積換算需乘上0.018

70 g/天 × 0.018 = 1.26 g/天

→ 換算大鼠每公斤體重攝取劑量

1.26 g/日 ÷ 0.2 kg（200g）= 6.3 g/kg

2. 小鼠

若一個70 kg 成人的一日建議劑量1 g/kg為

→ 70kg × 1g/kg ＝ 70 g/天

→ 成人（70 kg）與小鼠（20 g）體表面積換算需乘上0.0026

70 g/天 × 0.0026 = 0.182 g/天

→ 換算小鼠每公斤體重攝取劑量

0.182 g/天 ÷ 0.02 kg（20g）= 9.1 g/kg

以第20頁茄紅素的例子，廠商推出之產品中一般成人男性每日可攝取16.3 mg。

若以大鼠劑量換算：

70 kg成人與200 g大鼠體表面積換算因子為0.018，故 16.3 mg/天 × 0.018 = 0.2934 mg/天，換算成大鼠每公斤體重攝取劑量為 0.2934 mg/天÷0.2 kg = 1.467 mg/kg，因此可提供相關文獻證明攝取此劑量的茄紅素對於大鼠沒有負面生理影響，則可反映其對一個70公斤的成人亦無不良的影響。例如可舉的文獻：使用雄性及雌性大鼠，給予雄性大鼠高劑量組：茄紅素0, 145, 291,及586 mg/kg體重/天；給予雌性大鼠高劑量組：茄紅素0, 156, 312,及616 mg/kg體重/天。連續餵食9天，發現並無生理毒性反應。(Konker et al., 2003)

假設已有相關人體實驗上的文獻證明，某特定族群中，X kg 重的人每天服用 Y mg 茄紅素對其生理功能並不會造成負面影響，那麼此廠商亦可提供這樣的文獻以佐證食用這些產品對此特定族群是安全的。

四、討論

1. 非傳統性食品相關審查基準規範

目前相關單位對於健康食品的管理已有相關的法案，然而針對非傳統食物或原料產品的審查，則被列於健康食品類申請流程之內：即業者當申請之健康食品為「第三類食品-非傳統食用食品」必須提供以下相關安全性評估數據：(1) 90 日餵食試驗 (2) 基因毒性試驗 (3) 致畸試驗，以及產生過敏、副作用及藥理作用相關等營養毒性資料。亦由於非傳統性食品被歸類於傳統性食品的一部份，因此我們建議可以現有健康食品之法規，制定添加有非傳統性食品原料之食品安全規範。然而，與健康食品不同的是，非傳統性食品或原料一般皆缺乏長久食用安全的歷史，同時這一類食品的來源、結構或製造過程與國人一般食用之傳統食品或原料可能不同，所以為非傳統性食品原料制定更嚴格之安全性審查基準卻是必行的，必須明確指出原料來源、特性、使用目的及加工安全性、用量等原料基本資料。食用者及其攝食方式亦是需要深入討探之處，消費者的攝取上限，及其建議食用對象、排除對象等不同人的適用性都需考慮其中。

而對於其非傳統性食品或原料安全性方面資訊的了解目前大多來自於動物性的實驗；此外，許多此類食品或原料，可能是外國傳入而本國國人從未攝食過之原料；部份僅產自於部份特定的區域 (例

如：石蓮花)、或者一直以來不曾為民眾食用但目前卻又直接以添加物的形式出現在市面食品內(例如：竹碳、黃金)；也包括經科學方法萃取或純化的特定成分之濃縮原料；甚至亦可能有於人類飲食歷史中從未出現之原料。由於目前尚無相關法規予以規範，因此對於攝取此類相關產品民眾的健康將有所威脅。所以，為了保障民眾食用的安全，為這些不同種類的原料制定一套標準的安全性審查基準是必須的。然而亦因為這些原料來源複雜而多元，於設定審查基準時較無法針對特定種類的產品一一制定標準或規範，所以僅能就方法學制定一個通用的原則。

2. 每日估計攝取量 (EDI) 計算公式之應用及限制

本計劃參考美國食品藥物檢驗局於估算美國民眾攝取營養素時之公式作為估算非傳統性食品或原料 EDI 之公式。計算時須使用三個數據：(1) 含有計算成份各種食物的每日攝食頻率；(2) 含有計算成份各種食物的每次攝食份量；(3) 計算成份在食物中的含量。此三數據可取自於全國性大規模的飲食調查(如：我國之國民營養大調查)。由於這些數據是取自於該區域或國家大規模與大樣本的調查，因此再相關的資料中應具有相當的代表性以及可信度。

此公式於使用上亦會有一些限制：(1) 由於為大規模大群體的調查，個體差異性極大(平均值-標準差後為負值)；(2)除了成年人的數據之外，其他一些特定族群，包括老年人、學童或孕婦與哺乳婦等數據較不完整，因而我們使用間接的方法推算其 EDI 值；(3)對於極端消費者的 EDI，使用攝取量的平均值+標準差作為標準計算，如同第(1)點所述，標準差異極大，因此亦可能造成計算上的誤差。然而，或許以此公式計算之 EDI 其在應用上並無法那麼完善，但是在估計安全性未明之非傳統性食品原料時，我們認為寧願高估其危害性，以降低對民眾健康之危害風險。

3.老年人及國小學童以及其他族群各類食物攝取數據

第三次台灣國民營養健康狀況變遷調查尚於進行中，目前所使用的國民營養調查數據皆是取自第一次及第二次台灣國民營養健康狀況變遷調查結果。這兩次調查結果中，尚有許多數值未統計，舉例而言，在本次計劃內使用的台灣老年人每日各類食物食用頻率數值，由於只有"熱量"統計，缺乏"食物份量"統計，不得不以代換數值的方式計算；另外台灣國小學童的部份也是一樣缺乏完整的統計數值，雖然大部份各類食物所提供的熱量已統計，但是並沒有像成人或老年人一般依照性別及制定好的食物分類直接以表格的方式呈現，缺

少的數據都須用代換的方式取得，如此在估算不同族群每人每日特定成份攝取量時是有困難的，若是之後可以完整提供不同的族群不同的攝取情況，像是青少年、孕婦、學齡前兒童等，對於廠商參考數據會方便許多。

4.上限攝取量制訂

目前已制定之傳統營養素上限攝取量，為經過長期民眾食用歷史以及動物長短期不同劑量試驗後逐步推論出之安全食用劑量；另外，食品添加物之上限添加劑量亦為經由多種不同劑量及不同動物模式測試後，反覆選用不同劑量經由人體臨床試驗後制定。此外，目前最嚴格的上限攝取量制訂流程乃應用在新藥的開發與使用。新藥在上市前皆須經過嚴格的安全性試驗，自細胞、動物模式以及人體臨床前期、人體臨床期，最後才得以制定出 NOAEL、LOAEL、UL 等等數值。然而，對於缺乏使用歷史之非傳統性食物及原料之上限攝取量的制定較受到限制，因而我們建議以風險評估之系統逐步推算之。

5.市售含有非傳統性原料食品營養標示

為了解非傳統性食品原料在市面上販售的情形，實地走訪大小超市進行簡單市調，確實發現目前市面上許多宣稱含有非傳統性原料的食品，其中有些已經販售多年，打著有益或促進健康的口號，宣稱產

品含有特定的成份，例如:某些廠牌之綠茶飲料，多年前推出時並未於營養標示表列出含有多少濃度的兒茶素，然而隨著兒茶素功效的相關研究越來越多，兒茶素亦成為茶類產品的銷售主角；另外，有一些則是跟著潮流，亦趁機推出類似宣稱有特殊功效的非傳統性食品，如"膠原蛋白"，在以往或許只是提倡多吃含有膠質的食物來增加膠原蛋白的攝取，例如豬腳，現在已有廠商將膠原蛋白萃取製成錠劑方便民眾服用。此外經過市調後發現，市面上產品在營養標示的部份大多含糊不清，例如"錠劑"，並無明確標示每一錠有效成份含量以及整瓶有效成份含量；又或者"飲品"，也只是在瓶身文案宣稱含有特定成分，卻未於營養標示中明列成份含量等，這些的部份或許可以比照健康食品法之規定處理。

6. 評估方法應用上的限制

如前所述，非傳統性食品或原料較缺乏長久食用的歷史，因此相關的科學文獻亦有限，亦因為如此，雖然評估 ADME 的方法有許多，但以非傳統性食品而言，應多以實驗動物或是體外培養細胞的數據為主，所以在換算至人體的劑量、吸收血液內的濃度或是其他的一些作用上，與實際人體內的代謝會有一些限制，因此我們於此報告內亦提供人體與動物之間劑量換算的參考，以其儘量縮減期間的誤差。

五、結論與建議

針對特定族群的飲食估計攝取量建議可以以下公式計算:

$$EDI_x = \sum_{f=1}^{F} Freq_f \, x \, Port_f \, x \, Conc_{xf}$$

各族群相關數據之取得，可由衛生署出版之“國民營養現況”及“國民營養健康狀況調查”中查閱；以一般成年族群而言，採用資料中攝取量之平均值數據計算，以成年極端族群而言，則採用平均值+標準差計算之。而老年人及學童的族群，因為部份數據的缺乏，則以與成年人之“熱量-食物重量換算因子“間接的推算之。有關攝取上限的部份，因為非傳統性類食品較缺乏長久攝食的歷史或一些相關安全性的文獻資料，則建議由風險評估的系統逐步推論之。

營養毒理的相關資料與評估方法，我們亦彙整一些已於文獻中使用評估吸收、分佈、代謝與排泄的方法，整體而言，可給予人體或動物特定的物質後，於特定時間採集血液、尿液或組織，再利用儀器分析之並配合特定的公式計算，即可獲得相關的數據，此外，亦可使用體外的方法評估部份的項目以節省時間與經費。由動物實驗所得知結果，在使用劑量轉換因子換算成於人體的劑量，這些數據將有助於業者提供相關文獻資料的參考。

由於飲食資料的欠缺，部份數據無法計算出，建議未來相關單位

或許可針對特定的族群進行更完整的營養或飲食調查，使國人的飲食資料更趨完整。

六、九十六年度計畫執行成果報告表

九十六年度計畫執行成果報告表
（本資料須另附乙份於成果報告中）

<table>
<tr><td>計畫名稱</td><td colspan="3">非傳統性食品原料安全性評估資料之蒐集及我國審查基準之建立</td></tr>
<tr><td>計畫編號</td><td>DOH96-TD-F-113-033</td><td>填寫日期</td><td>97/02/27</td></tr>
<tr><td>執行機構</td><td>台北醫學大學</td><td>計畫主持人</td><td>謝明哲</td></tr>
<tr><td>計畫期程</td><td colspan="3">■一年期計畫 ； □多年期計畫，共_____年，本年度為第____年</td></tr>
<tr><td>原計畫書擬達成目標</td><td colspan="3">(一)飲食攝取資料的參考，包括：
1. 建議攝取之方式
2. 一般消費者、極端消費者之預估攝取量及上限
3. 特定族群消費者之預估攝取量及上限
4. 建議食用對象及排除對象
(二)營養及毒性之相關資料
1.各種原料於人體吸收、分佈、代謝、排出、生物利用率及耐受性實驗相關報告或文獻的研讀與彙整</td></tr>
<tr><td>已達成目標及其他成果</td><td colspan="3">(一)飲食攝取資料的參考
除了學童極端消費者之估計攝取量以及有關非傳統性食品之上限攝取量，因為部份資料的欠缺無法完整的給予建議之外，其他飲食的部份皆以提出建議的計算方式。此外，非傳統性食品因為種類的多樣性，相關的建議攝取方式以及建議食用對象及排除對象亦依特定的食品而有所差異，但建議孕產婦應被列於排除對象。
(二)營養及毒性之相關資料
已彙整常用於評估特定成份於體內吸收、分佈、代謝、排出、生物利用率及耐受性的相關研究方法。</td></tr>
</table>

（計畫主持人以條列方式逐項填寫，若篇幅不足，可另附頁說明）

七、九十六年度計畫重要研究成果及對本署之具體建議

1.本計畫之新發現或新發明

1. 提供相關單位針對不同族群非傳統食品估計攝取量計算方法的建議。
2. 有關此類食品建議攝取之方式、建議食用對象及排除對象，因此類食品種類繁多之故，故建議應依特定食品而應有不同的建議，但孕產婦應被列於排除對象。
3. 提供業者未來於提供毒理學相關文獻時有助於舉證的評估方法，同時亦提供於動物實驗及人體實驗劑量轉換的計算因子。

2.本計畫對民眾具教育宣導之成果

本計畫對於民眾教育宣導之部份，較無直接具體的成果。

3.本計畫對醫藥衛生政策之具體建議

由於生活品質的提升，民眾越來越注重本身的健康狀況，也因而使得市面上各種宣稱可促進健康的食品或補充品越來越多，非傳統性食品或原料的使用亦在此情況下日趨流行。然而特別針對此類的食品使用的相關法規制定仍在進行中，也由於缺少法規的依據與限制，市場上此類食品的種類繁多，的品質亦可能

參差不齊，真正促進健康的效果則不得而知。因此，於繁多的種類中，民眾一方面可能無從選擇，另一方面可能增加金錢上的損失，嚴重的狀況甚至可能因攝取這一類的食品而危害到自己的健康。由本次研究的成果，將有助於法規的制定以及業者評估攝取量與搜尋毒理學相關文獻資料的參考。此外，亦建議相關單位於法規制定的階段，可增加有關這些食品的宣導，使民眾對此類的食物多一層認識，同時亦可節省民眾不必要的開銷或是降低民眾於攝食此類食品的風險。

八、參考文獻

行政院衛生署 a：食品衛生處食品資訊網。http://food.doh.gov.tw/chinese/Academic/PDF/academic3_3/04.pdf

吳幸娟、章雅惠、方佳雯、潘文涵(民 87)台灣地區成人攝取的食物總重量、熱量值及三大營養素的食物來源。In: 國民營養現況：1993-1996 國民營養健康狀況變遷調查結果，p.51-82．行政院衛生署。

行政院衛生署 b：食品衛生處食品資訊網。http://food.doh.gov.tw/chinese/academic/PDF/academic3_1/200411_04.pdf

吳幸娟、章雅惠、魏燕蘭、高美丁、潘文涵。 台灣地區老人營養健康狀況調查 1997-2002: 老年人攝入之食物、熱量與各營養素的食物來源。In: 台灣國民營養健康狀況變遷調查（1997-2002）「台灣地區老人營養健康狀況調查 1999-2000 調查結果」P. 35-68。行政院衛生署。

行政院衛生署 c：食品衛生處食品資訊網。http://food.doh.gov.tw/chinese/academic/B.pdf

吳幸娟、潘文涵、葉乃華、張新儀。台灣國小學童營養健康狀況調查 2001-2002: 以 24 小時飲食回顧法評估國小學童膳食營養狀況。In: 台灣國民營養健康狀況變遷調查（1997-2002）「國小學童國民

營養健康狀況變遷調查 2001-2002 調查結果」P. 25-69。行政院衛生署。

行政院衛生署d。國人膳食營養素參考攝取量及其說明，修訂第六版。行政院衛生署。

王金玉,謝有容(2001)。應用毛細管電泳分析食品添加物之研究。Chemistry (The Chinese Chem. Soc., Taipei) 59, pp. 435~442。

何士慶。2006。中草藥開發計畫。

台灣生態碳產業發展協會，http://www.ecocarbon.org.tw/first5-1.htm (2007/8/25)

Balon K, Riebesehl BU and Müller BW: Drug liposome partitioning as a tool for the prediction of human passive intestinal absorption. *Pharm Res* 1999; 16: 882-888.

Chiho O, Atsushi T and Ryo A: Absorption, distribution, and excretion of DJ-927, a novel orally effective taxane, in mice, dogs, and monkeys. *Biol Pharm Bull* 2004; 27: 345-351.

Ekins S, Nikolsky Y and Nikolskaya T: Techniques: application of systems biology to absorption, distribution, metabolism, excretion and toxicity. *Trends Pharmacol Sci* 2005; 26: 202-209.

Eriksson UG, Bredberg U, Hoffmann KJ, Thuresson A, Gabrielsson M, Ericsson H, Ahnoff M, Gislén K, Fager G and Gustafsson D: Absorption, distribution, metabolism, and excretion of ximelagatran, an oral direct thrombin inhibitor, in rats, dogs, and humans. *Drug Metab Dispos* 2003; 31: 294-305.

Grindel JM, Jaworski T, Piraner O, Emanuele RM and Balasubramanian M: Distribution, metabolism, and excretion of a novel surface-active agent, purified poloxamer 188, in rats, dogs, and humans. *J Pharm Sci* 2002; 91: 1936-1947.

Guo J, Zhang X, Li Q and Li W: Biodistribution of functionalized multiwall carbon nanotubes in mice. *Nucl Med Biol* 2007; 34: 579-583.

Jonker D, Kuper CF, Fraile N, Estrella A and Rodríguez Otero C: Ninety-day oral toxicity study of lycopene from Blakeslea trispora in rats. *Regul Toxicol Pharmacol* 2003; 37: 396-406.

Kapitza SB, Michel BR, van Hoogevest P, Leigh ML and Imanidis G: Absorption of poorly water soluble drugs subject to apical efflux using phospholipids as solubilizers in the Caco-2 cell model. *Eur J Pharm Biopharm* 2007; 66:146-158.

Katoh M, Sawada T, Soeno Y, Nakajima M, Tateno C, Yoshizato K and Yokoi T: In vivo drug metabolism model for human cytochrome P450 enzyme using chimeric mice with humanized liver. *J Pharmacol Sci* 2006; 96: 428-437.

Kim SK, Lee DY, Lee E, Lee YK, Kim CY, Moon HT and Byun Y: Absorption study of deoxycholic acid-heparin conjugate as a new form of oral anti-coagulant. *J Control Release* 2007; 120: 4-10.

Konishi Y and Kobayashi S: Microbial metabolites of ingested caffeic acid are absorbed by the monocarboxylic acid transporter (MCT) in intestinal Caco-2 cell monolayers. *J Agric Food Chem* 2004: 52: 6418-6424.

Konishi Y, Hitomi Y, Yoshida M and Yoshioka E: Absorption and

bioavailability of artepillin C in rats after oral administration. *J Agric Food Chem* 2005: 53: 9928-9933.

Laitinen L, Takala E, Vuorela H, Vuorela P, Kaukonen AM and Marvola M: Anthranoid laxatives influence the absorption of poorly permeable drugs in human intestinal cell culture model (Caco-2). *Eur J Pharm Biopharm* 2007; 66: 135-145.

Lee HS, Ji HY, Park EJ and Kim SY: In vitro metabolism of eupatilin by multiple cytochrome P450 and UDP-glucuronosyltransferase enzymes *Xenobiotica* 2007; 37: 803–817.

Lee J, Yoo HH, Rhim KJ, Sohn DR and Kim DH: Metabolism and excretion of 5-ethyl-2-{5-[4-(2-hydroxyethyl)piperazine-1-sulfonyl]-2-propoxyphenyl}-7-propyl-3,5-dihydropyrrolo[3,2-d]-pyrimidin-4-on e (SK3530) in rats. R*apid Commun Mass Spectrom* 2007; 21: 1139-1149.

Mälkiä A, Murtomäki L, Urtti A and Kontturi K: Drug permeation in biomembranes: in vitro and in silico prediction and influence of physicochemical properties. *Eur J Pharm Sci* 2004; 23: 13-47.

Mangold JB, Gu H, Rodriguez LC, Bonner J, Dickson J and Rordorf C: Pharmacokinetics and metabolism of lumiracoxib in healthy male subjects. *Drug Metab Dispos* 2004; 32: 566-571.

Motlekar NA, Srivenugopal KS, Wachtel MS and Youan BB: Oral delivery of low-molecular-weight heparin using sodium caprate as absorption enhancer reaches therapeutic levels. *J Drug Target* 2005; 13: 573-583.

Puttonen J, Laine T, Ramela M, Häkkinen S, Zhang W, Pradhan R, Pentikäinen P and Koskinen M: Pharmacokinetics and excretion

balance of OR-1896, a pharmacologically active metabolite of levosimendan, in healthy men. *Eur J Pharm Sci* 2007; 32: 271-277.

Stott WT, Waechter JM, Rick DL and Mendrala AL: Absorption, distribution, metabolism and excretion of intravenously and dermally sdministered triethanolamine in mice. *Food Chem Toxicol* 2000; 38: 1043-1051.

Suzuki K and Kamimura H: Pharmacokinetics and metabolism of an alpha,beta-blocker, amosulalol hydrochloride, in mice: biliary excretion of carbamoyl glucuronide. *Biol Pharm Bull* 2007; 30: 1580-1585.

Tirumalasetty PP and Eley JG: Permeability enhancing effects of the alkylglycoside, octylglucoside, on insulin permeation across epithelial membrane in vitro. *J Pharm Pharm Sci* 2006; 9: 32-39.

Tsukura Y, Mori M, Hirotani Y, Ikeda K, Amano F, Kato R, Ijiri Y and Tanaka K: Effects of capsaicin on cellular damage and monolayer permeability in human intestinal Caco-2 cells. *Biol Pharm Bull* 2007; 30: 1982-1986.

U.S. FDA. Guidance for Industry Estimating Dietary Intake of Substances in Food. http://www.cfsan.fda.gov/~dms/opa2cg8.html

van de Waterbeemd H: Which in vitro screens guide the prediction of oral absorption and volume of distribution? *Basic Clin Pharmacol Toxicol* 2005; 96: 162-166.

Yasoshima K, Kuwabara T, Fuse E, Kuramitu T, Kurata N, Nishiie H, Oishi T, Kobayashi H and Kobayashi S: Pharmacokinetics, distribution, metabolism and excretion of [^{3}H]-UCN-01 in rats and dogs after intravenous administration. *Cancer Chemother Pharmacol*

2001; 47: 106-112.

Yu C, Shin YG, Chow A, Li Y, Kosmeder JW, Lee YS, Hirschelman WH, Pezzuto JM, Mehta RG and Breemen1 RB van: Human, rat, and mouse metabolism of resveratrol. *Pharmaceutical Res* 2002; 19: 1907-1914.

參考文獻附件

Drug Liposome Partitioning as a Tool for the Prediction of Human Passive Intestinal Absorption

K. Balon,[1] B. U. Riebesehl,[1,3] and B. W. Müller[2]

Received October 14, 1998; accepted March 5, 1999

Purpose. Appropriate physicochemical parameters are desired for the prediction of passive intestinal drug absorption during lead compound selection and drug development.

Methods. Liposome distribution coefficients measured titrimetrically and solubility data at pH 6.8 were used to characterize 21 structurally diverse ionizable drugs covering a range from <5% to almost complete absorption.

Results. A sigmoidal relationship was found between the percentage of human passive intestinal absorption and a new absorption potential parameter calculated from liposome distribution data and the solubility-dose ratio. In contrast, the human absorption data did not correlate with an octanol-based absorption potential or partitioning data alone. Poor correlations were found between liposome and octanol partitioning of ionic species or nonionic bases indicating the profound differences of the partitioning systems.

Conclusions. Liposome distribution coefficients of ionizable drugs derived by a pH-metric titration were successfully used to calculate a parameter that correlates with the percentage of passive intestinal absorption in humans. Profound differences between liposome and octanol partitioning were found for a highly diverse set of species. This titration technique may serve to generate liposome partitioning data for the selection and optimization of lead compounds and in drug development.

KEY WORDS: liposomes; octanol; partitioning; solubility; absorption; phospholipids.

INTRODUCTION

The implementation of combinatorial chemistry and high throughput screening in drug research has led to a much higher number of active drug candidates. The new screening methods tend to suggest also compounds with properties critical to absorption such as low solubility, high lipophilicity and high molecular weight (1). Therefore bioavailability surrogate parameters are utilized for selecting lead compounds with a promising bioavailability. Caco-2 cell permeability has been used successfully as an *in vitro* absorption parameter. Unfortunately Caco-2 cell cultures tend to show variable permeability and require laborious cultivation (2). Another disadvantage is the often observed steep correlation between permeation and absorption even on logarithmic scales. Physicochemical parameter-based estimation methods are attractive because of their throughput capacity, reproducibility and because they do not involve cumbersome cell cultivation. Some of the limitations associated with these estimations include their inability, to predict active transport as well as to catalyze enzymatic degradation of drugs. Many attempts have been made for correlating the *in vivo* absorption with drug lipophilicity. 1-octanol has been extensively used as it appeared to give the best correlations among the bulk solvents showing phase separation (3). However, good correlations were only found within homologous series of compounds. Octanol can interact with solutes by hydrophobic and H-bond interactions but fails to mimic the pronounced interfacial character of the bilayer structure of biomembranes and ionic interactions between membrane phospholipids and solutes. Historically it was hypothesized that only neutral molecules can penetrate through membranes (4). Therefore, attention was paid to the partition coefficients of the neutral forms of ionizable compounds. Numerous well-absorbed drug substances appear as ions at the absorptive sites in the small intestine. The relatively low partition coefficients in octanol for the ionic species cannot explain the absorption of these drugs. Studies with membrane lipid vesicles (5) and immobilized artificial membrane (IAM) columns (6) have shown important differences in interactions between drugs with phospholipids and octanol, especially of the ionic forms. Liposomes made from phospholipids are a partition system with characteristics similar to those of biomembranes. The Sirius pH metric logP titration method now allows the convenient and automated determination of liposome partitioning. Drug-liposome interactions are characterized by hydrophobic, H-bond and ionic interactions. High partition coefficients of ionic species are a combined effect of direct ionic interaction between drug and phospholipids and also interactions with the lipophilic part of the bilayer (7). The highly ordered bilayer structure of the phospholipid vesicles mimics also the impact of the membrane bilayer structure on the ability of a drug to permeate (8). A flexible molecule may be more suited for membrane penetration than a rather bulky molecule. A linear correlation between octanol and liposome logP for small neutral molecules has been proposed (9). Another publication describes a correlation between the octanol and liposome logP of the neutral species of ionizable drugs (10). Phagocytosis of solid drug through the intestinal mucosa is quantitatively negligible. Prior to absorption the administered single dose has to be able to dissolve in the intestinal fluid. Consequently, a factor for the solubility/dose relationship has to be included in the equation toward prediction for oral absorption.

MATERIALS AND METHODS

Materials

The chemical structures of the drug substances used in this investigation are given in Fig. 1. Acetylsalicylic acid(1), acyclovir (acycloguanosine)(2), allopurinol(3), amiloride hydrochloride(4), atenolol(5), diclofenac sodium(6), famotidine(7), furosemide(9), ibuprofen(10), miconazole nitrate(11), paromomycin sulfate(15), and propranolol hydrochloride(16) were purchased from Sigma Chemie Vertriebs GmbH (Deisenhofen, Germany). Fluoxetine hydrochloride(8), moxonidine(12), nizatidine(13), olanzapine(14), and xipamide(19) were supplied by Lilly Forschung GmbH (Hamburg, Germany).

[1] Lilly Forschung GmbH, Pharmaceutical Product Development, Wiesingerweg 25, D-20253 Hamburg, Germany.

[2] Department of Pharmaceutics and Biopharmaceutics, Christian Albrecht University, Gutenbergstrasse 76, D-24118 Kiel, Germany.

[3] To whom correspondence should be addressed. (e-mail: riebesehl_bernd@lilly.com)

0724-8741/99/0600-0882$16.00/0

1 Acetylsalicylic acid	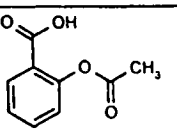	12 Moxonidine	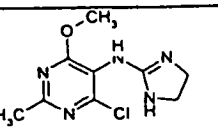
2 Acyclovir	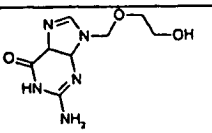	13 Nizatidine	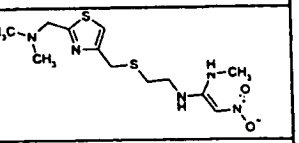
3 Allopurinol	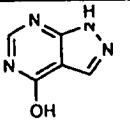	14 Olanzapine	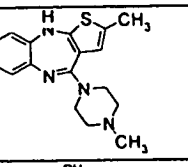
4 Amiloride	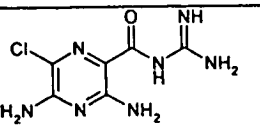	15 Paromomycin	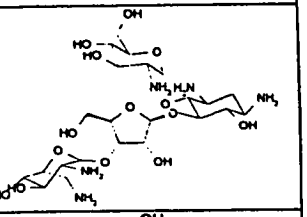
5 Atenolol	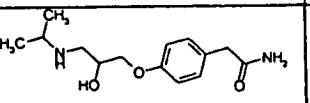	16 Propranolol	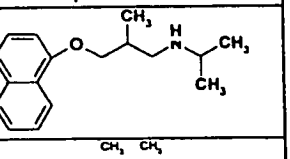
6 Diclofenac	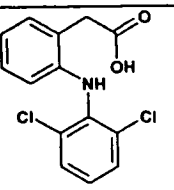	17 Rifabutine	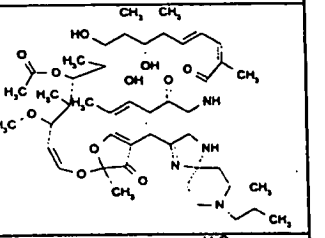
7 Famotidine	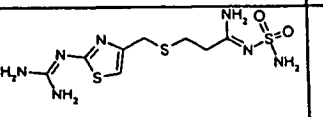	18 Terbinafine	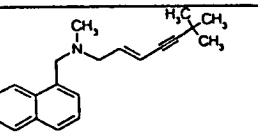
8 Fluoxetine	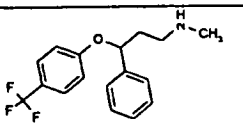	19 Xipamide	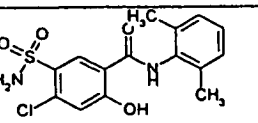
9 Furosemide	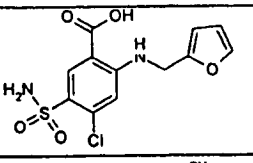	20 Zidovudine	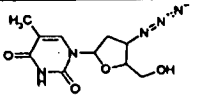
10 Ibuprofen	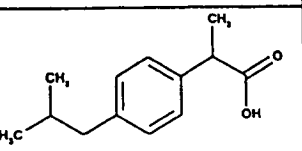	21 Zopiclone	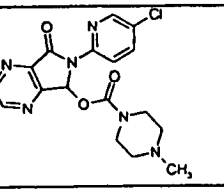
11 Miconazole	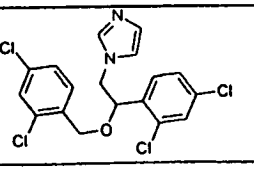		

Fig. 1. Structures of drug substances.

Rifabutine(17) was supplied by Pharmacia Spa. (Italy). Terbinafine hydrochloride(18) was supplied by Novartis Pharma AG (Basel, Switzerland). Zidovudine(20) was supplied by The Wellcome Foundation Ltd. (London, UK). Zopiclone(21) was supplied by Rhône-Poulenc Rorer GmbH (Köln, Germany). Potassium chloride, potassium dihydrogenphosphate, 1-octanol, HCl-Titrisol® and KOH-Titrisol® were purchased from Merck KGaA (Darmstadt, Germany). Polysorbate 80 was purchased from Caelo (Hilden, Germany). Epikuron 200® was supplied by Lucas Meyer GmbH (Hamburg, Germany). Epikuron 200 is a purified soybean phosphatidylcholine with a phospholipid content of >92% consisting of glycerophosphocholin esters with various mainly unsaturated fatty acids, <3% lyso-phosphatidylcholine, <2% other phosphatidylcholines, <0.8% water, <2% oil and <0.2% α-tocopherol. With 56 – 60% of total fatty acids, linoleic acid is the most commonly encountered acid.

Experimental

Liposome Preparation

Sonicated Small Unilamellar Vesicles (S-SUV) were prepared as follows: 1.6 grams of phospholipid were dissolved in a small amount of methanol in a 200 ml round bottom flask. A solid phospholipid film was formed by vacuum evaporation of methanol at 50°C using a rotary evaporator. As determined by thermogravimetry, the resulting film contained less than 5% volatiles after 30 min vacuum drying. The phospholipid film was dispersed with 14.4 ml of a 0.15 M potassium chloride solution, resulting in a phospholipid concentration of 100 mg/ml; 15 ml of this phospholipid dispersion was sonicated for 20 min. in a 20 ml vial using a Bandelin Sonopuls HD70 sonifier equipped with a TT13 sonotrode (Bandelin Electronic GmbH, Berlin, Germany) at 50% amplitude setting with argon purge and cooling with ice water.

Determination of Partition Coefficients

Titrations were performed on PCA101® and GLPKA® automatic titrators (Sirius Analytical Instruments Ltd., Forest Row, UK). The processing of titration data was carried out using the PKALOGP® version 5.01 software. Four titrations at different ratios of phospholipid to water and phospholipid to drug were carried out for each compound to evaluate the partitioning of both the neutral and the ionized species (see Table I). Titrations were carried out at 37°C at an ionic strength of 0.15 M potassium chloride as acidimetric assay starting at pH 10.5. Zopiclon had to be titrated alkalimetrically starting at pH 3.5 respecting its instability under alkaline conditions. Olanzapine had to be dissolved at pH 3.5 before starting the assay at pH 10.5. The determination of octanol/water partition coefficients by pH-metric titration is described in detail elsewhere (11–12).

Table I. General Assay Protocol for $logP_{SUV}$ Titrations

[Lipid]:[Drug][a]	ml Lipid	ml H_2O	Lipid/Water[b]
3	0.025	20	0.0013
10	0.1	15	0.0067
40	0.2	8	0.0250
100	1	20	0.0500

[a] [Lipid]:[Drug]: molar ratio of phospholipid to drug.
[b] (Lipid/Water): volume ratio of phospholipid to water.

Solubility

Solubility was determined in Simulated Intestinal Fluid (USP XXIII) at pH 6.8 without addition of pancreatin (KH_2PO_4 6.8 g = 0.05 M, polysorbate 80 0.01 g, KOH qs pH 6.8, distilled water ad 1000.0). The surface tension was adjusted with polysorbate 80 to a value of approximately 40 dyn/cm as reported for human gastric juice (13). The polysorbate 80 concentration was below the CMC (14). The procedure used for the solubility determination gives ranges of solubility from 0.02–10 mg/ml. The solubilities given in Table II are the mean values for the respective solubility ranges.

RESULTS AND DISCUSSION

Liposome Versus Octanol Partitioning

Figure 2 shows the comparison of partitioning of neutral and anionic species of acids in the liposome and octanol-water system. A linear correlation with a low slope of 0.37 and an intercept at 2.2 was found for the neutral acids. This implies that the liposomal systems is less discriminating than octanol and that especially compounds with a low octanol lipophilicity may show unexpected high partitioning to phospholipid bilayers. In contrast, the partitioning of the neutral forms of the most lipophilic acids diclofenac and ibuprofen is almost as high in the liposomal system as in the octanol system. The logP values of the neutral species of the acids ranged from log −1.8 to 4.2 in the octanol and only from log 1.7 to 4.3 in the liposomal system. A poor correlation with a low slope of 0.33 and an intercept at 2.6 was found for the anionic species. Here the partitioning of the anions was higher by at least two orders of magnitude in the liposomal system except for rifabutine. A consequence of the considerable anion partitioning in the liposomal system is also a small difference between the partition

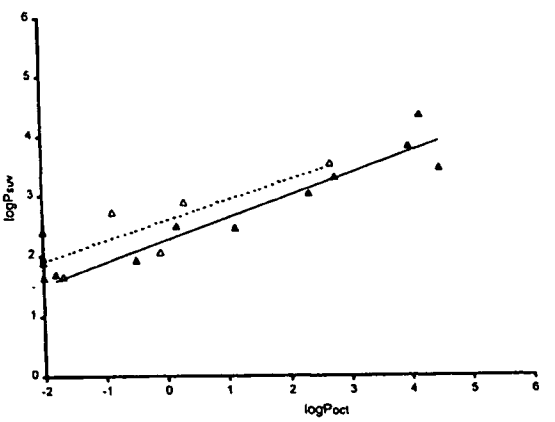

Fig. 2. Liposome versus octanol partitioning of the acids. ▲ - neutral forms ($logP_{SUV} = 0.37\ logP_{Oct} + 2.2$, $R^2 = 0.89$), Δ - anionic forms ($logP_{SUV} = 0.33\ logP_{Oct} + 2.6$, $R^2 = 0.72$). The solid line represents the correlation for the neutral forms. The dotted line represents the correlation for the anionic forms.

Table II. Properties of Drug Substances

No.	Compound	pK_a 37°C	log P_{suv} neutral	Error	log P_{suv} ion	Error	logP_{Oct} neutral	Error	log P_{Oct} ion	Error	log D_{suv} pH6.8	logD_{Oct} pH6.8	Solubility pH6.8 [mg/ml]	Dose [mg]	AP_{SUV}	AP_{Oct}	Intestinal absorption %
1	Acetylsalicylic acid	3.41	2.4	0.1	1.6	0.1	1.1	0.1	−2.0	0.1	1.6	−2.0	0.8	500	1.2	−2.4	90 (19)
2	Acyclovir	2.16 9.04	1.7	0.1	2.0	0.1	−1.8	0.1	−2.0	0.1	1.7	−1.8	0.8	200	1.7	−1.3	20 (20)
3	Allopurinol	9.00	2.5	0.1	2.7	0.1	0.2	0.1	−0.9	0.2	2.5	0.1	0.4	300	2.0	−0.6	90 (21)
4	Amiloride[a]	8.35	1.8	0.1	1.6	0.1	0.1	0.1	−0.7	0.2	1.6	−0.6	0.1	5	2.3	0.4	50 (22)
5	Atenolol	9.25	2.2	0.1	1.0	0.2	0.5	0.1	−1.5	0.3	1.0	−1.3	10.0	50	2.7	0.4	56 (23)
6	Diclofenac	4.01	4.3	0.1	2.9	0.1	4.2	0.1	0.3	0.1	2.9	1.4	0.8	50	3.5	2.3	99 (24)
7	Famotidine	6.56 11.02	2.3	0.1	1.7	0.1	−0.8	0.1	−0.2	0.1	2.1	−1.0	0.8	40	2.8	−0.5	45 (25)
8	Fluoxetine	9.62	3.0	0.1	2.2	0.1	4.5	0.1	1.5	0.1	2.1	1.9	2.5	30	3.5	3.3	80 (26)
9	Furosemide	3.61 10.24	3.0	0.1	1.9	0.1	2.6	0.1	−2.0	0.1	1.9	−1.0	0.8	40	2.6	−0.1	65 (22)
10	Ibuprofen[a]	4.45	3.8	0.1	2.1	0.1	4.0	0.1	−0.1	0.1	2.1	1.6	2.5	200	2.6	1.6	80 (27)
11	Miconazole	6.12	3.7	0.3	2.9	0.3	4.9	0.1	1.2	0.3	3.6	4.5	0.02	250	1.9	3.1	25 (22)
12	Moxonidine[b]	7.36	1.8	0.1	1.3	0.1	0.9	0.1	−0.2	0.1	1.5	0.4	0.8	0.3	4.3	3.1	99 (28)
13	Nizatidine	2.44 6.75	3.0	0.4	2.8	0.4	−0.2	0.1	−0.9	0.1	2.9	−0.3	10.0	300	3.8	0.5	99 (25)
14	Olanzapine	5.44 7.80	3.7	0.1	2.7 2.3	0.1 0.1	3.0	0.1	0.0	0.1	3.0	2.0	0.02	10	2.7	1.7	75 (29)
15	Paromomycin	5.99 7.05 7.57 8.23 8.90	1.7	0.1	1.2	0.1	−2.0	0.1	−2.0	0.1	−0.6	−2.0	10.0	250	0.4	−1.0	3 (22)
16	Propranolol	9.14	3.2	0.1	2.5	0.1	3.4	0.1	0.5	0.1	2.5	1.2	7.5	80	3.9	2.9	99 (30)
17	Rifabutine	6.90 9.37	3.4	0.1	3.5 2.7	0.1 0.1	4.5	0.1	2.7 2.0	0.3 0.1	3.2	4.3	0.1	150	2.4	2.8	53 (31)
18	Terbinafine	7.05	5.0	0.2	3.0	0.2	6.0	0.1	2.3	0.1	4.6	5.5	0.02	250	2.9	3.5	80 (32)
19	Xipamide	4.58 10.47	3.3	0.1	1.7	0.1	2.8	0.1	−1.7	0.3	1.7	0.5	0.8	20	2.7	1.5	70 (22)
20	Zidovudine	9.45	1.9	0.1	2.4	0.1	−0.5	0.1	−2.0	0.1	1.9	−0.7	7.5	100	3.2	1.6	90 (33)
21	Zopiclone	6.76	1.8	0.2	1.4	0.2	1.5	0.1	−0.8	0.2	1.6	1.3	0.1	8	2.1	1.5	80 (34)

[a] All data at 25°C.
[b] SUV data at 25°C for Dioleoylphosphatidylcholine-liposomes.

$$AP_{SUV} = \log\left(\text{Distribution } pH_{6.8} \times \frac{\text{Solubility } pH_{6.8} \times V}{\text{Dose}}\right)$$

coefficients of neutral and anionic species. The differences were smaller for the hydrophilic acids than for the more lipophilic acids. For the three hydrophilic weak acids, acyclovir, allopurinol and zidovudine, the liposome partitioning of the anionic species were even higher than that of the neutral form. An even worse correlation was found between the distribution coefficients of the acids at pH 6.8 in both systems (Fig. 4). Figure 3 shows the comparison of partitioning of neutral and cationic species of bases in the liposome and octanol-water system. A poor correlation with a low slope of 0.33 and an intercept at 2.2 was found for the 13 neutral bases. The lipophilicity ranged between −2.0 and 6.0 in the octanol and between 1.0 and 5.0 in the liposomal system. Again the differences between neutral and ion partitioning in the liposomal system were small. In most of the cases, the difference was less than one log unit. Generally, the partition coefficients of the neutral forms are higher for liposomes than for octanol. Only for the neutral forms of the most lipophilic bases with a logP of 4 and higher the octanol partitioning exceeded the liposome partitioning. A poor correlation with a low slope of 0.37 and an intercept at 2.0 was found for the cationic species. A correlation between octanol and liposome distribution coefficients of the bases at pH 6.8 was also poor (Fig. 4). A general similarity between octanol and liposome partition coefficients of nonionized acids and bases as reported by Avdeef *et al.* could not be verified for all of the compounds discussed here. Such a similarity could be seen for propranolol and the most lipophilic acids ibuprofen and diclofenac. With regard to the flat and erratic correlations between liposome and octanol partitioning, this coincidence of similar partitioning coefficients may be limited to this particular range of lipophilicities. Furthermore, a linearity of correlation between octanol and phospholipid systems for small nonionic molecules as reported by Gobas *et al.* is not representative for more complex drug molecules (9,15).

Correlations with Human Intestinal Absorption

For the correlation of physicochemical parameters with human intestinal absorption data, a new type of Absorption Potential (AP_{SUV}) based on liposome partitioning (Eq. 1) was

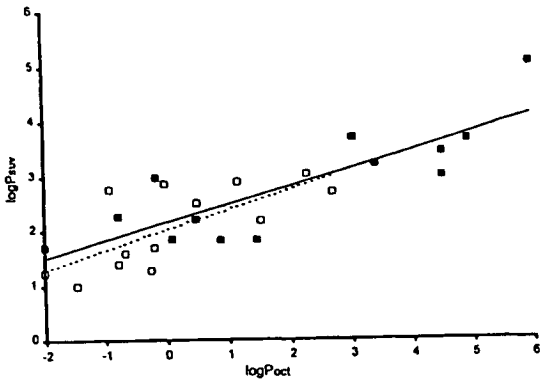

Fig. 3. Liposome versus octanol partitioning of the bases. ■—neutral forms ($logP_{SUV}$ = 0.33 $logP_{Oct}$ + 2.2, R^2 = 0.69), □—cationic forms ($logP_{SUV}$ = 0.37 $logP_{Oct}$ + 2.0, R^2 = 0.49). The solid line represents the correlation for the neutral forms. The dotted line represents the correlation for the cationic forms.

calculated from distribution, solubility, mean single oral dose, and the volume of the intestinal fluids. In contrast to the Absorption Potential introduced by Dressman *et al.* (16), the distribution coefficient at pH 6.8 is used instead of the partition coefficient. The Absorption Potential results for liposomes and octanol ($AP_{Octanol}$) and the references for the human absorption data are listed in Table II. pH 6.8 is considered to be a relevant pH for the fasted small intestine where most of the absorption takes place (17). Therefore, distribution coefficients were calculated for pH 6.8 and solubility was determined at pH 6.8. Figure 5 (a) shows the noncorrelation of intestinal absorption with liposome distribution at pH 6.8 ($logD_{SUV}$pH 6.8). Most of the drugs tested had a $logD_{SUV}$ of 1.5 to 3 absorption scattered between 20 and 100%. In contrast, a sigmoidal correlation of human intestinal absorption with AP_{SUV} was found (Fig. 5b). The high absorption of acetylsalicylic acid (1) and allopurinol (3) appears to be reached even with low AP_{SUV} values. This may be explained by their particularly low molecular weight, enabling additional paracellular diffusion through membranes (18). No correlations were found between $logD_{Oct}$ or $AP_{Octanol}$

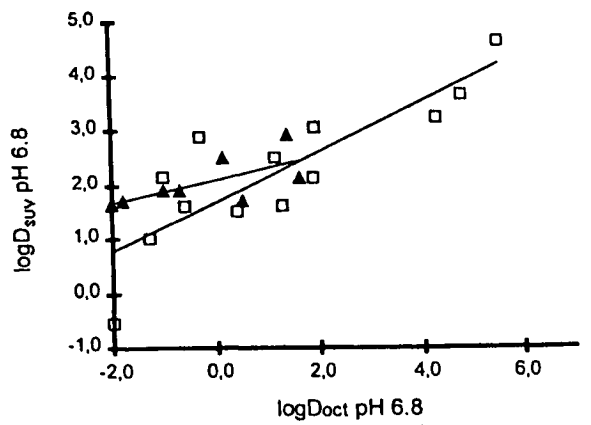

Fig. 4. Liposome versus octanol distribution at pH6.8. ▲ - Acids ($logD_{SUV}$ pH 6.8 = 0.22 $logD_{Oct}$ + 2.1, R^2; = 0.45), □—Bases ($logD_{SUV}$ pH 6.8 = 0.45 $logD_{Oct}$ + 1.7, R^2 = 0.71).

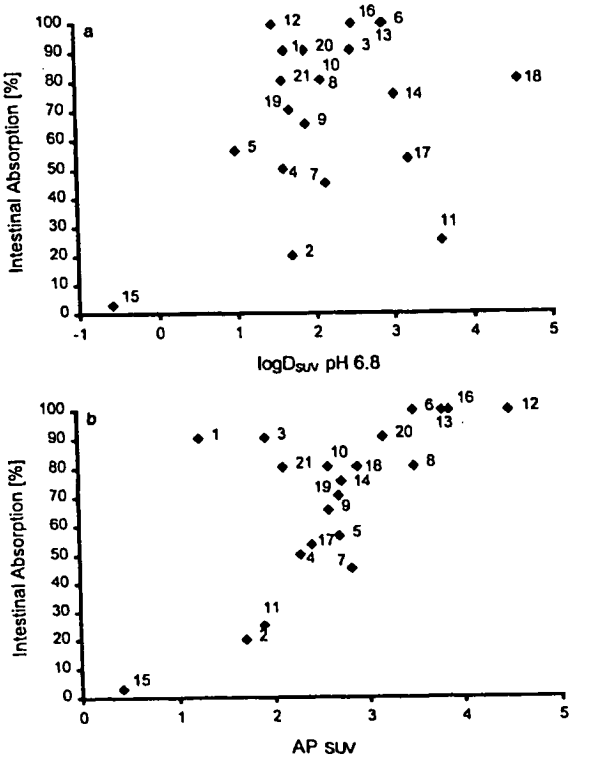

Fig. 5. (a) Intestinal Absorption versus $logD_{SUV}$ pH 6.8. The numbers in the graph refer to the substance numbers in Table II. Number 8 and 10 have identical values of absorption and logD. (b) Intestinal Absorption versus AP_{SUV}. The numbers in the graph refer to the substance numbers in Table II.

and the percentage of intestinal absorption (Fig. 6a and 6b). Particularly the low percentage of absorption of miconazole(11) and rifabutine(17) could not be predicted correctly using the octanol logD values. Their bulky lipophilic moiety may hinder, particularly, their integration in ordered phospholipid bilayers as it is expressed by lower liposome than octanol logD values. The most striking difference between the two systems is the much higher partitioning of ionic molecules in the liposomal system. This is first of all an effect of interactions between ionic drug molecules and the ionic functional groups in the phospholipid bilayer. It results in a higher affinity to membranes even of hydrophilic compounds than would be estimated from the low partitioning of drugs into organic bulk solvents. Another important factor for prediction of passive intestinal absorption is the solubility of the drug at intestinal pH. The prediction of intestinal absorption by logD values alone fails. Octanol as well as liposome distribution results do not correlate with the percentage of intestinal absorption as shown in Figs. 5a and 6a. A sufficient solubility relative to the single oral dose is a prerequisite for intestinal absorption. It could be shown that a high solubility to dose ratio may outweigh a low lipophilicity resulting in a high percentage of absorption. On the other hand even highly lipophilic compounds can be poorly absorbed when the solubility to dose ratio is small as, e.g., for miconazole[11] and rifabutine[17]. These two together with terbinafine [18] approach the main field of data points (Figs. 6b, 5b) or the

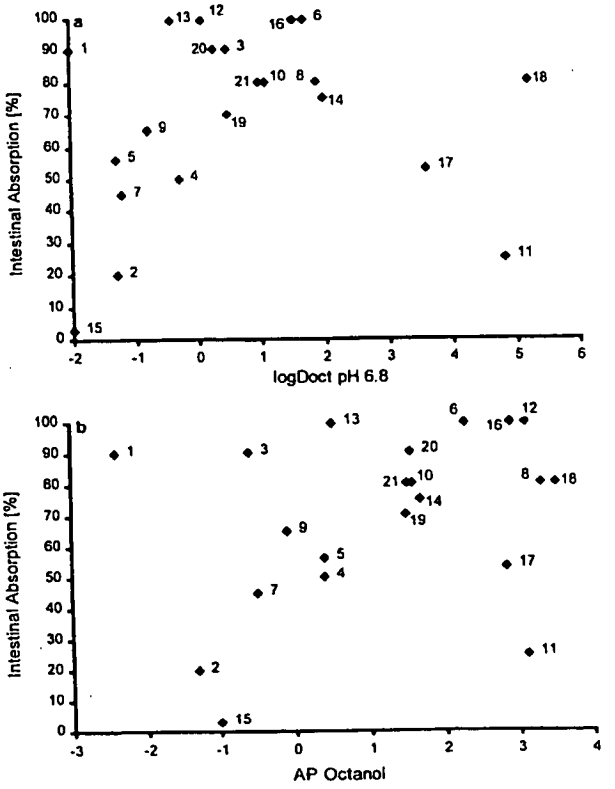

Fig. 6. (a) Intestinal Absorption versus $logD_{Oct}$ pH 6.8. The numbers in the graph refer to the substance numbers in Table II. (b) Intestinal Absorption versus $AP_{Octanol}$. The numbers in the graph refer to the substance numbers in Table II.

center line of data points when the correlation of absorption is changed from simple partitioning to the absorption potential.

CONCLUSIONS

Drug partitioning in the liposomal system can be measured conveniently by an automated potentiometric titration technique. It could be shown that octanol partitioning is poorly correlated with interactions between ionizable drugs and phospholipid bilayers. Liposome partitioning of structurally diverse acids and bases is characterized by much higher partitioning of ionic species compared to octanol so that the differences in logP between neutral and ionic species are smaller. Partitioning of hydrophilic compounds was found to be increased and partitioning of the neutral forms of highly lipophilic compounds to be similar or decreased compared to 1-octanol. As most drugs are ionizable and many exist in the ionic state at intestinal pH, this result is of relevance for *in vitro-in vivo* correlations with lipophilicity data. Liposome distribution coefficients of ionizable drugs have been successfully used to calculate a parameter, AP_{SUV}, that correlates with the percentage of passive intestinal absorption in humans. In contrast, the human absorption data did not correlate with an octanol-based absorption potential or partitioning data alone. This technique may serve for selection and optimization of lead compounds and in drug development. Limitations of this model are its inability to account for membrane passage via paracellular routes or any active transport mechanisms.

REFERENCES

1. C. A. Lipinski, F. Lombardo, B. W. Dominy, and P. J. Feeney. Experimental and computational approaches to estimate solubility and permeability in drug discovery and development settings. *Adv. Drug Del. Rev.* 23:3–25 (1997).
2. S. Yee. *In vitro* permeability across Caco-2 cells (colonic) can predict *in vivo* (small intestinal) absorption in man—fact or myth. *Pharm. Res.* 14:763–766 (1997).
3. K. J. Schaper. Absorption of ionizable drugs: nonlinear dependence on logP, pKa and pH-quantitative relationships. *Quant.Struct.-Act.Relat.* 1:13–27 (1982).
4. P. A. Shore, B. B. Brodie, and C. A. M. Hogben. The gastric secretion of drugs: A pH partition hypothesis. *J. Pharmacol. Exp. Ther.* 119:361–369 (1957).
5. C. J. Alcorn, R. J. Simpson, D. E. Leahy, and T. J. Peters. Partition and distribution coefficients of solutes and drugs in brush border membrane vesicles. *Biochem. Pharmacol.* 45:1775–1782 (1993).
6. F. Barbato, M. I. la Rotonda, and F. Quaglia. Interactions of nonsteroidal antiinflammatory drugs with phospholipids: comparison between octanol/buffer partition coefficients and chromatographic indexes on immobilized artificial membranes. *J. Pharm. Sci.* 86:225–229 (1997).
7. H.-Y. Cheng, C. S. Randall, W. W. Holl, P. P. Constantinides, T.-L. Yue, and G. Z. Feuerstein. Carvedilol-liposome interaction: evidence for strong association with the hydrophobic region of the lipid bilayers. *Biochim. Biophys. Acta* 1284:20–28 (1996).
8. G. V. Betageri, Y. Theriault, and J. A. Rogers. NMR Study of the interaction of beta-blockers with sonicated dimyritoylphosphatidylcholine liposomes in the presence of praseodymium cation. *Membrane Biochem.* 8:197–206 (1989).
9. F. A. P. C. Gobas, J. M. Lahittete, G. Garofalo, W. Y. Shiu, and D. MacKay. A novel method for measuring membrane-water partition coefficients of hydrophobic organic chemicals: comparison with 1-octanol-water partitioning. *J. Pharm. Sci.* 77:265–272 (1988).
10. A. Avdeef, K. J. Box, J. E. A. Comer, C. Hibbert, and K. Y. Tam. pH-metric logP 10: Determination of vesicle membrane–water partition coefficients of ionisable drugs. *Pharm. Res.* 15:209–215 (1998).
11. A. Avdeef. pH-Metric logP. Part 1: Difference plots for determining ion-pair octanol-water partition coefficients of multiprotic substances. *Quant. Struct.-Act. Relat.* 11:510–517 (1992).
12. A. Avdeef. pH-metric logP-2. Refinement of partition coefficients and ionisation constants of multiprotic substances. *J. Pharm. Sci.* 82:183–190 (1993).
13. P. Finholt and S. Solvang. Dissolution kinetics of drugs in human gastric juice—the role of surface tension. *J. Pharm. Sci.* 57:1322–1326 (1968).
14. L. S. C. Wan and P. F. S. Lee. CMC of Polysorbates. *J. Pharm. Sci.* 63:136–137 (1974).
15. G. Camenisch, G. Folkers, and H. van de Waterbeemd. Review of passive drug absorption models: historical background, recent developments and limitations. *Pharm. Acta Helv.* 71:309–327 (1996).
16. J. B. Dressman, G. L. Amidon, and D. Fleisher. Absorption potential: Estimating the fraction absorbed for orally administered compounds. *J. Pharm. Sci.* 74:588–589 (1985).
17. J. B. Dressman, and V. A. Gray. Change of pH intestinal fluid. *Pharmacopeial Forum* 22:1943–1945 (1996).
18. H. Lennernäs. Does fluid flow across the intestinal mucosa affect quantitative oral drug absorption? Is it time for a reevaluation? *Pharm. Res.* 12:1573–1582 (1995).
19. K. Hartke (ed). *DAB10 Kommentar* Wiss. Verl.-Ges. Stuttgart, 1991.
20. P. de Miranda, and M. R. Blum. Pharmacokinetics of acyclovir after intravenous and oral administration. *J. Antimicrob. Chemother.* 12 Suppl. B:29–37 (1983).
21. H. Breithaupt and M. Tittel. Kinetics of allopurinol after single intravenous and oral doses. *Eur. J. Clin. Pharmacol.* 22:77–84 (1982).
22. F. von Bruchhausen (ed.). *Hagers Handbuch der pharmazeutischen Praxis. 5. Aufl.*, Springer Verlag Berlin, 1993.

23. W. F. Frishman. Atenolol and timolol, two new systemic b-adrenoceptor antagonists. *N. Engl. J. Med.* **306**:1456–1462 (1982).
24. J. E. F. Reynolds, (ed), *Martindale, The Extra Pharmacopoeia, 31st Edition*, The Royal Pharmaceutical Society London, 1996.
25. K. Lauritsen, L. S. Laursen, and J. Rask-Madsen. Clinical Pharmacokinetics of drugs used in the treatment of gastrointestinal diseases (Part1). *Clin. Pharmacokinet.* **19**:11–31 (1990).
26. L. Lemberger, R. F. Bergstrom, R. L. Wollen, N. A. Farid, G. G. Enas, and G. R. Aronoff. Fluoxetine: Clinical pharmacology and physiological disposition. *J. Clin. Psychiatry* **46**:14–19 (1985).
27. R. F. N. Mills, S. S. Adams, E. E. Cliffe *et al.* The metabolism of ibuprofen. *Xenobiotica* 3:589–598 (1973a).
28. R. A. Theodor, H.-J. Weimann, W. Weber *et al.* Absolute bioavailability of moxonidine. *Eur. J. Drug Metab. Pharmacokinet.* **16**:153–159 (1991).
29. B. Fulton, and K. L. Goa. Olanzapine A review of its pharmacological properties and therapeutic efficacy in the management of schizophrenia and related psychoses. *Drugs* **53**:281–298 (1997).
30. P. A. Routledge and D. G. Shand. Clinical pharmacokinetics of propranolol. *Clin. Pharmacokinet.* **4**:73–90 (1979).
31. M. H. Skinner, and T. F Blaschke. Clinical pharmacokinetics of rifabutin. *Clin. Pharmacokinet.* **28**:115–125 (1995).
32. J. C. Jensen. Clinical pharmacokinetics of terbinafine. *Clin. Exp. Dermatol.* **14**:110–113 (1989).
33. H. D. Langtry and D. M. Campoli-Richards. Zidovudin. *Drugs* **37**:407–450 (1989).
34. A. N. Wadworth and D. McTavish. Zopiclone A review of its pharmacological properties and therapeutic efficacy. *Drugs & Aging* **3**:441–459 (1993).

Absorption, Distribution, and Excretion of DJ-927, a Novel Orally Effective Taxane, in Mice, Dogs, and Monkeys

Chiho ONO,*[,a] Atsushi TAKAO,[b] and Ryo ATSUMI[a]

[a] *Drug Metabolism & Physicochemical Property Research Laboratory, Daiichi Pharmaceutical Co., Ltd.; 1–16–13 Kita-Kasai, Edogawa-ku, Tokyo 134–8630, Japan: and* [b] *Daiichi Pure Chemicals Co., Ltd.; 2117 Muramatsu, Tokai, Ibaraki 319–1182, Japan.* Received September 24, 2003; accepted December 9, 2003; published online December 16, 2003

DJ-927, currently undergoing Phase I clinical trial, is a new orally effective taxane with potent antitumor effects. The absorption, tissue distribution, and excretion of DJ-927 were investigated in mice, dogs, and monkeys after a single oral administration. After oral administration of [^{14}C]DJ-927, radioactivity was rapidly absorbed, with the C_{max} occurring within 1—2 h in all species. The blood and plasma radioactivity elimination was biphasic and species-dependent. Elimination half-life of plasma in dogs was much longer than those in monkeys or mice. In mice, radioactivity was rapidly distributed to all tissues except for the central nervous system, especially to adrenal glands, liver, pituitary glands, kidneys, lungs, and spleen. In all species, radioactivity was mainly excreted in feces. Following a single oral administration to mice, more than 80% of the radioactivity was excreted within 48 h; in dogs and monkeys, 80% of the radioactivity was excreted within 168 h. Urinary excretion was less than 7% of radioactive dose in all species. *In vitro* plasma protein binding of [^{14}C]DJ-927 in the mouse, dog, and monkey plasma ranged from 92—98%. These studies showed that, the novel oral taxane DJ-927 was rapidly absorbed in all three species when administered by the oral route. The long biological half-life and slow elimination of radioactivity were distinctive in particular, compared with commercial taxanes. DJ-927 (as parent compound and its metabolites) is widely distributed to tissues except the brain. These preclinical data are useful for the design of clinical trials of DJ-927 and also for their interpretation.

Key words DJ-927; oral taxane; pharmacokinetics; preclinical study

Taxanes are important anti-tumor drugs endowed with a unique mechanism of action: they inhibit microtubule disassembly.[1,2] The taxanes in current clinical use, paclitaxel (PTX) and docetaxel (DTX), are effective against a broad spectrum of human tumors, in particular, ovarian and breast carcinomas.[3] PTX and DTX are usually administered by i.v. infusion. However, for cancer therapy, oral administration of such cytotoxic agents is the preferred administration route because it is convenient for patients, reduces administration costs, and allows the use of more chronic treatment regimens.[4—6] Unfortunately, the bioavailability of orally administered PTX is very low,[7,8] and neither it nor orally administered DTX have shown efficacy in preclinical studies.[9] Metabolic instability and active efflux mediated by the P-glycoprotein, (P-gp) in the gut wall and liver are considered to be the major barriers to oral bioavailability.[10,11]

There are a number of important mechanisms that can explain the variable and/or low bioavailability. To improve oral bioavailability, it should be considered not only physicochemical property but also affinity for drug trasnsporter and/or metabolic stability in the intestine and/or liver (first pass effect). A new, orally active taxane derivative, DJ-927 (Fig. 1), with high solubility, a better safety profile, and more potent antitumor activity against multi-drug resistant (MDR) tumors than PTX or DTX has been found.[12] *In vitro* DJ-927 is more cytotoxic than other taxanes against a broad range of tumor cell lines, especially against P-gp expressing cells. Additionally, orally administered DJ-927 shows potent antitumor effects against several kinds of human solid tumors that were xenografted into nude mice, against which neither PTX nor DTX was effective.[12] These profiles suggest DJ-927 is well absorbed from the gut of tumor-bearing mice. Finally, preclinical pharmacologic and toxicologic studies of DJ-927 in several animal species did not present any evidence of drug-induced neurotoxicity or cardiotoxicity.[13] In this paper, the absorption, distribution, and excretion of ^{14}C-labeled DJ-927 ([^{14}C]DJ-927, Fig. 1) were investigated after a single oral administration to male mice to clarify the pharmacokinetic profile of DJ-927. Moreover, these studies of [^{14}C]DJ-927 was investigated in two other species commonly used in toxicologic evaluations, beagle dogs and cynomolgus monkeys.

MATERIALS AND METHODS

Chemicals and Reagent DJ-927, (−)-(1*S*,2*S*,3*R*,4*S*,5*R*,8*R*,9*S*,10*R*,13*S*)-4-acetoxy-2-benzoyloxy-9,10-[(1*S*)-2-(dimethylamino)ethylidenedioxy]-5,20-epoxy-1-hydroxytax-11-en-13-yl (2*R*,3*S*)-3-(*tert*-butoxycarbonylamino)-3-(3-fluoro-2-pyridyl)-2-hydroxypropionate was synthesized by Daiichi Pharmaceutical Co., Ltd. (Tokyo, Japan). ^{14}C-labeled DJ-927 ([^{14}C]DJ-927) was synthesized by Daiichi Pure Chemical Co., Ltd. (DPC; Tokyo, Japan), and had a specific radioactivity of 1.76 GBq/mmol. Its chemical structure and site of labeling are shown in Fig. 1. [^{14}C]DJ-927 was purified by HPLC to a radiochemical purity of more than 97% just before use. Other reagents and solvents used were of analytical

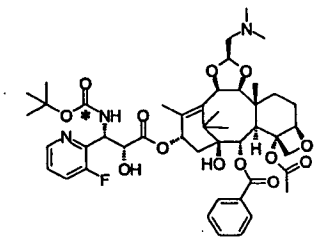

Fig. 1. Chemical Structure of DJ-927
The asterisk represents the ^{14}C labeling position.

* To whom correspondence should be addressed. e-mail: onoch74g@daiichipharm.co.jp

grade obtained commercially.

Animals Male mice were obtained from SLC Japan, Inc. (Shizuoka, Japan), and were used when they were 7 weeks old. Male beagle dogs were obtained from Toyota Tsusho Co. (Tokyo, Japan), and were used when they were 10—12 months old. Male cynomolgus monkeys were obtained from SLC Japan, Inc., and were used when they were 3 years old. The animals fasted for about 16 h before administration, and feedings resumed 4 h after administration. All animal experiments were performed in accordance with the in-house guidelines of the Institutional Animal Care and Use Committee of DPC.

Preparation of Dosing Solutions In all studies, McIlvaine buffer solution (0.2 M disodium hydrogen phosphate aqueous solution, 0.1 M citric acid aqueous solution, pH 4.0) was used as the vehicle for the dosing solution. [^{14}C]DJ-927 ethanol solution was taken and evaporated to dryness under a stream of nitrogen gas. The residue was dissolved in the vehicle to prepare the dosing solution. Solutions of [^{14}C]DJ-927 were prepared at concentrations of 0.4 mg/ml for mice, 0.6 mg/ml for dogs, and 0.5 mg/ml for monkeys.

Absorption and Excretion Study in Mice [^{14}C]DJ-927 was orally administered at a dose of 4 mg/kg to male mice for a single-dose pharmacokinetic and excretion study. Blood samples were collected from the inferior *vena cava* of mice under ether anesthesia at 0.5, 1, 2, 4, 8, 12, 24, 48, 72, 96, 120, 144, and 168 h after administration into heparinized microtubes. A portion of each blood sample was used for direct measurement of radioactivity, and plasma samples were obtained by centrifugation of each remaining sample at 8000 ***g*** for 5 min at 4 °C. For the excretion studies, three mice were individually housed in metabolic cages after single oral administration. Samples of urine and feces samples were collected during the following periods up to 168 h after dosing: 0—4, 4—8, 8—24, and every 24 h thereafter for urine; and 0—24 and every 24 h thereafter for feces. The fecal samples were homogenized with distilled water. After sample collection, an overdose of diethylether was used to sacrifice the animals. The carcasses were placed in 200 ml of 0.5 N sodium hydroxide and 30 ml of toluene and then homogenized with water. All samples were stored at −20 °C until analyzed.

Absorption and Excretion Study in Dogs [^{14}C]DJ-927 was orally administered at a dose of 0.6 mg/kg to male dogs for the single-dose pharmacokinetic and excretion study. Blood samples were collected from the abdominal aorta at 0.25 0.5, 1, 2, 4, 8, 12, 24, 48, 72, 96, 120, 144, 168 h, and every 24 h periods up to 336 h after administration into a vacuum tube containing heparin. A portion of each blood sample was used for direct measurement of radioactivity, and plasma samples were obtained by centrifugation of each remaining sample at 1800 ***g*** for 15 min at 4 °C. For the excretion studies, three dogs were individually housed in metabolic cages after single oral administration. Samples of urine and feces were collected during the following periods up to 336 h after dosing: 0—4, 4—8, 8—24 and every 24 h thereafter for urine; and 0—8, 8—24, and every 24 h thereafter for feces. The fecal samples were homogenized with distilled water. After sample collection, each dog was sacrificed by exsanguination from the abdominal aorta while under anesthesia induced by an intramuscular administration of ketamine hydroxide and xylazine hydroxide mixture. Tissues were collected from animal at the last time point (336 h) to determine the concentration and distribution of radioactivity in the tissues and to calculate the residual radioactivity in carcasses. The metabolic cages were washed with water, and radioactivity in washings was also determined.

Absorption and Excretion Study in Monkeys [^{14}C]DJ-927 was orally administered at a dose of 1 mg/kg to male monkeys for a single-dose pharmacokinetic and excretion study. Blood samples were collected from the abdominal aorta at 0.25 0.5, 1, 2, 4, 8, 12, 24, 48, 72, 96, 120, 144, 168 h, and every 24 h periods up to 336 h after administration into a vacuum tube containing heparin. A portion of each blood sample was used for direct measurement of radioactivity, and plasma samples were obtained by centrifugation of each remaining sample at 1800 ***g*** for 15 min at 4 °C. For the excretion studies, the monkeys were individually housed in metabolic cages after single oral administration. Samples of urine and feces were collected during following periods up to 336 h after dosing: 0—4, 4—8, 8—24, and every 24 h thereafter for urine, and 0—8, 8—24, and every 24 h thereafter for feces. The fecal samples were homogenized with distilled water. After sample collection, each monkey was sacrificed by exsanguinations from the abdominal aorta while under anesthesia induced by an intramuscular administration of a ketamine hydroxide. Tissues were collected at the last time point (336 h) to determine the concentration and distribution of radioactivity in the tissues and to calculate the residual radioactivity in carcasses. The metabolic cages were washed with water, and radioactivity in washings was also determined.

Tissue Distribution Study in Mice After oral administration of [^{14}C]DJ-927 to male mice at dose of 4 mg/kg, mice for each time point were anesthetized with ether and bleeding from the inferior *vena cava* 1, 8, 24, 72, and 168 h after administration. Immediately after blood collection, the tissues and organs indicated in Table 2 were removed and the wet mass of each was measured. The liver, small intestine, and large intestine were homogenized in a 2-fold volume (w/v) of saline. The other samples and homogenates described above were dissolved in 2 ml of the tissue solubilizer Soluene-350™ while heating. The concentration and percentage distribution of radioactivity in these tissues and tissue homogenates were then determined.

In Vitro* Distribution to Blood Cells and Plasma Protein Binding** The partitioning of DJ-927 into erythrocytes was determined by incubating the radiolabeled compound with fresh, heparin-treated whole blood from mice, dogs, or monkeys. [^{14}C]DJ-927 was added to blood from each animal to yield three concentrations of 25, 50, and 500 ng/ml, and the samples were incubated at 37 °C for 5 min. Plasma was separated by centrifugation (8000 ***g, 4 °C, 5 min), and aliquots were taken for scintillation counting. The ratio of the radioactivity in erythrocytes to that in blood (RBC) was calculated from the following equation:

$$\mathrm{RBC}\,(\%)=[1-(1-H_t)/R_b]\times 100$$

where H_t is the hematocrit and R_b is the ratio of the blood to the plasma concentration.

The binding of DJ-927 to plasma protein was determined by incubating the compound with pooled plasma from mice, dogs, and monkeys in the concentration range of 0.1—

10 μg/ml. [^{14}C]DJ-927 was added to plasma samples and incubated for 15 min at 37 °C. An aliquot of each sample was taken to determine total radioactivity (concentration of radioactivity in plasma, C_p). Another aliquot of each sample was transferred to 0.23PC tubes and centrifuged at 200000 g for 16 h at 4 °C. An aliquot of each supernatant (concentration of radioactivity in the unbound fraction, C_f) was taken for scintillation counting. The ratio of protein binding was calculated from the following equation:

$$\text{protein binding ratio (\%)} = (1 - C_f/C_p) \times 100$$

Determination of Radioactivity in the Samples Radioactivity in the samples was measured using an LSC (2700TR, Packard; Meriden, CT, U.S.A.). The radioactivity of samples in glass vials was measured, and radioactivity (dpm) was counted for 2 min after addition of a scintillator. The counting efficiency was automatically corrected using an external standard. Samples from control animals treated by the same methods were used to obtain background counts. The radioactivity detection limit was defined as twice the value of the corresponding background count. The radioactive concentration in blood, plasma, and each tissue sample was calculated as the equivalent concentration of [^{14}C]DJ-927 from the specific radioactivity of each dosing solution. The excreted radioactivity in urine and feces is expressed as a percentage of the administered radioactivity.

Pharmacokinetic Calculations A noncompartmental methods was used to determine the pharmacokinetics of DJ-927. The maximum plasma and blood concentration (C_{max}) and the time (t_{max}) to reach this value were determined from the observed highest concentration and the time of its occurrence, respectively. The concentrations of radioactivity in plasma and blood were converted to logarithms and plotted against time. TOPFIT computer software (ver. 2, Gustav Fischer Verlag, Stuttgart, Germany) was used to calculate the terminal elimination half-life ($t_{1/2}$) and the area under the concentration–time curve (AUC) for plasma and blood.

RESULTS

Blood and Plasma Radioactivity Concentration–Time Profiles in Mice, Dogs, and Monkeys Mean plasma and blood levels of radioactivity after a single oral administration of [^{14}C]DJ-927 to male mice, dogs, and monkeys are shown in Fig. 2 and the pharmacokinetic parameters are shown in Table 1. After a single oral administration of [^{14}C]DJ-927 to male mice at a dose of 4 mg/kg, the radioactive concentration of in plasma (mean of three mice at each time point) was a maximum (C_{max}) of 545.0 ng eq./ml at 2 h, and then declined

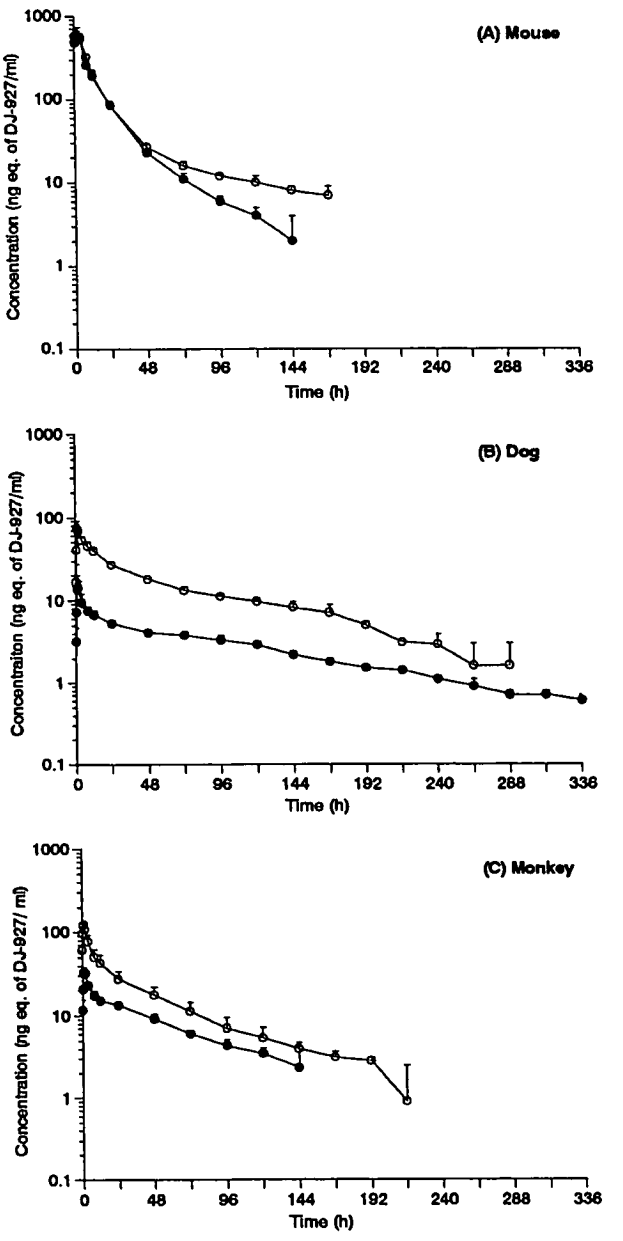

Fig. 2. Mean Blood (○) and Plasma (●) Levels of Radioactivity after a Single Oral Administration of [^{14}C]DJ-927 to Male Mice at a Dose of 4 mg/kg (A), to Male Dogs at a Dose of 0.6 mg/kg (B) and to Male Monkeys at a Dose of 1 mg/kg (C)

Each point with bar represents the mean±S.D. from three animals.

Table 1. Pharmacokinetic Parameters of [^{14}C]DJ-927 in Blood and Plasma after a Single Oral Administration of [^{14}C]DJ-927 at Dose of 4 mg/kg to Mice, 0.6 mg/kg to Dogs, and 1 mg/kg to Monkeys

PK parameters	Mouse		Dog		Monkey	
	Blood[a)]	Plasma[a)]	Blood	Plasma	Blood	Plasma
t_{max} (h)	1	2	1.0±0.0	2.0±1.0	1.0±0.0	2.0±1.0
C_{max} (ng eq./ml)	581.0	545.0	75.0±14.6	15.4±4.8	120.1±18.0	34.7±3.8
$t_{1/2}$ (d)	2.7	1.2	3.0±0.4	4.0±0.4	2.1±0.1	2.2±0.4
$AUC_{0-\infty}$ (μg eq.·h/ml)	10.1	8.3	3.5±0.09	0.9±0.05	3.0±0.7	1.4±0.2

Each value represents the mean±S.D. (n=3). *a*) PK parameters were calculated from the mean values of concentration at each time point.

Table 2. Cumulative Excretion of Radioactivity in Urine and Feces after a Single Oral Administration of [^{14}C]DJ-927 at a Dose of 4 mg/kg to Mice, 0.6 mg/kg to Dogs, and 1 mg/kg to Monkeys

Time period (h)	% of administered dose					
	Mouse		Dog		Monkey	
	Urine	Feces	Urine	Feces	Urine	Feces
0—4	0.4±0.3	—[a]	0.1±0.2	—[a]	1.4±1.4	—[a]
0—8	2.2±0.7	—[a]	0.1±0.2	0.0±0.0	2.1±1.5	0.0±0.0
0—24	5.1±0.7	68.0±3.8	1.4±0.3	28.5±6.3	3.1±1.6	6.5±7.8
0—48	5.9±0.9	86.1±2.9	2.3±0.3	46.6±3.8	3.9±1.6	32.0±25.7
0—72	6.1±1.0	89.7±3.2	2.9±0.3	60.5±3.5	4.3±1.6	62.5±16.4
0—96	6.2±1.0	90.9±3.1	3.4±0.3	68.8±1.4	4.6±1.6	78.4±7.4
0—120	6.3±1.0	91.6±3.1	3.7±0.3	75.3±2.3	4.8±1.6	84.2±4.9
0—144	6.4±1.2	92.2±3.0	4.1±0.3	78.8±1.4	4.9±1.6	87.4±4.2
0—168	6.4±1.1	92.5±2.9	4.3±0.3	83.0±1.0	5.0±1.6	89.2±4.1
0—192			4.4±0.3	85.3±0.9	5.0±1.5	90.1±3.9
0—216			4.6±0.3	86.7±1.1	5.0±1.5	90.7±3.8
0—240			4.7±0.3	88.0±0.6	5.1±1.6	91.0±3.8
0—264			4.8±0.3	89.4±0.3	5.1±1.6	91.3±3.7
0—288			4.8±0.3	90.2±0.3	5.1±1.5	91.4±3.7
0—312			4.9±0.2	90.7±0.3	5.1±1.5	91.5±3.7
0—336			4.9±0.2	91.3±0.4	5.1±1.5	91.6±3.7

Each value represents the mean±S.D. (n=3). *a*) Not collected.

biphasically with a terminal biologic half-life ($t_{1/2}$) of 1.2 d (Fig. 2A, Table 1). The radioactive concentration in whole blood was similar to the level in plasma, and disappeared biphasically with $t_{1/2}$ of 2.7 d. The $AUC_{0-\infty}$ values for plasma and blood were 8.3 and 10.1 μg eq.·h/ml, respectively. After a single oral administration of [^{14}C]DJ-927 to male dogs at a dose of 0.6 mg/kg, the radioactive concentration in plasma (mean of three dogs) was a C_{max} of 15.4 ng eq./ml at 2 h and disappeared biphasically with $t_{1/2}$ of 4.0 d (Fig. 2B, Table 1). The plasma $AUC_{0-\infty}$ was 0.9 μg eq.·h/ml. The radioactive concentration in blood was much higher than that in plasma. The blood $AUC_{0-\infty}$ was 3.5 μg eq.·h/ml. The calculated RBC values were 76.9% to 91.3% up to 288 h after administration (data not shown). After a single oral administration of [^{14}C]DJ-927 to male monkeys at a dose of 1 mg/kg, the radioactive concentration in the plasma (mean of three monkeys) reached a C_{max} (34.7 ng eq./ml) at 2 h after administration (Fig. 2C, Table 1). The $t_{1/2}$ was 2.2 d. The plasma $AUC_{0-\infty}$ was 1.4 μg eq.·h/ml. The C_{max} (120.1 ng eq./ml) of blood at 1 h after administration was about 4-fold higher than that of plasma. The blood $AUC_{0-\infty}$ was 3.0 μg eq.·h/ml. The calculated RBC values were 50.5% to 88.3% by 144 h after administration (data not shown).

Excretion in Mice, Dogs, and Monkeys Cumulative excretions of radioactivity in urine and feces of mice, dogs, and monkeys after a single oral administration of [^{14}C]DJ-927 are shown in Table 2. In mice, the radioactivity was mainly excreted in feces, of which 68.0±3.8% (mean±S.D., n=3) of the administered amount (4 mg /kg) was excreted during the initial 24 h after administration and 92.5±2.9% was excreted by 168 h after administration. The urinary excretion was very low, only 6.4% up to 168 h after administration. The excretion of radioactivity in the expired air was 1.3% by 48 h, and then no radioactivity was excreted in expired air (data not shown). The radioactivity remaining in the carcass was 0.6% at 168 h after administration. The total excretion of radioactivity in the excreta was 100.1% at 168 h after administration. In contrast, the radioactivity excreted in the feces of dogs was 28.5±6.3%, and in the urine was 1.4±0.3% over the first 24 h after administration (0.6 mg/kg). Over 336 h, 91.3±0.4% of the administered dose was excreted in feces and 4.9±0.2% of the administered dose excreted in urine. The total amount of radioactivity excreted was 96.2±0.4% of the administered dose at 336 h, and the radioactivity. As in mice, fecal excretion was also the main route, but dogs excreted radioactivity more slowly than mice did. The percentages of radioactivity distributed in the liver, skin, skeletal muscles, fat, bile in the gall bladder, and gastro-intestinal contents ranged from 0.1 to 0.8% of the administered dose at the end of the study period (data not shown). In monkeys, the amount of radioactivity excreted in the feces was 6.5±7.8% of the administered dose and in the urine was 3.1±1.6% over the first 24 h after administration (1 mg/kg). A total of 96.7±2.6% administered dose was recovered in the excreta, of which 91.6±3.7% was in the feces and 5.1±1.5% was in the urine, by 336 h after administration. The percentages of radioactivity distributed in the skeletal muscles, liver, and gastro-intestinal contents were 0.1—0.2% of the administered dose at the end of the study period (data not shown). Fecal excretion was also the main route, as previously described for mice and dogs; moreover, the rate of excretion in monkeys was slower than the rate in mice, but not as slow as rate in dogs.

Tissue Distribution in Mice The concentration of radioactivity in tissues after a single oral administration of [^{14}C]DJ-927 to mice is shown in Table 3. The radioactivity in all the tissues except for the brain was higher than in plasma at 1 h after administration. Most tissues showed their highest concentration at 1 h after administration, indicating that [^{14}C]DJ-927 rapidly distributes to tissues. The highest concentration of radioactivity was observed in the adrenal glands (11410 ng eq./g), followed by the liver (11269 ng eq./g), pituitary gland (10431 ng eq./g), kidneys (9324 ng eq./g), and lungs (8762 ng eq./g) at 1 h after oral administration. Approximately 99% of the radioactivity was eliminated by 168 h

Table 3. Tissue Distribution of Radioactivity after a Single Oral Administration of [^{14}C]DJ-927 to Mice at a Dose of 4 mg/kg

Tissue	Radioactivity concentration (ng eq. of DJ-927/g or ml)				
	1 h	8 h	24 h	72 h	168 h
Plasma	455±161	268±30	79±12	11±0	1±1
Blood	491±126	309±20	76±7	19±2	9±0
Cerebrum	54±24	104±9	81±21	40±2	22±3
Cerebellum	86±40	121±33	74±13	24±2	9±2
Pituitary gland[a)]	10431	15980	3490	169	0
Eyeball	462±220	842±100	467±95	122±1	25±2
Harderian gland	3564±1708	4388±270	713±127	49±6	3±5
Thyroid gland[a)]	5341	4750	564	91	46
Mandibular gland	4914±2322	5122±363	932±134	67±3	14±2
Mandibular lymph node	3143±2164	3730±483	399±65	0±0	0±0
Thymus	1563±838	3611±575	1337±405	37±6	3±6
Heart	3558±861	1879±27	211±21	25±2	7±3
Lung	8762±2223	4761±60	612±50	71±5	19±2
Liver	11269±2006	10482±348	4940±498	1188±57	250±30
Kidney	9324±3203	5663±282	831±158	66±3	20±2
Adrenal gland[a)]	11410	3694	511	73	0
Spleen	8060±2787	6243±693	601±91	47±4	12±3
Pancreas	4807±2233	3501±46	717±118	48±3	10±1
Fat	4935±2477	1647±222	162±25	12±1	6±1
Skeletal muscle	1199±548	946±39	132±17	13±1	5±1
Skin	733±291	1038±172	284±48	17±4	6±1
Bone marrow[a)]	4765	10016	890	51	0
Aorta[a)]	4584	3539	490	30	0
Testis	85±50	336±56	392±162	146±14	44±4
Epididymis	552±267	1534±237	734±124	127±23	31±3
Prostate gland[a)]	1171	1879	866	89	10
Stomach	3246±340	2233±311	512±37	41±5	13±3
Small intestine	5878±957	3557±662	682±103	31±3	14±5
Large intestine	1429±771	3268±824	726±40	34±4	13±5
Urinary bladder	1250±846	2363±571	685±33	45±17	3±5

Each value represents the mean±S.D. (n=3). *a*) Pooled samples of three animals.

Table 4. *In Vitro* Distribution to Blood Cells Varying Concentrations of [^{14}C]-DJ-927 in Mouse, Dog, and Monkey Blood

Concentration (ng/ml)	RBC (%)		
	Mouse	Dog	Monkey
25	53.1±1.7	86.3±3.3	77.0±2.9
50	—[a)]	87.3±3.9	76.8±3.5
500	52.9±0.5	—[a)]	—[a)]
Mean[b)]	53.0	86.8	76.9

Each value represents the mean±S.D. of three experiments. *a*) Not determined. *b*) Each value represents the mean of two concentrations.

Table 5. *In Vitro* Protein Binding Varying Concentrations of [^{14}C]-DJ-927 in Mouse, Dog, and Monkey Plasma

Concentration (μg/ml)	Protein binding ratio (%)		
	Mouse	Dog	Monkey
0.1	97.8±0.22	94.9±0.46	91.8±0.24
1	98.5±0.23	95.1±0.25	92.9±0.2
5	98.1±0.12	95.1±0.09	92.5±0.04
10	97.4±0.04	94.8±0.27	92.7±0.06
Mean±S.D.[a)]	98.0±0.35	95.0±0.12	92.5±0.56

Each value represents the mean±S.D. of three experiments. *a*) Each value represents the mean±S.D. of four concentrations.

after dosing. Similar tissue distribution patterns were found in whole body autoradiography (data not shown).

***In Vitro* Distribution to Blood Cells and Plasma Protein Binding** *In vitro*, the distribution of radioactivity into erythrocytes (RBC) were 53.0%, 86.8%, and 76.9% in mice, dogs, and monkeys in a three concentration range of 25, 50, and 500 ng/ml (Table 4). RBC for dogs was higher than the value for mice and monkeys, which was consistent with *in vivo* results for these animals. This binding was reversible.

The plasma protein binding of [^{14}C]DJ-927 was similar in the three species studied, with mean percent bound values in mice, dogs, and monkeys plasma were 98.0%, 95.0%, and 92.5%, respectively (Table 5). [^{14}C]DJ-927 was highly bound to plasma proteins but concentration independently over the concentration range from 0.1 to 10 μg/ml.

DISCUSSION

The taxanes, PTX and DTX are widely used hydrophobic antineoplastic agents that demonstrate significant antitumor activity against a broad spectrum of human tumors such as refractory ovarian, breast, and non-small-cell lung carcinomas.[3,14] Unfortunately, neither agent can be used orally, because of low oral bioavailability.[7—9] The poor absorption characteristics of PTX appear to be related to the presence of the P-glycoprotein (P-gp) drug efflux transport protein in intestinal cells,[8,10,15] since the systemic exposure of orally administered PTX in mice is significantly enhanced by coadministration of a P-gp blocker such as PSC833 or cyclosporin A.[16,17] However, in regard to DTX, it is suggested that efficient first-pass metabolism in gut and liver, probably

by CYP3A enzymes in mice, is the most important factor determining its low bioavailability.[18]

P-gp is an energy-dependent multi-drug efflux pump that was initially discovered by its ability to confer multidrug resistance (MDR).[19] P-gp is found not only tumor cells but also in healthy tissues and organs such as kidneys, liver adrenal glands, and intestines, where it is predominantly located on the apical side of epithelial cells.[20,21] Recently, many reports have shown that P-gp is involved in intestinal absorption of drugs.[22] On the other hand, CYP is the main oxidative drug metabolizing enzyme system. Especially, CYP3A subfamily is the predominant drug metabolizing enzymes and accounts for approximately 30% of hepatic CYP and more than 70% of intestinal CYP expression.[23] CYP 3A is responsible for significant first-pass metabolism of orally administered drugs. It is reported that many substrates for P-gp and CYP3A are overlapping and both proteins are responsible for the poor bioavailability observed for many orally administered drugs.[22,23] These observations suggest that oral cytotoxic agents would be natural targets of this elimination system, and that drugs designed to elude capture by this system would have better bioavailability. In our preliminary studies, oral bioavailability of DJ-927 was 107% in mice, 47% in dogs, and 63% in monkeys after intravenous and oral administration of non-labeled DJ-927.[24] The bioavailability of DJ-927 exhibits a species difference. Several PK studies indicate that DJ-927 is highly permeable in gut lumen. Dogs are considered to have extensive first-pass metabolism (unpublished data). In addition, *in vitro* study using human liver microsome revealed that metabolic rate of DJ-927 is slow and that CYP 3A family is the responsible enzyme for its metabolism.[24] Intrinsic clearance ($V_{max}/K_{m,app}$) of DJ-927 major metabolite was scaled up to predict the human clearance. The human clearance is estimated to be very low. In pharmacologic studies, DJ-927 is more effective than PTX and DTX against P-gp-expressing cells lines.[12] These results suggest that DJ-927 is a poor substrate for P-gp and CYP3A and that it escapes biological barriers in the gut and liver.

Other factors for low bioavailability are considered physicochemical properties such as solubility, pK_a of compound. PTX has very poor solubility in water, therefore, the commercial injection formulation consists of a sterile solution of the drug in Cremophor EL and hydrated alcohol to dissolve PTX.[25] Cremophor EL brings a number of pharmacologic, pharmacokinetic, and pharmaceutic drawbacks such as hypersensitivity reactions, nonlinear PK and difficulty of handling.[26—28] Low solubility also causes variability in the extent and rate of absorption. DJ-927 is relatively soluble in water especially in acidic condition. In the present study, oral formulation of [^{14}C]DJ-927 was made as solutions in McIlvine buffer (pH 4.0). The variability in the *AUC*, which is often a problem with oral chemotherapy, was small in dogs and monkeys (Table 1).

In the present study, we clarified absorption, distribution, and excretion of DJ-927 in the three kinds of species to compare the other taxanes. After a single oral administration of [^{14}C]DJ-927 to mice, dogs, and monkeys, the radioactivity was rapidly absorbed, with the C_{max} occurring within 1—2 h after oral administration in all animals, and the elimination of radioactivity from plasma was biphasic and species-dependent (Fig. 2). The elimination half-life in dogs was much longer than those in the monkeys or mice (Table 1). In mice, the radioactivity was rapidly distributed throughout all tissues except for the central nervous system (CNS), especially to the adrenal glands, liver, pituitary glands, kidneys, lungs, and spleen (Table 2); this is similar to the pattern observed for other taxanes.[30] The radioactivity was mainly excreted in the feces in all species with less than 7% excreted in the urine as same as other taxanes (Table 3). DJ-927 highly binds to plasma proteins concentration-independently, which is also observed for other taxanes.[29,30] A slightly higher protein binding ratio was observed in mouse plasma (98.0%) than in dog (95.0%) or monkey plasma (92.5%) (Table 5). In short, DJ-927 has similar pharmacokinetic characteristics to both taxanes in current clinical use, which includes elimination route, high plasma protein binding, and rapid distribution to most tissues except for the CNS.[7,9,29,30] However, PTX and DTX have short terminal biologic half-lives in plasma of approximately 1 h, and they are largely inactive when administered orally.[9] In contrast, DJ-927 has quite different characteristics; the pharmacokinetics results from the present study show that DJ-927 related radioactivity has a very long biologic terminal half-life after oral administration, especially in dogs and monkeys.

In conclusion, the pharmacokinetic profiles of DJ-927 were characterized after oral administration of the radiolabeled drug to the three species. The results of present study show that, in contrast to both commercially available taxanes PTX and DTX, the novel taxane DJ-927 is well absorbed in all three species and have long biological half lives especially dogs and monkeys when administered orally. DJ-927 is rapidly distributed to almost tissues except CNS but may not recognize MDR. DJ-927 is currently investigated in a Phase I clinical trial according to a global develop plan. PII clinical trials are planned in Europe and the USA. It is expected that the high oral bioavailability of this novel analog will lead to high pharmacologic efficacy.

REFERENCES AND NOTES

1) Gueritte-Voegelein F., Guenard D., Lavelle F., Le Goff M. T., Mangatal L., Potier P., *J. Med. Chem.*, **34**, 992—998 (1991).
2) Horwitz S. B., Cohen D., Rao S., Ringel I., Shen H.-J., Yang C.-P. H., *J. Natl. Cancer Inst. Monogr.*, **15**, 55—61 (1993).
3) Rowinsky E. K., *Annu. Rev. Med.*, **48**, 353—374 (1997).
4) DeMario M. D., Ratin M. J., *J. Clin. Oncol.*, **16**, 2557—2567 (1998).
5) Liu G., Franssen E., Fitch M. I., Warner E., *J. Clin. Oncol.*, **15**, 110—115 (1997).
6) Malingre M. M., Beijnen J. H., Schellens J. H. M., *Investigational New Drugs*, **19**, 155—162 (2001).
7) Eiseman J. L., Eddington N. D., Leslie J., MacAuley C., Sentz D. L., Zuhowski M., Kujawa J. M., Young D., Egorin M. J., *Cancer Chemother. Pharmacol.*, **34**, 465—471 (1994).
8) Sparreboom A., van Asperen J., Mayer U., Schinkel A. H., Smit J. W., Meijer D. K. F., Borst P., Nooijen W. J., Beijnen J. H., van Tellingen O., *Proc. Natl. Acad. Sci. U.S.A.*, **94**, 2031—2035 (1997).
9) Bissery M.-C., Nohynek G., Sanderink G.-J., Lavelle F., *Anti-Cancer Drugs*, **6**, 339—368 (1995).
10) Schellens J. H. M., Malingre M. M., Kruijtzer C. M., Bardelmeijer H. A., van Tellingen O., Schinkel A. H., Beijnen J. H., *Eur. J. Pharm. Sci.*, **12**, 103—110 (2000).
11) Shirakawa K., Takara K., Tanigawara Y., Aoyama N., Kasuga M., Komada F., Sakaeda T., Okumura K., *Jpn. J. Cancer Res.*, **90**, 1380—1386 (1999).
12) Shionoya M., Jimbo T., Kitagawa M., Soga T., Tohgo A., *Cancer Sci.*, **94**, 459—466 (2003).
13) Tohgo A., Shionoya M., Iwahana M., Uesugi Y., Jimbo T., Soga T.,

Proc. Am. Assoc. Cancer Res., **43**, 790 (2002).
14) Eisenhauer E. A., Vermorken J. B., *Drugs*, **55**, 5—30 (1998).
15) Terao T., Hisanaga E., Sai Y., Tamai I., Tsuji A., *J. Pharm. Pharmacol.*, **48**, 1083—1089 (1996).
16) Van Asperen J., Van Tellingen O., Sparreboom A., Schinkel A. H., Borst P., Nooijen W. J., Beijnen J. H., *Br. J. Cancer*, **76**, 1181—1183 (1997).
17) van Asperen J., van Tellingen O., van der Valk M. A., Rozenhart M., Beijnen J. H., *Clin. Cancer Res.*, **4**, 2293—2297 (1998).
18) Bardelmeijer H. A., Ouwehand M., Buckle T., Huisman M. T., Schellens J. H., Beijnen J. H., van Tellingen O., *Cancer Res.*, **62**, 6158—6164 (2002).
19) Chin K. V., Pastan I., Gottesman M. M., *Adv. Cancer Res.*, **60**, 157—180 (1993).
20) Thiebaut F., Tsuruo T., Hamada H., Gottesman M. M., Pastan I., Willingham M. C., *Proc. Natl. Acad. Sci. U.S.A.*, **84**, 7735—7738 (1987).
21) Van Asperen J., Van Tellingen O., Beijnen J. H., *Pharmacol. Res.*, **37**, 429—435 (1998).
22) Wacher V. J., Salphati L., Benet L. Z., *Adv. Drug Deliv. Rev.*, **46**, 89—102 (2001).
23) Wacher V. J., Wu C.-Y., Benet L. Z., *Mol. Carcinog.*, **13**, 129—134 (1995).
24) Ono C., Takao A., Hayashi K., Atsumi R., *Proc. Am. Assoc. Cancer Res.*, **43**, 790 (2002).
25) Adams J. D., Flora K. P., Goldspiel B. R., Wilson J. W., Arbuck S. G., Finley R., *J. Natl. Cancer Inst. Monogr.*, **15**, 141—147 (1993).
26) Nannan Pandy V. R., Huizing M. T., ten Bokkel Huinink W. W., Vermorken J. B., Beijnen J. H., *Clin. Drug Invest.*, **14**, 418—427 (1997).
27) Sparreboom A., van Tellingen O., Nooijen W. J., Beijnen J. H., *Cancer Res.*, **56**, 2112—2115 (1996).
28) van Tellingen O., Huizing M. T., Panday V. R., Schellens J. H., Nooijen W. J., Beijnen J. H., *Br. J. Cancer*, **81**, 330—335 (1999).
29) Clarke S. J., Rivory L. P., *Clin. Pharmacokinet.*, **36**, 99—114 (1999).
30) Sparreboom A., van Tellingen O., Nooijen W. J., Beijnen J. H., *Anti-Cancer Drugs*, **9**, 1—17 (1998).

Review TRENDS in Pharmacological Sciences Vol.26 No.4 April 2005

Techniques: Application of systems biology to absorption, distribution, metabolism, excretion and toxicity

Sean Ekins, Yuri Nikolsky and Tatiana Nikolskaya

GeneGo, 500 Renaissance Drive, Suite 106, St Joseph, MI 49085, USA

It is widely recognized that either predicting or determining the absorption, distribution, metabolism, excretion and toxicity (ADME/Tox) properties of molecules helps to prevent the failure of some compounds before they reach the clinic. Consequently, there has been considerable research into developing better *in silico*, *in vitro* and *in vivo* methods and models. Toxicogenomics, proteomics, metabonomics and pharmacogenomics represent the latest experimental approaches that can be combined with high-throughput molecular screening of targets to provide a view of the complete biological system that is modulated by a compound. The functional interpretation and relevance of these complex multidimensional data to the phenotype observed in humans is the focus of current research in toxicology. Multiple content databases, data mining and predictive modeling algorithms, visualization tools, and high-throughput data-analysis solutions are being integrated to form systems-ADME/Tox. In this review, we focus on the most recent advances and applications in this area.

An introduction to systems-ADME/Tox

In our quest to cure important diseases we encounter the complexity of the whole organism. At the molecular level, a coordinated system of transporters, channels, receptors and enzymes act as gatekeepers to foreign molecules; this system affects the absorption, distribution, metabolism, excretion and toxicity (ADME/Tox) of a molecule in humans (Figure 1). Understanding the interactions between small molecules and their molecular targets should improve our ability to predict the toxic consequences that are responsible for the withdrawal of many marketed drugs and late-stage failures of drugs in development [1].

The focus is now on preclinical ADME/Tox studies, but the complexities of different model systems mean that better predictive approaches are needed [2], preferably based purely on molecular structure [3,4]. Accurate predictions of toxicity mechanisms are complicated because the whole organism comprises thousands of endobiotic and xenobiotic molecules that interact in different cellular organelles and tissues. Species differences in protein expression and ligand specificity should also be considered. Methods are needed that account for the complexity of the biological data and enable prediction of the complete system, including metabolic, regulatory, signaling and transport processes [5,6]. Systems biology uses the relationships between all elements rather than approaching them separately, and attempts to unite biological fields [7]. This approach can be taken from either the 'top down' (by using a conceptual framework to integrate data) or the 'bottom up' (by combining individually modeled biochemical processes) [8]. Interpreting ADME/Tox in the systems context might improve our understanding and, ultimately, predictions of toxicity. Potentially, the perturbing effect of a molecule on the complete biological system can be observed either experimentally, using high-throughput screening against many proteins, or theoretically, using computational models [9]. This should enable an understanding of the effects of binding to multiple proteins simultaneously. The iterative approach of data generation and modeling cycles can create dynamic hypotheses with broader applications than static models. Systems-ADME/Tox requires the collection of high-throughput data, including global gene-expression, protein content and metabolic profiles for the same samples plus genetic, clinical and phenotypic data. To date, empirical data have been used to build computational models and 'score' many virtual molecules for enzyme inhibition [10]. These computational predictions require multidimensional analysis to target affinity and improve the efficiency of lead selection [11]. Computational predictions might also be used as input parameters for systems-biology models to quantitatively predict clearance or molecule disposition.

In this review, we describe the integration and relevant applications of several types of biological data, databases, computational algorithms and predictive methods. We illustrate that the systems-ADME/Tox approach can use data from all experiments and computational methods to provide a deeper understanding of the effects of xenobiotic and endobiotic molecules on the recursive human ADME/Tox properties.

OMICS data and their integration

Presently, in addition to high-throughput screening assays for binding to receptors and other proteins of interest, much data generated in at least four 'OMICS'

Corresponding author: Ekins, S. (sean@genego.com).

Available online 3 March 2005

 0165-6147/$ - see front matter doi:10.1016/j.tips.2005.02.006

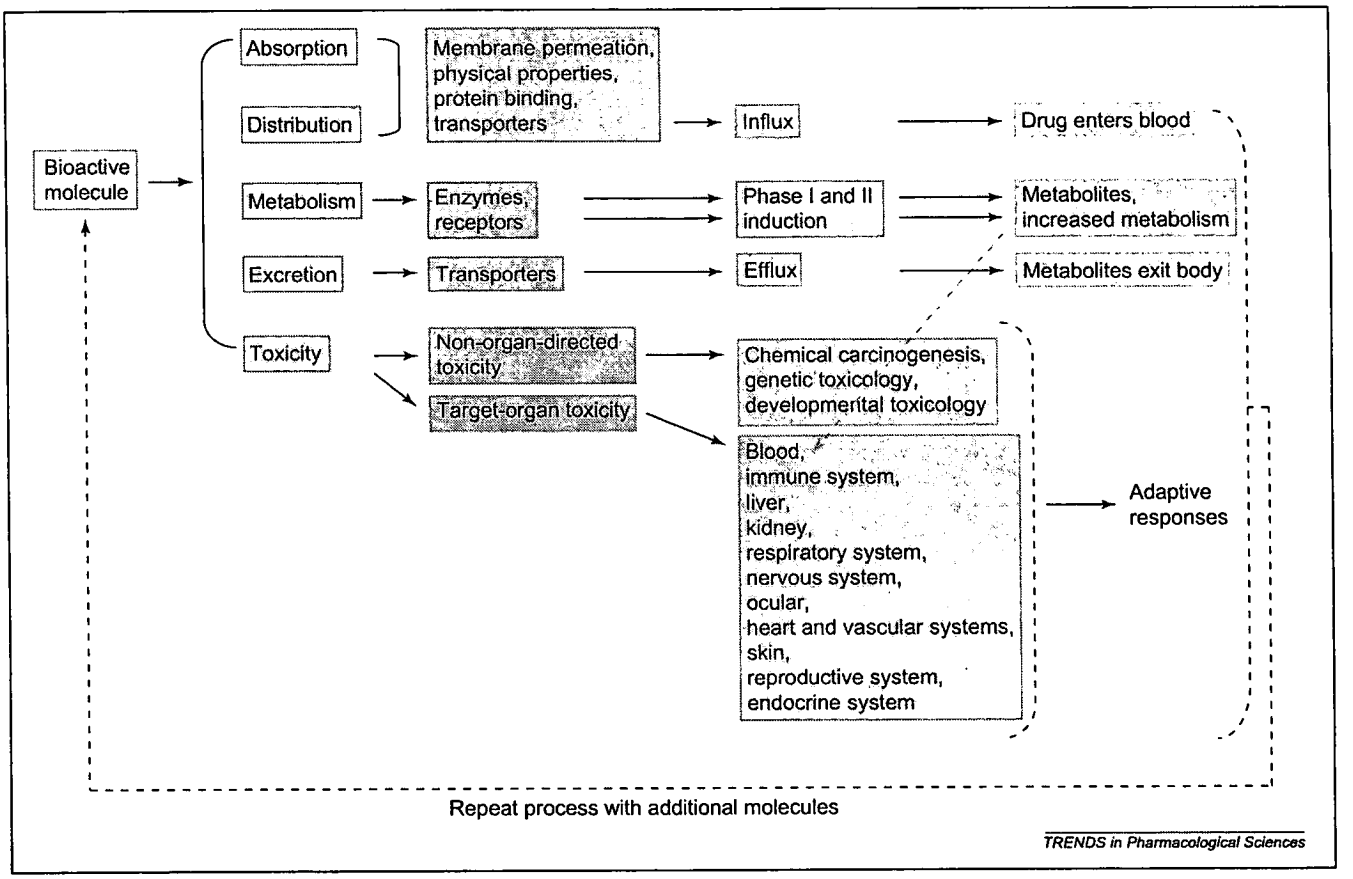

Figure 1. The iterative ADME/Tox optimization process. This figure demonstrates that a bioactive molecule is required to possess many favorable ADME/Tox properties before it can become a drug, and indicates the multidimensional nature of drug discovery. The proteins and endpoint associated with each ADME/Tox function are outlined. Adaptive responses represent the transcriptional and post-transcriptional effects following a toxic insult. Solid arrows represent the links between ADME/Tox properties, functions and endpoints. The grey dashed line represents reactive metabolites that can cause toxicity.

areas are related to the interaction of a drug with proteins involved in ADME/Tox. These areas are toxicogenomics, proteomics, metabonomics and pharmacogenomics.

Toxicogenomics

Toxicogenomics deals with global changes in gene expression in response to either a drug or a toxin, and is usually measured using microarrays (mRNA transcription). Drug discovery provides large numbers of molecules and data regarding the binding of these molecules to multiple proteins [12] and the quantity of toxicology information used in decision making during the drug discovery process has increased because of toxicogenomics. Generally, these studies can be divided into predictive toxicology and mechanism-based risk assessment [13]. Changes in the global patterns of gene expression in animals and in cells in response to drugs given at different doses and time-points identify 'signature' genes that can be used as predictors of toxicity [13] in humans.

In addition to predictive toxicology, the second toxicogenomics area to use microarrays is mechanistic toxicology. This is aimed at understanding the biochemical and biological responses in a particular type of toxicity and is important for compound risk assessment. Most biologically active compounds affect the function of cells at many levels, including nuclear hormone receptors (NHRs), which regulate the transcription of genes that encode cytochrome P450 enzymes (CYPs), phase II enzymes, transporters and other genes [14]. Microarray data have been used to identify a detailed mechanism of benzene-induced hematotoxicity and leukemogenicity that involves inhibition of p53-mediated apoptosis and oxidative stress [15] and that can be illustrated using both static (gene ontology) (Figure 2) and dynamic models using the software that is described later. Normally, carcinogenicity is evaluated in mouse bioassays that take up to 2 years, but microarray methods have been used to identify gene markers that speed up the identification of carcinogens. In an *in vivo* toxicology study, cDNA microarray data have been generated following 5-day, repeat-dose treatment of rats with several prototype rodent genotoxic and non-genotoxic carcinogens, and two non-carcinogenic hepatotoxicants. Correlating the gene-expression data from this study with the known carcinogenic potential of these compounds has identified transforming growth factor β-stimulated clone 22 and NAD(P)H CYP450 oxidoreductase as molecular markers of non-genotoxic carcinogenicity in rodents [16].

Proteomics

Assessing the effects of a compound on the activity and concentration of proteins can provide results that

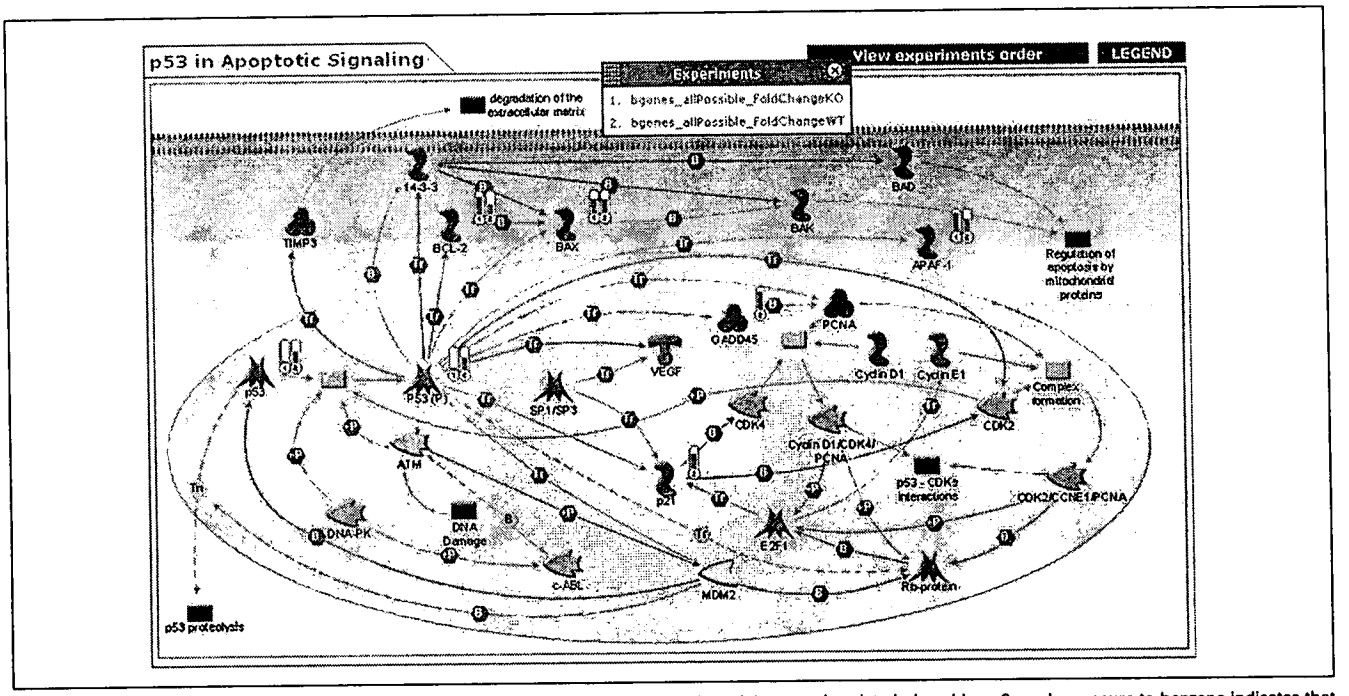

Figure 2. Visualizing OMICS data in networks. Visualization and network analysis of differential-expression data induced by a 2-week exposure to benzene indicates that hematotoxicity and leukemogenicity occurs via inhibition of p53-mediated apoptosis and oxidative stress [15]. Microarray-data mapping on the p53 apoptotic signaling map in MetaCore™ (http://www.genego.com) demonstrates the difference in expression of cell-cycle pathways between p53-knockout mice (1) and wild-type mice (2) (the height of the red bars indicates relative differences in expression). The colored, differently shaped nodes on the network represent enzymes (orange), transcription factors (red) and binding proteins (blue). The small colored hexagons encode the interactions between two connected nodes (e.g. binding (B), transcriptional regulation (Tr) and phosphorylation (+P)]. The green lines indicate a positive effect whereas the red lines indicate a negative effect.

compliment gene-expression data and are more consistent with the overall mechanism of toxicity [17]. Proteomics deals with the quantitative and qualitative measurement of protein concentrations in whole-tissue samples [18]. This is important because post-translational modification, proteolysis and other dynamic processes that cause functional changes in proteins means that the presence of a mature mRNA transcript does not always correspond to the presence of the active protein [19]. Expression-proteomics studies use two-dimensional (2D) protein electrophoresis and mass spectrometry to identify a set of proteins (hundreds to several thousand per sample) that are expressed in a particular tissue under different conditions [20–22], and they are a main method in both predictive and mechanistic toxicology studies [23]. A recent proteomics study of a proprietary lead compound that caused steatosis in rat liver identified 22 proteins in liver, many of which are involved in pathways that lead to the accumulation of acetyl-CoA and triglyceride. This indicates that steatosis is the result of perturbing the β-oxidation pathway in this tissue [24].

Metabonomics and metabolomics

Metabolites represent the endpoint of the response of an organism to a stimulus (Figure 1), and metabolic profiling is the most direct measure of physiology [25]. Metabolomics relates to the understanding of metabolic regulation and flux in cells, and metabonomics is a larger scale, systemic determination of biochemical profiles and their regulation in biofluids and tissues [26]. Both methods analyze all the low-molecular-weight molecules in cells. The quantification and identification of every metabolite in a cellular system is difficult because of the lack of analytical techniques that are reproducible, robust and automated, the chemical heterogeneity of metabolites, the lack of automated extraction techniques, and the low resolution of existing hardware [27].

Pharmacogeneomics

Pharmacogenomics uses genome-wide approaches to identify variations in the networks of genes that determine how individuals respond to a drug, and its efficacy and toxicity. During the past few decades many genes have been linked directly to the mechanisms of response and we know that 20–95% of the variability in drug response is inherited [28,29]. Examples of key genes that govern drug efficacy in humans and examples of ADME/Tox proteins that exhibit polymorphic variability to drug response [28,30] are also growing and their identification will assist drug discovery.

Integration

A few groups have integrated more than one OMICS dataset in a study. Examples include the assessment of toxicogenomics of bromobenezene in rats using both mRNA and protein, which shows a modest overlap in results and the complementary nature of the data [31]. Evaluating acetaminophen overdose in mice using microarray expression and proteomics [32] shows that protein concentrations change rapidly but RNA expression lags and there is little correlation between the two, possibly because of the small array size. In another study in mice,

microarray data and high-resolution ^{1}H nuclear-magnetic-resonance spectra from intact liver, tissue extracts and plasma after dosing with acetaminophen were used to identify the biochemical changes associated with hepatotoxicity. Increased hepatic glycolysis was observed, which is consistent with gene-expression data for lipid and energy metabolism [33]. The effect of carbon tetrachloride in rats has been evaluated using microarray and 2D-gel proteomics at several time points and doses [34]. Low doses of carbon tetrachloride caused the rapid upregulation of known markers of stress, early transcriptional factors and DNA-damage-control genes. These gene changes correlated with 21 out of 22 proteins, with at least one gene being differentially expressed [34]. Although it is, perhaps, too early to see the benefits of this integration in all but the few published cases [35], a comprehensive analysis of biological systems requires the integration of all the data to identify molecular markers of different toxic endpoints. The integration of metabolomics with gene-expression and proteomics data to unify metabolic regulatory networks and infer condition-specific metabolic networks [36] indicates that traditional metabolic pathways can be visualized as networks of subsystems [37].

New algorithms for integrative data analysis

After generating data by most high-throughput methods, commercially available clustering techniques [GeneSpring™ (http://www.silicongenetics.com/), Guided Analytic™ application (http://www.spotfire.com/) and Rosetta Resolver™ (http://www.rosettabio.com/)] are applied to extract the toxicity signatures as a phylogenetic tree in which the branch length corresponds to the similarity between datasets [38]. Recently, several approaches have been developed that enable more advanced, functional analysis of high-throughput molecular data. These algorithms can be used to combine protein-interaction information and expression data to find condition-specific modules in protein networks. This is achieved by clustering gene-expression data and mapping the resulting clusters onto interaction networks that are obtained from independent sources [39]. Other methods include superparamagnetic clustering (see Glossary), which identifies tightly connected sets of nodes [40], simulated annealing [41], probabilistic graphical models [42] and Monte Carlo optimization [43]. Most of the research in this area relies on interaction data from yeast two-hybrid assays. Thus, analysis is limited to direct physical interactions and also contains many false positives. Information on the type and direction of interaction is, generally, not represented in such datasets.

More recently, additional developments have been used to connect interacting, differentially expressed genes in condition-specific, functional, 'signature networks' [37]. Combining comprehensive databases with powerful analytical and network-building tools has resulted in the development of integrated, high-throughput, data-mining suites such as Pathway Assist™ (http://www.ariadnegenomics.com/), PathArt™ (http://jubilantbiosys.com/), MetaCore™ (http://www.genego.com) and Pathways Analysis™ (http://www.ingenuity.com/).

Glossary

Monte Carlo optimization: Random generation of values for uncertain variables to simulate a model. In the context of networks this method is used to find highly connected nodes in networks.
Nodes: An object (genes and molecules) connected in a network.
Probabilistic graphical models: A combination of graph theory and probability theory. They represent multivariate joint probability distributions via a product of terms, each of which involves only a few variables. The structure is represented by a graph that relates variables that appear in a common term.
Simulated annealing: A technique to find a good solution to an optimization problem by trying random variations of the current solution. A worse variation is accepted as the new solution with a probability that decreases as the computation proceeds. The slower the cooling schedule or rate of decrease, the more likely the algorithm is to find an optimal or near-optimal solution.
Superparamagnetic clustering: This method assigns a 'spin' to each node and spins in a highly connected cluster fluctuate in a correlated fashion, which is used to identify these nodes.

These tools enable visualization of the global cellular mechanisms that account for differences in expression. Most use manually curated content about the physical interactions between proteins in humans, which enables different levels of cellular functionality to be captured as either maps of the current biological knowledge or custom-built interaction networks (Figure 2).

Complex computational models have been generated iteratively to simulate networks that regulate transcription and metabolism in *Escherichia coli* [44]. Researchers have also constructed minimal-cell models as a first step to multicellular organisms, which are likely to provide insights into pharmacokinetics and pharmacodynamics [45]. Although the mathematical algorithms derived for simple organisms and pathways are unlikely to be reliable predictors of toxicity in mammals, we can learn from the gene responses of these organisms to xenobiotics. Yeast-cell-based assays are used increasingly for high-throughput screens to test for toxicity of xenobiotics because they mimic the well-conserved stress response [46], and produce chemical and genetic profiles of compounds that provide insights into their mechanisms of action [47,48]. The combination of algorithmic analysis of these types of higher throughput experimental approaches will enrich the mammalian data that are available.

Databases, modeling and predictive tools: ADME/Tox

Since the 1970s, industry and academia have organized databases on proteins, enzyme-encoding genes, and metabolic- and cell-signaling pathways (Figure 3) [49]. Although there have been limited efforts to organize ADME/Tox data, separate focused databases of ADME-associated proteins and pathways such as PharmaGKB [50], the nuclear receptor database [51], human membrane-transporter database [52] and the ADME-AP database [53] can be integrated. Commercial databases such as Metabolite™ (http://www.mdl.com), Metabolism™ (http://www.accelrys.com) and BioFrontier/P450™ (http://www.fqspl.com.pl/) represent a broad collection of metabolic data that are useful for calculating probabilities for a metabolic reaction [54]. Several companies market content databases of gene-expression profiles, histopathology, multi-parameter clinical chemistry tests and morphology in rat organs after treatment with several hundred marketed drugs and toxicants that use different array

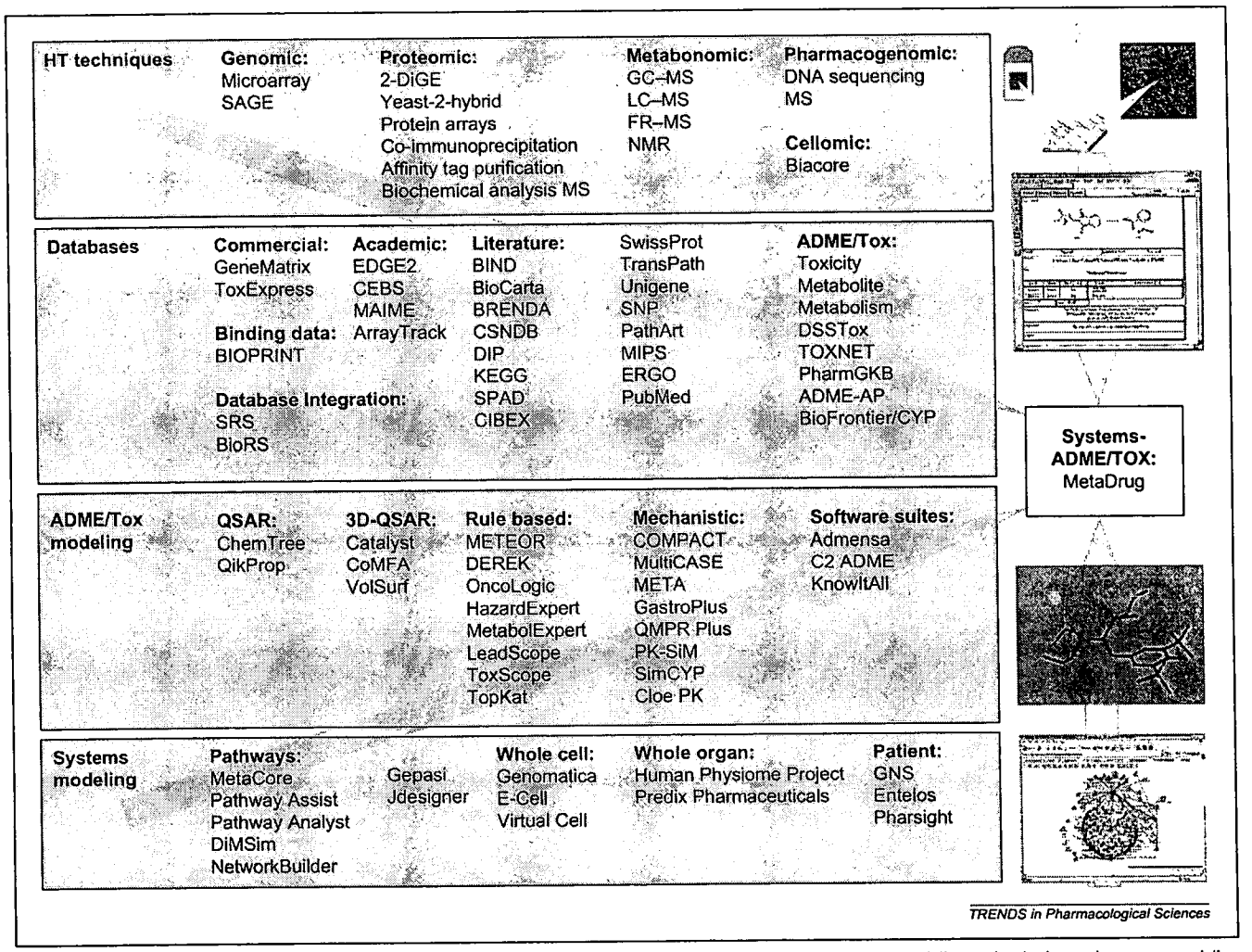

Figure 3. Developing systems-ADME/Tox. The convergence of high-throughput techniques, databases, small-molecule modeling technologies and systems modeling technologies forms the foundation of systems-ADME/Tox. Abbreviations: 2-DiGE, two-dimensional gel electrophoresis; FR–MS, Fourier transformation–mass spectrometry; GC–MS, gas chromatography–mass spectrometry; HT, high throughput; LC–MS, liquid chromatography–mass spectrometry; MS, mass spectrometry; NMR, nuclear magnetic resonance; SAGE, serial analysis of gene expression.

platforms and represent predictive toxicogenomic screening tools. These include Iconix (Drug Matrix™; http://www.iconixpharm.com/), GeneLogic (ToxExpress™; http://www.genelogic.com/) [55], Curagen (http://www.curagen.com/) and Icoria (formerly Paradigm Genetics; http://www.icoria.com/). Pattern-recognition analysis depends, ultimately, on the content and quality of these databases coupled with data on the phenotypic endpoint.

Many ongoing projects will contribute to the availability of public databases. The most promising are two databases that are being developed at the National Institutes of Health (NIH) and the Food and Drug Administration (FDA). The National Center for Toxicogenomics at the National Institute of Environmental Health Sciences (NIEHS) and The European Molecular Biology Laboratory–European Bioinformatics Institute are developing a comprehensive Chemical Effects in Biological Systems (CEBS) knowledgebase (http://www.niehs.nih.gov/nct/cebs.htm) [56,57]. This will accommodate gene-expression profiles, proteomics and metabolomics data in the extended open-source CEBS Systems Biology object model, and enable complex queries [57,58]. Similar goals are being pursued by the National Center for Toxicological Research at the FDA in their development of the ArrayTrack database [59]. Finally, the EDGE^2 database (http://edge.oncology.wisc.edu/), a public effort at the University of Wisconsin contains gene-expression profiles following treatment of mice with different toxic molecules [60]. Microarray approaches and database development (Figure 3) provide valuable methods and data to help understand toxicity, which is seen as increasingly important for future submissions to regulatory authorities [61].

Computational models are widely available for predicting ADME/Tox properties using software for either custom-model building [4,49] or pre-built modeling suites [Cerius^{2}™ ADME (http://www.accelrys.com) and KnowItAll™ (http://www.bio-rad.com)] (Figure 3). Generally, these systems are based around quantitative structure–activity relationships (QSARs) that generate descriptors based on molecular structure and use computational algorithms to relate the key descriptors to the biological activity [62]. The accumulation of drug-metabolism data from the literature has resulted in expert systems for predicting metabolism with

products such as MetabolExpert™ (http://www.compudrug.com/), META™ (http://www.multicase.com/) and METEOR™ (http://www.chem.leeds.ac.uk/luk/), with the caveat that these contain data from many different mammalian species. Simulation methods have also been developed, including physiologically based pharmacokinetic modeling (PBPK) and methods such as Cloe PK™ (http://www.cyprotex.com), GastroPlus™ (http://www.simulations-plus.com), Simcyp™ (http://www.simcyp.com/) and others that include toxicokinetic methods. PBPK approaches can be used with either empirical data, *in vitro* data or *in silico* predictions to derive human pharmacokinetic parameters such as area under the curve (AUC) [63]. By contrast, computational approaches for predicting toxicity are studied infrequently [3,64] but are complementary to research on ADME parameters [62]. These methods for individual toxicology properties tend to be rule-based systems such as DEREK™ (http://www.chem.leeds.ac.uk/luk/), Hazard Expert™ (http://www.compudrug.com/), LeadScope™ (http://www.leadscope.com/) or the mechanistic methods COMPACT [65] and MultiCASE™ (http://www.multicase.com/).

Applications of systems-ADME/Tox

Traditional ADME/Tox studies provide a detailed understanding of individual proteins. Now, we consider whether the molecule also binds to receptors that affect the regulation of other proteins, and if it interferes with endogenous metabolic, regulatory and transport proteins. Alternatively, the primary metabolic route might be mediated by a polymorphic enzyme and affect the likely therapeutic dose. Many of these questions are now answered earlier in the drug-discovery process *in vitro*. Because xenobiotics and their metabolites influence multiple genes and pathways simultaneously, predicting a response in a heterogeneous population is complex and depends on drug dose, genes, physiological state and other factors. The transcriptional regulation of CYPs, phase II enzymes and many transporters are regulated by numerous NHRs, which affect endogenous metabolism, cell growth, proliferation and oxidative stress [66,67]. Therefore, combining different experimental and predictive approaches will help explain the metabolism and toxicity of unknown compounds.

The development of a systems-ADME/Tox platform (MetaDrug™; http://www.genego.com) that links empirical, biological-pathway-centered data, OMICS-based models and ligand-based QSAR models, is the latest step in this research [6]. From an input molecular structure, the major metabolites in humans are predicted and scored with multiple ADME/Tox models (predicting K_m, V_{max}, IC_{50} and K_i values). This can be used to filter molecules before visualization as objects on regulatory networks. The visualization tool also uses the scores for many proteins to predict a network of proteins that are likely to be responsible for ADME/Tox interactions and provides a visual perspective of the most important pathways (Figure 4). This software has also been applied to illustrate the complexity of NHR interactions in humans [14]. Toxicogenomics data (microarrays, protein profiles and metabolic profiles) and pharmacogenomics data [single nucleotide polymorphisms (SNPs) and haplotypes] can also be visualized and compared on the same networks. This represents a valuable starting point for the development of rational, mechanism-driven hypotheses and models that uses a combined approach rather than relying on either a single type of high-throughput data or QSAR models. Systems-ADME/Tox methods might also help to determine the toxicity of molecules and the genes that might be involved [68] by reconstructing functional networks.

The future of systems-ADME/Tox

Studies of drug safety increasingly use OMICS data, which provides a starting point for a systems-ADME/Tox approach. However, many compounds can be co-administered and thus more studies that describe the effects of dosing with multiple compounds simultaneously are needed to indicate positive and negative interactions [69]. However, extensive experimental studies are expensive and require collaborations between different groups [70]. Presently, therefore, we are witnessing the parallel development and maturation of several databases [57], visualization software and predictive algorithms. The integration of these tools is likely to be synergistic, unlike the complimentary combination of OMICS methods seen to date. We suggest that the ideal study would include all types of experiments for the same sample and genetic background, such that the data are analyzed in a computational system to better understand and explain the discrepancies between the data types [49]. A systems-based approach to ADME/Tox might improve the efficiency of drug discovery by integrating these disparate technologies.

Each of the technologies described above faces considerable challenges. These include controlling experimental variability followed by effective verification, storage, utilization and dissemination of the massive amount of data that is generated. The data derived from animals and *in vitro* models (even human models) must be extrapolated to humans *in vivo*, which is another complex process. Generating computational predictions also requires validation before such models are accepted generally, which takes time and financial investment. Without doubt, the development of new technologies will benefit from the incorporation of relevant OMICS content to identify the specific interaction networks for groups of new chemical entities and toxins: linking the databases that are being developed, such as CEBS and commercially available databases, might be a first step toward this, This could be followed by providing reliable network comparisons using algorithms, and the resultant networks should reflect the responses to specific chemotypes and toxicophores. In parallel, the compounds for which toxicogenomics data are already collected should be processed through the chemical rules and models with the expectation that the resulting data intersects at the level of networks. This represents a starting point for the iterative generation of predicted interaction networks based on molecular structure.

Concluding remarks

Humans are sophisticated organisms who require that multiple cellular processes operate in parallel to ensure survival. Although understanding gene-expression

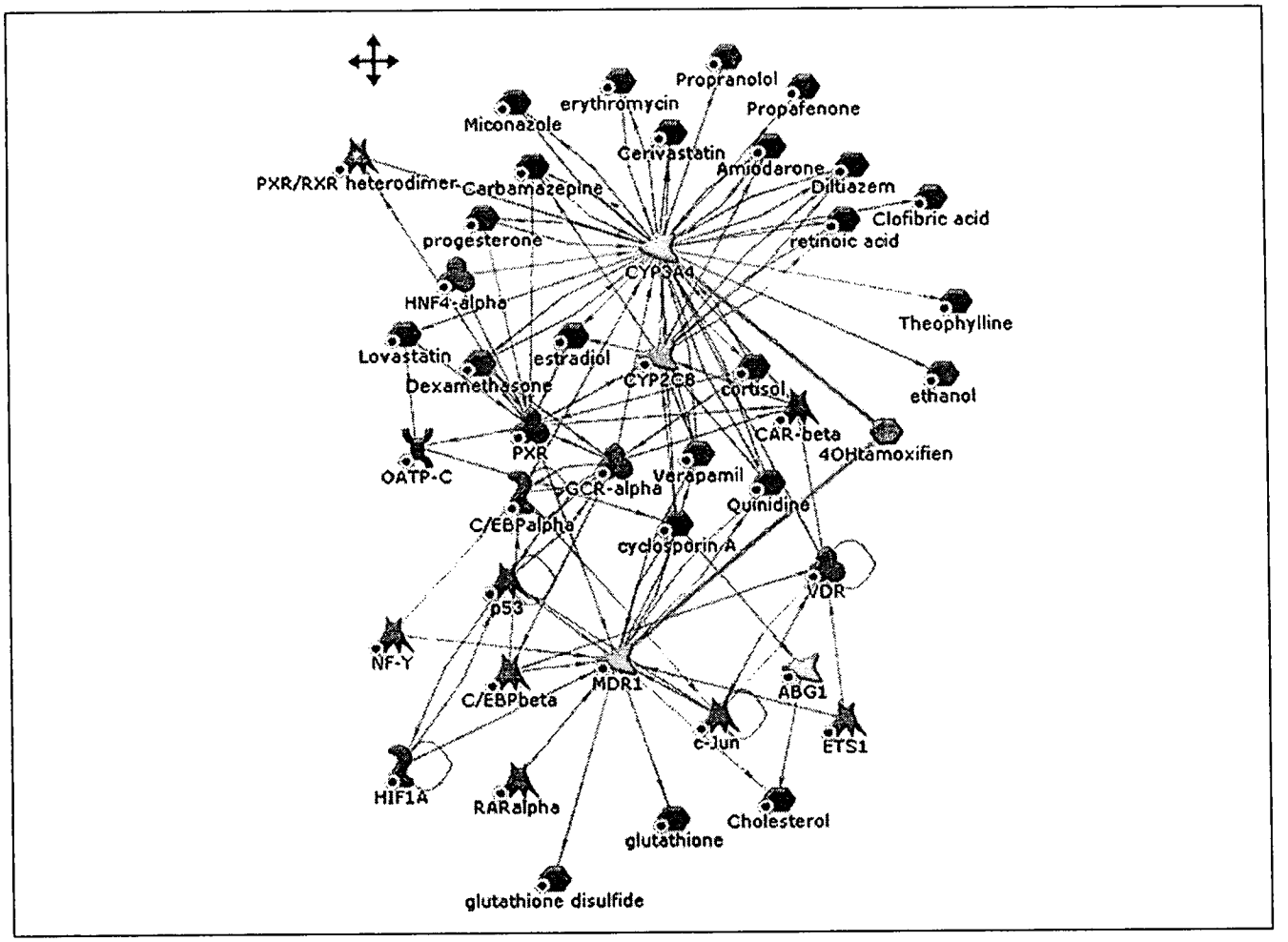

Figure 4. Simultaneous visualization of predicted and empirical protein–ligand interactions. A regulatory network generated with MetaDrug™ (http://www.genego.com) shows the predicted binding interactions for 4-hydroxytamoxifen (pink hexagon connected to thick blue lines) derived from QSAR models for P-glycoprotein (P-gp) and CYP3A4 built with literature data. The colored, differently shaped nodes represent enzymes (yellow/orange arrows), ligands (purple hexagons), transcription factors (red) and other proteins (blue). 4-Hydroxytamoxifen is known to be metabolized by (and inhibits) CYP3A4 [72] and to inhibit P-gp (IC_{50}=7.4 μM) [73].

networks *in silico* and *in vivo* in unicellular and multicellular systems is essential for drug discovery [71], these are not the only important factors. In conclusion, many separate tools and datasets are being integrated in software products that should improve our understanding of the effects of xenobiotics in humans because it is apparent that, used separately, top-down approaches and bottom-up methods are not sufficient.

Acknowledgements

S.E. gratefully acknowledges Maggie A.Z. Hupcey and Craig Giroux (Wayne State University) for editorial comments and suggestions, and our colleagues at GeneGo for software development. This work was supported by NIH grant 1-R43-GM069124–01.

References

1 Rawlins, M.D. (2004) Cutting the cost of drug development? *Nat. Rev. Drug Discov.* 3, 360–364
2 FDA (2004) Innovation stagnation: challenge and opportunity on the critical path to new medicinal products. http://www.fda.gov/oc/initiatives/criticalpath/whitepaper.pdf
3 Ekins, S. (2003) In silico approaches to predicting metabolism, toxicology and beyond. *Biochem. Soc. Trans.* 31, 611–614
4 van de Waterbeemd, H. and Gifford, E. (2003) ADMET *in silico* modelling: towards prediction paradise? *Nat. Rev. Drug Discov.* 2, 192–204
5 Ekins, S. *et al.* (2002) Towards a new age of virtual ADME/TOX and multidimensional drug discovery. *J. Comput. Aided Mol. Des.* 16, 381–401
6 Bugrim, A. *et al.* (2004) Early prediction of drug metabolism and toxicity: systems biology approach and modeling. *Drug Discov. Today* 9, 127–135
7 Hood, L. and Galas, D. (2003) The digital code of DNA. *Nature* 421, 444–448
8 Ideker, T. and Lauffenburger, D. (2003) Building with a scaffold: emerging strategies for high- to low-level cellular modeling. *Trends Biotechnol.* 21, 255–262
9 Ekins, S. *et al.* (2004) Applying computational and *in vitro* approaches to lead selection. In *Pharmaceutical Profiling in Drug Discovery for Lead Selection* (Borchardt, R.T. *et al.*, eds), pp. 361–389, AAPS Press
10 Ekins, S. *et al.* (2003) Generation and validation of rapid computational filters for CYP2D6 and CYP3A4. *Drug Metab. Dispos.* 31, 1077–1080
11 Shimada, J. *et al.* (2002) Integrating computer-based *de novo* drug design and multidimensional filtering for desirable drugs. *Targets* 1, 196–205
12 Ulrich, R. and Friend, S.H. (2002) Toxicogenomics and drug discovery: will new technologies help us produce better drugs? *Nat. Rev. Drug Discov.* 1, 84–88
13 Lord, P.G. (2004) Progress in applying genomics in drug development. *Toxicol. Lett.* 149, 371–375

14 Ekins, S. *et al.* A novel method for visualizing nuclear hormone receptor networks relevant to drug metabolism. *Drug Metab. Dispos.* (in press)
15 Yoon, B. *et al.* (2003) Mechanisms of benzene-induced hematotoxicity and leukemogenicity: cDNA microarray analyses using mouse bone marrow tissue. *Environ. Health Perspect.* 111, 1411–1420
16 Kramer, J.A. *et al.* (2004) Acute Molecular markers of rodent hepatic carcinogenesis identified by transcription profiling. *Chem. Res. Toxicol.* 17, 463–470
17 Walgren, J.L. and Thompson, D.C. (2004) Application of proteomic technologies in the drug development process. *Toxicol. Lett.* 149, 377–385
18 Anderson, N.L. and Anderson, N.G. (1998) Proteome and proteomics: new technologies, new concepts, and new words. *Electrophoresis* 19, 1853–1861
19 Klein, J.B. and Thongboonkerd, V. (2004) Overview of proteomics. *Contrib. Nephrol.* 141, 1–10
20 Fountoulakis, M. (2000) Two-dimensional electrophoresis. In *Encyclopedia of separation science, II/electrophoresis*, pp. 1356–1363, Academic Press
21 Aebersold, R. and Mann, M. (2003) Mass spectrometry-based proteomics. *Nature* 422, 198–207
22 Lahm, H.W. and Langen, H. (2000) Mass spectrometry: a tool for the identification of proteins separated by gels. *Electrophoresis* 21, 2105–2114
23 Kennedy, S. (2002) The role of proteomics in toxicology: identification of biomarkers of toxicity by protein expression analysis. *Biomarkers* 7, 269–290
24 Meneses-Lorente, G. *et al.* (2004) A proteomic investigation of drug-induced steatosis in rat liver. *Chem. Res. Toxicol.* 17, 605–612
25 Glassbrook, N. *et al.* (2000) Metabolic profiling on the right path. *Nat. Biotechnol.* 18, 1142–1143
26 Nicholson, J.K. and Wilson, I.D. (2003) Understanding 'global' systems biology: metabonomics and the continuum of metabolism. *Nat. Rev. Drug Discov.* 2, 668–676
27 Goodacre, R. *et al.* (2004) Metabolomics by numbers: acquiring and understanding global metabolite data. *Trends Biotechnol.* 22, 245–252
28 Evans, W.E. and McLeod, H.L. (2003) Pharmacogenomics–drug disposition, drug targets, and side effects. *New Engl. J. Med.* 348, 538–549
29 Weinshilboum, R. (2003) Inheritance and drug response. *New Engl. J. Med.* 348, 529–537
30 Trotta, R. *et al.* (2004) Trends in pharmacogenomics of drugs acting on hypertension. *Pharmacol. Res.* 49, 351–356
31 Heijne, W.H. *et al.* (2003) Toxicogenomics of bromobenzene hepatotoxicity: a combined transcriptomics and proteomics approach. *Biochem. Pharmacol.* 65, 857–875
32 Ruepp, S.U. *et al.* (2002) Genomics and proteomics analysis of acetaminophen toxicity in mouse liver. *Toxicol. Sci.* 65, 135–150
33 Coen, M. *et al.* (2004) Integrated application of transcriptomics and metabonomics yields new insight into the toxicity due to paracetamol in the mouse. *J. Pharm. Biomed. Anal.* 35, 93–105
34 Fountoulakis, M. *et al.* (2002) Modulation of gene and protein expression by carbon tetrachloride in the rat liver. *Toxicol. Appl. Pharmacol.* 183, 71–80
35 Klapa, M.I. and Quackenbush, J. (2003) The quest for the mechanisms of life. *Biotechnol. Bioeng.* 84, 739–742
36 Weckwerth, W. and Fiehn, O. (2002) Can we discover novel pathways using metabolomic analysis? *Curr. Opin. Biotechnol.* 13, 156–160
37 Barabasi, A-L. and Oltvai, Z.N. (2004) Network biology: understanding the cell's functional organization. *Nat. Rev. Genet.* 5, 101–113
38 Eisen, M.B. *et al.* (1998) Cluster analysis and display of genome-wide expression patterns. *Proc. Natl. Acad. Sci. U. S. A.* 95, 14863–14868
39 Tornow, S. and Mewes, H.W. (2003) Functional modules by relating protein interaction networks and gene expression. *Nucleic Acids Res.* 31, 6283–6289
40 Hanisch, D. *et al.* (2002) Co-clustering of biological networks and gene expression data. *Bioinformatics* 18, S145–S154
41 Ideker, T. *et al.* (2002) Discovering regulatory and signalling circuits in molecular interaction networks. *Bioinformatics* 18, S233–S240
42 Segal, E. *et al.* (2003) Discovering molecular pathways from protein interaction and gene expression. *Bioinformatics* 19, i264–i272
43 Spirin, V. and Mirny, L.A. (2003) Protein complexes and functional modules in molecular networks. *Proc. Natl. Acad. Sci. U. S. A.* 100, 12123–12128
44 Covert, M.W. *et al.* (2004) Integrating high-throughput and computational data elucidates bacterial networks. *Nature* 429, 92–96
45 Werner, E. (2003) In silico multicellular systems biology and minimal genomes. *Drug Discov. Today* 8, 1121–1127
46 Weiss, A. *et al.* (2004) High-throughput phenotypic profiling of gene-environment interactions by quantitative growth curve analysis in *Saccharomyces cerevisiae*. *Anal. Biochem.* 327, 23–34
47 Stockwell, B.R. (2004) The biological magic behind the bullets. *Nat. Biotechnol.* 22, 37–38
48 Parsons, A.B. *et al.* (2004) Integration of chemical-genetic and genetic interaction data links bioactive compounds to cellular target pathways. *Nat. Biotechnol.* 22, 62–69
49 Ekins, S. *et al.* Systems biology: applications in drug discovery. In *Drug Discovery Handbook* (Gad, S., ed.), Wiley (in press)
50 Oliver, D.E. *et al.* (2002) Ontology development for a pharmacogenetics knowledge base. *Pac Symp Biocomput.* 2002, 88–99
51 Nakata, K. *et al.* (2002) A nuclear receptor database that maps pathways to diseases. *Genome Infomatics* 13, 515–516
52 Yan, Q. and Sadee, W. (2000) Human membrane transporter database: a web-accessible relational database for drug transport studies and pharmacogenomics. *AAPS PharmSci* 2, E20
53 Sun, L.Z. *et al.* (2002) ADME-AP: a datbase of ADME associated proteins. *Bioinformatics* 18, 1699–1700
54 Boyer, S. and Zamora, I. (2002) New methods in predictive metabolism. *J. Comp. Aided Mol. Des.* 16, 403–413
55 Castle, A.L. *et al.* (2002) Toxicogenomics: a new revolution in drug safety. *Drug Discov. Today* 7, 728–736
56 Waters, M. *et al.* (2003) Systems toxicology and the Chemical Effects in Biological Systems (CEBS) knowledge base. *EHP Toxicogenomics* 111, 15–28
57 Mattes, W.B. *et al.* (2004) Database development in toxicogenomics: issues and efforts. *Environ. Health Perspect.* 112, 495–505
58 Hood, E. (2003) Proteomics: characterizing the cogs in the machinery of life. *Environ. Health Perspect.* 111, A816–A825
59 Tong, W. *et al.* (2003) ArrayTrack–supporting toxicogenomic research at the U.S. Food and Drug Administration National Center for Toxicological Research. *Environ. Health Perspect.* 111, 1819–1826
60 Thomas, R.S. *et al.* (2001) Identification of toxicologically predictive gene sets using cDNA microarrays. *Mol. Pharmacol.* 60, 1189–1194
61 Hackett, J.L. and Lesko, L.J. (2003) Microarray data- the US FDA, industry and academia. *Nat. Biotechnol.* 21, 742–743
62 Ekins, S. and Swaan, P.W. (2004) Computational models for enzymes, transporters, channels and receptors relevant to ADME/TOX. In (Lipkowitz, K.B. *et al.*, eds), pp. 333–415, Wiley-VCH
63 Leahy, D.E. (2004) Drug discovery information integration: virtual humans for pharmacokinetics. *DDT: BIOSILICO* 2, 78–84
64 Greene, N. (2002) Computer systems for the prediction of toxicity: an update. *Adv. Drug Deliv. Rev.* 54, 417–431
65 Lewis, D.F.V. (1996) *Cytochromes P450*, Taylor & Francis
66 Ulrich, R.G. (2003) The toxicogenomics of nuclear receptor agonists. *Curr. Opin. Chem. Biol.* 7, 505–510
67 Ulrich, R.G. *et al.* (2004) Overview of an interlaboratory collaboration on evaluating the effects of model hepatotoxicants on hepatic gene expression. *Environ. Health Perspect.* 112, 423–427
68 Williams, D.P. and Park, B.K. (2003) Idiosyncratic toxicity: the role of toxicophores and bioactivation. *Drug Discov. Today* 8, 1044–1050
69 Borisy, A.A. *et al.* (2003) Systematic discovery of multicomponent therapeutics. *Proc. Natl. Acad. Sci. U. S. A.* 100, 7977–7982
70 Clish, C.B. *et al.* (2004) Integrative biological analysis of the APOE*3-leiden transgenic mouse. *OMICS* 8, 3–13
71 Christopher, R. *et al.* (2004) Data-driven computer simulation of human cancer cell. *Ann. New York Acad. Sci.* 1020, 132–153
72 Desta, Z. *et al.* (2004) Comprehensive evaluation of tamoxifen sequential biotransformation by the human cytochrome P450 system *in vitro*: prominent roles for CYP3A and CYP2D6. *J. Pharmacol. Exp. Ther.* 310, 1062–1075
73 Bekaii-Saab, T.S. *et al.* (2004) Interactions of tamoxifen, N-desmethyltamoxifen and 4-hydroxytamoxifen with P-glycoprotein and CYP3A. *Biopharm. Drug Dispos.* 25, 283–289

Distribution, Metabolism, and Excretion of a Novel Surface-Active Agent, Purified Poloxamer 188, in Rats, Dogs, and Humans

J. MICHAEL GRINDEL,[1] TED JAWORSKI,[2] OLGA PIRANER,[3] R. MARTIN EMANUELE,[1] M. BALASUBRAMANIAN[4]

[1]CytRx Corporation, 154 Technology Parkway, Suite 200, Norcross, Georgia 30092

[2]PPD Development, 3900 Paramount Parkway, Morrisville, North Carolina 27560

[3]Center for Disease Control, 4770 Buford Highway, Atlanta, Georgia 30341

[4]Innoconcepts, 750 Brookfield Parkway, Roswell, Georgia 30075

Received 9 October 2001; revised 12 March 2002; accepted 13 March 2002

ABSTRACT: Purified poloxamer 188 (PP188) is a nonionic, block copolymer surfactant with hemorheologic, antithrombotic, and anti-adhesive properties. PP188 is being studied in phase III clinical trials in sickle cell disease and has been found to be well tolerated and has demonstrated benefit in ameliorating the effects of acute painful vasoocclusive crisis. The disposition of PP188 was studied in rats, dogs, and humans to establish a basis for understanding the safety parameters in support of clinical trials. PP188 was primarily distributed in extracellular water with little or no uptake by red blood cells, and had its highest concentrations in highly perfused tissues such as the kidney, liver, spleen, lymph nodes, and gastrointestinal tract. PP188 had no apparent effect on P450 isozymes *in vitro*. Metabolism was limited (< 5% of dose) with a higher molecular weight copolymer being the only other material detected in plasma or urine. Renal clearance was the controlling route of clearance for PP188 from the body. The 48-h intravenous infusion doses of PP188 were cleared in all species by approximately 1 week after the cessation of dose administration. PP188's disposition is a model for other nonionic block copolymers with similar physical and chemical properties. © 2002 Wiley-Liss, Inc. and the American Pharmaceutical Association J Pharm Sci 91:1936–1947, 2002

Keywords: surfactant; renal clearance; species comparison; disposition

INTRODUCTION

Purified poloxamer 188 (PP188) is a nonionic, block copolymer surfactant with hemorheologic and antithrombotic properties (Fig. 1). PP188 was purified by supercritical fluid extraction to remove potentially toxic lower molecular weight components found in the commercially available material.[1,2] PP188 improves microvascular blood flow by reducing blood viscosity, especially under low shear conditions and by reducing adhesive and frictional forces.[3] The mechanism of action of PP188 is not fully understood, but it is hypothesized that the polyoxypropylene core of the molecule binds to hydrophobic portions of cells, leaving the hydrophilic polyoxyethylene chains free to interact with the surrounding aqueous environment.[4,5] Consequently, PP188 provides a hydrated, relatively noncompressible barrier that appears to block hydrophobic adhesive interactions (e.g., cell–cell, cell–protein, and protein–protein) in the blood. As a result, there is a reduction in whole blood viscosity, erythrocyte aggregation, and adhesion to the vascular endothelium,[6] and an improvement in microvascular

Correspondence to: J. Michael Grindel (Telephone: 770-453-0120; Fax: 770-368-0622.; E-mail: grindelm@cytrx.com)

Journal of Pharmaceutical Sciences, Vol. 91, 1936–1947 (2002)

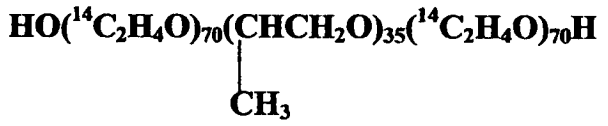

Figure 1. Structure of ^{14}C-purified poloxamer 188 (^{14}C-PP188).

blood flow.[7–10] PP188 has been studied in more than 300 patients with sickle cell disease.[11–14] Tolerability and pilot efficacy studies have been completed in sickle cell disease patients experiencing a vasoocclusive crisis[11,12] as well as in patients with acute chest syndrome.[13] PP188 has been shown to be safe and well tolerated after continuous intravenous infusion over 24 h at cumulative doses as high as 2960 mg/kg.[14] PP188 is also being evaluated preclinically in spinal cord injury and muscular dystrophy.

In this report, we describe the disposition of PP188 in rats, dogs, and humans. The data were collected to provide a comparative assessment of the disposition of PP188 across species used in safety and efficacy evaluations. The radiolabeled studies were conducted to closely pattern the conduct of the 30-day intravenous (IV) infusion toxicology studies.

MATERIALS AND METHODS

Materials

Purified poloxamer 188 was obtained from Hitex, Vannes, France. Propylene glycol, ethylene oxide (EO), and propylene oxide (PO) were purchased from Fluka (Munich, Germany). Cesium hydroxide and Celite were purchased from Aldrich, whereas Magnesol was obtained from The Dallas Group of America (New Iberia, LA). ^{14}C-Ethylene oxide (^{14}C-EO) was obtained from Amersham (Piscataway, NJ). The scintillation cocktail (Ultima Gold XR) and liquid scintillation counting solvents (Carbo-Sorb E and Permafluor E+) as well as all other HPLC or reagent grade solvents were commercially available. A model 307 sample oxidizer (Packard Instruments, Boston, MA) and model 1900TR or 2300TR liquid scintillation counter (Packard Instruments) were used for radioactive samples. Gel permeation chromatography (GPC) was performed using Plgel 1000A, 5 μ, 300 × 7.5 mm columns (Polymer Laboratories) or Ultrastyragel 1000A columns (Waters, Milford, MA), a Waters HPLC model 600 pump with controller, model 717 autosampler, model 410 refractive index detector, with data processed using Millenium32 software (Waters). pH measurements were taken on an Orion model 410A pH meter.

Animals

Purebred male and female beagle dogs were obtained from Covance Research Products. The absorption, distribution, metabolism, excretion (ADME) dogs were housed in individual stainless steel cages designed for the collection of urine and feces. Male and female Sprague-Dawley rats were purchased from Charles River Laboratories. The ADME rats were individually housed in Nalgene metabolism cages designed for the collection of urine and feces and for some rats expired air.

Synthesis of ^{14}C-PP188

Propylene glycol initiator (0.24 g, 3.16 mmol) was allowed to react with PO monomer (6.58 g, 113.5 mmol) in the presence of cesium hydroxide monohydrate catalyst (0.06 g, 0.35 mmol). The reaction was conducted by heating the reactor in an oil bath at 100°C in a specially designed glass reactor to handle small quantities of radioactive raw materials. After reacting the entire added PO, a polypropylene oxide polymer of approximately 1800 Da molecular weight (MW) was produced. 1.12 g (0.59 mmol) of polypropylene oxide polymer was transferred into another glass reactor and the polymerization was continued by adding a mixture of 4.81 g (109.3 mmol) of cold EO and 5.9 mg of ^{14}C-EO (30 mCi/mmol). The reaction mixture was heated at approximately 97°C with stirring for 48 h. The reaction product was treated with magnesol, water, and Celite to absorb the cesium hydroxide catalyst.

The radioactive reaction product was mixed with 39.57 g of non-labeled PP188 dissolved in methylene chloride and the polymer solution was filtered under nitrogen to remove Celite and magnesol. The final product was isolated from the solution by precipitating with petroleum ether and dried under vacuum to remove residual solvent.

The yield was 44.38 g of ^{14}C-PP188 (specific activity = 175.6 μCi/g; radiopurity of 99.6%) (Fig. 1). The final product was a white free-flowing powder with a peak MW of 8622 Da, and the low MW content (<4500 Da) was <1%. The pH of the aqueous polymer solution was 7.3. The GPC MW characteristics and pH were in agreement with the specifications for PP188. The ^{14}C-PP188

was further diluted with non-radiolabeled PP188 before dosing the animals to achieve the correct radioactive dose required for each study and species.

Determination of PP188 in Plasma [GPC Method with Refractive Index (RI) Detection]

The plasma samples were analyzed by a GPC method using RI detection. The method had a linear range of 0.025 to 2.50 mg/mL. A 1.0-mL plasma sample was added to a Teflon-lined tube and vortexed with 2.0 mL of acetonitrile (AcCN) and 0.15 g of sodium chloride. After separation of the phases, the AcCN phase was evaporated under a stream of nitrogen, reconstituted in 200 μL of tetrahydrofuran containing 0.02% polystyrene (MW ~50,400 Da) and filtered. The GPC mobile phase was 95% tetrahydrofuran/5% H_2O on two Plgel 1000A columns in series at 1 mL/min with a column temperature of 40°C and detector temperature of 40°C. All samples, including the calibration curve and quality control samples, were processed by the same procedure. The only exceptions to the above procedure were samples in which predicted concentrations exceeded the range of the calibration curve (> 2.5 mg/mL). These samples were diluted with control (blank) plasma to give final values within the range of the calibration curve.

The GPC method with RI detection for PP188 was validated across species for plasma samples obtained from rats, rabbits, dogs, and humans under Good Laboratory Practice (GLP) guidelines. The method validation consisted of system precision, linearity, method precision/accuracy from spiked samples, ruggedness from spiked samples, recovery from extraction, specificity, freeze–thaw sample stability, and standard stability. Extraction recovery ranged from 89 to 94%. The limit of quantitation for the assay was 0.025 mg/mL using a 1-mL plasma sample and the concentration range was 0.025–2.5 mg/mL.

Determination of PP188 in Urine (GPC Method with RI Detection)

The urine samples were analyzed by a GPC method using RI detection. The method had a linear range of 0.075 to 5.0 mg/mL. A 0.5-mL urine sample was mixed with 0.5-mL 60% alcohol solution. Dichloroethane (DCE), 2.5 mL, was added, the tube was capped tightly, rotated on a rocker for 45 min, and centrifuged for 20 min at 3500 rpm. Two milliliters of the DCE phase (bottom) was accurately transferred to a clean test tube. The DCE phase was evaporated under a stream of nitrogen, reconstituted in 300 μL of internal standard solution, and after filtration analyzed by GPC with RI detection as described above. All samples, including the calibration curve and quality control samples, were processed by the same procedure. The only exceptions to the above procedure were samples in which predicted concentrations exceeded the range of the calibration curve (0.075–5.0 mg/mL). These samples were diluted with control (blank) urine to give final values within the range of the calibration curve. The GPC method with RI detection for PP188 was validated (GLP guidelines) for human urine similar to that completed for plasma. Extraction recovery ranged from 85 to 92%. The limit of quantitation for the assay was found to be 0.075 mg/mL using a 0.5-mL urine sample.

Determination of PP188 in Feces (GPC Method with RI Detection)

The fecal samples were analyzed by a GPC method using RI detection. The method had a linear range of 0.075 to 5.0 mg/mL. A 5.0-g fecal aliquot sample was mixed 1:1 w/v with phosphate buffered normal saline (PBS). An aliquot of the sample homogenate was vortexed with AcCN; the AcCN phase was removed and evaporated to dryness under nitrogen. The dried sample was resuspended in hexane and extracted with PBS. The PBS phase was separated and extracted again with hexane, discarding the hexane layer. AcCN and sodium chloride were added to the PBS layer, centrifuged, the AcCN layer removed, and evaporated under a stream of nitrogen, reconstituted in 300 μL of internal standard solution, and after filtration analyzed by GPC as described above. All samples including the calibration curve and quality control samples were processed by the same procedure.

The assay demonstrated recoveries ranging from 74 to 86% at 0.075, 0.5, and 2.0 mg/mL. Recovery increased with increasing concentration.

Radioactive Analysis and Sample Preparation Methods

All sample combustion $^{14}CO_2$ was trapped in Carbo-Sorb E, and Permafluor E+ was added to the samples before liquid scintillation counting analysis. All samples were analyzed for radioactivity for at least 5 min or 100,000 accumulated

counts. All samples that were directly analyzed were diluted with Ultima Gold XR scintillation cocktail. Each sample was homogenized before radioanalysis (unless the entire sample was used for analysis) and assayed in duplicate. Scintillation counting data were automatically corrected for counting efficiency using the external standardization method and an instrument-stored quench curve generated from a series of sealed quenched standards.

Feces, brain, ovaries, pancreas, spleen, and testes were blotted dry and then homogenized in water and combusted. Blood was combusted directly. Cage wipes, dose wipes, dose cannulae, and cage debris were soaked in water overnight, homogenized, and combusted. Plasma, urine, cage wash and rinse, bile, and cerebrospinal fluid (CSF) were counted directly. Bone, fat, colon, kidneys, skeletal muscle, stomach, liver, and gastrointestinal contents were frozen in liquid nitrogen, homogenized in water, and aliquots counted. Adrenal glands, aorta, cecum, eyes, gall bladder, injection site, mesenteric lymph nodes, thyroid, and urinary bladder were digested in 1 N sodium hydroxide solution at 40°C, homogenized, and counted.

Autoradiographic Methods

Before sectioning the carboxymethylcellulose blocks containing rat carcasses, standards fortified with ^{14}C-radioactivity were placed into the frozen blocks and used for section thickness quality control. Sections were collected on adhesive tape (Nakagawa NA-70 MAG, Japan) at 40-μm thickness, in a Leica CM 3600 cryomicrotome maintained at −18°C. Sections were collected at four to six levels of interest and dried in the cryomicrotome chamber. The sections for each animal were mounted, wrapped with Mylar film, and exposed on Molecular Dynamics phosphorimaging screens along with ^{14}C-autoradiographic standards. The exposed screens were scanned using a Molecular Dynamics 445 SI (Amersham, Boston, MA). The autoradiographic standard imaging data, generated using American Radiolabeled Chemicals Inc. (St. Louis, MO). (ARC 146) were sampled using Imaging Research Inc. (St. Catherine's, Ontario, Canada). AIS software to create a calibrated standard curve. Specified tissues, organs, and fluids were analyzed and tissue concentrations interpolated from each standard curve as nanocuries per gram and then converted to microgram-equivalents/gram of tissue.

Enzyme Inhibition Studies

Characterized, pooled, human liver microsomal fractions from 10 individuals (lot number HHM-0257) were obtained from IIAM (Exton, PA) and stored at −70°C. The following isozymes and substrates were tested using conditions based on the literature: 7-ethoxyresorufin *O*-deethylase (CYP1A2)[15]; tolbutamide methyl hydroxylase (CYP2C9)[16]; *S*-mephenytoin 4′-hydroxylase (CYP2C19)[17]; dextromethorphan *O*-demethylase (CYP2D6)[18]; *p*-nitrophenol hydroxylase (CYP2E1)[19]; and erythromycin *N*-demethylase (CYP3A4).[20] A single substrate concentration was used, approximating the concentration of the substrate that gives half-maximal reaction velocity (K_m) for human liver microsomes in these assays. Assays were performed in the presence and absence of PP188 (10–1000 μM). The concentration of PP188 that inhibited 50% of the activity (IC_{50}) of each specific isozyme of cytochrome P450 was estimated by evaluating the effect of various PP188 concentrations on isozyme activity. The data were plotted (percent of activity remaining versus log of PP188 concentration).

Rat Pilot ADME Study

One male and one female rat were given 300 mg/kg/h (17.1 μCi/animal, 14,400 mg/kg) dose of ^{14}C-PP188 by continuous IV infusion over 48 h. Urine, feces, and expired air were collected daily for 96 h.

Rat ADME Study

Twenty male and 20 female rats in 10 groups of four rats/sex/dose (under GLP conditions) were given continuous IV infusion doses over 48 h of ^{14}C-poloxamer 188 at 30, 100, or 300 mg/kg/h (1440, 4800, or 14,400 mg/kg, 15–16 μCi/animal). Groups 1–3 were designated for collection of urine and feces, Groups 4–6 for blood collection during infusion and tissue collection, groups 7–9 for blood collection at the end of infusion, and group 10 for whole body autoradiography. Urine and feces were collected daily for 0–168 h. Blood (0.5 mL) samples (heparinized for plasma) were collected at predose, 0.25, 0.5, 2, 4, 8, and 48 h from the start of infusion in three groups of male and female rats and at predose, 1, 3, 6, 24, 27, 30, and 48 h in three other groups. Tissues (lung, liver, and kidney) were collected at the end of infusion from three groups (one per dose). Blood (2 mL)

was collected from one rat per sex at 48, 52, 56, 72, and 96 h after the start of infusion for one group at 300 mg/kg/h. Then, the animals were sacrificed and evaluated by whole body autoradiography. The carcasses were frozen in hexane/dry ice, drained, blotted dry, and placed on dry ice for at least 2 h and then bagged and stored frozen at −20°C. The frozen carcasses were embedded in chilled carboxymethylcellulose and frozen into blocks.

Dog ADME Study

Nine male and nine female purebred beagle dogs (under GLP conditions) were randomly assigned in groups of three/sex/dose for phase I and phase II of the study. The dogs received ^{14}C-PP188 by continuous IV infusion at 30, 100, or 300 mg/kg/h for 48 h (1440, 4800, or 14,400 mg/kg) with a target dose level of 5 μCi/kg per animal in phase I and again for phase II. The phases were separated by a 7-day washout period. Blood, urine, feces, and cage rinse were collected from phase I animals. Blood (3 mL) was collected predose and at 48.25, 48.5, 49, 50, 51, 52, 54, 72, and 96 h after the start of infusion. Urine and feces were collected separately at 24-h intervals through 168 h. Blood, urine, feces, CSF, bile, and tissues were collected from phase II animals. Blood (3 mL) was collected predose and at 0.25, 0.5, 1, 2, 3, 4, 6, 24, 27, 30, and 48 h after the start of infusion. Urine and feces were collected separately at 24-h intervals. Shortly after the last blood collection, the animals were anesthetized with sodium pentobarbital, CSF was collected, the animals were exsanguinated, and the following tissues were removed for radioanalysis from the 300 mg/kg/h dose group only: adrenal glands, aorta, bile, bone, brain, cecum, cecum contents, colon, colon contents, duodenum, duodenum contents, eyes, fat (abdominal), gall bladder, heart, ileum, ileum contents, injection site, jejunum, jejunum contents, kidneys, liver, lungs, mesenteric lymph nodes, ovaries, pancreas, skeletal muscle (thigh), spleen, stomach, stomach contents, thyroid, testes, and urinary bladder. The tissues were excised, rinsed with saline, blotted dry, weighed, and placed on ice. After identification, the tissue samples were frozen at −20°C until analyzed.

Human ADME Study

After receiving IRB approval and obtaining written informed consent, five male and one female healthy volunteer subjects were enrolled in this open-label, single-dose IV infusion (100 mg/kg × 1 h plus 30 mg/kg/h × 47 h, 1510 mg/kg) pharmacokinetic study. Blood was collected over EDTA from 0 to 72 h and plasma was separated. Urine and feces were collected quantitatively daily over 0 to 96 h after the start of infusion. All samples were measured or weighed, frozen, and shipped to the analytical laboratory for further testing. The concentrations of PP188 were determined by a GPC method with RI detection for all samples collected (plasma, urine, and feces). Subject safety was assessed by physical examination, clinical laboratory evaluations, vital signs, and adverse events reported by the subjects or the investigator.

Metabolite Profile

Rat

Plasma samples from the toxicokinetics studies in rats were analyzed by GPC to detect parent PP188 as well as a higher molecular weight entity. Urine samples from individual male and female rats in the ADME studies were prepared at 0–24, 24–48, and 48–72 h and were subjected to GPC analysis using a radiochemical flow detector.

Dog

Plasma samples from the toxicokinetics studies in dogs were analyzed by GPC to detect parent PP188 as well as a higher molecular weight entity. Urine samples from the ADME study were prepared separately for male and female dogs at 0–24, 24–48, and 48–72 h. These samples were subjected to GPC analysis using a radiochemical flow detector.

Human

The plasma, urine, and fecal samples from the volunteers in the above-described study were analyzed by GPC to detect parent PP188 as well as a higher molecular weight entity.

Statistical Methods

Statistical analysis included descriptive statistics for all urine and fecal excretion data as well as tissue concentration data where applicable.

RESULTS

Enzyme Inhibition

The inhibitory effects of PP188 on selected human cytochrome P450 isozymes were examined in human liver microsomal incubations. The concentration of PP188 that inhibited 50% of the control activity was determined for six isozyme specific assays with pooled human liver microsomes at fixed substrate concentrations and with five concentrations of PP188. The IC_{50} values for CYP1A2, CYP2C9, CYP2C19, CYP2D6, CYP2E1, and CYP3A4 were all >1000 μM (>850 mg/mL). PP188 did not significantly inhibit the activities of any of the six human P450 isozymes.

Metabolism and Excretion

Rat

The metabolic stability of the radiolabel in ^{14}C-PP188 was evaluated in two rats after the administration of a continuous IV infusion of ^{14}C-PP188 for 48 h at 300 mg/kg/h. There were no apparent gender differences in the rate or extent of excretion of radioactivity. The major route of excretion was the urine whereas expired air accounted for < 0.15% of the dose. The radiolabel in ^{14}C-PP188 was determined to be metabolically stable (data not shown).

The excretion of ^{14}C-PP188 was determined after a 48-h IV infusion to 10 groups of male and female rats at dose levels of 30, 100, or 300 mg/kg/h. The rates and extent of excretion of radioactivity were similar in male and female rats. The major route of excretion of ^{14}C-PP188-derived radioactivity in both sexes was urine with means of 75.1 to 88.5% dose recovered over 168 h. Fecal excretion averaged 4% of the dose and residual carcass contained 2% of the dose at 168 h postdose. The total mean mass balance for all groups for males and females was > 93.9% dose (Table 1 and Fig. 2). GPC analysis of urine samples showed ^{14}C-PP188 to be the primary component but a longer retention time material was present in all samples and was maximal at 24–48 h (0.79–1.39% dose). Similarly, plasma samples analyzed by GPC from rats in the toxicokinetics studies also demonstrated the presence of a longer retention time material at low concentrations at the highest doses. This material was not evident in the chromatograms from plasma samples obtained during the excretion study. This may be due to the

Table 1. Mean (SD) Cumulative Excretion (% Dose) of Radioactivity in Rats, Dogs, and Humans After Continuous IV Administration for 48 h of ^{14}C-PP188[a]

Species	Dose (mg/kg)	Interval (h)	Urine		Feces		Cage Wash		Cage Wipe		Total	
			Male	Female	Male	Female	Male	Female	Male	Female	Male	Female
Rat	1440[b]	0–168	88.4 (6.00)	87.1 (5.42)	4.43 (0.58)	4.46 (1.75)	2.38 (2.43)	2.39 (0.81)	0.33 (0.02)	0.46 (0.19)	95.5 (3.29)	94.4 (3.37)
	4800[c]	0–168	88.5 (1.71)	75.1 (21.8)	3.10 (0.89)	16.2 (16.9)	1.50 (0.49)	2.04 (1.69)	0.79 (0.37)	0.74 (0.25)	93.9 (2.29)	94.1 (3.26)
	14,400[d]	0–168	86.1 (8.52)	86.3 (3.88)	3.38 (0.99)	3.70 (1.94)	3.13 (2.49)	2.55 (1.48)	1.21 (1.15)	0.61 (0.08)	95.7 (6.21)	95.2 (3.21)
Dog	1440[b]	0–168	86.0 (2.14)	90.6 (3.73)	1.67 (1.23)	1.08 (0.69)	6.31 (0.76)	6.22 (3.92)	0.84 (0.49)	0.37 (0.29)	94.8 (1.63)	98.3 (1.03)
	4800[c]	0–168	88.1 (0.67)	90.5 (6.86)	2.35 (0.34)	1.19 (0.55)	5.55 (1.65)	3.37 (1.30)	0.78 (0.54)	0.75 (0.80)	96.7 (1.26)	95.8 (4.25)
	14,400[d]	0–168	94.4 (0.72)	90.1 (5.05)	0.87 (0.03)	1.12 (0.65)	2.52 (0.63)	5.85 (4.37)	0.46 (0.21)	0.43 (0.15)	98.2 (0.55)	97.5 (0.99)
Human[e]	1510[f]	0–96	84.53 (4.32)		0.025 (0.014)		NA[g]		NA		84.56 (4.33)	

[a]Human subjects received non-radioactive purified PP188 at 100 mg/kg × 1 h plus 30 mg/kg/h × 47 h.
[b]1440 mg/kg = 30 mg/kg/h × 48 h.
[c]4800 mg/kg = 100 mg/kg/h × 48 h.
[d]14,400 mg/kg = 300 mg/kg/h × 48 h.
[e]Five male and one female healthy volunteers.
[f]1510 mg/kg = 100 mg/kg × 1 h + 30 mg/kg/h × 47 h.
[g]NA, not available.

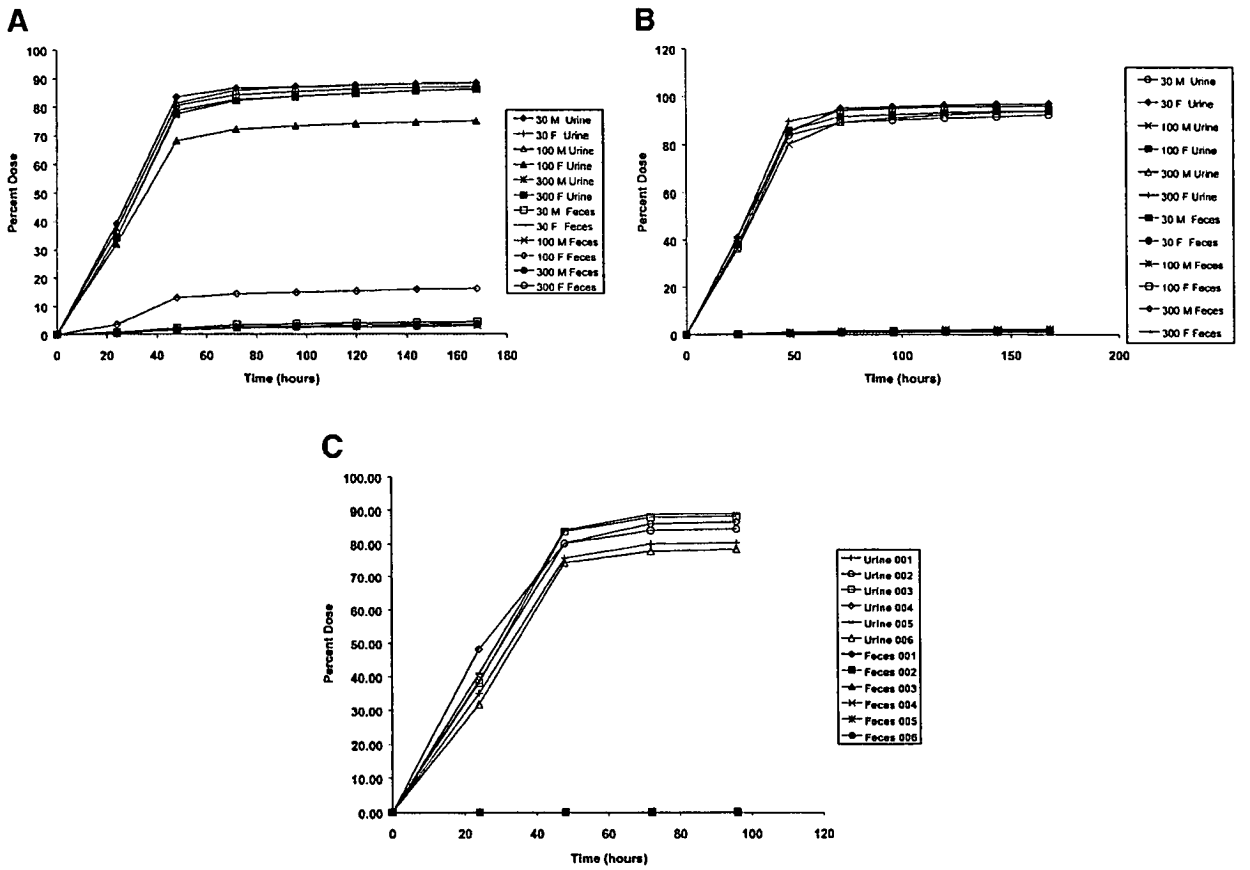

Figure 2. Cumulative excretion of total radioactivity (^{14}C-PP188) in urine and feces in rat (A), and dog (B), and cumulative excretion of PP188 in urine and feces from healthy humans (C).

shorter duration of dosing (48 h) compared with the toxicokinetics studies (30 days).

Dog

The excretion of ^{14}C-PP188-derived radioactivity was determined after a 48-h IV infusion of ^{14}C-PP188 to male and female dogs at doses of 30, 100, and 300 mg/kg/h. The rates and extent of excretion of radioactivity were similar in male and female dogs. The major route of excretion of radioactivity in both sexes was via the urine with means ranging from 86.0 to 94.4% dose. At 168 h, feces accounted for < 2.35% dose. The total mean mass balance ranged from 94.8 to 98.3% dose (Table 1 and Fig. 2). GPC analysis of the urine demonstrated the presence of a longer retention time species, which was present at > 5% of the dose. The primary component in urine was ^{14}C-PP188. GPC analysis of the plasma samples from this study only demonstrated the presence of parent PP188. However, dog plasma from the toxicokinetics studies demonstrated the presence of a longer retention time material at low concentrations in dogs from the highest doses. This difference may be attributable to the differing lengths of infusion (48 h versus 30 days, ADME versus toxicokinetics studies).

Human

The excretion and pharmacokinetics of PP188 were studied in five male and one female healthy subjects after a 48-h IV infusion of PP188 at a dose of 100 mg/kg × 1 h plus 30 mg/kg/h × 47 h. The major route of excretion of unchanged PP188 was the urine with 84.5% dose excreted over 96 h. Fecal excretion of PP188 accounted for 0.025% dose over the same time period (Table 1). The plasma samples demonstrated the presence of a longer retention time material at low concentrations, which was cleared slowly from the plasma. This species was not observed in urine or feces samples. Plasma samples were fractionated by

GPC, pooled, and analyzed by MALDI-TOF mass spectrometry to better understand the structure of the longer retention time material. This material had an apparent MW of approximately 16,000 Da and had fragmentation patterns consistent with a block copolymer. It appears to be the high molecular weight fraction of the polymeric distribution for PP188.

Tissue Distribution

Rat

Blood and plasma were analyzed for total radioactivity. The mean concentration of radioactivity was higher in plasma than blood in both sexes, indicating that ^{14}C-PP188-derived radioactivity distributed preferentially into the extracellular fraction of the whole blood. The plasma concentrations of radioactivity peaked at the end of the infusion and increased with increasing dose in a linear manner. (Fig. 3) The pharmacokinetic parameters for total radioactivity derived from ^{14}C-PP188 are summarized in Table 2. Autoradiographic data (Fig. 4) indicated that ^{14}C-PP188-derived radioactivity was widely distributed throughout the organs and tissues in both male and female rats. At 48 h postdose (end of infusion), the highest concentration of radioactivity occurred in the gastrointestinal tract, kidney, axillary lymph nodes, popliteal lymph nodes, adrenal gland, salivary gland, cervical lymph nodes, thyroid gland, inguinal lymph nodes, liver, lungs, and bone marrow as measured by autoluminography (Table 3) which does not allow for correction of background blood or urine in the tubules. Generally, tissue concentrations decreased over time, but elimination was not complete at 96 h postdose. Differential intra-organ distribution was apparent in the kidney with radioactivity unevenly distributed in the renal cortex and medulla (Table 3 and Fig. 4). Again this was probably attributable to the increased vascularization of the renal cortex.

Dog

The mean concentrations of radioactivity were higher in plasma than blood in both sexes indicating that ^{14}C-PP188-derived radioactivity distributed preferentially into the extracellular fraction. The peak concentrations of radioactivity occurred at the end of infusion and the concentrations increased with increasing dose in a linear manner. The pharmacokinetic parameters for total radioactivity derived from ^{14}C-PP188 as well as those for parent PP188 are summarized in Table 2. The tissues from male dogs with the highest mean concentrations at 48 h included the kidneys, mesenteric lymph nodes, adrenal glands, liver, urinary bladder, and spleen. The tissues from female dogs with the highest mean concentration at 48 h included the kidneys, adrenal glands, mesenteric lymph nodes, liver, ovaries, urinary bladder, and spleen (Table 3).

DISCUSSION

PP188 is a nonionic, block copolymer that is currently being evaluated in phase III clinical trials for the treatment of vasoocclusive crisis in sickle

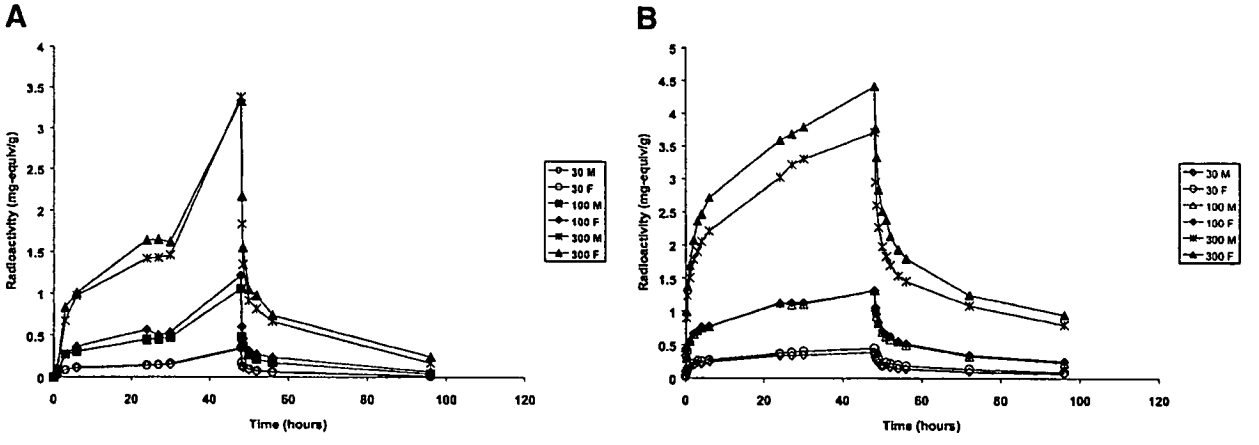

Figure 3. Mean plasma concentrations of total radioactivity in rats (A) and dogs (B) after a 48-h continuous IV infusion of ^{14}C-PP188.

Table 2. Pharmacokinetic Parameters for Total Radioactivity (Milligram-Equivalents/Gram) in Rats and Dogs and for PP188 in Dogs After 48-h Continuous IV Infusion Doses of ^{14}C-PP188

Entity Measured	Dose (mg/kg/h)	Species	Sex	C_{max} (mg/mL)	T_{max} (h)	$T_{1/2}$ (h)
Radioactivity	30	Rat	M	0.139	48.25	22.3
			F	0.173	48.25	19.8
	100		M	0.482	48.25	18.7
			F	0.602	48.25	21.0
	300		M	1.84	48.25	20.0
			F	2.17	48.25	23.2
Radioactivity	30	Dog	M	0.318	49.20	38.7
			F	0.404	48.25	37.7
	100		M	1.07	48.25	36.3
			F	1.06	48.25	37.6
	300		M	2.95	48.25	45.2
			F	3.77	48.25	42.2
PP188	100	Dog	M	1.27	48.25	9.8
			F	1.33	48.25	9.0
	300		M	5.33	48.25	13.5
			F	3.51	48.25	13.4

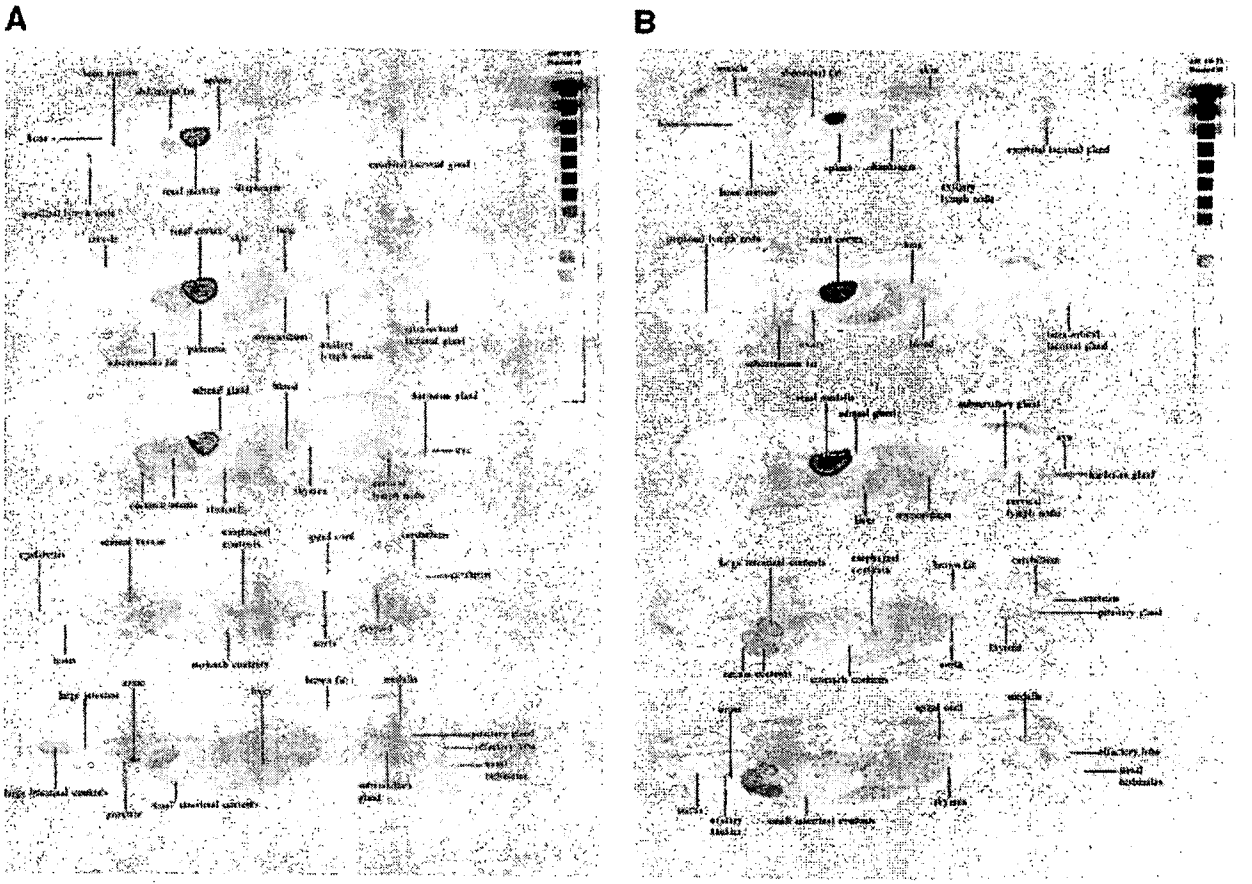

Figure 4. Whole body autoradioluminograph of male (A) and female (B) rats at 48 h after a 48-h IV infusion of ^{14}C-PP188 (14,400 mg/kg/day).

Table 3. Mean (SD) Concentration of Radioactivity in Tissues at 48 h (End of Infusion) for Male and Female Rats and Dogs After a 48-h IV Infusion of ^{14}C-PP188 (14,400 mg/kg)

	Microgram Equivalents of ^{14}C-PP188/g Tissue			
	Rats[a]		Dogs[b]	
Matrix	Male	Female	Male	Female
Adrenal glands	826	1150	2110 (226)	2410 (560)
Aorta	1020	769	ND[c]	ND
Bile (from gall bladder)	NA[d]	NA	569 (137)	186 (322)
Bone, including marrow	1140	ND	86.4 (150)	133 (230)
Brain	ND	ND	ND	20.4 (35.3)
Cecum	1090	1350	669 (75.4)	731 (70.6)
Cecum contents	2290	3180	445 (210)	249 (132)
CSF	NA	NA	52.8 (91.5)	ND
Colon	928	881	641 (69.9)	667 (85.6)
Colon contents	2110	3490	706 (369)	803 (595)
Duodenum	851	901	624 (72.6)	626 (43.8)
Duodenum contents	1610	912	140 (55.5)	151 (151)
Eyes (both)	ND	ND	ND	ND
Fat (abdominal)	ND	ND	527 (331)	508 (174)
Gall bladder	NA	NA	642 (163)	616 (162)
Heart	724	633	424 (73.2)	478 (51.3)
Ileum	NA	NA	612 (56.8)	583 (56.6)
Ileum contents	NA	NA	503 (225)	327 (108)
Injection site	NA	NA	156 (76.6)	353 (341)
Jejunum	NA	NA	566 (62.3)	571 (86.9)
Jejunum contents	NA	NA	356 (117)	354 (300)
Kidneys (both)[e]	7170	11,800	8390 (1070)	7470 (1120)
Liver	1370	1560	1450 (86.9)	1520 (123)
Lungs	1140	1170	784 (108)	991 (106)
Mesenteric lymph nodes	550	835	2340 (424)	2360 (253)
Ovaries	NA	767	NA	1200 (216)
Pancreas	812	803	487 (67.3)	559 (81.4)
Skeletal muscle (thigh)	ND	ND	144 (29.8)	144 (40.5)
Spleen	654	766	1000 (20.7)	1000 (69.1)
Stomach	566	695	653 (67.5)	666 (57.8)
Stomach contents	690	ND	39.3 (68.1)	ND
Testes	428	NA	324 (74.2)	NA
Thyroid	1050	1120	445 (405)	263 (456)
Urinary bladder	1040	875	1090 (138)	1150 (271)

[a]One rat/sex by whole body autoradiography.
[b]Three dogs/sex.
[c]ND, not detectable.
[d]NA, not available.
[e]Dog kidney radioactivity was corrected for background blood levels of ^{14}C. Rat data were not corrected.

cell disease,[12] and in preclinical studies for spinal cord injury and muscular dystrophy. PP188's distribution, metabolism, and excretion were evaluated in rats, dogs, and humans as part of the overall safety program in support of the clinical trials. This report presents the first comprehensive evaluation of a polyoxypropylene–polyoxyethylene block copolymer's distribution, metabolism, and excretion across species, including humans. Previous articles have discussed the distribution and excretion of similar polymers in rodents,[21–24] indicating that these agents were distributed in extracellular water and excreted primarily via the kidneys with minimal to no metabolism.[25]

As would be expected for a highly water soluble nonionic polymer, PP188 was primarily distributed in extracellular water with little to no uptake by red blood cells. The tissues with the highest concentration of PP188 in rats and dogs were the kidneys, lymph nodes, liver, spleen, and urinary bladder with the gastrointestinal tract and lungs also being prominent in the rats. These are all well perfused organs and tissues and the level of radioactivity detected was probably related to the concentration of compound in the extracellular fluid.

Metabolism was limited (< 5% of dose) as noted on GPC analysis with radiochemical detection. The longer retention time material identified in plasma from all three species had a MW of approximately 16,000 Da and a MALDI-MS fragmentation pattern suggesting a block copolymer. This material was present as part of the high molecular weight distribution of the PP188. The clearance from the body of this material is much slower than the parent compound leading to the observation of low levels in urine at later time periods as well as low plasma concentrations at the higher doses. PP188 had no apparent effect on any of the P450 isozymes that were studied. This would be consistent with PP188's surface-active properties and limited metabolism. These data suggest a low probability of drug interactions caused by interference of PP188 with P450 isozyme metabolism.

Clearance from the body was almost entirely by renal excretion in rats, dogs, and humans with the preponderance being intact PP188. Fecal/biliary excretion was low in all three species (< 5% of dose). The radiolabel used was metabolically stable as noted by the lack of excretion of $^{14}CO_2$ in the expired air.

Overall, PP188 was well tolerated clinically in all species studied even at the highest dose level of 300 mg/kg/h × 48 h (14,400 mg/kg). Renal clearance was the controlling route of clearance for PP188 from the body. The 48-h infusion doses of PP188 were cleared in all species by approximately 1 week after the cessation of dose administration. A similar pattern of distribution, metabolism, and excretion could be expected for other nonionic block copolymers with physical and chemical characteristics similar to PP188.

ACKNOWLEDGMENTS

The authors thank Covance Laboratories, Madison, WI for conducting the ADME studies and isozyme inhibition studies, Bio-Kinetic Laboratories, Springfield, MO for conducting the human ADME study, and Richard Okerholm, PhD, for advice and counsel in the design of the ADME studies.

REFERENCES

1. Bentley PK, Davis SS, Johnson OL, Lowe KC, Washington C. 1989. Purification of pluronic F-68 for perfluorochemical emulsification. J Pharm Pharmacol 41:661–663.
2. Lowe KC, Furmidge BA, Thomas S. 1995. Haemolytic properties of pluronic surfactants and effects of purification. Artif Cells Blood Substit Immobil Biotechnol 23:135–139.
3. Smith CM, Hebbel RP, Tukey DP, Clawson CC, White JG, Vercellotti GM. 1987. Pluronic F-68 reduces the endothelial adherence and improves the rheology of liganded sickle erythrocytes. Blood 69:1631–1636.
4. Carr ME, Powers PL, Jones MR. 1991. Effects of poloxamer 188 on the assembly, structure and dissolution of fibrin clots. Thromb Haemost 66:565–568.
5. Carter C, Fisher TC, Hamai H, Johnson CS, Meiselman HJ, Nash GB, Stuart J. 1992. Haemorheological effects of a nonionic copolymer surfactant (poloxamer 188). Clin Hemorheol 12:109–120.
6. Hsu LL, Liu XW, Pierangeli S, Eckman JR, Aguayo SM, Jack D, Wick TM. 2000. Microcirculatory effects of blocking cell adhesion molecules in transgenic sickle cell mice. Blood 96:528a.
7. McKenna R, Cole E, MacLeod C, Emanuele M, Hunter R. 1989. The effects of RheothRx on platelet function and coagulation in man. Blood 74:411.
8. Grover FL, Kahn RS, Heron MW, Paton BC. 1973. A nonionic surfactant and blood viscosity. Arch Surg 106:307–310.
9. Toth K, Bogar L, Juricskay I, Keltai M, Yusuf S, Haywood LJ, Meiselman HJ. 1997. The effect of RheothRx injection on the hemorheological parameters in patients with acute myocardial infarction. Clin Hemorheol Microcirc 17:117–125.
10. Armstrong JK, Meiselman HJ, Fisher TC. 1995. Inhibition of red blood cell-induced platelet aggregation in whole blood by a nonionic surfactant, poloxamer 188 (RheothRx injection). Thromb Res 79:437–450.
11. Adams-Graves P, Kedar A, Koshy M, Steinberg M, Veith R, Ward D, Crawford R, Edwards S, Bustrack J, Emanuele M. 1997. RheothRx (poloxamer 188) injection for the acute painful episode of sickle cell disease: A pilot study. Blood 90:2041–2046.
12. Orringer EP, Casella JF, Ataga KI, Koshy M, Adams-Graves P, Luchtman-Jones L, Wun T, Watanabe M, Shafer F, Kutlar A, Abboud M,

Steinberg M, Adler B, Swerdlow P, Terregino C, Saccente S, Files B, Ballas S, Brown R, Wojtowicz-Praga S, Grindel JM. 2001. Purified poloxamer 188 for the treatment of acute vaso-occlusive crisis of sickle cell disease: A double-blind, randomized, placebo-controlled study. JAMA 286:2099–2106.

13. Files BA, Ballas SK, Benjamin LJ, Wojtowicz-Praga S, Grindel JM. 1998. Multicenter trial of FLOCOR in patients with sickle cell disease and acute chest syndrome. Blood 92:30b.
14. Luchtman-Jones L, Files B, Ballas SK, Swerdlow P, Benjamin L, Hilliard L, Coates TD, Abboud M, Wojtowicz-Praga S, Grindel JM. 1999. Phase I study of FLOCOR in patients with acute chest syndrome of sickle cell disease. Blood 94:25b.
15. Plopper CG, Weir AJ, Morin D, Chang A, Philpot RM, Buckpitt AR. 1993. Postnatal changes in the expression and distribution of pulmonary cytochrome P450 monooxygenases during Clara cell differentiation in rabbits. Mol Pharmacol 44:51–61.
16. Ho JW, Moody DE. 1993. Determination of tolbutamide hydroxylation in rat liver microsomes by high-performance liquid chromatography: Effect of psychoactive drugs on *in vitro* activity. Life Sci 52: 21–28.
17. Chiba K, Manabe K, Kobayashi K, Takayama Y, Tani M, Ishizaki T. 1993. Development and preliminary application of a simple assay of S-mephenytoin 4′-hydroxylase activity in human liver microsomes. Eur J Clin Pharmacol 44:559–562.
18. Jacqz-Aigrain E, Funck-Brentano C, Cresteil T. 1993. CYP2D6- and CYP3A-dependent metabolism of dextromethorphan in humans. Pharmacogenetics 3:197–204.
19. Duescher RJ, Elfarra AA. 1993. Determination of *p*-nitrophenol hydroxylase activity of rat liver microsomes by high-pressure liquid chromatography. Anal Biochem 212:311–314.
20. Zhang XJ, Thomas PE. 1996. Erythromycin as a specific substrate for cytochrome P4503A isozymes and identification of a high-affinity erythromycin *N*-demethylase in adult female rats. Drug Metab Dispos 24:23–27.
21. Wang ZY, Stern IJ. 1975. Disposition in rats of a polyoxypropylene–polyoxyethylene copolymer used in plasma fractionation. Drug Metab Dispos 3:536–542.
22. Moghimi SM. 1999. Re-establishing the long circulatory behavior of poloxamine-coated particles after repeated intravenous administration: Applications in cancer drug delivery and imaging. Biochim Biophys Acta 472:399–403.
23. Leu D, Manthey B, Kreuter J, Speiser P, Deluca PP. 1984. Distribution and elimination of coated polymethyl [2-^{14}C]methacrylate nanoparticles after intravenous injection in rats. J Pharm Sci 73: 1433–1437.
24. Clarke MSF, Prendergast MA, Terry AV Jr. 1999. Plasma membrane ordering agent pluronic F-68 (PF-68) reduces neurotransmitter uptake and release and produces learning and memory deficits in rats. Learn Mem 6:634–649.
25. Rodriguez SC, Singer EJ. 1996. Toxicology of polyoxyalkylene block copolymers. In: Nace VM, editor. Nonionic surfactants, Vol. 60; New York: Marcel Dekker. pp 211–241.

0090-9556/03/3103-294-305$7.00
DRUG METABOLISM AND DISPOSITION
Copyright © 2003 by The American Society for Pharmacology and Experimental Therapeutics
DMD 31:294–305, 2003

Vol. 31, No. 3
810/1044816
Printed in U.S.A.

ABSORPTION, DISTRIBUTION, METABOLISM, AND EXCRETION OF XIMELAGATRAN, AN ORAL DIRECT THROMBIN INHIBITOR, IN RATS, DOGS, AND HUMANS

ULF G. ERIKSSON, ULF BREDBERG, KURT-JÜRGEN HOFFMANN, ANNELI THURESSON, MARGARETH GABRIELSSON, HANS ERICSSON, MARTIN AHNOFF, KRISTINA GISLÉN, GUNNAR FAGER, AND DAVID GUSTAFSSON

AstraZeneca R&D Mölndal, Mölndal, Sweden

(Received May 29, 2002; accepted November 26, 2002)

This article is available online at http://dmd.aspetjournals.org

ABSTRACT:

The absorption, metabolism, and excretion of the oral direct thrombin inhibitor, ximelagatran, and its active form, melagatran, were separately investigated in rats, dogs, and healthy male human subjects after administration of oral and intravenous (i.v.) single doses. Ximelagatran was rapidly absorbed and metabolized following oral administration, with melagatran as the predominant compound in plasma. Two intermediates (ethyl-melagatran and OH-melagatran) that were subsequently metabolized to melagatran were also identified in plasma and were rapidly eliminated. Melagatran given i.v. had relatively low plasma clearance, small volume of distribution, and short elimination half-life. The oral absorption of melagatran was low and highly variable. It was primarily renally cleared, and the renal clearance agreed well with the glomerular filtration rate. Ximelagatran was extensively metabolized, and only trace amounts were renally excreted. Melagatran was the major compound in urine and feces after administration of ximelagatran. Appreciable quantities of ethyl-melagatran were also recovered in rat, dog, and human feces after oral administration, suggesting reduction of the hydroxyamidine group of ximelagatran in the gastrointestinal tract, as demonstrated when ximelagatran was incubated with feces homogenate. Polar metabolites in urine and feces (all species) accounted for a relatively small fraction of the dose. The bioavailability of melagatran following oral administration of ximelagatran was 5 to 10% in rats, 10 to 50% in dogs, and about 20% in humans, with low between-subject variation. The fraction of ximelagatran absorbed was at least 40 to 70% in all species. First-pass metabolism of ximelagatran with subsequent biliary excretion of the formed metabolites account for the lower bioavailability of melagatran.

Thrombin plays a central role in the processes of hemostasis and thrombus formation. Among its numerous functions are the catalysis of the transformation of fibrinogen to fibrin monomers producing the fibrin network that reinforces the fragile, platelet-rich plug and the stimulation of platelet aggregation. A number of agents, including warfarin and low-molecular-weight heparins, are available for the prevention and treatment of thromboembolic complications. Indeed, warfarin and other vitamin K antagonists are the only oral anticoagulants available today. However, patients receiving these agents require frequent monitoring of prothrombin time because of the narrow therapeutic window and slow on- and offset of action of these agents (Hirsh et al., 2001), characteristics that make it difficult to predict their anticoagulant effect. Warfarin is also subject to large variability in its pharmacokinetic (PK[1]) properties due to drug and food interactions (Hirsh et al., 2001). Despite monitoring, these agents are associated with a high incidence of bleeding and drug-related deaths (Anonymous, 1993). Low-molecular-weight heparins can be administered without routine coagulation monitoring (Hull and Pineo, 1995), but the fact that they can only be administered parenterally limits their use. Currently available anticoagulants therefore have a number of drawbacks, and there is an ongoing quest for a new anticoagulant that is effective, safe, and can be administered orally without routine coagulation monitoring.

Melagatran is a novel, direct thrombin inhibitor that binds rapidly, reversibly, and competitively to the active site of thrombin with a K_i of 0.002 μM (Gustafsson et al., 1998). It has shown promise as an antithrombotic drug, both in animal models of experimental thrombosis (Elg et al., 1997, 1999; Eriksson et al., 1997; Mattsson et al., 1997; Gustafsson et al., 1998; Metha et al., 1998) and in clinical trials in orthopedic surgery patients (Heit et al., 2001; Eriksson et al., 2002a,b,c) and patients with deep venous thrombosis (Eriksson et al., 1999a, 2003). Because of low membrane permeability, melagatran is not suited to oral administration, however, its favorable pharmacodynamic properties were the impetus for the development of ximelagatran, a novel, direct thrombin inhibitor that can be administered orally, whereupon it is rapidly transformed to melagatran, its active form (Gustafsson el al., 2001). Melagatran may be formed from ximelagatran via two different pathways, as shown in Fig. 1. The primary compounds formed during the bioconversion of ximelagatran to melagatran are OH-melagatran (formed by hydrolysis of the ethyl ester) and ethyl-melagatran (formed by reduction of the hydroxyamidine), which are both subsequently converted to melagatran. The thrombin-inhibiting activity of ximelagatran and OH-melagatran is about 1% of

[1] Abbreviations used are: PK, pharmacokinetic; LC, liquid chromatographic; LC-MS, liquid chromatography-mass spectrometry; LOQ, limit of quantification; CV, coefficient of variation; Y_{pred}, the model-predicted plasma concentration; AUC, area under the plasma concentration–time curve; AUMC, area under the first moment curve; CL, plasma clearance; F, bioavailability; CL_R, renal clearance.

Address correspondence to: Ulf G. Eriksson Ph.D., Experimental Medicine, AstraZeneca R&D Mölndal, S-431 83 Mölndal, Sweden. E-mail: ulf.eriksson@astrazeneca.com

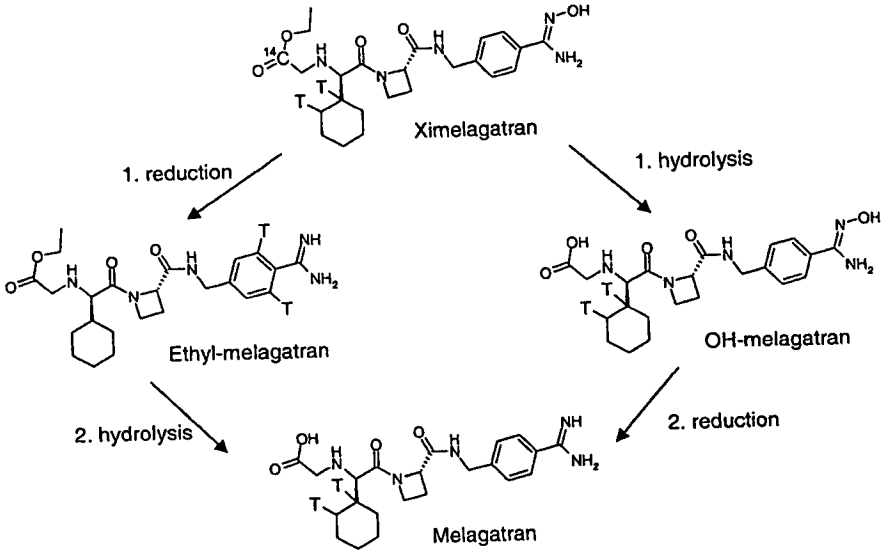

FIG. 1. *The proposed metabolic pathway of ximelagatran showing the formation of melagatran via two intermediate compounds, ethyl-melagatran, and OH-melagatran, by reduction of the OH-group and hydrolysis of the ethyl ester.*

The ^{14}C- and tritium (T)-labeled positions are indicated in the figure.

that of melagatran, whereas ethyl-melagatran has about the same inhibitory potency as melagatran (Gustafsson et al., 2001).

The aim of the studies described here was to examine the metabolism and excretion patterns and the PK properties of ximelagatran and melagatran following the administration of single oral and i.v. doses to animals and humans. The main focus was on evaluating the bioavailability of melagatran, the active thrombin inhibitor, following oral administration of ximelagatran.

Materials and Methods

Ximelagatran and melagatran were synthesized by AstraZeneca (Mölndal, Sweden), using methods analogous to those described previously (Antonsson et al., 1994, 1997). Ethyl-melagatran and OH-melagatran, used as reference compounds for metabolite identification in biological samples, and radiolabeled compounds were prepared at the Department of Medicinal Chemistry, AstraZeneca. The chemical structures of these compounds are shown in Fig. 1. The radiolabeled compounds (specific radioactivity and radiochemical purity given in parentheses) used were [^{14}C]ximelagatran (2.0 kBq/nmol, >97%), [^{3}H]ximelagatran (55 kBq/nmol, >97%), [^{3}H]melagatran (521 kBq/nmol, 97%), OH-melagatran-^{3}H (55 kBq/nmol, >95%), and ethyl-melagatran-^{3}H (900 kBq/nmol, >98%). In essentially all studies, aqueous solutions (pH adjusted to 3–5) of melagatran (chemical purity 99.3%) and ximelagatran (chemical purity >97%) were used for dosing to animals and humans. In the food interaction study for melagatran in human subjects, an immediate-release tablet of melagatran was administered. All other chemicals used were of analytical grade.

Design of Studies in Animals

Sprague-Dawley rats and beagle dogs were used in studies to examine the mass balance and PK properties of melagatran and ximelagatran after i.v. and oral (by gastric gavage) administration. All animal studies described were approved by the regional ethics committee.

Mass Balance and Pharmacokinetics in Rats. The rats were starved overnight until after drug administration but retained free access to drinking water at all times. In mass balance studies, the rats were placed in all-glass metabolic cages that allowed separate collection of urine and faeces. PK studies were performed in separate groups of rats. Two days before dosing, these rats were anesthetized, and a catheter was placed in the carotid artery for collection of blood samples. For i.v. dosing, a catheter was also inserted in the right jugular vein. The catheters were exteriorized at the nape of the neck and sealed. After surgery, the rats were housed individually and had free access to water and food.

Mass balance studies. Single, 2 μmol/kg (3.5 MBq/kg) i.v. doses of [^{3}H]melagatran were administered (via a catheter placed in the right vena jugularis) to one group of four rats, and single, 30 μmol/kg (2 MBq/kg), oral doses of [^{3}H]melagatran were administered by gavage to a separate group of four rats. The rats used were 12 to 14 weeks old and weighed 339 to 355 g. Urine and feces were collected during the 19-h period before dosing and at 24-h intervals for 7 days after dosing. Urine samples collected during the 0- to 24-h time period and feces collected during the 0- to 24- and 24- to 48-h time periods postdosing were used in the analysis of metabolic patterns of melagatran.

Single, 40 μmol/kg (19.4 MBq/kg), oral doses of [^{14}C]ximelagatran were administered to one group of eight rats (four male and four female) and single, 10 μmol/kg (21.9 MBq/kg), i.v. doses of [^{14}C]ximelagatran were administered by bolus injection in the tail vein to a separate group of eight rats (four male and four female). The rats used were 6- to 7-weeks old. At the time of dosing, the females weighed from 173 to 255 g and the males from 145 to 218 g. Urine and feces were collected at 24-h intervals for 7 days postdosing. Urine samples were also collected during the 0- to 6- and 6- to 24-h time periods postdosing. Metabolic patterns were determined in the urine samples collected during the 0- to 6- and 6- to 24-h time periods postdosing and in fecal samples collected during the 0- to 24- and 24- to 48-h time periods postdosing.

Excretion in bile was determined in bile-duct-fistulated rats (three male and three female rats, starved overnight), each of which received a single, 40 μmol/kg (20 MBq/kg), oral dose of [^{3}H]ximelagatran. The rats were housed individually in metabolic cages, and bile was collected during the 0- to 2-, 2- to 4-, 4- to 8-, and 8- to 24-h time periods postdosing.

PK studies. Unlabeled melagatran was administered as an i.v. bolus dose (2 μmol/kg) or orally (30 μmol/kg) to separate groups of four male or four female rats. A higher oral dose of 100 μmol/kg was also given to another group of four male rats. The rats used were 12- to 14-weeks old. At the time of dosing, the females weighed from 209 to 240 g and the males from 338 to 365 g. Blood samples (0.2 ml) were collected from all rats 60 min or less before and at regular intervals until 240 min after i.v. dosing and 480 min after oral dosing.

PK properties of ximelagatran in rats were examined following oral and i.v. administration of [^{14}C]ximelagatran. Oral administration involved a single dose of 10 μmol/kg (8.89 MBq/kg) ximelagatran, administered by gavage to five male and five female rats, and a single dose of 40 μmol/kg (35.6 MBq/kg) ximelagatran administered to a separate group of five male rats. Administration (i.v.) involved a single, 5 μmol/kg (4.39 MBq/kg), dose of ximelagatran administered by bolus injection to three male and four female rats and a single, 10 μmol/kg (8.78 MBq/kg) dose of ximelagatran administered to a separate group of four male rats. Each rat received only one dose of drug. The rats used

were 12-week-old males and females weighing 200 to 450 g. Blood samples (250 μl) were collected from the carotid artery before and up to 24 h after oral and i.v. administration. After oral administration, nine blood samples were taken from each rat. After i.v. administration, 12 samples were taken from each male rat and six from each female rat.

Mass Balance and Pharmacokinetics in Dogs. Male and female dogs that were 2- to 6-years old and weighing 10 to 17 kg were used in the experiments. Two groups of four dogs (two males and two females) were administered single doses of [^{3}H]melagatran either as an i.v. infusion over 1 min in a front leg vein (2 μmol/kg, 2MBq/kg), or orally by gavage (30 μmol/kg, 6 MBq/kg). Just before administration of both the oral and i.v. doses of melagatran, the dogs were placed in metabolic cages. Blood samples (5 ml) were collected from a front leg vein before and then at frequent intervals until 300 min after i.v. dosing and 360 min after oral dosing. Additional blood samples were then collected every 24 h for 5 days. Urine was collected in the cage during the 0- to 12- and 12- to 24-h time periods postdosing and thereafter at 24-h intervals for 5 days. Feces were collected at 24-h intervals for 5 days postdosing.

The influence of food on the absorption of melagatran was the subject of a second study in four dogs who were administered a single oral dose of 30 μmol/kg melagatran on two study days separated by a washout period of 5 days. On one study day, the dogs were administered melagatran under fasting conditions, whereas on the other study day, they were administered the drug 1 h after food intake in a crossover design. Blood samples were collected before dosing and then frequently until 6 h postdosing. In both studies, the dogs were fasted from approximately 3:00 PM on the day before dosing until approximately 6 h after dosing but retained free access to water throughout the experiments.

Two male and two female dogs received a single, 40 μmol/kg (5.16 MBq/kg) oral dose of [^{14}C]ximelagatran, by gastric gavage. After a washout period of 4.5 weeks, the same dogs were each given a single, 10 μmol/kg (5.09 MBq/kg), i.v. dose of [^{14}C]ximelagatran, by bolus injection into the cephalic vein over a period of approximately 1 min. The dogs were housed individually in metabolic cages immediately following each dose of drug. Venous blood samples (approximately 8 ml) were collected from a leg vein into lithium heparin tubes before and up to 48 h after oral and i.v. administration. Urine was collected before and 6 and 24 h after both oral and i.v. drug administration, and then at 24-h intervals until 168 h post drug administration. Feces were collected predose and at 24-h intervals for 7 days postdosing. In addition, two male and two female dogs were given a 10 μmol/kg oral dose of unlabeled ximelagatran. After a washout period of 2 weeks, the same dogs received a 5 μmol/kg i.v. dose of ximelagatran. The dogs were starved overnight before dosing and until approximately 5 h postdosing but had free access to water at all times. Blood samples (1.5 ml) from a front leg vein were collected predose and up to 24 h postdosing.

Excretion in bile was determined in a chronically bile-duct canulated female fasted dog (15.3 kg) administered a single, 40 μmol/kg (5 MBq/kg), oral dose of [^{3}H]ximelagatran. Bile was collected during the 0- to 2-, 2- to 4-, 4- to 8-, and 8- to 24-h time periods postdosing.

Design of Studies in Humans

Subjects. Young healthy white male subjects, from whom informed consent was obtained prior to enrollment, were included in the studies that were performed in compliance with current good clinical practice guidelines and the Declaration of Helsinki. The subjects included in three melagatran studies were 20- to 40-years old and weighed 66 to 86 kg. These studies were performed in Sweden and approved by the Medical Products Agency of Sweden and the Göteborg University Ethics Committee. For the ximelagatran study, the subjects were 31- to 50-years old and weighed 76 to 86 kg. This study was performed in Scotland and approved by the local independent ethics committee.

For all studies, eligibility for entry was assessed at a screening visit that took place within 14 days of the start of the study. No medication, including aspirin, other nonsteroidal anti-inflammatory drugs, or prescribed medication, were allowed within the 2 weeks prior to the first dose of study drug and until the end the study period. None of the subjects had received another investigational drug within 2 to 3 months prior to the first treatment day.

Melagatran Studies. *Mass balance and pharmacokinetics.* Fixed doses of [^{3}H]melagatran were administered to 12 healthy male volunteers in an open-label, crossover study. Each subject was to receive two single doses of [^{3}H]melagatran, one as an iv infusion and the second as an oral solution, with at least 2 weeks between doses. The iv dose consisted of 5.3 μmol (2.3 mg) melagatran containing 5.2 MBq of [^{3}H]melagatran in a volume of 15 ml infused over 10 min. The oral dose consisted of 256 μmol (110 mg) melagatran containing 7.4 MBq [^{3}H]melagatran in a volume of 40 ml followed by 60 ml of water to rinse the vial. On the evening before each investigational day, subjects were instructed to have dinner no later than 7:00 PM and to abstain from food and drink from 10:00 PM until a standardized meal (lunch) was served 3 h after drug administration. Other standardized meals were served 6 h (snack), 10 h (dinner) and 13 h (snack) after drug administration. Venous blood samples were drawn by repeated venipuncture (Venoject; Terumo Europe N.V., Leuven, Belgium) from a forearm (the forearm contralateral to that of the infusion for subjects receiving i.v. melagatran) before and then frequently during the 24-h period after administration of both the i.v. and the oral doses of melagatran. Urine was collected predose, during the 0- to 4-, 4- to 12-, and 12- to 24-h time periods postdosing and thereafter at 24-h intervals for 5 days postdosing. Feces were collected at 24-h intervals over the 5-day period postdosing. The amounts of urine and feces collected were determined by weighing.

Dose linearity. This was examined in two studies as follows: 1) an open-label, dose-escalation study in 26 healthy male volunteers, in which melagatran was administered as gradually increasing single i.v. doses (administered as a constant infusion over 10 min) from 1.7 to 82 μg/kg (0.004–0.19 μmol/kg) to groups of two or four subjects per dosing level; 2) an open-label, dose-escalation study in 23 healthy, male volunteers, in which melagatran was administered as gradually increasing single oral doses (in solution) from 0.02 to 3.28 μg/kg (0.05–7.6 μmol/kg) to groups of two or four subjects per dosing level. Each subject received a maximum of two doses of melagatran separated by at least 1 week. On the evening before each investigational day, subjects were instructed to have dinner no later than 7:00 PM and to abstain from food and drink from 10:00 PM until a standardized meal was served postdrug administration. In the i.v.-dosing study, standardized meals were served 1 h (breakfast) and 4 h (lunch) after the start of the i.v. infusion, whereas in the oral dosing study, they were served 3 h (lunch), 6 h (snack), 10 h (dinner), and 13 h (snack) after drug administration. In the i.v.-dosing study, blood samples were collected immediately before and then frequently until 4 h after dosing for doses up to 50 nmol/kg, and additionally at 6 and 8 h after dosing for doses of 50 nmol/kg and above. In the oral dosing study, blood samples were drawn before and at frequent intervals until 24 h after dosing.

Effect of food. Six healthy human volunteers received melagatran as a 50-mg tablet on three investigational days separated by washout periods of at least 1 week, in an open-label, three-way, randomized crossover study. Administration of melagatran occurred under fasting conditions, together with breakfast, or 2 h after breakfast, in randomized order.

Ximelagatran study. The mass balance and pharmacokinetics of ximelagatran was examined in an open-label, sequential, nonrandomized study, in which each subject received a single, 50 mg (105 μmol), oral dose of [^{14}C]ximelagatran (2.52 MBq), at a concentration of 1.25 mg/ml. This was followed 20 days later by a single, 10 mg (21 μmol), i.v. dose of unlabeled ximelagatran infused over 10 min with the aid of an infusion pump. Subjects were required to remain at the study site for 7 to 9 days following drug administration in the first study session and for 24 h following drug administration in the second study session. Subjects were required to fast from 11:00 PM on the evenings before drug administration until a standardized lunch was served 4 h postdosing. Subjects also abstained from food for 2 h before each laboratory investigation.

Blood (10–12 ml), urine, and feces samples for PK analysis were collected before and up to 168 h post oral administration, by which time excretion of drug was essentially complete. Blood (5 ml) and urine samples were collected before and up to 12 h and 24 h post i.v. administration, respectively. Whole blood samples were collected via a venous catheter or by venopuncture.

Plasma Protein Binding and Blood–Plasma Partitioning.

The plasma protein binding and the partitioning between blood and plasma were determined in vitro in freshly collected blood and plasma. For ximelagatran and the two intermediates, ethyl-melagatran and OH-melagatran, blood from four dogs and four healthy human subjects (two male and two female

animals/subjects) were used in the experiments. For melagatran, pooled blood from three male dogs, ten male rats, and individually in four healthy human subjects (two male and two female) was used. The blood samples from the different species were treated separately, and all experiments were carried out in triplicate. Blood and plasma were incubated separately with [^{3}H]ximelagatran at concentrations of 0.1, 1, and 10 μM, and with ^{3}H-labeled ethyl-melagatran and OH-melagatran at concentrations of 0.05, 0.5, and 5 μM. [^{3}H]melagatran was incubated at the following concentrations: 0.05, 0.5, and 5 μM in humans; 0.05, 5, and 100 μM in dogs; and 0.05, 5, and 30 μM in rats. Plasma protein binding, determined using ultrafiltration, was given as the ratio of concentrations in ultrafiltrate and plasma. No adsorption to the membrane or the ultrafiltration device was observed for any of the compounds. The whole blood to plasma concentration ratio was calculated as the concentration of radioactivity in whole blood divided by the concentration of radioactivity in the corresponding plasma samples.

Sample Analysis

Handling and Stability of Biological Samples. All urine and feces samples were directly frozen and stored at −20°C until analysis. Blood samples were collected in heparinized test tubes, kept on ice until plasma was separated by centrifugation (within 1 h of collection), and then kept frozen at −20°C until analysis. The stability of ximelagatran in freshly collected dog and human blood was evaluated by incubation for 1 h at 37°C. In these incubation experiments, more than 90% of the initial ximelagatran concentrations were remaining, supporting that the stability of ximelagatran was satisfactory when the blood samples were handled as described above.

The stability of ximelagatran in human feces was studied by addition of [^{3}H]ximelagatran (50 μM) to feces homogenate from blank human feces. Incubation of the samples was performed under anaerobic conditions at 37°C. At selected incubation times (5, 15, 30, and 60 min, 24 h, and 14 days), the feces slurry was centrifuged at 15,000*g* for 10 min and the supernatant analyzed using the reversed-phase gradient liquid chromatographic (LC) system with on-line radioactivity and mass spectrometry (MS) detection described below.

Concentration of Total Radioactivity. In melagatran studies, the concentration of total radioactivity in the biological samples was determined by liquid scintillation counting after mixing the samples with liquid scintillation fluid. Fecal samples were homogenized in approximately twice their volume in tap water. For ximelagatran studies, all samples except whole blood and bile were analyzed as described for melagatran studies. Whole blood, feces homogenate, and bile were combusted using a Packard Tri-Carb Automatic Sample Oxidizer (PerkinElmer Life Sciences, Boston, MA). For mass balance studies, the amounts of radioactivity in urine and feces were expressed as a percentage of the administered dose.

Metabolic Patterns in Urine, Bile, and Feces. For both melagatran and ximelagatran studies, a reversed-phase gradient LC system with on-line radioactivity detection was used to determine the metabolic pattern in urine and feces. Urine samples were injected directly onto the LC column. Bile samples were diluted with mobile phase A and centrifuged at 15,000*g* for 10 min. Feces homogenates (100-mg aliquot from samples containing >3% of the dose) were mixed with 0.5 ml of phosphoric acid (1 M), shaken for 5 min, and centrifuged at 10,000*g*. The resultant supernatant was injected onto the LC column. Complete recovery of radioactivity for the extraction from fecal samples was demonstrated by liquid scintillation counting.

The LC system consisted of a high-pressure LC pump (Pharmacia LKB 2248; Pharmacia AB, Uppsala, Sweden) connected to an autosampler (CMA/200, 200-μl loop volume) and a Symmetry C_{18} (150 × 3.9 mm) analytical column protected by a precolumn (Symmetry C_{18}, 20 × 3.9 mm; Waters, Milford, MA). A gradient of two mobile phases was pumped at a flow rate of 1 ml/min. The mobile phases A and B consisted of 10 and 50% acetonitrile in 0.05 M phosphate buffer (pH 7). After sample injection (100–150 μl), the mobile phase B was increased linearly from 0 to 30% in 15 min and then to 100% in 10 min. An equilibration time of at least 6 min with 0% mobile phase B was allowed before injection of the next sample. The radioactivity in the eluate was continuously measured using a Radiomatic FLO-ONE (PerkinElmer Life Sciences) detector with a 1-ml flow cell and a scintillation fluid (Ultima-FLO AP) at a flow rate of 3 ml/min. The radioactivity signal was stored in a PC-based evaluation system (Radiomatic 500TR FLO-ONE). The LC retention times of ximelagatran, ethyl-melagatran, OH-melagatran, and melagatran were 25 to 26, 22 to 23, 10, and 9 min, respectively. The recovery of radioactivity from the LC column was determined by collecting the eluate from the radioactivity detector, analyzing aliquots of the eluate by liquid scintillation counting, and then comparing with the amount injected. The recovery was consistently greater than 95%. The amounts of unchanged ximelagatran, ethyl-melagatran, OH-melagatran, melagatran, and unknown metabolites were calculated by integration of the radioactivity signal and expressed as a percentage of the total amount of radioactivity detected in the sample. For melagatran studies, the LC gradient was slightly modified to give a retention time of 17 min and a sample recovery of greater than 90%.

The chemical structure of metabolites was determined by liquid chromatography-mass spectrometry (LC-MS) using an ion trap mass spectrometer (LCQ Classic, Thermo Finnigan MAT; San Jose, CA) equipped with an electrospray interface. The gradient LC system was the same as described above, except that the mobile phase consisted of an ammonium acetate buffer (2.5 mM, pH 7.1). The LC-MS interface conditions consisted of a heated capillary temperature of 250°C, a spray voltage of +4.5 kV and a source current of 80 μA. Positive ion mass spectra were recorded (mass range *m/z* 100–700) in a data-dependent mode (base peak, collision energy at 25 eV). The normal scan and product ion mass spectra were stored in the computer system (Xcalibur 1.0; Thermo Finnigan MAT), and data were obtained by subtracting background scans from before and after the averaged spectrum of the chromatographic peak.

Plasma and Urine Concentrations. For the melagatran PK studies, the plasma concentration of melagatran was determined by reversed-phase liquid chromatography and positive electrospray ionization mass spectrometry. For quantification, an analog to melagatran was used as internal standard. Melagatran was isolated from plasma by solid-phase extraction on octylsilica. LC separation of the extracts was performed on an octadecylsilica column using a mobile phase consisting of 40% acetonitrile and 0.08% formic acid in 0.0013 mol/l ammonium acetate solution. Molecular ions $(M + H)^+$ of melagatran and the internal standard were measured by selected ion monitoring at *m/z* 430.2 and 444.2, respectively.

The limit of quantification (LOQ) for the method ranged from 0.020 to 0.050 μM depending on the plasma volume used in the sample workup procedure of the study. For human subjects, a 500-μl aliquot of plasma was analyzed. Using this sample volume, the method was linear (accuracy within ± 15%) over the 0.020 to 20 μM range, and the lower LOQ [coefficient of variation (CV)<20%] was 0.020 μM. A 200-μl aliquot was used for plasma from the rat and dog. The corresponding linear range was 0.050 to 50 μM, and the LOQ was 0.050 μM. Precision was typically <±5% for concentrations approximately 2.5 times LOQ and higher.

In the ximelagatran PK studies, the plasma concentrations of ximelagatran, ethyl-melagatran, OH-melagatran, and melagatran, were determined using reversed-phase LC and positive electrospray ionization tandem mass spectometry. For quantification, isotope-labeled ximelagatran ($D_7{}^{13}C_2$) and melagatran ($D_2{}^{13}C_2$) were used as internal standards. The analytes were isolated from plasma (0.5 ml) by solid-phase extraction on octylsilica. The procedure involved elution with ammonia in methanol so as to achieve adequate recovery of all four analytes. After solvent evaporation, 30 μl of the residues dissolved in 500 μl were injected for LC-tandem mass spectometry analysis. Chromatographic separation was carried out on an octadecylsilica column using a mobile phase obtained by mixing 600 ml of acetonitrile, 400 ml of ammonium acetate (4 mM), and 1 ml of formic acid. Molecular ions $(M + H)^+$ of the analytes and internal standards, formed by electrospray ionization, were fragmented, and selected product ions were recorded (selected reaction monitoring). In the human studies, the LOQ for ximelagatran, ethyl-melagatran, and melagatran was 0.010 μM, whereas that for OH-melagatran was 0.020 μM. In the rat study, LOQ was 0.025 μM for ximelagatran and 0.050 μM for OH-melagatran and melagatran. Plasma from dogs was analyzed with an LOQ of 0.025 μM for ximelagatran, ethyl-melagatran, and melagatran, and 0.050 μM for OH-melagatran. Urine from the human ximelagatran study was also analyzed using LC-MS with an LOQ for all compounds of 0.10 μM. These analytical methods for determination of melagatran only (Larsson et al., 2002) and for determination of all four analytes (Larsson et al., 2003) in biological fluids, with several enhancements, have recently been published.

TABLE 1

Mean (S.D.) percentage of administered dose of [^{3}H]melagatran excreted in urine and feces following oral and iv administration to rats, dogs, and humans

	Rats	Dogs	Humans
n; Gender	4; M	4; 2 M, 2 F	12 M
Oral dose	30 μmol/kg	30 μmol/kg	256 μmol
Urine[a]	9.8 (2.9)	26.1 (4.5)	7.6 (5.5)
Feces	82.6 (3.2)	56.4 (4.5)	77.5 (8.6)
Total	92.4 (1.2)	82.5 (3.1)	85.1 (7.8)
i.v. dose	2 μmol/kg	2 μmol/kg	5.3 μmol
Urine[a]	65.9 (3.5)	42.5 (7.8)	82.6 (3.9)
Feces	24.3 (4.3)	38.9 (15.5)	5.7 (2.2)
Total	90.3 (2.2)	81.4 (16.1)	88.3 (3.4)

M, male; F, female.
[a] Includes cage-wash.

Pharmacokinetic Assessments.

A bi-exponential model was fit to the data obtained after i.v. dosing in the human melagatran study whereas noncompartmental analysis was used for all other data. Weighted least-squares nonlinear regression using PCNONLIN (version 4.2; Statistical Consultants Inc., Lexington, KY) was used to fit the bi-exponential model to the data for i.v. melagatran in human subjects. The weights used were $(Y_{pred})^{-2}$ or $(Y_{pred})^{-1}$, where Y_{pred} is the model-predicted plasma concentration. Basic PK parameters were derived from the bi-exponential model in a standard manner. The C_{max} was the highest plasma concentration observed, and t_{max} was the time at which C_{max} occurred. The area under the plasma concentration−time curve (AUC) was calculated using the log-linear trapezoidal rule from time 0 to t_{last}, the last sampling time with a measurable plasma concentration, and extrapolated to infinity by addition of the quantity C_{last}/k, where C_{last} was the predicted plasma concentration at t_{last}, and k was the elimination rate constant. C_{last} and k were estimated by linear least-squares regression of log plasma concentration−time data in the terminal phase of the decline. The $t_{1/2}$ was calculated as $\ln 2/k$. The area under the first moment curve (the curve of the product of concentration and time versus time; AUMC) was calculated using the linear trapezoidal rule and extrapolated to infinity by adding the quantity $(C_{last} \cdot t_{last}/k) + (C_{last}/k^2)$. Plasma clearance (CL) and volume of distribution at steady state (V_{ss}) were also calculated following i.v. dosing; CL as $dose_{i.v.}/AUC_{i.v.}$ and V_{ss} as CL × MRT, where MRT is the mean residence time calculated as $AUMC_{i.v.}/AUC_{i.v.}$.

Oral bioavailability was calculated as $100 \cdot (AUC_{oral}/AUC_{i.v.})/(dose_{i.v.}/dose_{oral})$, where the oral and i.v. suffixes denote the quantities for oral and i.v. dosing, respectively. After both oral and i.v. administration of ximelagatran, the bioavailability of melagatran (F_{Mel}) was calculated as $(AUC \times CL_{Mel})/dose$, where CL_{Mel} is the mean value of melagatran clearance. Renal clearance (CL_R) of melagatran was estimated as A_e/AUC, where A_e was the amount of melagatran excreted in urine.

In the food interaction study in dogs, differences in the parameters C_{max}, AUC, and $t_{1/2}$ between the two treatments (administration with and without food) were tested by the Student's paired *t* test. Log-transformed values were used for AUC and C_{max}. In the human study, analysis of variance analysis was used to test for between-treatment differences in C_{max} and AUC using log-transformed values. Differences were considered significant at $p < 0.05$.

Results

Mass Balance and Metabolic Profile of Melagatran. The mean cumulative recovery of total radioactivity excreted in urine and feces, following i.v. and oral administration of [^{3}H]melagatran to rats, dogs, and human subjects, is shown in Table 1. In rats and dogs, the major portion of radioactivity excreted in feces and urine following both oral and i.v. administration of melagatran was identified as unchanged melagatran. However, a few minor peaks in the chromatogram eluted from the reversed-phase LC system with a shorter retention time than melagatran, suggesting that metabolites with a more polar nature than melagatran were formed. The concentration of these metabolites was low in relation to melagatran, except in the urine of dogs, where they were present in somewhat larger amounts. The structure of these polar metabolites remains to be identified.

As in animals, LC-analysis of samples of human urine and feces showed that most of both the oral and the i.v. doses were excreted as unchanged melagatran. However, in contrast with the animal studies, no peak other than that belonging to unchanged melagatran was detected in urine after both oral and i.v. administration, showing that there were no metabolites of melagatran excreted in human urine. After i.v. administration, the amount of radioactivity in samples of feces was too low to allow detection of any metabolites. For both human and animals, the LC analysis of urine and feces showed no evidence of formation of tritiated water indicating that the tritium-labeled position of melagatran was stable in vivo.

Mass Balance and Metabolic Profile of Ximelagatran. The mean cumulative recovery of total radioactivity in urine and feces, following oral and i.v. administration of [^{14}C]ximelagatran is shown in Table 2. The excretion of radioactivity was rapid and essentially complete for both animals and human subjects.

LC analysis of samples of urine from male and female rats and dogs showed that most of the radioactivity in urine was melagatran (Fig. 2), whereas ximelagatran, ethyl-melagatran, and OH-melagatran accounted for only small fractions of the administered dose excreted. No ximelagatran was detected in the urine of male or female rats after either oral or i.v. administration, and only trace amounts were found in the urine of dogs. Melagatran was also the dominant compound recovered in feces (Table 3). Only small amounts of metabolites with retention times other than that of ximelagatran or its three main products were observed in the chromatograms of urine and feces. Most of these eluted earlier than melagatran, with retention times ranging from 2.1 to 3.8 min, suggesting that they are more polar than melagatran. In urine, the fraction of the dose accounted for by these unknown metabolites after i.v. administration of ximelagatran to male rats, female rats, and dogs was 10.6, 3.1, and 9.5%, respectively. The corresponding fractions in urine after oral administration of ximelagatran were 1.7, 1.8, and 9.1%, respectively. The amounts of unknown metabolites in feces are given in Table 3.

The amount of radioactivity excreted in bile (mean ± S.D.) expressed as a percentage of the administered dose of [^{3}H]ximelagatran was 16.4 ± 3.3% for male rats, 7.2 ± 0.7% for female rats, and 33.5% for one female dog. LC-MS analysis with radiochemical detection of the collected bile samples showed that most of the radioactivity was melagatran. For male and female rats, 80 and 88% of the radioactivity in bile was melagatran, respectively. Trace amounts of OH-melagatran and ethyl-melagatran (only for male rats) accounted for the remainder of the radioactivity in rat bile. In bile from the dog, 51% of the radioactivity was melagatran, and 41% was ethyl-melagatran.

The compounds in human urine were positively identified as ximelagatran, ethyl-melagatran, OH-melagatran, and melagatran using LC-MS analysis, based on comparison with the chromatographic retention times, molecular ions, and product ion spectra of available synthetic compounds. The predominant compound in urine after both oral and i.v. administration of ximelagatran was melagatran (Fig. 2). Melagatran was excreted rapidly, with maximal concentrations in urine samples collected 4 h postdosing. However, by 24 to 48 h postdosing, melagatran was either present in urine in very small quantities or was below LOQ. Low levels of the parent compound, ximelagatran, and the two intermediates, ethyl-melagatran and OH-melagatran, were also detected, with maximal concentrations also observed 4 h post oral and i.v. dosing.

The metabolic pattern in urine determined by radiochemical detection methods supported the results from the LC-MS measurements shown in Fig. 2 and also revealed unknown metabolites in the urine

TABLE 2

Mean (S.D.) percentage of administered dose of [^{14}C]ximelagatran excreted in urine and feces following oral and i.v. administration to rats, dogs and humans

	Rats	Rats	Dogs	Humans
n; gender	4; M	4; F	4; 2 M, 2 F	5 M
Oral dose	40 μmol/kg	40 μmol/kg	40 μmol/kg	105 μmol
Urine	21.3 (1.9)	16.5 (1.7)	22.6 (2.4)	25.2 (4.3)
Feces	71.3 (1.1)	77.0 (2.0)	66.9 (3.1)	71.1 (4.5)
Total[a]	94.9 (1.5)	96.6 (1.0)	90.5 (2.2)	96.3 (0.8)
i.v. dose	10 μmol/kg	10 μmol/kg	10 μmol/kg	
Urine	45.8 (3.5)	34.6 (15.1)	32.3 (1.3)	N.D.
Feces	37.4 (4.4)	54.9 (8.7)	57.9 (2.8)	N.D.
Total[a]	88.8 (0.9)	96.0 (6.1)	91.3 (1.6)	N.D.

M, male; F, female; N.D., not determined as only unlabeled compound was given.
[a] Includes cage-wash.

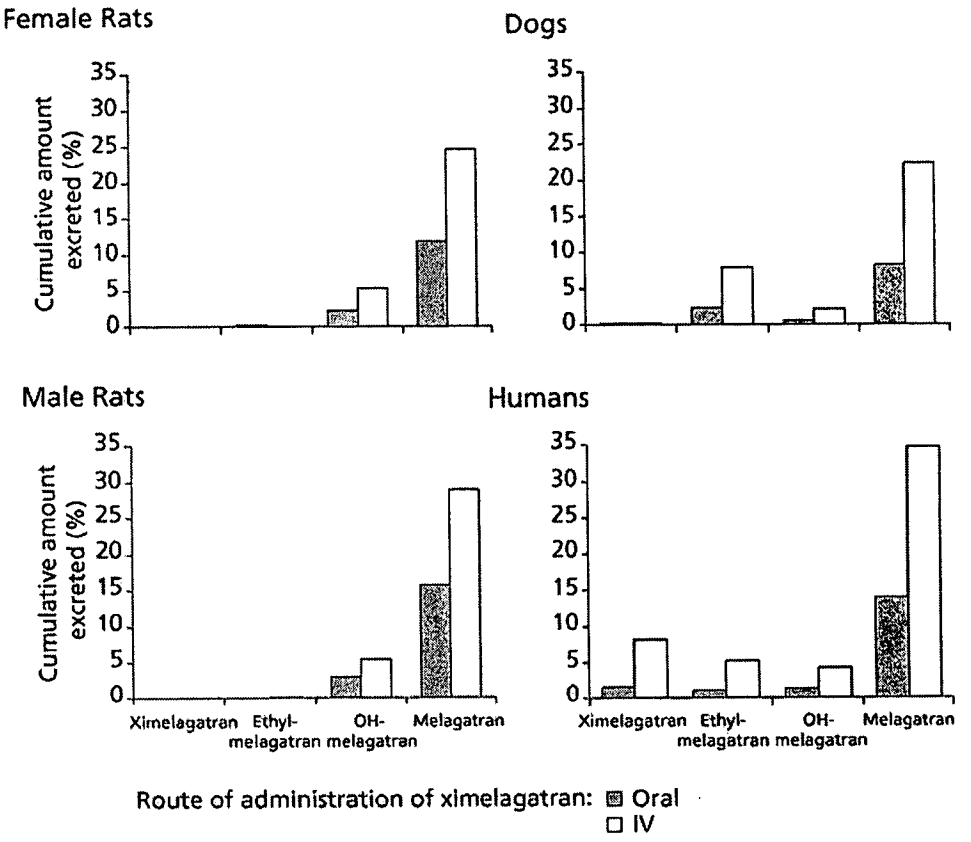

FIG. 2. *Cumulative amounts of ximelagatran, melagatran, ethyl-melagatran, and OH-melagatran excreted in urine in the 0- to 24-h period following oral and i.v. administration of ximelagatran to rats, dogs, and humans (as determined using radiochemical detection methods in rats and dogs and LC-MS in humans).*

Results are expressed as mean percentages of administered dose.

and feces of human subjects administered oral ximelagatran. These accounted for 1.8% of the oral ximelagatran dose excreted in the urine collected up to 24 h postdosing. As in the animal experiments, melagatran was the dominant compound in feces (Table 3).

In vitro, the disappearance of ximelagatran and the formation of ethyl-melagatran and melagatran in human feces homogenate were rapid under anaerobic conditions. The half-life for the reduction of ximelagatran to ethyl-melagatran was about 30 min. The subsequent ester-hydrolysis with formation of melagatran was slower, with detectable concentrations (about 10% of the radioactivity) after 24 h of anaerobic incubation. Polar metabolites, with about the same retention times as the unknown metabolites found in feces samples collected from the human subjects who had been administered oral ximelagatran, were also detected and accounted for about 50% of the radioactivity after 14 days of anaerobic incubation. The remaining radioactivity had retention times corresponding to ethyl-melagatran (26%) and melagatran (22%).

Pharmacokinetics of Melagatran. The mean plasma concentration–time profiles in rats, dogs, and human subjects, after oral and i.v. administration of melagatran, are shown in Fig. 3. The PK parameters of melagatran are presented in Tables 4 and 5. For rats, the apparent $t_{1/2}$ of melagatran after oral administration (mean values of 1.1–1.6 h) was longer than after i.v. administration indicating absorption-rate limited elimination. Renal clearance of melagatran was estimated to 8.6 ml/min/kg for male rats and 119 ± 10 ml/min for human subjects.

In the ascending dose study in humans, both C_{max} and AUC increased linearly with dose for i.v. dosing (Fig. 4). PK parameters

TABLE 3

Cumulative amounts of melagatran, ethyl-melagatran, and unknown metabolites excreted in feces following i.v. and oral administration of ximelagatran to rats, dogs, and humans (M, male; F, female; as determined using radiochemical detection methods)

Results are expressed as mean percentages of administered dose.

Route of Administration (i.v./oral)	Rats 4 (M)	Rats 4 (F)	Dogs 4 (2 M, 2 F)	Humans 5 (M)
Melagatran				
i.v.	24.5	42.6	34.1	N.D.
Oral	35.9	43.5	37.8	33.6
Ethyl-melagatran				
i.v.	0.1	0.7	17.7	N.D.
Oral	20.6	23.1	21.1	21.2
Unknown metabolites				
i.v.	10.5	8.6	3.0	N.D.
Oral	9.1	8.4	11.0	14.7

N.D., not determined as only unlabeled compound was given.

estimated for dose levels with sufficient number of measurable plasma concentrations (16–191 nmol/kg) were consistent and showed low interindividual variability (CV of melagatran CL was 13%). In contrast, the PK variability for oral dosing was large. The mean (±S.D.) estimates for melagatran bioavailability in the ascending oral dose study ranged from 3.9 ± 1.8% at the lowest evaluable dose (1.61 μmol/kg) to 7.6 ± 2.4% at the 6.1 μmol/kg dose, with a mean value across all doses of 5.8 ± 2.3%. In addition, a tendency for dose dependence was observed in both C_{max} and AUC as shown by the fact that there was a slight increase in the dose-normalized values of both C_{max} and AUC with dose (Fig. 4). There was a linear correlation between C_{max} and AUC ($r^2 = 0.96$).

Food markedly decreased the oral bioavailability of melagatran in both dogs and humans. AUC and C_{max} of melagatran (6.9 ± 2.7 μmol · h/l and 2.2 ± 1.0 μM) was significantly decreased ($p < 0.05$) when dogs received the oral dose with food compared with under fasting conditions (39.7 ± 18 μmol · h/l and 21.6 ± 13 μM). In humans, the median (range) of AUC and C_{max} was decreased from 1.02 (0.31–1.38) μmol · h/l and 0.18 (0.06–0.27) μmol/l under fasting conditions to 0.14 (0.01–0.31) μmol · h/l and 0.03 (0.02–0.06) μmol/l when the tablet of melagatran was given together with food. The bioavailability of melagatran, calculated using the median value of AUC to be 7.6% when melagatran was administered to fasting subjects, was reduced to 1.1% when it was administered with breakfast. Likewise, when melagatran was administered 2 h after breakfast, its median AUC and C_{max} were both decreased approximately 3-fold, compared with fasting conditions, and the bioavailability was estimated to 2.4%.

Pharmacokinetics of Ximelagatran. The mean plasma concentration–time profiles for those compounds with measurable plasma concentrations in rats, dogs, and human subjects are shown in Fig. 5. Melagatran was formed rapidly and was the predominant compound in plasma after both oral and i.v. administration. Consequently, the PK analysis was focused on melagatran. The PK parameters of melagatran following oral and i.v. administration of ximelagatran are presented in Tables 6 and 7. CL_R of melagatran after i.v. administration of ximelagatran was 23.1 and 4.37 ml/min per kg body weight for rats and dogs, respectively, and 120 ml/min for humans.

In rats, the metabolism of ximelagatran was so rapid that no measurable concentrations of ximelagatran or ethyl-melagatran were detected in any of the rat plasma samples (Fig. 5). Besides melagatran, only OH-melagatran was detectable in rat plasma. After oral administration of ximelagatran to rats, the AUC of OH-melagatran was about 30% of that of melagatran. Following i.v. administration of ximelagatran, the AUC of OH-melagatran was higher than for melagatran, but the concentration of OH-melagatran declined rapidly and was below LOQ 30 min postdosing.

In the plasma of dogs, t_{max} of ximelagatran occurred 15 to 30 min post oral administration, and both intermediates were measurable (Fig. 5). The concentration of ximelagatran decayed faster in dogs after i.v. than after oral administration ($t_{1/2}$ of 1.9 and 3.9 min for the 5 and 10 μmol/kg i.v. doses, respectively, compared with 32 min for the 40 μmol/kg oral dose), indicating absorption-limited kinetics for orally administered ximelagatran. F_{Ximel} was 37% after administration of the 40 μmol/kg oral dose. The exposure of ximelagatran was approximately 30 and 8% of that of melagatran after i.v. and oral administration of ximelagatran, respectively. The corresponding figures for the exposure of ethyl-melagatran were 12 to 21% and 17 to 22%, and for OH-melagatran were 23 to 25% and 7.5 to 13% of that of melagatran after i.v. and oral administration of ximelagatran, respectively.

In both rats and dogs, the mean plasma concentration of total radioactivity peaked at the same level and at the same time as did the sum of the plasma concentrations of those compounds that were detectable using LC-MS (ximelagatran, ethyl-melagatran, OH-melagatran, and melagatran). However, the total radioactivity in plasma declined with a longer $t_{1/2}$ than did the total concentration of metabolites (14 to 24 h and 45 h in rats and dogs, respectively, after oral administration; 13 to 27 h and 54 h, respectively, after i.v. administration).

As in rats and dogs, ximelagatran was rapidly absorbed (mean t_{max}, 0.33 h postdosing) and metabolized (mean $t_{1/2}$ of ximelagatran, 0.34 and 0.18 h post oral and i.v. administration, respectively) in the human subjects. Ximelagatran and both intermediates were observed in plasma in humans, although their exposure was low relative to that of melagatran. At sampling times where concentrations were <LOQ for some subjects, these were set to LOQ/2 for calculation of mean plasma concentrations shown in Fig. 5. The mean value of F_{Ximel} after oral administration was 21.9 ± 1.7%. The exposure of ximelagatran was 18.3 and 36.1% of that of melagatran after oral and i.v. administration of ximelagatran, respectively. After oral administration the mean AUC estimates for ethyl-melagatran and OH-melagatran were 3.2 and 10.6% of that of melagatran, respectively, Likewise after i.v. administration, the mean AUC estimates for ethyl-melagatran and OH-melagatran were 4.2 and 12.8% of that of melagatran, respectively.

Following oral administration of [^{14}C]ximelagatran, maximal total radioactivity in plasma reached a peak of 0.88 μM, 40 min postdosing, and declined with a $t_{1/2}$ of 4.2 h in the 5 min to 8 h time period post drug administration. The plasma concentration of total radioactivity at t_{max} and times after t_{max} was consistently 0.1 to 0.2 μM higher than the sum of the plasma concentrations of ximelagatran, the intermediates, and melagatran. The total radioactivity in whole blood mirrored that in plasma but at lower levels.

Plasma Protein Binding and Blood–Plasma Partitioning. The degree of plasma protein binding and the partitioning between blood and plasma was low and concentration-independent for all species and compounds. The mean values for the plasma protein binding of melagatran were 10.6 and 10.0% in dogs and rats, respectively, with low variability. Of the human subjects, one male and one female had essentially no plasma protein binding of melagatran, whereas the other two had values of 13.3 and 15.3%. For ximelagatran, the mean percentage binding was 79% in humans and 76% in dogs. For ethyl-melagatran, the corresponding estimates were 44 and 63%, and for OH-melagatran they were 10 and 12% in humans and dogs, respectively. The mean blood-to-plasma concentration ratios of melagatran were 0.55 in dogs and 0.62 in rats. The individual mean values in humans ranged from 0.56 to 0.62. The mean

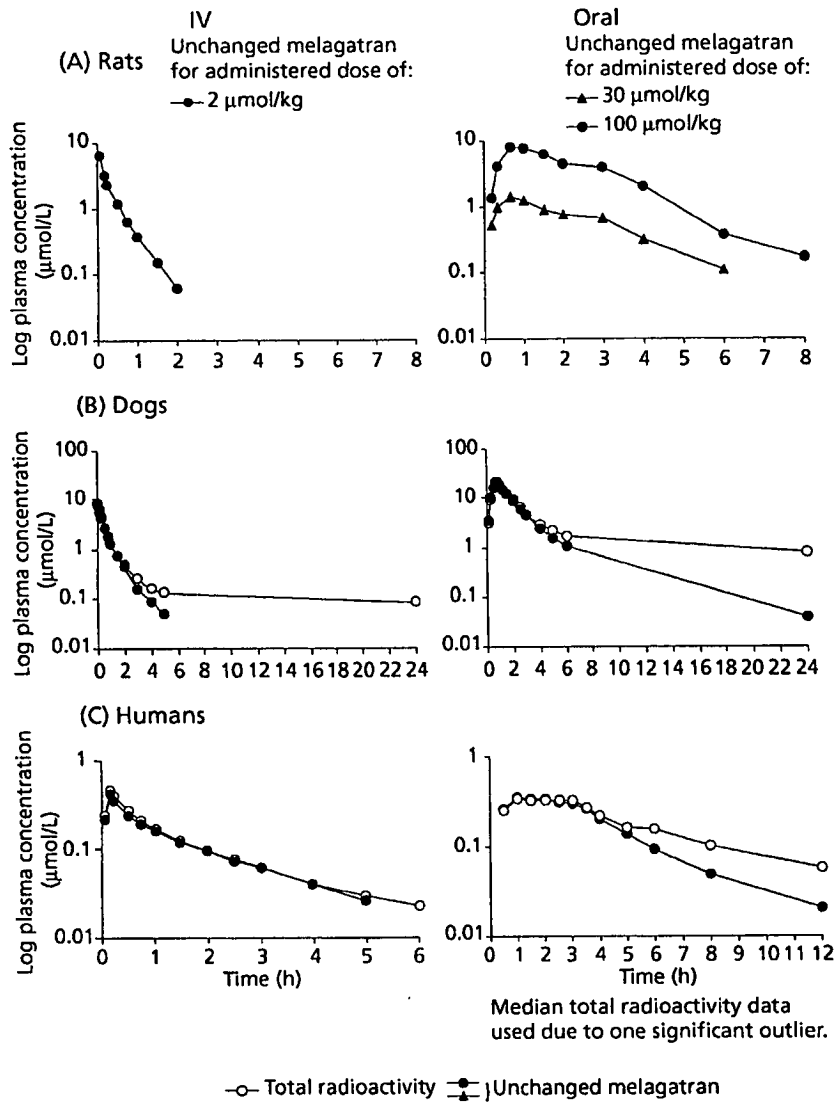

FIG. 3. *Mean plasma concentrations (log scale) of total radioactivity (B and C only) and of unchanged melagatran (A, B, and C) versus time (h) since oral and i.v. administration of melagatran to rats (A), dogs (B), and humans (C).*

TABLE 4

Mean (S.D.) PK parameters of melagatran following oral administration of melagatran to rats, dogs, and humans

Species and Dose	Gender	*n*	C_{max}	t_{max}	*t*	F_{Mel}
			μmol/l	*h*	*h*	*%*
Rat						
30 μmol/kg	M	4	1.63(0.43)	1.4(1.1)	N.D.	13 (39)
30 μmol/kg	F	4	1.39(0.38)	0.7(0.3)	N.D.	12 (42)
100 μmol/kg	M	4	8.42(1.94)	0.8(0.2)	N.D.	20 (15)
Dog						
30 μmol/kg	M/F	4	21.7 (1.3)	0.8(0.1)	1.4 (0.2)	72 (22)
Human						
110 mg (256 μmol)	M	12	0.6 (0.6)	1.2(0.7)	2.3 (0.4)	7.7(6.8)

M, male; F, female; N.D., not determined because of absorption-rate limited elimination.

TABLE 5

Mean (S.D.) PK parameters of melagatran following intravenous administration of melagatran to rats, dogs, and humans

Species and Dose	Gender	*n*	CL	V_{ss}	*t*
			ml/min/kg	*l/kg*	*h*
Rat					
2 μmol/kg	M	4	15.8(2.1)	0.37(0.02)	0.4(0.03)
2 μmol/kg	F	4	18.0(3.6)	0.40(0.10)	0.4(0.05)
Dog					
2 μmol/kg	M/F	4	7.0(1.0)	0.36(0.04)	1.2(0.2)
Human[a]					
2.3 mg (5.3 μmol)	M	12	145 (15)[b]	17.3 (1.7)[c]	1.6(0.2)

M, male; F, female.
[a] Analyzed by fitting a bi-exponential equation to the data.
[b] Units of milliliters per minutes in humans.
[c] Units of liters in humans.

ratios of ximelagatran, ethyl-melagatran, and OH-melagatran ranged from 0.54 to 0.67 in dogs and humans.

Discussion

The PK properties of the oral direct thrombin inhibitor, ximelagatran, and in particular the formation and bioavailability of its active form, melagatran, were examined in animals and healthy male human subjects. Ximelagatran was rapidly absorbed and metabolized following oral administration to rats, dogs, and humans. Melagatran was the dominant compound in the plasma of all three species. It was demonstrated that the bioconversion of ximelagatran to its active form,

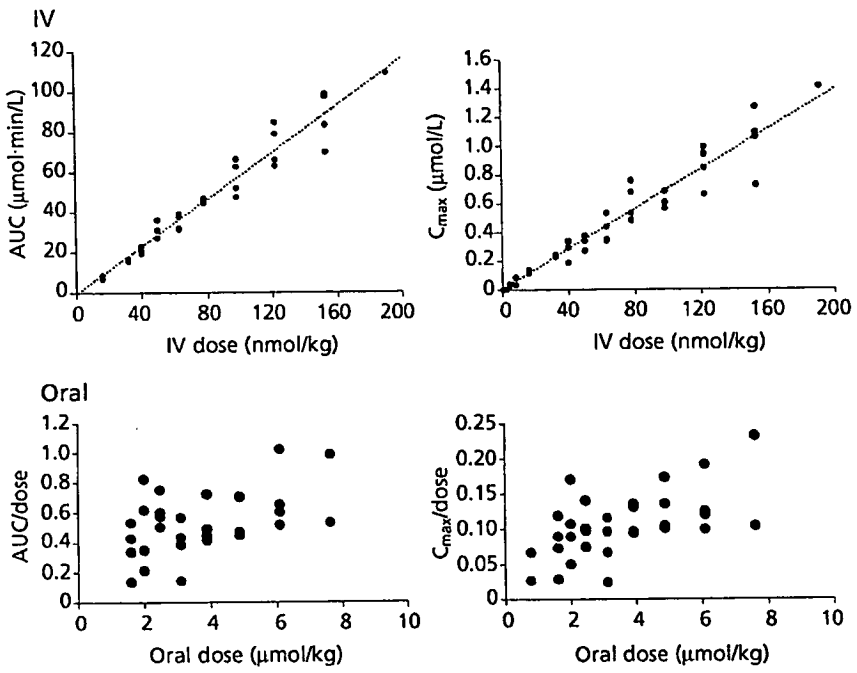

FIG. 4. *AUC and C_{max} versus i.v. dose of melagatran and dose-normalized AUC and C_{max} versus oral dose of melagatran in humans.*

melagatran, occurs by ester hydrolysis and reduction via two intermediates, ethyl-melagatran and OH-melagatran (Fig. 1). Ethyl-melagatran is formed by reduction of the hydroxyamidine and OH-melagatran by ester hydrolysis. In vivo reduction of an amidoxime derivative, pentamidoxime, to its corresponding amidine has been demonstrated previously (Clement, 1998). The PK properties of melagatran, following oral and i.v. administration, were also consistent between the animal species and humans. Melagatran has a relatively low plasma clearance, negligible plasma protein binding, a small volume of distribution, and a short elimination half-life. Renal excretion of unchanged melagatran was the main route of elimination. In humans, linear PK of melagatran were observed after i.v. dosing over the entire dose range studied with low interindividual variability. The calculated renal clearance of melagatran in rats and humans was similar to the glomerular filtration rate (Davies and Morris, 1993). The polar nature of melagatran, which prevents passive reabsorption from the proximal and distal tubules, and the fact that plasma protein binding is negligible, suggests that glomerular filtration is the mechanism of elimination in the kidneys. After i.v. administration of ximelagatran to rats, the renal clearance of melagatran was higher than that determined after administration of melagatran and higher than the glomerular filtration rate. This may be due to metabolism of ximelagatran and the formation of melagatran in the kidneys. In dogs and humans, CL_R of melagatran was after i.v. administration of ximelagatran approximately equal to the glomerular filtration rate.

The low and dose-dependent oral bioavailability of melagatran in rats and humans is consistent with its polar properties and poor membrane permeability determined in the Caco-2 cell line (Gustafsson et al., 2001). The markedly higher bioavailability observed in dogs compared with rats and humans is probably the result of greater absorption across the gut wall in this species. This is consistent with a recent report reviewing the absorption data for a large number of compounds, which concluded that the fraction absorbed was markedly higher in dogs than in humans, whereas the absorption data obtained in rats were in much better agreement with data in humans (Chiou et el, 2000). The interindividual variability in melagatran exposure following its oral administration to humans was also large. The combination of low interindividual variability after i.v. administration and the strong correlation between C_{max} and AUC after oral administration suggest that the variability in plasma levels after oral administration is mainly due to variability in the extent of absorption. In the presence of food, the bioavailability of melagatran was significantly reduced in both dogs and humans.

Ximelagatran, for which the membrane permeability is 80 times higher than for melagatran (Gustafsson et al., 2001), was rapidly absorbed and metabolized following oral administration. In rats, the bioconversion of ximelagatran was so rapid that no detectable concentrations of ximelagatran were found in plasma after either i.v. or oral administration. Ethyl-melagatran was also undetectable in rat plasma. However, by using sodium dodecyl sulfate as an esterase inhibitor in the blood collection test tube (Holm et al., 1985), it was shown that both male and female rats had measurable concentrations of ximelagatran and ethyl-melagatran. This finding indicates that ester hydrolysis of ximelagatran occurred to some extent ex vivo in blood after collection of the sample. The levels of ximelagatran and ethyl-melagatran were much lower than that of melagatran, and the clearance of ximelagatran exceeded cardiac output (data on file), suggesting a high esterase activity in blood and tissues of rats. Also, OH-melagatran was present in rat plasma with high peak concentrations after both i.v. and oral administration but declined rapidly. In dogs and humans, the plasma concentrations of the intermediates were low compared with that of melagatran. The plasma concentration of OH-melagatran appeared to be higher than that of ethyl-melagatran, suggesting that the ester hydrolysis occurred more readily than the reduction.

In dogs and rats, there was a dose-dependent increase in the bioavailability of melagatran after both oral and i.v. administration of ximelagatran. In a previous study in which healthy male human subjects received escalating single oral doses of ximelagatran ranging from 5 to 98 mg, the bioavailability of melagatran was dose-independent and estimated to be about 20% (Eriksson et al., 1999b). This is consistent with the value of 19% observed at the dose of 50 mg

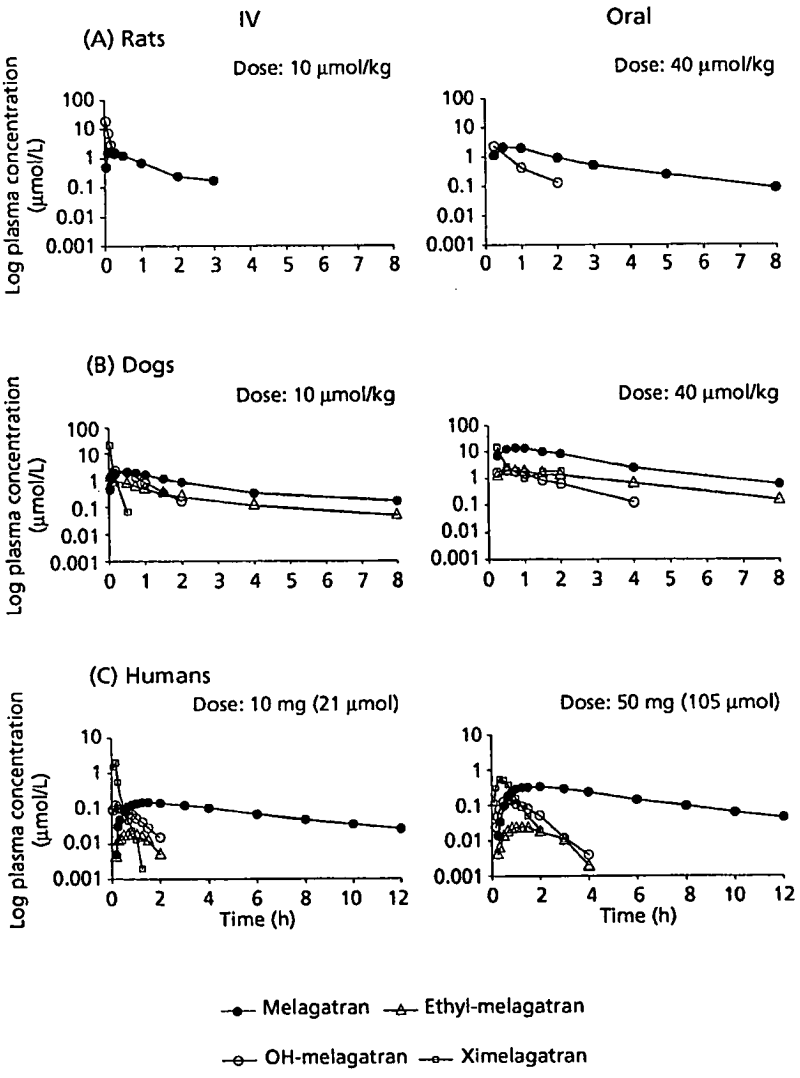

FIG. 5. *Mean plasma concentrations (log scale) of ximelagatran, melagatran, ethyl-melagatran, and OH-melagatran versus time (h) since oral and i.v. administration of ximelagatran to rats, dogs, and humans.*

TABLE 6

Mean (S.D.) PK parameters of melagatran following oral administration of ximelagatran to rats, dogs, and humans (M, male; F, female)

Species and Dose	Gender	n	C_{max}	t_{max}	AUC	t	F_{Mel}
			μmol/l	h	μmol · h/l	h	%
Rat							
10 μmol/kg	M	5	0.24(0.06)	0.5 (0.0)	0.50(0.13)[a]	1.3(0.3)	5(1)
10 μmol/kg	F	5	0.32(0.26)	0.80(0.27)	0.73(0.25)[b,c]	1.5(0.8)[c]	9(2)
40 μmol/kg	M	5	2.16(0.22)	0.80(0.27)	4.81(1.49)	1.4(0.4)	13(3)
Dog							
10 μmol/kg	M/F	4	0.93(0.16)	0.63(0.15)	2.37(0.31)	13[d]	10(1)
40 μmol/kg	M/F	4	15.9 (5.0)	1.13(0.6)	45.6 (12.1)	11 (3)	50(13)
Human							
50 mg (105 μmol)	M	5	0.36(0.03)	1.85(0.78)	2.28(0.75)	3.6(0.7)	19(6)

[a] 17 to 30% of AUC extrapolated.
[b] 16 to 63% of AUC extrapolated.
[c] $n = 4$.
[d] No S.D. as estimate based on data from one dog.

(equivalent to approximately 0.3 μmol/kg) given to the male human subjects in the present study. Consequently, the dose-dependent increase in F_{Mel} observed in the animal experiments is likely due to the higher doses (40 μmol/kg) that were given to the rats and dogs. Possible reasons for the observed dose-dependent increase in F_{Mel} are an increase in the fraction of ximelagatran absorbed, increased metabolism of ximelagatran to melagatran, or decreased elimination of melagatran at higher doses. Dose proportional PK for i.v. melagatran was shown in humans and has also been demonstrated in rats and dogs for a wide range of doses (data on file), which supports that the elimination of melagatran is independent of dose.

The bioavailability of melagatran and the amount of melagatran

TABLE 7

Mean (S.D.) PK parameters of melagatran following i.v. administration of ximelagatran to rats, dogs, and humans (M, male; F, female)

Species and Dose	Gender	n	C_{max}	t_{max}	AUC	t	F_{Mel}
			μmol/l	*h*	*μmol · h/l*	*h*	%
Rat							
5 μmol/kg	M	3	0.52 (0.15)	0.14 (0.05)	0.44 (0.10)[a]	0.52 (0.07)	9 (2)
5 μmol/kg[c]	F	5	0.59	0.17	0.60	0.72	13
10 μmol/kg	M	4	1.72 (0.67)	0.15 (0.04)	1.86 (0.82)	0.77 (0.13)	20 (9)
Dog							
5 μmol/kg	M/F	4	0.46 (0.12)	0.5 (0.0)	3.00 (0.48)[b]	19 (5)	25 (4)
10 μmol/kg	M/F	4	2.14 (0.56)	0.57 (0.13)	8.51 (2.12)	13 (5)	36 (9)
Human							
10 mg (21 μmol)	M	5	0.15 (0.03)	1.25 (0.18)	1.05 (0.22)	4.29 (0.53)	43 (9)

[a] 23 to 31% of AUC extrapolated.
[b] 24 to 44% of AUC extrapolated.
[c] PK parameters calculated using mean plasma concentration.

recovered in urine was higher after i.v. than after oral administration of ximelagatran, which suggests incomplete absorption. The relative bioavailability of melagatran after oral versus i.v. administration of ximelagatran, obtained as the ratio of the AUC estimates of melagatran and corrected for difference in dose, was 40 to 70% at the 10 μmol/kg dose given to rats and dogs. In humans, the relative bioavailability of melagatran was 43%. Similar estimates were obtained for the relative bioavailability of the intermediates, ethyl-melagatran (34%) and OH-melagatran (37%). Assuming that the metabolism of ximelagatran is the same after oral and i.v. administration, this means that 40 to 70% of the oral dose of ximelagatran is absorbed. As F_{Ximel} after oral administration to humans was only 21.9%, this suggests that first-pass metabolism of ximelagatran during absorption reduces its oral bioavailability. If the absorption of ximelagatran is incomplete, there is a possibility that it may be increased at the higher doses that were given to animals.

The estimate of the fraction of oral ximelagatran absorbed is uncertain because presystemic metabolism and sequential biliary excretion of ximelagatran or its products appeared to occur. It is therefore likely that the fraction absorbed is even higher than 40 to 70%. The principal route of excretion of the orally administered dose of ximelagatran was fecal in rats, dogs, and humans. High recovery of radioactivity in the feces was also observed after i.v. administration to rats and dogs, suggesting biliary excretion of ximelagatran and/or formed metabolites. In fact, this was demonstrated by the substantial fraction of the dose excreted in bile collected after oral administration of ximelagatran to rats and one dog. The predominant compound in the bile of rats was melagatran whereas about equal amounts of melagatran and ethyl-melgatran were found in bile from the dog. The dose-dependent increase in F_{Mel} observed in the animal experiments could therefore be caused by saturation of the biliary excretion of melagatran and ethyl-melagatran.

In addition to being the major circulating compound in the plasma of all three species following oral and i.v. administration of ximelagatran, melagatran was also the major product found in urine and feces collected after oral and i.v. administration. Appreciable quantities of ethyl-melagatran were also recovered in fecal samples, whereas neither OH-melagatran nor ximelagatran were detected. Polar metabolites were also found that in general were present in larger amounts in feces than in urine. This may be due to instability of ximelagatran in the gastrointestinal tract. Anaerobic incubation of ximelagatran in human feces homogenate showed rapid disappearance of ximelagatran and formation of melagatran, ethyl-melagatran, and unknown polar metabolites. In the human subjects, the concentration of total radioactivity in plasma was higher than the sum of the plasma concentrations of ximelagatran, the intermediates, and melagatran. This supports the premise that unknown metabolites were present in plasma, but it is also possible that this is an artifact, as the two assay methods may give slightly different results.

The plasma protein binding of ximelagatran, ethyl-melagatran, OH-melagatran, and melagatran was relatively low in both human and dog plasma, although that of ximelagatran and ethyl-melagatran was higher than that of OH-melagatran, the binding of which was similar to that of melagatran. The low blood-to-plasma concentration ratios for ximelagatran, ethyl-melgatran, OH-melagatran, and melagatran suggest a low affinity for, and a low penetration into, red blood cells.

In conclusion, ximelagatran was rapidly absorbed and converted to melagatran, the predominant compound in plasma and the active form of ximelagatran, following oral administration. The bioavailability of melagatran in humans was about 20%, presumably because of incomplete oral absorption of ximelagatran, but also first-pass metabolism of ximelagatran with subsequent biliary excretion of the formed metabolites.

Acknowledgments. We thank Roger Simonsson and Göran Nilsson for the synthesis of radiolabeled compounds; Annika Janefeldt, Arja Schedwin, and Marie Strimfors for carrying out the animal experiments; and Andreas Landin for performing the feces homogenate incubations.

References

Anonymous (1993) Biverkningsnytt. Rekordantal rapporter 1992. *Läkartidningen* 90:2533–2534.

Antonsson T, Bylund R, Gustafsson D, and Nilsson I (1994) inventors, Trypsin-like protease-inhibiting peptide derivatives, their synthesis and therapeutic use. PTC patent application WO 94/29336.

Antonsson T, Gustafsson D, Hoffmann K-J, Nyström J-E, Sörensen H, and Sellén M (1997) inventors, Preparation of peptide derivatives as prodrug of thrombin inhibitors. PTC patent application WO 97/23499.

Chiou WL, Jeong HY, Chung SM, and Wu TC (2000) Evaluation of using dog as an animal model to study the fraction of oral dose absorbed of 43 drugs in humans. *Pharm Res (NY)* 17:135–140.

Clement B (1998) inventor, Pharmaceutical preparation. Patent application US 5,786,383.

Davies B and Morris T (1993) Physiological parameters in laboratory animals and humans. *Pharm Res (NY)* 10:1093–1095.

Elg M, Gustafsson D, and Carlsson S (1999) Antithrombotic effects and bleeding time of thrombin inhibitors and warfarin in the rat. *Thromb Res* 94:187–197.

Elg M, Gustafsson D, and Deinum J (1997) The importance of enzyme inhibition kinetics for the effect of thrombin inhibitors in a rat model of arterial thrombosis. *Thromb Haemost* 78:1286–1292.

Eriksson BI, Arfwidsson A-C, Frison L, Eriksson UG, Bylock A, Kälebo P, Fager G, and Gustafsson D (2002a) A dose-ranging study of the oral direct thrombin inhibitor, ximelagatran and its subcutaneous form, melagatran, compared with dalteparin in the prophylaxis of thromboembolism after hip or knee replacement: METHRO I. MElagatran for THRombin inhibition in Orthopaedic surgery. *Thromb Haemost* 87:231–237.

Eriksson BI, Bergqvist D, Kälebo P, Dahl OE, Lindbratt S, Bylock A, Frison L, Eriksson UG, Welin L, and Gustafsson D (2002b) The oral direct thrombin inhibitor, ximelagatran and its active form, melagatran, in ascending doses compared with dalteparin for prevention of venous thromboembolism after total hip or total knee replacement: The METHRO II study. *Lancet* 360:1441–1447.

Eriksson BI, Carlsson S, Halvarsson M, Risberg B, and Mattsson C (1997) Antithrombotic effect

of two low molecular weight thrombin inhibitors and a low molecular weight heparin in a caval vein thrombosis model in the rat. *Thromb Haemost* **78**:1404–1407.

Eriksson BI, Ogren M, Eriksson UG, Kälebo P, Ahnfelt L, Björkström S, Sjöstedt Å, Folestad A, Arfwidsson A-C, Elvander CS, and Frison L (2002c) Prophylaxis of venous thromboembolism with subcutaneous melagatran in total hip or total knee replacement: results from phase II studies. *Thromb Res* **105**:371–378.

Eriksson H, Eriksson UG, Frison L, Hansson PO, Held P, Holmström M, Hägg A, Jonsson T, Lapidus L, Leijd B, Stockelberg D, Säfwenberg U, and Taghavi A (1999a) Pharmacokinetics and pharmacodynamics of melagatran, a novel synthetic LMW thrombin inhibitor, in patients with acute DVT. *Thromb Haemost* **81**:358–363.

Eriksson H, Wåhlander K, Gustafsson D, Welin L, Frison L, and Schulman S. (2003) A randomised, controlled, dose-guiding study of the oral direct thrombin inhibitor ximelagatran compared with standard therapy for the treatment of acute deep vein thrombosis: THRIVE I. *J Thromb Haemost* **1**:1–7.

Eriksson UG, Johansson L, Frison F, Bredberg U, and Gustafsson D (1999b) Single and repeated oral dosing of H 376/95, a prodrug of the direct thrombin inhibitor melagatran, to young healthy subjects. *Blood* **94**:26a.

Gustafsson D, Antonsson T, Bylund R, Eriksson U, Gyzander E, Nilsson I, Elg M, Mattson C, Deinum J, Pehrsson S, et al. (1998) Effects of melagatran, a new low-molecular-weight thrombin inhibitor, on thrombin and fibrinolytic enzymes. *Thromb Haemost* **79**:110–118.

Gustafsson D, Nyström J-E, Carlsson S, Bredberg U, Eriksson U, Gyzander E, Elg M, Antonsson T, Hoffmann K-J, Ungell A-L, et al. (2001) The direct thrombin inhibitor melagatran and its oral prodrug H 376/95: intestinal absorption properties, biochemical and pharmacodynamic effects. *Thromb Res* **101**:171–181.

Heit JA, Colwell CW, Francis CW, Ginsberg JS, Berkowitz SD, Whipple J, and Peters G (2001) Comparison of the oral direct thrombin inhibitor ximelagatran with enoxaparin as prophylaxis against venous thromboembolism after total knee replacement. *Arch Intern Med* **161**: 2215–2221.

Hirsh J, Dalen JE, Anderson DR, Poller L, Bussey H, Ansell J, and Deykin D (2001) Oral anticoagulants. Mechanism of action, clinical effectiveness and optimal therapeutic range. *Chest* **119**:8S–21S.

Holm G, Hanssen K, and Svensson L (1985) Use of dodecyl sulfate as an esterase inhibitor before gas-chromatographic determination of labile β-adrenoceptor blocking drugs. *Clin Chem* **31**:868–870.

Hull RD and Pineo GF (1995) Treatment of venous thromboembolism with low-molecular weight heparin. *J Thromb Thrombolysis* **1**:279–284.

Larsson M, Ahnoff M, Abrahamsson A, Logren U, Fakt C, Ohrman I, and Persson B-A (2003) Determination of ximelagatran, an oral direct thrombin inhibitor, its active metabolite melagatran, and the intermediate metabolites, in biological samples by liquid chromatography-mass spectrometry. *J Chromatogr B* **783**:335–347.

Larsson M, Logren U, Ahnoff M, Lindmark B, Abrahamsson P, Svennberg H, and Persson B-A (2002) Determination of melagatran, a novel, direct thrombin inhibitor, in human plasma and urine by liquid chromatography-mass spectrometry. *J Chromatogr B* **766**:47–55.

Mattsson C, Björkman JA, and Ulvinge JC (1997) Melagatran, hirudin and heparin as adjuncts to tissue-type plasminogen activator in the canine model of coronary artery thrombolysis. *Fibrinolysis Proteolysis* **11**:121–128.

Metha J, Chen L, Nichols WW, Mattsson C, Gustafsson D, and Saldeen GP (1998) Melagatran, an oral active site inhibitor of thrombin, prevents or delays formation of electrically induced occlusive thrombus in the canine coronary artery. *J Cardiovasc Pharmacol* **31**:345–351.

Distribution, Metabolism, and Excretion of a Novel Surface-Active Agent, Purified Poloxamer 188, in Rats, Dogs, and Humans

J. MICHAEL GRINDEL,[1] TED JAWORSKI,[2] OLGA PIRANER,[3] R. MARTIN EMANUELE,[1] M. BALASUBRAMANIAN[4]

[1]CytRx Corporation, 154 Technology Parkway, Suite 200, Norcross, Georgia 30092

[2]PPD Development, 3900 Paramount Parkway, Morrisville, North Carolina 27560

[3]Center for Disease Control, 4770 Buford Highway, Atlanta, Georgia 30341

[4]Innoconcepts, 750 Brookfield Parkway, Roswell, Georgia 30075

Received 9 October 2001; revised 12 March 2002; accepted 13 March 2002

ABSTRACT: Purified poloxamer 188 (PP188) is a nonionic, block copolymer surfactant with hemorheologic, antithrombotic, and anti-adhesive properties. PP188 is being studied in phase III clinical trials in sickle cell disease and has been found to be well tolerated and has demonstrated benefit in ameliorating the effects of acute painful vasoocclusive crisis. The disposition of PP188 was studied in rats, dogs, and humans to establish a basis for understanding the safety parameters in support of clinical trials. PP188 was primarily distributed in extracellular water with little or no uptake by red blood cells, and had its highest concentrations in highly perfused tissues such as the kidney, liver, spleen, lymph nodes, and gastrointestinal tract. PP188 had no apparent effect on P450 isozymes *in vitro*. Metabolism was limited (< 5% of dose) with a higher molecular weight copolymer being the only other material detected in plasma or urine. Renal clearance was the controlling route of clearance for PP188 from the body. The 48-h intravenous infusion doses of PP188 were cleared in all species by approximately 1 week after the cessation of dose administration. PP188's disposition is a model for other nonionic block copolymers with similar physical and chemical properties. J Pharm Sci 91:1936–1947, 2002

Keywords: surfactant; renal clearance; species comparison; disposition

INTRODUCTION

Purified poloxamer 188 (PP188) is a nonionic, block copolymer surfactant with hemorheologic and antithrombotic properties (Fig. 1). PP188 was purified by supercritical fluid extraction to remove potentially toxic lower molecular weight components found in the commercially available material.[1,2] PP188 improves microvascular blood flow by reducing blood viscosity, especially under low shear conditions and by reducing adhesive and frictional forces.[3] The mechanism of action of PP188 is not fully understood, but it is hypothesized that the polyoxypropylene core of the molecule binds to hydrophobic portions of cells, leaving the hydrophilic polyoxyethylene chains free to interact with the surrounding aqueous environment.[4,5] Consequently, PP188 provides a hydrated, relatively noncompressible barrier that appears to block hydrophobic adhesive interactions (e.g., cell–cell, cell–protein, and protein–protein) in the blood. As a result, there is a reduction in whole blood viscosity, erythrocyte aggregation, and adhesion to the vascular endothelium,[6] and an improvement in microvascular

Correspondence to: J. Michael Grindel (Telephone: 770-453-0120; Fax: 770-368-0622.; E-mail: grindelm@cytrx.com)

Journal of Pharmaceutical Sciences, Vol. 91, 1936–1947 (2002)

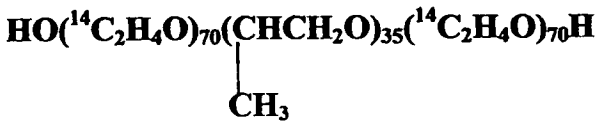

Figure 1. Structure of ^{14}C-purified poloxamer 188 (^{14}C-PP188).

blood flow.[7–10] PP188 has been studied in more than 300 patients with sickle cell disease.[11–14] Tolerability and pilot efficacy studies have been completed in sickle cell disease patients experiencing a vasoocclusive crisis[11,12] as well as in patients with acute chest syndrome.[13] PP188 has been shown to be safe and well tolerated after continuous intravenous infusion over 24 h at cumulative doses as high as 2960 mg/kg.[14] PP188 is also being evaluated preclinically in spinal cord injury and muscular dystrophy.

In this report, we describe the disposition of PP188 in rats, dogs, and humans. The data were collected to provide a comparative assessment of the disposition of PP188 across species used in safety and efficacy evaluations. The radiolabeled studies were conducted to closely pattern the conduct of the 30-day intravenous (IV) infusion toxicology studies.

MATERIALS AND METHODS

Materials

Purified poloxamer 188 was obtained from Hitex, Vannes, France. Propylene glycol, ethylene oxide (EO), and propylene oxide (PO) were purchased from Fluka (Munich, Germany). Cesium hydroxide and Celite were purchased from Aldrich, whereas Magnesol was obtained from The Dallas Group of America (New Iberia, LA). ^{14}C-Ethylene oxide (^{14}C-EO) was obtained from Amersham (Piscataway, NJ). The scintillation cocktail (Ultima Gold XR) and liquid scintillation counting solvents (Carbo-Sorb E and Permafluor E+) as well as all other HPLC or reagent grade solvents were commercially available. A model 307 sample oxidizer (Packard Instruments, Boston, MA) and model 1900TR or 2300TR liquid scintillation counter (Packard Instruments) were used for radioactive samples. Gel permeation chromatography (GPC) was performed using Plgel 1000A, 5 μ, 300 × 7.5 mm columns (Polymer Laboratories) or Ultrastyragel 1000A columns (Waters, Milford, MA), a Waters HPLC model 600 pump with controller, model 717 autosampler, model 410 refractive index detector, with data processed using Millenium32 software (Waters). pH measurements were taken on an Orion model 410A pH meter.

Animals

Purebred male and female beagle dogs were obtained from Covance Research Products. The absorption, distribution, metabolism, excretion (ADME) dogs were housed in individual stainless steel cages designed for the collection of urine and feces. Male and female Sprague-Dawley rats were purchased from Charles River Laboratories. The ADME rats were individually housed in Nalgene metabolism cages designed for the collection of urine and feces and for some rats expired air.

Synthesis of ^{14}C-PP188

Propylene glycol initiator (0.24 g, 3.16 mmol) was allowed to react with PO monomer (6.58 g, 113.5 mmol) in the presence of cesium hydroxide monohydrate catalyst (0.06 g, 0.35 mmol). The reaction was conducted by heating the reactor in an oil bath at 100°C in a specially designed glass reactor to handle small quantities of radioactive raw materials. After reacting the entire added PO, a polypropylene oxide polymer of approximately 1800 Da molecular weight (MW) was produced. 1.12 g (0.59 mmol) of polypropylene oxide polymer was transferred into another glass reactor and the polymerization was continued by adding a mixture of 4.81 g (109.3 mmol) of cold EO and 5.9 mg of ^{14}C-EO (30 mCi/mmol). The reaction mixture was heated at approximately 97°C with stirring for 48 h. The reaction product was treated with magnesol, water, and Celite to absorb the cesium hydroxide catalyst.

The radioactive reaction product was mixed with 39.57 g of non-labeled PP188 dissolved in methylene chloride and the polymer solution was filtered under nitrogen to remove Celite and magnesol. The final product was isolated from the solution by precipitating with petroleum ether and dried under vacuum to remove residual solvent.

The yield was 44.38 g of ^{14}C-PP188 (specific activity = 175.6 μCi/g; radiopurity of 99.6%) (Fig. 1). The final product was a white free-flowing powder with a peak MW of 8622 Da, and the low MW content (<4500 Da) was <1%. The pH of the aqueous polymer solution was 7.3. The GPC MW characteristics and pH were in agreement with the specifications for PP188. The ^{14}C-PP188

was further diluted with non-radiolabeled PP188 before dosing the animals to achieve the correct radioactive dose required for each study and species.

Determination of PP188 in Plasma [GPC Method with Refractive Index (RI) Detection]

The plasma samples were analyzed by a GPC method using RI detection. The method had a linear range of 0.025 to 2.50 mg/mL. A 1.0-mL plasma sample was added to a Teflon-lined tube and vortexed with 2.0 mL of acetonitrile (AcCN) and 0.15 g of sodium chloride. After separation of the phases, the AcCN phase was evaporated under a stream of nitrogen, reconstituted in 200 μL of tetrahydrofuran containing 0.02% polystyrene (MW ~50,400 Da) and filtered. The GPC mobile phase was 95% tetrahydrofuran/5% H_2O on two Plgel 1000A columns in series at 1 mL/min with a column temperature of 40°C and detector temperature of 40°C. All samples, including the calibration curve and quality control samples, were processed by the same procedure. The only exceptions to the above procedure were samples in which predicted concentrations exceeded the range of the calibration curve (> 2.5 mg/mL). These samples were diluted with control (blank) plasma to give final values within the range of the calibration curve.

The GPC method with RI detection for PP188 was validated across species for plasma samples obtained from rats, rabbits, dogs, and humans under Good Laboratory Practice (GLP) guidelines. The method validation consisted of system precision, linearity, method precision/accuracy from spiked samples, ruggedness from spiked samples, recovery from extraction, specificity, freeze–thaw sample stability, and standard stability. Extraction recovery ranged from 89 to 94%. The limit of quantitation for the assay was 0.025 mg/mL using a 1-mL plasma sample and the concentration range was 0.025–2.5 mg/mL.

Determination of PP188 in Urine (GPC Method with RI Detection)

The urine samples were analyzed by a GPC method using RI detection. The method had a linear range of 0.075 to 5.0 mg/mL. A 0.5-mL urine sample was mixed with 0.5-mL 60% alcohol solution. Dichloroethane (DCE), 2.5 mL, was added, the tube was capped tightly, rotated on a rocker for 45 min, and centrifuged for 20 min at 3500 rpm. Two milliliters of the DCE phase (bottom) was accurately transferred to a clean test tube. The DCE phase was evaporated under a stream of nitrogen, reconstituted in 300 μL of internal standard solution, and after filtration analyzed by GPC with RI detection as described above. All samples, including the calibration curve and quality control samples, were processed by the same procedure. The only exceptions to the above procedure were samples in which predicted concentrations exceeded the range of the calibration curve (0.075–5.0 mg/mL). These samples were diluted with control (blank) urine to give final values within the range of the calibration curve. The GPC method with RI detection for PP188 was validated (GLP guidelines) for human urine similar to that completed for plasma. Extraction recovery ranged from 85 to 92%. The limit of quantitation for the assay was found to be 0.075 mg/mL using a 0.5-mL urine sample.

Determination of PP188 in Feces (GPC Method with RI Detection)

The fecal samples were analyzed by a GPC method using RI detection. The method had a linear range of 0.075 to 5.0 mg/mL. A 5.0-g fecal aliquot sample was mixed 1:1 w/v with phosphate buffered normal saline (PBS). An aliquot of the sample homogenate was vortexed with AcCN; the AcCN phase was removed and evaporated to dryness under nitrogen. The dried sample was resuspended in hexane and extracted with PBS. The PBS phase was separated and extracted again with hexane, discarding the hexane layer. AcCN and sodium chloride were added to the PBS layer, centrifuged, the AcCN layer removed, and evaporated under a stream of nitrogen, reconstituted in 300 μL of internal standard solution, and after filtration analyzed by GPC as described above. All samples including the calibration curve and quality control samples were processed by the same procedure.

The assay demonstrated recoveries ranging from 74 to 86% at 0.075, 0.5, and 2.0 mg/mL. Recovery increased with increasing concentration.

Radioactive Analysis and Sample Preparation Methods

All sample combustion $^{14}CO_2$ was trapped in Carbo-Sorb E, and Permafluor E+ was added to the samples before liquid scintillation counting analysis. All samples were analyzed for radioactivity for at least 5 min or 100,000 accumulated

counts. All samples that were directly analyzed were diluted with Ultima Gold XR scintillation cocktail. Each sample was homogenized before radioanalysis (unless the entire sample was used for analysis) and assayed in duplicate. Scintillation counting data were automatically corrected for counting efficiency using the external standardization method and an instrument-stored quench curve generated from a series of sealed quenched standards.

Feces, brain, ovaries, pancreas, spleen, and testes were blotted dry and then homogenized in water and combusted. Blood was combusted directly. Cage wipes, dose wipes, dose cannulae, and cage debris were soaked in water overnight, homogenized, and combusted. Plasma, urine, cage wash and rinse, bile, and cerebrospinal fluid (CSF) were counted directly. Bone, fat, colon, kidneys, skeletal muscle, stomach, liver, and gastrointestinal contents were frozen in liquid nitrogen, homogenized in water, and aliquots counted. Adrenal glands, aorta, cecum, eyes, gall bladder, injection site, mesenteric lymph nodes, thyroid, and urinary bladder were digested in 1 N sodium hydroxide solution at 40°C, homogenized, and counted.

Autoradiographic Methods

Before sectioning the carboxymethylcellulose blocks containing rat carcasses, standards fortified with ^{14}C-radioactivity were placed into the frozen blocks and used for section thickness quality control. Sections were collected on adhesive tape (Nakagawa NA-70 MAG, Japan) at 40-μm thickness, in a Leica CM 3600 cryomicrotome maintained at −18°C. Sections were collected at four to six levels of interest and dried in the cryomicrotome chamber. The sections for each animal were mounted, wrapped with Mylar film, and exposed on Molecular Dynamics phosphorimaging screens along with ^{14}C-autoradiographic standards. The exposed screens were scanned using a Molecular Dynamics 445 SI (Amersham, Boston, MA). The autoradiographic standard imaging data, generated using American Radiolabeled Chemicals Inc. (St. Louis, MO). (ARC 146) were sampled using Imaging Research Inc. (St. Catherine's, Ontario, Canada). AIS software to create a calibrated standard curve. Specified tissues, organs, and fluids were analyzed and tissue concentrations interpolated from each standard curve as nanocuries per gram and then converted to microgram-equivalents/gram of tissue.

Enzyme Inhibition Studies

Characterized, pooled, human liver microsomal fractions from 10 individuals (lot number HHM-0257) were obtained from IIAM (Exton, PA) and stored at −70°C. The following isozymes and substrates were tested using conditions based on the literature: 7-ethoxyresorufin *O*-deethylase (CYP1A2)[15]; tolbutamide methyl hydroxylase (CYP2C9)[16]; *S*-mephenytoin 4′-hydroxylase (CYP2C19)[17]; dextromethorphan *O*-demethylase (CYP2D6)[18]; *p*-nitrophenol hydroxylase (CYP2E1)[19]; and erythromycin *N*-demethylase (CYP3A4).[20] A single substrate concentration was used, approximating the concentration of the substrate that gives half-maximal reaction velocity (K_m) for human liver microsomes in these assays. Assays were performed in the presence and absence of PP188 (10–1000 μM). The concentration of PP188 that inhibited 50% of the activity (IC_{50}) of each specific isozyme of cytochrome P450 was estimated by evaluating the effect of various PP188 concentrations on isozyme activity. The data were plotted (percent of activity remaining versus log of PP188 concentration).

Rat Pilot ADME Study

One male and one female rat were given 300 mg/kg/h (17.1 μCi/animal, 14,400 mg/kg) dose of ^{14}C-PP188 by continuous IV infusion over 48 h. Urine, feces, and expired air were collected daily for 96 h.

Rat ADME Study

Twenty male and 20 female rats in 10 groups of four rats/sex/dose (under GLP conditions) were given continuous IV infusion doses over 48 h of ^{14}C-poloxamer 188 at 30, 100, or 300 mg/kg/h (1440, 4800, or 14,400 mg/kg, 15–16 μCi/animal). Groups 1–3 were designated for collection of urine and feces, Groups 4–6 for blood collection during infusion and tissue collection, groups 7–9 for blood collection at the end of infusion, and group 10 for whole body autoradiography. Urine and feces were collected daily for 0–168 h. Blood (0.5 mL) samples (heparinized for plasma) were collected at predose, 0.25, 0.5, 2, 4, 8, and 48 h from the start of infusion in three groups of male and female rats and at predose, 1, 3, 6, 24, 27, 30, and 48 h in three other groups. Tissues (lung, liver, and kidney) were collected at the end of infusion from three groups (one per dose). Blood (2 mL)

was collected from one rat per sex at 48, 52, 56, 72, and 96 h after the start of infusion for one group at 300 mg/kg/h. Then, the animals were sacrificed and evaluated by whole body autoradiography. The carcasses were frozen in hexane/dry ice, drained, blotted dry, and placed on dry ice for at least 2 h and then bagged and stored frozen at −20°C. The frozen carcasses were embedded in chilled carboxymethylcellulose and frozen into blocks.

Dog ADME Study

Nine male and nine female purebred beagle dogs (under GLP conditions) were randomly assigned in groups of three/sex/dose for phase I and phase II of the study. The dogs received ^{14}C-PP188 by continuous IV infusion at 30, 100, or 300 mg/kg/h for 48 h (1440, 4800, or 14,400 mg/kg) with a target dose level of 5 μCi/kg per animal in phase I and again for phase II. The phases were separated by a 7-day washout period. Blood, urine, feces, and cage rinse were collected from phase I animals. Blood (3 mL) was collected predose and at 48.25, 48.5, 49, 50, 51, 52, 54, 72, and 96 h after the start of infusion. Urine and feces were collected separately at 24-h intervals through 168 h. Blood, urine, feces, CSF, bile, and tissues were collected from phase II animals. Blood (3 mL) was collected predose and at 0.25, 0.5, 1, 2, 3, 4, 6, 24, 27, 30, and 48 h after the start of infusion. Urine and feces were collected separately at 24-h intervals. Shortly after the last blood collection, the animals were anesthetized with sodium pentobarbital, CSF was collected, the animals were exsanguinated, and the following tissues were removed for radioanalysis from the 300 mg/kg/h dose group only: adrenal glands, aorta, bile, bone, brain, cecum, cecum contents, colon, colon contents, duodenum, duodenum contents, eyes, fat (abdominal), gall bladder, heart, ileum, ileum contents, injection site, jejunum, jejunum contents, kidneys, liver, lungs, mesenteric lymph nodes, ovaries, pancreas, skeletal muscle (thigh), spleen, stomach, stomach contents, thyroid, testes, and urinary bladder. The tissues were excised, rinsed with saline, blotted dry, weighed, and placed on ice. After identification, the tissue samples were frozen at −20°C until analyzed.

Human ADME Study

After receiving IRB approval and obtaining written informed consent, five male and one female healthy volunteer subjects were enrolled in this open-label, single-dose IV infusion (100 mg/kg × 1 h plus 30 mg/kg/h × 47 h, 1510 mg/kg) pharmacokinetic study. Blood was collected over EDTA from 0 to 72 h and plasma was separated. Urine and feces were collected quantitatively daily over 0 to 96 h after the start of infusion. All samples were measured or weighed, frozen, and shipped to the analytical laboratory for further testing. The concentrations of PP188 were determined by a GPC method with RI detection for all samples collected (plasma, urine, and feces). Subject safety was assessed by physical examination, clinical laboratory evaluations, vital signs, and adverse events reported by the subjects or the investigator.

Metabolite Profile

Rat

Plasma samples from the toxicokinetics studies in rats were analyzed by GPC to detect parent PP188 as well as a higher molecular weight entity. Urine samples from individual male and female rats in the ADME studies were prepared at 0–24, 24–48, and 48–72 h and were subjected to GPC analysis using a radiochemical flow detector.

Dog

Plasma samples from the toxicokinetics studies in dogs were analyzed by GPC to detect parent PP188 as well as a higher molecular weight entity. Urine samples from the ADME study were prepared separately for male and female dogs at 0–24, 24–48, and 48–72 h. These samples were subjected to GPC analysis using a radiochemical flow detector.

Human

The plasma, urine, and fecal samples from the volunteers in the above-described study were analyzed by GPC to detect parent PP188 as well as a higher molecular weight entity.

Statistical Methods

Statistical analysis included descriptive statistics for all urine and fecal excretion data as well as tissue concentration data where applicable.

RESULTS

Enzyme Inhibition

The inhibitory effects of PP188 on selected human cytochrome P450 isozymes were examined in human liver microsomal incubations. The concentration of PP188 that inhibited 50% of the control activity was determined for six isozyme specific assays with pooled human liver microsomes at fixed substrate concentrations and with five concentrations of PP188. The IC_{50} values for CYP1A2, CYP2C9, CYP2C19, CYP2D6, CYP2E1, and CYP3A4 were all >1000 μM (>850 mg/mL). PP188 did not significantly inhibit the activities of any of the six human P450 isozymes.

Metabolism and Excretion

Rat

The metabolic stability of the radiolabel in ^{14}C-PP188 was evaluated in two rats after the administration of a continuous IV infusion of ^{14}C-PP188 for 48 h at 300 mg/kg/h. There were no apparent gender differences in the rate or extent of excretion of radioactivity. The major route of excretion was the urine whereas expired air accounted for < 0.15% of the dose. The radiolabel in ^{14}C-PP188 was determined to be metabolically stable (data not shown).

The excretion of ^{14}C-PP188 was determined after a 48-h IV infusion to 10 groups of male and female rats at dose levels of 30, 100, or 300 mg/kg/h. The rates and extent of excretion of radioactivity were similar in male and female rats. The major route of excretion of ^{14}C-PP188-derived radioactivity in both sexes was urine with means of 75.1 to 88.5% dose recovered over 168 h. Fecal excretion averaged 4% of the dose and residual carcass contained 2% of the dose at 168 h post-dose. The total mean mass balance for all groups for males and females was > 93.9% dose (Table 1 and Fig. 2). GPC analysis of urine samples showed ^{14}C-PP188 to be the primary component but a longer retention time material was present in all samples and was maximal at 24–48 h (0.79–1.39% dose). Similarly, plasma samples analyzed by GPC from rats in the toxicokinetics studies also demonstrated the presence of a longer retention time material at low concentrations at the highest doses. This material was not evident in the chromatograms from plasma samples obtained during the excretion study. This may be due to the

Table 1. Mean (SD) Cumulative Excretion (% Dose) of Radioactivity in Rats, Dogs, and Humans After Continuous IV Administration for 48 h of ^{14}C-PP188[a]

Species	Dose (mg/kg)	Interval (h)	Urine		Feces		Cage Wash		Cage Wipe		Total	
			Male	Female	Male	Female	Male	Female	Male	Female	Male	Female
Rat	1440[b]	0–168	88.4 (6.00)	87.1 (5.42)	4.43 (0.58)	4.46 (1.75)	2.38 (2.43)	2.39 (0.81)	0.33 (0.02)	0.46 (0.19)	95.5 (3.29)	94.4 (3.37)
	4800[c]	0–168	88.5 (1.71)	75.1 (21.8)	3.10 (0.89)	16.2 (16.9)	1.50 (0.49)	2.04 (1.69)	0.79 (0.37)	0.74 (0.25)	93.9 (2.29)	94.1 (3.26)
	14,400[d]	0–168	86.1 (8.52)	86.3 (3.88)	3.38 (0.99)	3.70 (1.94)	3.13 (2.49)	2.55 (1.48)	1.21 (1.15)	0.61 (0.08)	95.7 (6.21)	95.2 (3.21)
Dog	1440[b]	0–168	86.0 (2.14)	90.6 (3.73)	1.67 (1.23)	1.08 (0.69)	6.31 (0.76)	6.22 (3.92)	0.84 (0.49)	0.37 (0.29)	94.8 (1.63)	98.3 (1.03)
	4800[c]	0–168	88.1 (0.67)	90.5 (6.86)	2.35 (0.34)	1.19 (0.55)	5.55 (1.65)	3.37 (1.30)	0.78 (0.54)	0.75 (0.80)	96.7 (1.26)	95.8 (4.25)
	14,400[d]	0–168	94.4 (0.72)	90.1 (5.05)	0.87 (0.03)	1.12 (0.65)	2.52 (0.63)	5.85 (4.37)	0.46 (0.21)	0.43 (0.15)	98.2 (0.55)	97.5 (0.99)
Human[e]	1510[f]	0–96	84.53 (4.32)		0.025 (0.014)		NA[g]		NA		84.56 (4.33)	

[a]Human subjects received non-radioactive purified PP188 at 100 mg/kg × 1 h plus 30 mg/kg/h × 47 h.
[b]1440 mg/kg = 30 mg/kg/h × 48 h.
[c]4800 mg/kg = 100 mg/kg/h × 48 h.
[d]14,400 mg/kg = 300 mg/kg/h × 48 h.
[e]Five male and one female healthy volunteers.
[f]1510 mg/kg = 100 mg/kg × 1 h + 30 mg/kg/h × 47 h.
[g]NA, not available.

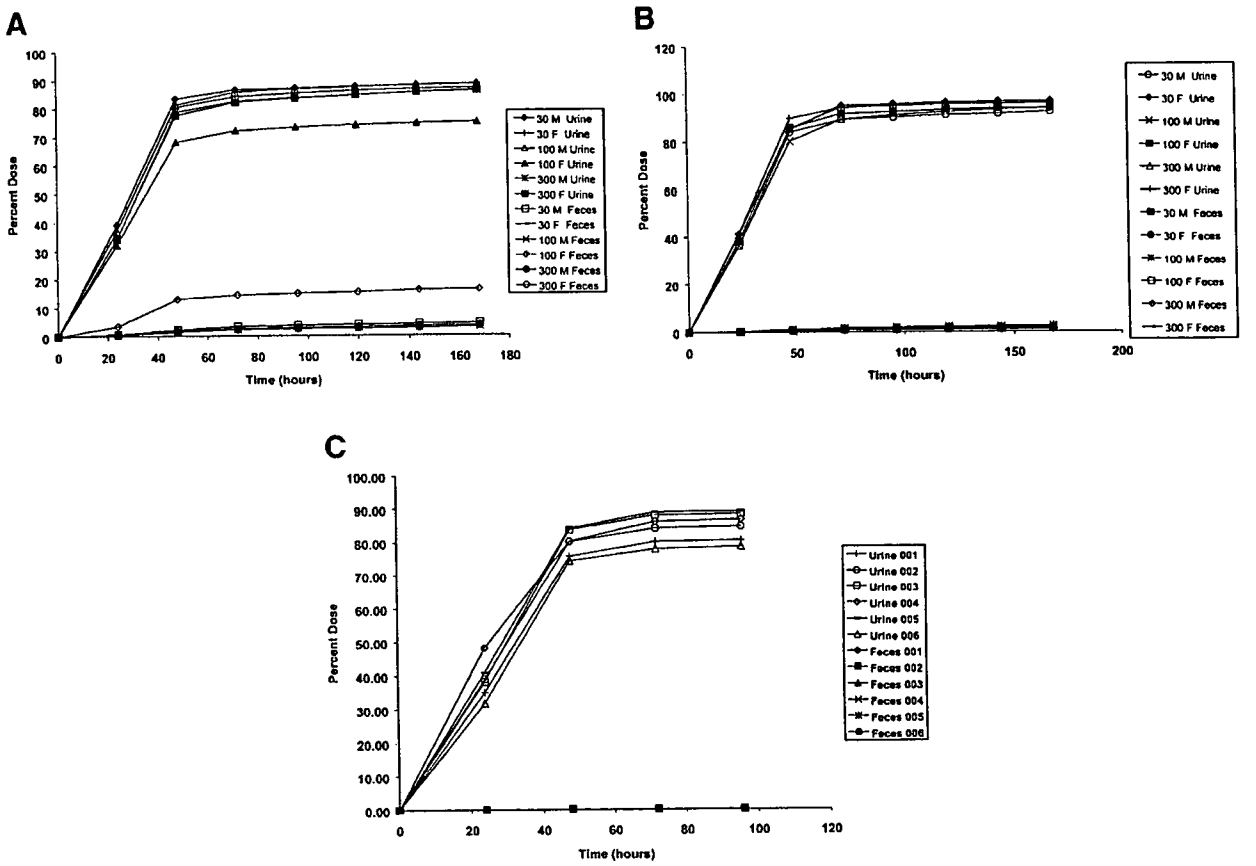

Figure 2. Cumulative excretion of total radioactivity (^{14}C-PP188) in urine and feces in rat (A), and dog (B), and cumulative excretion of PP188 in urine and feces from healthy humans (C).

shorter duration of dosing (48 h) compared with the toxicokinetics studies (30 days).

Dog

The excretion of ^{14}C-PP188-derived radioactivity was determined after a 48-h IV infusion of ^{14}C-PP188 to male and female dogs at doses of 30, 100, and 300 mg/kg/h. The rates and extent of excretion of radioactivity were similar in male and female dogs. The major route of excretion of radioactivity in both sexes was via the urine with means ranging from 86.0 to 94.4% dose. At 168 h, feces accounted for $< 2.35\%$ dose. The total mean mass balance ranged from 94.8 to 98.3% dose (Table 1 and Fig. 2). GPC analysis of the urine demonstrated the presence of a longer retention time species, which was present at $> 5\%$ of the dose. The primary component in urine was ^{14}C-PP188. GPC analysis of the plasma samples from this study only demonstrated the presence of parent PP188. However, dog plasma from the toxicokinetics studies demonstrated the presence of a longer retention time material at low concentrations in dogs from the highest doses. This difference may be attributable to the differing lengths of infusion (48 h versus 30 days, ADME versus toxicokinetics studies).

Human

The excretion and pharmacokinetics of PP188 were studied in five male and one female healthy subjects after a 48-h IV infusion of PP188 at a dose of 100 mg/kg × 1 h plus 30 mg/kg/h × 47 h. The major route of excretion of unchanged PP188 was the urine with 84.5% dose excreted over 96 h. Fecal excretion of PP188 accounted for 0.025% dose over the same time period (Table 1). The plasma samples demonstrated the presence of a longer retention time material at low concentrations, which was cleared slowly from the plasma. This species was not observed in urine or feces samples. Plasma samples were fractionated by

GPC, pooled, and analyzed by MALDI-TOF mass spectrometry to better understand the structure of the longer retention time material. This material had an apparent MW of approximately 16,000 Da and had fragmentation patterns consistent with a block copolymer. It appears to be the high molecular weight fraction of the polymeric distribution for PP188.

Tissue Distribution

Rat

Blood and plasma were analyzed for total radioactivity. The mean concentration of radioactivity was higher in plasma than blood in both sexes, indicating that ^{14}C-PP188-derived radioactivity distributed preferentially into the extracellular fraction of the whole blood. The plasma concentrations of radioactivity peaked at the end of the infusion and increased with increasing dose in a linear manner. (Fig. 3) The pharmacokinetic parameters for total radioactivity derived from ^{14}C-PP188 are summarized in Table 2. Autoradiographic data (Fig. 4) indicated that ^{14}C-PP188-derived radioactivity was widely distributed throughout the organs and tissues in both male and female rats. At 48 h postdose (end of infusion), the highest concentration of radioactivity occurred in the gastrointestinal tract, kidney, axillary lymph nodes, popliteal lymph nodes, adrenal gland, salivary gland, cervical lymph nodes, thyroid gland, inguinal lymph nodes, liver, lungs, and bone marrow as measured by autoluminography (Table 3) which does not allow for correction of background blood or urine in the tubules. Generally, tissue concentrations decreased over time, but elimination was not complete at 96 h postdose. Differential intra-organ distribution was apparent in the kidney with radioactivity unevenly distributed in the renal cortex and medulla (Table 3 and Fig. 4). Again this was probably attributable to the increased vascularization of the renal cortex.

Dog

The mean concentrations of radioactivity were higher in plasma than blood in both sexes indicating that ^{14}C-PP188-derived radioactivity distributed preferentially into the extracellular fraction. The peak concentrations of radioactivity occurred at the end of infusion and the concentrations increased with increasing dose in a linear manner. The pharmacokinetic parameters for total radioactivity derived from ^{14}C-PP188 as well as those for parent PP188 are summarized in Table 2. The tissues from male dogs with the highest mean concentrations at 48 h included the kidneys, mesenteric lymph nodes, adrenal glands, liver, urinary bladder, and spleen. The tissues from female dogs with the highest mean concentration at 48 h included the kidneys, adrenal glands, mesenteric lymph nodes, liver, ovaries, urinary bladder, and spleen (Table 3).

DISCUSSION

PP188 is a nonionic, block copolymer that is currently being evaluated in phase III clinical trials for the treatment of vasoocclusive crisis in sickle

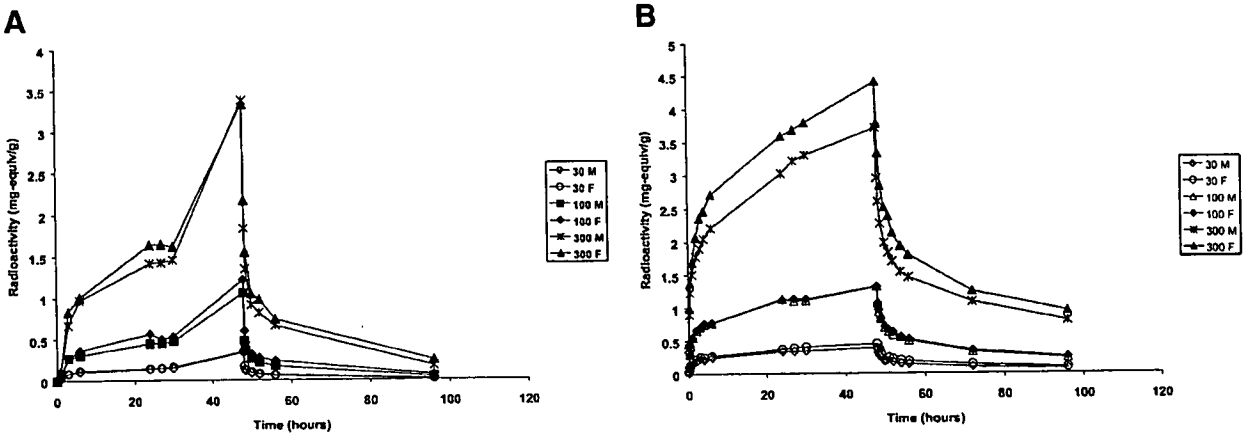

Figure 3. Mean plasma concentrations of total radioactivity in rats (A) and dogs (B) after a 48-h continuous IV infusion of ^{14}C-PP188.

Table 2. Pharmacokinetic Parameters for Total Radioactivity (Milligram-Equivalents/Gram) in Rats and Dogs and for PP188 in Dogs After 48-h Continuous IV Infusion Doses of ^{14}C-PP188

Entity Measured	Dose (mg/kg/h)	Species	Sex	C_{max} (mg/mL)	T_{max} (h)	$T_{1/2}$ (h)
Radioactivity	30	Rat	M	0.139	48.25	22.3
			F	0.173	48.25	19.8
	100		M	0.482	48.25	18.7
			F	0.602	48.25	21.0
	300		M	1.84	48.25	20.0
			F	2.17	48.25	23.2
Radioactivity	30	Dog	M	0.318	49.20	38.7
			F	0.404	48.25	37.7
	100		M	1.07	48.25	36.3
			F	1.06	48.25	37.6
	300		M	2.95	48.25	45.2
			F	3.77	48.25	42.2
PP188	100	Dog	M	1.27	48.25	9.8
			F	1.33	48.25	9.0
	300		M	5.33	48.25	13.5
			F	3.51	48.25	13.4

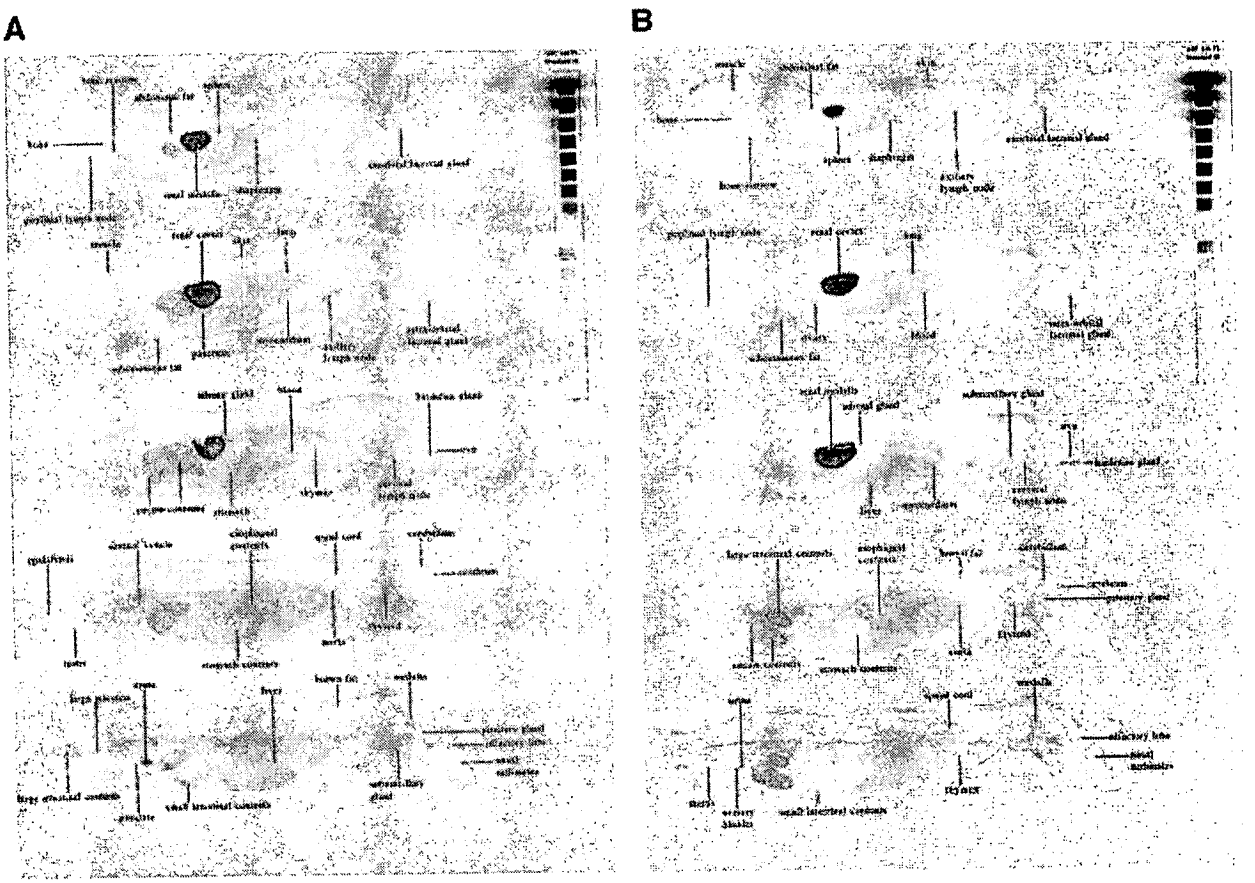

Figure 4. Whole body autoradioluminograph of male (A) and female (B) rats at 48 h after a 48-h IV infusion of ^{14}C-PP188 (14,400 mg/kg/day).

Table 3. Mean (SD) Concentration of Radioactivity in Tissues at 48 h (End of Infusion) for Male and Female Rats and Dogs After a 48-h IV Infusion of ^{14}C-PP188 (14,400 mg/kg)

	Microgram Equivalents of ^{14}C-PP188/g Tissue			
	Rats[a]		Dogs[b]	
Matrix	Male	Female	Male	Female
Adrenal glands	826	1150	2110 (226)	2410 (560)
Aorta	1020	769	ND[c]	ND
Bile (from gall bladder)	NA[d]	NA	569 (137)	186 (322)
Bone, including marrow	1140	ND	86.4 (150)	133 (230)
Brain	ND	ND	ND	20.4 (35.3)
Cecum	1090	1350	669 (75.4)	731 (70.6)
Cecum contents	2290	3180	445 (210)	249 (132)
CSF	NA	NA	52.8 (91.5)	ND
Colon	928	881	641 (69.9)	667 (85.6)
Colon contents	2110	3490	706 (369)	803 (595)
Duodenum	851	901	624 (72.6)	626 (43.8)
Duodenum contents	1610	912	140 (55.5)	151 (151)
Eyes (both)	ND	ND	ND	ND
Fat (abdominal)	ND	ND	527 (331)	508 (174)
Gall bladder	NA	NA	642 (163)	616 (162)
Heart	724	633	424 (73.2)	478 (51.3)
Ileum	NA	NA	612 (56.8)	583 (56.6)
Ileum contents	NA	NA	503 (225)	327 (108)
Injection site	NA	NA	156 (76.6)	353 (341)
Jejunum	NA	NA	566 (62.3)	571 (86.9)
Jejunum contents	NA	NA	356 (117)	354 (300)
Kidneys (both)[e]	7170	11,800	8390 (1070)	7470 (1120)
Liver	1370	1560	1450 (86.9)	1520 (123)
Lungs	1140	1170	784 (108)	991 (106)
Mesenteric lymph nodes	550	835	2340 (424)	2360 (253)
Ovaries	NA	767	NA	1200 (216)
Pancreas	812	803	487 (67.3)	559 (81.4)
Skeletal muscle (thigh)	ND	ND	144 (29.8)	144 (40.5)
Spleen	654	766	1000 (20.7)	1000 (69.1)
Stomach	566	695	653 (67.5)	666 (57.8)
Stomach contents	690	ND	39.3 (68.1)	ND
Testes	428	NA	324 (74.2)	NA
Thyroid	1050	1120	445 (405)	263 (456)
Urinary bladder	1040	875	1090 (138)	1150 (271)

[a]One rat/sex by whole body autoradiography.
[b]Three dogs/sex.
[c]ND, not detectable.
[d]NA, not available.
[e]Dog kidney radioactivity was corrected for background blood levels of ^{14}C. Rat data were not corrected.

cell disease,[12] and in preclinical studies for spinal cord injury and muscular dystrophy. PP188's distribution, metabolism, and excretion were evaluated in rats, dogs, and humans as part of the overall safety program in support of the clinical trials. This report presents the first comprehensive evaluation of a polyoxypropylene–polyoxyethylene block copolymer's distribution, metabolism, and excretion across species, including humans. Previous articles have discussed the distribution and excretion of similar polymers in rodents,[21–24] indicating that these agents were distributed in extracellular water and excreted primarily via the kidneys with minimal to no metabolism.[25]

As would be expected for a highly water soluble nonionic polymer, PP188 was primarily distributed in extracellular water with little to no uptake by red blood cells. The tissues with the highest concentration of PP188 in rats and dogs were the kidneys, lymph nodes, liver, spleen, and urinary bladder with the gastrointestinal tract and lungs also being prominent in the rats. These are all well perfused organs and tissues and the level of radioactivity detected was probably related to the concentration of compound in the extracellular fluid.

Metabolism was limited (< 5% of dose) as noted on GPC analysis with radiochemical detection. The longer retention time material identified in plasma from all three species had a MW of approximately 16,000 Da and a MALDI-MS fragmentation pattern suggesting a block copolymer. This material was present as part of the high molecular weight distribution of the PP188. The clearance from the body of this material is much slower than the parent compound leading to the observation of low levels in urine at later time periods as well as low plasma concentrations at the higher doses. PP188 had no apparent effect on any of the P450 isozymes that were studied. This would be consistent with PP188's surface-active properties and limited metabolism. These data suggest a low probability of drug interactions caused by interference of PP188 with P450 isozyme metabolism.

Clearance from the body was almost entirely by renal excretion in rats, dogs, and humans with the preponderance being intact PP188. Fecal/biliary excretion was low in all three species (< 5% of dose). The radiolabel used was metabolically stable as noted by the lack of excretion of $^{14}CO_2$ in the expired air.

Overall, PP188 was well tolerated clinically in all species studied even at the highest dose level of 300 mg/kg/h × 48 h (14,400 mg/kg). Renal clearance was the controlling route of clearance for PP188 from the body. The 48-h infusion doses of PP188 were cleared in all species by approximately 1 week after the cessation of dose administration. A similar pattern of distribution, metabolism, and excretion could be expected for other nonionic block copolymers with physical and chemical characteristics similar to PP188.

ACKNOWLEDGMENTS

The authors thank Covance Laboratories, Madison, WI for conducting the ADME studies and isozyme inhibition studies, Bio-Kinetic Laboratories, Springfield, MO for conducting the human ADME study, and Richard Okerholm, PhD, for advice and counsel in the design of the ADME studies.

REFERENCES

1. Bentley PK, Davis SS, Johnson OL, Lowe KC, Washington C. 1989. Purification of pluronic F-68 for perfluorochemical emulsification. J Pharm Pharmacol 41:661–663.
2. Lowe KC, Furmidge BA, Thomas S. 1995. Haemolytic properties of pluronic surfactants and effects of purification. Artif Cells Blood Substit Immobil Biotechnol 23:135–139.
3. Smith CM, Hebbel RP, Tukey DP, Clawson CC, White JG, Vercellotti GM. 1987. Pluronic F-68 reduces the endothelial adherence and improves the rheology of liganded sickle erythrocytes. Blood 69:1631–1636.
4. Carr ME, Powers PL, Jones MR. 1991. Effects of poloxamer 188 on the assembly, structure and dissolution of fibrin clots. Thromb Haemost 66:565–568.
5. Carter C, Fisher TC, Hamai H, Johnson CS, Meiselman HJ, Nash GB, Stuart J. 1992. Haemorheological effects of a nonionic copolymer surfactant (poloxamer 188). Clin Hemorheol 12:109–120.
6. Hsu LL, Liu XW, Pierangeli S, Eckman JR, Aguayo SM, Jack D, Wick TM. 2000. Microcirculatory effects of blocking cell adhesion molecules in transgenic sickle cell mice. Blood 96:528a.
7. McKenna R, Cole E, MacLeod C, Emanuele M, Hunter R. 1989. The effects of RheothRx on platelet function and coagulation in man. Blood 74:411.
8. Grover FL, Kahn RS, Heron MW, Paton BC. 1973. A nonionic surfactant and blood viscosity. Arch Surg 106:307–310.
9. Toth K, Bogar L, Juricskay I, Keltai M, Yusuf S, Haywood LJ, Meiselman HJ. 1997. The effect of RheothRx injection on the hemorheological parameters in patients with acute myocardial infarction. Clin Hemorheol Microcirc 17:117–125.
10. Armstrong JK, Meiselman HJ, Fisher TC. 1995. Inhibition of red blood cell-induced platelet aggregation in whole blood by a nonionic surfactant, poloxamer 188 (RheothRx injection). Thromb Res 79:437–450.
11. Adams-Graves P, Kedar A, Koshy M, Steinberg M, Veith R, Ward D, Crawford R, Edwards S, Bustrack J, Emanuele M. 1997. RheothRx (poloxamer 188) injection for the acute painful episode of sickle cell disease: A pilot study. Blood 90:2041–2046.
12. Orringer EP, Casella JF, Ataga KI, Koshy M, Adams-Graves P, Luchtman-Jones L, Wun T, Watanabe M, Shafer F, Kutlar A, Abboud M,

Steinberg M, Adler B, Swerdlow P, Terregino C, Saccente S, Files B, Ballas S, Brown R, Wojtowicz-Praga S, Grindel JM. 2001. Purified poloxamer 188 for the treatment of acute vaso-occlusive crisis of sickle cell disease: A double-blind, randomized, placebo-controlled study. JAMA 286:2099–2106.

13. Files BA, Ballas SK, Benjamin LJ, Wojtowicz-Praga S, Grindel JM. 1998. Multicenter trial of FLOCOR in patients with sickle cell disease and acute chest syndrome. Blood 92:30b.
14. Luchtman-Jones L, Files B, Ballas SK, Swerdlow P, Benjamin L, Hilliard L, Coates TD, Abboud M, Wojtowicz-Praga S, Grindel JM. 1999. Phase I study of FLOCOR in patients with acute chest syndrome of sickle cell disease. Blood 94:25b.
15. Plopper CG, Weir AJ, Morin D, Chang A, Philpot RM, Buckpitt AR. 1993. Postnatal changes in the expression and distribution of pulmonary cytochrome P450 monooxygenases during Clara cell differentiation in rabbits. Mol Pharmacol 44:51–61.
16. Ho JW, Moody DE. 1993. Determination of tolbutamide hydroxylation in rat liver microsomes by high-performance liquid chromatography: Effect of psychoactive drugs on *in vitro* activity. Life Sci 52: 21–28.
17. Chiba K, Manabe K, Kobayashi K, Takayama Y, Tani M, Ishizaki T. 1993. Development and preliminary application of a simple assay of S-mephenytoin 4′-hydroxylase activity in human liver microsomes. Eur J Clin Pharmacol 44:559–562.
18. Jacqz-Aigrain E, Funck-Brentano C, Cresteil T. 1993. CYP2D6- and CYP3A-dependent metabolism of dextromethorphan in humans. Pharmacogenetics 3:197–204.
19. Duescher RJ, Elfarra AA. 1993. Determination of *p*-nitrophenol hydroxylase activity of rat liver microsomes by high-pressure liquid chromatography. Anal Biochem 212:311–314.
20. Zhang XJ, Thomas PE. 1996. Erythromycin as a specific substrate for cytochrome P4503A isozymes and identification of a high-affinity erythromycin *N*-demethylase in adult female rats. Drug Metab Dispos 24:23–27.
21. Wang ZY, Stern IJ. 1975. Disposition in rats of a polyoxypropylene–polyoxyethylene copolymer used in plasma fractionation. Drug Metab Dispos 3:536–542.
22. Moghimi SM. 1999. Re-establishing the long circulatory behavior of poloxamine-coated particles after repeated intravenous administration: Applications in cancer drug delivery and imaging. Biochim Biophys Acta 472:399–403.
23. Leu D, Manthey B, Kreuter J, Speiser P, Deluca PP. 1984. Distribution and elimination of coated polymethyl [2-^{14}C]methacrylate nanoparticles after intravenous injection in rats. J Pharm Sci 73: 1433–1437.
24. Clarke MSF, Prendergast MA, Terry AV Jr. 1999. Plasma membrane ordering agent pluronic F-68 (PF-68) reduces neurotransmitter uptake and release and produces learning and memory deficits in rats. Learn Mem 6:634–649.
25. Rodriguez SC, Singer EJ. 1996. Toxicology of polyoxyalkylene block copolymers. In: Nace VM, editor. Nonionic surfactants, Vol. 60; New York: Marcel Dekker. pp 211–241.

Available online at www.sciencedirect.com
ScienceDirect
Nuclear Medicine and Biology 34 (2007) 579–583
NUCLEAR MEDICINE — AND — BIOLOGY
www.elsevier.com/locate/nucmedbio

Biodistribution of functionalized multiwall carbon nanotubes in mice

Jinxue Guo[a,b,*], Xiao Zhang[b], Qingnuan Li[a,*], Wenxin Li[a]

[a]*Shanghai Institute of Applied Physics, Chinese Academy of Sciences, Shanghai 201800, China*
[b]*College of Chemistry and Molecular Engineer, Qingdao University of Science and Technology, Qingdao 266042, China*

Received 9 November 2006; recieved in revised 10 February 2007; accepted 7 March 2007

Abstract

With the application of carbon nanotubes in biomedical and pharmaceutical sciences, its basic biological properties in vivo have become an issue of strong concern. Water-soluble functionalized multiwall carbon nanotubes (MWNTs) were labeled with radioactive ^{99m}Tc atoms, and then a tracer was used to study the distribution of MWNTs modified with glucosamine in mice. It shows that MWNTs moved easily among the compartments and tissues of the body, behaving like active molecules although their apparent mean molecular weight is tremendously large. In this study, water-soluble MWNTs were labeled with ^{99m}Tc for the first time, and all results on the distribution of MWNTs in animals provide useful data for their use in the biomedical field.

Keywords: ^{99m}Tc labeled; Distribution; Multiwall carbon nanotubes; In vivo

1. Introduction

Because of their unique and fascinating one-dimensional nanostructure, carbon nanotubes are currently under careful scrutiny as novel tools for biomedical and pharmaceutical applications [1–8]. With the progress of methods for carbon nanotubes functionalization [9–12], the biocompatibility of functionalized carbon nanotubes is clearly improved [13–15]. As a consequence, functionalized carbon nanotubes were proposed as novel types of carrier system for therapeutic agents in vivo [6,7,16–18]. Thus, the biodistribution and kinetics of functionalized carbon nanotubes have raised many concerns as they are introduced into living systems.

Yet, studies about the biodistribution and kinetics of functionalized carbon nanotubes in living systems have seldom been reported because of the shortage of a suitable analytical method. In recent decades, radioisotope tracing has been an effective and straightforward method to study the in vivo quantitative distribution of xenobiotics [19]. Among the radioisotopes used in tracing studies, technetium-99 (^{99m}Tc; $T_{1/2}$=6.02 h, E_γ=141 keV) is widely used due to the stability of labeled compound and appropriate photo energies for measurement.

In this study, we modified multiwall carbon nanotubes (MWNTs) with glucosamine to get water-soluble MWNT glucosamine (MWNT-G), and then ^{99m}Tc-labeled MWNT-G (^{99m}Tc-MWNT-G) was synthesized, which was water-soluble and highly compatible with body fluid in vivo. Finally, the tissue distribution of ^{99m}Tc-MWNT-G in mice was measured. The quantity of MWNT-G accumulated in organs was determined by radioisotopes, and quantitative valuable information on MWNTs in vivo was afforded.

2. Materials and methods

2.1. Materials

MWNTs commercially prepared by chemical vaporization deposition were obtained from Shenzhen Nanotech Port Co. Ltd. China. Determined with transmission electron microscopy (TEM), MWNTs are several tens of micrometers in length, with a diameter of 20–40 nm. Purity was >95%, containing <3% amorphous carbon according to thermal gravity analysis (TGA) and ca. 0.6% Ni as determined by inductively coupled plasma mass spectrometry. The purification of MWNTs was performed according to the method of Liu et al. [20]; the purity was >96%, and the concentration of Ni decreased to <0.2%. Thionyl chloride was of analytical reagent (99% purity). Glucosamine (99% purity) was purchased from Aldrich

* Corresponding authors. Tel.: +86 532 8402275.
E-mail address: gjx1213@126.com (J. Guo).

0969-8051/$ – see front matter © 2007 Elsevier Inc. All rights reserved.
doi:10.1016/j.nucmedbio.2007.03.003

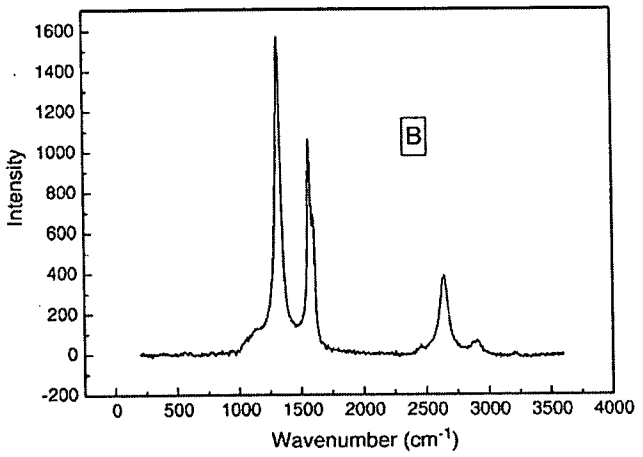

Fig. 1. Raman spectra of water-soluble MWNT-G.

(Germany). $^{99m}TcO_4^-$ (18 mCi) was purchased from the China Institute of Atomic Energy.

2.2. Preparation of MWNT-G

MWNTs were functionalized with glucosamine according to the method of Pompeo and Resasco [21]. MWNTs were placed in a mixture of concentrated sulfuric and nitric acids (3:1; 98% and 70%) and heated at 40°C with ultrasonic for 24 h to synthesize MWNTs with carboxyl. In order to synthesize MWNTs functionalized with acyl chloride, 100 mg of MWNTs was suspended in 30 ml of thionyl chloride ($SOCl_2$). This suspension was stirred at 70°C for 24 h. After centrifugation, the brown-colored supernatant was decanted, and the remaining solid was washed with anhydrous tetrahydrofuran (THF). After centrifugation, the pale yellow-colored supernatant was decanted. The remaining solid was dried at 60°C under vacuum. Finally, a mixture of resulting MWNTs and 10 g of glucosamine was dissolved in anhydrous THF, which was kept in the presence of Na wires to eliminate any traces of water. The mixture was then refluxed for 48 h at room temperature. Glucosamine excess was removed by washing the product with anhydrous THF four times. The remaining solid was dried at 60°C under vacuum, and the final MWNT-G was obtained. Fourier transform infrared (FTIR) spectroscopy, Raman spectra, element analysis, TGA and TEM were applied to determine the characteristics of MWNT-G.

2.3. ^{m}Tc labeling of MWNT-G

MWNTs-G were labeled with ^{99m}Tc according to the method of Li et al. [22]. In brief, MWNTs were dissolved in deionized water with ultrasonic device for 5 min, and then ascorbic acid, stannous chloride and $^{99m}TcO_4^-$ were added to the suspension. This mixture was stirred at 90°C for 20 min. After centrifugation, the supernatant was decanted, and the remaining solid was ^{99m}Tc-MWNT-G.

2.4. Biodistribution study in mice

All animal experiments were performed in compliance with the local ethics committee. Kunming mice (female, 18–22 g, 5–6 weeks old) were obtained from the Shanghai SLAC Laboratory Animal Co. Ltd., Chinese Academy of Sciences (Shanghai, China).

In this study, each mouse in all five groups (five mice per group) was intraperitoneally injected with 300 μl of ^{99m}Tc-MWNT-G suspension (0.5 mCi). They were sacrificed at 1, 3, 6, 10 and 24 h postinjection, respectively. Their tissues, including the heart, lung, liver, spleen, kidney, stomach (emptied), intestine (emptied), skin, muscle (leg) and enterogastric area, were immediately dissected, and blood, feces and urine were collected. Each tissue was wrapped in foil, weighted and counted for ^{99m}Tc activity. Data were corrected for physical decay of radioactivity. Distribution in tissues was presented in percent injected dose per gram of wet tissue (% ID/g), which could be calculated by the percent injected dose (tissue activity/total activity dosed) per gram of wet tissue. The excretion of MWNT-G from mice was investigated by counting ^{99m}Tc in the urine and feces of mice at different time intervals from 0 to 24 h postdosing. Results were expressed as percent injected dose per gram of wet tissue.

2.5. In vivo stability

Normal female mice were intraperitoneally injected with 300 μl of the ^{99m}Tc-MWNT-G suspension containing 0.5 mCi of radioactivity. The mice were then sacrificed at 6, 10 and 24 h postinjection, and urine was collected. Urine radioactivity was measured with NaI(Tl) scintillor. Urine was centrifuged at 10,000 rpm for 4 min, the supernatant was decanted and the remaining solid was washed with

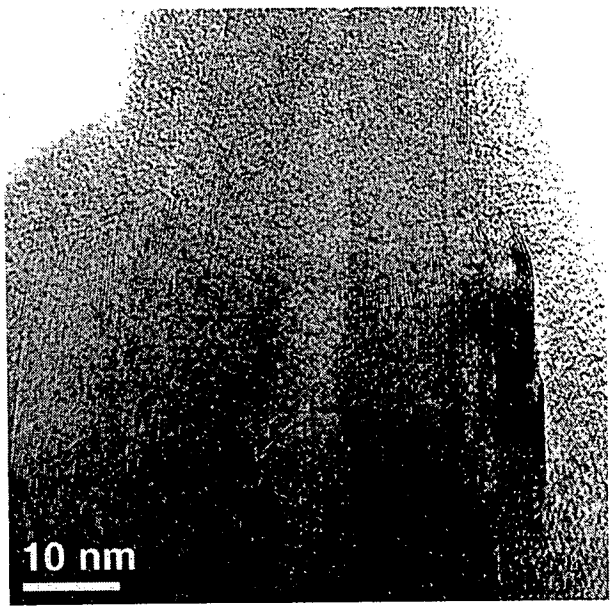

Fig. 2. TEM image of MWNT-G.

Table 1
Biodistribution of ^{99m}Tc-MWNT-G in mice (% ID/g; mean±S.D.)

Tissue	T (h)				
	1 h	3 h	6 h	10 h	24 h
Blood	2.38±0.242	1.82±0.171	1.12±0.102	0.42±0.031	0.13±0.009
Heart	0.86±0.073	0.65±0.072	0.51±0.037	0.30±0.021	0.29±0.013
Lung	2.16±0.189	1.57±0.144	1.19±0.097	0.61±0.047	0.39±0.026
Liver	2.13±0.193	2.28±0.232	1.84±0.065	1.81±0.074	0.42±0.031
Spleen	1.16±0.103	0.98±0.093	0.77±0.068	0.42±0.033	0.23±0.011
Kidney	1.44±0.112	1.32±0.121	1.05±0.093,	0.62±0.053	0.29±0.023
Stomach	9.80±0.092	15.93±1.680	12.91±1.370	6.55±0.781	2.09±0.201
Intestines	1.19±0.135	1.165±0.027	0.98±0.083	0.32±0.018	0.27±0.016
Coat	2.41±0.251	3.49±0.332	2.36±0.233	2.12±0.193	1.49±0.132
Muscle	0.84±0.071	0.48±0.050	0.41±0.026	0.28±0.012	0.14±0.013
Enterogastric area	27.43±2.961	37.21±3.621	53.67±6.332	4.80±0.436	0.81±0.076
Feces			11.81±1.316	30.70±4.120	18.31±2.012
Urine			5.43±0.497	4.61±0.386	4.90±0.456

deionized water. The solid was analysis with paper chromatography using Whatman 1 chromatography paper strips to establish whether ^{99m}Tc was still bound to MWNT-G, and its radioactivity was measured with NaI(Tl) scintillor for comparison with urine radioactivity.

3. Results and discussion

3.1. Synthesis of MWNT-G

MWNT-G was characterized by FTIR spectra, Raman spectra (Fig. 1, the peak at 1324 cm^{-1} is assigned to the "D" band, and the peak at 1570 cm^{-1} is assigned to the "G" band of MWNTs [23]) and TEM (Fig. 2). The FTIR spectra (KBr pellets) of MWNT-G depict the presence of two major signals ($\nu_{c=o}$=1647 cm^{-1} and ν_{N-H}=3400 cm^{-1}) indicating the formation of amide bond [24].

3.2. ^{m}Tc labeling of MWNT-G and in vitro stability

Radiochemical yields of ^{99m}Tc-MWNT-G and $^{99m}TcO_4^-$ were determined by paper chromatography using Whatman 1 chromatography paper strips (1.5×15 cm). Ten-microliter portions of the test solution were applied at 1.5 cm from the lower end of the strips. The strips were developed in 0.9% saline until the solvent reached the top of the strips. The strips were dried and cut into equal segments (1 cm), and radioactivity was measured using NaI(Tl) scintillor. $^{99m}TcO_4^-$ and ^{99m}Tc-MWNT-G migrated with respective R_f values of 0.9 and 0 in saline. The results showed that the purity of ^{99m}Tc-MWNT-G was >90%. The tests were routinely measured at 1, 3, 6, 10 and 24 h postinjection, and it showed that ^{99m}Tc-MWNT-G was stable at 24 h.

3.3. Biodistribution of ^{99m}Tc-MWNT-G in mice

The results of distribution studies of ^{99m}Tc-MWNT-G in mice by intraperitoneal injection are presented in Table 1. ^{99m}Tc-MWNT-G was quickly delivered and was present in measurable levels throughout the entire body. It has been shown that it can easily pass through a number of compartments to reach targets around the whole mouse body, behaving like typical small molecules. A significant percentage of total activity was retained throughout the 24-h study, particularly in the stomach.

In contrast to the results of Wang et al. [25], who examined the organ distribution of carboxylic carbon nanotubes after intraperitoneal injection, there was no sign of renal or other severe acute toxicity responses occurring in the animals in our studies. But Singh et al. [26], who examined the tissue biodistribution and blood clearance rates of intravenously administrated carbon nanotube radiotracers, obtained results similar to those of our studies. In the studies of Wang et al., the materials were carbon nanotubes, but the materials used in the studies of Singh et al. and ours were functionalized carbon nanotubes. Singh et al. modified carbon nanotubes with diethylenetriamine pentaacetic acid (DTPA), and carbon nanotubes were functionalized with glucosamine in our work. Our work indicated that functionalization of carbon nanotubes may have improved the biocompatibility of carbon nanotubes, so there was no severe acute toxicity response observed in the studies of Singh et al. and ours.

The excretion experiment at 24 h demonstrated that >70% of total activity was collected from urine and feces. It indicated that MWNT-G was excreted predominantly via

Table 2
Comparison of solid radioactivity and urine radioactivity (% ID/g; mean±S.D.)

Urine radioactivity			Solid radioactivity		
6 h	12 h	24 h	6 h	12 h	24 h
5.43±0.497	4.61±0.386	4.90±0.456	4.93±0.448	4.16±0.358	4.45±0.417

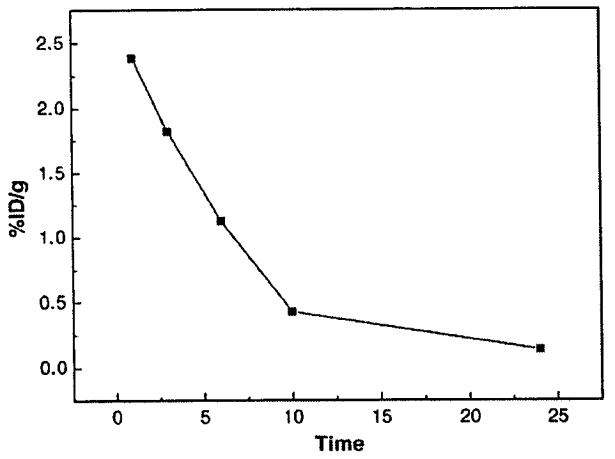

Fig. 3. Clearance of ^{99m}Tc-MWNT-G in the blood.

urine and feces. This result is in accord with that of Wang et al. [25], but is different from the results of ^{99m}Tc–$C_{60}(OH)_x$ [22], which is probably due to the different sizes of MWNTs and C_{60}.

3.4. In vivo stability

With paper chromatography analysis using Whatman 1 chromatography paper strips, a shift assay was performed on solid samples that were centrifuged from urine. The solid migrated with an R_f value of 0 in saline, and the signal with an R_f value of 0.9 was not detected. The data included in Table 2 show that the ratio of solid radioactivity to urine radioactivity is >90%. All results indicated that ^{99m}Tc was still bound to MWNT-G in urine and that there was no free ^{99m}Tc. Thus, ^{99m}Tc-MWNT-G in vivo was stable at 24 h.

3.5. Clearance of ^{99m}Tc-MWNT-G in the blood

The blood clearance rates of ^{99m}Tc-MWNT-G were accumulated in order to expatiate the pharmacokinetic profile of functionalized carbon nanotubes. As is shown in Fig. 3, the blood circulation half-life of ^{99m}Tc-MWNT-G was about 5.5 h. Singh et al. [26] found that the blood circulation half-life of DTPA-SWNT 5 was about 3 h and that of DTPA-SWNT 3 was >3.5 h, which is shorter than ours. In order to elucidate the reason for the different blood circulation half-life in the experiments of Singh et al. and ours, further studies need to be performed.

4. Conclusion

Water-soluble MWNT-G was labeled with ^{99m}Tc for the first time, and the distribution and excretion of ^{99m}Tc-MWNT-G in mice were studied. After intraperitoneal injection, there were no severe acute toxicity responses observed in the studies because the functionalization of carbon nanotube with glucosamine improved the biocompatibility of carbon nanotube. ^{99m}Tc-MWNT-G was quickly delivered around the whole mice body and was excreted mainly via urine and feces. It was determined that the blood circulation half-life of ^{99m}Tc-MWNT-G is about 5.5 h. The study provides basic information for the application of water-soluble MWNTs in biomedical and pharmaceutical sciences, such as carrier systems for therapeutic agents in vivo.

Acknowledgment

The authors thank Tiecheng Ran PhD, Jingying Xu and Ying Zhu for their technical assistance. This work was supported by MOST 973 program (no. 2006CB705600) and the foundation of QUST.

References

[1] Martin CR, Kohli P. The emerging field of nanotube biotechnology. Nat Rev Drug Discov 2003;2:29–37.
[2] Lin Y, Taylor S, Li H, Fernando KA, Qu L, Wang W, et al. Advances toward bioapplications of carbon nanotubes. J Mater Chem 2004;14: 527–41.
[3] Bianco A, Kostarelos K, Partidos CD, Prato M. Biomedical applications of functionalised carbon nanotubes. Chem Commun 2005571–7.
[4] Bianco A. Carbon nanotubes for the delivery of therapeutic molecules. Expert Opin Drug Deliv 2004;1:57–65.
[5] Bianco A, Prato M. Can carbon nanotubes be considered useful tools for biological applications? Adv Mater 2003;15:1765–8.
[6] Wu W, Wieckowski S, Pastorin G, Benincasa M, Klumpp C, Bianco A, et al. Targeted delivery of amphotericin B to cells using functionalized carbon nanotubes. Angew Chem Int Ed 2005;44: 6358–62.
[7] Kam NWS, O'Connell M, Wisdom JA, Dai H. Carbon nanotubes as multifunctional biological transporters and near-infrared agents for selective cancer cell destruction. Proc Natl Acad Sci U S A 2005;102: 11600–5.
[8] Kam NWS, Liu Z, Dai H. Functionalization of carbon nanotubes via cleavable disulfide bonds for efficient intracellular delivery of siRNA and potent gene silencing. J Am Chem Soc 2005;127:12492–3.
[9] Tasis D, Tagmatarchis N, Bianco A, Prato M. Chemistry of carbon nanotubes. Chem Rev 2006;106:1105–36.
[10] Tasis D, Tagmatarchis N, Georgakilas V, Prato M. Soluble carbon nanotubes. Chem Eur J 2003;9:4000–8.
[11] Dyke CA, Tour JM. Overcoming the insolubility of carbon nanotubes through high degrees of sidewall functionalization. Chem Eur J 2004; 10:812–7.
[12] Wu Y, Hudson JS, Lu Q, Moore JM, Mount AS, Ke PCJ, et al. Coating single-walled carbon nanotubes with phospholipids. Phys Chem B 2006;110:2475–8.
[13] Sayes CM, Liang F, Hudson JL, Mendez J, Guo W, Colvin VL, et al. Functionalization density dependence of single-walled carbon nanotubes cytotoxicity in vitro. Toxicol Lett 2006;161:135–42.
[14] Nimmagadda A, Thurston K, Nollert MU, McFetridge PSJ. Chemical modification of SWNT alters in vitro cell–SWNT interactions. Biomed Mater Res 2006;76A:614–25.
[15] Murugesan S, Park TJ, Yang H, Mousa S, Linhardt RJ. Blood compatible carbon nanotubes — nano-based neoproteoglycans. Langmuir 2006;22:3461–3.
[16] Pantarotto D, Briand JP, Prato M, Bianco A. Translocation of bioactive peptides across cell membranes by carbon nanotubes. Chem Commun 200416–7.
[17] Kam NWS, Jessop TC, Wender PA, Dai H. Nanotube molecular transporters: internalization of carbon nanotube–protein conjugates into mammalian cells. J Am Chem Soc 2004;126:6850–1.

[18] Kam NWS, Dai H. Carbon nanotubes as intracellular protein transporters: generality and biological functionality. J Am Chem Soc 2005;127:6021–6.

[19] Dalvie D. Recent advances in the applications of radioisotopes in drug metabolism, toxicology and pharmacokinetics. Curr Pharm Design 2000;6:1009.

[20] Liu J, Rinzler AG, Dai H, Hafner JH, Bradley RK, Smalley RE, et al. Fullerene pipes. Science 1998;280:1253–6.

[21] Pompeo F, Resasco DE. Water solubilization of single-walled carbon nanotubes by functionalization with glucosamine. Nano Lett 2002;2:369–73.

[22] Li Q, Xiu Y, Zhang X. Preparation of ^{99m}Tc–$C_{60}(OH)_x$ and its biodistribution studies. Nucl Med Biol 2002;29:707–10.

[23] Lefrant S. Raman and SERS studies of carbon nanotube systems. Curr Appl Phys 2002;2:479–82.

[24] Chen J, Hamon MA, Hu H, Chen YS, Rao AM, Haddon RC, et al. Solution properties of single-walled carbon nanotubes. Science 1998; 282:95–8.

[25] Wang HF, Wang J, Deng XY, Sun HF, Shi ZJ, Zhao YL, et al. Biodistribution of carbon single-wall carbon nanotubes in mice. J Nanosci Nanotechnol 2004;4:1019–24.

[26] Singh R, Pantarotto D, Lacerda L, Pastorin G, Klumpp C, Prato M, et al. Tissue biodistribution and blood clearance rates of intravenously administrated carbon nanotube radiotracers. Proc Natl Acad Sci U S A 2006;103:3357–62.

ACADEMIC PRESS

Available online at www.sciencedirect.com

SCIENCE DIRECT®

Regulatory Toxicology and Pharmacology 37 (2003) 396–406

Regulatory Toxicology and Pharmacology

www.elsevier.com/locate/yrtph

Ninety-day oral toxicity study of lycopene from *Blakeslea trispora* in rats

D. Jonker,[a] C.F. Kuper,[a] N. Fraile,[b] A. Estrella,[b] and C. Rodríguez Otero[c,*]

[a] *TNO Nutrition and Food Research, Utrechtseweg 48, P.O. Box 360, 3700 AJ Zeist, The Netherlands*
[b] *Antibioticos S.A., R & D Center, Avda. de Antibioticos, 59/61, 24080 Léon, Spain*
[c] *Vitatene S.A., Avda. de Antibióticos, 59/61, 24080 León, Spain*

Received 21 October 2002

Abstract

Lycopene, as a suspension in sunflower oil (20% w/w), was tested for subchronic toxicity by administration at dietary concentrations of 0, 0.25, 0.50, and 1.0% to groups of 20 male and 20 female Wistar rats for a period of 90 days. The lycopene examined in this study was derived from a fungal biomass (*Blakeslea trispora*). Lycopene intake was calculated to be 0, 145, 291, and 586 mg/kg body weight/day in control through high-dose males and 0, 156, 312, and 616 mg/kg body weight/day in control through high-dose females. The results from this study do not provide any evidence of toxicity of lycopene at dietary levels up to 1.0% as demonstrated by the findings of clinical observations, neurobehavioral observations, motor activity assessment, body weight and food consumption measurements, ophthalmoscopic examinations, hematology, clinical chemistry, urinalysis, organ weights, gross pathology, or histopathology. The No-Observed-Effect Level (NOEL) was 1.0% in the diet, the highest dietary concentration tested.

Keywords: Lycopene; Subchronic toxicity; Wistar rat; Oral; Diet; NOEL

1. Introduction

Lycopene, an aliphatic hydrocarbon, is one of the 600 known naturally occurring carotenoids. Fruits and vegetables, particularly tomatoes, contain high concentrations of lycopene (Cronin, 2000). Various epidemiology studies have provided evidence to indicate that diets containing high concentrations of carotenoids may lower risks for the development of chronic diseases such as cancer and heart disease (Bramley, 2000; Nguyen and Schwartz, 1999). Lycopene has received particular attention in recent years as a result of studies that have reported that it is a highly efficient antioxidant and has a high singlet-oxygen and free-radical scavenging capacity (Cronin, 2000). In the European Community (EC), lycopene derived from tomatoes is authorized as a food color and listed as E 160d in Directive 94/36/EC.

Published standard repeated dose animal toxicity data on lycopene include 4- and 14-week feeding studies and an embryotoxicity/teratogencity study, all conducted in rats using lycopene produced by chemical synthesis and stabilized by the preparation of a beadlet formulation containing about 10% of lycopene (SCF, 1999). In the 4-week study, the lycopene beadlet formulation was well tolerated by rats at a dose of 1000 mg lycopene/kg body weight/day. Treatment of rats for 14 weeks with beadlet formulation did not produce any signs of toxicity at doses up to 500 mg lycopene/kg body weight/day. A dose-related orange-red discoloration of the liver and adipose tissue was observed, particularly in females, which only partially resolved following a 5-week recovery phase. There were slight changes in hematological and clinical chemistry values at the high- and mid-dose (150 mg/kg body weight/day) and, in one sex only, changes in the relative weight of the thyroid and brain at the high dose. No treatment-related morphological or histopathological changes were recorded in this study. The embryotoxicity study revealed an increase in the number of complete additional thoracic ribs (14th rib) in the pups at a dose of 1000 mg lycopene/kg body weight/day. Two other synthetic lycopene

* Corresponding author. Fax: +34-987-895-957.
E-mail address: crodriguez@antibioticos.it (C. Rodríguez Otero).

0273-2300/03/$ - see front matter © 2003 Elsevier Science (USA). All rights reserved.
doi:10.1016/S0273-2300(03)00013-8

products, consisting of a stabilizing formulation matrix containing about 10% synthetic lycopene, were recently examined in a GLP-compliant, 13-week oral toxicity study in which rats received the products by daily oral gavage using water as the vehicle (Mellert et al., 2002). In this study, the highest dose level evaluated, viz. about 300 mg lycopene/kg body weight/day was a No-Observed-Adverse-Effect Level (NOAEL).

Other studies on lycopene are limited to those that have investigated the potential antioxidant/protective effects of this carotenoid or to studies in which lycopene was fed along with a mixture of other carotenoids (e.g., Zhao et al., 1998).

A GLP-compliant, subchronic toxicity study to underscore the safety of lycopene prepared from a natural source has not appeared in the open, peer-reviewed scientific literature.

A number of previously conducted studies have shown that lycopene is detected in the plasma and tissues of rats following incorporation into the daily diet. Such studies indicate that lycopene is absorbed intact in rats and subsequently distributed to the tissues. Similar plasma and tissue concentrations of lycopene have been reported in humans consuming lycopene as part of the diet. While the level of absorption may be greater in humans, current published data suggest no toxicodynamic differences occur between rats and humans. Given that the lycopene molecule has been proven to be absorbed and that it showed a similar tissue distribution in rats and humans, the rat can therefore be regarded as a useful and appropriate animal model for assessing the potential toxicity of lycopene in humans (Boileau et al., 2000; Bramley, 2000; Carughi and Hooper, 1994; Ferreira et al., 2000; Kaplan et al., 1990; Mayne et al., 1999; Nierenberg and Nann, 1992; Schierle et al., 1997; Schmitz et al., 1991; Stahl et al., 1992; Zhao et al., 1998). The objective of the present study was to assess the oral toxicity of lycopene, derived from a fungal biomass (*Blakeslea trispora*), following administration to rats via dosed feed for a period of 90 days.

2. Materials and methods

2.1. Animals

Young (about 4 weeks old) male and female Wistar rats (Crl:(WI)WU BR) (85 rats/sex) were obtained from a colony maintained under SPF conditions at Charles River Deutschland, Sulzfeld, Germany. On the day of arrival, they were allocated randomly to four groups of 20 rats/sex. The animals were quarantined and acclimatized for 13 days prior to the initiation of treatment. During the quarantine period, the animals were checked for health and normal growth, and serological evaluation of bacterial and viral infections was performed on randomly selected rats. The age of the animals at study initiation was approximately 6 weeks. The weights of the animals were 136–215 g (mean 170 g) and 108–150 g (mean 129 g) for males and females, respectively. Just prior to the start of treatment, 2 males and 2 females were replaced with reserve animals since their weight was more than 20% below the mean weights for each respective sex. After the start of treatment, extra animals (5/sex) were kept as sentinel animals, but were not used in any part of the study.

The welfare of the animals was maintained in accordance with the general principles of the European Communities (Directive 86/609/EEC) and Dutch legislation (The Experiments on Animals Act 1997), governing the use of animals in toxicity experiments of the European Communities (Directive 86/609/EEC) and Dutch legislation (The Experiments on Animals Act, 1997). The rats were housed in conventional conditions in macrolon cages in groups of 5 (either all males or all females). The cages contained wood chips (Woody Clean, type 3/4) for bedding material. Cages were allocated to treatment groups based on the output of a computerized randomization program. Temperature and relative humidity of the animal room were maintained at 19–23 °C and 40–70%, respectively. The experimental room was ventilated at a rate of approximately 10 air changes per hour and the animals were maintained on a 12-h light and 12-h dark cycle.

2.2. Diets and test materials

The test article lycopene was obtained from Vitatene SAU, León, Spain, in the form of a suspension in sunflower oil (nominal concentration 20% w/w). For this study, two batches of lycopene were used (viz. LC-027-PILOTO in diet batches 1 and 2, and LC-029-PILOTO in diet batches 3 and 4). All batches of lycopene/sunflower oil suspension complied with the current chemical and microbiological specifications for the product. Sunflower oil was used to balance the level of added fat in the experimental diets. The control diet (0% lycopene), low-dose diet (0.25% lycopene), and mid-dose diet (0.5% lycopene) were supplemented with sunflower oil to obtain the same level of added fat as that in the high-dose diet (1.0% lycopene), viz. about 4% (see Table 1 for composition of the experimental diets).

Feed and drinking water were provided ad libitum. During the quarantine and acclimatization period, the rats were fed a commercial pelletized rodent chow (Rat and Mouse No. 3 Breeding Diet, RM3) obtained from SDS Special Diets Services, Witham, England. From initiation of treatment, the rats were fed experimental diets that were prepared by supplementing finely ground RM3 diet with lycopene sunflower oil suspension and/or sunflower oil (see Table 1). The experimental diets were provided in powdered form in stainless steel cans

Table 1
Experimental dose groups

Group	Dietary level (%, w/w)[a]			Average lycopene intake (mg/kg body weight/day)	
	Lycopene	Lycopene oil suspension	Added sunflower oil	Male	Female
Control	0	0	4.40[b]/4.26[c]	0	0
Low-dose group	0.25	1.35[b]/1.32[c]	3.30[b]/3.19[c]	145	156
Mid-dose group	0.50	2.70[b]/2.63[c]	2.20[b]/2.13[c]	291	312
High-dose group	1.0	5.40[b]/5.26[c]	0	586	616

[a] Basal diet for all groups was Rat and Mouse No. 3 Breeding Diet (RM3).
[b] Levels in batches 1 and 2; the level of lycopene oil suspension was calculated on the basis of the concentration of lycopene in the suspension measured by high performance liquid chromatography (HPLC) (18.5% measured; nominal 20%).
[c] Levels in batches 3 and 4; the level of lycopene oil suspension was calculated on the basis of the concentration of lycopene in the suspension measured by HPLC (19.0% measured; nominal 20%).

covered by a perforated stainless steel plate to prevent spillage. Feed was replaced twice per week. Fresh batches of experimental diets were prepared at least once per month, using a mechanical blender. Following preparation, each diet was divided up into portions sufficient for one-half week and stored at <−18 °C. Analyses to demonstrate the stability, homogeneity, and content of lycopene in the experimental diets were conducted using high performance liquid chromatography (HPLC) methodology. Stability was assessed by measuring the concentration of lycopene on the day of diet preparation, after storage in the animal room for up to 4 days, and after up to 4 weeks in the freezer at <−18 °C. There was appropriate homogenous distribution of lycopene within the feed, and the dietary level of lycopene remained constant under the storage conditions examined. Also, the achieved concentration of lycopene in the experimental diets was generally close to the intended level.

2.3. Experimental design

Testing was performed by TNO Nutrition and Food Research (Zeist, The Netherlands) in compliance with Good Laboratory Practice (GLP) regulations established by the Organization for Economic Co-operation and Development (OECD), Paris, ENV/MC/CHEM(98)17. The study protocol was drafted in accordance with Food and Drug Administration (FDA) Guidelines for Toxicological Testing (1982) and the OECD Guideline for the Testing of Chemicals 408 (adopted 21 September 1998).

Four groups of rats (20 rats/sex/group) received diets containing lycopene at a level of 0 (controls), 0.25, 0.5, or 1.0% for a period of at least 90 days. The animals were checked twice daily Monday through Friday, and once daily on Saturdays, Sundays, and holidays, for signs of morbidity and mortality. General clinical observations were made once daily. Neurobehavioral functioning was evaluated by weekly, detailed clinical observations made outside the home cage in a standard arena, and a functional observational battery and motor activity assessment conducted in the 13th exposure week. This neurobehavioral evaluation was conducted on those 10 rats per sex per group that were not used for collection of blood and urine.

Body weights were recorded once during the acclimation period (day-6 of the study), at initiation of treatment (study day 0), once weekly thereafter, and on the day of necropsy. Food consumption was measured weekly by cage (5 animals of 1 sex per cage) and expressed in terms of grams consumed per rat per day. Food conversion efficiency was calculated from the food consumption and body weight data. The amount of lycopene ingested, in terms of milligram per kilogram body weight per day, was calculated weekly from the nominal dietary concentrations of lycopene and the weekly food consumption and body weight data. Water consumption was measured on a cage basis during a 5-day period in weeks 1, 6, and 12. Ophthalmologic examinations were performed once prior to initiation of treatment on all animals and once in week 13 on the control and high-dose animals.

Prior to necropsy, while the animals were under CO_2/O_2 anesthesia, blood samples for clinical chemistry and hematological evaluations were obtained from the abdominal aorta of 10 non-fasted rats per sex per group. Blood samples were analyzed for the following hematological parameters, using K_2-EDTA as anticoagulant: hemoglobin (HB), packed cell volume (PCV), red blood cell count (RBC), reticulocytes, total white blood cell count, thrombocyte count (ABX Pentra 120 hematology analyzer from ABX Diagnostics, France), differential white blood cell counts (microscopic examination of stained blood smears), and prothrombin time (Normotest, Nyegaard A/S, Norway). Mean corpuscular volume, mean corpuscular hemoglobin concentration, and mean corpuscular hemoglobin were calculated from HB, PCV, and RBC.

Plasma samples, obtained from heparinized centrifuged whole blood, were analyzed for the following clinical chemistry parameters: alkaline phosphatase,

aspartate aminotransferase, alanine aminotransferase, gamma glutamyl transferase, total protein, albumin, albumin:globulin ratio, urea, creatinine, total bilirubin, total cholesterol, triglycerides, phospholipids, calcium, inorganic phosphate, chloride, potassium, and sodium (Automatic analyzer model 911 from Hitachi, Japan). Fasting glucose was determined separately in blood collected from the tip of the tail at the end of the urine collection period (study day 87).

For collection of urine samples, the same 10 rats/sex/group as used for hematology and clinical chemistry were deprived of water for 24 h and food for the last 16 h, during study days 86–87. For the last 16 h of this period, the rats were held in stainless steel metabolism cages (1 rat/cage) and urine was collected and analyzed for volume, density, appearance, and dipstick parameters (pH, glucose, occult blood, ketones, protein, bilirubin, and urobilinogen). Urine sediment was examined microscopically for the presence of red and white blood cells, epithelial cells, amorphous material, casts, crystals, bacteria, sperm cells, and worm eggs.

At the end of the study (males on days 91 and 92; females on days 93 and 94), all animals were killed by exsanguination from the abdominal aorta while under CO_2/O_2 anesthesia. On each day, the animals were sacrificed in such a sequence that the average time of killing was about the same for each group. All animals were subjected to gross necropsy, which included an external examination of all body orifices and surfaces, and an examination of all cranial, thoracic, and abdominal organs. Gross pathology findings were recorded. Samples of tissues and organs were removed and preserved in neutral phosphate-buffered 4% formaldehyde solution. The adrenal glands, brain, epididymides, heart, kidneys, liver, ovaries, spleen, testes, thymus, thyroid (with parathyroids), and uterus of all animals were weighed (paired organs together) as soon as possible after dissection. Relative organ weights (gram per kilogram body weight) were calculated on the basis of the terminal body weight of the rats. Histopathological examination of paraffin-embedded, haematoxylin, and eosin-stained sections of the following organs and tissues was performed on all control and high-dose animals: adrenal glands, aorta, axillary lymph nodes, brain, cecum, colon, epididymides, eyes, gut-associated lymphoid tissue (GALT) including Peyer's patches, Harderian gland, heart, kidneys, liver, lungs, mammary gland (females), mesenteric lymph nodes, sciatic nerve, esophagus, ovaries, pancreas, parathyroid, pituitary, prostate, rectum, skin, small intestine (duodenum, jejunum, and ileum), spinal cord (three levels), spleen, sternum with bone marrow, stomach, sublingual salivary gland, submaxillary salivary gland, testes, thymus, thyroid, trachea/bronchi, urinary bladder, uterus (with cervix), Zymbals gland, and all gross lesions. The kidneys, liver, lungs, and all gross lesions were also evaluated microscopically in all rats of the intermediate-dose groups. In addition, 1 low-dose group male rat (B142) that was killed in extremis was subjected to complete histopathological examination.

2.4. Statistical analysis

Data on body weights were evaluated by one-way analysis of covariance (covariable: body weight at initiation of treatment), followed by Dunnett's test to compare the mean of each dose group with the control group. Food and water consumption, food efficiency, continuous neurobehavioral parameters and motor activity, clinical chemistry parameters, quantitative urinalysis parameters, red blood cell and clotting variables, white blood cell counts (total and absolute differential), and organ weights were evaluated using one-way analysis of variance. Where significant differences were found ($p < 0.05$), Dunnett's tests were also applied. Homogeneity of variance was tested using Bartlett's test. Parameters for which significant differences in variance were found ($p < 0.01$) were re-evaluated using Kruskal–Wallis non-parametric analysis of variance followed by Mann–Whitney U tests. Reticulocytes, relative differential white blood cell counts, rank order neurobehavioral parameters, and semi-quantitative urinalysis data were evaluated using Kruskal–Wallis non-parametric analysis of variance followed by Mann–Whitney U tests. Histopathological changes were assessed using Fisher's Exact test. All tests were two-sided.

3. Results and conclusion

The mean intake of lycopene was calculated to be 0, 145, 291, and 586 mg/kg body weight/day in control through high-dose males and 0, 156, 312, and 616 mg/kg body weight/day in control through high-dose females.

On study day 36, one of the low-dose male rats (B142) was killed in extremis. At this time the animal displayed a distended stomach and pale eyes. During the prior 2 weeks this animal also lost weight. Macroscopic and microscopic examination revealed that the conditional decline of this rat was due to severe hydronephrosis. This finding was considered unrelated to treatment because it occurred in a single animal only and, moreover, hydronephrosis is a background finding in Wistar rats. Within a few days of the commencement of treatment, all of the high-dose and many of the mid-dose animals of both sexes displayed pink discoloration of the fur. This was the result of the direct contact of the animals with the red staining lycopene mixed into their diet. No other clinical sign was found to be related to lycopene treatment.

The results of the neurobehavioral testing, including functional observational battery and motor activity, gave no indication of a neurotoxic effect of treatment

Table 2a
Functional observational battery results for Wistar rats fed lycopene at up to 1.0% in the diet for 90 days

Endpoint	Dose group[a]			
	0% Lycopene	0.25% Lycopene	0.50% Lycopene	1.0% Lycopene
Males				
Palpebral closure in homecage (scores 1–4)	2.2 ± 0.5	2.5 ± 0.5	2.1 ± 0.5	2.4 ± 0.5
Rears (number)	3.3 ± 1.1	4.1 ± 1.1	3.5 ± 1.1	4.9 ± 1.3
Arousal (scores 1–6)	3.6 ± 0.2	3.7 ± 0.2	3.8 ± 0.1	3.6 ± 0.2
Handling reactivity (scores 1–4)	2.0 ± 0.0	2.0 ± 0.0	2.0 ± 0.0	2.0 ± 0.0
Urine spots (number)	0.0 ± 0.0	0.1 ± 0.1	0.2 ± 0.1	0.0 ± 0.0
Gait score (scores 1–4)	1.0 ± 0.0	1.0 ± 0.0	1.0 ± 0.0	1.0 ± 0.0
Righting reflex (scores 1–4)	1.0 ± 0.0	1.0 ± 0.0	1.0 ± 0.0	1.4 ± 0.3
Mean forelimb gripstrength (g)	1897 ± 57	1950 ± 50	1860 ± 40	1895 ± 46
Mean hindlimb gripstrength (g)	974 ± 42	1031 ± 44	949 ± 38	1000 ± 42
Mean landing footsplay (mm)	96.1 ± 2.8	97.8 ± 3.3	97.0 ± 2.7	95.0 ± 5.6
Approach response (scores 1–5)	2.0 ± 0.0	1.9 ± 0.1	1.9 ± 0.1	1.8 ± 0.1
Touch response (scores 1–5)	2.0 ± 0.0	2.0 ± 0.0	2.0 ± 0.0	2.0 ± 0.0
Click response (scores 1–5)	2.8 ± 0.2	3.1 ± 0.2	2.3 ± 0.2	2.6 ± 0.2
Tail pinch response (scores 1–5)	3.2 ± 0.3	2.2 ± 0.2	3.0 ± 0.4	2.5 ± 0.3
Mean body temperature (°C)	37.3 ± 0.2	37.4 ± 0.2	37.3 ± 0.2	37.6 ± 0.2
Females				
Palpebral closure in homecage (scores 1–4)	2.0 ± 0.4	1.3 ± 0.3	1.9 ± 0.5	2.0 ± 0.4
Rears (number)	14.9 ± 2.2	17.8 ± 2.7	11.3 ± 0.8	15.6 ± 2.3
Arousal (scores 1–6)	3.9 ± 0.1	4.1 ± 0.1	3.9 ± 0.1	4.0 ± 0.0
Handling reactivity (scores 1–4)	2.0 ± 0.0	2.2 ± 0.1	2.0 ± 0.0	2.0 ± 0.0
Urine spots (number)	0.3 ± 0.3	0.2 ± 0.1	0.1 ± 0.1	0.8 ± 0.7
Gait score (scores 1–4)	1.2 ± 0.1	1.2 ± 0.1	1.1 ± 0.1	1.1 ± 0.1
Righting reflex (scores 1–4)	1.0 ± 0.0	1.0 ± 0.0	1.0 ± 0.0	1.0 ± 0.0
Mean forelimb gripstrength (g)	1368 ± 41	1390 ± 53	1423 ± 44	1377 ± 38
Mean hindlimb gripstrength (g)	599 ± 32	663 ± 52	724 ± 32	642 ± 41
Mean landing footsplay (mm)	74.7 ± 3.7	74.4 ± 3.2	78.9 ± 3.2	73.1 ± 3.2
Approach response (scores 1–5)	1.9 ± 0.1	1.8 ± 0.1	1.8 ± 0.1	1.8 ± 0.1
Touch response (scores 1–5)	2.0 ± 0.0	2.0 ± 0.0	2.0 ± 0.0	2.3 ± 0.2
Click response (scores 1–5)	2.1 ± 0.2	2.2 ± 0.1	2.2 ± 0.2	2.7 ± 0.3
Tail pinch response (scores 1–5)	2.4 ± 0.3	3.0 ± 0.3	3.0 ± 0.3	2.4 ± 0.3
Mean body temperature (°C)	37.9 ± 0.3	38.5 ± 0.3	37.8 ± 0.2	38.0 ± 0.2

[a] Values are means ± SEM for groups of 10 rats. Statistical analysis showed no significant differences between the lycopene groups and controls. The endpoints ease of removal, palpebral closure during handling, fecal boli, salivation, lacrimation, and mobility had the same value (in the normal response range) in all animals, controls included, and none of the animals showed abnormal pupil reflex, clonic or tonic movements, and stereotypy or bizarre behavior (data not shown).

Table 2b
Results of motor activity assessment for Wistar rats fed lycopene at up to 1.0% in the diet for 90 days

Endpoint	Dose group[a]			
	0% Lycopene	0.25% Lycopene	0.5% Lycopene	1.0% Lycopene
Males				
Total distance moved (cm)	3011 ± 201	2967 ± 177	3379 ± 167	3376 ± 133
Number of movements	868 ± 54	857 ± 49	978 ± 46	980 ± 40
Mean velocity (cm/s)	8.4 ± 0.5	8.5 ± 0.3	8.3 ± 0.4	8.4 ± 0.3
Females				
Total distance moved (cm)	3708 ± 284	3698 ± 312	3738 ± 273	3709 ± 250
Number of movements	1028 ± 70	1027 ± 83	1039 ± 72	1023 ± 66
Mean velocity (cm/s)	10.0 ± 0.7	11.0 ± 0.3	10.4 ± 0.6	10.6 ± 0.6

[a] Values are means ± SEM for groups of 10 rats. Statistical analysis showed no significant differences between the lycopene groups and controls.

(see Tables 2a and 2b). Similarly, there were no effects of treatment apparent from the results of the ophthalmologic evaluations (data not shown).

There were no statistically significant differences in mean body weight between the treated and control groups (see Figs. 1 and 2). There were no significant

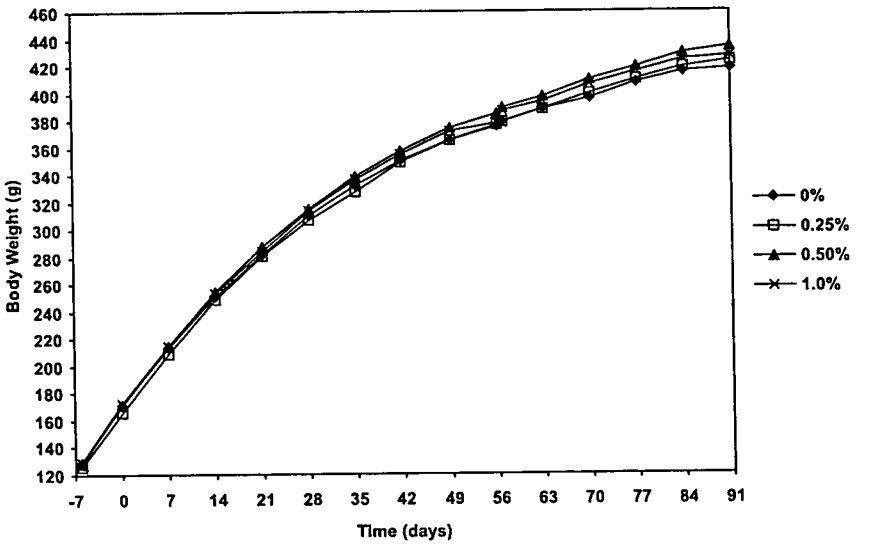

Fig. 1. Body weights (g) for male Wistar rats fed lycopene at up to 1.0% in the diet for 90 days.

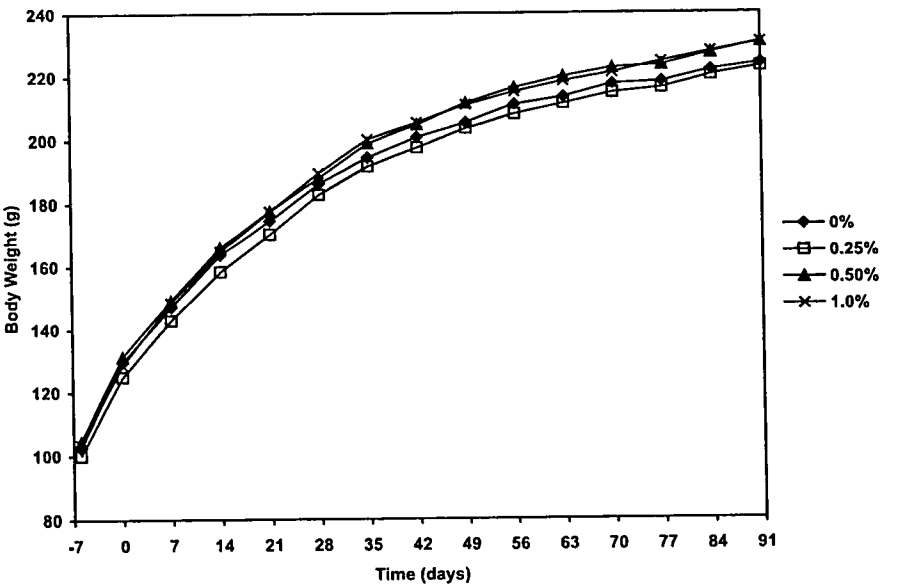

Fig. 2. Body weights (g) for female Wistar rats fed lycopene at up to 1.0% in the diet for 90 days.

Table 3
Mean food consumption of Wistar rats fed lycopene at up to 1.0% in the diet for 90 days

Groups	Overall mean food intake during weeks 1–13 (g/rat/day)[a]	
	Males	Females
0% Lycopene	18.2	11.7
0.25% Lycopene	18.2	11.6
0.50% Lycopene	18.9	12.0
1.0% Lycopene	18.8	11.9

[a] Food consumption was measured per cage (5 rats/cage; 4 cages/sex/group) over successive periods of 7 days and expressed as grams per rat per day.

effects of treatment on food or water consumption or on food conversion efficiency (see Tables 3 and 4).

The results of the hematological and clinical chemistry analyses revealed no statistically significant differences between the treated and control groups. A summary of the hematology and clinical chemistry data is presented in Tables 5 and 6, respectively. Similarly, there were no effects on the quantitative and semi-quantitative urinalysis parameters evaluated (see Table 7).

As shown in Table 8, there were no statistically significant effects of treatment on absolute organ weights. Similarly, there were no significant differences in the

Table 4
Mean water consumption of Wistar rats fed lycopene at up to 1.0% in the diet for 90 days

Groups	Mean water intake (g/rat/day)[a]					
	Week 1		Week 6		Week 12	
	Males	Females	Males	Females	Males	Females
0% Lycopene	29.6	21.5	28.8	20.2	26.2	20.0
0.25% Lycopene	30.2	20.8	29.4	19.9	25.5	19.8
0.50% Lycopene	29.9	22.0	28.7	21.1	28.0	20.2
1.0% Lycopene	31.6	21.8	30.7	21.2	28.0	20.9

[a] Water consumption was measured daily per cage (5 rats/cage; 4 cages/sex/group) on five successive days in the weeks indicated and expressed as grams per rat per day.

Table 5
Terminal hematological values for Wistar rats fed lycopene at up to 1.0% in the diet for 90 days

Parameter	Dose group[a]			
	0% Lycopene	0.25% Lycopene	0.50% Lycopene	1.0% Lycopene
Males				
RBC ($\times 10^{12}$/L)	8.61 ± 0.13	8.26 ± 0.08	8.51 ± 0.08	8.44 ± 0.10
HB (mmol/L)	9.8 ± 0.1	9.6 ± 0.1	9.8 ± 0.1	9.8 ± 0.1
PCV (L/L)	0.435 ± 0.006	0.428 ± 0.005	0.434 ± 0.004	0.432 ± 0.006
MCV (fl)	50.6 ± 0.5	51.8 ± 0.4	51.0 ± 0.4	51.1 ± 0.4
MCH(fmol)	1.14 ± 0.01	1.17 ± 0.01	1.15 ± 0.01	1.16 ± 0.01
MCHC (mmol/L)	22.6 ± 0.1	22.6 ± 0.1	22.5 ± 0.1	22.6 ± 0.1
Reticulocytes (per 1000)	24.5 ± 2.0	22.8 ± 1.4	22.4 ± 1.4	23.2 ± 1.1
Thrombocytes ($\times 10^9$/L)	921 ± 32	966 ± 28	927 ± 20	946 ± 28
Prothrombin time (s)	41.3 ± 0.7	40.8 ± 0.4	41.6 ± 0.4	40.1 ± 0.7
WBC (10^9/L)	9.1 ± 0.6	10.7 ± 0.6	10.1 ± 0.4	9.8 ± 0.6
Eosinophils (10^9/L)	0.1 ± 0.0	0.1 ± 0.0	0.1 ± 0.0	0.1 ± 0.0
Neutrophils (10^9/L)	0.6 ± 0.1	0.5 ± 0.1	0.6 ± 0.1	0.9 ± 0.2
Lymphocytes (10^9/L)	8.2 ± 0.6	9.9 ± 0.7	9.2 ± 0.5	8.7 ± 0.6
Monocytes (10^9/L)	0.2 ± 0.0	0.2 ± 0.1	0.2 ± 0.0	0.1 ± 0.0
Basophils (10^9/L)	0.0 ± 0.0	0.0 ± 0.0	0.0 ± 0.0	0.0 ± 0.0
Females				
RBC ($\times 10^{12}$/L)	7.42 ± 0.08	7.53 ± 0.12	7.52 ± 0.12	7.44 ± 0.10
HB (mmol/L)	9.4 ± 0.1	9.4 ± 0.1	9.4 ± 0.1	9.3 ± 0.1
PCV (L/L)	0.407 ± 0.003	0.407 ± 0.005	0.406 ± 0.005	0.401 ± 0.006
MCV (fl)	55.0 ± 0.6	54.1 ± 0.4	54.1 ± 0.6	53.9 ± 0.3
MCH (fmol)	1.27 ± 0.01	1.24 ± 0.01	1.25 ± 0.02	1.25 ± 0.01
MCHC (mmol/L)	23.1 ± 0.1	23.0 ± 0.1	23.2 ± 0.1	23.2 ± 0.1
Reticulocytes (per 1000)	27.2 ± 1.8	26.7 ± 1.9	31.3 ± 3.3	24.8 ± 1.5
Thrombocytes ($\times 10^9$/L)	821 ± 26	832 ± 22	838 ± 20	834 ± 23
Prothrombin time (s)	34.9 ± 0.5	34.0 ± 0.5	35.1 ± 0.4	34.8 ± 0.7
WBC (10^9/L)	7.5 ± 0.6	8.2 ± 0.8	7.5 ± 0.6	7.3 ± 0.4
Eosinophils (10^9/L)	0.1 ± 0.0	0.1 ± 0.0	0.0 ± 0.0	0.0 ± 0.0
Neutrophils (10^9/L)	0.6 ± 0.1	0.7 ± 0.1	0.7 ± 0.1	0.6 ± 0.1
Lymphocytes (10^9/L)	6.7 ± 0.6	7.3 ± 0.8	6.7 ± 0.6	6.6 ± 0.3
Monocytes (10^9/L)	0.1 ± 0.0	0.1 ± 0.0	0.1 ± 0.0	0.1 ± 0.0
Basophils (10^9/L)	0.0 ± 0.0	0.0 ± 0.0	0.0 ± 0.0	0.0 ± 0.0

[a] Values are means ± SEM for groups of 10 rats (exception: $n = 9$ for control males). Statistical analysis showed no significant differences between the lycopene groups and controls. RBC, red blood cell count; HB, hemoglobin; PCV, packed cell volume; MCV, mean corpuscular volume; MCH, mean corpuscular hemoglobin; MCHC, mean corpuscular hemoglobin concentration; and WBC, total white blood cell count.

relative organ weights of the treated animals versus the controls (data not shown).

Gross necropsy findings did not demonstrate any adverse effects in any organ system (data not shown). All rats of the treated groups showed reddish discoloration of the contents of the gastro-intestinal tract due to ingestion of the red-staining lycopene. Neither the gut tissue itself nor any other organ exhibited a treatment-related discoloration. Histopathological examination did not reveal adverse changes attributable to the ingestion of lycopene (Table 9). The statistically significant decrease in the incidence of 'mononuclear cell aggregates/necrotic hepatocytes' (a background lesion with a highly variable incidence) in high-dose females compared to concurrent

Table 6
Terminal clinical chemistry values for Wistar rats fed lycopene in the diet at up to 1.0% for 90 days

Parameter	Dose group[a]			
	0% Lycopene	0.25% Lycopene	0.50% Lycopene	1.0% Lycopene
Males				
Glucose (mmol/L)	3.96 ± 0.13	4.66 ± 0.42	4.15 ± 0.23	4.07 ± 0.14
Alkaline phosphatase (U/L)	196 ± 10	189 ± 14	175 ± 9	193 ± 10
Alanine aminotransferase (U/L)	77 ± 4	76 ± 4	76 ± 6	76 ± 2
Aspartate aminotransferase (U/L)	110 ± 9	103 ± 4	106 ± 5	124 ± 6
Gamma glutamyl transferase (U/L)	0.0 ± 0.0	0.0 ± 0.0	0.0 ± 0.0	0.0 ± 0.0
Protein (g/L)	73 ± 1	72 ± 1	72 ± 0	71 ± 1
Albumin (g/L)	45 ± 1	44 ± 0	44 ± 0	43 ± 1
Albumin/globulin ratio	1.59 ± 0.05	1.58 ± 0.03	1.60 ± 0.03	1.57 ± 0.03
Urea (mmol/L)	8.1 ± 0.4	7.7 ± 0.3	7.7 ± 0.5	8.1 ± 0.4
Creatinine (μmol/L)	37 ± 1	35 ± 1	35 ± 1	36 ± 1
Total bilirubin (μmol/L)	1.3 ± 0.2	1.4 ± 0.1	1.5 ± 0.1	1.7 ± 0.1
Cholesterol (mmol/L)	2.20 ± 0.08	2.50 ± 0.09	2.22 ± 0.09	2.43 ± 0.11
Triglycerides (mmol/L)	1.85 ± 0.21	1.82 ± 0.23	2.36 ± 0.29	1.95 ± 0.18
Phospholipids (mmol/L)	2.12 ± 0.07	2.26 ± 0.09	2.20 ± 0.09	2.29 ± 0.09
Inorganic phosphate (mmol/L)	2.63 ± 0.06	2.50 ± 0.11	2.41 ± 0.12	2.49 ± 0.13
Calcium (mmol/L)	3.27 ± 0.04	3.23 ± 0.03	3.24 ± 0.01	3.24 ± 0.02
Chloride (mmol/L)	99 ± 0	99 ± 0	99 ± 0	99 ± 0
Potassium (mmol/L)	5.3 ± 0.1	5.3 ± 0.1	5.2 ± 0.1	5.4 ± 0.1
Sodium (mmol/L)	151 ± 0	151 ± 0	151 ± 0	151 ± 0
Females				
Glucose (mmol/L)	3.96 ± 0.15	4.09 ± 0.12	4.28 ± 0.23	5.09 ± 0.64
Alkaline phosphatase (U/L)	136 ± 7	146 ± 8	160 ± 11	129 ± 7
Alanine aminotransferase (U/L)	67 ± 4	70 ± 4	65 ± 3	66 ± 5
Aspartate aminotransferase (U/L)	93 ± 5	92 ± 5	93 ± 4	87 ± 5
Gamma glutamyl transferase (U/L)	0.0 ± 0.0	0.0 ± 0.0	0.0 ± 0.0	0.0 ± 0.0
Protein (g/L)	71 ± 1	72 ± 0	70 ± 1	71 ± 1
Albumin (g/L)	49 ± 0	49 ± 0	48 ± 1	49 ± 0
Albumin/globulin ratio	2.21 ± 0.06	2.12 ± 0.04	2.14 ± 0.04	2.15 ± 0.05
Urea (mmol/L)	8.5 ± 0.5	7.7 ± 0.5	7.2 ± 0.2	8.2 ± 0.7
Creatinine (μmol/L)	39 ± 1	38 ± 1	37 ± 1	38 ± 1
Total bilirubin (μmol/L)	1.2 ± 0.1	1.2 ± 0.1	1.1 ± 0.1	0.9 ± 0.1
Cholesterol (mmol/L)	2.24 ± 0.14	2.34 ± 0.12	2.33 ± 0.08	2.20 ± 0.11
Triglycerides (mmol/L)	0.80 ± 0.07	0.80 ± 0.11	0.80 ± 0.07	1.01 ± 0.18
Phospholipids (mmol/L)	2.27 ± 0.09	2.36 ± 0.11	2.36 ± 0.04	2.34 ± 0.06
Inorganic phosphate (mmol/L)	2.56 ± 0.24	2.43 ± 0.20	2.28 ± 0.23	2.17 ± 0.16
Calcium (mmol/L)	3.23 ± 0.06	3.23 ± 0.07	3.20 ± 0.06	3.17 ± 0.06
Chloride (mmol/L)	101 ± 0	101 ± 0	101 ± 0	101 ± 1
Potassium (mmol/L)	5.2 ± 0.1	5.3 ± 0.1	5.2 ± 0.1	5.1 ± 0.1
Sodium (mmol/L)	149 ± 0	149 ± 0	150 ± 0	149 ± 0

[a] Values are means ± SEM for groups of 10 rats. Statistical analysis showed no significant differences between the lycopene groups and controls.

Table 7
Urinalysis results for Wistar rats fed lycopene at up to 1.0% in the diet for 90 days

Endpoint	Dose group[a]			
	0% Lycopene	0.25% Lycopene	0.5% Lycopene	1.0% Lycopene
Males				
Urinary volume (mL)	3.3 ± 0.3	3.6 ± 0.5	3.9 ± 0.5	2.8 ± 0.2
Urinary density (kg/L)	1.046 ± 0.002	1.044 ± 0.005	1.046 ± 0.003	1.054 ± 0.002
Females				
Urinary volume (mL)	2.1 ± 0.2	1.7 ± 0.2	1.9 ± 0.2	2.0 ± 0.2
Urinary density (kg/L)	1.048 ± 0.006	1.057 ± 0.004	1.055 ± 0.003	1.051 ± 0.003

[a] Values are means ± SEM for groups of 10 rats. Statistical analysis showed no significant differences between the lycopene groups and controls. Semi-quantitative dipstick measurements and microscopic examination of the urinary sediment showed no intergroup differences either (data not shown).

Table 8
Mean terminal body weight and absolute organ weights (grams) of Wistar rats fed lycopene in the diet at up 1.0% for 90 days

Organ	Dose group[a]			
	0% Lycopene	0.25% Lycopene	0.5% Lycopene	1.0% Lycopene
Males				
Body weight (g)	418.6 ± 5.5	423.4 ± 5.8	433.1 ± 6.7	427.6 ± 9.1
Thyroid (g)	0.027 ± 0.001	0.026 ± 0.001	0.029 ± 0.001	0.027 ± 0.001
Adrenals (paired) (g)	0.050 ± 0.002	0.048 ± 0.001	0.053 ± 0.002	0.052 ± 0.001
Kidneys (paired) (g)	2.37 ± 0.04	2.48 ± 0.05	2.47 ± 0.05	2.44 ± 0.06
Thymus (g)	0.389 ± 0.013	0.378 ± 0.018	0.439 ± 0.026	0.372 ± 0.026
Brain (g)	1.95 ± 0.01	1.96 ± 0.01	1.95 ± 0.01	1.96 ± 0.01
Spleen (g)	0.677 ± 0.013	0.648 ± 0.024	0.674 ± 0.017	0.666 ± 0.017
Heart (g)	1.28 ± 0.03	1.27 ± 0.02	1.31 ± 0.03	1.27 ± 0.03
Liver (g)	14.64 ± 0.32	14.63 ± 0.35	15.06 ± 0.35	14.81 ± 0.39
Testes (g)	3.44 ± 0.06	3.39 ± 0.06	3.45 ± 0.06	3.36 ± 0.09
Epididymides (g)	1.43 ± 0.03	1.41 ± 0.04	1.39 ± 0.02	1.39 ± 0.03
Females				
Body weight (g)	225.4 ± 2.9	224.1 ± 4.1	232.0 ± 3.4	233.1 ± 3.6
Thyroid (g)	0.019 ± 0.001	0.020 ± 0.001	0.021 ± 0.001	0.021 ± 0.001
Adrenals (paired) (g)	0.061 ± 0.002	0.062 ± 0.002	0.061 ± 0.002	0.060 ± 0.002
Kidneys (paired) (g)	1.46 ± 0.02	1.43 ± 0.04	1.44 ± 0.02	1.49 ± 0.02
Thymus (g)	0.266 ± 0.009	0.256 ± 0.014	0.262 ± 0.011	0.290 ± 0.011
Brain (g)	1.76 ± 0.02	1.73 ± 0.02	1.76 ± 0.01	1.74 ± 0.01
Spleen (g)	0.436 ± 0.011	0.426 ± 0.014	0.439 ± 0.010	0.453 ± 0.011
Heart (g)	0.81 ± 0.02	0.82 ± 0.02	0.83 ± 0.02	0.80 ± 0.02
Liver (g)	7.22 ± 0.15	7.28 ± 0.15	7.47 ± 0.15	7.29 ± 0.14
Ovaries (paired) (g)	0.074 ± 0.002	0.072 ± 0.003	0.075 ± 0.002	0.076 ± 0.002
Uterus (g)	0.537 ± 0.024	0.646 ± 0.062	0.604 ± 0.041	0.675 ± 0.061

[a] Values are means ± SEM for groups of 20 rats (exception: $n = 19$ for the 0.25% group of males). Statistical analysis showed no significant differences between the lycopene groups and controls.

Table 9
Histopathological findings in Wistar rats fed lycopene at up to 1.0% in the diet for 90 days

Organ/tissue[a]	Incidence of lesion (number of animals examined in parentheses)							
	Males				Females			
	Control	0.25% Lycopene	0.50% Lycopene	1.0% Lycopene	Control	0.25% Lycopene	0.50% Lycopene	1.0% Lycopene
Axillary lymph nodes	(20)	(1)		(20)	(20)			(20)
Sinusoidal blood	0	0		1	0			0
Brain	(20)	(1)		(20)	(20)			(20)
Mineralization of small vein	0	0		1	0			0
Epididymides	(20)	(1)		(20)				
No spermatozoa	0	0		1				
Periarteritis	0	1		0				
Focal mononuclear cell infiltrate	2	1		0				
Eyes	(20)	(1)		(20)	(20)			(20)
Focal mononuclear cell infiltrate	1	0		0	0			0
GALT	(20)	(1)		(20)	(20)			(20)
Mineralization	0	0		0	1			0
Harderian glands	(20)	(1)		(20)	(20)			(20)
Focal mononuclear cell infiltrate	4	0		2	0			0
Unilateral dacryoadenitis	0	0		0	0			1
Heart	(20)	(1)		(20)	(20)			(20)
Focal myocardial mixed inflammatory-cell infiltrate	1	0		0	0			0
Focal myocardial mononuclear cell infiltrate	3	0		0	0			0
Multifocal myocardial fibrosis	0	1		0	0			0
Periarteritis	0	1		0	0			0
Kidneys	(20)	(20)	(20)	(20)	(20)	(20)	(20)	(20)
Basophilic tubules	10	14	12	16	2	0	1	2
Increased hyaline droplet nephropathy	7	4	3	6	0	0	0	0

Table 9 (*continued*)

Organ/tissue[a]	Incidence of lesion (number of animals examined in parentheses)							
	Males				Females			
	Control	0.25% Lycopene	0.50% Lycopene	1.0% Lycopene	Control	0.25% Lycopene	0.50% Lycopene	1.0% Lycopene
Focal mononuclear cell infiltrate	0	1	0	0	0	0	1	0
Focal mineralization	3	4	1	4	4	2	2	6
Hydronephrosis	1	4	2	1	1	0	1	3
Focal glomerular sclerosis	1	0	0	0	0	0	0	0
Periarteritis	0	1	0	0	0	0	0	0
Focal simple transitional epithelial cell hyperplasia	0	0	1	3	0	0	0	0
Intra-tubular proteinaceous cast(s)	0	0	0	1	0	0	0	1
Focal necrosis	0	0	0	0	0	2	0	0
Liver	(20)	(20)	(20)	(20)	(20)	(20)	(20)	(20)
Mononuclear cell aggregates/necrotic hepatocytes	9	5	9	10	10	9	8	3*
Hepatocellular vacuolization	0	1	1	0	0	0	1	0
Lungs	(20)	(20)	(20)	(20)	(20)	(20)	(20)	(20)
Inflammatory cell infiltrate	1	0	0	0	1	0	0	0
Ovaries					(20)			(20)
Hemorrhage					0			1
Cyst(s)					1			0
Mineralization					2			1
Pancreas	(20)	(1)		(20)	(20)			(19)
Focal mononuclear cell infiltrate	0	0		1	0			1
Multifocal degeneration	0	0		0	1			0
Pituitary gland	(17)	(1)		(20)	(20)			(20)
Pars neuralis salivary gland remnants)	0	0		0	1			0
Pars distalis cyst(s)	0	1		1	0			0
Skin/subcutis	(20)	(1)	(1)	(20)	(20)	(3)		(20)
Subcutaneous edema	0	0	1	0	0	0		0
Follicular keratotic plug(s)	0	0	0	0	1	0		0
Focal hypotrichosis	0	0	0	0	1	0		0
Focal parakeratosis	0	0	0	0	1	0		0
Focal acanthosis	0	0	0	0	0	1		0
Spleen	(20)	(1)		(20)	(20)			(20)
Increased extramedullary hematopoiesis	0	1		0	0			0
Sublingual salivary glands	(20)	(1)		(20)	(20)			(20)
Focal serous metaplasia	0	0		1	0			0
Testes	(20)			(20)				
Seminiferous tubular mineralization	0			1				
Seminiferous tubular atrophy	1			1				
Thymus	(20)	(2)	(2)	(20)	(20)			(20)
Focal ductular structures	0	0	0	3	2			4
Corticomedullary hemorrhage(s)	3	1	2	6	2			0
Thyroid	(20)	(1)		(20)	(19)			(20)
Mononuclear cell infiltrate	0	0		0	0			1
Trachea/Bronchi	(20)	(1)		(20)	(20)			(20)
Focal mononuclear cell infiltrate	0	0		3	0			1
Tracheal gland dilatation	0	0		0	2			1
Urinary bladder	(20)	(1)		(20)	(20)			(19)
Subepithelial mononuclear cell infiltrate	0	0		0	0			1
Uterus					(20)			(20)
Endometrial glandular detritus/debris					1			1
Focal mononuclear cell infiltrate					1			0

[a] Organs/tissues in which no abnormalities were observed are not listed in this table (Fisher's exact test, $^*p < 0.05$).

controls was considered a fortuitous finding unrelated to treatment. All other changes observed represent common findings in rats of this strain and age and/or occurred in one or a few animals only or at comparable incidences in the treated group(s) and controls.

Summarizing, the results of the present study in rats did not show any adverse effects of lycopene derived from a natural source (fungal biomass) when administered at dietary levels up to 1.0% for 13 weeks. The dietary level of 1.0% provided a mean daily intake of about 600 mg

lycopene/kg body weight/day which is much higher than estimated to occur in humans (SCF, 1999). The current estimated daily intake from all dietary sources ranges between 0.5 and 27 mg/person/day or 0.08 and 0.45 mg/kg/day (Agarwal et al., 2001; Forman et al., 1993; Järvinen, 1995; Olmedilla et al., 1994; SCF, 1999; Scott et al., 1996; Yong et al., 1994). A 4- and a 14-week feeding study in rats with synthetic lycopene similarly demonstrated absence of any overt toxic effects although discoloration of the liver and adipose tissue occurred along with some marginal changes in relative thyroid and brain weights at the high-dose level in the 14-week feeding study (up to 1000 and 500 mg/kg body weight/day were tested in the 4- and 14-week study, respectively) (SCF, 1999). No marginal changes in organ weights were found in the present study and discoloration was limited to the contents of the gastro-intestinal tract and did not extend to any tissue. In a 13-week study in which rats received synthetic lycopene by oral gavage, discoloration was also limited to the contents of the gastro-intestinal tract and the highest dose tested (about 300 mg lycopene/kg body weight/day) was considered a NOAEL (Mellert et al., 2002).

In conclusion, since the results from this study did not provide any evidence of toxicity of lycopene, the NOEL was considered to be 1.0% in the diet, the highest concentration tested.

References

Agarwal, A., Shen, H., Agarwal, S., Rao, A.V., 2001. Lycopene content of tomato products: its stability, bioavailability and in vivo antioxidant properties. J. Med. Food 4 (1), 9–15.

Boileau, T.W., Clinton, S.K., Erdman, J.W., 2000. Tissue lycopene concentrations and isomer patterns are affected by androgen status and dietary lycopene concentration in male F344 rats. J. Nutr. 130, 1613–1618.

Bramley, P.M., 2000. Is lycopene beneficial to human health? Phytochemistry 54, 233–236.

Carughi, A., Hooper, F.G., 1994. Plasma carotenoid concentrations before and after supplementation with a carotenoid mixture. Am. J. Clin. Nutr. 59, 896–899.

Cronin, J.R., 2000. Lycopene: the powerful antioxidant that makes tomatoes red. Altern. Complement. Ther. 6, 92–94.

Ferreira, A.L.A., Yeum, K.-J., Liu, C., Smith, D., Krinsky, N.I., Wang, X.D., Russell, R.M., 2000. Tissue distribution of lycopene in ferrets and rats after lycopene supplementation. J. Nutr. 130, 1256–1260.

Forman, M.R., Lanza, E., Yong, L.C., Holden, J.M., Graubard, B.I., Beecher, G.R., Meltiz, M., Brown, E.D., Smith, J.C., 1993. The correlation between two dietary assessments of carotenoid intake and plasma carotenoid concentrations: application of a carotenoid food-composition database. Am. J. Clin. Nutr. 58, 519–524.

Järvinen, R., 1995. Carotenoids, retinoids, tocopherols and tocotrienols in the diet: the Finnish Mobile Clinic Health Examination survey. Int. J. Vitam. Nutr. Res. 65, 24–30.

Kaplan, L.A., Lau, J.M., Stein, E.A., 1990. Carotenoid composition, concentrations, and relationships in various human organs. Clin. Physiol. Biochem. 8, 1–10.

Mayne, S.T., Cartmel, B., Silva, F., Kim, C.S., Fallon, B.G., Briskin, K., Zheng, T., Baum, M., Shor-Posner, G., Goodwin Jr., W.J., 1999. Plasma lycopene concentrations in humans are determined by lycopene intake, plasma cholesterol concentrations and selected demographic factors. J. Nutr. 129, 849–854.

Mellert, W., Deckardt, K., Gembardt, C., Schulte, S., Van Ravenzwaay, B., Slesinski, R.S., 2002. Thirteen-week oral toxicity study of synthetic lycopene products in rats. Food Chem. 40, 1581–1588.

Nguyen, M.L., Schwartz, S.J., 1999. Lycopene: chemical and biological properties. Food Technol. 53, 38–45.

Nierenberg, D.W., Nann, S.L., 1992. A method for determining concentrations of retinol, tocopherol, and five carotenoids in human plasma and tissue samples. Am. J. Clin. Nutr. 56, 417–426.

Olmedilla, B., Grandado, F., Blanco, I., Rojas-Hidalgo, E., 1994. Seasonal and sex-related variations in six serum carotenoids, retinol, and α-tocopherol. Am. J. Clin. Nutr. 60 (1), 106–110.

SCF, 1999. Opinion on Synthetic Lycopene as a Colouring Matter for Use in Foodstuff (Expressed on 2 December 1999). Annex V to the Minutes of the 119th Plenary Meeting. European Commission, Health & Consumer Protection Directorate-General, Scientific Committee on Food (SCF): Brussels, Belgium, SCF/CS/ADD/COL/160 Final 6/12/99.

Schierle, J., Bretzel, W., Buhler, I., Faccin, N., Hess, D., Steiner, K., Schuep, W., 1997. Content and isometric ratio of lycopene in food and human blood plasma. Food Chem. 59, 459–465.

Schmitz, H.H., Poor, C.L., Wellman, R.B., Erdman Jr., J.W., 1991. Concentrations of selected carotenoids and vitamin A in human liver, kidney and lung tissue. J. Nutr. 121, 1613–1621.

Scott, K.J., Thurngham, D.I., Hart, D.J., Bingham, S.A., Day, K., 1996. The correlation between the intake of lutein, lycopene and β-carotene from vegetables and fruits, and blood plasma concentrations in a group of women aged 50–65 years in the UK. Br. J. Nutr. 75 (3), 409–418.

Stahl, W., Schwarz, W., Sundquist, A.R., Sies, H., 1992. *Cis–trans* isomers of lycopene and β-carotene in human serum and tissues. Arch. Biochem. Biophys. 294, 173–177.

Yong, L.-C., Forman, M.R., Beecher, G.R., Graubard, B.I., Campbell, W.S., Reichman, M.E., Taylor, P.R., Lanza, E., Holden, J.M., Judd, J.T., 1994. Relationship between dietary intake and plasma concentrations of carotenoids in premenopausal women: application of the USDA-NCI carotenoid food-composition database. Am. J. Clin. Nutr. 60 (2), 223–230.

Zhao, Z., Khachik, F., Rihie Jr., J.P., Cohen, L.A., 1998. Lycopene uptake and tissue disposition in male and female rats. Proc. Soc. Exp. Biol. Med. 218, 109–114.

Available online at www.sciencedirect.com
ScienceDirect
European Journal of Pharmaceutics and Biopharmaceutics 66 (2007) 146–158
European Journal of Pharmaceutics and Biopharmaceutics
www.elsevier.com/locate/ejpb

Research paper

Absorption of poorly water soluble drugs subject to apical efflux using phospholipids as solubilizers in the Caco-2 cell model

Susanne B. Kapitza [a], Bettina R. Michel [a], Peter van Hoogevest [a,b], Mathew L.S. Leigh [b], Georgios Imanidis [a,*]

[a] *Institute of Pharmaceutical Technology, University of Basel, Basel, Switzerland*
[b] *Phares Drug Delivery AG, Muttenz, Switzerland*

Received 17 June 2006; accepted in revised form 16 August 2006
Available online 23 August 2006

Abstract

The purpose of this work was to determine the influence of liposomal solubilization of poorly water soluble drugs exhibiting apical efflux on permeation kinetics and cell toxicity in Caco-2 cells. The HIV-protease inhibitors indinavir and saquinavir were incorporated in phosphatidylcholine liposomes at maximal drug-to-lipid mass ratios and their absorption was determined in Caco-2 cell cultures grown on Transwell inserts using purely aqueous drug solutions as reference. A novel mathematical model was developed to quantitatively delineate the contribution of passive membrane permeation and carrier mediated efflux to transport across the cell monolayer and passive permeability coefficient and maximal efflux rate and affinity constant of the transporter system were determined. Cell toxicity of phospholipids was evaluated by the 3-(4,5-dimethylthiazol-2-yl)-2,5-diphenyl-2*H*-tetrazolium bromide (MTT) and the lactate dehydrogenase (LDH) assay. Cell integrity was not significantly affected by phospholipid concentrations of up to 150 mg/ml with respect to the used standard tests. Maximum drug concentration was increased 10- and 750-fold for indinavir and saquinavir, respectively, by the use of liposomes. The passive membrane permeability coefficient differed between the two drugs in accordance with their lipophilicity and the affinity for apical efflux transporters was on average 4-fold greater for saquinavir than for indinavir. Liposomal solubilization diminished the passive permeability coefficient of both drugs but the passive apical-to-basal delivery rate was increased by the liposomes compared to the purely aqueous solutions at maximal donor concentrations for at least one of the two drugs. Efflux rate reached a maximum for the liposomal formulations reflecting transporter saturation. Hence, liposomal solubilization considerably increased drug concentration in the media and altered absorption behavior by affecting both the passive diffusion and the carrier mediated efflux components of cell monolayer permeation.

Keywords: Caco-2; Drug absorption; HIV-protease inhibitors; Efflux; Liposomes; Phospholipids; Kinetic modeling

1. Introduction

As guide for formulation development work aimed at optimizing bioavailability, drugs are classified by the biopharmaceutic classification system (BCS), which considers four classes of drugs having either a low or high solubility in water and either a high or low permeability for the biological membrane [1,2]. The intestinal permeation kinetics of candidate drugs is routinely measured using the Caco-2 cell model and the PAMPA method [3]. The characteristics of the Caco-2 cell monolayer model have been well described [4–6]. The Caco-2 cell monolayer can be easily used for testing water soluble drugs. The necessary concentration gradient can be generated by simply using high concentrations of the drug in the donor compartment. However, poorly water soluble compounds are much harder to test in the Caco-2 cell model because of the insufficiently steep concentration gradient over the cell monolayer requiring very sensitive analytical tools such as radio-labelling for monitoring drug permeation. For this reason, addition of solubilizing agents is necessary to allow

* Corresponding author. Institute of Pharmaceutical Technology, University of Basel, CH-4056 Basel, Switzerland. Tel.: +41 61 267 1513; fax: +41 61 267 1516.
E-mail address: georgios.imanidis@unibas.ch (G. Imanidis).

0939-6411/$ - see front matter © 2006 Elsevier B.V. All rights reserved.
doi:10.1016/j.ejpb.2006.08.010

measurement of the permeation at readily detectable drug levels in the receiver compartment. Unfortunately, the concentration of solubilizing excipient cannot be infinitely increased because of the detrimental effects of solubilizers such as surfactants, chelating agents and organic solvents to the cell membrane [7–10]. In general, most solubilizers could only be used at very low levels. Consequently, it is to be expected that for some poorly soluble drugs it may be almost impossible to assess the membrane permeation characteristics using the Caco-2 cell model. This deficit is reflected in a recent article [11] showing that a major part of the drugs listed by the WHO as essential drugs cannot be classified in the BCS because of lack of reliable membrane permeation data of these drugs.

Liposomes are phospholipid vesicles, comprising a phospholipid bilayer surrounding an aqueous compartment. In the lipid domain of the bilayer membrane, lipophilic drugs can be dissolved. This principle has been used to solubilize lipophilic drugs like amphotericin B [12] and cyclosporin A [13]. Compared to detergents or solvents, it might be expected that liposomes do not perturbate the plasma membrane of the Caco-2 cells.

A major objective of this work was to explore the possibility of using liposomal solubilization of lipophilic, poorly water soluble drugs for studying their permeation in the Caco-2 model and to investigate the influence of liposomal solubilization on the Caco-2 permeation. This included determining the maximally applicable phospholipid concentration with respect to Caco-2 cell toxicity for increasing drug concentration in solution. Two HIV-protease inhibitors, indinavir and saquinavir with an aqueous solubility at pH 7.4 of 70 and 36 μg/ml, respectively, were used as model poorly water soluble compounds [14]. Both drugs are known to be subject to apical cellular efflux mediated by P-glycoprotein and MRP2 [15–18]. These transporters have been identified in Caco-2 cells [19–21]. The measured cell monolayer permeability in this case is the result of two transport mechanisms taking place in parallel, i.e., passive cell membrane permeation and active apical efflux. In order to gain a basic understanding of the effect of liposomes on absorption, the contribution of each of these two mechanisms to cell layer permeation of the two drugs must be determined, which should allow the effect of liposomes on them to be separately assessed. Therefore, the second major objective of this work was to develop a method for quantitatively delineating passive membrane permeation and carrier mediated apical efflux from experimental transport data in the Caco-2 cell model. This was accomplished by introducing a mathematical model for the kinetics of cellular transport.

2. Materials and methods

2.1. Materials

The human colon adenocarcinoma cell line Caco-2 was a gift of Prof. H. P. Hauri, Biocenter, University of Basel, and originated from the American Type Culture Collection (Rockville, MD, USA). Dulbecco's modified Eagle's medium (DMEM) with high glucose without foetal calf serum (FCS) and without sodium pyruvate, L-glutamine, MEM non-essential amino acids solution (100×), FCS and phosphate-buffered saline (PBS) were all purchased from Gibco (Gaithersburg, MD, USA). For cell culture, DMEM was supplemented with 2 mM L-glutamine, 1% MEM solution and 10% FCS.

Transport media used for the permeation studies were made with Dulbecco's modified Eagle's medium (DMEM) base (Sigma, St. Louis, MO, USA) which did not contain phenol red, sodium pyruvate, FCS and $NaHCO_3$. This was dissolved in bi-distilled water and supplemented with glucose (4.5 g/l), Hepes (4.76 g/l), NaCl (1.987 g/l) and L-glutamine (0.876 g/l), the pH was adjusted to 7.4 and the final medium was subjected to sterile filtration.

Plastic dishes (56.7 cm^2) and 24-well plates were from Nunc (Roskilde, Denmark) and the 12 and 6-well Transwell plates were from Costar, Corning (NY, USA).

Indinavir was kind gift of the University of Applied Sciences, (FHNW, Muttenz, Switzerland), and was synthesized by Sequoia Research Products (Oxford, UK). The base of saquinavir was a kind gift of F. Hoffmann-La Roche, Ltd. (Basel, Switzerland). Vinblastine sulfate was obtained from Sigma Chemicals (St. Louis, MO, USA). Thiazolyl blue for the MTT assay was purchased from Fluka (Buchs, Switzerland) and the LDH Cytotoxicity Detection Kit from Roche Diagnostics (Mannheim, Germany).

Phosphatidylcholine (PC) (>94%) and phosphatidylglycerol (PG) (1-palmitoyl-2-oleoyl-*sn*-glycero-3-phosphatidylglycerol ammonium salt) were purchased from Lipoid AG (Ludwigshafen, Germany).

2.2. Cell culture

Caco-2 cells were grown in petri dishes and maintained at 37 °C in an atmosphere of 8% CO_2 and in equilibrium with distilled water. Their doubling time under these conditions was about 20 h. They were passaged by treatment with 0.25% trypsin and 2.65 mM EDTA with a splitting ratio of 1:14. The medium was changed every alternate day until the petri dishes reached 90% confluence. Cells were used in the experiments at passage number 60–65.

2.3. Preparation of liposomes

Liposomes for the experiments with indinavir were prepared by adding PC to transport media and homogenizing the dispersion with a Polytron mixer (Kinematica AG, Littau, Switzerland) for 5 min at 15,000 rpm. Subsequently the dispersions were extruded at room temperature through polycarbonate filters (Nucleopore® Track-Etch Membrane, Sterico, Wangen, Switzerland) with pore size of 0.4 μm (3 extrusions), 0.2 μm (5 extrusions) and 0.1 μm (20 extrusions) by applying a pressure of 10 bar. The

liposome dispersions finally underwent sterile filtration (0.2 μm sterile filter, Minisart® Sartorius AG, Goettingen, Germany). The phospholipid concentration of the produced vesicle dispersions was 150 mg/ml.

Liposome dispersions with a PC of 50 mg/ml were loaded with indinavir at a pre-defined drug-to-lipid weight ratio (see Section 4 below). A 200 mg/ml solution of the drug was first prepared in DMSO which also contained 20 mg/ml PG. This solution was slowly added to the liposomes under vigorous agitation with a vortex mixer whereas the indinavir partitions spontaneously into the liposomal membrane. The final liposome formulation contained no more than 0.25% DMSO.

To prepare saquinavir-loaded liposomes, the film method was used. PC, saquinavir and PG were dissolved in ethanol 96%. The PC concentration was 100 mg/ml and those of saquinavir and PG varied depending on the desired final drug-to-lipid weight ratio (see below). Ethanol was removed in a rotary evaporator at 40 °C and an initial pressure of 800 mbar that was gradually reduced to 20 mbar. The film was dispersed in transport medium by agitation with a vortex mixer and mild heating to a final PC concentration of 50 mg/ml. This dispersion was extruded and subjected to sterile filtration as described above.

The size of the liposomes was determined with a Zetasizer 1000 HSA photon correlation spectrometer (Malvern Instruments Ltd, Malvern, UK). Prior to the measurements, vesicle dispersions were diluted in transport media until counting rates between 100 and 200 KCts/s were reached. Measurements were performed at room temperature. Vesicle size was typically between 130 and 150 nm with a polydispersity index of around 0.1. The addition of the drugs had no measurable effect on the size of the liposomes.

2.4. MTT-assay

Mitochondrial activity of the cell was evaluated by the 3-(4,5-dimethylthiazol-2-yl)-2,5-diphenyl-2*H*-tetrazolium bromide (MTT) assay. This assay is based on the reduction of MTT by hydrogenase activity in functionally intact mitochondria. The hydrogenase catalyses the conversion of the yellow MTT reagent to blue formazan crystals. Caco-2 cells were seeded on 24-well plates or 12-well Transwell plates at a density of 114,000 cells/cm^2 and allowed to attach for 7–9 days. Medium was changed every other day. Liposome formulations were added to the cells using 4 wells and 3 wells per group for the 24-well plate and the Transwell plate, respectively, and were incubated for 2.5 and 5 h. The liposomes were removed, the cells washed twice with PBS and MTT solution at a concentration of 0.45 mg/ml in culture medium that was prepared from a stock solution of MTT in PBS was added to the cells and incubated for 4 h. Subsequently, lysis buffer containing 10% SDS in 0.01 M HCl was added to solubilize the cells and the formed formazan crystals. The mixture was kept overnight in humidified atmosphere at 37 °C and the amount of formazan was quantified in quadruplicate by transferring to a 96-well plate and measuring the absorbance at 580 nm (reference wavelength 650 nm) using an ELISA plate reader (VERSAmax, Molecular Devices, Sunnyvale, CA, USA). Mitochondrial activity was expressed relative to a control group treated with transport media.

2.5. LDH-assay

Release of the cytoplasmic enzyme lactate dehydrogenase (LDH) into the medium supernatant of the cells was used as a marker for cell membrane integrity. LDH activity was assayed in the supernatants by a reaction in which the tetrazolium salt 2-(4-iodophenyl)-3-(4-nitrophenyl)-5-phenyltetrazolium chloride is reduced to a red formazan salt. Cells were grown as for the MTT-assay. Liposome formulations were added to the cells using 3 wells per group and were incubated for 5 h at 37 °C. After incubation the supernatant of each well was diluted 1:40 with transport media, transferred into a 96-well plate and LDH activity of the diluted medium was determined using the Cytotoxicity Detection Kit according to the manufacturer's instructions. The absorbance of the red formazan was measured at 492 nm (reference wavelength 650 nm) with a plate reader. Absorption values were in the linear range.

Cultures exposed to 1% Triton X-100 were used as high control (100% lysis) and cultures exposed to transport media as low control. Transport medium was also used as background. Cytotoxicity was expressed as follows:

$$\%\ \text{cytotoxicity} = \frac{\text{sample value} - \text{low control}}{\text{high control} - \text{low control}} \times 100 \qquad (1)$$

A potential interaction of the liposomes with the assay was tested using pure LDH (hog muscle, Roche Diagnostics). A LDH solution diluted to 0.05 U/ml with transport media was mixed with liposome formulations that were diluted to concentrations corresponding to the assay with the cells and LDH activity was determined as above. Transport media instead of liposomes were used as a control.

2.6. TEER

The transepithelial electrical resistance (TEER) of cultured cells on Transwell inserts was monitored before and after each permeation experiment with an EVOM epithelial voltohmmeter (World Precision Instruments, Sarasota, FL, USA). Before the experiment, Caco-2 monolayers were washed with Dulbecco's PBS (containing Ca^{2+} and Mg^{2+}) and incubated with transport media for 1 h at 37 °C before the TEER measurement. Physiologically and morphologically well-developed confluent Caco-2 monolayers (at least 19 days old) with TEER values typically between 500 and 650 Ω cm^2 were used in the experiments.

2.7. Drug permeation across Caco-2 monolayers

Liposomal formulations with an indinavir concentration of 500 μg/ml and a saquinavir concentration of 7.5 and 2.2 mg/ml were used in the permeation studies. The concentration of PC was always 50 mg/ml and the concentration of PG was in each case one-tenth of the corresponding drug concentration. These formulations were stable under the conditions of the experiment while at higher drug loadings precipitation of the drug was observed. In addition, purely aqueous solutions of the drugs in transport media were used for permeation studies. Concentrations of these solutions were 50 and 10 μg/ml for indinavir and 10 and 3 μg/ml for saquinavir. These solutions were prepared by adding stock solutions of the drugs in DMSO to the transport media under stirring. The final DMSO concentration in these solutions was 0.25% for indinavir and 1% for saquinavir. The respective high concentration of each drug approached its solubility in the media.

Cells were seeded at a density of 114,000 cells/cm^2 onto 6-well Transwell® plates with an insert area of 4.7 cm^2 and a pore size of the polycarbonate membrane of 0.4 μm. Culture medium was changed every other day and cell monolayers were used between 19 and 21 days post seeding.

The drug solution/formulation was added either in the apical or in the basal compartment with respect to the cell monolayer. Three Transwells were used in each group. When liposomal drug formulations were used, the respective receiver compartment contained a blank liposomal dispersion in transport media with the same phospholipid and DMSO concentration. For the non-liposomal drug solutions the receiver compartment contained transport medium with the same DMSO concentration as the drug solution. In one experiment, the efflux inhibitor vinblastine was added at a concentration of 70 μM to the solution in both compartments.

Permeation of drug across the cell monolayer was monitored by sampling the solutions in both compartments at predefined time points for a duration of 5 h. Sampling volume was 100 μl for the non-liposomol drug solutions and 25 or 50 μl for the liposomal formulations. The withdrawn volume was not replaced. The starting volume of the apical solution was 1.6 ml and of the basal solution 2.8 ml. During the permeation experiment the Transwell plates were kept at 37 °C in a vapour saturated atmosphere and agitated on an orbital shaker at 50 min^{-1} (Edmund Bühler, Hechingen, Germany).

2.8. HPLC

Drug concentration in the samples was determined by HPLC-UV-MS (Agilent series 1100) with an isocratic pump G1310A, an autosampler G1313A, a variable wave length detector G1314A, and a mass spectrometer detector G1946C. The MS detector employed atmospheric pressure electrospray ionization and was operated in the scan mode at positive polarity with capillary voltage 4000 V, fragmentor 140 V, drying gas flow 10 l/min, drying gas temperature 350 °C and nebulizer pressure 30 psig. A C-18 reversed phase column (CC125/2 lispher sel.B 5 μm, Macherey-Nagel, Switzerland) and the following mobile phases were used: For indinavir MeOH/THF/20 mM CH_3COONH_4–1 mM CH_3COONa (aq.) = 40/10/50 and for saquinavir MeOH/THF/20 mM CH_3COONH_4 (aq.) = 50/10/40. The flow rate was 0.25 ml/min. Indinavir was detected at 214 nm in UV and at *m/z* 615 and 637 in MS, corresponding to the protonated form and the sodium adduct, respectively, and saquinavir at 238 nm in UV and at *m/z* 671, 693 and 709 in MS, corresponding to the protonated form, the sodium and the potassium adduct, respectively. Vinblastine was detected at 214 nm in UV concurrently with indinavir at longer retention times. Purely aqueous samples were injected undiluted and samples containing phospholipids were diluted at ratios between 1:10 and 1:40 with transport medium prior to injection. Quantification was performed against a set of external standard solutions within the linear response concentration range.

2.9. Theoretical modeling

A kinetic model describing cell permeation was developed in order first, to delineate the contribution of passive diffusion and active efflux on the overall cell permeation of the drug and second, to evaluate the effect of the liposomes on permeation in terms of these two contributing factors. This model was based on the following assumptions:

1. Three different compartments are considered in which drug concentration varies with time, the apical, the cellular and the basal compartment.
2. Drug may move between the apical and the cellular and the cellular and the basal compartment in both directions by passive diffusion. Permeation through the apical and the basal cell membrane is symmetrical and is characterized in both cases by the permeability coefficient, *P*. No effect of electrical membrane potential on the transport is considered.
3. Drug is subject to carrier mediated active efflux from the cellular to the apical compartment. This follows saturable kinetics that may be characterized by two macroscopic kinetic parameters, v_{max}, the maximum transport rate and *K*, the mass in the cellular compartment for which one-half of the maximum rate is attained, often referred to as affinity or dissociation constant. One global set of parameters is used to describe carrier mediated efflux.
4. No two different orientations or conformations of the carrier at the two faces of the membrane are explicitly involved, the drug concentration in the apical compartment does not influence efflux transport and the entire mass of drug present in the cellular compartment is substrate of the transporter.

5. The total mass of drug in the three compartments is preserved.

According to this model, the following differential equations describe the change of drug concentration or mass as a function of time in the three compartments during permeation in both directions.

$$\frac{dC_{Aab}}{dt} = -P(C_{Aab} - C_{Cab})\frac{S_m}{V_A} + \frac{v_{max}m_{Cab}}{K + m_{Cab}}\frac{1}{V_A} \quad (2)$$

$$\frac{dC_{Bab}}{dt} = P(C_{Cab} - C_{Bab})\frac{S_m}{V_B} \quad (3)$$

$$\frac{dm_{Cab}}{dt} = P(C_{Aab} - C_{Cab})S_m - \frac{v_{max}m_{Cab}}{K + m_{Cab}} - P(C_{Cab} - C_{Bab})S_m \quad (4)$$

$$\frac{dC_{Aba}}{dt} = P(C_{Cba} - C_{Aba})\frac{S_m}{V_A} + \frac{v_{max}m_{Cba}}{K + m_{Cba}}\frac{1}{V_A} \quad (5)$$

$$\frac{dC_{Bba}}{dt} = -P(C_{Bba} - C_{Cba})\frac{S_m}{V_B} \quad (6)$$

$$\frac{dm_{Cba}}{dt} = P(C_{Bba} - C_{Cba})S_m - \frac{v_{max}m_{Cba}}{K + m_{Cba}} - P(C_{Cba} - C_{Aba})S_m \quad (7)$$

where C is concentration, m is mass, the indices A, B, and C (upper case) denote the apical, basal and cellular compartment, respectively, the indices ab and ba (lower case) denote permeation in the apical-to-basal and the basal-to-apical direction, respectively, S_m is the surface area of the monolayer and V is volume of solution in each compartment. A cell monolayer volume of 0.0094 ml was used based on a monolayer thickness of 20 μm.

For high drug concentrations and accordingly large drug mass in the cellular compartment, the validity of the following approximation was tested.

$$\frac{v_{max}m_C}{K + m_C} \approx v_{max} \quad (8)$$

The reduction of the volume of solution in the apical and the basal compartment due to sampling as a function of time was accounted for by the following relations that were determined empirically using regression analysis.

$$V = V(0) - 0.0037189t + 3.68 \times 10^{-6}t^2 + 6.87 \times 10^{-9}t^3 \quad (9)$$

$$V = V(0) - 0.0018594t + 1.84 \times 10^{-6}t^2 + 3.43 \times 10^{-9}t^3 \quad (10)$$

$$V = V(0) - 0.0009297t + 9.2 \times 10^{-7}t^2 + 1.72 \times 10^{-9}t^3 \quad (11)$$

where $V(0)$ is volume at time zero. Eqs. (9)–(11) apply to both compartments and to sampling volumes of 100, 50 and 25 μl, respectively.

3. Results

3.1. Cell toxicity of liposomes

The results of the MTT assay are shown in Figs. 1, 2. For a 2.5 h incubation with liposomal formulations, mitochondrial activity of the cells was reduced to values between 88% and 97% of the control. This reduction was statistically significant (Student's t-test) at $p < 0.05$ for 100 mg/ml phospholipid and at $0.05 < p < 0.1$ for 50 mg/ml phospholipid with 3.75 mg/ml saquinavir. For the 5 h incubation in the 24-well plates, no statistically

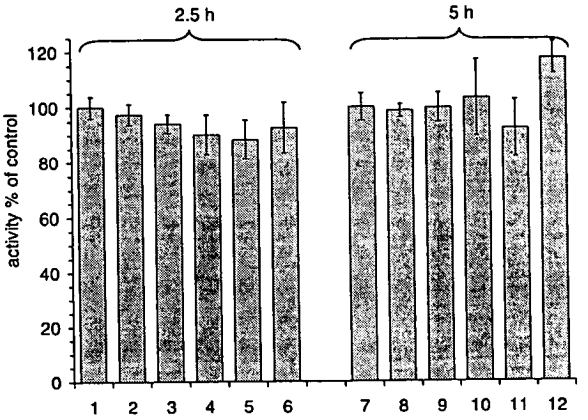

Fig. 1. Mitochondrial dehydrogenase activity of the cells determined by the MTT assay following 2.5 and 5 h incubation with different liposomal formulations in 24-well plates. Results are expressed in percent of control obtained with transport medium and given as mean and standard deviation with $n = 4$. Columns: 1 and 7, transport medium. 2 and 8, phospholipid 150 mg/ml. 3 and 9, phospholipid 100 mg/ml. 4 and 10, phospholipid 50 mg/ml. 5 and 11, phospholipid 50 mg/ml with 3.75 mg/ml saquinavir. 6 and 12, phospholipid 50 mg/ml with 7.5 mg/ml saquinavir.

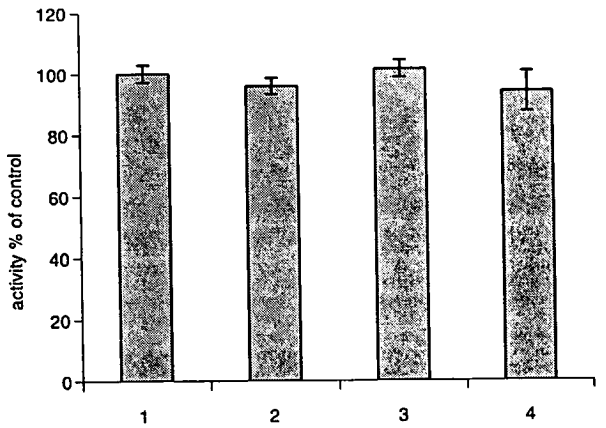

Fig. 2. Mitochondrial dehydrogenase activity of the cells determined by the MTT assay following 5 h incubation with liposomes added either to the apical (column 2) or the basal (column 3) or both compartments (column 4) of Transwell plates. Phospholipid concentration 150 mg/ml. Results are expressed in percent of control obtained with transport medium (column 1) and given as means and standard deviation with $n = 3$.

significant reduction of activity was found except for the 50 mg/ml phospholipid with 7.5 mg/ml saquinavir formulation for which an increase of activity was detected ($p < 0.01$). No positive correlation between phospholipid concentration and reduction of mitochondrial activity in the studied phospholipid concentration range was observed. Also, no effect of the presence of saquinavir was found in this respect. In the Transwell plates, addition of liposomes only to the apical or the basal or to both compartments about the cell monolayer reduced mitochondrial activity to 94% at the most, this reduction of 6% not being statistically significant.

In the LDH assay, no marked increase of lactate dehydrogenase activity was measured in the culture supernatant of the cells after incubation with liposomes with a phospholipid concentration of 50 and 150 mg/ml for 5 h. Cytotoxicity values remained consistently below 1% of the values measured with Triton X-100 as positive control Eq. (1). A maximum value of 0.81% was measured for a phospholipid concentration of 50 mg/ml. The phospholipids did not suppress the LDH enzymatic activity that this assay relies upon and did not negatively interfere with the assay as determined using pure LDH. On the contrary, a roughly 20% increase of activity of the pure LDH in the presence of liposomes was measured as compared to transport medium. A comparable increase was also found in the presence of 1% Triton.

3.2. Cell permeation of drugs from aqueous solutions and liposomal formulations

Measurement of drug permeation in the Caco-2 model was possible with purely aqueous solutions at the employed drug concentrations. Permeation of indinavir through the Caco-2 monolayer in the apical-to-basal direction was rather limited. In the basal-to-apical direction, extensive permeation took place against the concentration gradient after approximately 90 min of the experiment (Fig. 3). For saquinavir, apical-to-basal permeation was even more limited than for indinavir and the basal-to-apical permeation was more extensive, such that the apical concentration exceeded the basal concentration already after approximately 50 min of the experiment in the latter direction of permeation (Fig. 4). The presence of vinblastine in the apical and the basal compartment increased apical-to-basal permeation of indinavir and diminished the extent of its basal-to-apical permeation although the latter remained more pronounced than the former (Fig. 5). The asymmetric transport of both drugs across the Caco-2 cells and the partial reversal of this asymmetry by vinblastine, a known inhibitor of P-glycoprotein and MRP, confirm that the drugs are subject to active apical efflux by these transporters that are present in these cells [14,15].

Indinavir and saquinavir were used in permeation studies as liposomal dispersions at concentrations 10- to 2500-fold higher than those in the purely aqueous solutions. Typical results are shown in Figs. 6 and 7 for indinavir

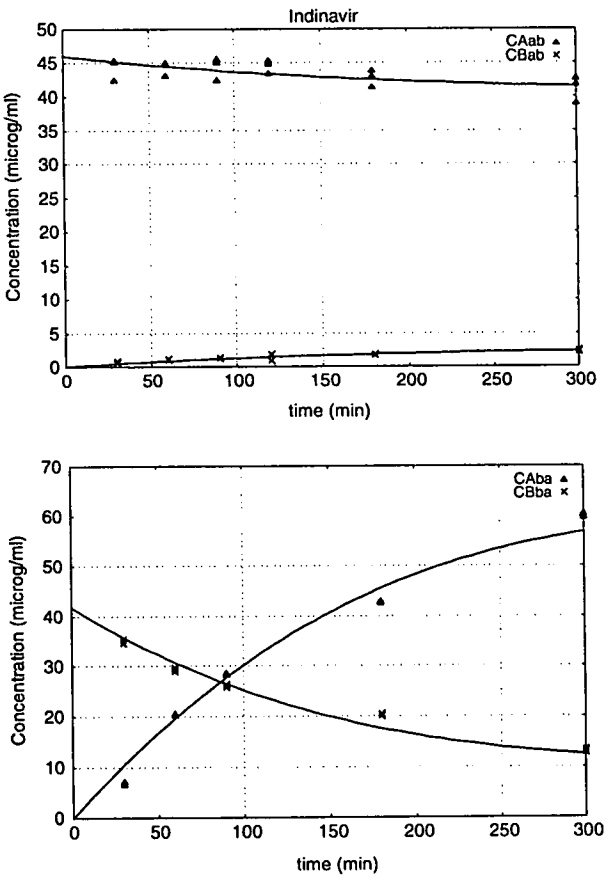

Fig. 3. Permeation of indinavir in Caco-2 cells from purely aqueous solution; experimental points and model-based fitted curves. Upper panel, apical-to-basal direction; lower panel, basal-to-apical direction. (▲) Apical concentration. (×) Basal concentration.

and saquinavir, respectively. In the apical-to-basal direction, percentage of permeation was for both drugs smaller than that observed when the drugs were applied in purely aqueous solution. Basal-to-apical permeation of indinavir was greater than in the opposite direction but it was smaller in relative terms compared to when the drug was applied with no liposomes. Basal-to-apical permeation of saquinavir was diminished by the liposomes to a larger extent than that of indinavir compared to the purely aqueous solution. Thus, formulation of the drugs in a liposomal dispersion appears to profoundly influence their permeation behavior through the Caco-2 monolayer.

3.3. Quantification of passive and carrier mediated transport parameters

Permeation data were analyzed using the theoretical model for the kinetics of cellular transport presented in Section 2. The concentration variables defined by the system of differential Eqs. (2)–(7) were fitted to the experimental concentration data and optimal values of the parameters P, v_{max} and K applicable to the different experimental conditions were deduced. Numerical solution of

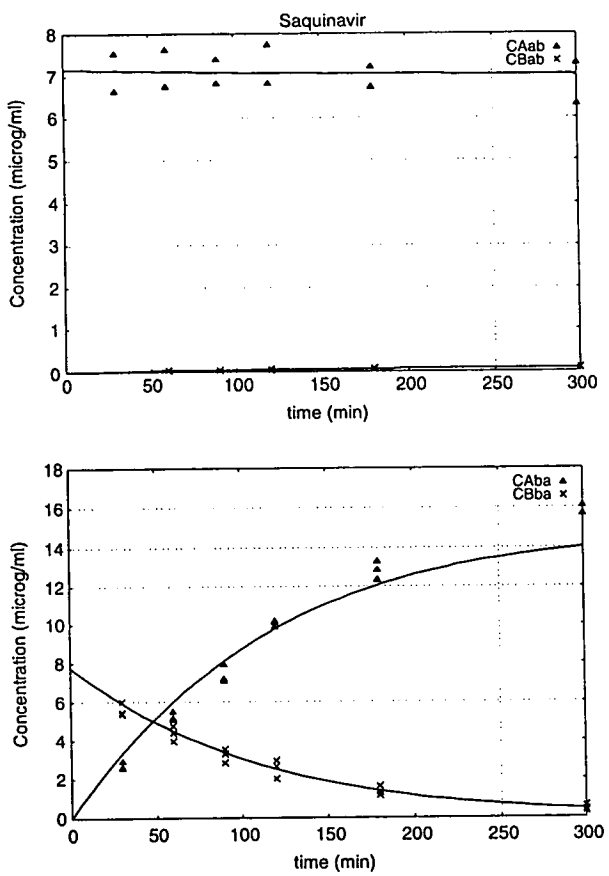

Fig. 4. Permeation of saquinavir in Caco-2 cells from purely aqueous solution; experimental points and model-based fitted curves. Upper panel, apical-to-basal direction; lower panel, basal-to-apical direction. (▲) Apical concentration. (×) Basal concentration.

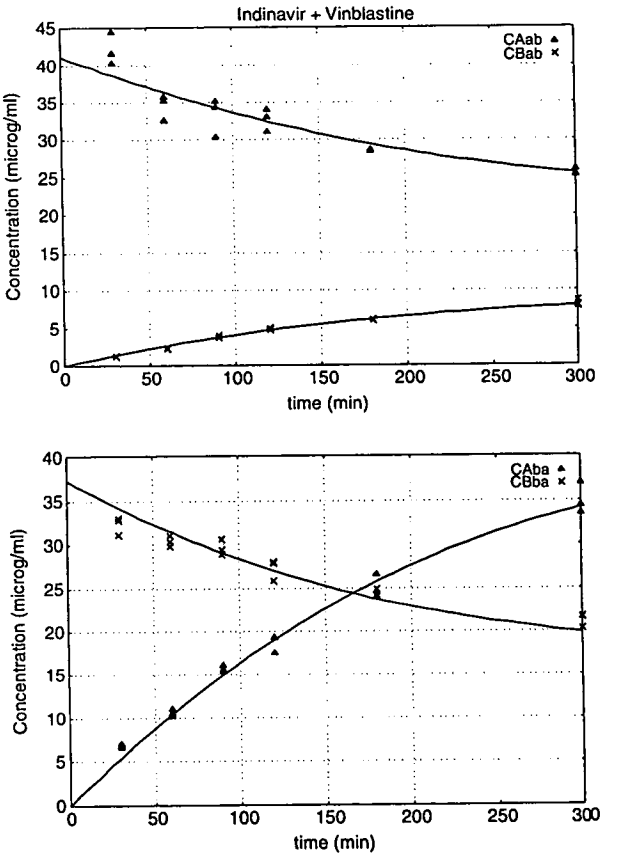

Fig. 5. Permeation of indinavir in Caco-2 cells from purely aqueous solution in the presence of 70 μM vinblastine; experimental points and model-based fitted curves. Upper panel, apical-to-basal direction; lower panel, basal-to-apical direction. (▲) Apical concentration. (×) Basal concentration.

the equations and least squares fit were performed using the software EASY-FIT (Prof. K. Schittkowski, University of Bayreuth, Germany). Concentration data of both compartments obtained from the apical-to-basal and the basal-to-apical direction of permeation were used simultaneously in the fitting. This provided a more stable regression analysis compared to the separate evaluation of each permeation direction. The drawn lines in Figs. 3–7 represent the best fit. This is considered in all cases to be satisfactory.

The estimated transport parameters are given in Table 1. Consistent values of the passive permeability coefficient were always obtained. In the instances typically involving the purely aqueous solutions of the drugs, a high level correlation ($r \approx 1$) between v_{max} and K occurred in the regression analysis (correlation matrices not shown) which meant that these parameters could not be deduced individually from each of these experiments. For indinavir-liposomes, the best fit was obtained when Eq. (8) was substituted into Eqs. (2)–(7) i.e., for a constant transporter mediated efflux rate independent of drug mass in the cellular compartment. This was assumed to represent v_{max}. For the saquinavir-liposomes with high drug concentration, the same value of v_{max} as for the indinavir-liposomes resulted using Eqs. (2)–(7) and the deduced K value had a rather high standard error indicating that this parameter did not significantly influence the goodness of fit. These results of the indinavir-liposomes and the saquinavir-liposomes, hence, were in mutual agreement and suggest that the carrier mediated efflux took place at a constant rate corresponding to a saturation of the carrier probably because of the high drug concentration of these formulations. Therefore, in all experiments involving no liposomes, the value of v_{max} deduced from the liposome formulations was introduced in the calculation and kept constant. This allowed the parameter K to be estimated also in these situations where otherwise a correlation between v_{max} and K occurred. Only in the studies with saquinavir liposomes and low drug concentration in which the experimental data were close to the detection limit and thus rather variable, a reliable estimation of K or v_{max} was not possible. The deduced parameter values given in Table 1 were overall consistent as evidenced by the small standard error and the absence of correlation between them.

The drug concentrations at time zero, $C(0)_A$ and $C(0)_B$, obtained from the best fit were smaller than the theoretical

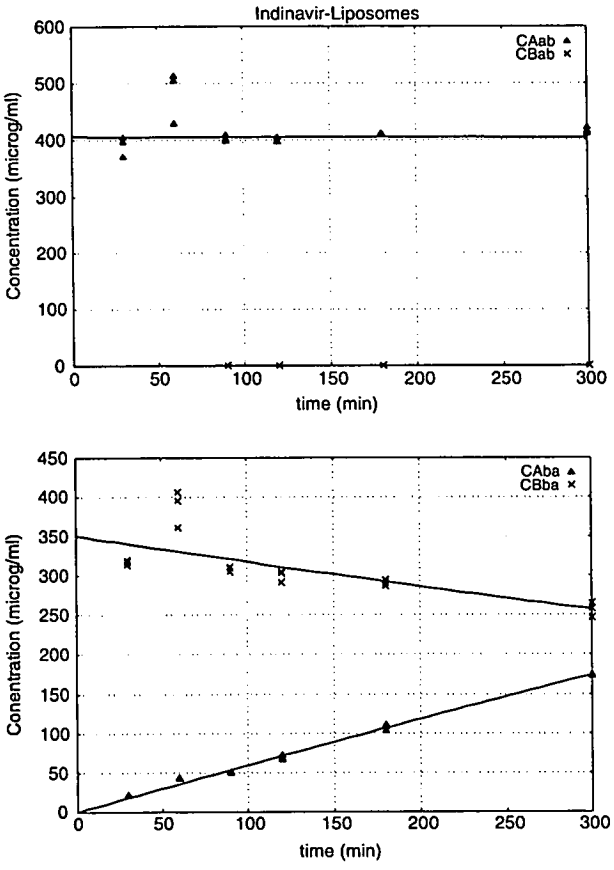

Fig. 6. Permeation of indinavir in Caco-2 cells from a liposomal formulation with 50 mg/ml lipid; experimental points and model-based fitted curves. Upper panel, apical-to-basal direction; lower panel, basal-to-apical direction. (▲) Apical concentration. (×) Basal concentration.

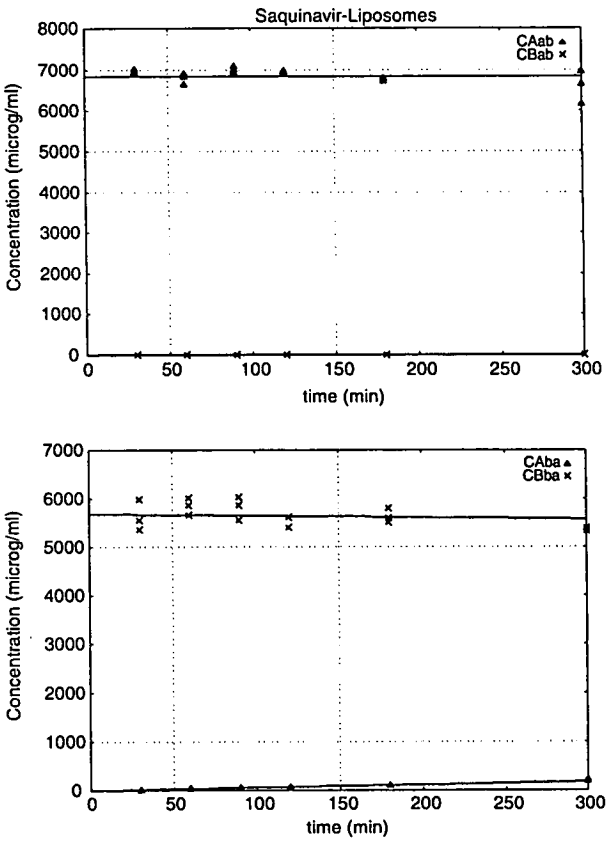

Fig. 7. Permeation of saquinavir in Caco-2 cells from a liposomal formulation with 50 mg/ml lipid; experimental points and model-based fitted curves. Upper panel, apical-to-basal direction; lower panel, basal-to-apical direction. (▲) Apical concentration. (×) Basal concentration.

concentrations of the prepared aqueous solutions and the liposomal formulations (given in Section 2). This was because of some loss of drug firstly during preparation, which was confirmed by measuring the drug concentration of the ready-to-use preparations, and secondly at the onset of the transport experiment possibly because of an initial adsorption of the drug to the plastic container walls of the Transwell plates. Time dependent mass balance demonstrated that total drug mass was constant after the first sampling point of 30 min. Therefore, the estimation of kinetic parameters was not affected by this initial decrease of drug content of the preparations. No relevant metabolism of the drugs was evident in the Caco-2 cells. For saquinavir, which is metabolized predominantly by hydroxylation [28], a signal at m/z 687 corresponding to the hydroxylate was detectable at early retention times that amounted however to less than 2% of the parent compound. Fragments of the parent compound in the MS with very small abundances were detected at m/z 570, 433, and 242. Indinavir reportedly is less metabolized than saquinavir [28].

Passive membrane permeability and carrier mediated transport expressed by P and v_{max} and K, respectively, were thus separately assessed and were found to depend on the drug in use and on whether it was formulated as a liposomal dispersion. Drug mass in the cellular compartment obtained from model simulation was comparable for both permeation directions and differed greatly between the groups as discussed below. The calculated mass values were of the same order of magnitude as experimental values found by extracting the cell monolayer. The deduced kinetic parameters of apical efflux are global in the sense that they do not differentiate between different transporters that may be involved. This is sufficient for the delineation of the contributions of passive and carrier mediated transport processes which was the objective of the present work. Distinguishing between parameters for individual transporters in the employed Caco-2 experimental model entails the availability and use of high specificity, high affinity inhibitors for the transporters, a task that can currently not be resolved.

4. Discussion

4.1. Cell toxicity of liposomes

The possibility of adverse effects elicited by the liposome formulations on cultured Caco-2 cell monolayers was evaluated by determining the mitochondrial dehydrogenase

Table 1
Kinetic parameters of transport of drugs in the Caco-2 cell monolayer[a]

Composition	$C(0)_A$ (μg/ml)	$C(0)_B$ (μg/ml)	$P \times 10^5$ (cm/s)	v_{max} (μg/s)	K (μg)
Indinavir	45.9 (1.1)	41.5 (0.87)	5.19 (0.23)	0.0175[c]	0.022 (0.0031)
		8.47 (0.17)[b]	5.45 (0.22)	[d]	[d]
Indinavir + vinblastine	41.2 (0.45)	37.4 (0.39)	4.1 (0.078)	0.0175[c]	0.489 (0.025)
Saquinavir	7.17 (0.2)	7.79 (0.17)	8.97 (0.34)	0.0175[c]	0.0034 (0.00025)
	2.24 (0.05)	2.08 (0.035)	8.83 (0.29)	0.0175[c]	0.012 (0.00066)
Indinavir-liposomes	405 (19.4)	351 (13.8)	0.933 (0.057)	0.0175 (0.00098)	
Saquinavir-liposomes	6839 (8.38)	5684 (5.43)	0.0587 (0.0016)	0.0175 (0.00098)	0.068 (0.098)
	1933 (143)	1587 (118)	0.041 (0.004)	[d]	[d]

[a] Estimated parameters from regression analysis; numbers in parenthesis are standard error of estimates. Transport experiments in apical-to-basal and basal-to-apical direction except where otherwise noted.
[b] Experiment only in the basal-to-apical direction.
[c] Set value (not adjustable).
[d] No estimation possible due to data variability and correlation between parameters.

activity and the plasma membrane integrity of the cells. The former was assessed using the MTT assay and the latter using the LDH assay. These are both established methods addressing different aspects of cell functionality and are widely used as general criteria of cytotoxicity. While the MTT assay detects specifically mitochondrial metabolic activity and ability of the cells for proliferation, the LDH assay detects leakage of cytosolic lactate dehydrogenase out of the cells indicating cell membrane dysfunction. The employed liposome formulations had overall no significant cytotoxic effect on the cells and caused no perturbation of the cell membrane. The latter is especially relevant in the present study which is dealing with drug permeation across the cells. The statistically significant effects observed in a few instances in the MTT assay in the 24-well plates were not consistent between the two incubation times or within the series of applied phospholipid concentrations and were not confirmed in the Transwell plates. Hence, they do not appear to be systematic. The test in the Transwell plates corresponds exactly to the experimental setup used in the permeation studies.

The results presented, therefore, provide strong indication that the liposomes composed of phosphatidylcholine and phosphatidylglycerol may be considered safe with respect to the employed assays for use in drug permeation studies with Caco-2 cell cultures up to concentrations of 150 mg phospholipid per ml. This finding is even more striking in view of the very small molar ratio of cell membrane lipid to liposome lipid used here that was of the order of 1:100,000. This ratio can be derived from the assumption that the 4.7 cm^2 surface area is a monolayer of phospholipids, a surface area per phospholipid molecule of 67 $Å^2$ [27], the concentration of employed liposomal phospholipid of 50 mg/ml and the apical donor compartment volume of 1.6 ml. Reports about interaction of the MTT assay with high concentrations of some P-glycoprotein and MRP substrates leading to false cell viability values exceeding 100% [29] were not confirmed in this study for the phospholipids. A masking of cytotoxicity of the phospholipids by such an interaction is further refuted by the result of the LDH assay.

No toxicity data of liposomes with the present phospholipid composition and concentration for Caco-2 cells were previously available. Reports on the intravenous in vivo toxicity of liposomes with different compositions including those with cationic lipids used for cell transfection are not relevant in the context of the present study. As a consequence of the safe use of high phospholipid concentrations in the Caco-2 experimental setting, the concentration of lipophilic drugs may, dependent on their maximal solubility in the liposomal membrane, be manifold higher than when the drugs are solubilized with detergents or solvents [7,9]. This in turn may facilitate the performance of permeation experiments.

4.2. Cell permeation kinetics

The model-based evaluation of the experimental results of this study shows that the developed model for describing the kinetics of permeation in the Caco-2 cell monolayer makes it possible to distinguish in a quantitative fashion between the contribution of passive permeation and carrier mediated efflux to drug transport in this system.

The passive permeability coefficient of saquinavir was greater than that of indinavir in the purely aqueous drug solutions (Table 1), this trend being consistent with the lipophilicity of the compounds in terms of octanol/water partition coefficient that was higher for the former ($\log K_{o/w} = 4.1$) compared to the latter ($\log K_{o/w} = 2.9$) [14]. In this respect it should be realized that both compounds existed mostly in the unprotonated form at the physiological pH of 7.4 (pK_a 6.9 and 5.7, respectively). This result is also in agreement with the greater solubility in the liposomal membrane found for saquinavir, i.e., 1/6.7 drug to lipid mass ratio, compared to indinavir, i.e., 1/100 drug to lipid mass ratio. The passive permeability coefficient of both indinavir and saquinavir did not depend on the employed concentration of either drug. This is in agreement with diffusion theory and validates the model.

Apical efflux for the purely aqueous drug solutions was stronger for saquinavir than for indinavir as evidenced by

the smaller K value of the former compared to the latter. From this, a higher affinity of saquinavir for the efflux transporters P-glycoprotein and/or MRP may be inferred. This reflects the more limited apical-to basal permeation and the more extensive basal-to-apical permeation observed for saquinavir compared to indinavir (Figs. 3, 4). The drug mass in the cellular compartment yielded by the model-based simulation was 0.02–0.07 μg and 0.0008 to 0.0018 μg for indinavir and saquinavir, respectively. The smaller cellular accumulation of saquinavir compared to indinavir is in line with the stronger apical efflux of the former compound. Hence, the different propensity of the two drugs to be apically effluxed can be quantitatively assessed with the present analysis. The mass of both drugs in the cellular compartment was not negligible compared to the respective values of the parameter K indicating that in the used concentration range saturable efflux kinetics applied. In this analysis, the value of v_{max} obtained from the liposome formulations of the drugs was used (see Section 3). As discussed below, the presence of phospholipids was not expected to alter the v_{max} of the drugs. The value of v_{max} was assumed to be the same for both drugs because equal values of this parameter were determined from the fitting of the data of the liposome formulations. This assumption is supported by the fact that these drugs are known to be both substrates of the same efflux transporters [14,15].

The presence of vinblastine in the media caused an increase of K of indinavir by more than 10-fold (Table 1). In these experiments, vinblastine was added at equal concentrations to both the apical and the basal solution. In the course of the experiment, vinblastine concentration increased in the apical and decreased in the basal solution (Fig. 8), evidencing transport against a concentration gradient which is consistent with active apical efflux. This demonstrates that vinblastine itself is a substrate of efflux transporters. Therefore, the established inhibitory action of this compound on P-glycoprotein and MRP may be assumed to take place by a competitive mechanism whereas the extent of inhibition likely depends on the comparative affinity of the compounds in question for the carrier. A competitive inhibition of indinavir efflux by vinblastine is perfectly consistent with the deduced increase of the value of the K parameter of indinavir. The value of v_{max} was assumed not to be influenced by the presence of vinblastine in line with a mechanism of competitive inhibition. The model-simulated drug mass in the cells was increased to 0.1–0.15 μg (compared to indinavir being used alone, see above) suggesting that inhibition of apical efflux resulted in an accumulation of the drug in the cells.

The presence of indinavir in the apical or the basal compartment did not seem to influence the magnitude of apical efflux of vinblastine (Fig. 8). This result in combination with the finding that the cellular content of indinavir is roughly comparable for the two directions of permeation of the drug is supportive of the inherent assumption of the presented model that performance of apical efflux does not depend on the side of the cell membrane on which the compound is originally added. The presence of vinblastine caused a rather small reduction of the passive permeability of indinavir. This result could not be anticipated on theoretical grounds and, being marginal in magnitude, cannot be further discussed unless rigorously reproduced.

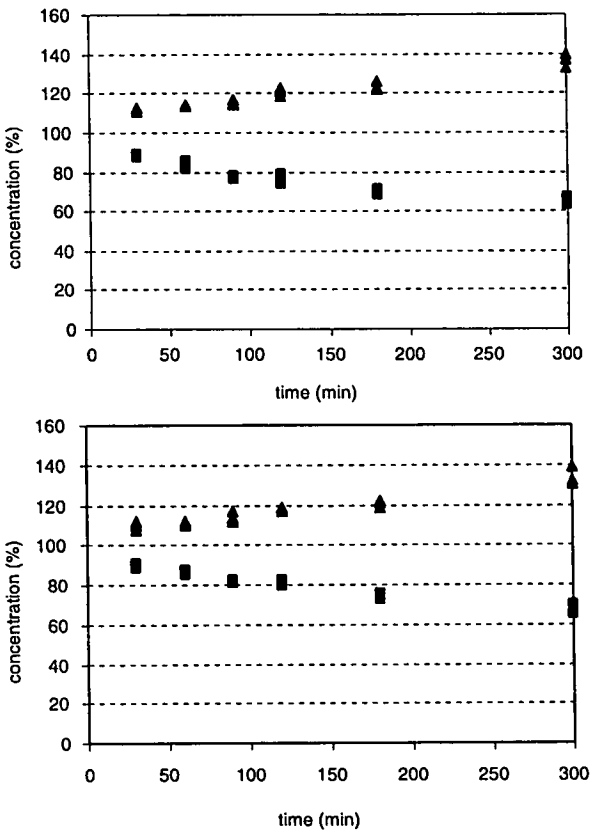

Fig. 8. Transport of vinblastine in Caco-2 cells in the presence of 50 μg/ml indinavir. Upper panel, indinavir added to the apical solution; lower panel, indinavir added to the basal solution Concentration expressed in % of the concentration at time zero. (▲) Apical concentration. (■) Basal concentration.

Concluding this section it is pointed out that the present theoretical analysis provides congruent results for the passive membrane permeability and the apical efflux transport of the used drugs and of the effect of the efflux inhibitor on these parameters; therefore, this analysis is proposed as a tool for independently determining the contribution of the individual transport processes to the over-all cellular permeation.

4.3. Effect of liposomes

The drug concentration of the liposomal formulations was much greater than the concentration used in the purely aqueous solutions that approached solubility level, demonstrating that liposomes can be effectively used as vehicles for solubilizing these drugs in water. A maximal drug-to-lipid mass ratio of 1/100 for indinavir and 1/6.7 for saquinavir provided stable liposomal formulations

for the duration of the experiment. Photon correlation spectroscopy measurements showed no change of particle size during the incubation of these liposomes in the assay medium at 37 °C for at least 8 hours. Higher ratios gave rise to crystallization/precipitation of the drugs. Evidently, saquinavir is more effectively solubilized by liposomes than indinavir. These results imply that liposomal solubilization may facilitate the handling of drugs with an aqueous solubility <1 ppm in in vitro experiments.

The localization of drug inside the liposome, although not studied in detail, may be indirectly proven by the increase of the apparent solubility of the compounds in the aqueous liposomal dispersion compared to their purely aqueous solubility. Since under these conditions, the liposomes are the only lipid reservoir for the drugs preventing their precipitation, it can be assumed that the lipophilic drugs (as indicated by their $\log K_{o/w}$ values of 4.1 and 2.9 for saquinavir and indinavir, respectively) are associated with the lipophilic domain of the liposomal membrane.

Passive permeability coefficients obtained with the liposomal formulations of indinavir and saquinavir were considerably diminished compared to the ones for the purely aqueous solutions (Table 1). This result may be interpreted in terms of a reduced availability of the drug for passive permeation through the cell membrane because of its incorporation in the liposomes that would be related to the large excess of liposomal lipid versus cell membrane lipid (molar ratio of the order of 100,000:1, see above). Mechanistically, the permeation rate of the drug will depend on the mode of interaction of the liposomes with the cells. This may occur in various ways [32]: (1) collision and possibly adsorption of the liposome and extracellular release of its contents and subsequent transport of these contents into the cells; (2) collision and possibly adsorption of the liposome followed by selective transfer of lipophilic compounds from the liposomal bilayer directly to the plasma membrane; (3) endocytotic internalization of the liposomes followed by intracellular release of its content; (4) fusion of the liposomal membrane with the plasma membrane or, intracellularly with the endosomal membrane and thereby release of the liposomal contents in the cytoplasm. For lipophilic compounds associated with the liposomes, the selective inter-membrane transfer described above may be a very important way of interaction. This transfer of the drug from the liposomal to the cell plasma membrane could be rate determining and depend on the comparative interaction of the drug with the lipid pool of the cell monolayer and that of the liposomes. Alternatively, the permeation of these lipophilic drugs may be defined by the equilibrium of the drug between liposomal lipid domain and water phase, whereas the concentration in the water phase is determining for permeation [22]. Both alternatives conceivably give rise to the diminished passive permeability coefficients. In order to understand the complex underlying mechanisms, detailed studies of passive cell membrane permeation of liposomally solubilized drugs involving the equilibria of solubilization are underway in this laboratory.

With respect to drug delivery, the product $C(0)_A \cdot P$ providing the initial passive flux of drug across the membrane is relevant. For this product, using the highest concentrations given in Table 1, one obtains 2.38×10^{-3} μg/cm^2/s for indinavir in purely aqueous solution as compared to 3.78×10^{-3} μg/cm^2/s for indinavir liposomes and 0.641×10^{-3} μg/cm^2/s for saquinavir in purely aqueous solution compared to 4.01×10^{-3} μg/cm^2/s for saquinavir liposomes. $C(0)_B \cdot P$ yields an analogous picture. Since the used concentrations are nearly the highest attainable in the respective formulations, the results of this calculation are comparable to each other in terms of absolute effectiveness of delivery. This calculation demonstrates that passive delivery of the drugs would be more efficient with the liposomes than the purely aqueous solution, this difference being far more evident for saquinavir than indinavir. The use of liposomes in Caco-2 cell cultures to solubilize a lipophilic immunomodulator drug, PSC 833, also demonstrated that, when encapsulated in liposomes the PSC 833 exhibited a stronger interaction with the cells than when the compound was dispersed in the media [31].

The findings of this study point to the possible pharmaceutical relevance of investigating the permeation in the Caco-2 cell model of formulated lipophilic drugs instead of unformulated drugs. Besides achieving high enough drug concentrations to allow detection in the in vitro test, formulations may change the rate of passive drug absorption. The relevance of this finding is underscored by the need of delivery systems to achieve sufficiently high blood levels of lipophilic drugs by peroral administration, and, perhaps more importantly, by the fact that most lipophilic drugs are solubilized in vivo in mixed micelles of phospholipids and bile salts. Thus, even if liposomes are altered after peroral administration, drug solubilization in colloidal dispersion systems may still take place in the intestine. The presence of micellar systems and phospholipids reportedly influences intestinal absorption of lipophilic drugs [26,30]. As a result of solubilization in lipids, the lipophilic drugs may be shifted in the biopharmaceutic classification system from a low to a high solubility class [23]. In agreement with the argumentation in reference [23], this study shows also that, because of formulation effects or possible in vivo relevant interaction with phospholipids, the drugs may be shifted to another class of the BCS with a higher solubility and another permeation rate. A system that perfectly simulates the intestinal juice remains, of course, difficult to ascertain. Liposome dispersions represent a safe, high capacity solubilization vehicle for studying the absorption of lipophilic drugs in the Caco-2 model.

The apical efflux rate of indinavir-liposomes and saquinavir-liposomes reached a constant value corresponding to v_{max} (Table 1). This value was the same for the liposome formulations of both drugs, this being consistent with the fact that these drugs have been shown to be substrates of the same efflux transporters [14,15]. The deduced value of $v_{max} = 0.0175$ μg/s or 3.72×10^{-3} μg/cm^2/s is strikingly similar to the initial passive influx of

drug in the cells for both liposomal formulations given by $C(0)_A \cdot P$ (see above). This confirms that with the liposomal formulations the maximum value of efflux rate was reached because of saturation of the transporters due to the high drug concentration of these formulations. This is also corroborated by the drug mass in the cellular compartment that was found by the model simulation to be larger for the indinavir-liposomes (0.025–0.15 μg) and especially the saquinavir-liposomes (0.5–3 μg) compared to the respective purely aqueous drug solutions.

Phospholipids have been previously reported to be substrates of P-glycoprotein and possibly inhibit P-glycoprotein transport of other compounds [24,25]. This inhibition was discussed to be of competitive mode. Based on this, no effect of the phospholipids on the v_{max} of drugs should be expected. An effect of phospholipids on the value of parameter K could not be assessed from the present data because it was not possible to deduce this parameter for the liposomal formulations of the drugs as a result of saturation of the transporters at the employed drug concentrations.

Liposomal formulations, therefore, appear to influence passive permeation and carrier mediated efflux rate of the two drugs. The effect of the liposomes on apical efflux appears to consist in eliciting a maximal efflux rate of the drugs corresponding to transporter saturation due to the high drug concentrations, while their effect on passive permeation seems to be related to the readiness of transfer of the drug from the liposomal to the cellular phospholipid bilayer membrane. Fig. 9 shows the experimental basal concentrations of the drugs formulated with and without liposomes permeating in the apical-to-basal direction. For saquinavir, the basal concentration with liposomes was much greater than those without liposomes while for indinavir the opposite is true, albeit far less pronounced. The much more effective transcellular delivery of saquinavir, in absolute terms, from the liposomal formulation is because of the overwhelmingly more effective passive delivery of this drug discussed above. For indinavir, on the other hand, the slight advantage of the liposomal formulation in terms of passive delivery is offset by the maximal efflux rate attained at saturation.

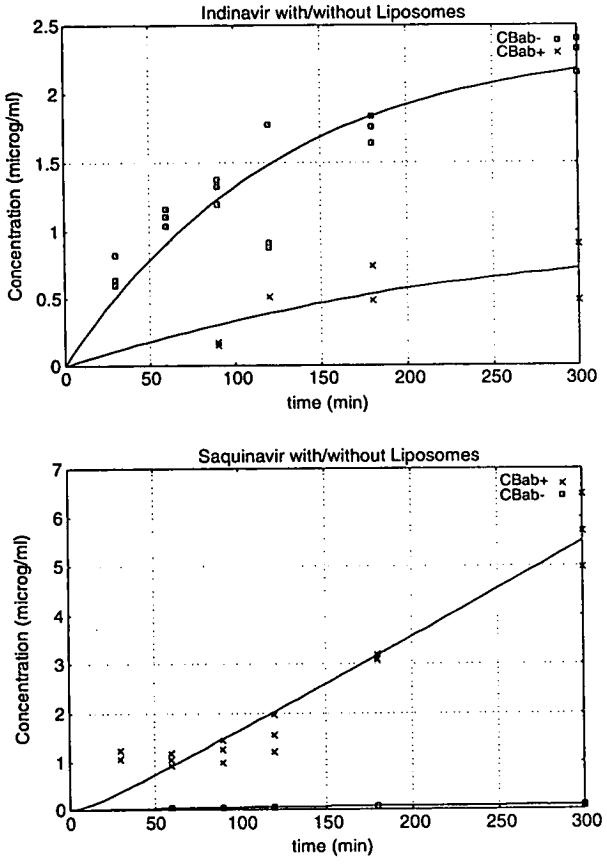

Fig. 9. Basal concentration of indinavir (upper panel) and saquinavir (lower panel) for apical-to-basal permeation in Caco-2 cells; experimental points and model-based fitted curves. (■) Purely aqueous drug solution. (×) Liposomal formulation with 50 mg/ml lipid.

In conclusion, whereas liposomes can be effectively used as solubilizers of these drugs increasing their concentration in solution many fold without exhibiting cell toxicity, their impact on drug delivery depends on the combination of their influence on passive and active cellular transport processes and may vary with the drug in use. Furthermore, purely aqueous solutions and formulations of lipophilic drugs may reveal different absorption behavior of the drugs pointing to the possible relevance of performing Caco-2 cell studies with formulated drugs. A quantitative analysis of the contributing factors is shown to be indispensable for a mechanistic understanding of the final outcome of absorption and can be accomplished using the methodology based on mathematical modeling proposed in this report.

Acknowledgements

We thank F. Hoffmann-La Roche, Ltd, Basel for generous supply of saquinavir and Prof. D. Gygax of the School of Life Sciences, Swiss Northwestern University of Applied Sciences for the gift of indinavir and technical support.

References

[1] G.L. Amidon, H. Lennernäs, V.P. Shah, J.R. Crison, A theoretical basis for a biopharmaceutic drug classification: the correlation of in vitro drug product dissolution and in vivo bioavailability, Pharm. Res. 12 (1995) 413–420.

[2] M.N. Martinez, G.L. Amidon, A mechanistic approach to understanding the factors affecting drug absorption: a review of fundamentals, J. Clin. Pharmacol. 42 (2002) 620–643.

[3] M. Kansy, F. Senner, K. Gubernator, Physicochemical high throughput screening: parallel artificial membrane permeation assay in the description of passive absorption process, J. Med. Chem. 41 (1998) 1007–1010.

[4] I.J. Hidalgo, T.J. Raub, R.T. Borchardt, Characterization of human colon carcinoma cell line (Caco-2) as a model system for intestinal epithelial permeability, Gastroenterology 96 (1989) 736–749.

[5] P. Artursson, K. Palm, K. Luthman, Caco-2 monolayers in experimental and theoretical predictions of drug transport, Adv. Drug Deliv. Rev. 46 (2001) 27–43.
[6] P. Artursson, Cell cultures as models for drug absorption across the intestinal mucosa, Crit. Rev. Ther. Drug Carrier Syst. 8 (1991) 305–350.
[7] B.J. Aungst, N.H. Nguyen, J.P. Bulgarelli, K. Oates-Lenz, The influence of donor and reservoir additives on Caco-2 permeability and secretory transport of HIV inhibitors and other lipophilic compounds, Pharm. Res. 17 (2000) 1175–1180.
[8] R.B. Shah, A. Palamakula, M.A. Khan, Cytotoxicity evaluation of enzyme inhibitors and absorption enhancers in Caco-2 cells for oral delivery of salmon calcitonin, J. Pharm.Sci. 93 (2004) 1070–1078.
[9] F.M. Ingels, P.F. Augustijns, Biological, pharmaceutical and analytical considerations with respect to the transport media used in the absorption screening system Caco-2, J. Pharm. Sci. 92 (2003) 1545–1558.
[10] B.J. Aungst, Intestinal permeation enhancers, J. Pharm. Sci. 89 (2000) 429–442.
[11] M. Lindenberg, S. Kopp, J.B. Dressman, Classification of orally administered drugs on the World Health Organization model list of essential medicines according to the biopharmaceutics classification system, Eur. J. Pharm. Biopharm. 58 (2004) 265–278.
[12] P. van Hoogevest, B. de Kruijff, Effect of amphotericin B on cholesterol-containing liposomes of egg phosphatidylcholine and didocosenoyl-phosphatidylcholine. A refinement of the model for the formation of pores by amphotericin B in membranes, Biochim. Biophys. Acta 511 (1978) 397–407.
[13] A. Fahr, M. Holz, G. Fricker, Liposomal formulations of cyclosporin A: influence of lipid type and dose on pharmacokinetics, Pharm. Res. 12 (1995) 1189–1198.
[14] G.C. Williams, P.J. Sinko, Oral absorption of the HIV protease inhibitors: a current update, Adv. Drug Deliv. Rev. 39 (1999) 211–238.
[15] L.M.S. Chan, S. Lowes, B.H. Hirst, The ABCs of drug transport in intestine and liver: efflux proteins limiting drug absorption and bioavailability, Eur. J. Pharm. Sci. 21 (2004) 25–51.
[16] B.J. Aungst, P-glycoprotein, secretory transport, and other barriers to the oral delivery of anti-HIV drugs, Adv. Drug Deliv. Rev. 39 (1999) 105–116.
[17] A.E. Kim, J.M. Dintaman, D.S. Waddell, J.A. Silverman, Saquinavir, an HIV protease inhibitor, is transported by P-glycoprotein, J. Pharmacol. Exp. Ther. 286 (1998) 1439–1445.
[18] C.G. Lee, M.M. Gottesman, C.O. Cardarelli, M. Ramachandra, K.T. Jeang, S.V. Ambudkar, S. Dey, HIV-1 protease inhibitors are substrates for the MDR1 multidrug transporter, Biochemistry 37 (1998) 3594–3601.
[19] I.J. Hidalgo, J. Li, Carrier-mediated transport and efflux mechanisms in Caco-2 cells, Adv. Drug Deliv. Rev. 22 (1996) 53–66.
[20] H. Gutmann, G. Fricker, M. Török, S. Michael, C. Beglinger, J. Drewe, Evidence for different ABC-transporters in Caco-2 cells modulating drug uptake, Pharm. Res. 16 (1999) 402–407.
[21] J. Hunter, B.H. Hirst, Intestinal secretion of drugs. The role of P-glycoprotein and related drug efflux systems in limiting oral drug absorption, Adv. Drug Deliv. Rev. 25 (1997) 129–157.
[22] A. Fahr, P. van Hoogevest, S. May, N. Bergstrand, M.L.S. Leigh, Transfer of lipophilic drugs between liposomal membranes and biological interfaces: consequences for drug delivery, Eur. J. Pharm. Sci. 26 (2005) 251–265.
[23] C.J.H. Porter, W.N. Charman, In vitro assessment of oral lipid based formulations, Adv. Drug Deliv. Rev. 50 (2001) 127–147.
[24] Y.-L. Lo, Phospholipids as multidrug resistance modulators of the transport of epirubicin in human intestinal epithelial Caco-2 cell layers and everted gut sacs of rats, Biochem. Pharmacol. 60 (2000) 1381–1390.
[25] I. Bosch, K. Dunussi-Jannopoulos, R.-L. Wu, S.T. Furlong, J. Croop, Phosphatidylcholine and phosphatidylethanolamine behave as substrates of the human MDR1 P-glycoprotein, Biochemistry 36 (1997) 5685–5694.
[26] T. Sugawara, M. Kushiro, H. Zhang, E. Nara, H. Ono, A. Nagao, Lysophosphatidylcholine enhances carotenoid uptake from mixed micelles by Caco-2 human intestinal cells, J. Nutr. 131 (2001) 2921–2927.
[27] R.A. Demel, L.L.M. van Deenen, B.A. Pethica, Monolayer interactions of phospholipids and cholesterol, Biochim. Biophys. Acta 135 (1967) 11–19.
[28] M.E. Fitzsimmons, J.M. Collins, Selective biotransformation of the human immunodeficiency virus protease inhibitor saquinavir by human small intestinal cytochrome P4503A4, Drug Metab. Dispos. 25 (1997) 256–266.
[29] K.-S. Vellonen, P. Honkakoski, A. Urtti, Substrates and inhibitors of efflux proteins interfere with the MTT assay in cells and may lead to underestimation of drug toxicity, Eur. J. Pharm. Sci. 23 (2004) 181–188.
[30] M.O. Reynier, H. Lafont, C. Crotte, P. Sauve, A. Gerolami, Intestinal cholesterol uptake: comparison between mixed micelles containing lecithin or lysolecithin, Lipids 20 (1985) 145–150.
[31] Y. Lo, F. Liu, J. Cherng, Effect of PSC 833 liposomes and intralipid on the transport of epirubicin in Caco-2 cells and rat intestines, J. Control. Release 76 (2001) 1–10.
[32] V.P. Torchilin, V. Weissig, in: Liposomes, a Practical Approach, second ed., Oxford University Press, Oxford, 2003, p. 268.

In Vivo Drug Metabolism Model for Human Cytochrome P450 Enzyme Using Chimeric Mice with Humanized Liver

MIKI KATOH,[1] TOSHIRO SAWADA,[1] YOSHINORI SOENO,[2] MIKI NAKAJIMA,[1] CHISE TATENO,[3] KATSUTOSHI YOSHIZATO,[3,4] TSUYOSHI YOKOI[1]

[1]Division of Pharmaceutical Sciences, Graduate School of Medical Science, Kanazawa University, Kanazawa 920-1192, Japan

[2]PhoenixBio Co. Ltd., Hiroshima, Japan

[3]Hiroshima Prefectural Institute of Industrial Science and Technology, Cooperative Link of Unique Science and Technology for Economy Revitalization, Hiroshima, Japan

[4]Graduate School of Science, Hiroshima University, Hiroshima, Japan

Received 20 June 2006; revised 12 August 2006; accepted 24 August 2006

Published online in Wiley InterScience (www.interscience.wiley.com). DOI 10.1002/jps.20783

ABSTRACT: We previously clarified that major human drug metabolizing enzymes were expressed in a chimeric urokinase-type plasminogen activator $(uPA)^{+/+}$/severe combined immunodeficient (SCID) mouse line established recently, in which the liver could be replaced by more than 80% with human hepatocytes. In the present study, we investigated the *in vivo* drug metabolism of a CYP2D6 substrate, debrisoquin (DB), in chimeric mice with high (High) or low (Low) human albumin (hAlb) concentrations and in control $uPA^{-/-}$/SCID mice. The hAlb in the mouse blood is one of the indices of humanized liver because the chimeric mice produce hAlb. After oral administration of DB at 2.0 mg/kg, the AUC_{0-8} value of a major CYP2D6 metabolite of DB, 4′-hydroxydebrisoquin (4-OH DB), in High was 3.6-fold higher than those of Low and $uPA^{-/-}$/SCID mice. By pre-treatment with a typical CYP2D6 inhibitor, quinidine, the AUC_{0-8} value of 4-OH DB in High was decreased although such values in Low and $uPA^{-/-}$/SCID mice did not change. The *in vitro* kinetic analyses and the K_i values of quinidine on the DB 4′-hydroxylase activity in liver microsomes also supported the humanization of the chimeric mice. In conclusion, the chimeric mice exhibited a humanized profile of drug metabolism and the inhibition of P450. J Pharm Sci 96:428–437, 2007

Keywords: cytochrome P450 2D6; debrisoquin 4′-hydroxylation; pharmacokinetic; inhibition; quinidine; humanization; *in vivo* model

INTRODUCTION

Chimeric mice with humanized liver, which were established using urokinase-type plasminogen activator $(uPA)^{+/+}$/severe combined immunodeficient (SCID) mice by Tateno et al.[1] were previously used by the present authors to clarify the expressions of cytochrome P450 (P450) and phase II enzymes in the livers of the chimeric mice and the *in vivo* induction of P450.[2–5] Chimeric mice with humanized liver can become a useful model for investigating the metabolism of drugs in humans. However, *in vivo* drug metabolism studies in the chimeric mice have not been performed.

P450 plays an important role in the biotransformation of endogenous compounds and xenobiotics including drugs. Approximately 80% of oxidative metabolism can be catalyzed by P450s.[6]

Correspondence to: Tsuyoshi Yokoi, (Telephone/Fax: +81-76-234-4407;
E-mail: TYOKOI@kenroku.kanazawa-u.ac.jp)

Journal of Pharmaceutical Sciences, Vol. 96, 428–437 (2007)

In many cases, hepatic metabolism by P450s is a major determinant of a drug's pharmacokinetics since P450 is predominantly expressed in the liver. One of the most important isoforms, CYP2D6, has been reported to represent approximately 2% of the total P450 content in human livers,[7] but the metabolism of 25% of known drugs may be catalyzed by CYP2D6.[8] The CYP2D6 substrates include antidepressants such as selective serotonin reuptake inhibitors and tricyclic antidepressants, codeine, and some β-adrenergic blocking agents. Such drugs are often prescribed for long periods of time. The inhibition of the CYP2D6 enzyme activity by the selective serotonin reuptake inhibitors could be observed in clinical settings.[9] A typical CYP2D6 inhibitor, quinidine, is a frequently prescribed antiarrhythmic drug. The clinical implications of the inhibition by quinidine of the CYP2D6 enzyme activity are well known.[10] In short, drug interactions caused by the inhibition of CYP2D6 require further clarification.

Many isoforms of the CYP2D subfamily exist in rats and mice.[11] The large interspecies difference in the CYP2D6 enzyme activity may be caused by differences in the expressed isoforms,[11] the expression levels, and substrate specificities.[12] We considered that investigation of the pharmacokinetics of a CYP2D6 substrate using chimeric mice would be of great worth.

In the present study, the *in vivo* and *in vitro* metabolism of a CYP2D6 substrate, debrisoquin (DB), in chimeric mice was investigated. DB was selected due to a typical and well-known CYP2D6 substrate. In humans, urinary recovery of 4-OH DB was higher than that of DB, suggesting that the hepatic metabolism is the important process of DB elimination.[13] Moreover, we determined whether the DB 4′-hydroxylase (DBOH) activity in the chimeric mice was inhibited by typical CYP2D6 inhibitors, quinidine and paroxetine, in *in vivo* and *in vitro* studies.

MATERIALS AND METHODS

Materials

DB sulfate and 4-OH DB were purchased from Sigma-Aldrich (St. Louis, MO). Imipramine hydrochloride and quinidine sulfate were from Wako Pure Chemical Industries (Osaka, Japan). Paroxetine was from Toronto Research Chemicals (Toronto, Canada). Nicotinamide adenine dinucleotide phosphate (oxidized form, $NADP^+$) and glucose-6-phosphate dehydrogenase were from Oriental Yeast (Tokyo, Japan). All other chemicals and solvents were of the highest or analytical grade commercially available.

Generation of the Chimeric Mice with Humanized Liver

The present study was approved by the Ethics Committees of Kanazawa University and the Hiroshima Prefectural Institute of Industrial Science and Technology Ethics Board. The cryopreserved human hepatocytes from a donor (9-month-old Caucasian male) were purchased from In Vitro Technologies (Catonsville, MD). The chimeric mice with humanized liver were generated by the method described previously.[1] The concentration of human albumin (hAlb) in the blood of the chimeric mice and the replacement index (RI, the rate of the replacement from mice to humans) were well correlated.[1] The 11–14-week-old chimeric mice were divided into two groups, high and low hAlb concentration, designated as High (more than 5.0 mg/mL hAlb and 70% of RI) and Low (less than 0.6 mg/mL hAlb and 10% of RI) at 1 day before the administration of DB. The $uPA^{+/+}$/SCID and $uPA^{-/-}$/SCID mice used in the present study were obtained as previously reported.[1] The $uPA^{-/-}$/SCID mice were used as the control.

In Vivo DB Metabolic Study and Inhibition Study

DB was administered orally by gavage at 2.0 mg/kg (Day 1). This was designated as Test I for determining the DB metabolism in mice without inhibitors. Blood samples (100 μL of volume) were collected from eyes at 0, 0.5, 1.0, 2.0, 4.0, 6.0, and 8.0 h after the DB administration, the series of collections was performed. Serum was separated by centrifugation from blood. After 3 days of DB administration (Days 2–4), quinidine (100 mg/kg/day) or paroxetine (30 mg/kg/day) was administered intraperitoneally for 3 days (Days 5–7). On Day 8, DB was administered again orally by gavage at 2.0 mg/kg, and the blood sampling was performed as on Day 1. This was designated as Test II for determining the inhibitory effects of DB metabolism by the pre-treatment with quinidine or paroxetine. Each group consisted of four mice.

Quantification of DB and 4-OH DB by Liquid Chromatography/Tandem Mass Spectrometry

The serum concentrations of DB and 4-OH DB were measured according to the method by Corchero et al.[14] with slight modifications. Briefly, 10 μL of serum supplemented with 400 μL of H_2O were spiked with 40 μL of internal standard (20 nM imipramine), and 780 μL of dichloromethane and 520 μL of isopropanol were added. The mixture was vortexed and centrifuged at 1000 *g* for 10 min. The organic phase was evaporated to dryness under a gentle stream of nitrogen. The residue was dissolved in 30 μL of the mobile phase and a 10 μL portion was injected into a liquid chromatography (LC)/tandem mass system.

The LC system was employed using an HP 1100 system including a binary pump, an automatic sampler, and a column oven (Agilent Technologies, Waldbronn, Germany), which was equipped with a Symmetry Shield C_{18} column (Waters, Tokyo, Japan). The column temperature was 35°C. The mobile phase was 40% acetonitril/0.1% formic acid (v/v). The flow rate was 0.3 mL/min. The LC was connected to a PE Sciex API2000 tandem mass spectrometer (Applied Biosystems, Langen, Germany) operated in the positive electrospray ionization mode. The turbo gas was maintained at 550°C. Nitrogen was used as the nebulizing gas, turbo gas, and curtain gas at 65, 85, and 30 psi, respectively. Parent and/or fragment ions were filtered in the first quadruple and dissociated in the collision cell using nitrogen as the collision gas. The collision energy ranged from 25 to 27 V. Two mass/charge (m/z) ion transitions were recorded in the multiple reaction monitoring mode: m/z 176 and 134 for DB, m/z 192 and 132 for 4-OH DB, m/z 281 and 86 for internal standard. The detection limits of DB and 4-OH DB were 30 nM and 2 nM, respectively.

Pharmacokinetic Analysis

The pharmacokinetic parameters for DB and 4-OH DB were estimated from the serum concentration-time data by a moment analysis (MULTI). The area under the serum concentration time curves from 0 to 8 h (AUC_{0-8}) was obtained using the trapezoidal rule. The apparent oral clearance was calculated from dose/AUT_{0-8}. Statistical analyses were performed with GraphPad Instat computer program (GraphPad Software, San Diego, CA) by Mann–Whitney *U*-test.

Liver Microsomes

For the kinetic analyses and the *in vitro* inhibition study, liver microsomes from High, Low, and the control uPA$^{-/-}$/SCID mice were prepared as described previously[15] and were stored at −80°C until analysis. The chimeric mice used in the *in vitro* study were 13–16 weeks old. The protein concentration was determined using Bradford protein assay reagent (Bio-Rad, Hercules, CA) with bovine gamma globulin as the standard.

Kinetic Analyses of DBOH Activity in Chimeric Mice

DBOH activity was measured as described previously[16] with slight modifications. Briefly, the typical incubation mixtures (total volume of 0.20 mL) consisted of 0.2 mg/mL microsomes in 100 mM potassium phosphate buffer (pH 7.4) containing an NADPH-generating system [0.5 mM nicotinamide adenine dinucleotide phosphate (oxidized form), 5 mM glucose-6-phosphate, 5 mM $MgCl_2$, and 1 U/mL glucose-6-phosphate dehydrogenase] and DB. The concentration of DB ranged from 10 to 600 μM. The reaction was initiated by the addition of the NADPH-generating system and was then incubated for 10 min at 37°C. The reaction was terminated by adding 20 μL of ice-cold 60% perchrolic acid. The product formation was determined using LC with a C_{18} 5-μm analytical column (Mightysil RP-18, Kanto Chemical, Tokyo, Japan). The mobile phase was 12% acetonitrile/20 mM sodium perchlorate and the flow rate was 0.8 mL/min. The eluent was monitored fluorometrically with a noise-base clean Uni-3 (Union, Gunma, Japan). The kinetic parameters were estimated from the fitted curves using a KaleidaGraph computer program (Synergy, Reading, PA) designed for nonlinear regression analysis. The kinetic parameters of each group were averaged from the results of more than eight individual liver microsomes.

In Vitro Inhibition by Quinidine and Mechanism-Based Inactivation by Paroxetine on DB Metabolism

The liver microsomes from High, Low, and control uPA$^{-/-}$/SCID mice were used for the inhibition study. In the inhibition by quinidine, the concentration of DB ranged as follows: High (30–240 μM), Low (50–400 μM), and uPA$^{-/-}$/SCID (75–600 μM), respectively. The concentrations of

 DOI 10.1002/jps

quinidine ranged as follows: High (0–60 nM), Low (0–90 μM), and uPA$^{-/-}$/SCID (0–90 μM), respectively. Because the K_m values and the inhibition potency of quinidine in liver microsomes from High, Low, and the control uPA$^{-/-}$/SCID mice were different in the kinetic analyses or a preliminary study, the concentrations of DB and quinidine were selected to be suitable for calculating the inhibition constants.

In the mechanism-based inactivation by paroxetine, the concentration of DB was 200 μM. Liver microsomes were pre-incubated at 37°C for 5, 10, and 20 min with various concentrations of paroxetine (0–500 nM) in the presence of the NADPH-generating system. After pre-incubation, the DBOH activity at a 200 μM substrate concentration was measured according to the method described above. Kinetic parameters of the inactivation process, k_{inact} and K_i, were calculated as described previously.[17] The kinetic parameters of each group were averaged from the results of more than eight individual liver microsomes. The final concentration of the methanol to dissolve paroxetine in the incubation mixture was <1%. All data were analyzed using the average of duplicate determinations.

Genotyping for *CYP2D6*3*, *CYP2D6*4*, and *CYP2D6*5* Alleles

The *CYP2D6*3*, *CYP2D6*4*, and *CYP2D6*5* alleles have been reported to account for approximately 95% of the alleles of poor metabolizers in Caucasians.[18,19] Genomic DNA from the donor hepatocytes and the livers of the chimeric mice were used for the genotyping of *CYP2D6*3*, *CYP2D6*4*, and *CYP2D6*5* described previously.[20,21]

RESULTS

In Vivo DB Metabolism in Test I

The average DB serum concentrations versus the time curves in High, Low, and uPA$^{-/-}$/SCID mice were determined (Fig. 1). The AUC_{0-8} values of DB among three groups were not statistically different (Table 1). The oral clearance values of DB were 9.6, 10.1, and 6.9 L/h/kg in High, Low, and control uPA$^{-/-}$/SCID mice, respectively. The mean residence time (MRT) of DB was 2.9, 3.4, and 3.9 h in High, Low, and control uPA$^{-/-}$/SCID mice, respectively. The decrease of the serum DB concentration in High seemed to be faster than that of the uPA$^{-/-}$/SCID mice. On the other hand, the AUC_{0-8} value of 4-OH DB in High (887 ± 90 nM · h) was significantly higher by 3.6-fold than those of Low (218 ± 26 nM · h) and uPA$^{-/-}$/SCID mice (279 ± 32 nM · h).

Inhibition of 4-OH DB Formation by Quinidine

The average DB and 4-OH DB concentrations versus the time curves after a 3-day treatment with quinidine in High, Low, and uPA$^{-/-}$/SCID mice are shown in Figure 2. The average AUC_{0-8} value of 4-OH DB in High in Test II (345.0 ± 41.4 nM · h) was 42% of that in Test I (815.0 ± 91.3 nM · h). The AUC_{0-8} value of 4-OH DB was significantly decreased by the pre-treatment with

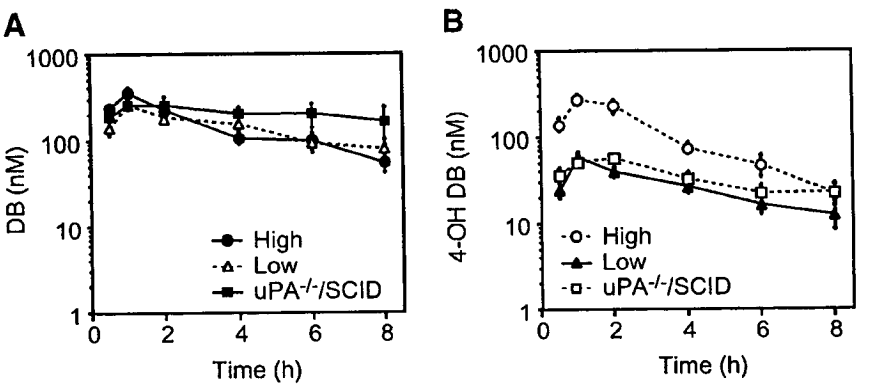

Figure 1. Serum concentrations of DB (A) and 4-OH DB (B) in the chimeric mice and uPA$^{-/-}$/SCID mice in Test I. DB was orally administered at 2.0 mg/kg. Data represent the mean ± SE ($n = 8$). Circle, triangle, and square represent the values of High (>5.0 mg/mL hAlb concentration and >70% of RI), Low (<0.6 mg/mL hAlb concentration and <10% of RI), and uPA$^{-/-}$/SCID mice, respectively.

Table 1. Pharmacokinetic Parameters of DB and 4-OH DB in Chimeric Mice and uPA$^{-/-}$/SCID Mice after Single Oral Administration of DB

	DB			4-OH DB		
Mouse	C_{max} (nM)	T_{max} (h)	AUC_{0-8} (nM · h)	C_{max} (nM)	T_{max} (h)	AUC_{0-8} (nM · h)
High	359.6 ± 37.0	1.00 ± 0.12	1451 ± 153	297.1 ± 37.7***	1.22 ± 0.07*	887 ± 90***
Low	249.2 ± 16.2	1.36 ± 0.13	1456 ± 267	53.3 ± 3.1	1.37 ± 0.14	218 ± 26
uPA$^{-/-}$/SCID	306.4 ± 72.8	1.59 ± 0.28	1693 ± 362	61.4 ± 9.0	1.71 ± 0.19	279 ± 32

Data represent the mean ± SE ($n = 8$).
High, >5.0 mg/mL hAlb concentration (>70% of RI); Low, <0.6 mg/mL hAlb concentration (<10% of RI).
*$P < 0.05$, compared with uPA$^{-/-}$/SCID mice.
***$P < 0.001$, compared with uPA$^{-/-}$/SCID mice.

quinidine (Table 2). The MRT value of 4-OH DB in High in Test II (3.7 h) was longer than that in Test I (2.6 h). However, AUC_{0-8} and MRT values in Low and uPA$^{-/-}$/SCID mice did not change between Test I and Test II. The AUC_{0-8} value of DB tended to increase in High, but the difference was not statistically significant compared to the other groups (data not shown). The MRT value of DB in High in Test II (3.7 h) was longer than that in Test I (3.0 h).

Inhibition of 4-OH DB Formation by Paroxetine

The average DB and 4-OH DB concentrations versus the time curves after 3-day treatment with paroxetine in High, Low, and uPA$^{-/-}$/SCID mice are shown in Figure 3. In all groups, the serum concentrations of 4-OH DB between 0 to 8 h in Test II were decreased as compared with those in Test I. The AUC_{0-8} values of 4-OH DB in all groups decreased by the treatment with paroxetine (data not shown). Only in High was the AUC_{0-8} value of DB in Test II (2971 ± 595 nM · h) statistically higher than that in Test I (1350 ± 225 nM · h, $P < 0.05$).

Kinetic Analysis of DBOH Activity *In Vitro*

The kinetic parameters of DBOH activity in liver microsomes from High, Low, and uPA$^{-/-}$/SCID mice are shown in Table 3. The K_m value of High was 72 ± 8 μM, which was lower than those of Low (145 ± 14 μM) and uPA$^{-/-}$/SCID mice (213 ± 12 μM). The V_{max} value of High was similar to that of Low, but was significantly lower than that of uPA$^{-/-}$/SCID mice. The V_{max}/K_m value of High was significantly higher than those of Low and uPA$^{-/-}$/SCID mice.

Inhibition of DBOH Activity by Quinidine *In Vitro*

The DBOH activity was strongly inhibited by quinidine in liver microsomes from High, but not

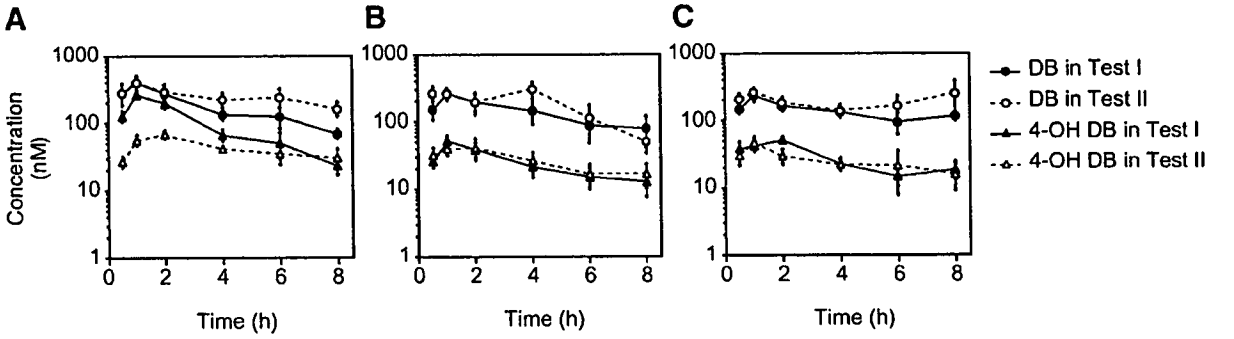

Figure 2. Effect of quinidine treatment on serum concentration of DB and 4-OH DB in High (A), Low (B), and uPA$^{-/-}$/SCID mice (C) in Test II. DB and quinidine were administered as described in Materials and Methods. Data represent the mean ± SE ($n = 4$). High, >5.0 mg/mL hAlb concentration (>70% of RI); Low, <0.6 mg/mL hAlb concentration (<10% of RI).

DOI 10.1002/jps

Table 2. Pharmacokinetic Parameters of 4-OH DB in Chimeric Mice and uPA$^{-/-}$/SCID Mice after 3-Day-Treatment of Quinidine

	4-OH DB		
	C_{max} (nM)	T_{max} (h)	AUC_{0-8} (nM · h)
High			
Test I	293.3 ± 71.7	1.22 ± 0.10	815.0 ± 91.3
Test II	65.2 ± 7.0*	2.03 ± 0.20*	345.0 ± 41.4**
Low			
Test I	52.2 ± 5.5	1.33 ± 0.12	203.4 ± 50.8
Test II	46.5 ± 3.1	0.84 ± 0.29	180.8 ± 47.6
uPA$^{-/-}$/SCID			
Test I	61.0 ± 18.1	1.85 ± 0.36	219.7 ± 28.5
Test II	42.6 ± 6.4	1.14 ± 0.28	196.2 ± 46.0

Data represent the mean ± SE ($n = 4$).
High, >5.0 mg/mL hAlb concentration (>70% of RI); Low, <0.6 mg/mL hAlb concentration (<10% of RI).
Test I, no pre-treatment; Test II, pre-treatment with quinidine.
*$P < 0.05$, compared with those in Test I.
**$P < 0.01$, compared with those in Test I.

in those from Low and uPA$^{-/-}$/SCID mice. The K_i value of quinidine for DBOH activity in High was much lower than those in Low and uPA$^{-/-}$/SCID mice (Table 4). The inhibition pattern was competitive in High. However, the K_i values of Low and uPA$^{-/-}$/SCID mice were 592- to 633-fold higher than that of High.

Mechanism-Based Inactivation of DBOH Activity by Paroxetine *In Vitro*

The DBOH activity was inactivated by paroxetine in all liver microsomes from High, Low, and uPA$^{-/-}$/SCID mice. The k_{inact} (0.050–0.057 min^{-1}) and K_i (94–115 nM) values were similar among the three groups.

Genotyping for *CYP2D6*3*, *CYP2D6*4*, and *CYP2D6*5* Alleles

By using genomic DNA prepared from the donor hepatocytes and from the liver of the chimeric mice, the donor did not have *CYP2D6*3*, *CYP2D6*4*, and *CYP2D6*5* alleles (data not shown).

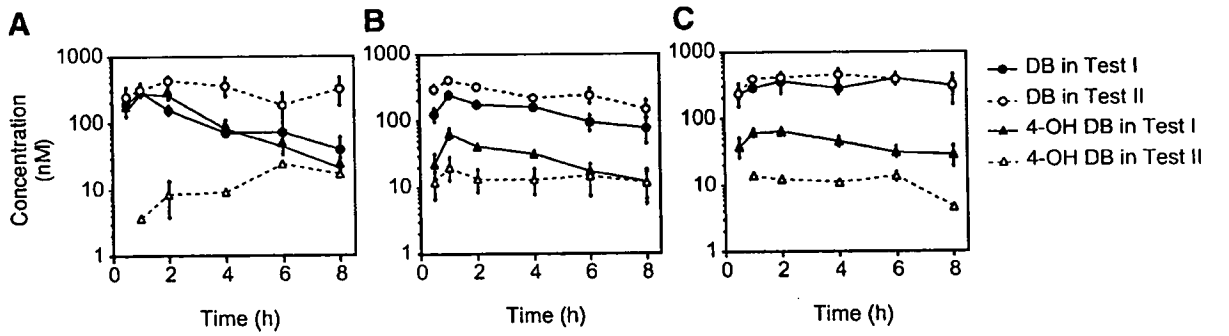

Figure 3. Effect of paroxetine treatment on serum concentration of DB and 4-OH DB in High (A), Low (B), and uPA$^{-/-}$/SCID mice (C) in Test II. DB and paroxetine were administered as described in Materials and Methods. Data represent the mean ± SE ($n = 4$) except the values of 4-OH DB of High in Test II, which represent the mean from two or three mice. High, >5.0 mg/mL hAlb concentration (>70% of RI); Low, <0.6 mg/mL hAlb concentration (<10% of RI).

Table 3. Kinetic Parameters of DBOH Activity in Liver Microsomes from Chimeric Mice and uPA$^{-/-}$/SCID Mice

Microsomes	K_m (μM)	V_{max} (pmol/mg/min)	V_{max}/K_m (μL/mg/min)
High	72 ± 8	39 ± 2	0.59 ± 0.05
Low	145 ± 14**	43 ± 4	0.31 ± 0.02***
uPA$^{-/-}$/SCID	213 ± 12***	82 ± 7***	0.40 ± 0.04*

Data represent the mean ± SE ($n > 8$).
High, >5.0 mg/mL hAlb concentration (>70% of RI); Low, <0.6 mg/mL hAlb concentration (<10% of RI).
*$P < 0.05$, compared with those of High.
**$P < 0.01$, compared with those of High.
***$P < 0.001$, compared with those of High.

DISCUSSION

DB is one of the typical substrates of CYP2D6 and was clarified to be oxidized polymorphically in humans.[22] Masubuchi et al.[23] reported that the DBOH activity in liver microsomes from mice was low, suggesting that a species difference exists. In the present study, we evaluated whether the chimeric mouse model with humanized liver established by transplanting human hepatocytes into uPA$^{+/+}$/SCID mice[1] could be applied for the prediction of *in vivo* drug interactions involving human CYP2D6. In our previous report,[2] the chimeric mice generated using hepatocytes from the same donor as the present study were clarified to express sufficient human CYP2D6 and have CYP2D6 enzyme activity. Moreover, it was clarified that the donor did not have *CYP2D6*3*, *CYP2D6*4*, and *CYP2D6*5* alleles, suggesting that the donor might not be a poor metabolizer. Thus, the *in vivo* pharmacokinetic study could evaluate the enzyme activity and the inhibition of CYP2D6 in the chimeric mice.

In the *in vivo* metabolic study (Test I), the AUC_{0-8} and C_{max} values of 4-OH DB in High were significantly higher than those in Low and the control uPA$^{-/-}$/SCID mice. Such a difference resulted from the hepatic expression level of human CYP2D6 in chimeric mice, suggesting that the chimeric mice with a high hAlb concentration would exhibit humanized metabolism *in vivo* as well as *in vitro*.[2] The chimeric mice with a low hAlb concentration may be classified as mice not humanized mice. The K_m values of High in Table 1 was similar to the value obtained by Nakajima et al. ($K_m = 62.0–106.8$ μM).[16] In the present study, the differences in the K_m and V_{max}/K_m values for DBOH activity among the three groups indicated that the murine Cyp2d was replaced by human CYP2D6 in the chimeric mice.[2] There was a small difference in the AUC_{0-8} values of DB among the three groups in the present study. Although the major metabolite of DB is 4-OH DB in humans,[24] the *in vivo* elimination of DB except for the 4-hydroxylation might be needed to investigate. To date, the metabolite of DB in mice is not fully understood. A small but not statistically significant difference in the DB levels among the three groups might have been caused by other minor metabolic pathways, but further

Table 4. Inhibition and Inactivation of DBOH Activity by Quinidine and Paroxetine in Liver Microsomes from Chimeric Mice and uPA$^{-/-}$/SCID Mice

	Quinidine	Paroxetine	
Microsomes	K_i (μM)	k_{inact} (10^{-3}/min)	K_i (nM)
High	0.049 ± 0.012	57 ± 5	94 ± 15
Low	31 ± 6***	55 ± 4	109 ± 18
uPA$^{-/-}$/SCID	29 ± 3***	50 ± 7	115 ± 24

Data represent the mean ± SE (n > 8).
High, >5.0 mg/mL hAlb concentration (>70% of RI); Low, <0.6 mg/mL hAlb concentration (<10% of RI).
***$P < 0.001$, compared with those of High.

DOI 10.1002/jps

study is needed to clarify this issue. The DBOH activity was also catalyzed by CYP1A1 using B-lymphoblastoid cells expressing human CYP1A1 *in vitro*.[25] The hepatic CYP1A1 expression exhibited large interindividual variation in humans.[26] However, the human CYP1A1 protein could not be detected in the liver of the chimeric mice,[3] that were generated with the same hepatocytes. Therefore, there may have been no contribution of human CYP1A1 in the liver. Although DBOH in mice was lower than that in humans, mouse enzymes catalyzed by DBOH are still unclear. In High, the expression levels of mouse drug metabolizing enzymes were much lower than those in uPA$^{-/-}$/SCID mice.[3] Therefore, the contribution of mouse Cyp1a1 in DBOH in High may be minor or negligible.

Paine et al.[27] reported that the intestinal CYP2D6 expressed was approximately 1% of the total intestinal P450 content and that the jejunal CYP2D6 content was less than 8% of the hepatic CYP2D6 in humans. They surmised that the intestinal CYP2D6 would contribute minimally to the overall first-pass metabolism of drugs except some drugs known to reside for a long time in the enterohepatic circulation.[27] Serious drug interactions involving CYP2D6 in human intestine have not been reported. Therefore, the liver is the predominant organ for CYP2D6 drug interactions, and the liver but not other organs was humanized in the chimeric mice.

Quinidine is one of the typical CYP2D6 inhibitors, which is clinically used for long periods as an antiarrhythmic drug. It has not been clarified whether quinidine can affect the DBOH activity in mice. Due to the pre-treatment with quinidine, the AUC_{0-8} values of 4-OH DB in High decreased as compared with the control (Test I). However, in both Low and uPA$^{-/-}$/SCID mice, the AUC_{0-8} values did not change with quinidine, indicating that the inhibition by quinidine on DBOH activity was specific to humans. The possibility that the changes of quinidine pharmacokinetic by the humanization of the liver in the chimeric mice is still remained, because the serum concentration of quinidine was not measured due to limited volume of serum from the same mouse. In the *in vitro* study, quinidine exhibited strong competitive inhibition in liver microsomes from High. The K_i values of Low and uPA$^{-/-}$/SCID mice were approximately 600-fold higher than that of High, which supported the findings of our *in vivo* study described above. Therefore, the chimeric mice with high hAlb concentrations can be used to evaluate the *in vitro* inhibitory effect of P450. Paroxetine was reported to be a mechanism-based inactivator of CYP2D6.[28] In the present study, after the pretreatment with paroxetine the serum 4-OH DB concentrations in all groups were reduced and a potent *in vitro* inactivation by paroxetine was observed using liver microsomes from the chimeric mice. Although the species differences in the mechanism-based inactivation of the CYP2D enzyme activity have not been clarified, the human CYP2D6 expressed in the chimeric mice was shown to be inhibited by a typical inhibitor of CYP2D6.

In conclusion, the chimeric mice were shown to exhibit a humanized profile of drug metabolism and inhibition of P450 in both the *in vivo* and *in vitro* studies. The chimeric mice could be a better *in vivo* model for investigating drug interactions caused by the inhibition as well as the induction of human P450.[3,5] The chimeric mice can produce hAlbs and the binding of drugs to albumin may be different between humans and mice. It is necessary to keep the species difference of the protein binding in mind, but the existence of hAlb can make the experimental condition more humanized. There have been many studies that attempted to extrapolate the pharmacokinetics from experimental animals to humans. Although the prediction methods can be expected to improve, chimeric mice could still be one of the most useful models to estimate the pharmacokinetics in humans.

ACKNOWLEDGMENTS

This work was supported by a Research on Advanced Medical Technology, Health, and Labor Sciences Research Grant from the Ministry of Health, Labor, and Welfare of Japan. We acknowledge Mr. Brent Bell for reviewing the manuscript.

REFERENCES

1. Tateno C, Yoshizane Y, Saito N, Kataoka M, Utoh R, Yamasaki C, Tachibana A, Soeno Y, Asahina K, Hino H, Asahara T, Yokoi T, Furukawa T, Yoshizato K. 2004. Near completely humanized liver in mice shows human-type metabolic responses to drugs. Am J Pathol 165:901–912.

2. Katoh M, Matsui T, Nakajima M, Tateno C, Kataoka M, Soeno Y, Horie T, Iwasaki K, Yoshizato K, Yokoi T. 2004. Expression of human cytochromes P450 in chimeric mice with humanized liver. Drug Metab Dispos 32:1402–1410.
3. Katoh M, Matsui T, Nakajima M, Tateno C, Soeno Y, Horie T, Iwasaki K, Yoshizato K, Yokoi T. 2005. In vivo induction of human cytochrome P450 enzymes expressed in chimeric mice with humanized liver. Drug Metab Dispos 33: 754–763.
4. Katoh M, Matsui T, Okumura H, Nakajima M, Nishimura M, Naito S, Tateno C, Yoshizato K, Yokoi T. 2005. Expression of human phase II enzymes in chimeric mice with humanized liver. Drug Metab Dispos 33:1333–1340.
5. Katoh M, Watanabe M, Tabata T, Sato Y, Nakajima M, Nishimura M, Naito S, Tateno C, Iwasaki K, Yoshizato K, Yokoi T. 2005. In vivo induction of human cytochrome P450 3A4 by rifabutin in chimeric mice with humanized liver. Xenobiotica 35:863–875.
6. Wilkinson GR. 2005. Drug metabolism and variability among patients in drug response. N Engl J Med 352:2211–2221.
7. Shimada T, Yamazaki H, Mimura M, Inui Y, Guengerich FP. 1994. Interindividual variations in human liver cytochrome P-450 enzymes involved in the oxidation of drugs, carcinogens and toxic chemicals: Studies with liver microsomes of 30 Japanese and 30 Caucasians. J Pharmacol Exp Ther 270:414–423.
8. Ingelman-Sundberg M. 2005. Genetic polymorphisms of cytochrome P450 2D6 (CYP2D6): Clinical consequences, evolutionary aspects and functional diversity. Pharmacogenomics J 5:6–13.
9. Hemeryck A, Belpaire FM. 2002. Selective serotonin reuptake inhibitors and cytochrome P-450 mediated drug-drug interactions: An update. Curr Drug Metab 3:13–37.
10. Caporaso NE, Shaw GL. 1991. Clinical implications of the competitive inhibition of the debrisoquin-metabolizing isozyme by quinidine. Arch Intern Med 151:1985–1992.
11. Nelson DR, Koymans L, Kamataki T, Stegeman JJ, Feyereisen R, Waxman DJ, Waterman MR, Gotoh O, Coon MJ, Estabrook RW, Gunsalus IC, Nebert DW. 1996. P450 superfamily: Update on new sequences, gene mapping, accession numbers and nomenclature. Pharmacogenetics 6:1–42.
12. Hiroi T, Chow T, Imaoka S, Funae Y. 2002. Catalytic specificity of CYP2D isoforms in rat and human. Drug Metab Dispos 30:970–976.
13. Dalen P, Dahl ML, Eichelbaum M, Bertilsson L, Wilkinson GR. 1999. Disposition of debrisoquine in Caucasians with different *CYP2D6*-genotypes including those with multiple genes. Pharmacogenetics 9:697–706.
14. Corchero J, Granvil CP, Akiyama TE, Hayhurst GP, Pimprale S, Feigenbaum L, Idle JR, Gonzalez FJ. 2001. The CYP2D6 humanized mouse: Effect of the human CYP2D6 transgene and HNF4α on the disposition of debrisoquine in the mouse. Mol Pharmacol 60:1260–1267.
15. Yamazaki H, Shibata A, Suzuki M, Nakajima M, Shimada N, Guengerich FP, Yokoi T. 1999. Oxidation of troglitazone to a quinone-type metabolite catalyzed by cytochrome P-450 2C8 and P-450 3A4 in human liver microsomes. Drug Metab Dispos 27:1260–1266.
16. Nakajima M, Tane K, Nakamura S, Shimada N, Yamazaki H, Yokoi T. 2002. Evaluation of approach to predict the contribution of multiple cytochrome P450s in drug metabolism using relative activity factor: Effects of the differences in expression levels of NADPH-cytochrome P450 reductase and cytochrome b5 in the expression system and the differences in the marker activities. J Pharm Sci 91:952–963.
17. Nakajima M, Suzuki M, Yamaji R, Takashina H, Shimada N, Yamazaki H, Yokoi T. 1999. Isoform selective inhibition and inactivation of human cytochrome P450s by methylenedioxyphenyl compounds. Xenobiotica 29:1191–1202.
18. Broly F, Gaedigk A, Heim M, Eichelbaum M, Morike K, Meyer UA. 1991. Debrisoquine/sparteine hydroxylation genotype and phenotype: Analysis of common mutations and alleles of CYP2D6 in a European population. DNA Cell Biol 10:545–558.
19. Dahl ML, Johansson I, Palmertz MP, Ingelman-Sundberg M, Sjoqvist F. 1992. Analysis of the *CYP2D6* gene in relation to debrisoquin and desipramine hydroxylation in a Swedish population. Clin Pharmacol Ther 51:12–17.
20. Heim M, Meyer UA. 1990. Genotyping of poor metabolisers of debrisoquine by allele-specific PCR amplification. Lancet 336:529–532.
21. Johansson I, Lundqvist E, Dahl ML, Ingelman-Sundberg M. 1996. PCR-based genotyping for duplicated and deleted CYP2D6 genes. Pharmacogenetics 6:351–355.
22. Mahgoub A, Idle JR, Dring LG, Lancaster R, Smith RL. 1977. Polymorphic hydroxylation of debrisoquine in man. Lancet 2:584–586.
23. Masubuchi Y, Iwasa T, Hosokawa S, Suzuki T, Horie T, Imaoka S, Funae Y, Narimatsu S. 1997. Selective deficiency of debrisoquine 4-hydroxylase activity in mouse liver microsomes. J Pharmacol Exp Ther 282:1435–1441.
24. Allen JG, East PB, Francis RJ, Haigh JL. 1975. Metabolism of debrisoquine sulfate. Identification of some urinary metabolites in rat and man. Drug Metab Dispos 3:332–337.

 DOI 10.1002/jps

25. Granvil CP, Krausz KW, Gelboin HV, Idle JR, Gonzalez FJ. 2002. 4-Hydroxylation of debrisoquine by human CYP1A1 and its inhibition by quinidine and quinine. J Pharmacol Exp Ther 301: 1025–1032.
26. Schweikl H, Taylor JA, Kitareewan S, Linko P, Nagorney D, Goldstein JA. 1993. Expression of CYP1A1 and CYP1A2 genes in human liver. Pharmacogenetics 3:239–249.
27. Paine MF, Hart HL, Ludington SS, Haining RL, Rettie AE, Zeldin DC. 2006. The human intestinal cytochrome P450 "PIE". Drug Metab Dispos 34: 880–886.
28. Bertelsen KM, Venkatakrishnan K, von Moltke LL, Obach RS, Greenblatt DJ. 2003. Apparent mechanism-based inhibition of human CYP2D6 in vitro by paroxetine: Comparison with fluoxetine and quinidine. Drug Metab Dispos 31:289–293.

Available online at www.sciencedirect.com
ScienceDirect
Journal of Controlled Release 120 (2007) 4–10
journal of controlled release
www.elsevier.com/locate/jconrel

Absorption study of deoxycholic acid-heparin conjugate as a new form of oral anti-coagulant

Sang Kyoon Kim [a,1], Dong Yun Lee [b,1], Eunhye Lee [c], Yong-kyu Lee [d], Choong Yong Kim [e], Hyun Tae Moon [f], Youngro Byun [b,f,*]

[a] Department of Materials Science and Engineering, Gwangju Institute of Science and Technology, Gwangju 500-712, South Korea
[b] College of Pharmacy, Seoul National University, Seoul 151-742, South Korea
[c] Department of Life Science, Gwangju Institute of Science and Technology, Gwangju 500-712, South Korea
[d] Department of Chemical and Biological Engineering, Chungju National University, Chungbuk 380-702, South Korea
[e] Korea Institute of Toxicology, Korea Research Institute of Chemical Technology, Daejon 305-600, South Korea
[f] Mediplex Corp., Seoul 135-729, South Korea

Received 7 August 2006; accepted 13 March 2007
Available online 20 March 2007

Abstract

The oral delivery of macromolecules is a topic of much interest as this would undoubtedly improve patient acceptance and compliance with chronic regimens. Heparin and insulin are perhaps among the first candidates that should be considered for oral macromolecule delivery systems. Heparin is the most potent anti-coagulant known for the prevention of deep vein thrombosis and pulmonary embolism, and an orally active heparin would undoubtedly effectively reduce chronic thrombotic events. Here, we report on the development of an orally administrable chemical conjugate of heparin and hydrophobic deoxycholic acid (DOCA), which we refer to as LHD. LHD was pre-formulated with dimethyl sulfoxide (DMSO) as solubilizer to further improve its oral bioavailability (9.1% in monkey). LHD was found to be absorbed mainly in the jejunum and ileum of the small intestine, although it is in the ileum that the absorption is most notable. From the mechanism studies of LHD absorption using Caco-2 cell monolayers for mimicking the intestine, we found that LHD highly permeated by passive diffusion through the transcellular route and its permeation was partially affected by bile acid transporters. This study demonstrates the feasibility of chemically modified heparin for long-term oral administration as an effective therapy for venous thromboembolism in clinical trials.

Keywords: Oral absorption; Anti-coagulant; Low molecular weight heparin; Deoxycholic acid

1. Introduction

The oral route of delivery of macromolecular drugs, *i.e.*, heparin and insulin, is a topic of intense interest as it is likely to markedly improve patient acceptance and compliance. Moreover, heparin is the most potent anti-coagulant known in terms of deep vein thrombosis (DVT) and pulmonary embolism (PE) prevention. Venous thromboembolisms, *i.e.*, DVT and PE, are diagnosed in ~250,000 hospitalized patients annually; and ~100,000 patients die each year of PE, [1,2] and without therapy, there is a 50% chance of a recurrent thromboembolism [3]. Currently 5 days of parenteral heparin injections followed by 3 months of oral warfarin therapy, the so-called 'gold-standard' treatment, successfully prevents PE in 95% of patients with proximal DVT [4]. However, although heparin and warfarin are effective anti-coagulants, individual patient response to oral warfarin therapy varies, and doses must be monitored closely to determine the duration of treatment, because warfarin has a slow onset, is pre-dominantly protein bound, and is subject to drug–drug interactions [5]. However, heparin does not have teratogenic effects, and has a rapid onset anti-coagulant effect with a half-life of <4 h, which allows its

* Corresponding author. College of Pharmacy, Seoul National University, San 56-1, Sillim-dong, Gwanak-gu, Seoul 151-742, South Korea. Tel.: +82 2 880 7866; fax: +82 2 872 7864.
E-mail address: yrbyun@snu.ac.kr (Y. Byun).
[1] The authors equally contributed in this study as first author.

0168-3659/$ - see front matter © 2007 Elsevier B.V. All rights reserved.
doi:10.1016/j.jconrel.2007.03.008

anti-coagulant effect to be readily reversed if necessary [6]. Therefore, chronic heparin administration is a highly attractive alternative therapy for the prevention of venous thromboembolism. Unfortunately, heparin cannot be absorbed orally because of its high charge density and its large molecular weight, and thus, can only be given parenterally. Thus, there is a need for an orally absorbable heparin, because currently the long-term use of intravenous heparin is not a practical option. In addition, oral heparin would facilitate venous thromboembolism treatment in an outpatient setting.

To increase heparin absorption in the intestine, various approaches, such as, liposomes, enteric coatings, and enhancers have been investigated [7–10]. Recently, we developed an orally active heparin derivative that enhances heparin absorption in the intestine [11–13]. This derivative is a chemical conjugate of low molecular weight heparin (LMWH) and deoxycholic acid (DOCA), which we refer to as LHD. This conjugated DOCA in LHD promotes intestinal absorption by enhancing the hydrophobic properties of LMWH and by increasing the interaction between heparin and the intestinal membrane [14,15]. Moreover, when we designed this conjugate system it was envisaged that DOCA would more easily interact with bile acid transporters expressed on the intestinal membrane, and that this would increase the absorption of macromolecules into the intestinal membrane. In the previous study, it was confirmed that LHD was highly absorbed in mice and did not induce any systemic toxicities as well as local toxicities in the GI tract at 10 mg/kg dose [16]. In the current study, we explored the oral absorption of LHD in a non-human primate model (cynomolgus monkeys) and investigated the absorption mechanism involved.

2. Methods

2.1. Materials

Low molecular weight heparin (LMWH; Fraxiparin®, 4500 Da) was obtained from GlaxoSmithKline (Brentford, Middlesex, UK). Deoxycholic acid (DOCA), dicyclohexylcarbodiimide (DCC), hydroxysuccinimide (HOSu), 1-ethyl-3-(3-dimethylamino propyl) carbodiimide hydrochloride (EDAC), ethylenediamine, dimethyl sulfoxide (DMSO), sodium taurocholate, ethylene glycol tetra acetic acid (EGTA), and colchicine were purchased from Sigma Chemical Co. (St. Louis, MO). Dimethylformamide (DMF) was obtained from Merck (Darmstadt, Germany). Fluorescein-5-isothiocyanate (FITC) and tetramethylrhodamine B isothiocyanate (TRITC)-labeled phalloidin were obtained from Fluka (Buchs, Switzerland). Coatest anti-Factor Xa assay kits were purchased from Chromogenix (Milano, Italy).

2.2. Synthesis of LHD

The chemical conjugate of LMWH and deoxycholic acid (DOCA) was synthesized by conjugating the carboxylic group of DOCA with the carboxylic group of LMWH. Briefly, the carboxylic group of DOCA (196 mg) was activated using DCC (165 mg) and HOSu (92 mg) in 15 ml of DMF. Then the activated carboxylic group of DOCA was further reacted with ethylenediamine in DMF for 5 h at 25 °C, thereby forming deoxycholylethylamine. The feed mole ratio of activated DOCA to ethylenediamine was 3:1. The carboxylic groups of LMWH (100 mg) were also activated by using formamide (2 ml) and EDAC (11.49 mg), and then further reacted with an amine group of deoxycholylethylamine at 25 °C for 12 h. The feed mole ratio of deoxycholylethylamine to LMWH was 2:1. After the product was lyophilized and precipitated in acetone, the LMWH–DOCA conjugate, *i.e.*, LHD, was obtained as a white powder.

Fluorescein-labeled LMWH or LHD were synthesized to confirm the absorption of LMWH derivatives *in vitro* and *in vivo*. For fluorescein (FITC; fluorescein isothiocyanate) labeling LMWH derivatives a binding molar ratio of 1:1 (w/w) was used, *i.e.*, FITC to LMWH or LHD. The absence of an effect by fluorescein on the particle sizes of LMWH derivatives in water or in 10% DMSO solution was confirmed by dynamic light scattering.

2.3. Oral absorption of LMWH derivatives in monkeys

Cynomolgus male monkeys, each weighing about 2.5–3.0 kg, were individually housed at Korea Research Institute of Chemical Technology (KRICH; Daejon, Korea). Animal care and all animal-related procedures were approved by KRICH. After fasting for 12 h, different doses (5, 10, 50 mg/kg) of LMWH or LHD were administered singly to monkeys by oral gavage. For pharmacokinetic analysis, 1 mg/kg of LMWH or LHD was intravenously injected into monkeys. After administering LMWH or LHD, monkey blood samples were collected from vein at each time and directly mixed with 50 μl of sodium citrate (3.8%). The plasma concentrations of LMWH or LHD were calculated from their anti-Factor Xa (FXa) activity, as determined by anti-FXa chromogenic assays [12]. In brief, the samples were diluted with human normal plasma at heparin concentrations above 0.7 IU/ml. LHD sample (100 μl) was mixed with 100 μl of anti-thrombin III (ATIII) solution, where ATIII concentration was in excess of the LHD concentration, followed by incubating at 37 °C for 3 min. FXa (100 μl) was added to the solution, and the resulting solution was then incubated for an additional 30 s. The concentration of FXa was also in excess of the LHD concentration. The substrate (200 μl, 0.8 μmol/ml) was then added and incubated at 37 °C for 3 min. The reaction was terminated by adding 300 μl of 20% acetic acid. The bioactivity and the concentration of LHD were calculated from the absorbance at 405 nm. The detection limit of anti-FXa chromogenic assay was 0.05 IU/ml, and the coefficient of variation was 2.6% in the range from 0.05 to 0.7 IU/ml.

In order to evaluate the absorption site of orally administered LHD, tissues from the duodenum, jejunum, and ileum were harvested and washed in lysis buffer for 30 min after fluorescein-labeled LHD (10 mg/kg) in 10% DMSO formulation was orally administered to mice. The tissue from each part was ground and homogenized with Ultra Turrax T 25 (JANKE

& KUNKEL, IKA Labotrchnik). After centrifugation of tissue extract, their supernatants were filtered, and fluorescences of all samples were measured with synergy HT (BioTek Instruments, Inc, VT).

2.4. Permeability study using a Caco-2 cell transport model

The human colon cancer cell line Caco-2 (American Type Culture Collection, Manasassas, VA) were used as the transport model since they express bile acid transporters [17,18]. The cells were cultured in DMEM medium (pH 7.4) supplemented with 1% NEAA, 10% fetal bovine serum, 1% antibiotics at 37 °C in a 5% CO_2 an atmosphere at 95% RH. Caco-2 cells (3×10^5 cells/ml) were seeded on the collagen-coated filter membranes of Transwell® cell culture inserts (3.0 μm pore diameter; Costar, Cambridge, MA) and further cultured for 4 weeks to reach confluence. The culture media were placed into the apical (0.5 ml) and basolateral (1.5 ml) chambers, and changed every other day for a week and then daily.

Caco-2 cell monolayers with a transendothelial electrical resistance (TEER) value of more than 400 Ω cm^2 were used for permeability studies. Briefly, Caco-2 cell monolayers were washed twice with cold phosphate buffered saline (PBS; Biowhittaker) and pre-incubated with pre-warmed transport media (pH 7.4), comprised of: hanks balanced salt solution (HBSS; Biowhittaker), 10 mM HEPES (*N*-2-hydroxyethyl piperazine-*N'*-2-ethanesulfonic acid, Biowhittaker), 25 mM d-glucose, and metabolic inhibitor (sodium azide, 10 mM) for 30 min at 37 °C in a 5% CO_2 incubator. In addition, 4% bovine serum albumin (BSA; GIBCO) was pre-treated into the basolateral part as a cytoprotective agent. To evaluate the main absorption routes of LMWH or LHD, sodium taurocholate, colchicine, EGTA, or glucose free media were placed in the apical or basolateral region of transwell, respectively. Culture medium in the opposite part was collected at 10, 20, 30, 60, 90, 120 min after treating with LMWH derivatives (0.5 mg/ml) and the various blockers such as sodium taurocholate, sodium azide, colchicine and EGTA. The amounts of LMWH or LHD that permeated through the filter were measured indirectly using anti-FXa activity chromogenic assays. The apparent permeability (P_{app}, cm/s) was calculated from the slope at the steady state in the plot of the amount of permeated drug versus time.

To visualize LMWH or LHD permeation, 0.5 mg/kg of fluorescein-labeled LMWH or LHD with or without 10% DMSO was administered to Caco-2 cell monolayers. At 30 min after treatment, monolayers were washed and observed under a confocal laser scanning microscope. To confirm patent tight junctions between Caco-2 cells in the presence of 10% DMSO, RITC-phalloidin (a stain for actin filament) was treated and observed under a confocal laser scanning microscope.

2.5. Statistical analysis

All data are expressed as means±SEM. The paired *t*-test was used to compare before and after treatment data and ANOVA was used to compare groups. P values of ≤ 0.05 were considered statistically significant.

3. Results

3.1. Oral absorption of LMWH derivatives in monkeys and mice

The anti-coagulant activity of LHD measured by Factor Xa chromogenic assay was 86 IU/mg, whereas that of LMWH was 97 IU/mg [16]. In addition, the partition coefficient of LHD in octanol/water was 15 folds higher than LMWH. To evaluate the oral absorption of LHD in a primate model, LHD was orally administered to fasted male cynomolgus monkeys. Furthermore, because LHD itself tended to form self-assembled particle in water due to the hydrophobic nature of the conjugated DOCA molecules, LHD was pre-formulated with 10% dimethyl sulfoxide (DMSO) as a solution. When LMWH (10 mg/kg) in 10% DMSO formulation, *i.e.*, DMSO–LMWH, was orally administered, plasma anti-Xa activity of LMWH remained below 0.1 IU/ml; the minimum effective concentration (MEC) required for treating venous thromboembolism (Fig. 1A). However, LHD (10 mg/kg) in an identical DMSO formulation, *i.e.*, DMSO–LHD, was rapidly absorbed with a maximum plasma anti-FXa activity at 4 h, and its plasma level

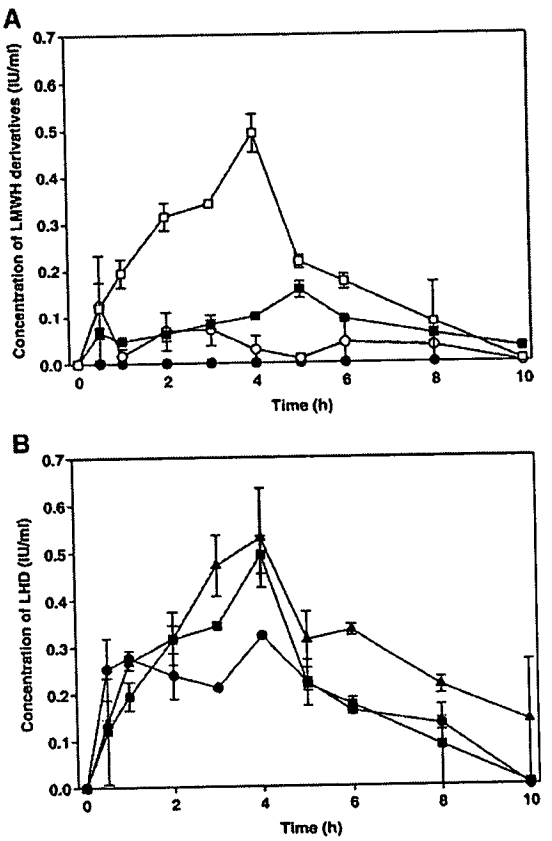

Fig. 1. Oral absorption profiles of LHD or LMWH in monkeys are shown. (A) Absorption profiles of LMWH or LHD alone or pre-formulated with 10% DMSO. After the oral administration of 10 mg/kg of LMWH (●), DMSO–LMWH (○), LHD (■) or DMSO–LHD (□), anti-FXa activity in plasma was measured ($n=3$) for each case. (B) Absorption profiles of 5 mg/kg (●), 10 mg/kg (■), and 50 mg/kg (▲) of DMSO–LHD in monkeys ($n=3$).

was maintained above the minimum effective anti-Xa activity of 0.1 IU/ml for 8 h. On the other hand, the AUC of LHD at 5, 10 and 50 mg/kg were 94.6±9.7, 104.0±13.0 and 153.1±24.9 μg/ml/min, respectively (Fig. 1B). The absorption of LHD was not increased proportionally according to its dose. This result was related to the solubility of LD2 in 10% DMSO solution. For 5 mg/kg dosage, the concentration of LD2 in the dosage was 1 mg/ml, and it was completely dissolved. However, 50 mg/kg dosage (10 mg/ml) was administered in a dispersed state. Therefore, the solubility of LD2 might be important to the absorption in the intestine. Also, the specific interaction of LD2 with bile acid transporters might be an additional factor which affected the absorption of LD2 in the intestine. Moreover, when we pharmacokinetically analyzed the absorption profiles of LHD with/without DMSO in the formulation, we found that its bioavailabilities were 9.2 and 3.5%, respectively (Table 1).

To study the absorption site of LHD in the intestine, fluorescein-labeled DMSO–LHD was orally administered in mice (Fig. 2). Fluorescein-labeled DMSO–LHD was mostly absorbed in the jejunum (26%) and ileum (72%) parts of the small intestine, although it is most notable in the ileum; the absorption in the duodenum and the colon was negligible.

3.2. Permeation of LMWH derivatives in the Caco-2 cell transport model

Having found that LHD can be orally absorbed in monkeys, we sought to investigate the absorption pathway involved. First, we developed an *in vitro* model in which 10% DMSO formulation did not affect the integrity of confluent Caco-2 cell monolayer in the presence of bovine serum albumin (4%) as a cytoprotective agent. Then, to observe the absorption mechanism of DMSO–LHD, we determined the optimum concentration of LHD for transport by studying the correlation between the drug concentration and its absorption by Caco-2 cell monolayers formed in transwell. At 2 h after treating the

Table 1
Pharmacokinetic parameters of low molecular weight heparin (LMWH) derivatives in Cynomolgus monkeys

LMWH derivatives	Dose (mg/kg)	$AUC_{0-600\ min}$ (μg/ml/min)	V_d (l/kg)	CL (ml/min/kg)	$T_{1/2}$ (h)
Intravenous					
LMWH	1	118.9±1.0	0.11±0.0	0.3±0.0	4.3±0.0
LHD	1	113.6±6.0	0.25±0.0	0.8±0.0	3.4±0.1
	Dose (mg/kg)	$AUC_{0-600\ min}$ (μg/ml/min)	C_{max} (IU/ml)	T_{max} (h)	F (%)
Oral					
DMSO–LHD	10	104.0±13.0	0.49±0.0	4	9.2
LHD	10	45.9±3.0	0.16±0.0	5	3.5
DMSO-LMWH	10	13.4±10.0	0.13±0.10	0.5	1.1
LMWH	10	ND	ND	ND	ND

LMWH, low molecular weight heparin; LHD, LMWH-deoxycholic acid (DOCA) conjugate; DMSO, 10% dimethyl sulfoxide (DMSO) formulation; $AUC_{0-600\ min}$, area under curve from 0 to 600 min (10 h) to plasma profile after LMWH derivative administration orally; V_d, volume of distribution; CL, clearance; $T_{1/2}$, half-life time; C_{max}, maximum concentration; T_{max}, the time at C_{max}; F, bioavailability; ND, not detectable.

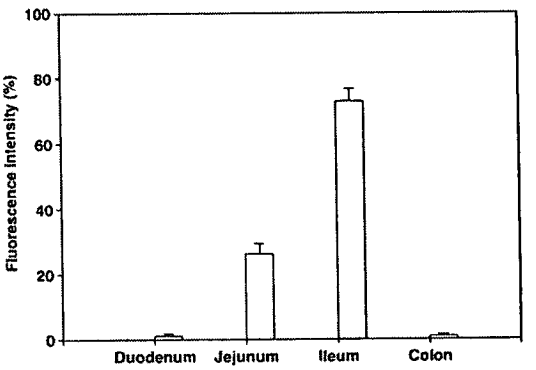

Fig. 2. The amount of fluorescein-labeled LHD in intestinal tissues.

apical region of Caco-2 cell monolayers with different concentrations of LHD or LMWH, the amounts of LHD or LMWH that permeated to the basolateral region was measured. The apparent permeability ($P_{app} \times 10^{-7}$ cm/s) values of 0.1, 0.5, 1, and 5 mg/ml of LHD were 45.6±10.9, 42.3±4.6, 26.0±2.3, and 2.6±0.3, respectively (Fig. 3A, white bar). Moreover, the P_{app} values of 0.1 and 0.5 mg/ml of LHD, which were not statistically different, were significantly higher than those of 1

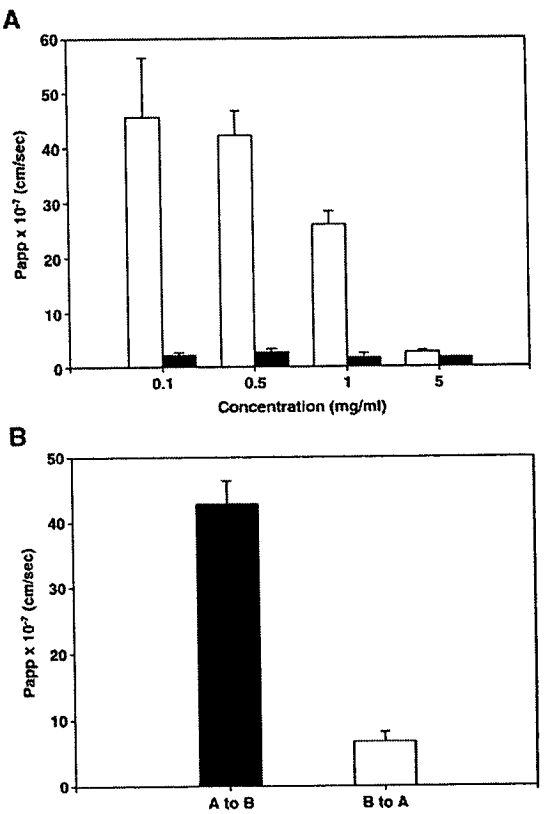

Fig. 3. Permeation of DMSO–LMWH or DMSO–LHD through a Caco-2 cell monolayer. (A) Apparent permeability (P_{app}) at 0.1, 0.5, 1, and 5 mg/ml of DMSO–LMWH (black bar) or DMSO–LHD (white bar) from the apical (A) to basolateral (B) direction for 2 h. (B) The permeability of 0.5 mg/kg of DMSO–LHD from A to B direction (black bar) or from B to A direction (white bar) for 2 h. Data are expressed as means±SEM (n=5).

and 5 mg/ml of LHD. On the other hand, the P_{app} values of the same concentrations of LMWH were below 3.0×10^{-7} cm/s (Fig. 3A, black bar). Fig. 3B shows that the permeability of LHD (0.5 mg/ml) from apical (A) to basolateral (B) direction was six times greater than that from B to A.

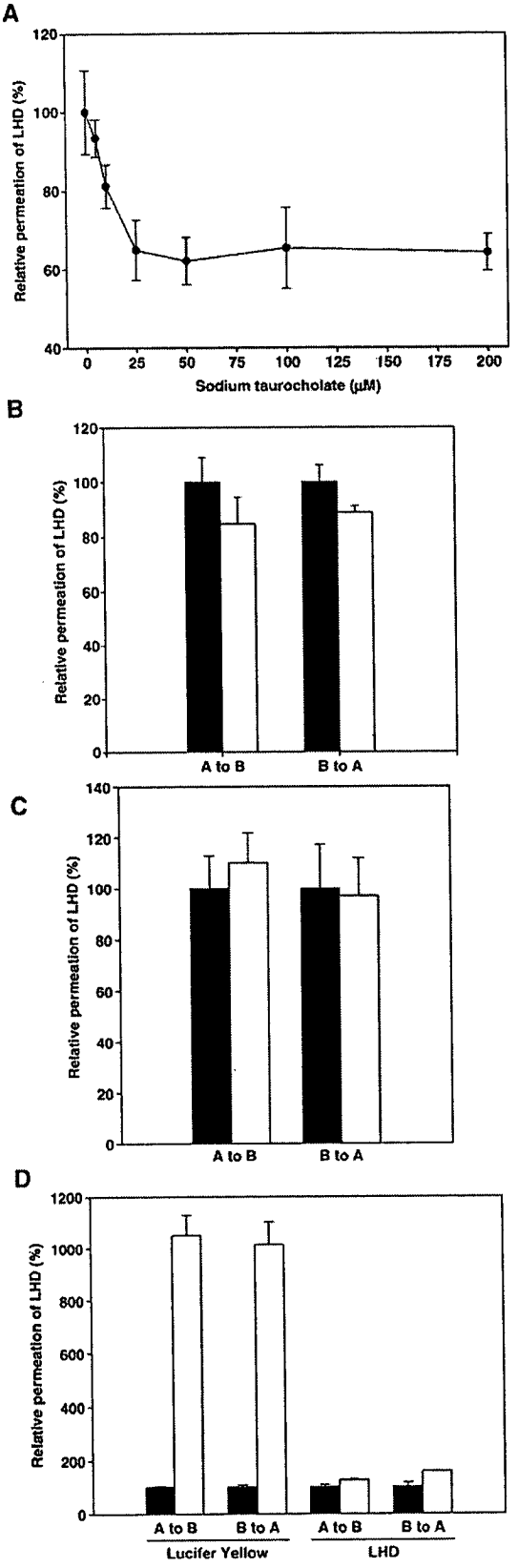

3.3. Mechanism study to the LHD permeation through Caco-2 cell monolayer

To evaluate whether the oral absorption of LHD was aided by an adhesive effect between the conjugated DOCA molecule and intestinal membrane, Caco-2 cell monolayers were treated with sodium taurocholate. Sodium taurocholate is used as competitive inhibitor to bile acid transporter because of its high affinity for IBAT. Compared to the permeated amount of LHD in the absence of sodium taurocholate, the relative amounts of LHD that permeated for 120 min at 5, 10, 25, 50, 100, and 200 μM of sodium taurocholate were 94.3±2.5, 81.9±5.1, 64.9±7.7, 62.1±6.0, 65.4±10.3 and 64.2±4.7%, respectively. We found that as the permeated amount of LHD was significantly decreased with the increase of the sodium taurocholate concentration; however, the permeation of LHD was not further reduced when the concentration of sodium taurocholate was above 25 μM (Fig. 4A).

We evaluated the absorption of LHD in the presence of sodium azide to inhibit an active transport. As shown in Fig. 4B, the amounts of LHD that permeated from A to B and from B to A directions under glucose deprivation conditions with sodium azide were not significantly different with each other as compared with LHD permeation under the normal condition. Also, the permeated amount of LHD in the presence of colchicine (endocytosis inhibitor by blocking polymerization of microtubules) was not significantly different from that in the absence of colchicine, that is, the relative amounts of permeated LHD from A to B and from B to A directions in the presence of colchicine were 110.3±11.6 and 96.9±15.1%, respectively (Fig. 4C). This result indicated that LHD did not permeate Caco-2 cell monolayer by endocytosis.

To evaluate the involvement of paracellular route, in the permeation of LHD, we used ethylene glycol tetra acetic acid (EGTA; a calcium chelating agent) to open the tight junction in Caco-2 cell monolayer. The relative permeated amounts of LHD in the presence of EGTA from A to B and from B to A directions were 127.0±1.8 and 158.7±1.6%, respectively (Fig. 4D). Under the same condition, however, the relative amounts of

Fig. 4. The mechanism studies of DMSO–LHD permeation through a Caco-2 cell monolayer. (A) The relative permeation of 0.5 mg/ml of DMSO–LHD in the A to B direction in the presence of different concentrations (0, 5, 10, 25, 50, 100, and 200 μM) of sodium taurocholate to inhibit active transport. (B) The relative permeability of 0.5 mg/ml of DMSO–LHD in the A to B and the B to A directions for 2 h in the glucose presence (black bar) or deprivation with 10 mM sodium azide (white bar). (C) The relative permeation of 0.5 mg/ml of DMSO–LHD for 2 h in the A to B and the B to A directions through Caco-2 cell monolayers (black bar) or Caco-2 cell monolayers pre-treated with 2.5 μM colchicine for 30 min (white bar). (D) Relative permeation of 0.5 mg/ml of DMSO–LHD for 2 h in the A to B and the B to A directions through Caco-2 cell monolayer pre-treated with 2.5 mM EGTA. As a paracellular marker, Caco-2 cell monolayers were separately treated with 100 μM of Lucifer yellow. Data are expressed as means±SEM (n=5). Black bar: no treatment (control); white bar: absence of glucose or treatment with colchicine or EGTA.

permeated Lucifer yellow (a general paracellular transport marker) from A to B and from B to A directions were 1050.1 ± 78.0 and 1013.6±88.6%, respectively. Therefore, the increase of permeated amount of LHD due to EGTA was negligible, compared to Lucifer yellow.

3.4. Visualization of LHD permeation through Caco-2 cell monolayer

To visualize LHD permeation through Caco-2 cell monolayers, fluorescein-labeled LHD or LMWH with or without DMSO pre-formulation were treated to Caco-2 cell monolayers for 2 h. The fluorescein-LMWH failed to completely permeate through monolayers, whereas fluorescein-labeled DMSO–LMWH was intermittently detected in Caco-2 cell monolayers (Fig. 5A, B). On the other hand, the fluorescein-labeled DMSO–LHD showed a typical image pattern of transcellular permeation (Fig. 5C). The fluorescent image intensity of the fluorescein-labeled LHD was reduced, compared to Fig. 5C, since LHD was not completely dissolved in buffer (Fig. 5D).

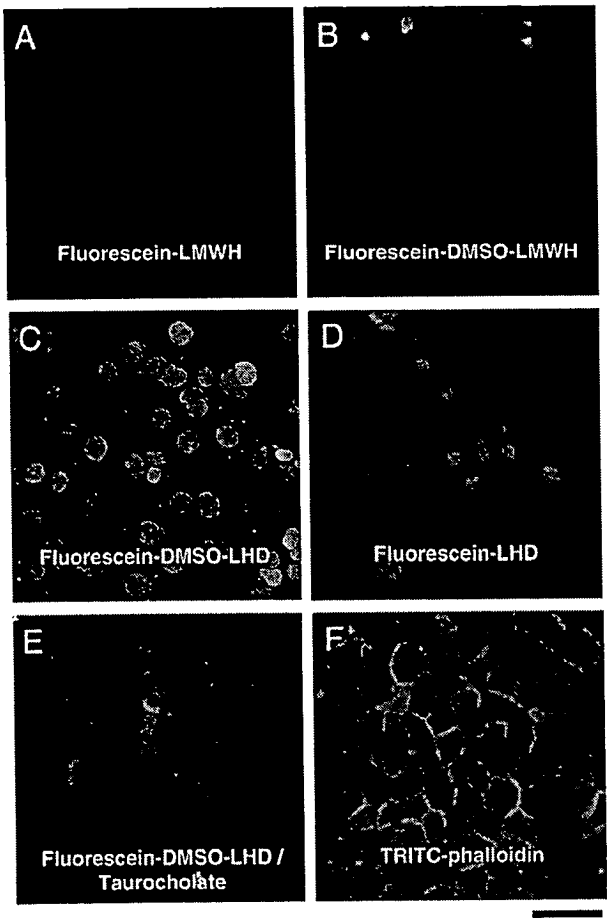

Fig. 5. Confocal laser scanning microscopic images of Caco-2 cell monolayers. Caco-2 cell monolayers treated with fluorescein-labeled LMWH for 30 min (A), DMSO–LMWH for 30 min (B), DMSO–LHD for 30 min (C), LHD for 30 min (D), DMSO–LHD for 30 min after pre-treatment with 200 μM taurocholate for 30 min (E). Confirmation that DMSO caused no tight junction damage between Caco-2 cells by staining with TRITC-phalloidin after treatment of 10% DMSO for 30 min (F) (bar 10 μm).

Moreover, the fluorescein-labeled DMSO–LHD in the presence of 200 mM sodium taurocholate (Fig. 5E) also showed a reduced fluorescent image, compared to Fig. 5C. The actin filament (F-actin) in tight junction was stained using TRITC-labeled phalloidin after incubating Caco-2 cell monolayers for 2 h in 10% DMSO solution (Fig. 5F).

4. Discussion

We describe here the absorptive properties of an orally active low molecular weight heparin conjugate with DOCA, *i.e.*, LHD. The conjugated hydrophobic DOCA molecules increase the hydrophobicity of heparin and aid its ability to penetrate the intestinal membrane. In addition, DOCA can interact with bile acid transporters in the intestine and thus aid heparin absorption. LHD absorption occurs in mainly jejunum and ileum of the small intestine, especially, in the ileum because IBAT is highly expressed in this region. Moreover, the absorption of LHD was found to occur primarily via a transcellular route.

It was possible that LHD formed a self-assembled particle in aqueous solution because it has amphiphilic characteristics due to the presence of hydrophilic heparin and hydrophobic DOCA. Therefore, we used DMSO as a solubilizer, since it is a good solvent of DOCA. Compared to the DMSO free formulation, the bioavailability of LHD was 3 folds higher in DMSO formulation. On the other hand, the oral absorption of DMSO–LMWH, *i.e.*, without DOCA, in the monkey model was negligible. This result suggested that DMSO itself did not have any enhancing effect on the absorption of LMWH in the intestine.

After treating monkeys with 10 mg/kg DMSO–LHD, the plasma concentration of LHD was maintained at higher than 0.1 IU/ml for 8 h, which is a therapeutic concentration for treating DVT and PE. Therefore, this study suggested that the designed orally active heparin derivative, LHD, could be potentially administered for a long term to prevent venous thromboembolism in hospitalized patients and/or in outpatients.

In the mechanism study, the permeation of LHD in Caco-2 cell monolayer from A to B was higher than that from B to A, indicating the possibility of the interaction between LHD and the cell membrane. The dose dependency of LHD permeation, that the LHD permeability was decreased with the increase of LHD concentration, also showed the possibility of the interaction of LHD to the cell membrane. Such a low apparent permeability of LHD at high concentration would be induced by the saturation of interaction between LHD and the Caco-2 cell membrane. The result of inhibition test using sodium taurocholate showed that the interaction mentioned above was between LHD and ileal bile acid transporters. These results were also supported by the animal study that the amount of permeated fluorescein-labeled LHD in the ileum was higher than jejunum. However, the permeation of LHD was not further reduced above 25 μM of sodium taurocholate and the relative permeated amount of LHD reached at a constant level about 65%. This result suggested that about 35% of LHD permeation was attributed to the bile acid transporter and about 65% LHD permeation was due to non-specific absorption. On the other

hand, the permeation result using sodium azide did not show any differences from that in the absence of sodium azide, that is, there was no active transport. Therefore, LHD did not permeate through the bile acid transporters even though LHD interacted with ileal bile acid transporters. However, the interaction between LHD and bile acid transporters would be important to enhance the concentration gradient of LHD across the intestinal wall, and LHD permeated through the transcellular pathway by a simple diffusion.

5. Conclusion

The proposed heparin derivative, LHD, in a DMSO formulation could be highly absorbable in the intestine, that is, 10 mg/kg of LHD could match the dose for the prevention of deep vein thrombosis. The conjugated DOCA could interact with ileal bile acid transporters, thereby increasing its concentration at the intestinal wall, and LHD permeate intestinal wall through the transcellular pathway by a simple diffusion. Therefore, LHD showed a high potential to be applied to prevent deep vein thrombosis for a long term, and it could provide a clinically effective option as a new strategy for oral macromolecule drug delivery.

Acknowledgement

This study was supported by the grant from the Mediplex Corp. in Republic of Korea.

References

[1] C.S. Landefiled, P. Hanus, Economic burden of venous thromboembolism, in: S.Z. Goldhaber (Ed.), Prevention of Venous Thromboembolism, Marcel Dekker, New York, 1993, pp. 69–85.
[2] J.S. Alpert, J.E. Dalen, Epidemiology and natural history of venous thromboembolism, Prog. Cardiovasc. Dis. 36 (1994) 417–422.
[3] R. Hull, T. Delmore, E. Genton, J. Hirsh, M. Gent, D. Sackett, D. McLoughlin, P. Armstrong, Warfarin sodium versus low-dose heparin in the long-term treatment of venous thrombosis, N. Engl. J. Med. 301 (1979) 855–858.
[4] T.M. Hyers, R.D. Hull, J.G. Weg, Antithrombotic therapy for venous thromboembolic disease, Chest 108 (1995) 335S–351S (suppl).
[5] R. Hull, T. Delmore, C. Carter, J. Hirsh, E. Genton, M. Gent, G. Turpie, D. McLaughlin, Adjusted subcutaneous heparin versus warfarin sodium in the long-term treatment of venous thrombosis, N. Engl. J. Med. 306 (1982) 189–194.
[6] J.G. Hardman, L.E. Limbird, P.B. Molinoff, R.W. Ruddon, A.G. Gilman, The Pharmacological Basis of Therapeutics, vol. 9, McGraw-Hill, New York, 1996.
[7] M.D. Gonze, K. Salartash, W.C. Sternbergh III, R.A. Baughman, A. Leone-Bay, S.R. Money, Orally administered unfractionated heparin with carrier agent is therapeutic for deep venous thrombosis, Circulation 101 (2000) 2658–2661.
[8] F.G.P. Welt, T.C. Woods, E.R. Edelman, Oral heparin prevents neointimal hyperplasia after arterial injury. Inhibitory potential depends on type of vascular injury, Circulation 104 (2001) 3121–3124.
[9] R.A. Baughman, S.C. Kapoor, R.K. Agarwal, J. Kisicki, F. Catella-Lawson, G.A. FitzGerald, Oral delivery of anticoagulant doses of heparin. A randomized, double-blind, controlled study in humans, Circulation 98 (1998) 1610–1615.
[10] Y. Jiao, N. Ubrich, V. Hoffart, M. Marchand-Arvier, C. Vigneron, M. Hoffman, P. Maincent, Anticoagulant activity of heparin following oral administration of heparin-loaded microparticles in rabbits, J. Pharm. Sci. 91 (2002) 760–768.
[11] Y. Lee, H.T. Moon, Y. Byun, Preparation of slightly hydrophobic heparin derivatives which can be used for solvent casting in polymeric formulation, Thromb. Res. 92 (1998) 149–156.
[12] Y. Lee, S.H. Kim, Y. Byun, Oral delivery of new heparin derivatives in rats, Pharm. Res. 17 (2000) 1259–1264.
[13] Y. Lee, J.H. Nam, H. Shin, Y. Byun, Conjugation of low-molecular-weight heparin and deoxycholic acid for the development of a new oral anticoagulation agent, Circulation 104 (2001) 3116–3120.
[14] W. Kramer, D. Corsiero, M. Fredrich, Intestinal absorption of bile acids: paradoxical behavior of the 14 kDa ileal lipid-binding protein in differential photoaffinity labeling, Biochem. J. 333 (1998) 335–341.
[15] W. Kramer, G. Wess, A. Enhen, Modified bile acids as carriers for peptides and drugs, J. Control. Release 46 (1997) 17–30.
[16] S. Kim, B. Vaishali, E. Lee, Y. Byun, Oral delivery of chemical conjugates of heparin and deoxycholic acid in aqueous formulation, Thromb. Res. 117 (2006) 419–427.
[17] I.J. Hidalgo, R.T. Borchardt, Transport of bile acids in human intestinal epithelial cell line Caco-2, Biochim. Biophys. Acta 1035 (1990) 97–103.
[18] C.E. Chandler, L.M. Zaccaro, J.B. Moberly, Transepithelial transport of cholyltaurine by Caco-2 cell monolayers is sodium dependent, Am. J. Physiol. 264 (1993) G1118–G1125.

JOURNAL OF AGRICULTURAL AND FOOD CHEMISTRY

Microbial Metabolites of Ingested Caffeic Acid Are Absorbed by the Monocarboxylic Acid Transporter (MCT) in Intestinal Caco-2 Cell Monolayers

YUTAKA KONISHI*,† AND SHOKO KOBAYASHI‡

Applied Bioresearch Center, Research & Development Department, Kirin Brewery Company, Ltd., 3 Miyaharacho, Takasaki-shi, Gunma 370-1295, Japan, and Department of Food and Life-science, Takasaki University of Health and Welfare, Takasaki 370-0033, Japan

It was previously reported that *m*-coumaric acid, *m*-hydroxyphenylpropionic acid (*m*HPP), and 3,4-dihydroxyphenylpropionic acid (DHPP) are major metabolites of ingested caffeic acid formed by gut microflora and would be transported by the monocarboxylic acid transporter (MCT). We have directly measured their absorption characteristics in Caco-2 cells using a coulometric detection method involving HPLC-ECD. The proton-coupled directional transport of *m*-coumaric acid, *m*HPP, and DHPP was observed, and the transport was inhibited by an MCT substrate. The permeation of *m*-coumaric acid and *m*HPP was concentration-dependent and saturable: The Michaelis constant for *m*-coumaric acid and *m*HPP was 32.5 and 12.9 mM, respectively, and the maximum velocity for *m*-coumaric acid and *m*HPP was 204.3 and 91.2 nmol $(min)^{-1}$ $(mg\ protein)^{-1}$, respectively. By contrast, the permeation of DHPP was nonsaturable even at 30 mM and was inversely correlated with the paracellular permeability of Caco-2 cells. Our results demonstrate that these compounds are absorbed by the MCT, although DHPP is mainly permeated across Caco-2 cells via the paracellular pathway. MCT-mediated absorption of phenolic compounds per se and their colonic metabolites would exert significant impact on human health.

KEYWORDS: Caffeic acid; monocarboxylic acid transporter; microbial metabolite; Caco-2

INTRODUCTION

Epidemiological studies indicate an association between consumption of whole grain products and prevention of chronic diseases such as coronary diseases (*1*) and certain forms of cancer (*2*). Various nutrients in whole grain cereals, such as fiber, vitamins, minerals, and phenolic compounds, have been assumed to exert gastrointestinal effects and antioxidant protection, although the exact mechanism is still unclear (*3*). The hydroxycinnamic acids are a major class of phenolic compounds in cereal bran, mainly present as esters linked to polymers in the cell wall (*4*, *5*). Caffeic acid is the main representative of the hydroxycinnamic acids and occurs in foods mainly as chlorogenic acid (5-caffeoylquinic acid), an ester of quinic acid. Coffee is a major source of chlorogenic acid in the diet; other dietary sources include fruit, such as apples, pears, and berries (*6*).

Caffeic acid has vicinal hydroxyl groups on an aromatic residue and exhibits antioxidant activities and antimutagenic and carcinogenic effects in vitro (*7*, *8*). This is consistent with the reported inverse correlation between coffee intake and colon cancer in some epidemiological studies (*9*–*11*). The physiological importance of caffeic acid is dependent upon its availability for intestinal absorption and subsequent interaction with target tissues. However, the microbial metabolites of the ingested parent compound and their biological properties must be fully investigated to understand the health benefits of dietary polyphenols. *m*-Coumaric acid, *m*-hydroxyphenylpropionic acid (*m*HPP), and 3,4-dihydroxyphenylpropionic acid (DHPP) are major metabolites of ingested caffeic acid, formed by gut microflora (**Figure 1**), and have been considered to exert physiological effects through the prevention of antioxidant stress

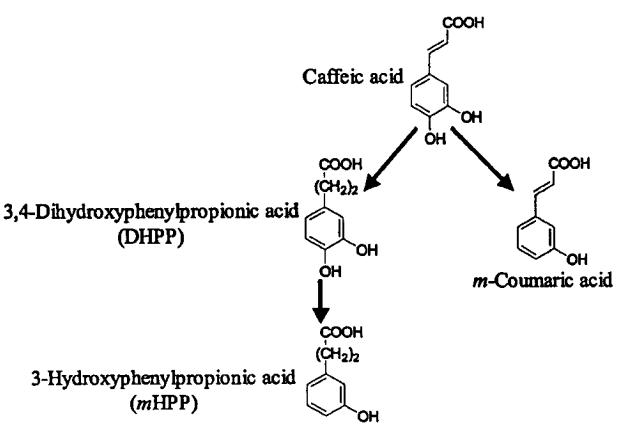

Figure 1. Metabolic pathway of caffeic acid metabolized by gut microflora.

* To whom correspondence should be addressed. Tel: +81-27-346-9441; fax: +81-27-346-9985; e-mail: konishiy@kirin.co.jp.
† Kirin Brewery Co., Ltd.
‡ Takasaki University of Health and Welfare.

10.1021/jf049560y CCC: $27.50
Published on Web 09/28/2004

(*12*, *13*). However, the absorption characteristics of caffeic acid per se and their colonic metabolites are still obscure.

Recently, we established that measuring the competitive effect of dietary substances on the transport of fluorescein, a substrate of the monocarboxylic acid transporter (MCT), is a useful means of identifying compounds that can be transported by the MCT (*14*). MCT-mediated transport of dietary phenolic acids, such as ferulic and *p*-coumaric acids, was demonstrated using this method (*15*, *16*). Furthermore, we previously reported that caffeic acid is mainly absorbed via the paracellular pathway, whereas *m*-coumaric acid and *m*HPP seem to be absorbed by the MCT since they showed competitive inhibition of fluorescein transport (*17*). This study was designed to reveal the absorption mechanisms of *m*-coumaric acid, *m*HPP, and DHPP by directly measuring their transepithelial transport across Caco-2 cells as an in vitro model of intestinal absorption and metabolism (*18*–*20*).

MATERIALS AND METHODS

Materials. The human colon adenocarcinoma cell line Caco-2 was obtained from the American Type Culture Collection (Rockville, MD). Dulbecco's modified Eagle's medium (DMEM) was purchased from Nissui Pharmaceuticals (Tokyo). Fetal calf serum, glutamine, nonessential amino acids, penicillin, streptomycin (10 000 units/mL and 10 mg/mL in 0.9% sodium chloride, respectively), phosphate-buffered saline, and Hank's balanced salt solution (HBSS) were all purchased from Invitrogen Corp. (Carlsbad, CA). Type I collagen was purchased from Nitta Gelatin Inc. (Osaka, Japan). Plastic dishes, plates, and Transwell inserts with 0.4-μm polycarbonate membranes (12 mm in diameter) were obtained from Corning (Corning, NY). *m*-Coumaric acid, *m*HPP, and DHPP were from Wako Pure Chemicals Inc, Ltd. (Osaka, Japan). All other chemicals used in this study were of analytical grade.

Cell Culture. Caco-2 cells were cultured in DMEM containing 10% fetal calf serum, 1% nonessential amino acids, 4 mM L-glutamine, 50 IU/mL penicillin, and 50 μg/mL streptomycin, together with sodium bicarbonate to adjust the pH to 7.4. The cells were incubated at 37 °C in a humidified atmosphere of 5% CO_2 in air. The monolayers became confluent 6 to 7 days after seeding with 1×10^5 cells per 100-mm dish. Cells were passaged at a split ratio of 4 to 8 by treatment with 0.1% trypsin and 0.02% EDTA acid in HBSS. All cells used were between passages 56 and 70.

Measurement of Transepithelial Electrical Resistance (TER). Cells were grown for TER measurement in Transwell inserts with the semipermeable membrane first coated with type I collagen (12-mm diameter and 0.4-μm pore size, Corning Costar, NY). The cells were seeded at a density of $1 \times 10^5/cm^2$, and the medium was changed every 1 or 2 days. Monolayers were formed after culturing for 2 weeks. The integrity of the cell layer was evaluated by measurement of TER with Millicell-ERS equipment (Millipore, MA). Monolayers with TER of more than 250 $\Omega \cdot cm^2$ were used for the experiments. The TER of the monolayer was measured before and after an assay sample was added to the insert.

Transepithelial Transport Experiments. To measure the apical-to-basolateral permeability, 1.5 mL of HBSS (pH 7.4, 37 °C) was added to the basal chamber of the Transwell insert, and 0.5 mL of the test solution (pH 6.0 or 7.4, 37 °C) containing *m*-coumaric acid (1 mM), *m*HPP (1 mM), or DHPP (5 mM) was added to the apical side. At a designated time after incubation at 37 °C, the basal solution was collected and replaced by an equal volume of HBSS. The amount of *m*-coumaric acid, *m*HPP, or DHPP transported by Caco-2 cells was estimated using an HPLC-electrochemical detector (ECD) with an ESA coulometric detection system (ESA Inc., Boston). The results were expressed in terms of specific permeability ($\mu L/cm^2$), which was calculated as the amount transported divided by the initial concentration in the donor compartment.

To examine the basolateral-to-apical transport, HBSS (pH 6.0 or 7.4, 37 °C) was added to the apical side, and 1.5 mL of the test solution (pH 7.4, 37 °C) was added to the basolateral side.

Chromatographic Conditions. An HPLC-ECD fitted with a coulometric detection system was used in the analysis, as previously reported (*17*). Chromatographic separation was performed on a C18 column (ODS150, MC Medical, Inc., Tokyo, Japan). The mobile phase A (Solvent A) was 50 mM sodium acetate containing 5% methanol (pH 3.0 adjusted with phosphoric acid), while mobile phase B (Solvent B) was 50 mM sodium acetate containing 40% acetonitrile and 20% methanol (pH 3.5 adjusted with phosphoric acid). The elution profile (0.6 mL/min) was as follows: 0−28.5 min, linear gradient from 85% solvent A/15% solvent B to 20% solvent A/80% solvent B; 28.5−31 min, isocratic elution 0% solvent A/100% solvent B; 31−35 min, isocratic elution 85% solvent A/15% solvent B. To measure the amount of *m*-coumaric acid, the eight electrode detector potentials measured at 100−800 mV in increments of 100 mV and were from 0 to 700 mV in increments of 100 mV to measure the amount of *m*HPP and DHPP.

Distribution of *m*-Coumaric Acid, *m*HPP, and DHPP after Transport Experiments. At the end of the transport experiments, the level of *m*-coumaric acid, *m*HPP, or DHPP in the apical and basolateral solutions was measured. Monolayer cells were rinsed with HBSS (pH 6.0 or 7.4) and extracted with methanol/Solvent A (10:1, v/v) for 30 min. *m*-Coumaric acid, *m*HPP, or DHPP in this extract was measured and used as an index of the intracellular fractions taken up by the Caco-2 cells.

Data Analysis. The amount transported [nmol (mg protein)$^{-1}$] against time (in minutes) was plotted and the permeation rate [nmol min^{-1} (mg protein)$^{-1}$], J, was evaluated from the slope of the initial linear part of the plot, calculated by linear regression analysis. The kinetic parameters for saturable transport across Caco-2 cells were estimated by fitting eq 1 using the nonlinear least-squares regression analysis program, MULTI (*21*):

$$J = J_{max}[C]/(K_t + [C]) \quad (1)$$

where C is the initial concentration of the substrate, J_{max} is the maximum permeation rate, and K_t is the Michaelis−Menten constant. Results are expressed as the means ± SD. Statistical analysis was performed using Student's two-tailed t-test, and differences with $P < 0.01$ were considered significant.

RESULTS

HPLC Analysis of *m*-Coumaric Acid, *m*HPP, and DHPP Transported across Caco-2 Cell Monolayers. Representative chromatograms of *m*-coumaric acid, *m*HPP, or DHPP transported (**Figure 2**) into the basolateral solution are presented in **Figure 2**. *m*-Coumaric acid, *m*HPP, or DHPP were determined at a detection limit of <0.5 pmol on the column: reproducibility was good and did not require any sample pretreatment. Peak purity was assessed using the peak area ratio accuracies from oxidation channels (lower or upper) adjacent to the dominant oxidation channel. The voltametric response of analyte across these channels was unique for each compound, and more than 70% ratio accuracy was considered to support the peak purity (*22*). The retention time (RT) and dominant oxidation potential for *m*-coumaric acid, *m*HPP, and DHPP are 17.3 min, 700mV; 15.9 min, 600mV; and 10.2 min, 200mV, respectively.

Characteristics of Transepithelial Transport of *m*-Coumaric Acid, *m*HPP, and DHPP. The bidirectional permeation of *m*-coumaric acid (1 mM), *m*HPP (1 mM), or DHPP (5 mM) across Caco-2 cell monolayers was examined in the presence and absence of an inwardly directed proton gradient (**Figure 3**). *m*-Coumaric acid, *m*HPP, and DHPP exhibited pH-dependent directional transport from the apical to the basolateral side ($J_{ap \to bl}$ and $J_{bl \to ap}$ being 7.23 and 0.44 nmol/min/mg protein, respectively, for *m*-coumaric acid; 7.47 and 0.34 nmol/min/mg protein, respectively, for *m*HPP; 2.27 and 0.33 nmol/min/mg protein, respectively, for DHPP: apical pH, 6.0; basolateral pH, 7.4). In the absence of a proton gradient (apical pH, 7.4; basolateral pH, 7.4), $J_{ap \to bl}$ of *m*-coumaric acid (0.48 nmol/min/mg protein)

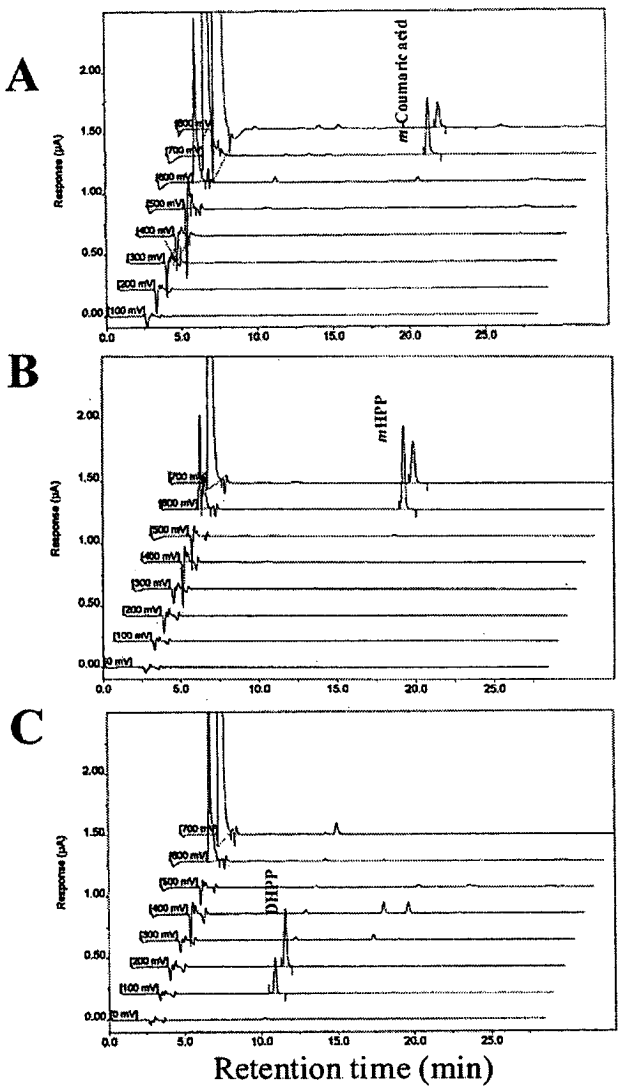

Figure 2. Chromatograms of *m*-coumaric acid (**A**), *m*HPP (**B**), and DHPP (**C**) transported across Caco-2 cell monolayers.

was almost the same as that of $J_{bl \rightarrow ap}$ (0.54 nmol/min/mg protein), whereas the $J_{ap \rightarrow bl}$ of *m*HPP and DHPP (0.57 or 0.43 nmol/min/mg protein) was greater than the $J_{bl \rightarrow ap}$ (0.36 or 0.24 nmol/min/mg protein), which is characteristic of polarized transport.

Distribution of *m*-Coumaric Acid, *m*HPP, and DHPP. After transport experiments in the absence of a proton gradient (apical pH, 7.4; basolateral pH, 7.4), >98% of apically loaded *m*-coumaric acid, *m*HPP, or DHPP was retained on the apical side, suggesting they were restricted by the tight junctions (**Table 1**). In the presence of a proton gradient (apical pH, 6.0; basolateral pH, 7.4), a considerable amount of *m*-coumaric acid, *m*HPP, and DHPP was transported to the basolateral side, although there was greater transport of *m*-coumaric acid and *m*HPP compared with DHPP. Transport to the basolateral side is likely to be dependent on the pH gradient; however, DHPP was mainly restricted by the tight junction, similar to caffeic acid (*17*).

Concentration Dependence of *m*-Coumaric Acid, *m*HPP, and DHPP Transport. **Figure 4** shows the relationship between the initial permeation rate of *m*-coumaric acid, *m*HPP, and DHPP and their concentration (apical pH, 6.0; basolateral pH, 7.4).

Table 1. Distribution of *m*-Coumaric Acid, *m*HPP, and DHPP after Transepithelial Transport Experiments in the Presence and Absence of a Proton Gradient[a]

	% compound recovered from		
pH gradient	apical side	basolateral side	cells
	m-Coumaric Acid		
6.0/7.4	85.84 ± 0.39	13.74 ± 0.39	0.42 ± 0.01
7.4/7.4	98.55 ± 0.05	1.34 ± 0.04	0.12 ± 0.09
	*m*HPP		
6.0/7.4	82.38 ± 0.51	16.90 ± 0.58	0.72 ± 0.07
7.4/7.4	98.49 ± 0.07	1.29 ± 0.08	0.22 ± 0.01
	DHPP		
6.0/7.4	97.75 ± 0.55	1.71 ± 0.06	0.54 ± 0.12
7.4/7.4	99.41 ± 0.06	0.40 ± 0.10	0.20 ± 0.04

[a] Transepithelial transport experiments were performed as described in Materials and Methods both in the presence and absence of a proton gradient (apical pH, 6.0 or 7.4; basolateral pH, 7.4). Values are the mean ± SD of three or more experiments.

Table 2. Effect of Various Compounds on *m*-Coumaric Acid, *m*HPP, and DHPP Transport across Caco-2 Cell Monolayers in the Presence of a Proton Gradient[a]

	relative permeation (% of control)		
	m-coumaric acid	*m*HPP	DHPP
NaN_3 10 mM	10.2 ± 2.1[b]	12.4 ± 2.1[b]	18.2 ± 2.6[b]
benzoic acid 20 mM	13.8 ± 1.2[b]	20.3 ± 2.8[b]	26.1 ± 3.2[b]
lactic acid 20 mM	104.8 ± 8.9	89.1 ± 9.1	107.2 ± 7.8
acetic acid 20 mM	51.8 ± 4.1[b]	48.7 ± 3.7[b]	33.7 ± 4.8[b]

[a] The amount of transported *m*-coumaric acid, *m*HPP, or DHPP was measured at 37 °C for 40 min by incubating Caco-2 cells in the absence or presence of each compound at the concentration indicated (apical pH, 6.0; basolateral pH, 7.4). Each value represents the mean ± SD of three or more experiments. [b] $P < 0.01$.

The permeation rates of *m*-coumaric acid and *m*HPP were concentration dependent and saturable. The Michaelis constant for *m*-coumaric acid and *m*HPP was 32.5 ± 2.8 and 12.9 ± 3.5 mM, respectively, and the maximum velocity for *m*-coumaric acid and *m*HPP was 204.3 ± 10.4 nmol and 91.2 ± 13.9 nmol $(min)^{-1}$ $(mg\ protein)^{-1}$, respectively. In contrast, the permeation of DHPP was not saturable even at 30 mM, suggesting passive diffusion might be involved. These results are in good agreement with a previous distribution study which suggested that DHPP is mainly permeated via the paracellular diffusion. Lucifer Yellow, a marker compound for paracellular transport, and caffeic acid also showed this trend (*14*, *17*).

Inhibition of Directional Transport of *m*-Coumaric Acid, *m*HPP, and DHPP. To investigate the transport characteristics responsible for proton-coupled polarized transport of *m*-coumaric acid, *m*HPP, or DHPP (apical pH, 6.0; basolateral pH, 7.4), we added 0.1 mM *m*-coumaric acid, 0.1 mM *m*HPP, or 1 mM DHPP to the apical chamber and the effects of various compounds on the permeation were examined (**Table 2**). A metabolic inhibitor, NaN_3, (10 mM) strongly reduced the permeation of *m*-coumaric acid, *m*HPP, and DHPP. Substrates for the MCT (20 mM), such as benzoic acid and acetic acid, significantly inhibited permeation, although lactic acid, a good substrate for MCT1-MCT4 (*23*), had no effect. The order of the inhibitory activity of the MCT substrates was benzoic acid > acetic acid > lactic acid. This order was the same as that for ferulic and *p*-coumaric acid transport, clearly demonstrating that they are transported at least in part by the MCT (*15*, *16*).

Paracellular Transport of DHPP across the Caco-2 Cell Monolayers. Caco-2 cell monolayers exhibiting different TER values were prepared by treating the cells with cytochalasin D

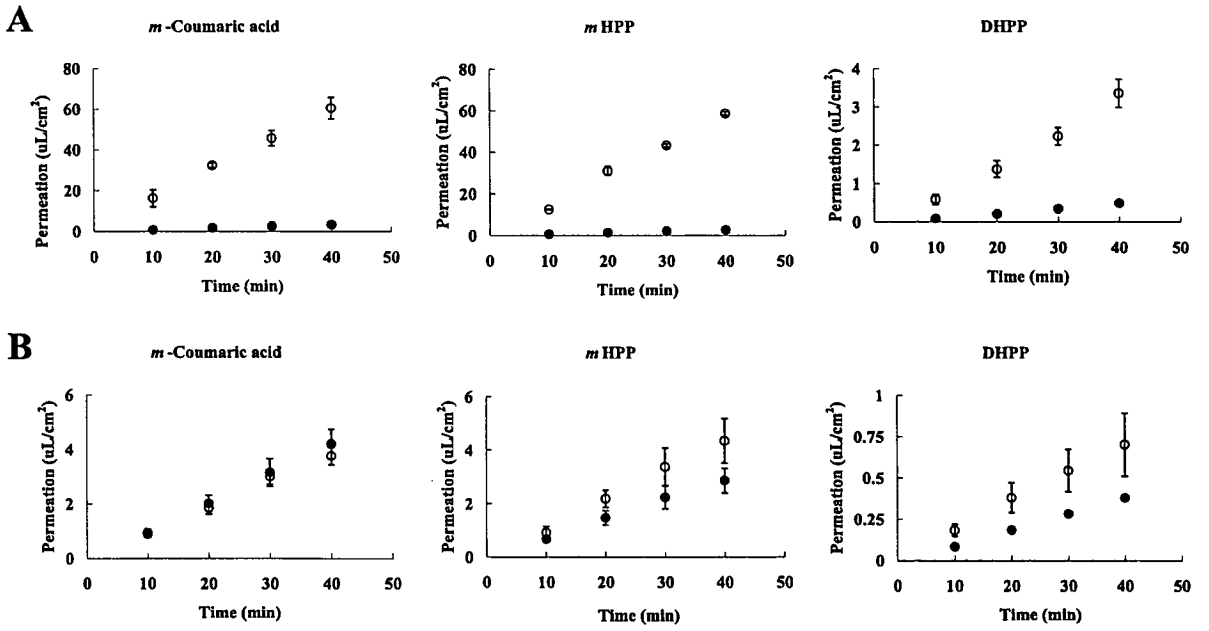

Figure 3. Characteristics of the transepithelial transport of *m*-coumaric acid, *m*HPP, and DHPP across Caco-2 cell monolayers in the presence (A) and the absence (B) of a proton gradient. Permeation of *m*-coumaric acid (1 mM), *m*HPP (1 mM), and DHPP (5 mM) from the apical side to the basolateral side (○) and from the basolateral side to the apical side (●) was measured at 37 °C both in the presence (A) and absence (B) of a proton gradient (apical pH, 6.0 or 7.4; basolateral pH, 7.4). Each point is the mean ± SD of three experiments.

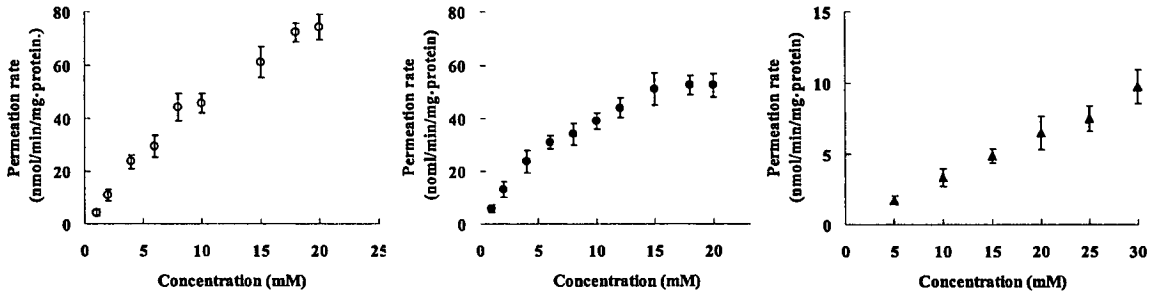

Figure 4. Concentration dependence of *m*-coumaric acid (○), *m*HPP (●), and DHPP (▲) transport across Caco-2 cell monolayers in the presence of a proton gradient. The initial permeation rate is shown. Values are the mean ± SD of three or more experiments.

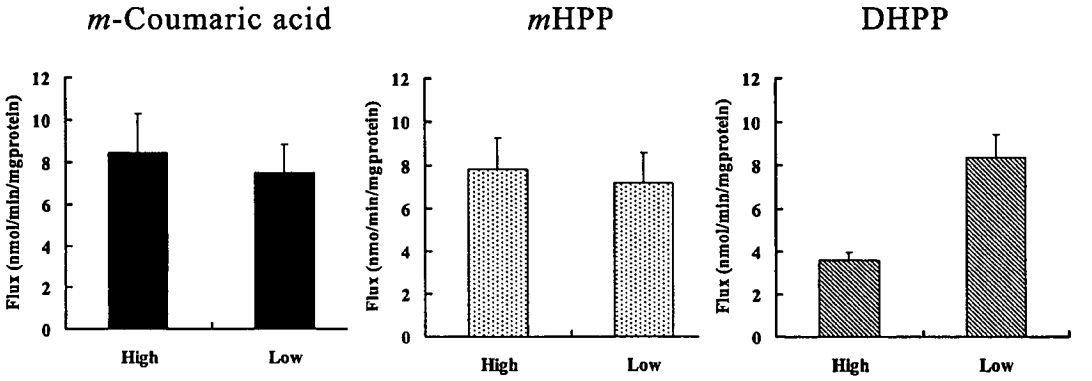

Figure 5. Correlation between TER and the transepithelial flux of *m*-coumaric acid, *m*HPP, and DHPP. *m*-Coumaric acid (1 mM), *m*HPP (1 mM), or DHPP (5 mM) were loaded in the apical side, and the flux from the apical side to the basolateral side was measured at 37 °C (apical pH, 6.0; basolateral pH, 7.4). TER values are indicated as follows: (*m*-coumaric acid), high: 1001 ± 20, low: 319 ± 30; (*m*HPP), high: 940 ± 12, low: 316 ± 28; (DHPP), high: 884 ± 60, low: 294 ± 15. Each point is the mean ± SD of three experiments.

(*14*). The apical-to-basolateral transport of DHPP was then characterized in comparison with that of *m*-coumaric acid and *m*HPP using these monolayers (apical pH, 6.0; basolateral pH, 7.4). As illustrated in **Figure 5**, the transepithelial flux of DHPP was inversely correlated with the TER, whereas the transepithelial flux of *m*-coumaric acid and *m*HPP was almost constant irrespective of the TER, suggesting that DHPP permeates across Caco-2 cells via the paracellular pathways. This result also agreed with the MCT-mediated transport of *m*-coumaric acid and *m*HPP, mentioned above.

DISCUSSION

In our previous study, we reported that *m*-coumaric acid and *m*HPP competitively inhibited fluorescein transport across Caco-2 cells, suggesting they were absorbed by the MCT (*17*). The results were in agreement with the structure of these compounds: both possess a monoanionic carboxyl group and a nonpolar side chain or aromatic hydrophobic moiety, which are thought to be necessary components of a substrate for a MCT (*24*). However, it was not known whether MCT could recognize and transport *m*-coumaric acid and *m*HPP in Caco-2 cells. Hence, the mechanism of intestinal transport of *m*-coumaric acid and *m*HPP together with DHPP, a precursor of *m*HPP, was investigated (**Figure 3**).

The apical-to-basolateral flux ($J_{ap\rightarrow bl}$) of *m*-coumaric acid and *m*HPP in the presence of the proton gradient (7.23 nmol/min/mg·protein for *m*-coumaric acid and 7.47 nmol/min/mg·protein for *m*HPP) was similar to that of ferulic acid (9.79 nmol/min/mg·protein) and greater than that of *p*-coumaric acid (3.73 nmol/min/mg·protein) (*15*, *16*). The $J_{ap\rightarrow bl}$ of *m*-coumaric acid and *m*HPP in the presence of the proton gradient was 13∼15-fold higher than the $J_{ap\rightarrow bl}$ of each in the absence of a proton gradient (0.48 nmol/min/mg·protein for *m*-coumaric acid and 0.57 nmol/min/mg·protein for *m*HPP). The $J_{ap\rightarrow bl}$ of *m*-coumaric acid and *m*HPP was 16∼22-fold higher than the basolateral-to-apical flux ($J_{bl\rightarrow ap}$) of each in the presence of the proton gradient (0.44 nmol/min/mg·protein for m-coumaric acid, 0.34 nmol/min/mg·protein for *m*HPP). The proton-coupled polarized transport of *m*-coumaric acid and *m*HPP is similar to other MCT substrates, such as ferulic acid, *p*-coumaric acid, and fluorescein (*14*−*16*). Considering the results of the distribution study (**Table 1**), and the specific inhibition of this polarized transport by MCT substrate (**Table 2**), the polarized transport seen in this study is presumably mediated by the MCT, as is the case for ferulic and *p*-coumaric acid (*15*, *16*). The concentration-dependent saturable transport of *m*-coumaric acid and *m*HPP (**Figure 4**) also supports this conclusion.

In addition, proton-coupled directional transport of DHPP (5 mM) from the apical to the basolateral side was observed ($J_{ap\rightarrow bl}$; 2.27 nmol/min/mg·protein, $J_{bl\rightarrow ap}$, 0.34 nmol/min/mg·protein: apical pH, 6.0; basolateral pH, 7.4), although the $J_{ap\rightarrow bl}$ was much lower than that of 1 mM *m*-coumaric acid and *m*HPP. The transport of DHPP increased linearly, even at 30 mM (**Figure 4**), and the permeation was inversely correlated with the TER, that is, paracellular permeability of Caco-2 cells (**Figure 5**). This findings were similar to that of caffeic acid at the concentration of 5 mM ($J_{ap\rightarrow bl}$; 2.69 nmol/min/mg·protein, $J_{bl\rightarrow ap}$, 0.59 nmol/min/mg·protein: apical pH, 6.0; basolateral pH, 7.4), indicating that the permeation of DHPP was mainly via paracellular diffusion across Caco-2 cells: DHPP may be absorbed by the MCT, but to a lesser extent (*17*). The result of the distribution study indicated that DHPP was restricted by a tight junction, irrespective of the proton gradient, which is in agreement with the measurements above (**Table 1**). Hydroxylation of MCT substrates, such as benzoic and cinnamic acids, would be predicted to decrease affinity for MCT (*25*). DHPP, a dihydroxy derivative of phenylpropionic acid, may still have some affinity for MCT, though the affinity would be expected to be lesser than that of *m*-coumaric acid and *m*HPP, monohydroxy derivatives of cinnamic or phenylpropionic acids.

We observed directional transport of *m*HPP and DHPP in the apical-to-basolateral direction in the absence of an inwardly directed proton gradient (**Figure 3**); however, this was not true for *m*-coumaric acid. The reason for the polarized transport is not clear; however, the characteristics of the two directional transport systems appear to differ. NaN_3 (10 mM) did not inhibit the directional transport of DHPP, indicating that transport was not energy-dependent, although DIDS (2 mM) inhibited the transport to some extent. On the contrary, HCO_3^- (25 mM) and benzoic acid (20 mM) seemed to increase the permeation of DHPP and decrease the TER of the Caco-2 cells (**Table 3**). Basolateral-loaded DHPP caused an increase in the TER of the Caco-2 monolayer, which would agree with the greater $J_{ap\rightarrow bl}$ over $J_{bl\rightarrow ap}$ (apical pH, 7.4; basolateral pH, 7.4). The inhibitory effect of DIDS is still unknown, but interaction of DIDS with DHPP may occur. In contrast, the permeation of *m*HPP was inhibited by NaN_3 (10 mM), HCO_3^- (25 mM), benzoic acid (20 mM), and, to a lesser extent, DIDS (2 mM). In the absence of a proton gradient, monocarboxylic acids such as lactic acid and benzoic acid are transported by an anion exchanger (*26*). Our results suggest the directional transport of *m*HPP would be via an anion exchanger.

Table 3. Transport Characteristics of *m*-Coumaric Acid, *m*HPP, and DHPP across Caco-2 Cell Monolayers in the Absence of a Proton Gradient[a]

	*m*HPP	DHPP
relative permeation (% of control)		
NaN_3 10 mM	62.4 ± 2.4[b]	93.9 ± 7.0
DIDS 2 mM	80.5 ± 6.5[b]	60.1 ± 7.3[b]
benzoic acid 20 mM	51.5 ± 7.9[b]	133.7 ± 10.4[b]
HCO_3^- 25 mM	45.9 ± 6.9[b]	150.3 ± 13.2[b]
relative TER		
$_{ap\rightarrow bl}$ control	0.80 ± 0.21	0.69 ± 0.16
$_{ap\rightarrow bl}$ NaN_3 10 mM	0.87 ± 0.20	0.65 ± 0.15
$_{ap\rightarrow bl}$ DIDS 2 mM	1.04 ± 0.22	0.70 ± 0.17
$_{ap\rightarrow bl}$ benzoic acid 20 mM	0.77 ± 0.15	0.55 ± 0.11
$_{ap\rightarrow bl}$ HCO_3^- 25 mM	0.73 ± 0.22	0.44 ± 0.03
$_{bl\rightarrow ap}$ control	0.96 ± 0.27	1.41 ± 0.12[b]

[a] The amount of *m*HPP or DHPP transported in the apical-to-basolateral direction was measured at 37 °C for 40 min by incubating Caco-2 cells in the absence or presence of each compound at the concentration indicated (apical pH, 7.4; basolateral pH, 7.4). TER values are expressed as relative to the initial value before the assay. Values are the mean ± SD of three or more experiments. [b] $P < 0.01$.

Recently, the biological effects of microbial metabolites of ingested polyphenols have been focused on, particularly for those poorly absorbed in the small intestine (*12*, *27*−*29*). The total microbial metabolites of ingested chlorogenic or caffeic acids accounted for 57.4% and 28.1%, respectively, of total intake: this includes *m*-coumaric acid, *m*HPP, DHPP, and other metabolites (*12*). Colonic metabolites formed by gut microflora in the gastrointestinal tract have also been reported from various dietary polyphenols. For instance, major phenolic metabolites identified were 3-(*p*)-hydroxyphenylpropionic and 3-phenylpropionic acid for naringin or naringenin and 3,4-dihydroxyphenylacetic acid, 3-(*m*)-hydroxyphenylpropionic acid, and 3-hydroxyphenylacetic acid for rutin or quercetin (*13*). The phenolic degradation products could be generally classified as hydroxylated 3-phenylpropionic acids and the hydroxylated phenylacetic acids, dependent on the structural characteristics of the parent polyphenol. Since these metabolites still possess a free phenolic group, they could have significant reducing and antioxidant properties and therefore protect against oxidative stress, although the monophenolic structure is generally a poorer antioxidant than ortho-diphenolic structures (*30*). Indeed, microbial metabolites such as 3,4-dihydroxyphenylacetic acid and 4-hydroxyphenylacetic acid were more effective than their rutin and quercetin precursors in inhibiting platelet aggregation in vitro (*31*). Considering the higher yield and biological properties of the microbial metabolites in vivo, these bioactive compounds

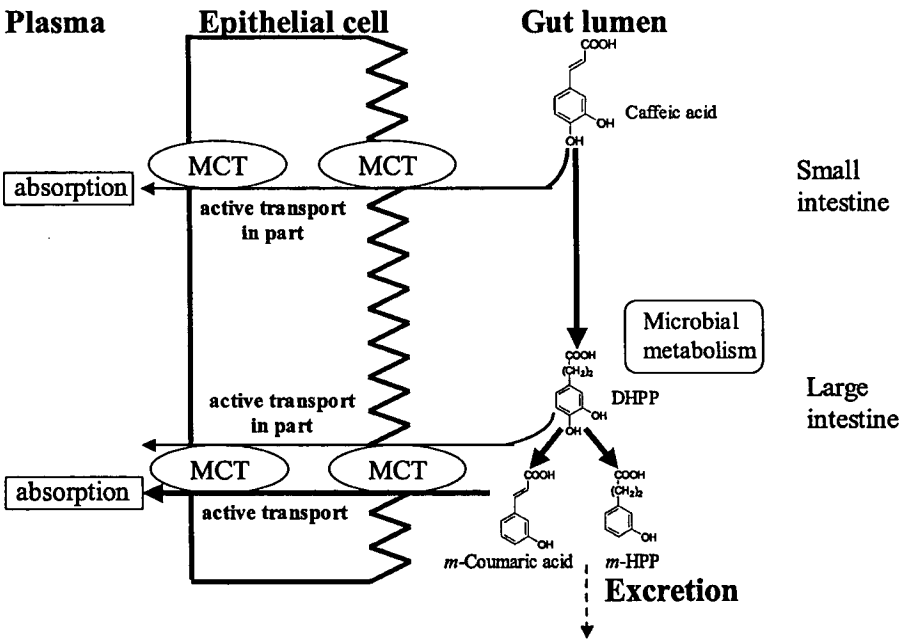

Figure 6. Possible routes for absorption of ingested caffeic acid.

might be responsible for the health effects of dietary polyphenols. However, there is too little information on their absorption and distribution within the body to investigate the health effects of these microbial metabolites. The results obtained in this study, together with data from the literature (*17*), suggest that caffeic acid is absorbed not only via paracellular diffusion, but it is actively absorbed in part by the MCT in the intestine. Furthermore, caffeic acid reaches the large intestine, is metabolized to DHPP, *m*-coumaric acid, and *m*HPP using gut microflora, which are then absorbed by the MCT (**Figure 6**). This clearly shows that the physiological significance of MCT-mediated absorption must be better understood to realize the full health benefits of dietary polyphenols. The high efficacy of MCT-mediated absorption was demonstrated in this study using hydroxylated 3-phenylpropionic acids, *m*HPP, and DHPP. Additional experiments are necessary to understand the absorption characteristics of the hydroxylated phenylacetic acids.

Short-chain fatty acids (SCFA), acetate, propionate, and butyrate, are the most abundant organic anions in the colonic lumen: they are the products of microbial fermentation of undigested carbohydrates and proteins, such as the poorly absorbed polyphenols. SCFA play a pivotal role in maintaining homeostasis in the colon. Butyrate is present in colonic epithelial cells at millimolar concentrations and is the principal energy source (*32*), exerting several biological effects to induce cell differentiation and regulate growth and proliferation of colonic mucosal epithelial cells (*33*, *34*). The mechanism of absorption of butyrate is still debated, although the nonelectrogenic $SCFA^-/HCO_3^-$ antiporter is at least in part involved in its absorption (*35*). Currently, nine isoforms of the MCT have been identified (*23*), but only MCT1-MCT4 are characterized in terms of their substrate and inhibitor kinetics. Each MCT isoform is likely to have a unique biological role, which is related to the different tissue distribution. MCT1 is the most well studied isoform and is found in almost all tissues, that is, heart, skeletal muscle, small intestine, colon, liver, brain, spinal cord, testis, ovary, placenta, and adrenal gland (*36*). It was reported that butyrate is transported by MCT1 (*37*, *38*). Recently, it was determined that butyrate induces an increase in the expression and activity of MCT1, which may serve as a physiological mechanism to maximize intracellular availability of butyrate (*39*). Furthermore, butyrate, taken up by the MCT, reduces colonic paracellular permeability by enhancing peroxisome proliferator-activated receptor γ (PPARγ), which is attributed to preventing inflammation of the colon (*40*). Further identification and characterization of MCT-mediated absorption of dietary components and their microbial metabolites is necessary to clarify the health benefits of whole grains ingested daily.

In conclusion, we have demonstrated that MCT is involved in the absorption of the major microbial metabolites of caffeic acid. *m*-Coumaric acid and *m*HPP are absorbed by the MCT, although DHPP is mainly transported via the paracellular pathways. This suggests a physiological significance of MCT-mediated absorption of dietary components. Further studies on MCT-mediated transport of dietary substances and their colonic metabolites are required to fully understand the health effects of dietary components.

ABBREVIATIONS USED

HBSS, Hanks' balanced salt solution; TER, transepithelial electrical resistance; MCT, monocarboxylic acid transporter; ECD, electrochemical detector, SCFA; short chain fatty acids; PPARγ, peroxisome proliferators-activated receptor γ; *m*HPP, *m*-hydroxyphenylpropionic acid; DHPP, 3,4-dihydroxyphenylpropionic acid

ACKNOWLEDGMENT

We thank K. Hagiwara and Dr. Makoto Shimizu for support during this work.

LITERATURE CITED

(1) Jacobs, D.; Pereira, M.; Slavin, J.; Marquart, L. Defining the impact of whole-grain intake on chronic disease. *Cereal Foods World* **2000**, *45*, 51−53.

(2) Jacobs, D. R.; Marquart, L.; Slavin, J. L.; Kushi, L. H. Whole grain intake and cancer: an expanded review and meta-analysis. *Nutr. Cancer* **1998**, *30*, 85−96.

(3) Slavin, J. L.; Jacobs, D.; Marquart, L.; Wiemer, K. The role of whole grains in disease prevention. *J. Am. Diet. Assoc.* **2001**, *101*, 780−785.

(4) Garcia-Conesa, M. T.; Plumb, G. W.; Waldron, K. W.; Ralph, J.; Williamson, G. Ferulic acid dehydrodimers from wheat bran: Isolation, purification, and antioxidant properties of 8-*O*-4′-diferulic acid. *Redox Rep.* **1997**, *3*, 319−323.

(5) Andreasen, M. F.; Christensen, L. P.; Meyer, A. S.; Hansen, A. Ferulic acid dehydrodimers in rye (*Secale ceresle* L.). *J. Cereal Sci.* **2000**, *31*, 303−307.

(6) Clifford, M. N. Chlorogenic acids and other cinnamates: nature, occurrence, and dietary burden. *J. Sci. Food Agric.* **1999**, *79*, 362−372.

(7) Rice-Evans, C. A.; Miller, N. J.; Paganga, G. Structure-antioxidant activity relationships of flavonoids and phenolic acids. *Free Radical Biol. Med.* **1996**, *20*, 933−956.

(8) Scalbert, A.; Morand, C.; Manach, C.; Remesy, C. Absorption and metabolism of polyphenols in the gut and impact on health. *Biomed. Pharmacother.* **2002**, *56*, 276−282.

(9) Giovannucci, E. Meta-analysis of coffee consumption and risk of colorectal cancer. *Am. J. Epidemiol.* **1998**, *147*, 1043−1052.

(10) Favero, A.; Franceschi, S.; La Vecchia, C.; Negri, E.; Conti, E.; Montella, M. Meal frequency and coffee intake in colon cancer. *Nutr. Cancer* **1998**, *30*, 182−185.

(11) Tavani, A.; Pregnolato, A.; La Vecchia, C.; Negri, E.; Talamini, R.; Franceschi, S. Coffee and tea intake and risk of cancers of the colon and rectum: a study of 3,530 cases and 7,057 controls. *Int. J. Cancer* **1997**, *73*, 193−197.

(12) Gonthier, M. P.; Verny, M. A.; Besson, C.; Remesy, C.; Scalbert, A. Chlorogenic acid bioavailability largely depends on its metabolism by the gut microflora in rats. *J. Nutr.* **2003** *133*, 1853−1859.

(13) Rechner, A. R.; Smith, M. A.; Kuhnle, G.; Gibson, G. R.; Debnam, E. S.; Srai, S. K. S.; Moore, K. P.; Rice-Evans, C. A. Colonic metabolism of dietary polyphenols: influence of structure on microbial fermentation products. *Free Radical Biol. Med.* **2004**, *36*, 212−225.

(14) Konishi, Y.; Hagiwara, K.; Shimizu, M. Transepithelial transport of fluorescein in Caco-2 cell monolayers and its use in *in vitro* evaluation of phenolic acids availability. *Biosci., Biotechnol., Biochem.* **2002**, *66*, 2449−2457.

(15) Konishi, Y.; Shimizu, M. Transepithelial transport of ferulic acid by monocarboxylic acid transporter in Caco-2 cell monolayers. *Biosci. Biotechnol. Biochem.* **2003**, *67*, 856−862.

(16) Konishi, Y.; Kobayashi S.; Shimizu, M. Transepithelial transport of *p*-coumaric acid and gallic acid by monocarboxylic acid transporter in Caco-2 cell monolayers. *Biosci., Biotechnol., Biochem.* **2003**, *67*, 2317−2324.

(17) Konishi, Y.; Kobayashi, S. Transepithelial transport of chrologenic acid, caffeic acid, and their colonic metabolites in intestinal Caco-2 cell monolayers. *J. Agric. Food Chem.* **2004**, *52*, 2518−2526.

(18) Hidalgo, I. J.; Raub, T. J.; Borchardt, R. T. Characterization of the human colon carcinoma cell line (Caco-2) as a model system for intestinal epithelial permeability. *Gastroenterology* **1989**, *96*, 736−749.

(19) Hilgers, A. R.; Conradi, R. A.; Burton, P. S. Caco-2 cell monolayers as a model for drug transport across the intestinal mucosa. *Pharm. Res.* **1990**, *7*, 902−910.

(20) Artursson, P.; Karlsson, J. Correlation between oral drug absorption in humans and apparent drug permeability coefficients in human intestinal epithelial (Caco-2) cells. *Biochem. Biophys. Res. Commun.* **1991**, *175*, 880−885.

(21) Yamaoka, K.; Tanigawara, Y.; Nakagawa, T.; Uno, T. A pharmacokinetics analysis program (MULTI) for microcomputer. *J. Pharmacobiodyn.* **1981**, *4*, 879−885.

(22) Guo, C.; Cao, G.; Sofic, E.; Prior, R. L. High-performance liquid chromatography coupled with coulometric array detection of electroactive components in fruits and vegetables: relationship to oxygen radical absorbance capacity. *J. Agric. Food Chem.* **1997**, *45*, 1787−1796.

(23) Price, N. T.; Jackson, V. N.; Halestrap, A. P. Cloning and sequencing of four new mammalian monocarboxylate transporter (MCT) homologues confirms the existence of a transporter family with an ancient past. *Biochem. J.* **1999**, *329*, 321−329.

(24) Rahman, B.; Schneider, H. P.; Broer, A.; Deitmer, J. W.; Broer, S. Helix 8 and Helix 10 are involved in substrate recognition in the rat monocarboxylate transporter MCT1. *Biochemistry* **1999**, *38*, 11577−11584.

(25) Konishi, Y.; Kubo, K.; Shimizu, M. Structural effects of phenolic acids on transepithelial transport of fluorescein in Caco-2 cell monolayers. *Biosci., Biotechnol., Biochem.* **2003**, *67*, 2014−2017.

(26) Ogihara, T.; Tamai, I.; Tsuji, A. Structural characterization of substrates for the anion exchange transporter in Caco-2 cells. *J. Pharm. Sci.* **1999**, *88*, 1217−1221.

(27) Rechner, A. R.; Kuhnle, G.; Bremner, P.; Hubbard, G. P.; Moore, K. P.; Rice-Evans, C. A. The metabolic fate of dietary polyphenols in humans. *Free Radical Biol. Med.* **2002**, *33*, 220−235.

(28) Chesson, A.; Provan, G. J.; Russell, W. R.; Scobbie, L.; Richardson, A. J.; Stewart, C. Hydroxycinnamic acids in the digestive tract of livestock and humans. *J. Sci. Food Agric.* **1999**, *79*, 373−378.

(29) Gonthier, M. P.; Cheynier, V.; Donovan, J. L.; Manach, C.; Morand C.; Mila, I.; Lapierre, C.; Remesy, C.; Scalbert, A. Microbial aromatic acid metabolites formed in the gut account for a major fraction of the polyphenols excreted in urine of rats fed red wine polyphenols. *J. Nutr.* **2003**, *133*, 461−467.

(30) Glasser, G.; Graefe, E. U.; Struck, F.; Veit, M.; Gebhardt, R. Comparison of antioxidative capacities and inhibitory effects on cholesterol biosynthesis of quercetin and potential metabolites. *Phytomedicine* **2002**, *9*, 33−40.

(31) Kim, D. H.; Jung, E. A.; Sohng, I. S.; Han, J. A.; Kim, T. H.; Han, M. J. Intestinal bacterial metabolism of flavonoids and its relation to some biological activities. *Arch. Pharm. Res.* **1998**, *21*, 17−23.

(32) Cummings J. H. The importance of SCFA in man. *Scand. J. Gastroenterol.* **1984**, *19*, 89−99.

(33) Roediger, W. E. W. Role of anaerobic bacteria in the metaolic welfare of the colonic mucosa in man. *Gut* **1980**, *21*, 793−798.

(34) Scheppach, W.; Bartram, H. P.; Richter, A.; Richter, F.; Liepold, H.; Dusel, G.; Hofstetter, G.; Ruthlein, J.; Kasper, H. Effect of short-chain fatty acid on the human colonic mucosa in vitro. *J. Parent. Enter. Nutr.* **1992**, *16*, 43−48.

(35) Stein, J.; Schroder, O.; Milovic, V.; Caspary, W. F. Mercaptopropionate inhibits butyrate uptake in isolated apical membrane vesicles of the rat distal colon. *Gastroenterologv* **1995**, *108*, 673−679.

(36) Lin, R. Y.; Vera, J. C.; Chaganti, R. S. K.; Golde, D. W. Human monocarboxylate transporter 2 (MCT2) is a high affinity pyruvate transporter. *J. Biol. Chem.* **1998**, *273*, 28959−28965.

(37) Stein, J.; Zores, M.; Schroder, O. Short-chain fatty acid (SCFA) uptake into Caco-2 cells by a pH-dependent and carrier mediated transport mechanism. *Eur. J. Nutr.* **2000**, *39*, 121−125.

(38) Hadjiagapiou, C.; Schmidt, L.; Dudeja, P. K.; Layden, T. J.; Ramaswamy, K. Mechanism of butyrate transport in Caco-2 cells: role of monocarboxylate transporter 1. *Am. J. Physiol. Gastrointest. Liver Physiol.* **2000**, *279*, G775−780.

(39) Cuff, M. A.; Lambert, D. W.; Shirazi-Beechey, S. P. Substrate-induced regulation of the human colonic monocarboxylate transporter, MCT1. *J. Physiol.* **2002**, *539*, 361−371.

(40) Kinoshita, M.; Suzuki, Y.; Saito, Y. Butyrate redices colonic paracellular permeability by enhancing PPARγ activation. *Biochem. Biophys. Res. Commun.* **2002**, *293*, 827−831.

Received for review March 17, 2004. Revised manuscript received July 14, 2004. Accepted August 6, 2003.

JF049560Y

JOURNAL OF AGRICULTURAL AND FOOD CHEMISTRY

Absorption and Bioavailability of Artepillin C in Rats after Oral Administration

YUTAKA KONISHI,*,† YOSHITAKA HITOMI,† MICHIKO YOSHIDA,‡ AND EIJI YOSHIOKA§

Central Laboratories for Frontier Technology, Kirin Brewery Co., Ltd., 1-13-5, Fukuura, Kanazawa-ku, Yokohama-shi, Kanagawa 236-0004, Japan, R&D Laboratory, Functional Food Division, Kirin Brewery Co., Ltd., 3 Miyaharacho, Takasaki-shi, Gunma 370-1295, Japan, and Pharmaceutical Development Laboratories, Pharmaceutical Division, Kirin Brewery Co., Ltd., 2−2 Souja-machi 1 chome, Maebashi-shi, Gunma 371-0853, Japan

Artepillin C (AC), an active ingredient of Brazilian propolis, permeates intact across Caco-2 cells by transcellular passive diffusion. The permeation of AC across Caco-2 cells is as efficient as that of phenolic acids and the microbial metabolites of poorly absorbed polyphenols, which are actively absorbed by the monocarboxylic acid transporter (MCT) (*Biochim. Biophys. Acta* **2005**, *1713*, 138−144). Here, the absorption of orally administered AC in rats has been studied to evaluate its pharmacokinetics and bioavailability in vivo in comparison with those of *p*-coumaric acid (CA), a substrate of MCT. Rats were given 100 μmol/kg of body weight of AC or CA, and blood was subsequently collected from the portal vein and abdominal artery. AC, CA, and their metabolites were quantified by coulometric detection using HPLC−ECD. The serum concentration of intact AC and CA in the portal vein peaked at 5−10 min after administration, with a C_{max} of 19.7 μmol/L for AC and 74.8 μmol/L for CA. The area under the curve (AUC) for intact AC and CA in the portal vein was calculated from the serum concentration as 182.6 and 3057.3 μmol·min·L^{-1}, respectively. The absorption efficiency of CA was about 17-fold higher than that of AC. Furthermore, the bioavailability of CA was about 278-fold higher than that of AC, and the ratio of AUC in the abdominal artery to AUC in the portal vein was 0.04 and 0.70, for AC and CA, respectively. Thus, AC is likely to be more susceptible to hepatic elimination than is CA. The bioactive compound of AC in vivo should be investigated further.

KEYWORDS: Artepillin C; p-coumaric acid; monocarboxylic acid transporter; intestinal absorption; rat

INTRODUCTION

Artepillin C (AC; 3,5-diprenyl-4-hydroxycinnamic acid) is one of the principal phenolic acids present in propolis extract and has been ascribed to various biological activities of the extract, such as its antibacterial, antiviral, and anticarcinogenic properties (*1*−*5*). However, there are very few reports in the literature concerning the absorption, distribution, and excretion of AC. Recently, it was reported that intact AC was readily absorbed by the intestine and gave protection against oxidative stress in vitro, suggesting that AC is the principal bioactive compound in propolis (*6*). As it is considered timely to reevaluate the biological activity and health effects of polyphenols in terms of their bioavailability (*7*), it would be desirable to determine the absorption characteristics and bioavailability of AC in detail.

We have recently elucidated the absorption characteristics of many phenolic acids (i.e. ferulic, *p*-coumaric, gallic, caffeic acids) and related compounds (i.e. chlorogenic, rosmarinic acids) in terms of their affinity for the monocarboxylic acid transporter (MCT) and have demonstrated the diverse nature of the absorption of phenolic compounds in Caco-2 cells (i.e. MCT-mediated absorption, partial MCT-mediated absorption, paracellular diffusion) (*8*−*11*). It has been also shown that the absorption characteristics of these compounds in Caco-2 cells in vitro correlates well with their absorption efficiencies and bioavailabilities in vivo (*12*, *13*). Furthermore, the physiological significance of the microbial metabolites of poorly absorbed parent polyphenols has now been firmly established (*7*); these metabolites are also thought to be absorbed and distributed by MCT, similar to phenolic acids (*14*, *15*). These observations highlight the physiological impact of MCT-mediated absorption and distribution in humans, which involves specific transport systems that act not only for phenolic acids but also for "metabonutrients", that is, microbial metabolites of poorly absorbed polyphenols or dietary fibers having biological activities (*14*, *15*).

The key features of a substrate for MCT are thought to be a monoanionic carboxylic acid group and a nonpolar side chain or aromatic hydrophobic moiety (*16*). Because AC seems to

* To whom correspondence should be addressed. (Tel: +81−45−788−7588; Fax: +81−45−788−4047; E-mail: konishiy@kirin.co.jp).
† Central Laboratories for Frontier Technology.
‡ R&D Laboratory.
§ Pharmaceutical Development Laboratories.

10.1021/jf051962y CCC: $30.25
Published on Web 12/06/2005

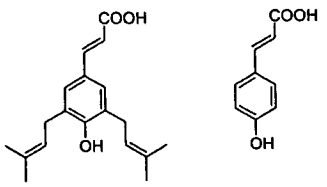

Artepillin C p-Coumaric acid

Figure 1. Chemical structures of AC and CA.

fulfill the structural criteria for a MCT substrate (**Figure 1**), we have previously examined whether AC is transported by MCT and have shown that it mainly permeates intact across Caco-2 cells by transcellular passive diffusion with a permeation efficiency as high as those of MCT substrates (*17*). It is generally considered, however, that the first hepatic elimination of hydrophobic compounds that are absorbed by transcellular passive diffusion is high and that their bioavailability is necessarily low. The current study was designed to examine the intestinal absorption efficiency and bioavailability of AC in vivo by means of pharmacokinetics and to compare them with those of the MCT substrate CA.

MATERIALS AND METHODS

Materials. AC, CA, and sulfatase type H-5 were purchased from Sigma-Aldrich, Inc. (St. Louis, MO). The other chemicals used in this study were of analytical grade.

Animals and Diets. Male Wistar rats (7 weeks old, Charles River Japan, Yokohama, Japan) were housed in an air-conditioned room (22 ± 1 °C) under 12-h dark/12-light cycles, with free access to tap water and a commercial nonpurified CE-2 diet (CLEA Japan, Inc., Tokyo, Japan). Three rats to be administered AC or CA were assigned to each time point of each experimental group. This study was approved by the Ethics Committee of Kirin Brewery Co., Ltd.

Sample Preparation. Rats were fasted for 20 h and their body weight was measured (182−213 g). They were given AC or CA (100 μmol/kg in 50% propyleneglycol) by gastric intubation. Blood was withdrawn from the portal vein and abdominal artery at each time point (5, 10, 20, 30, 60, and 90 min) after the administration of AC or CA. Serum was obtained by centrifugation and was stored at −80 °C until analysis.

HPLC−ECD Analysis. An HPLC−ECD fitted with a coulometric detection system was used to measure the amount of AC, CA, and their conjugates in serum samples according to a previously described method (*14*, *15*). In brief, to 25 μL of serum was added 25 μL of 0.1 mol/L sodium acetate buffer (pH 5.0), and 100 μL of 0.83 mol/L acetic acid in methanol. The mixture was vortexed, sonicated, and centrifuged (at 8500*g* for 5 min at 4 °C), and the supernatant was injected onto an HPLC C18 column (ODS150, MC Medical, Inc., Tokyo, Japan). For AC, mobile phase A (solvent A) was 50 mM sodium acetate containing 40% acetonitrile and 20% methanol (pH 3.0), and mobile phase B (solvent B) was 50 mM sodium acetate containing 80% methanol (pH 3.5). The elution profile (0.6 mL/min) was as follows: 0−28.5 min, linear gradient from 85% solvent A/15% solvent B to 0% solvent A/100% solvent B; 28.5−32 min, isocratic elution 0% solvent A/100% solvent B; 32−35 min, isocratic elution 85% solvent A/15% solvent B. Eight electrode detector potentials (from 200 to 760 mV in increments of 80 mV) were used. For CA, mobile phase A (solvent A) was 50 mM sodium acetate containing 5% methanol (pH 3.0), and mobile phase B (solvent B) was 50 mM sodium acetate containing 40% acetonitrile and 20% methanol (pH 3.5). The elution profile (0.6 mL/min) was as follows: 0−28.5 min, linear gradient from 85% solvent A/15% solvent B to 20% solvent A/80% solvent B; 28.5−31 min, isocratic elution 0% solvent A/100% solvent B; 31−35 min, isocratic elution 85% solvent A/15% solvent B. Eight electrode detector potentials (from 0 to 700 mV in increments of 100 mV) were used. The quantitative determination of AC and CA was performed by using an external standard method, which verified that the detector response was linear for concentrations of up to 400 μmol/L for AC and 600 μmol/L for CA.

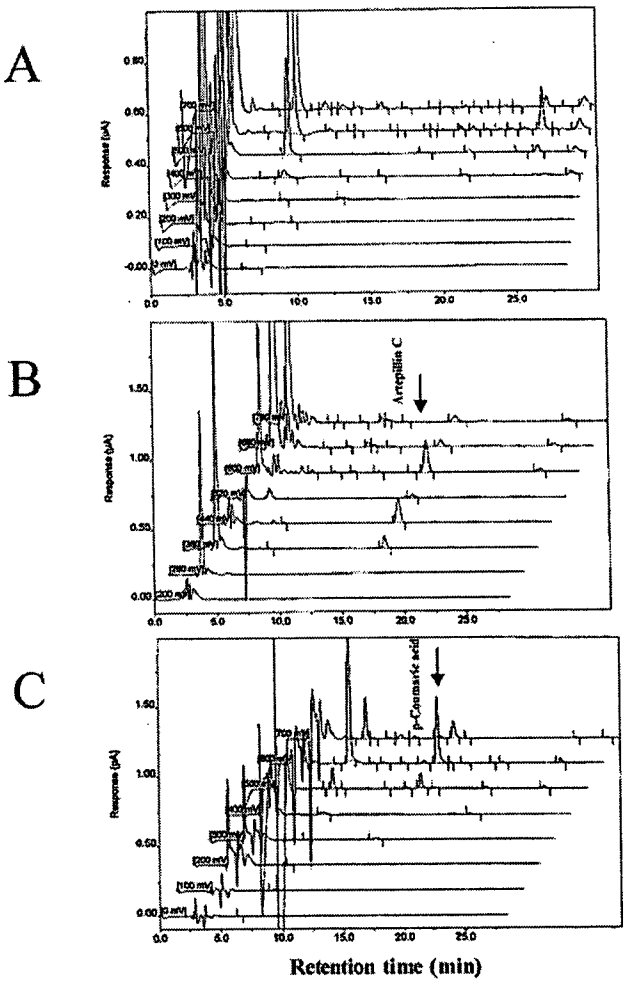

Figure 2. Chromatograms obtained by HPLC−ECD analysis of rat serum before (**A**) and after the administration of AC (**B**) or CA (**C**).

Enzymatic Hydrolysis and Determination of AC or CA Conjugates. Serum (25 μL) was mixed with 25 μL of sulfatase type H-5 solution in 0.1 mol/L acetate buffer (pH 5.0) containing both 12.5 units of sulfatase and about 270 units of β-glucuronidase activity. The mixture was incubated at 37 °C for 45 min. The difference in AC or CA content before and after sulfatase treatment was assumed to be due the amount of the respective sulfate and glucuronide conjugates in the sample.

Data Analysis. Noncompartmental pharmacokinetic parameters were calculated from the serum concentration−time data by using WinNonlin. The measured values were used to determine the maximum serum concentration, C_{max}, and the time, t_{max}, taken to reach C_{max}. The results of C_{max} are expressed as the mean ± SEM of three determinations. The area under the curve (AUC) for the serum concentration−time data from zero to the final sampling time at 1.5 h ($AUC_{0-1.5h}$) was calculated by using the linear/log trapezoidal rule. The elimination half-life ($t_{1/2}$) was calculated from a log−linear regression of the terminal phase of the serum concentration−time profile. AUC and $t_{1/2}$ were calculated by using the mean concentration value at each time point.

RESULTS

Determination of AC and CA in Serum Samples. **Figure 2** shows representative HPLC profiles of serum from a control rat (A), and serum from rats given AC (B) and CA (C). On the basis of a comparison in two dimensions (i.e. chromatographic and voltammetric), the identity of the AC or CA peak was

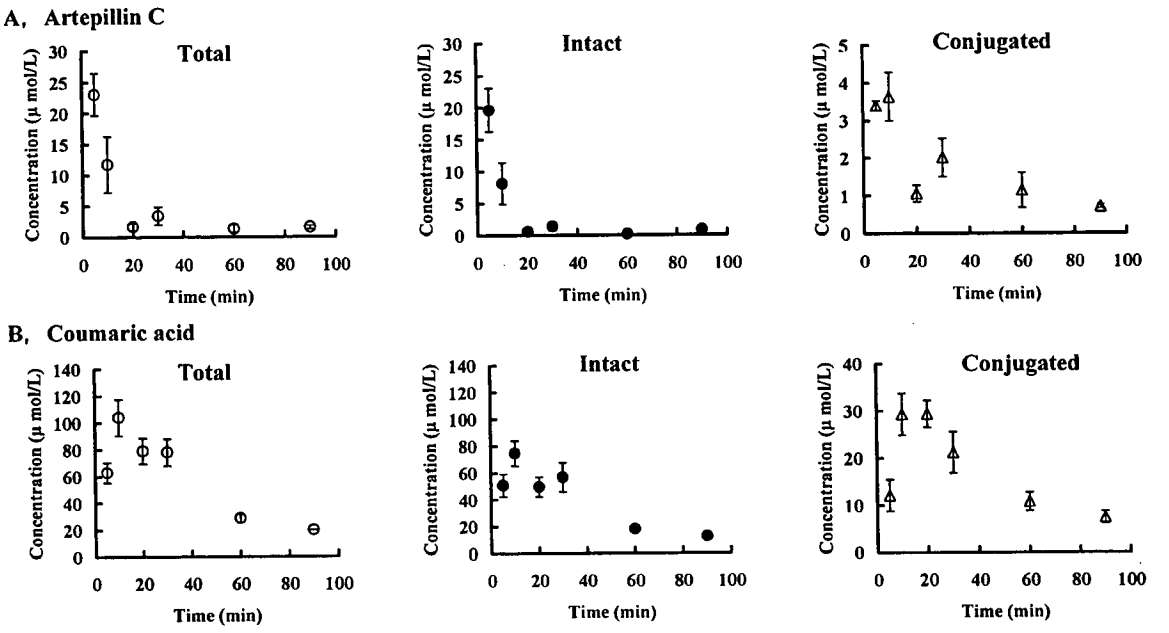

Figure 3. Serum concentration of phenolic acid in the portal vein as a function of time after the administration of AC (A) or CA (B). Each point is expressed as the mean ± SEM, $n = 3$.

determined by evaluating the peak area ratio for the oxidation channels (lower or upper) adjacent to the dominant oxidation channel. An accuracy in the ratio of more than 70% was considered to support peak purity (*18*). The retention time (t_R) and dominant oxidation potential were, respectively, 16.3 min and 440 mV for AC and 14.9 min and 600 mV for CA. Experiments with AC- or CA-spiked serum showed that this procedure gave more than 97% recovery for both compounds throughout the detection range.

Quantitative Changes in AC, CA, and Their Metabolites in Rat Serum. The mean serum concentrations of AC, CA, and their metabolites of sulfate and glucuronide in the portal vein as a function of time after administration are shown in **Figure 3**. The concentrations of total and intact AC and CA were measured after and before deconjugation with sulfatase treatment, and the results of the noncompartmental pharmacokinetics analysis are given in **Table 1**. The intestinal absorption of intact AC and CA was fast: the first and second peak levels were 5 min (19.67 μmol/L) and 30 min (1.39 μmol/L) for AC and 10 min (74.75 μmol/L) and 30 min (56.94 μmol/L) for CA. There was a difference in the AUC in the portal vein (AUC_{portal}) calculated for intact AC and CA. The absorption efficiency of CA was estimated to be 17-fold greater than that of AC. This finding shows that the intestinal absorption efficiency of CA is much higher than that of AC (**Table 1**).

Furthermore, the concentration of AC, CA, and their metabolites in the abdominal artery was investigated as a function of time after administration to clarify hepatic elimination (**Figure 4**), and the results of the noncompartmental pharmacokinetics analysis are also given in **Table 1**. At all time points after administration, there was much less intact AC in the abdominal artery than in the portal vein. In contrast, a large amount of intact CA was detected in the abdominal artery at all time points after administration, and the concentration of CA in the abdominal artery showed the same trend over time as that in the portal vein. Intriguingly, the AUC in the abdominal artery ($AUC_{abdominal}$) for CA was about 278-fold greater than that for AC (**Table 1**).

Table 1. Pharmacokinetic Parameters of Intact AC and CA in the Portal Vein and Abdominal Artery after the Administration of a Single Oral Dose of 100 μmol/kg AC or CA[a]

	AC	CA
Portal Vein		
C_{max},[b] μmol/L	19.67 ± 3.43	74.75 ± 9.27
t_{max}, min	5	10
$AUC_{0-1.5h}$, μmol·min·L^{-1}	182.6	3057.3
$t_{1/2}$, min	86.6	27.5
relative absorption efficiency	16.7	
Abdominal Artery		
C_{max}, μmol/L	0.55 ± 0.12	47.36 ± 9.54
t_{max}, min	5	10
$AUC_{0-1.5h}$, μmol·min·L^{-1}	7.72	2143.0
$t_{1/2}$, min	23.2	27.5
relative bioavailability	277.6	

[a] Abbreviations: AC, artepillin C; CA, *p*-coumaric acid; C_{max}, maximum serum concentration; t_{max}, time to reach the C_{max}; AUC, area under the serum concentration–time curve; $t_{1/2}$, elimination half-life. Relative absorption efficiency was calculated as follows: AUC_{portal} of CA/AUC_{portal} of AC. Relative bioavailability was calculated as follows: $AUC_{abdominal}$ of CA/$AUC_{abdominal}$ of AC. [b] Values of C_{max} are the mean ± SEM, $n = 3$.

The concentration of conjugated AC in the abdominal artery was also much lower than that in the portal vein, although the concentration of conjugated AC in the abdominal artery exhibited the same trend over time as that in the portal vein (**Figures 3** and **4**). In contrast, the concentration profile of conjugated CA in the abdominal artery was nearly the same as that in the portal vein. The noncompartmental pharmacokinetics analysis of conjugated AC and CA is shown in **Table 2**. The AUC and C_{max} of conjugated CA in the portal vein were nearly the same as the corresponding values in the abdominal artery, whereas the values of AUC and C_{max} of conjugated AC were much lower in the abdominal artery than those in the portal vein (**Table 2**).

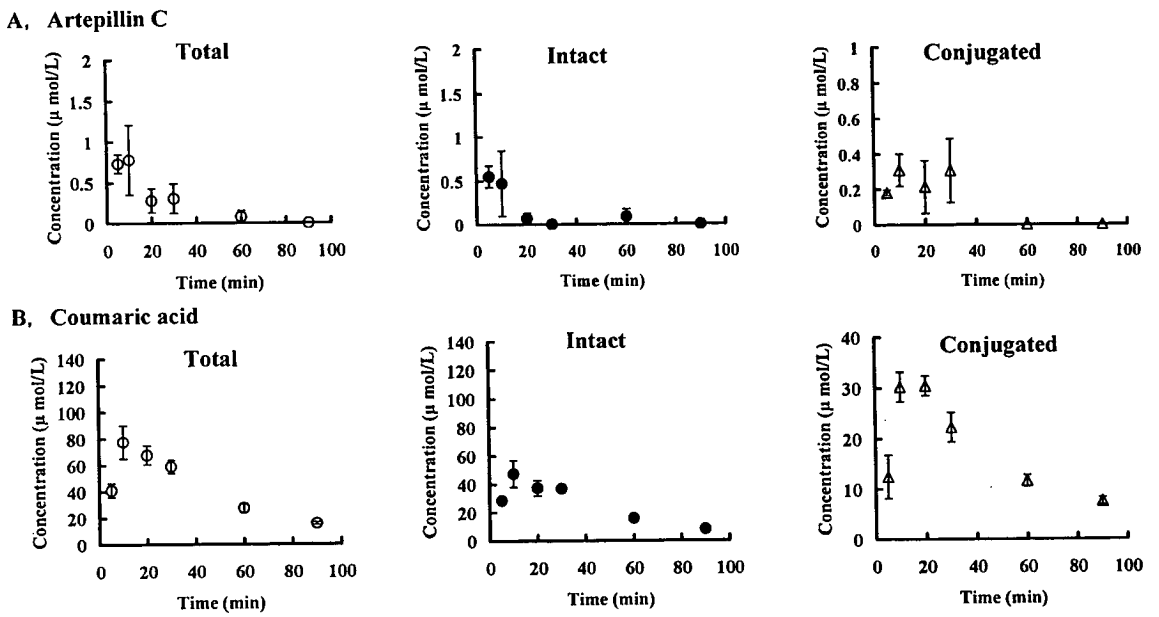

Figure 4. Serum concentration of phenolic acid in the abdominal artery as a function of time after the administration of AC (A) or CA (B). Each point is expressed as the mean ± SEM, $n = 3$.

Table 2. Pharmacokinetic Parameters of AC and CA Conjugates in the Portal Vein and Abdominal Artery after the Administration of a Single Oral Dose of 100 μmol/kg AC or CA[a]

	AC	CA
	Portal Vein	
C_{max},[b] μmol/L	3.64 ± 0.64	29.36 ± 2.83
t_{max}, min	10	20
$AUC_{0-1.5h}$, μmol·min·L^{-1}	135.4	1410.7
$t_{1/2}$, min	40.0	39.8
	Abdominal Artery	
C_{max}, μmol/L	0.31 ± 0.09	30.43 ± 1.94
t_{max}, min	10	20
$AUC_{0-1.5h}$, μmol·min·L^{-1}	6.8	1477.8
$t_{1/2}$, min	nc	38.6

[a] Abbreviation: AC, artepillin C; CA, *p*-coumaric acid; C_{max}, maximum serum concentration; t_{max}, time to reach the C_{max}; AUC, area under the serum concentration–time curve; nc, not calculated. [b] Values of C_{max} are the mean ± SEM, $n = 3$; $t_{1/2}$, elimination half-life.

DISCUSSION

In this study, we have demonstrated that the in vivo absorption efficiency of intact AC is lower than that of intact CA, indicating that there is a specific difference in the absorption characteristics of these two phenolic acids in vivo. Indeed, the absorption characteristics of AC are different from those of CA in Caco-2 cells (i.e. transcellular passive diffusion for AC versus MCT-mediated active transport for CA) (*9*, *17*). However, the absorption efficiency of intact AC and CA in vivo is apparently different from that observed in the in vitro Caco-2 cell system, because the absorption efficiency of AC was found to be as high as that of an MCT substrate such as CA in Caco-2 cells (*17*), in contrast to the lower absorption efficiency of rosmarinic and gallic acids, which are absorbed by paracellular diffusion (*9*, *11*). It is possible that this discrepancy in absorption efficiency between in vivo and in vitro studies might originate from such differences as an unstirred water layer, a mucin layer, or some other feature of the evaluation method employed. Further, the difference of absorption efficiency in stomach between CA and AC might cause this discrepancy. Indeed, it was reported that MCT expression was detected in mouse stomach (*19*) and that both transport systems for ferulic acid via transcellular passive diffusion and MCT-mediated absorption might operate (*20*), but at present the exact reason is unknown.

For gut absorption of dietary polyphenols, it is generally considered that the partition coefficient seems to govern their permeation across epithelial cells, because only passive diffusion appears to be involved (*21*). Indeed, it was reported that the lipophilicity of flavonoids and their affinity for liposomal membranes were well-correlated with their absorptivity into Caco-2 cells (*22*). Quercetin, one of the most typical and prevalent flavonoids in the human diet, and its glucosides were taken up into Caco-2 cells according to their own liphophilicity and were further conjugated across the epithelium (*23*). It was also reported that quercetin glucosides might be taken up intracellularly by SGLT1 (*24*) and transported by efflux into the intestinal lumen by MRP2 (*25*), indicating that the absorption and metabolism of quercetin and its glucosides are complex. Nevertheless, it is reasonable to assume that quercetin permeates across epithelial cells by transcellular passive diffusion (*22*), although a precise analysis of its absorption characteristics has not been performed, as it has in the case of AC (*17*). The same mechanism appears to govern the transport of isoflavonoids such as genistein and diazein, although isoflavones are transported as intact aglycons more efficiently than as flavonoids owing to their steric structure (*26*). In contrast to the deduced absorption characteristics in vitro, the absorption efficiency of quercetin or daizein in vivo is low in human or rat (*27*–*29*), which is in keeping with our findings for AC in this study. It is possible that an unknown but specific elimination mechanism might be involved in the low absorption efficiency in vivo to preserve homeostasis, because it would be harmful to living things if a xenobiotic compound with affinity for biomembranes could permeate across the epithelium easily and enter into enterocytes.

Furthermore, we also have demonstrated that the in vivo bioavailability of intact AC is much lower than that of intact CA. We found that the ratio of $AUC_{abdominal}$ to AUC_{portal} for intact AC and CA was 0.04 and 0.70, respectively, which suggests that intact AC is much more susceptible than intact

Table 3. Absorption Characteristics, Absorption Efficiency, and Bioavailability of Phenolics[a]

	CA[b]	CFA[c]	GA or RA[d]	AC[e]
phenolic characteristics	MCT-mediated active transport	paracellular diffusion[f]	paracellular diffusion	transcellular diffusion
efficiency	high	low	low	low
bioavailability	high	low	low	low

[a] Abbreviation: CA, p-coumaric acid; CFA, caffeic acid; GA, gallic acid; RA, rosmarinic acid; AC, artepillin C. [b] From refs *9*, *12*. [c] From refs *10*, *13*. [d] From refs *9*, *11–13*. [e] From ref *17*. [f] MCT-mediated active transport, in part.

CA to hepatic elimination. It is likely that a mechanism for eliminating AC in vivo might be involved, as mentioned above.

Considerable amounts of AC and CA conjugates were observed in the portal vein (**Figure 3**), although no AC and CA conjugates were transported in Caco-2 cells (*9*, *17*). This finding indicates that conjugation of AC and CA occurs during their permeation across the rat epithelium, consistent with results obtained in our previous in vivo studies (*12*, *13*). The discrepancy in conjugate formation between the in vivo and the in vitro Caco-2 cell system also might originate from differences in the evaluation method, as discussed above for the absorption efficiency or bioavailability. The $AUC_{abdominal}$ of conjugated AC was much lower than the AUC_{portal} of conjugated AC (ratio 0.05), and similar results were obtained for intact AC. This finding also suggests that AC may be eliminated by a specific mechanism. In contrast, because the AUC_{portal} of conjugated CA was nearly the same as the $AUC_{abdominal}$ of conjugated CA (**Table 2**), it is possible that CA is conjugated mainly during the absorption process and that further conjugation does not occur in the liver.

In this study, apart from the propyleneglycol concentration of the vehicle, which was 50% due to the lipophilicity of AC, the other experimental conditions were exactly the same as those used in previous in vivo studies (propyleneglycol concentration 10%). It has been reported that the vehicle used for oral administration can affect the absorption efficiency of flavonoids (*30*). Indeed, there are differences in the C_{max} values and concentration profiles of CA between this study and previous in vivo studies (*12*), but the AUC and t_{max} values were almost constant, indicating the high absorption efficiency and bioavailability of CA, similar to the results of the previous in vivo study. These results, together with a series of our previous works (*9–13*, *17*), have been used to summarize the diversity of absorption characteristics, absorption efficiency, and bioavailability of dietary phenolic compounds in **Table 3**, highlighting the unique physiological significance of the MCT-mediated transport system. We have focused on the physiological impact of MCT-mediated absorption and distribution in humans, which involves specific transport systems that act not only for phenolic acids but also for microbial metabolites of poorly absorbed polyphenols or dietary fibers (*14*, *15*). It is highly desirable to assess in full the health effects of phenolic acids and "metabo-nutrients", in other words, microbial metabolites with the biological activities of polyphenols or dietary fibers (*15*).

In conclusion, we have demonstrated that the absorption efficiency and bioavailability of AC are extremely low in vivo, in comparison to those of CA, which is absorbed and distributed by the MCT-mediated transport system. To evaluate the health effect of AC or propolis, further identification and characterization of its bioactive compounds in vivo are required.

ABBREVIATIONS USED

MCT, monocarboxylic acid transporter; AC, artepillin C; CA, *p*-coumaric acid; ECD, electrochemical detector.

ACKNOWLEDGMENT

We thank Mrs. K. Hagiwara for support during this work.

LITERATURE CITED

(1) Aga, H.; Shibuya, T.; Sugimoto, T.; Kurimoto, M.; Nakajima, S. Isolation and identification of anti-microbial compounds in Brazilian propolis, *Biosci., Biotechnol., Biochem.* **1994**, *58*, 945–946.

(2) Kimoto, T.; Arai, S.; Kohguchi, M.; Aga, M.; Nomura, Y.; Micallef, M. J.; Kurimoto, M.; Mito, K. 1998 Apoptosis and suppression of tumor growth by Artepillin C extracted from Brazilian propolis. *Cancer Detect. Prev.* **1998**, *22*, 506–515.

(3) Sugimoto, Y.; Iba, Y.; Kayasuga, R.; Kirino, Y.; Nishiga, M.; Alejandra Hossen, M.; Okihara, K.; Sugimoto, H.; Yamada, H.; Kamei, C. Inhibitory effects of propolis granular APC on 4-(methylnitrosamino)–(3-pyridyl)-1-butanone-induced lung tumorigenesis in A/J mice. *Cancer Lett.* **2003**, *193*, 155–159.

(4) Khayyal, M. T.; el-Ghazaly, M. A.; el-Khatib, A. S. Mechanisms involved in the antiinflammatory effect of propolis extract. *Drugs Exp. Clin. Res.* **1993**, *19*, 197–203.

(5) Dimov, V.; Ivanovska, N.; Bankova, V.; Popov, S. Immunomodulatory action of propolis. Prophylatic activity against gram-negative infections and adjuvant effect of the water-soluble derivative. *Vaccine* **1992**, *10*, 817–823.

(6) Shimizu, K.; Ashida, H.; Matsuura, Y.; Kanazawa, K. Antioxidative bioavailability of artepillin C in Brazilian propolis. *Arch. Biochem. Biophys.* **2004**, *424*, 181–188.

(7) Scalbert, A.; Johnson, I. T.; Saltmarsh, M. Polyphenols: Antioxidants and beyond. *Am. J. Clin. Nutr.* **2005**, *81*, 215S–217S.

(8) Konishi, Y.; Shimizu, M. Transepithelial transport of ferulic acid by monocarboxylic acid transporter in Caco-2 cell monolayers. *Biosci. Biotechnol. Biochem.* **2003**, *67*, 856–862.

(9) Konishi, Y.; Kobayashi, S.; Shimizu, M. Transepithelial transport of *p*-coumaric acid and gallic acid by monocarboxylic acid transporter in Caco-2 cell monolayers. *Biosci. Biotechnol. Biochem.* **2003**, *67*, 2317–2324.

(10) Konishi, Y.; Kobayashi, S. Transepithelial transport of chlorogenic acid, caffeic acid, and their colonic metabolites in intestinal Caco-2 cell monolayers. *J. Agric. Food Chem.* **2004**, *52*, 2518–2526.

(11) Konishi, Y.; Kobayashi, S. Transepithelial transport of rosmarinic acid in intestinal Caco-2 cell monolayers. *Biosci. Biotechnol. Biochem.* **2005**, *69*, 583–591.

(12) Konishi, Y.; Hitomi, Y.; Yoshioka, E. Intestinal absorption of p-coumaric and gallic acids in rats after oral administration. *J. Agric. Food Chem.* **2004**, *52*, 2527–2532.

(13) Konishi, Y.; Hitomi, Y.; Yoshida, M.; Yoshioka, E. Pharmacokinetic study of caffeic and rosmarinic acids in rats after oral administration. *J. Agric. Food Chem.* **2005**, *53*, 4740–4746.

(14) Konishi, Y.; Kobayashi, S. Microbial metabolites of ingested caffeic acid are absorbed by the monocarboxylic acid transporter (MCT) in intestinal Caco-2 cell monolayers. *J. Agric. Food Chem.* **2004**, *52*, 6418–6424.

(15) Konishi, Y. Transepithelial transport of microbial metabolites of quercetin in intestinal Caco-2 cell monolayers. *J. Agric. Food Chem.* **2005**, *53*, 601–607.

(16) Rahman, B.; Schneider, H. P.; Broer, A.; Deitmer, J. W.; Broer, S. Helix 8 and Helix 10 are involved in substrate recognition in the rat monocarboxylate transporter MCT1. *Biochemistry* **1999**, *38*, 11577–11584.

(17) Konishi, Y. Transepithelial transport of artepillin C in intestinal Caco-2 cell monolayers. *Biochim. Biophys. Acta* **2005**, *1713*, 138–144.

(18) Guo, C.; Cao, G.; Sofic, E.; Prior, R. L. High-performance liquid chromatography coupled with coulometric array detection of electroactive components in fruits and vegetables: Relationship to oxygen radical absorbance capacity. *J. Agric. Food Chem.* **1997**, *45*, 1787−1796.

(19) Koehler-Stec, E. M.; Simpson, I. A.; Vannucci, S. J.; Landschulz, K. T.; Landschulz, W. H. Monocarboxylate transporter expression in mouse brain. *Am. J. Physiol.* **1998**, *275*, E516-E524.

(20) Zhao, Z.; Egashira, Y.; Sanada, H. Ferulic acid is quickly absorbed from rat stomach as the free form and then conjugated mainly in liver. *J. Nutr.* **2004**, *134*, 3083−3088.

(21) Scalbert, A.; Williamson, G. Dietary intake and bioavailability of polyphenols. *J. Nutr.* **2000**, *130*, 2073S−2085S.

(22) Murota, K.; Terao, J. Antioxidative flavonoid quercetin: Implication of its intestinal absorption and metabolism. *Arch. Biochem. Biophys.* **2003**, *417*, 12−17.

(23) Murota, K.; Shimizu, S.; Chujo, H.; Moon, J. H.; Terao, J. Efficiency of absorption and metabolic conversion of quercetin and its glucosides in human intestinal cell line Caco-2. *Arch. Biochem. Biophys.* **2000**, *384*, 391−397.

(24) Walgren, R. A.; Lin, J. T.; Kinne, R. K. H.; Walle, T. Cellular uptake of dietary flavonoids quercetin 4′-beta-glucoside by sodium-dependent glucose transporter SGLT1. *J. Pharmacol. Exp. Ther.* **2000**, *294*, 837−843.

(25) Walgren, R. A.; Karnky, K. J. J.; Lindenmayer, G. E. Walle, T. Efflux of dietary flavonoids quercetin 4′-beta-gluoside across human intestinal Caco-2 cell monolayers by apical multidrug resistance-associated protein-2. *J. Pharmacol. Exp. Ther.* **2000**, *294*, 830−836.

(26) Murota, K.; Shimizu, S.; Miyamoto, S.; Izumi, T.; Obata, A.; Kikuchi, M.; Terao, J. Unique uptake and transport of isoflavone aglycones by human intestinal Caco-2 cells: Comparison of isoflavonoids and flavonoids. *J. Nutr.* **2002**, *132*, 1956−1961.

(27) Shimoi, K.; Yoshizumi, K.; Kido, T.; Usui, Y.; Yumoto, T. Absorption and urinary excretion of quercetin, rutin, and αG-rutin, a water soluble flavonoid, in rats. *J. Agric. Food Chem.* **2003**, *51*, 2785−2789.

(28) Scalbert, A.; Morand, C.; Manach, C.; Remesy, C. Absorption and metabolism of polyphenols in the gut and impact on health. *Biomed. Pharmacother.* **2002**, *56*, 276−282.

(29) Bloedon, L. T.; Jeffcoat, A. R.; Lopaczynski, W.; Schell, M. J.; Black, T. M.; Dix, K. J.; Thomas, B. F.; Albright, C.; Busby, M. G.; Crowell, J. A.; Zeisel, S. H. Safety and pharmacokinetics of purified soy isoflavones: Single dose administration to postmenopausal women. *Am. J. Clin. Nutr.* **2002**, *76*, 1126−1137.

(30) Piskula, M. K.; Terao, J. Quercetin's solubility affects its accumulation in rat plasma after oral administration. *J. Agric. Food Chem.* **1998**, *46*, 4313−4317.

Received for review August 10, 2005. Revised manuscript received October 16, 2005. Accepted October 19, 2005.

JF051962Y

Available online at www.sciencedirect.com
ScienceDirect
European Journal of Pharmaceutics and Biopharmaceutics 66 (2007) 135–145
European Journal of Pharmaceutics and Biopharmaceutics
www.elsevier.com/locate/ejpb

Research paper

Anthranoid laxatives influence the absorption of poorly permeable drugs in human intestinal cell culture model (Caco-2)

Leena Laitinen [a,b,*], Elina Takala [b], Heikki Vuorela [c], Pia Vuorela [a,1], Ann Marie Kaukonen [a], Martti Marvola [b]

[a] *Drug Discovery and Development Technology Center (DDTC), Faculty of Pharmacy, University of Helsinki, Finland*
[b] *Division of Biopharmaceutics and Pharmacokinetics, Faculty of Pharmacy, University of Helsinki, Finland*
[c] *Division of Pharmaceutical Biology, Faculty of Pharmacy, University of Helsinki, Finland*

Received 16 March 2006; accepted in revised form 20 September 2006
Available online 28 September 2006

Abstract

Interactions between widely used anthranoid laxatives and other simultaneously administered drugs are not known. In this paper, the influence of rhein, danthron, sennidins A/B, sennosides A/B, and senna leaf infusion was investigated on the permeability of furosemide, ketoprofen, paracetamol, propranolol, verapamil, digoxin, and Rhodamine 123 across Caco-2 monolayers. The effects on monolayer integrity ([^{14}C]mannitol permeability, TEER) were also determined.

The *in vitro* absorption of highly permeable drugs was not strongly affected during co-administration of the laxatives. Furosemide permeability was enhanced by rhein and danthron (3.6 and 3.0-fold), which may partly be due to opening of the paracellular spaces and/or effects on active efflux. However, the secretory permeability of digoxin and Rho 123 was not strongly affected by rhein and danthron, suggesting that inhibition of MDR1 was not responsible for the increased permeation of furosemide. The absorptive permeability of digoxin was decreased by rhein and danthron, offering evidence for effects on apical membranes. The effects on monolayer integrity were detectable, but reversible. According to presented experiments, daily use of laxatives with well-absorbing drugs would seem unlikely to affect drug permeability, but the effects on the absorption of poorly permeable drugs cannot be excluded.

Keywords: Anthranoid laxatives; Sennosides; Caco-2 permeability; Absorption of drugs

Abbreviations: AP-BL, apical-to-basolateral; BL-AP, basolateral-to-apical; C_0, initial concentration (μM, nM); DMSO, dimethyl sulfoxide; dpm, disintegrations per minute; FBS, foetal bovine serum; HBSS, Hank's balanced salt solution; DMEM, Dulbecco's modified Eagle's medium; Hepes, *N*-[2-hydroxyethyl]piperazine-*N'*-[2-ethanesulfonic acid]; HPLC, high-performance liquid chromatography; log *P*, octanol–water partitioning coefficient; MDR1, multidrug resistance protein 1; Mes, 2-(*N*-morpholino)-ethanesulfonic acid; MRP, multidrug resistance associated protein; MTT, 3-[4,5-dimethylthiazol-2-yl]-2,5-diphenyltetrazolum bromide; NEAA, non-essential amino acids; P_{app}, apparent permeability coefficient (cm/s); pK_a, ionisation constant; Rho 123, rhodamine 123; TEER, transepithelial electrical resistance.

* Corresponding author. Drug Discovery and Development Technology Center (DDTC), Faculty of Pharmacy, University of Helsinki, P.O. Box 56, 00014 Helsinki, Finland. Tel.: +358 50 9196290; fax: +358 9 191 59 725.
E-mail address: leena-laitinen@msn.com (L. Laitinen).
[1] Present address: Division of Biochemistry and Pharmacy, Biocity, Åbo Akademi University, Turku, Finland.

0939-6411/$ - see front matter © 2006 Elsevier B.V. All rights reserved.
doi:10.1016/j.ejpb.2006.09.006

1. Introduction

Anthranoid laxatives are widely used laxatives of natural origin. Sennosides, the most known anthranoid compounds, are extracted from the dried leaves and pods of senna plants *Cassia senna* L. (*Cassia acutifolia* Delile) and *Cassia angustifolia* Vahl. Other anthranoids, such as aloe-emodin, chrysophanol, and rhein, are obtained from *Rhamnus purshiana* DC and *Rheum palmatum* [1]. The basic structure of anthranoid laxatives is the anthracene ring (Fig. 1a), where C-9 is substituted with a hydroxyl or a carbonyl group. For the laxative function, C-8 is substituted with hydroxyl groups [2]. Based on the moiety present at C-10, anthranoids are called anthrones (H_2), anthraquinones (=O) or dianthrones (Fig. 1b).

In plants, the anthranoids are mostly present as sugar derivatives (=glycosides). Glucose or rhamnose molecules are bound by β-glycosidic linkages to the OH groups at C-8 or at C-1 (*O*-glycosides) (Fig. 1b). The β-glycosidic linkage between the sugar moiety and the anthranoid backbone stabilizes the molecule and protects it against hydrolysis in the stomach and α-glucosidase activity in the small intestine [3]. The glycosidic anthranoid laxatives are not absorbed from the small intestine. Bacterial enzymes, β-glycosidase and reductase, present in the large intestine transform the glycosidic sennosides first to sennidin monoglucosides and sennidin, and further to corresponding active aglycone anthrones, i.e., rhein anthrone, and rhein [2,4]. Unlike the glycones, which are absorbed after bacterial transformation to aglycones mainly in the large intestine, the orally ingested aglycones are absorbed in the upper parts of the gastrointestinal tract [5].

Direct interactions between rhein anthrone or anthraquinone (rhein, danthron) and the intestinal epithelium cause epithelial cell damage, which lead to motility changes and accelerated intestinal transit both in the small and large intestine [6,7]. Alterations in intestinal water absorption and secretion, which lead to fluid accumulation in the intestine [8,9], lead to further acceleration of intestinal transit. The effects on secretion and absorption are induced by a direct interaction between the laxative and the epithelial cells [10]. Additionally, anthranoids may cause decreased production of ATP by uncoupling mitochondrial oxidative phosphorylation [11]. Low ATP concentration and inhibition of the Na^+/K^+ ATPase lead to the breakdown of the ion gradient across the epithelial cell mem-

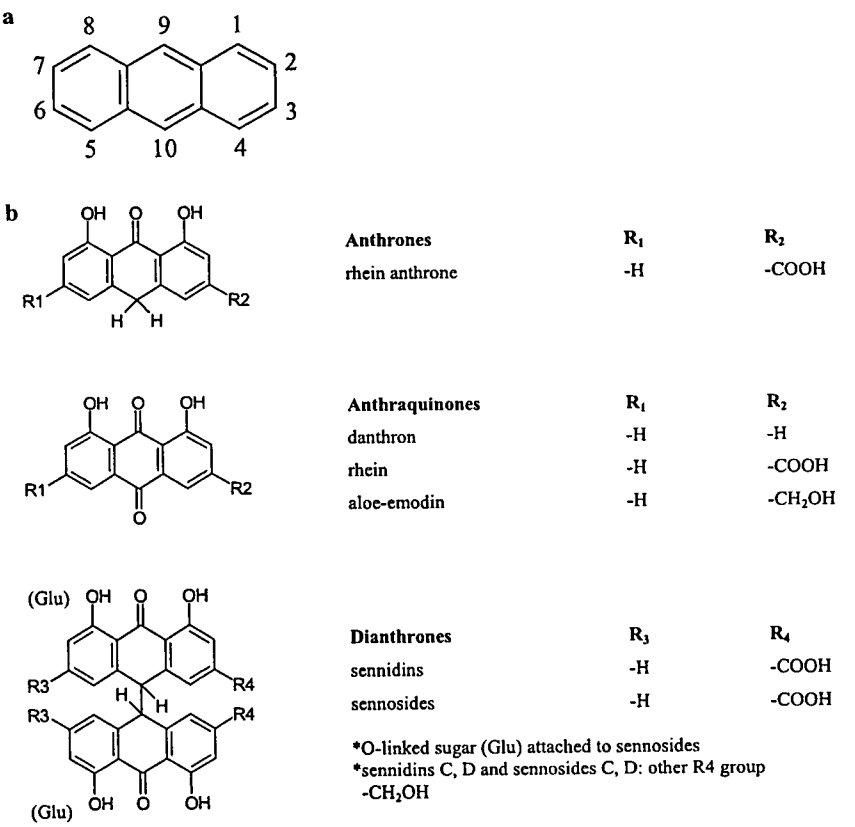

Fig. 1. (a) Anthracene ring, the basic structure of all anthranoid laxatives. (b) Three groups of anthranoid laxatives: anthrones with two hydrogen atoms in C-10, anthraquinones with carbonyl at C-10. Dianthrones consist of two linked anthrone molecules with or without O-linked sugar (=sennosides or sennidines, respectively). Two optic isomers can be distinguished depending on the configuration of the C-10; sennoside A is a dextrorotary *trans*-form and sennoside B is a *meso*-form.

brane. This prevents the absorption of sodium and water from the intestinal lumen to the blood, and may affect the permeability of co-administered drugs. Disruption of tight junctions between intestinal epithelial cells induces increased net secretion of water and electrolytes into the intestinal lumen [12]. This might inhibit the absorptive permeability of hydrophilic poorly absorbing drugs from the intestinal lumen or enhance the secretory permeability, even though a change of fluid flux from net secretion to net absorption has been shown not to increase the permeability of antipyrine, a highly permeable drug [13]. Although changes in water and electrolyte absorption and efflux in the small intestine caused by laxatives may be compensated for in the colon, they may affect the bioavailability of co-administered drugs at the main site of their absorption, the small intestine.

The aim of this paper was to probe whether anthranoid laxatives rhein, danthron, sennidin A/B, sennoside A/B (Fig. 1b), or a senna leaf infusion have the ability to affect the absorptive permeability of well-permeating drugs ketoprofen (active transport by monocarboxylic acid transporter), paracetamol (passive permeability), propranolol (passive permeability; interacts with MDR1), verapamil (substrate/inhibitor of MDR1), poorly permeating furosemide (active transport/efflux) and digoxin (active efflux by MDR1) across Caco-2 cell monolayers. Caco-2 cell cultures are widely used as *in vitro* model for intestinal absorption and secretion of nutritional and drug molecules [14–16]. These cell cultures are used as a model to investigate drug–drug (for example [17]), or drug–food interactions during the absorption phase [18,19]. Additionally, the effects of the anthranoid laxatives on the absorptive and secretory permeabilities of [^{14}C]mannitol (a paracellular marker molecule) and Rhodamine 123 (Rho 123) (paracellular absorption and MDR1-mediated active efflux) were determined.

2. Materials and methods

2.1. Materials

The anthranoid laxatives rhein, sennidin A/B, and sennoside A/B, purity 98%, with small amounts of sennosides C and D, were donated by Extracta Ltd. (Helsinki, Finland). Danthron was bought from ICN Biomedicals Inc. (Aurora, OH, USA) and senna leaves intended for laxative use were from Helsinki University Pharmacy (Helsinki, Finland).

Ketoprofen, propranolol, and verapamil were bought from ICN Biomedicals Inc. (Aurora, OH, USA). Furosemide and paracetamol were donated by Orion Pharma (Espoo, Finland). [^{14}C]mannitol (specific activity 58.0 mCi/ml) was bought from Amersham Pharmacia Biotech UK Ltd. (Amersham, England). Rhodamine 123 (Rho 123) was purchased from Fluka Chemie GmbH (Buchs, Switzerland) and [^{3}H]digoxin (specific activity 21.8 Ci/mmol) was from Perkin-Elmer Life Sciences (Boston, MA, USA). All chemicals for cell culturing were purchased from Gibco Invitrogen Corp. (Life Technologies Ltd., Paisley, Scotland) or from Sigma Chemical Co. (St. Louis, MO, USA). All of the organic solvents and other chemicals used in the analyses were of analytical or chromatographic grade and were bought from Riedel-de Haën (Seelze, Germany), Rathburn (Walkerburn, Scotland), Merck (Darmstadt, Germany), or ICN Biomedicals Inc. (Aurora, OH, USA).

2.2. Cell culture

The Caco-2 cell line was obtained from the American Type Culture Collection (Rockville, MD, USA). Cells were cultivated as described earlier [17,19] and seeded at a density of 6.8×10^4 cells/cm^2 onto tissue culture inserts (Transwell 3401, 12 mm diameter, 0.4 μm pore size, 1.1 cm^2 growth area polycarbonate filters, Corning Costar Corp., Cambridge, MA). Cells from passage numbers 31 to 42 at ages ranging from 21 to 28 days were used for the transport experiments.

2.3. Preparation of the solutions

The studied compounds ketoprofen, paracetamol, propranolol, verapamil, and furosemide were dissolved in HBSS (pH 5.8) to a concentration of 200 μM (100 μM Rho 123). After dissolution, the pH of the solution was re-adjusted, if needed. 1.6 μCi/ml [^{3}H]digoxin and 1.2 μCi/ml [^{14}C]mannitol in HBSS were prepared.

For drug-permeability experiments, the anthranoid laxatives (rhein, danthron, sennidin and sennoside) were first dissolved in DMSO. These solutions were added to HBSS, resulting in 200 μM laxative concentrations and 2% DMSO content. The senna leaf infusion (senna tea) was prepared according to package instructions: the senna leaves were infused for 15 min in boiling water and filtered after cooling to room temperature. HBSS 10× concentrate was added to final senna leaf concentration 20 mg/ml. All test solutions contained 10 mM Mes.

Prior to starting the experiment, the anthranoid and drug solutions were combined (1:1), and the pH of the final test solutions was measured and corrected, if needed.

2.4. MTT toxicity test

MTT test (a colorimetric assay) can be used to determine cell viability (mitochondrial activity) by measuring the extent of formazan formation after lysis of the living material and solubilisation of formazan crystals [20]. The seeding of Caco-2 cells and test procedure is explained in [19]. The cells were exposed over 60 min to ethanol (0.25–30%, v/v), 90 min to DMSO (0.2–35%, v/v), the drugs (1.0 and 10.0 μM, digoxin; 100 and 500 μM, other drugs), or laxatives (different concentrations, from 50 to 500 μM; 2.50, 5.00, and 10.00 mg/ml, senna infusion), at 37°C. Results ($n = 6$–8) were expressed as percentages of the control value (cells treated with HBSS only).

2.5. Permeability experiments

All of the permeability experiments were performed under "sink conditions", meaning that amounts of compound transported to the acceptor compartment during individual sampling intervals did not exceed 10% of the amounts in the donor compartment.

Before the permeability experiments, the cell monolayers were washed twice with HBSS containing 10 mM Hepes, pH 7.4. After equilibration in the experimental conditions, the transepithelial electrical resistance (TEER) was measured using a Millicell® ERS Voltohmmeter (Millipore Corp., Bedford, MA, USA). Cell monolayers with TEER values below 250 Ω cm^2 were not used.

The abilities of 100 μM ketoprofen, paracetamol, propranolol, verapamil, and furosemide to permeate across the Caco-2 monolayers without or with co-administration of 100 μM laxatives (senna infusion 10 mg/ml) were studied in an absorptive (apical-to-basolateral, AP-BL) direction at an apical pH of 5.8 and a basolateral pH of 7.4. For Rho 123, 50 and 5 μM donor concentrations were used in AP-BL and secretory (basolateral-to-apical, BL-AP) directions, respectively. For [^{3}H]digoxin, solutions with 0.8 μCi/ml activity were used in both directions.

After equilibration, the apical solutions were changed to HBSS containing the compounds without or with the laxatives. Samples were collected after 15, 30, 45, 60, and 90 min (ketoprofen, paracetamol, propranolol, and verapamil), or after 30, 60, 90, and 120 min (furosemide and digoxin) by moving the cell monolayers to a new well containing fresh HBSS. In the case of digoxin, BL-AP samples were collected by removing the whole acceptor (apical) volume and replacing it with fresh HBSS solution. All of the transport experiments were conducted in triplicate. Samples were kept at −22°C until analysed (for no longer than 35 days).

In Rho 123 experiments, a 60-min pre-incubation was performed with the anthranoids before the actual permeability test. After the pre-incubation, the laxatives were removed from the apical compartment, the cell monolayers were washed once with fresh HBSS (apical + basolateral compartments), and Rho 123 in HBSS was added in donor compartments. Samples were collected after 15, 30, 45, 60, 90, and 120 min by moving the monolayers to a new well with fresh pre-warmed HBSS (AP-BL), or by removing the whole acceptor (apical) volume and replacing it with fresh HBSS solution (BL-AP).

To determine monolayer integrity after each experiment, the cell cultures were washed once with HBSS, pH 7.4, and TEER values were measured. If values were below 220 Ω cm^2, the cell monolayers were further incubated with HBSS, and electrical resistance was measured again after 60 min. Monolayer integrity was further assessed after the drug-permeability tests with [^{14}C]mannitol. The apical washing solution was changed to test solution with [^{14}C]mannitol solution (0.6 μCi/ml, pH 5.8). After 60 min, 100 μl samples were withdrawn from the basolateral compartments for the activity measurements. Diffusion rates ≤0.5%/h were considered as "normal".

2.6. Long-term effects on monolayer integrity

In order to study long-term effects of the anthranoid laxatives on the paracellular permeability of the monolayers, an 8-h experiment with [^{14}C]mannitol was performed. The AP-BL and BL-AP permeability of [^{14}C]mannitol was monitored after 60-min pre-exposure to 100 μM laxative concentrations (senna infusion at 10 mg/ml). TEER of the monolayers was measured at $t = -5$, 30, and 55 min from the start of the pre-exposure. After 60 min, the laxative solutions were removed from the donor compartments and mannitol in DMEM (without additives used in growth medium) buffered to pH 5.8 (10 mM Mes) was added to the donor compartment, and DMEM buffered to 7.4 (10 mM Hepes) was added to the acceptor compartments. Mannitol samples were collected after 30, 60, 90, 120, 150, 180, 210, 240, 270, 300, 360, 420, and 480 min and TEER was measured at time points 60, 120, 180, 240, 300, 360, 420, and 480 min. Cumulative sample concentrations (dpm, ^{14}C-disintegrations per minute) between time points 90 and 270–300 min were used for permeability calculations.

2.7. Analytical methods

Drug concentrations in the acceptor compartments were determined using HPLC (Waters Millennium, Milford, USA). The determination conditions are explained in [19]. Propranolol was determined using same method with verapamil. Rho 123 concentrations in samples were determined by Wallac Victor^2 1420 Multilabel HTS Counter (Wallac, Turku, Finland), [^{14}C]mannitol and [^{3}H]digoxin with liquid scintillation counting, using a WinSpectral 1414 Liquid Scintillation Counter (Wallac, Turku, Finland), described elsewhere [19].

2.8. Data analysis

The AP-BL and BL-AP permeability (apparent permeability coefficient, P_{app}) of each compound was calculated according to the following equation where

$$P_{app}\ (\mathrm{cm/s}) = \frac{dQ}{dt}\left(\frac{1}{C_0 A}\right), \quad (1)$$

where dQ/dt is the cumulative rate of appearance of drugs on the acceptor side (μmol/s or nmol/s), C_0 is the initial drug concentration on the donor side (μmol/ml or nmol/ml), and A is the surface area (1.1 cm^2) of the monolayers.

The results were tested statistically using unpaired t-test combined with Dunn–Sidak Adjusted Probability and Bonferroni Adjusted Probability test using SYSTAT® version 10.2 for Windows® (SYSTAT Software Inc., Richmond, CA, USA). Significance level of 5% was used.

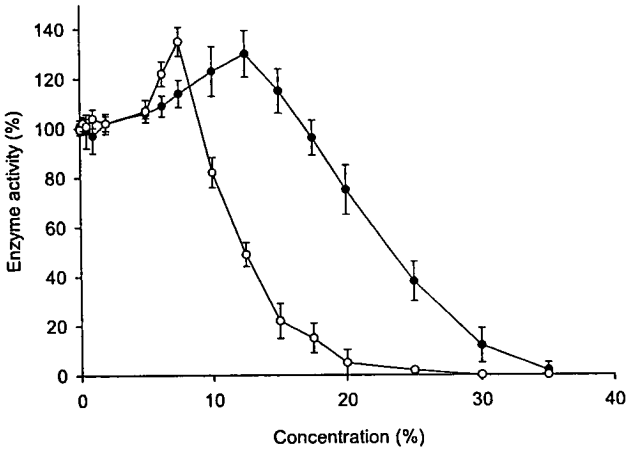

Fig. 2. Effects of DMSO (●) and ethanol (○) on the intracellular dehydrogenase activity of Caco-2 cells (means ± SD, $n = 4$). The cells were exposed to DMSO for 90 min and to ethanol for 60 min.

3. Results and discussion

3.1. MTT test

The effects of ethanol, DMSO, the drugs studied, and of the anthranoid laxatives on the mitochondrial dehydrogenase activity were studied on Caco-2 cell monolayers prior to the transport experiments. Slightly increased enzyme activities were observed at ethanol and DMSO concentrations (v/v) 5.0–10% and 5.0–15.0%, respectively, indicating sub-toxic effects on the cell line (Fig. 2). In order to ensure cell viability during the permeability experiments, the concentration of DMSO was restricted to 1.0% in the laxative solutions containing rhein, danthron, sennidin, and sennoside. Ethanol was not used as a solubility enhancing excipient in the experiments.

No toxic effects in relation to mitochondrial enzyme activity were seen with any of the studied drugs even at 500 μM concentration (Table 1), whereas laxatives caused a clear reduction in mitochondrial enzyme activity at higher concentrations (≥250 μM). In order to ensure the solubility of the laxatives at higher concentrations, the concentration of DMSO in the MTT test was 2.5% (v/v). This should, however, not compromise the results as DMSO effects at this concentration are still minor. The laxative concentrations for the permeability experiments were chosen according to the above results: rhein, danthron, sennidin A/B, and sennoside A/B were used at 100 μM (including 1.0% DMSO). The senna infusion exhibited no toxicity at the concentrations tested (2.5, 5.0 or 10.0 mg/ml) (Table 1). In the subsequent permeability experiments, the concentration of the senna infusion was 10.0 mg/ml.

Table 1
The MTT test

Compound	Concentration (μM)	Enzyme activity (%)
Digoxin	0.1	105 ± 8.0
	1.0	97 ± 2.9
Furosemide	100	101 ± 11
	500	102 ± 12
Ketoprofen	100	101 ± 3.1
	500	106 ± 3.1
Paracetamol	100	107 ± 2.0
	500	101 ± 2.2
Propranolol	100	97 ± 3.7
	500	101 ± 3.2
Verapamil	100	105 ± 2.6
	500	99 ± 9.0
Rho 123	100	98 ± 5.3
	500	96 ± 6.3
Rhein[a]	50	91 ± 5.9
	100	89 ± 9.2
	250	88 ± 8.9
	500	45 ± 9.9
Danthron[a]	50	95 ± 7.8
	100	89 ± 25
	250	32 ± 5.4
	500	28 ± 11
Sennidin A/B[a]	50	97 ± 19
	100	85 ± 22
	250	54 ± 27
Sennoside A/B[a]	100	102 ± 13
	250	111 ± 15
	500	45 ± 11
Senna infusion	2.50[b]	106 ± 23
	5.00[b]	102 ± 15
	10.00[b]	92 ± 12

Caco-2 cells (16×10^4 cells/cm^2) were exposed to the compounds studied and the anthranoid laxatives for 90 min. Results are expressed as percentage of control value (100%) obtained after exposure to HBSS only (means ± SD, $n = 8$).
[a] With 25 mg/ml DMSO.
[b] Concentration mg/ml.

3.2. Drug permeability

The abilities of the highly permeable drugs ketoprofen, paracetamol, propranolol, and verapamil to permeate across Caco-2 cell monolayers were to some extent affected by the anthranoid laxatives (Fig. 3). The permeability of paracetamol (pK_a 9.63, acid), a compound permeating mainly by passive transcellular diffusion, was one of the least affected besides propranolol and verapamil. As a very weak acid, which is practically 100% unionised at the apical pH 5.8, it should also be fairly insensitive to any small changes in the pH potentially caused by the co-administered compounds, especially since a further acidification is more likely.

The permeability of ketoprofen, which is, at least in part, actively transported by a pH-dependent carrier-mediated H^+ co-transporter in the AP-BL direction [21,22], was most affected by danthron (27% reduction) and the senna infusion (48% increment) (Fig. 3). Ketoprofen, a lipophilic acid, has a calculated $\log D_{5.8}$ of 1.34 (based on pK_a 3.98,

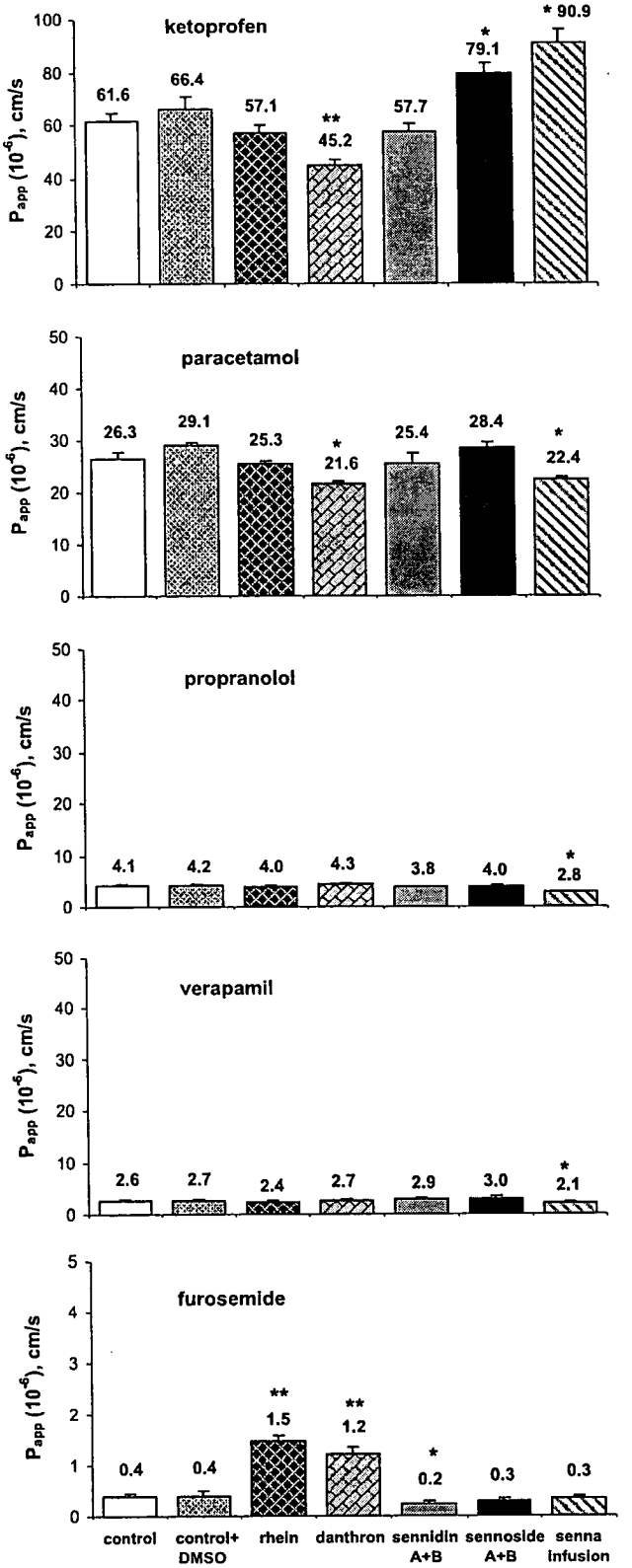

Fig. 3. P_{app} values for 100 μM ketoprofen, paracetamol, propranolol, verapamil and furosemide with co-administration of HBSS only (control), DMSO as a solvent in HBSS, rhein, danthron, sennidin, sennoside and senna infusion across Caco-2 cell monolayers (means ± SD, $n = 3$–4). $^{*}p < 0.05$; $^{**}p < 0.01$.

log$P$ 3.16 [23]), which as such would suggest fair passive absorptive permeability despite a high extent of ionisation. Anthranoids, such as danthron, are supposed to have the ability to uncouple mitochondrial oxidative phosphorylation, leading potentially to a decreased ATP production [24,11]. The pH-dependent carrier-mediated H^+ co-transporter might suffer from low ATP concentrations leading to diminished active transport. The reduced permeability values in the presence of danthron, 45.2 ± 1.7 (10^{-6}) cm/s, compared with the control values, 61.6 ± 2.8 (10^{-6}) cm/s, could therefore be explained by the reduction in ATP concentrations caused by danthron in Caco-2 cells.

The senna infusion contains mainly sennosides A and B, small amounts of sennosides C and D, aloe-emodin, rhein 8-glucosides, mucilage, flavonoids (kaemferol, its respective glycosides kaemferin and isorhamnetin), and naphthalene precursors, but also salicylic acid and oxalate [1,25] and resin, saponins, and polysaccharide hydrocolloids [26,1]. This infusion had the ability to enhance ketoprofen permeability almost 1.5-fold. Since senna leaves contain acids, which are stronger than ketoprofen (salicylic acid, oxalate), but also many active compounds capable of interacting with co-administered actively transported drugs, it is not easy to explain what could happen between drugs and these compounds. Small regional changes in the pH of the transport buffer at the site of absorption might cause changes in the permeabilities of co-administered drugs by strengthening the H^+ gradient across the Caco-2 cell membranes.

Propranolol and verapamil, which are considered MDR1 efflux transport substrates [27,28], were affected by co-administered senna infusion (Fig. 3). Some anthracyclines, which also belong to anthraquinones and are used in cancer treatment, are determined as MDR1 and/or MRP1 substrates [29]. The permeability of not only anthracyclines, but also other "natural" drugs (such as rhein and danthron), might be affected by the efflux proteins. No considerable effects of rhein or danthron were, however, detectable on propranolol and verapamil permeability (Fig. 3). For many substrates of MDR1, passive permeability dominates at high drug concentrations, if both the affinity to the MDR1 protein and the passive permeability are high as in the case of verapamil [30]. However, more recent studies do not confirm propranolol as a substrate for MDR1; it is considered a potential modulator (activator) of MDR1-associated ATPase activity [31,32]. Thus, the slight permeability reducing effect of the senna infusion might be due to small regional acidification of the transport buffer at the site of absorption, leading to increased degree of ionisation of the basic compounds.

The absorption of furosemide, a poorly permeable drug, is a mixture of trans- and paracellular diffusion and saturable active transport mediated potentially by several efflux proteins [33–35]. The actual efflux proteins involved in the poor absorption of furosemide have not been positively identified, but MDR1, MRP1, and/or MRP2 have been suggested. Rhein and danthron enhanced furosemide per-

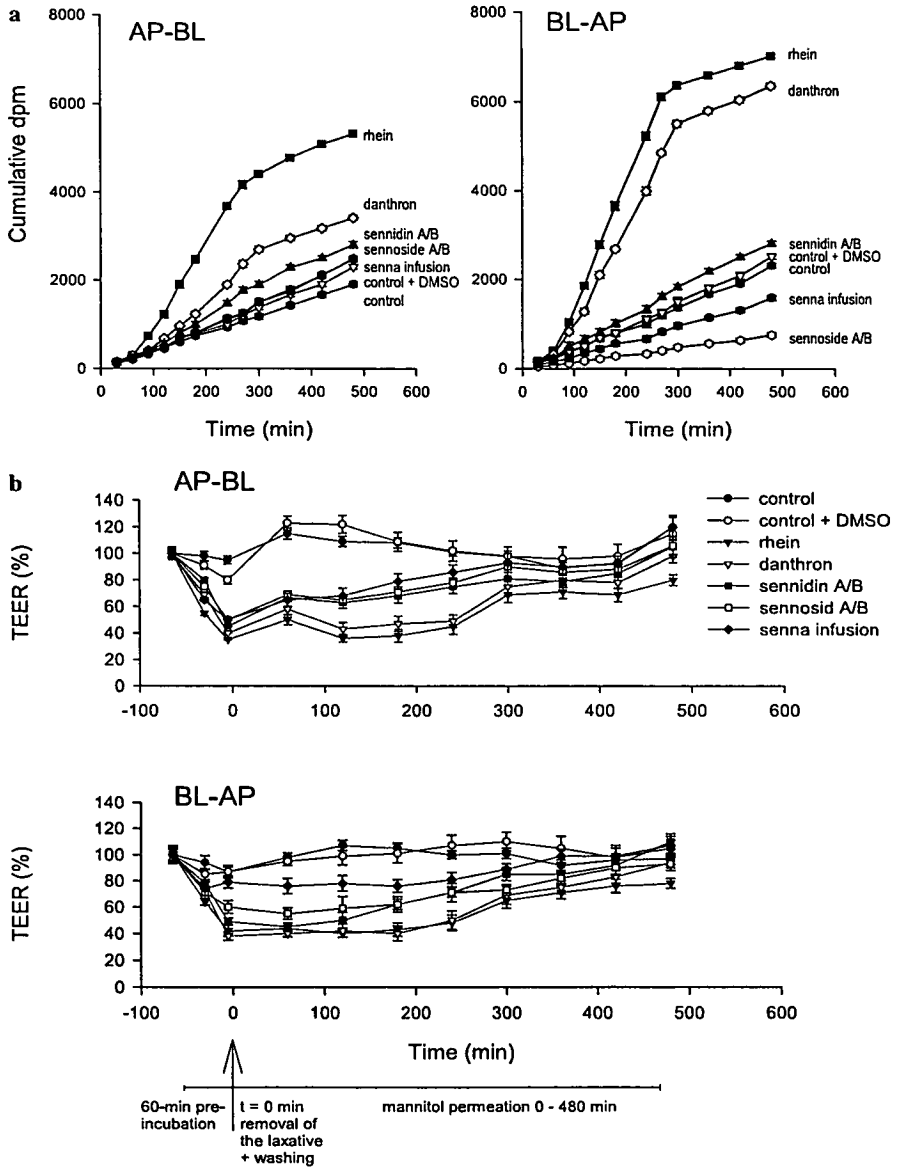

Fig. 4. Long-term effects of laxatives on monolayer integrity. The cell monolayers were pre-treated (60 min) with 100 μM rhein, danthron, sennidin A/B, sennoside A/B, or 10 mg/ml senna leaf infusion. At time point 0, the laxatives were removed and the monolayers washed with buffered DMEM, pH 7.4. The donor transport medium was changed to DMEM + [^{14}C]mannitol buffered to pH 5.8 (apical) or pH 7.4 (basolateral), and the acceptor medium to buffered DMEM, respectively. (a) Mannitol permeability. The cumulative paracellular diffusion of [^{14}C]mannitol (measured as disintegrations/min), dpm, after pre-treatment with HBSS only (control), 1% DMSO in HBSS (control + 1.0% DMSO), 100 μM rhein, danthron, sennidin, sennoside and 10 mg/ml senna infusion (means ± SD, $n = 3$). (b) % changes in monolayer electrical resistance (TEER; means ± SD, $n = 3$) after 60 min pre-treatment with HBSS only (control), 1% DMSO in HBSS, rhein, danthron, sennidin, sennosides and senna infusion, and during the 8-h mannitol permeability experiment. Initial TEER values prior to pre-incubation were used as 100%.

meability 3.6- and 3.0-fold, respectively (Fig. 3). This might be caused by interactions with the efflux protein(s), if the anthranoids had higher affinity to the secretory protein than furosemide. If the paracellular permeability were enhanced, opening of the paracellular spaces between Caco-2 cells would have been observed as decreased TEER values and enhanced mannitol permeability. Indeed, mannitol permeability was enhanced to 0.6 and 0.55%/h (control 0.2%/h) during the furosemide assay when co-administered with rhein and danthron, respectively (data not shown). TEER values decreased reversibly to about 40% as indicated also in Fig. 4b. However, due to the high acid strength of furosemide (determined pK_{a1} 3.70, pK_{a2} 9.93) and the presence of a pH gradient across the cell monolayer (pH 5.8 vs 7.4), a significant fraction is absorbed transcellularly at the used pH [33]. A partial opening of the paracellular spaces would, therefore, not lead to a very strong enhancement of permeability, since the paracellular route represents a relatively small fraction of the accessible absorptive area. Hence, inhibition of efflux would be likely

to contribute to the enhanced furosemide permeability in the presence of rhein and danthron.

Furosemide permeability was decreased by sennidin to about 60% and by sennoside to 70% of the control value (Fig. 3). Tight junctions between Caco-2 cells were to some extent affected, as indicated by TEER measurements (about 60% of the control values, Fig. 4b) and 60-min mannitol diffusion experiment after the permeability assay (0.32 and 0.30%/h, data not shown), but these changes would be more indicative of increased permeability. However, studies probing the transporters involved in furosemide secretion show decreased permeation of furosemide in both absorptive and secretive direction in the presence of sulfinpyrazone, an inhibitor of the efflux proteins MRP1 and 2 [34,35].

Rho 123 is a substrate of MDR1 efflux and its absorptive permeability is quite low. According to Troutman and Thakker [36], the AP-BL permeability is passive and mainly paracellular, with little contribution from transcellular diffusion. The permeability of Rho 123 without laxative pre-incubation was 0.67 ± 0.06, and 6.25 ± 0.52 (10^{-6}) cm/s (pH gradient) in AP-BL and BL-AP direction, respectively, which indicates the presence of active efflux (Fig. 5a). At equal pH conditions (iso-pH 7.4), the AP-BL permeability was 0.94 ± 0.06 and BL-AP permeability 8.0 ± 0.7 (10^{-6}) cm/s (Fig. 5a), which results in 8.5-fold directional difference. This offers evidence for the fact that the pH conditions are not responsible for the differences in absorption and excretion of Rho 123.

The AP-BL permeability of Rho 123 was not affected during the experiment time by any of the laxatives, the P_{app} values were very close to each other (Fig. 5a). If enhancement of paracellular absorptive permeability were noticed, low TEER values would indicate for opening of the paracellular spaces. This did indeed partly happen; TEER values measured after the pre-incubation with the anthranoids were about 50% of the initial value (Fig. 4b), but after the Rho 123 permeability assay TEER values were almost 90% and 80% in AP-BL and BL-AP experiments, respectively (Fig. 5c). According to Troutman and Thakker [36], the paracellular absorptive permeability of Rho 123 is not affected by MDR1-mediated efflux activity.

Rhein enhanced significantly (30%) the BL-AP permeability of Rho 123, whereas danthron and senna infusion inhibited it (25% and 20%, respectively). This was noticed as a slightly reduced ratio between BL-AP and AP-BL permeabilities ($P_{app[BL\text{-}AP]}$ vs $P_{app[AP\text{-}BL]}$) for danthron (8.4) and senna leaf infusion (9.0). Other laxatives had no effect on the secretory permeability of Rho 123 (Fig. 5a).

Digoxin is a well-known substrate of MDR1 [37]. MDR1 inhibitors, such as verapamil and GW918, have been shown to increase absorptive and decrease secretory permeability of digoxin [36]. Additionally, there is some evidence to suggest that other efflux proteins may partly contribute to digoxin secretory permeability [38].

The permeability of [^{3}H]digoxin was not affected by sennidines or sennosides (data not shown). Two hundred micromolar of verapamil enhanced AP-BL and decreased

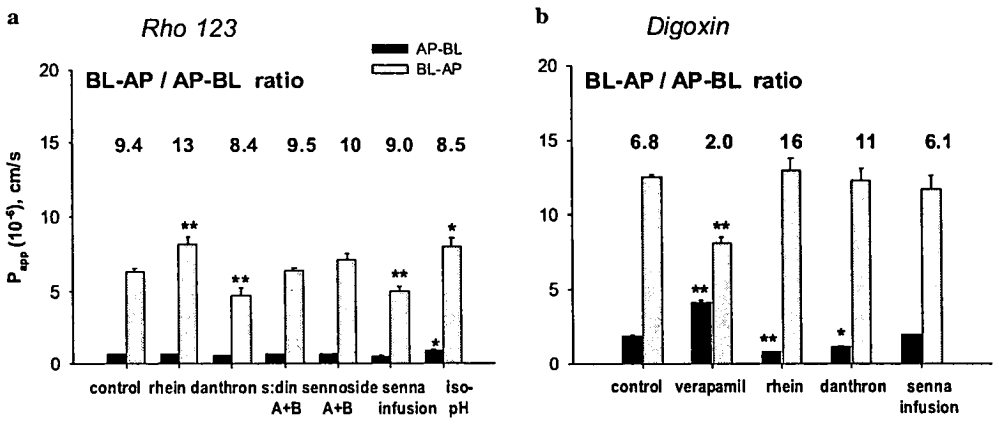

c **TEER, % of the control value (S.D.)**

	control	rhein	danthron	sennidin A+B	sennoside A+B	senna infusion
AP-BL	95 (2.6)	62 (2.7)*	86 (3.9)*	86 (6.7)*	89 (9.2)	85 (4.3)
BL-AP	98 (5.2)	69 (3.8)*	105 (5)*	81 (6)	77 (6.3)*	89 (7.3)

Fig. 5. Apparent permeabilities (P_{app}; means ± SD, $n = 3$–4) of Rho 123 and [^{3}H]digoxin across Caco-2 cell monolayers at apical pH 5.8 and basolateral pH 7.4. The permeability ratios $P_{app[BL\text{-}AP]}$ vs $P_{app[AP\text{-}BL]}$ are also indicated. (a) After 60-min pre-incubation with HBSS only (control), 100 μM rhein, danthron, sennidin, sennoside, and 10 mg/ml senna leaf infusion and at iso-pH conditions (with HBSS, when both apical and basolateral pH was 7.4). (b) Without (control) or with 200 μM verapamil, 100 μM rhein, danthron and 10 mg/ml senna infusion. (c) % changes in monolayer electrical resistance (TEER) after Rho 123 AP-BL and BL-AP permeability experiments. Initial TEER value at the start of the experiment (prior to pre-incubation) is 100% (means ± SD, $n = 3$).

BL-AP permeability of [^{3}H]digoxin (Fig. 5b), as expected. Rhein and danthron were able to decrease the AP-BL permeability of digoxin, but the BL-AP permeability was not affected (Fig. 5b). This leads to high BL-AP/AP-BL ratio (6.8, 16, and 11 for control, rhein, and danthron, respectively). Rhein and danthron are relatively small (m.w. < 300 g/mol) planar molecules (Fig. 1b), and are therefore possibly able to intercalate with cell membranes. This leads to changes in membrane fluidity (possibly to increased membrane rigidity) and effects capability of drugs to interfere with MDR1 in the apical membranes. This would not affect the secretory permeability, because in this case drugs enter apical membranes (and the efflux protein) from the basolateral side.

The mechanism behind the interactions during absorption between the senna infusion and drugs is not easily detected because of several active compounds present in the infusion. Besides several compounds of laxative effect, the infusion also contains flavonoids, such as kaemferol and respective glycosides kaemferin and isorhamnetin [25], which are able to interact with active transport proteins and cell membranes [39,40].

3.3. Long-term effects on monolayer integrity

The apparent permeabilities for mannitol without laxative pre-incubation were 0.48 ± 0.02 (AP-BL) and 0.52 ± 0.01 (BL-AP) (10^{-6}) cm/s during the 480 min assay, calculated between time points 90 and 270 min (Fig. 4a). Inclusion of 1% DMSO in the 60-min pre-treatment (apical compartment) solution (control + 1% DMSO) did not significantly enhance mannitol permeability. Pre-treatment with 100 μM rhein with 1% DMSO in HBSS enhanced long-term mannitol permeability; P_{app} values were 2.30 ± 0.23 and 3.38 ± 0.13 (10^{-6}) cm/s for AP-BL and BL-AP permeabilities, respectively. Corresponding P_{app} values after danthron pre-treatment were 1.19 ± 0.09 and 2.69 ± 0.11 (10^{-6}) cm/s. Characteristic for all enhanced mannitol permeabilities was that after the first 60 min of almost control-like permeability, a clear step for higher permeability was detected (Fig. 4a). Same phenomenon was observed also during cumulative AP-BL permeability of Rho 123 (paracellular route) after pre-incubation with rhein (data not shown). This phenomenon could be explained by the possibility of rhein and danthron to intercalate with apical cell membranes, leading to additional effects on paracellular spaces when increased rigidity of the membranes might inhibit normal flexibility of the paracellular spaces. However, again after 300 min, mannitol permeability evened out and the final slope (300–480 min) of the cumulative permeability curve was similar to that of the control (Fig. 4a). This happens because laxative molecules slowly leave the cell membranes. Sennidin pre-treatment caused only a slight enhancement in the P_{app} values (1.9- and 1.4-fold enhancements in AP-BL and BL-AP permeabilities) during the 8-h experiment. Sennoside A/B or senna infusion pre-treatment did not affect the absorptive permeability of mannitol (1.2-fold enhancement), but the BL-AP permeability was decreased to 35% (sennoside) and 71% (senna infusion) compared to the control value.

Transepithelial electrical resistance (TEER) of the monolayers was followed over the 8-h mannitol permeability experiment (Fig. 4b). As expected, high mannitol permeability is connected with low TEER values, indicating opening of the paracellular spaces between the Caco-2 cells. Rhein and danthron caused a strong decrement in the TEER values. However, all cell monolayers recovered during the 8-h experiment showing almost control-like values at the end of the experiment. This is indeed consistent with the results in mannitol permeability. Sennidin, sennoside and senna infusion caused also a strong decrement in the TEER, to about 55% of the control value, but the recovery of the monolayers was fast (at $t = 180$ min up to 75%), and therefore only slight effects on mannitol permeability were observed.

Anthraquinone laxatives have the ability to enhance fluid secretion to the small and large intestine [8,9]. This is caused by the disruption of tight junctions between colonic epithelial cells [12]. Mannitol, being a small paracellularly diffusing molecule (m.w. 182 g/mol), is a good marker molecule for tight junctional integrity of cell monolayers [15].

It has been observed that secretion of water, electrolytes, and [^{14}C]erythritol (a paracellular permeability marker molecule) into the rat colon happens 6 h after ingestion of sennosides [41]. In those experiments, it took several hours for sennosides to enter the colon, where bacterial β-glucosidase breaks down the β-glycosidic linkages between the glucose and the anthranoid molecules. In our experiments, sennosides did not cause prominent elevation of [^{14}C]mannitol permeability, but pre-treatment with sennidin (sennoside molecule without glucose moiety) caused a slight increment in AP-BL permeability. Because β-glucosidase was not present in our experiments, sennidin should act on Caco-2 monolayers as sennosides do when the glucose molecule is cleaved from the main dianthrone molecule in the colon. In fact, the TEER values had decreased by 40–45% after the sennidin and sennoside pre-treatment (Fig. 4b), but the cells recovered almost completely within 180 min, and the final TEER values were very close to the original values.

4. Conclusions

The abilities of highly permeable drugs paracetamol, propranolol, and verapamil to diffuse across Caco-2 cell monolayers were not strongly affected by any of the anthranoid laxatives. The effects of danthron and rhein on active transport of drugs may be due to reduced ATP production in Caco-2 cells, or by their affinity to intercalate with cell membranes, leading to changes in membrane fluidity. The effects of senna infusion on drug permeability are

variable, depending on several active compounds present in the infusion. The enhancement of paracellular permeability of drugs was evidenced by mannitol long-term assay and TEER measurements. Laxatives rhein and danthron were able to reversibly open the paracellular spaces between Caco-2 cells, leading to enhanced mannitol permeability and decreased TEER.

Our results indicate that anthranoid laxatives and drugs with high passive permeability can be contemporaneously ingested. However, if poorly permeable drugs are administered with anthranoid laxatives, effects on drug permeabilities cannot be predicted. *In vitro* experiments offer valuable information about possible interactions during absorption.

References

[1] G. Franz, The senna drug and its chemistry, Pharmacology 47 (1993) 2–6.

[2] P. de Witte, Metabolism and pharmacokinetics of anthranoids, Pharmacology 47 (1993) 86–97.

[3] J. Lemli, Metabolism of Sennosides – an overview, Pharmacology 36 (1988) 126–128.

[4] P. de Witte, J. Lemli, The metabolism of anthranoid laxatives, Hepatogastroenterology 37 (1990) 601–605.

[5] D.D. Breimer, A.J. Baars, Pharmacokinetics and metabolism of anthraquinone laxatives, Pharmacology 14 (1976) 30–47.

[6] T. Yagi, Y. Miyawaki, T. Nishikawa, K. Yamauchi, S. Kuwano, Involvement of prostaglandin-like material in the purgative action of rhein anthrone, the intraluminal active metabolite of sennosides A and B in mice, J. Pharm. Pharmacol. 40 (1988) 27–30.

[7] G. Nijs, P. de Witte, K. Geboes, J. Lemli, Influence of rhein anthrone and rhein on small intestine transit rate in rats: evidence of prostaglandin mediation, Eur. J. Pharmacol. 218 (1992) 199–203.

[8] E. Leng-Peschlow, Dual effect of orally administered sennosides on large intestine transit and fluid absorption in the rat, J. Pharm. Pharmacol. 38 (1986) 606–610.

[9] E. Beubler, G. Kollar, Prostaglandin-mediated action of sennosides, Pharmacology 36 (1988) 85–91.

[10] A. van Hoestenberghe, P. de Witte, K. Geboes, H. Eyssen, G. Nijs, J. Lemli, The effect of rhein and rhein anthrone on intestinal fluid transport and on large intestine transit in germfree rats, Eur. J. Pharmacol. 212 (1992) 121–123.

[11] R. Wanitschke, U. Karbach, Influence of rhein on rat colonic Na^+/K^+-ATPase and permeability in vitro, Pharmacology 36 (1988) 98–103.

[12] K. Ewe, The physiological basis of laxative action, Pharmacology 20 (1980) 2–20.

[13] D. Nilsson, U. Fagerholm, H. Lennernäs, The influence of net water absorption on the permeability of antipyrine and levodopa in the human jejunum, Pharm. Res. 11 (1994) 1540–1544.

[14] P. Artursson, Epithelial transport of drugs I. A model for studying the transport of drugs (β-blocking agents) over an intestinal epithelial cell line (Caco-2), J. Pharm. Sci. 79 (1990) 476–482.

[15] J.N. Cogburn, M.G. Donovan, C.S. Schaasteen, A model of human small intestinal absorptive cells. 1. Transport barrier, Pharm. Res. 8 (1991) 210–216.

[16] P. Artursson, K. Palm, K. Luthman, Caco-2 monolayers in experimental and theoretical predictions of drug transport, Adv. Drug Deliv. Rev. 22 (1996) 67–84.

[17] L. Laitinen, H. Kangas, A.M. Kaukonen, K. Hakala, T. Kotiaho, R. Kostiainen, J. Hirvonen, N-in-one permeability studies of heterogeneous sets of compounds across Caco-2 cell monolayers, Pharm. Res. 20 (2003) 187–197.

[18] D.G. Bailey, J. Malcolm, O. Arnold, J.D. Spence, Grapefruit juice–drug interactions, Br. J. Clin. Pharmacol. 46 (1998) 101–110.

[19] L. Laitinen, P. Tammela, A. Galkin, H. Vuorela, M. Marvola, P. Vuorela, Effects of extracts of commonly consumed food supplements and food fractions on the permeability of drugs across Caco-2 cell monolayers, Pharm. Res. 21 (2004) 1904–1916.

[20] T. Mosmann, Rapid colorimetric assay for cellular growth and survival: application to proliferation and cytotoxicity assays, J. Immunol. Methods 65 (1983) 55–63.

[21] T. Ogihara, I. Tamai, H. Takanaga, Y. Sai, A. Tsuji, Stereoselective and carrier-mediated transport of monocarboxylic acids across Caco-2 cells, Pharm. Res. 13 (1996) 1828–1832.

[22] J.-S. Choi, M.J. Jin, H.-K. Han, Role of monocarboxylic acid transporters in the cellular uptake of NSAIDs, J. Pharm. Pharmacol. 57 (2005) 1185–1189.

[23] A. Avdeef, C.M. Berger, C. Brownell, pH-metric solubility. 2: correlation between the acid-base titration and the saturation shake-flask solubility-pH methods, Pharm. Res. 17 (2000) 85–89.

[24] E.H.C. Verhaeren, Mitochondrial uncoupling activity as a possible base for a laxative and antiproriatic effect, Pharmacology 20 (1980) 43–49.

[25] J. Bruneton, Pharmacognosy, Phytochemistry, Medicinal Plants, Lavoisier Publishing, Paris, France, 1995.

[26] B.M. Müller, J. Kraus, G. Franz, Chemical structure and biological activity of water-soluble polysaccharides from *Cassia angustifolia* leaves, Planta Med. 55 (1989) 536–539.

[27] J. Yang, K.-J. Kim, V.H.L. Lee, Role of P-glycoprotein in restricting propranolol transport in cultured rabbit conjunctival epithelial cell layers, Pharm. Res. 17 (2000) 533–538.

[28] S. Orlowski, J. Mir, J. Belehradek, M. Garrigos, Effects of steroids and verapamil on P-glycoprotein ATPase activity: progesterone, desoxycorticosterone, corticosterone and verapamil are mutually non-exclusive modulators, Biochem. J. 317 (1996) 515–522.

[29] B.A.P. van Gorgom, H. Timmer-Bosscha, S. de Jong, D.M. van der Kolk, J.H. Kleibeuker, E.G.E. deVries, Cytotoxicity of rhein, the active metabolite of sennoside laxatives, is reduced by multidrug resistance-associated protein 1, Br. J. Cancer 86 (2002) 1494–1500.

[30] S. Döppenschmitt, H. Spahn-Langguth, C.G. Regårdh, P. Langguth, Role of P- glycoprotein-mediated secretion in absorptive drug permeability: an approach using passive membrane permeability and affinity to P-glycoprotein, J. Pharm. Sci. 88 (1999) 1067–1072.

[31] J. Polli, S. Wring, J. Humphreys, L. Huang, J. Morgan, L. Webster, C. Serabjit-Singh, Rational use of in vitro P-glycoprotein assays in drug discovery, J. Pharmacol. Exp. Ther. 299 (2001) 620–628.

[32] A. Collett, J. Tanianis-Hughes, G. Warhurst, Rapid induction of P-glycoprotein expression by high permeability compounds in colonic cells in vitro: a possible source of transporter mediated drug interactions? Biochem. Pharmacol. 68 (2004) 783–790.

[33] V. Pade, S. Stavchansky, Estimation of the relative contribution of the transcellular and paracellular pathway to the transport of passively absorbed drugs in the Caco-2 cell culture model, Pharm. Res. 14 (1997) 1210–1215.

[34] S.D. Flanagan, L.H. Takahashi, X. Liu, L.Z. Benet, Contributions of saturable active secretion, passive transcellular, and paracellular diffusion to the overall transport of furosemide across adenocarcinoma (Caco-2) cells, J. Pharm. Sci. 91 (2002) 1169–1177.

[35] S.D. Flanagan, C.L. Cummins, M. Susanto, X. Liu, L.H. Takahashi, L.Z. Benet, Comparison of furosemide and vinblastine secretion from cell lines overexpressing multidrug resistance protein (P-glycoprotein) and multidrug resistance-associated proteins (MRP1 and MRP2), Pharmacology 64 (2002) 126–134.

[36] M.D. Troutman, D.R. Thakker, Rhodamine 123 requires carrier-mediated influx for its activity as a P-glycoprotein substrate in Caco-2 cells, Pharm. Res. 20 (2003) 1192–1199.

[37] M.E. Cavet, M. West, N.L. Simmons, Transport and epithelial secretion of the cardiac glycoside, digoxin, by human intestinal epithelial (Caco-2) cells, Br. J. Pharmacol. 118 (1996) 1389–1396.

[38] S. Lowes, M.E. Cavet, N.L. Simmons, Evidence for a non-MDR1 component in digoxin secretion by human intestinal Caco-2 epithelial layers, Eur. J. Pharmacol. 458 (2003) 49–56.
[39] C. van Dijk, A.J.M. Driessen, K. Recour, The uncoupling efficiency and affinity of flavonoids for vesicles, Biochem. Pharmacol. 60 (2000) 1593–1600.
[40] P. Tammela, L. Laitinen, A. Galkin, T. Wennberg, R. Heczko, H. Vuorela, J.P. Slotte, P. Vuorela, Permeability characteristics and membrane affinity of flavonoids and alkyl gallates in Caco-2 cells and in phospholipid vesicles, Arch. Biochim. Biophys. 425 (2004) 193–199.
[41] E. Leng-Peschlow, Sennoside-induced secretion and its relevance for the laxative effect, Pharmacology 47 (1993) 14–21.

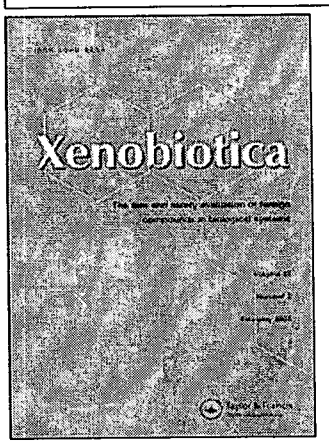

Xenobiotica
The fate and safety evaluation of foreign compounds in biological systems
Publication details, including instructions for authors and subscription information:
http://www.informaworld.com/smpp/title~content=t713698011

In vitro metabolism of eupatilin by multiple cytochrome P450 and UDP-glucuronosyltransferase enzymes

H. S. Lee [a]; H. Y. Ji [a]; E. J. Park [a]; S. Y. Kim [a]
[a] Drug Metabolism and Bioanalysis Laboratory, College of Pharmacy and Medicinal Resources Research Institute, Wonkwang University, Iksan, Korea

Online Publication Date: 01 August 2007
To cite this Article: Lee, H. S., Ji, H. Y., Park, E. J. and Kim, S. Y. (2007) '**In vitro** metabolism of eupatilin by multiple cytochrome P450 and UDP-glucuronosyltransferase enzymes', Xenobiotica, 37:8, 803 - 817
To link to this article: DOI: 10.1080/00498250701534877
URL: http://dx.doi.org/10.1080/00498250701534877

Xenobiotica, August 2007; 37(8): 803–817

In vitro metabolism of eupatilin by multiple cytochrome P450 and UDP-glucuronosyltransferase enzymes

H. S. LEE, H. Y. JI, E. J. PARK, & S. Y. KIM

Drug Metabolism and Bioanalysis Laboratory, College of Pharmacy and Medicinal Resources Research Institute, Wonkwang University, Iksan, Korea

(*Received 25 April 2007; revised 19 June 2007; accepted 25 June 2007*)

Abstract

Eupatilin, a pharmacologically active flavone derived from *Artemisia* plants, is extensively metabolized to eupatilin glucuronide, 4-*O*-desmethyleupatilin and 4-*O*-desmethyleupatilin glucuronide in human liver microsomes. This study characterized the human liver cytochrome P450 (CYP) and UDP-glucuronosyltransferase (UGT) enzymes responsible for the metabolism of eupatilin. The specific CYPs responsible for *O*-demethylation of eupatilin to the major metabolite, 4-*O*-desmethyleupatilin were identified using a combination of correlation analysis, immuno-inhibition, chemical inhibition in human liver microsomes and metabolism by human cDNA-expressed CYP enzymes. UGT enzymes involved in the eupatilin glucuronidation were identified using pooled human liver microsomes and human cDNA-expressed UGT enzymes. Eupatilin was predominantly metabolized by CYP1A2 and, to a lesser extent, CYP2C8 mediated *O*-demethylation of eupatilin to 4-*O*-desmethyleupatilin. Eupatilin glucuronidation was catalysed by UGT1A1, UGT1A3, UGT1A7, UGT1A8, UGT1A9, and UGT1A10.

Keywords: *Eupatilin metabolism, O-demethylation, CYP1A2, CYP2C8, UGT1A1, UGT1A3, UGT1A7, UGT1A8, UGT1A9, UGT1A10*

Introduction

Eupatilin, 2-(3,4-dimethoxy-phenyl)-5,7-dihydroxy 6-methoxy-chromen-4-one, is a pharmacologically active ingredient of *Artemisia asiatica* Nakai used as a traditional Asian medicinal plant (Seo and Surh 2001). Eupatilin has been shown to inhibit 5-lipoxygenase activity in cultured mastocytoma cells (Koshihara et al. 1983), and to induce apoptosis in human promyelocytic leukaemia cells and human gastric cancer cells (Seo and Surh 2001,

Correspondence: H. S. Lee, Drug Metabolism and Bioanalysis Laboratory, College of Pharmacy and Medicinal Resources Research Institute, Wonkwang University, Iksan 570-749, Korea. E-mail: hslee@wonkwang.ac.kr

ISSN 0049-8254 print/ISSN 1366-5928 online
DOI: 10.1080/00498250701534877

Kim et al. 2005a). The compound inhibits cellular protein tyrosine kinases and then blocks downstream multisignal pathways and Ca^{2+} influx during mast cell activation triggered by a specific antigen–antibody reaction (Kim et al. 2005b). Eupatilin also attenuates bile acid-induced hepatocyte apoptosis by suppressing bile acid-induced kinase activation (Park et al. 2006).

After intravenous administration of eupatilin in rats, 2.5 and 0.2% of the intravenous dose were excreted as an unchanged drug over 24 h in urine and bile, respectively, and the percentage of the intravenous doses excreted over 24 h in urine and bile as eupatilin glucuronide were 13.4 and 27.0%, respectively (Jang et al. 2003). Eupatilin is extensively metabolized to 6-*O*-desmethyleupatilin, 4-*O*-desmethyleupatilin, 4-*O*-desmethyleupatilin glucuronide, and eupatilin glucuronide in rats (Ji et al. 2004).

Knowledge of the specific cytochrome P450 (CYP) enzyme(s) and UDP-glucuronosyltransferases (UGTs) that biotransform a drug can be of considerable clinical importance with regard to potential drug–drug interactions and inter-individual variation in drug metabolism. Accordingly, the purpose of the current study was to characterize the human CYP enzyme(s) responsible for the biotransformation of eupatilin to a major phase I metabolite 4-*O*-desmethyleupatilin and the human UGT enzyme(s) involved in the formation of a major metabolite, eupatilin glucuronide from eupatilin

Materials and methods

Reagents

Eupatilin (>99.5% purity) was donated by Dong-A Pharmaceutical Co. (Yongin, Korea). 4-*O*-desmethyleupatilin was from Plant Diversity Research Center, Korea Research Institute of Bioscience and Biotechnology (Daejeon, Korea). NADPH, $NADP^+$, glucose 6-phosphate, glucose 6-phosphate dehydrogenase, alamethicin, uridine diphosphoglucuronic acid (UDPGA), diethyldithiocarbamate, coumarin, furafylline, ketoconazole, sulfaphenazole, quinidine, and triethylenethiophosphoramide were obtained from Sigma Chemical Co. (St. Louis, MO, USA). Acetonitrile and ethyl acetate (HPLC grade) were obtained from Burdick & Jackson, Inc. (Muskegon, MI, USA) and the other chemicals were of the highest quality available.

Human liver microsomes (coded H161, H003, H023, H042, H043, H056, H066, H070, H089, H093, HH18, HK23, and HK34), human CYP enzymes (CYPs 1A2, 2A6, 2B6, 2C8, 2C9, 2C19, 2D6, 2E1, and 3A4) and human UGT enzymes (UGTs 1A1, 1A3, 1A4, 1A6, 1A7, 1A8, 1A9, 1A10, 2B4, 2B7, 2B15, and 2B17) produced using a baculovirus-insect cell-expression system and *S*-benzylnirvanol were purchased from BD Gentest Co. (Woburn, MA, USA). Human selective antibodies for the immuno-inhibition of human CYPs, i.e. anti-CYP1A2, anti-CYP2D6, anti-CYP2C8, and anti-CYP2E1 were obtained from Gentest Co.

Metabolism of eupatilin in human liver microsomes or cDNA-expressed CYP enzymes

Incubation mixtures contained 50 mM potassium phosphate buffer (pH 7.4), human liver microsomes (0.2 mg protein ml^{-1}), or cDNA-expressed CYP1A2, 2C8, 2C9, 2C19, 2D6, 2E1, and 3A4 enzymes (4 pmol), an NADPH-generating system (1.3 mM NADP, 3.3 mM glucose 6-phosphate and 0.8 U ml^{-1} glucose 6-phosphate dehydrogenase),

3 mM magnesium chloride, and eupatilin (5 and 75 μM, final acetonitrile concentration not exceeding 0.5%, v/v) in a final volume of 200 μl. Preliminary experiments showed that the formation of a major metabolite, 4-*O*-desmethyleupatilin from eupatilin, was linear with respect to both incubation time over 20 min and liver microsomal protein concentration (0.1–0.3 mg ml^{-1}) at 37°C. Thus, a 15-min incubation time and a 0.2 mg ml^{-1} microsomal protein concentration were selected. The incubations were initiated by the addition of the NADPH-generating system and continued at 37°C for 15 min in a shaking water bath. The reactions were terminated by the addition of 10 μl of 1 M hydrochloric acid solution, 10 μl of linezolid (internal standard, 100 ng ml^{-1}), and 1000 μl of ethyl acetate. After vortex-mixing and centrifugation an aliquot of the organic layer was pipette-transferred and evaporated to dryness under nitrogen at 35°C. The residues were dissolved in 40 μl of 50% acetonitrile in water by vortex-mixing for 2 min, transferred to injection vials, and then 10 μl were injected into an LC-MS system.

In kinetic experiments of the metabolism of eupatilin to 4-*O*-desmethyleupatilin, eight concentrations of eupatilin (0.5, 1, 2, 5, 10, 25, 50, and 100 μM) were incubated in duplicate with three different human liver microsome samples (H043, H056, and H093) or cDNA-expressed CYP 1A2, 2C8, 2C9, 2C19, and 2D6 enzymes to obtain values for K_m and V_{max}.

Correlation of 4-O-desmethyleupatilin formation with probe substrate activities

The comparative metabolic rates of eupatilin in 12 different human liver microsome samples were investigated by incubating 5 and 75 μM of eupatilin with 0.2 mg ml^{-1} microsomal protein for 15 min. The formation rate of 4-*O*-desmethyleupatilin was correlated with specific CYP activities in human liver microsomes reported by Gentest using the Pearson Product Moment Correlation (SigmaStat software version 2.0, SPSS Science). A $p < 0.05$ was considered as being statistically significant.

Inhibition of 4-O-desmethyleupatilin formation by CYP-specific inhibitors and antibodies in human liver microsomes

Immuno-inhibition studies were performed by incubating pooled human liver microsomes (H161) with various amounts of human selective antibodies, anti-CYP1A2, anti-CYP2C8, anti-CYP2D6, or anti-CYP3A4 for 15 min on ice before the addition of 50 mM potassium phosphate buffer (pH 7.4), eupatilin (5 and 75 μM), 3 mM magnesium chloride, and NADPH-generating system. As a control, comparable incubations were done with microsomes and 25 mM Tris buffer (pH 7.4).

The inhibitory effects of selective CYP enzyme inhibitors on the metabolism of eupatilin to 4-*O*-desmethyleupatilin were evaluated in pooled human liver microsomes (H161). Well-characterized specific CYP inhibitors, i.e. 10 μM furafylline for CYP1A2 (Sesardic et al. 1990), 100 μM coumarin for CYP2A6 (Yun et al. 1991), 5 μM triethylenethiophosphoramide for CYP2B6 (Rae et al. 2002), 0.1 μM montelukast for CYP2C8 (Walsky et al. 2005), 10 μM sulfaphenazole for CYP2C9 (Baldwin et al. 1995), 1 μM *S*-benzylnirvanol for CYP2C19 (Suzuki et al. 2002), 10 μM quinidine for CYP2D6 (Newton et al. 1995), 10 μM diethyldithiocarbamate for CYP2E1 (Newton et al. 1995), and 1 μM ketoconazole for CYP3A4 (Baldwin et al. 1995) were incubated with 5 or 75 μM of eupatilin, pooled human liver microsomes (H161, 0.2 mg ml^{-1}) and an NADPH-generating system for 15 min at 37°C. Furafylline and diethyldithiocarbamate were pre-incubated for 10 min with human liver microsome and an NADPH-generating system before the addition

of eupatilin to initiate the reaction. The activity of each inhibitor was compared with a control incubation that did not contain the inhibitor.

Characterization of human UGTs involved in the formation of eupatilin glucuronide

To screen UGT enzymes involved in eupatilin glucuronidation, 200 µl reaction mixtures containing human liver microsomes (0.20 mg protein ml^{-1}) or cDNA-expressed UGT 1A1, 1A2, 1A3, 1A4, 1A5, 1A6, 1A7, 1A8, 1A9, 1A10, 2B4, 2B7, 2B15, and 2B17 enzymes (0.1 mg protein ml^{-1}), 1 mM UDPGA, 0.025 mg ml^{-1} alamethicin, 10 mM magnesium chloride, and eupatilin (20 µM, final acetonitrile concentration not exceeding 0.5%, v/v) in 50 mM Tris buffer (pH 7.5) were incubated at 37°C for 30 min. The reaction was stopped by the addition of 10 µl of 1 M hydrochloric acid solution, 10 µl of linezolid (internal standard, 100 ng ml^{-1}), and 1000 µl of ethyl acetate. After vortex-mixing and centrifugation, an aliquot of the organic layer was pipette-transferred and evaporated to dryness under nitrogen at 35°C. The residues were dissolved in 40 µl of 50% acetonitrile in water by vortex-mixing for 2 min, transferred to injection vials, and then 10 µl were injected into an LC-MS system.

In kinetic experiments of the metabolism of eupatilin to eupatilin glucuronide, eight concentrations of eupatilin (0.5, 1, 2, 5, 10, 25, 50, and 100 µM) were incubated in duplicate with pooled human liver microsomes (H161, 0.20 mg protein ml^{-1}) or cDNA-expressed UGT 1A1, 1A3, 1A8, 1A10 (0.10 mg protein ml^{-1}), 1A7 (0.025 mg protein ml^{-1}), and 1A9 (0.05 mg protein ml^{-1}) enzymes to obtain values for K_m and V_{max}.

LC-MS analysis of eupatilin and metabolites

For the analysis of eupatilin and its metabolites, a tandem quadrupole mass spectrometer (Quattro LC, Micromass) coupled with a Nanospace SI-2 LC system (Shizeido) was used. The separation was performed on a Luna phenylhexyl column (3 µm, 2 mm i.d. × 100 mm; Phenomenex, CA, USA) using a mixture of acetonitrile in 10 mM ammonium formate (pH 3.0) (40 : 60, v/v) at a flow rate of 0.2 ml min^{-1}. The column temperature was 35°C.

To allow identification of the metabolites, mass spectra were recorded by electrospray ionization in positive mode. The ion source and desolvation temperature were held at 120 and 350°C, respectively. The cone voltage was 40 V and the collision energy for daughter scanning was 24 eV. A selected ion monitoring (SIR) mode was employed for quantification: *m/z* 331.7 for 4-*O*-desmethyleupatilin, *m/z* 521.0 for eupatilin glucuronide, and *m/z* 338.2 for linezolid (internal standard). Peak areas for all components were automatically integrated using MassLynx Version 3.5 (Micromass UK Ltd, Manchester, UK). The calibration curve was linear over the concentration range of 0.5–200 pmol of 4-*O*-desmethyleupatilin. The inter-batch relative error value for 4-*O*-desmethyleupatilin ranged from 2.3 to 4.5% with coefficient of variation values of 1.8–3.4% at three QC levels, i.e. 1.0, 40, and 180 pmol.

Data analysis

Results are presented as the average of two determinations obtained from human liver microsomes, human cDNA-expressed CYPs and UGTs. The apparent kinetic parameters

for the oxidation of eupatilin to 4-*O*-desmethyleupatilin (K_m and V_{max}) were determined by fitting the Michaelis–Menten equation:

$$\left[V = \frac{V_{max} \cdot S}{K_m + S}\right]$$

or isozyme equation model:

$$\left[V = \frac{V_{max1} \cdot (S/K_{m1})}{1 + S/K_{m1}} + \frac{V_{max2} \cdot (S/K_{m2})}{1 + S/K_{m2}}\right]$$

to unweighted data on the formation rate of 4-*O*-desmethyleupatilin over a range of eupatilin concentrations using Enzyme Kinetics software (version 1.1, SPSS Science, Inc., Richmond, CA, USA). The apparent kinetic parameters for the formation of eupatilin glucuronide in cDNA-expressed UGT enzymes were determined by fitting the substrate-inhibition equation or Hill equation model:

$$\left[V = \frac{V_{max} \cdot S^n}{K_m^n + S^n}\right]$$

to unweighted data on the formation rate of eupatilin glucuronide over a range of eupatilin concentrations, where V is the velocity of the reaction at substrate concentration (S); V_{max} is the maximum velocity; and K_m is the substrate concentration at which the reaction velocity is 50% of V_{max}. The intrinsic clearance (Cl_{int}) of *in vitro* incubation was calculated as V_{max}/K_m. Contributions of each cytochrome to eupatilin oxidation were normalized for mean values of the relative abundance of individual cytochromes in human liver. The relative abundances of CYP1A2 (12.7%), CYP2C8 (7.0%), CYP2C9 (14.7%), CYP2C19 (3.5%), CYP2D6 (1.5%), and CYP2E1 (6.6%) have been previously reported (Shimada et al. 1994, Venkatakrishnan et al. 1998). The Cl_{int} attributable to CYPs 1A2, 2C8, 2C9, 2C19, 2D6, and 2E1 was multiplied by the relative abundance of each CYP in the liver. Percentages of the Cl_{int} of an individual CYP relative to the overall contribution of CYPs 1A2, 2C8, 2C9, 2C19, 2D6, and 2E1 were calculated.

Results

In vitro metabolic profiles of eupatilin in human liver microsomes

LC-MS analysis of organic extracts after the incubation of eupatilin with human liver microsomes in the presence of NADPH and UDPGA resulted in three metabolites (M1, M2, and M3 in the order of elution). M1, M2, and M3 showed pseudo-molecular ions (MH^+) at *m/z* 507, 521, and 331, respectively (Figure 1a) and LC-MS/MS analysis of unchanged eupatilin and its three metabolites produced informative and prominent product ions (Figure 1b).

The major metabolite M2 exhibited MH^+ ion at *m/z* 521 (176 amu more than parent eupatilin) and a product ion at *m/z* 345, and was produced from the incubation of eupatilin in the presence of UDPGA, suggesting that M2 might result from glucuronidation of eupatilin. M2 was therefore tentatively characterized as eupatilin glucuronide.

The major metabolite M3, produced from the incubation of eupatilin with pooled human liver microsome in the presence of an NADPH-generating system, generated an MH^+ ion at *m/z* 331 (14 amu less than the parent eupatilin) and product ions at *m/z* 316, *m/z* 301,

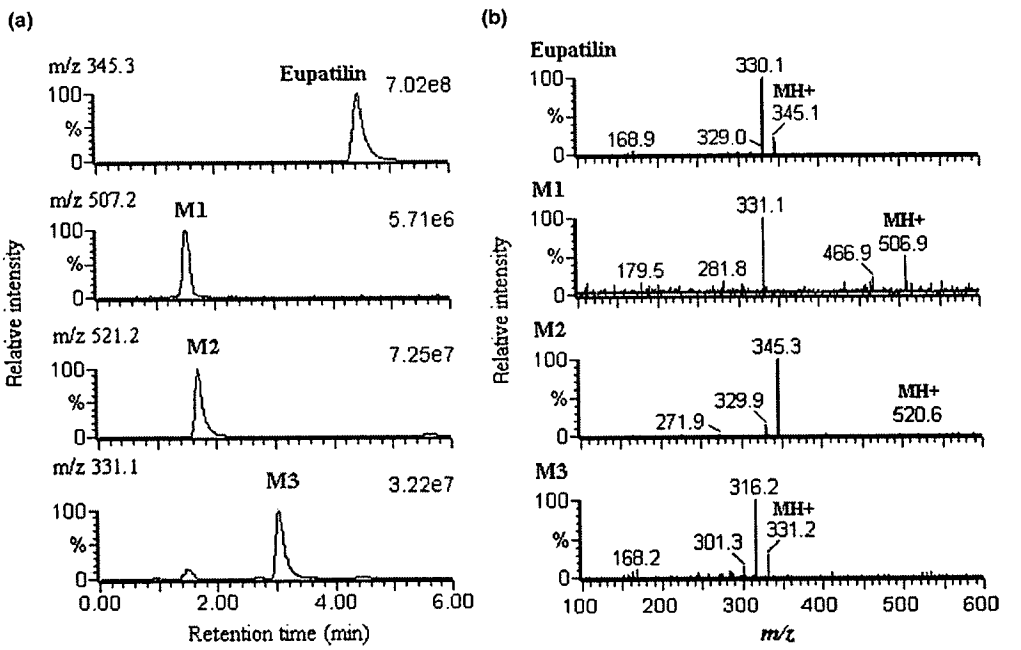

Figure 1. (a) Extracted ion chromatograms for the incubation of eupatilin with human liver microsomes in the presence of an NADPH-generating system and UDPGA; and (b) MS/MS spectra of eupatilin and its three metabolites, M1, M2, and M3.

and *m/z* 168. M3 was produced by 4-*O*-demethylation and identified as 4-*O*-desmethyleupatilin based on co-chromatography and MS/MS spectrum of the authentic standard.

Metabolite M1 was produced from the incubation of eupatilin with pooled human liver microsome in the presence of an NADPH-generating system and UDPGA and displayed an MH^+ ion at *m/z* 507 (176 amu more than 4-*O*-desmethyleupatilin) and a product ion at *m/z* 331. M1 was therefore tentatively identified as 4-*O*-desmethyleupatilin glucuronide. The possible metabolic pathways of eupatilin in human liver microsomes are shown in Figure 2.

Characterization of human CYPs involved in the formation of 4-O-desmethyleupatilin from eupatilin

The metabolism of eupatilin to 4-*O*-desmethyleupatilin in three human liver microsomes followed Michaelis–Menten kinetics (Figure 3). The apparent kinetic parameters for the formation of 4-*O*-desmethyleupatilin in three human liver microsomes were $K_{m1} = 7.2$ (± 3.3) μM, $K_{m2} = 246$ (± 151) μM, $V_{max1} = 44.0$ (± 27.8) pmol min^{-1} mg $protein^{-1}$, $V_{max2} = 244$ (± 123) pmol min^{-1} mg $protein^{-1}$, $Cl_{int1} = 6.0$ (± 2.3) μl min^{-1} mg $protein^{-1}$, and $Cl_{int2} = 1.2$ (± 0.5) μl min^{-1} mg $protein^{-1}$ (Table I).

A screen using microsomes containing either human cDNA-expressed CYPs 1A2, 2A6, 2B6, 2C8, 2C9, 2C19, 2D6, 2E1, or 3A4 for the metabolism of 5 and 75 μM eupatilin to 4-*O*-desmethyleupatilin identified possible roles of CYPs 1A2, 2C8, 2C9, 2C19,

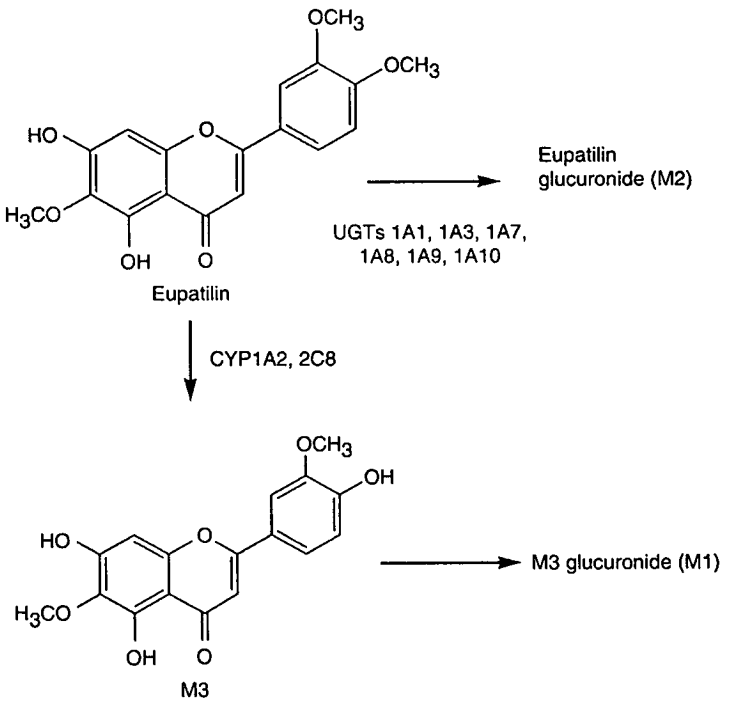

Figure 2. Proposed metabolic pathways of eupatilin in human liver microsome.

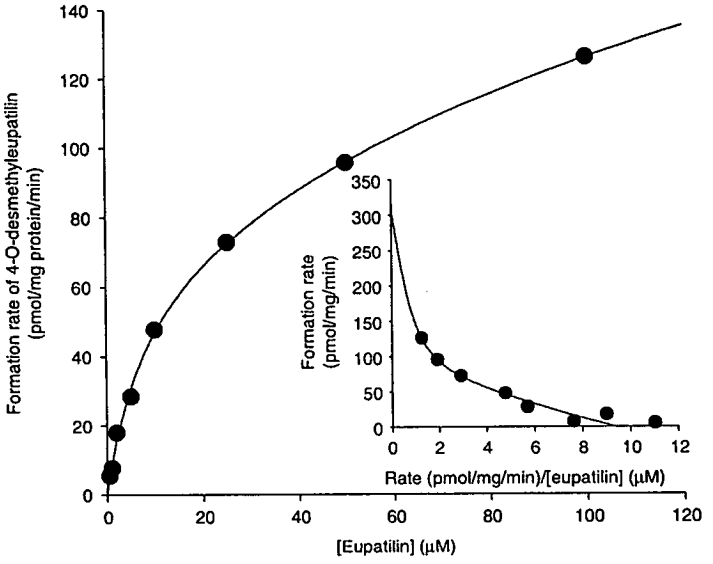

Figure 3. Michaelis–Menten plots for the biotransformation of eupatilin to 4-*O*-desmethyleupatilin in human liver microsome H056 with inset Eadie–Hostee plots demonstrating isozyme kinetics. Each data point represents the average of two determinations.

Table I. Kinetic parameters for eupatilin metabolism to 4-*O*-desmethyleupatilin in three human liver microsome samples.

Parameters	Human liver microsomes			Mean ± SD
	H043	H056	H093	
K_{m1} (μM)	9.6	8.5	3.4	7.2 ± 3.3
K_{m2} (μM)	358	304	74.6	246 ± 151
V_{max1} (pmol min^{-1} mg protein^{-1})	41.5	72.9	17.5	44.0 ± 27.8
V_{max2} (pmol min^{-1} mg protein^{-1})	370	238	124	244 ± 123
Cl_{int1} (μl min^{-1} mg protein^{-1})	4.3	8.6	5.1	6.0 ± 2.3
Cl_{int2} (μl min^{-1} mg protein^{-1})	1.2	0.5	1.1	1.2 ± 0.5

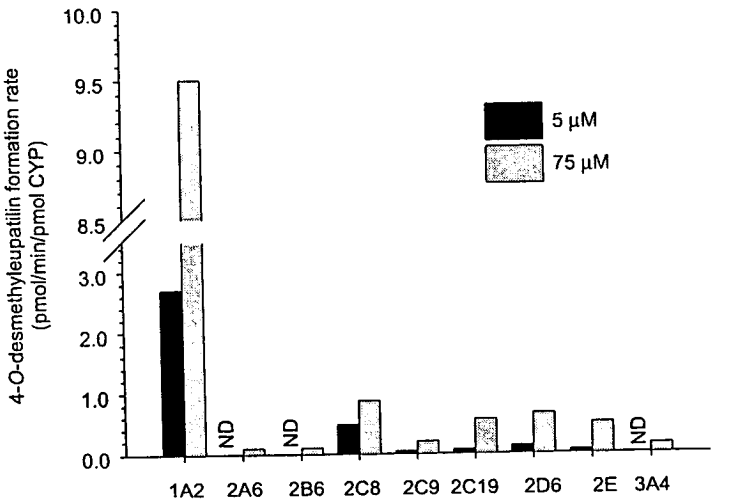

Figure 4. Formation rates of 4-*O*-desmethyleupatilin from eupatilin by human cDNA-expressed CYP enzymes. Each data point represents the average of two determinations. ND was less than 0.01 pmol min^{-1} pmol CYP^{-1}.

2D6, and 2E1 in the formation of 4-*O*-desmethyleupatilin (Figure 4). Table II details the single enzyme Michaelis–Menten kinetics for the formation of 4-*O*-desmethyleupatilin from eupatilin in human cDNA-expressed CYPs 1A2, 2C8, 2C9, 2C19, 2D6, and 2E1. The contributions of these CYPs were determined after normalization for the predicted relative abundance of each CYP, as described in the Materials and methods. Normalization for the relative abundance of CYPs confirmed that CYP1A2 played the predominant role in the formation of 4-*O*-desmethyleupatilin from eupatilin with minor contribution of CYP2C8.

The rates of 4-*O*-desmethyleupatilin formation from 5 and 75 μM eupatilin in 12 human liver microsomes were 19.4–52.1 and 94.3–314.6 pmol min^{-1} mg protein^{-1}, respectively. Table III shows correlations between the rate of 4-*O*-desmethyleupatilin formation in 12 human liver microsomal samples and their standard CYP-specific activities. A good correlation was observed between the rates of phenacetin *O*-deethylase, a marker of

Table II. Kinetic parameters for eupatilin metabolism to 4-*O*-desmethyleupatilin in human cDNA-expressed CYPs. Since the role of each CYP has been determined relative to others, their Cl_{int} (V_{max}/K_m) values have been normalized for the relative hepatic abundance of each CYP, as described in the Materials and methods.

Expressed human CYP	K_m (μM)	V_{max} (pmol min^{-1} pmol CYP^{-1})	Cl_{int} (μl min^{-1} pmol CYP^{-1})	Cl_{int} (% of total)
1A2	14.4	11.2	0.778	86.0
2C8	4.5	0.94	0.209	12.7
2C9	156	0.53	0.003	0.4
2C19	161	0.81	0.005	0.2
2D6	88.6	0.73	0.008	0.1
2E1	73.9	0.73	0.010	0.6

Table III. Correlation of CYP activities and the rates of formation of 4-*O*-desmethyleupatilin from eupatilin in 12 different human liver microsomes.

		Correlation coefficient	
Enzymatic activity	CYP	5 μM	75 μM
Phenacetin *O*-deethylase	1A2	0.594*	0.672*
Coumarin 7-hydroxylase	2A6	0.371	−0.120
Paclitaxel 6α-hydroxylase	2C8	0.525	0.110
Diclofenac 4′-hydroxylase	2C9	0.336	0.143
[*S*]-mephenytoin 4′-hydroxylase	2C19	0.126	−0.101
Bufuralol 1′-hydroxylase	2D6	0.158	0.111
Chlorozoxazone 6-hydroxylase	2E1	0.532	0.445
Testosterone 6β-hydroxylase	3A4	0.231	−0.010

*$p < 0.05$.

CYP1A2, and the formation of 4-*O*-desmethyleupatilin from eupatilin at 5 μM ($r = 0.594$, $p = 0.0387$) and 75 μM ($r = 0.672$, $p = 0.0167$).

Figure 5 shows the effects of selective inhibitors of CYP on 4-*O*-desmethyleupatilin formation from eupatilin in pooled human liver microsomes (H161). The CYP1A2 selective inhibitor, furafylline (10 μM) extensively inhibited 4-*O*-desmethyleupatilin formation by up to 50%. The effect of the other inhibitors tested on the formation of 4-*O*-desmethyleupatilin was less than a 20% reduction.

To confirm further which CYP is primarily responsible for the formation of 4-*O*-desmethyleupatilin from eupatilin, immuno-inhibition studies with anti-CYP1A2, anti-CYP2C8, anti-CYP2D6 or anti-CYP2E1 were performed in pooled human liver microsomes (H161) (Figure 6). 4-*O*-desmethyleupatilin formation was inhibited up to 50% and 20% by anti-CYP2C8 and anti-CYP1A2, respectively. Neither anti-CYP2D6 nor anti-CYP2E1 inhibited the metabolism of eupatilin to 4-*O*-desmethyleupatilin in pooled human liver microsomes.

Characterization of human UGT enzymes involved in glucuronidation of eupatilin

Eupatilin glucuronide was produced in incubations with human liver microsomes and human cDNA-expressed UGTs 1A1, 1A3, 1A7, 1A8, 1A9, and 1A10, but not with

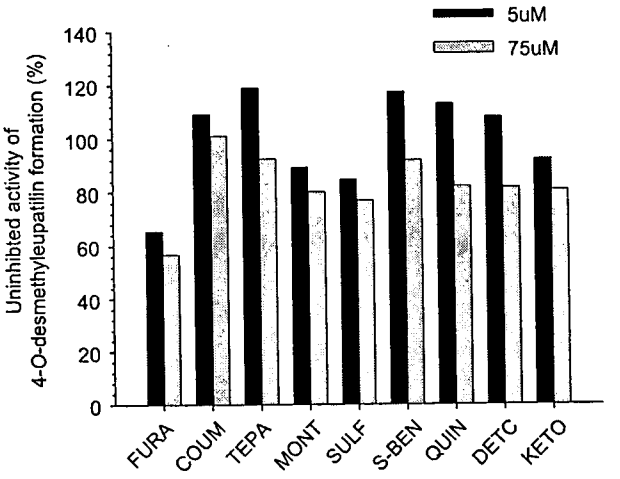

Figure 5. Effects of CYP-selective inhibitors on the metabolism of eupatilin to 4-*O*-desmethyleupatilin. Pooled human liver microsomes (H161, 0.2 mg protein ml^{-1}) were incubated with 5 or 75 μM eupatilin and an NADPH-generating system in the presence and absence of chemical inhibitors at 37°C for 15 min. Each bar represents the average of two determinations. FURA, furafylline (10 μM) for CYP1A2; COUM, coumarin (100 μM) for CYP2A6; TEPA, triethylenethiophosphoramide (5 μM) for CYP2B6; MONT, montelukast (0.1 μM) for CYP2C8; SULF, sulfaphenazole (10 μM) for CYP2C9; S-BEN, *S*-benzylnirvanol (1 μM) for CYP2C19; QUIN, quinidine (10 μM) for CYP2D6; DETC, diethyldithiocarbamate (10 μM) for CYP2E1; and KETO, ketoconazole (1 μM) for CYP3A4. Control formation rate for 4-*O*-desmethyleupatilin formation was 49.3 pmol mg protein^{-1} min^{-1} at 5 μM and 186 pmol mg protein^{-1} min^{-1} at 75 μM.

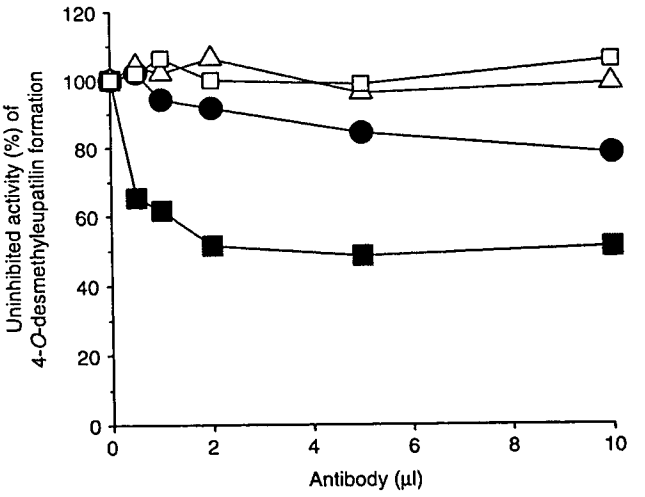

Figure 6. Effect of anti-CYP antibodies on the metabolism of 5 μM eupatilin to 4-*O*-desmethyleupatilin. Pooled human liver microsomes (H161, 0.2 mg protein ml^{-1}) were pre-incubated with anti-CYP1A2 (●), anti-CYP2C8 (■), anti-CYP2D6 (Δ) or anti-CYP2E1 (□). Each data point represents the average of two determinations. The control reaction rate for the formation of 4-*O*-desmethyleupatilin from 5 μM eupatilin was 49.3 min^{-1} mg protein^{-1}.

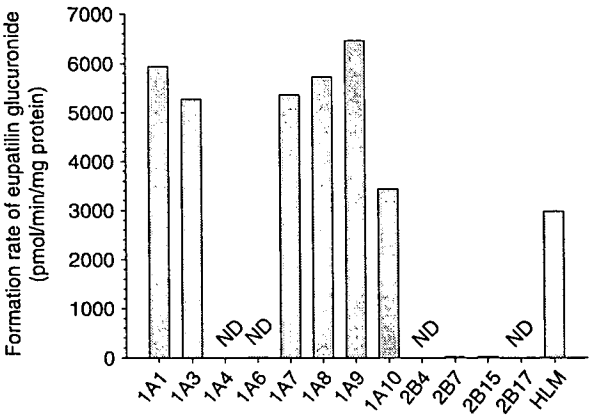

Figure 7. Formation of eupatilin glucuronide from 20 μM eupatilin in human cDNA-expressed UGT enzymes and pooled human liver microsomes (H161) in the presence of UDPGA. Each data point represents the average of two determinations. ND was less than 30 pmol min^{-1} mg $protein^{-1}$.

1A4, 1A6, 2B4, 2B7, 2B15, and 2B17 (Figure 7). Figure 8 shows the concentration-dependent formation rate for eupatilin glucuronide in UGTs 1A1, 1A3, 1A7, 1A8, 1A9, and 1A10. In UGT1A1, the substrate inhibition of eupatilin glucuronidation was observed at substrate concentrations higher than 10 μM. The rate of eupatilin glucuronidation revealed sigmoidal saturation curves that were fitted to the Hill equation for UGTs 1A3, 1A7, 1A8, 1A9, 1A10, and pooled human liver microsomes. The enzyme kinetic parameters of the formation of eupatilin glucuronide from eupatilin are listed in Table IV. The K_m values (6.2–40.1 μM) of eupatilin glucuronidation in UGTs 1A1, 1A3, 1A7, 1A8, and 1A9 were similar to that of pooled human liver microsomes (19.9 μM), except for UGT1A10 (240.7 μM).

Discussion

Eupatilin was metabolized to three metabolites (eupatilin glucuronide, 4-*O*-desmethyleupatilin, and 4-*O*-desmethyleupatilin glucuronide) in human liver microsomal incubations in the presence of UDPGA and NADPH (Figures 1 and 2). 6-*O*-desmethyleupatilin is a minor metabolite in rat liver microsomal incubations and rats (Ji et al. 2004), but was not detected in human microsomal incubations.

In order to identify the specific enzymes responsible for *O*-demethylation of eupatilin to 4-*O*-desmethyleupatilin, a combination of chemical inhibition, immuno-inhibition, correlation analysis in human liver microsomes and metabolism by recombinant cDNA-expressed CYP enzymes was employed. Two apparent kinetic parameters for 4-*O*-desmethyleupatilin formation in three human liver microsomes suggested the involvement of more than one CYP enzymes. Correlation analysis between known CYP activities and the rate of 4-*O*-desmethyleupatilin formation revealed a significant correlation with CYP1A2-catalysed phenacetin *O*-deethylase activity in the 12 human liver microsomes investigated. Furafylline, a selective CYP1A2 inhibitor, substantially inhibited 4-*O*-desmethyleupatilin

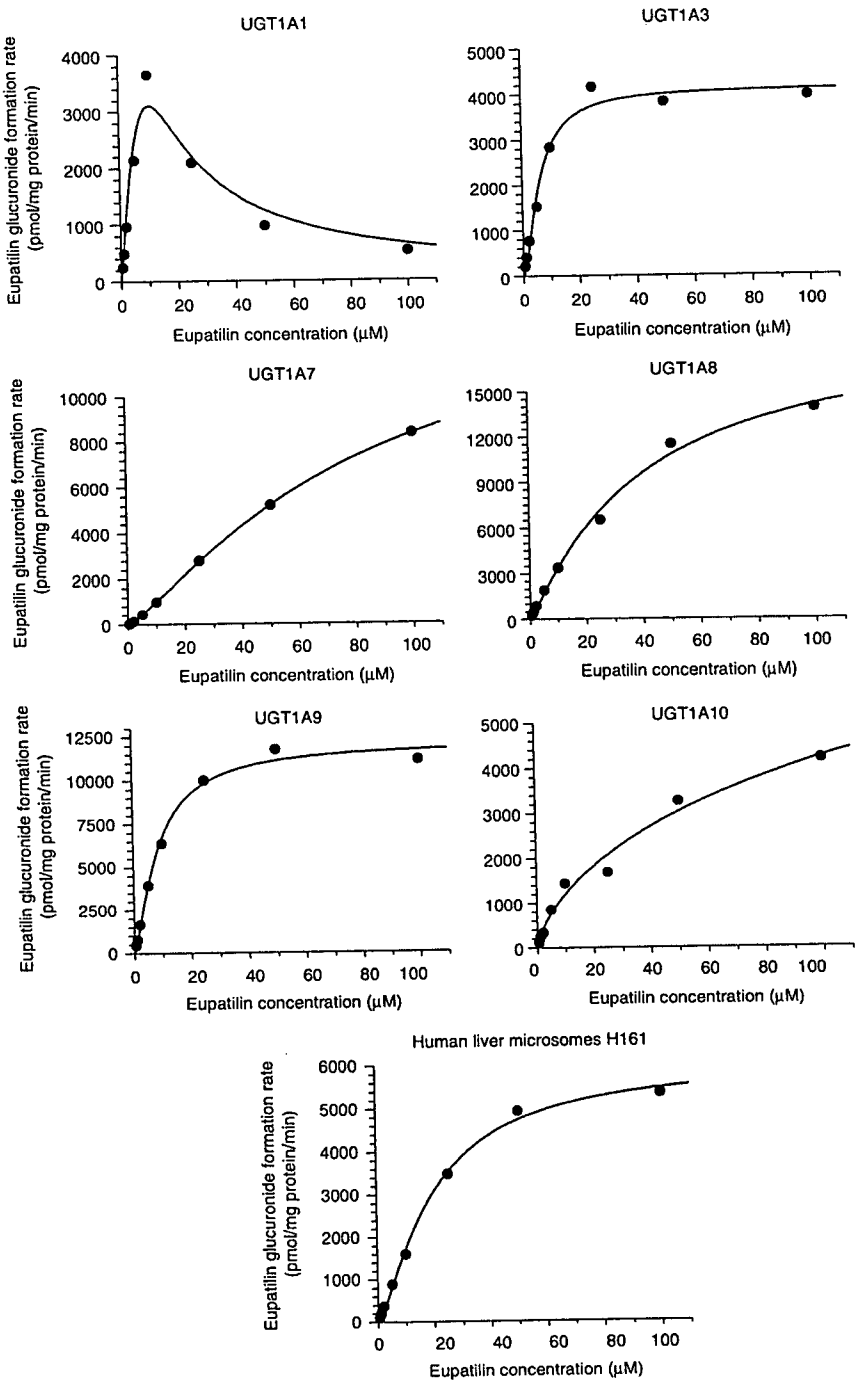

Figure 8. Michaelis–Menten plots for the glucuronidation of eupatilin to eupatilin glucuronide in UGT1A1, UGT1A3, UGT1A7, UGT1A8, UGT1A9, UGT1A10, and pooled human liver microsomes (H161). Each data point represents the average of two determinations.

Table IV. Kinetic parameters for glucuronidation of eupatilin in human cDNA-expressed UGT enzymes and pooled human liver microsomes.

UGT	K_m (μM)	V_{max} (pmol min^{-1} mg protein^{-1})	n	K_i
1A1	16.9	10010	–	6.5
1A3	6.2	4189.4	1.6	
1A7	9.2	19860	1.1	
1A8	40.1	19330	1.1	
1A9	8.4	11960	1.4	
1A10	240.7	12060	0.7	
H161	19.9	6055.8	1.3	

formation (Figure 5). CYP1A2 was calculated to contribute up to 86% of the formation of 4-*O*-desmethyleupatilin from eupatilin and to be the major enzyme catalysing eupatilin *O*-demethylation (Figure 4 and Table II). CYP2C8 was partly involved in the *O*-demethylation of eupatilin to 4-*O*-desmethyleupatilin. Anti-CYP1A2 and anti-CYP2C8 antibodies inhibited the metabolism of eupatilin to 4-*O*-desmethyleupatilin (Figure 6). These results collectively suggest that CYP1A2 plays the predominant role and CYP2C8 a lesser one in eupatilin *O*-demethylation to 4-*O*-desmethyleupatilin.

Human cDNA-expressed UGT1A1, 1A3, 1A7, 1A8, 1A9 and 1A10 enzymes were responsible for eupatilin glucuronidation (Figure 7 and Table IV). However, the relative contribution of each of these six UGT enzymes could not be estimated because the relative expression levels of different UGTs in expressed enzyme systems and the human liver have not been determined (Miners et al. 2006). K_m values for UGT1A1, UGT1A3 and UGT1A9, expressed in the human liver (Kiang et al. 2005), were similar to that of pooled human liver microsomes. UGT1A8 and UGT1A10 are exclusively present in the gastrointestinal tract, whereas UGT1A7 is expressed in the oesophagus, stomach, and lung (Strassburg et al. 1997, Cheng et al. 1998). Because of the tissue-specific distribution of these six UGT enzymes responsible for eupatilin glucuronidation, both the gastrointestinal tract and the liver may contribute to the glucuronidation of eupatilin.

CYP1A2, expressed in humans with wide inter-individual variability (Schweikl et al. 1993), was a major enzyme for *O*-demethylation of eupatilin to 4-*O*-desmethyleupatilin, suggesting that inter-individual variability in the pharmacokinetics of eupatilin may be expected due to variable rates of metabolism. CYP1A2 has been shown to be induced or inhibited by various drugs and chemicals (Miners and McKinnon 2000). Any co-administered drugs that can inhibit or induce CYP1A2 may alter the formation of 4-*O*-desmethyleupatilin from eupatilin.

Genetic polymorphisms have been identified for UGT1A1, UGT1A4, UGT1A6, UGT1A7, UGT1A8, UGT1A9, UGT1A10, UGT2B7, and UGT2B15 (Iyer et al. 1999, Guillemette 2003, Shipkova and Wieland 2005). UGT1A1, UGT1A7, UGT1A9, and UGT1A10 are inhibited or induced by various drugs, based on *in vitro* experiments using recombinant UGT enzymes, human liver microsomes, human hepatocytes or Caco-2 cells (Lyer et al. 1999, Galijatovic et al. 2001, Zhang et al. 2005, Naganuma et al. 2006). The clinical studies on the effects of putative UGT inhibitors or inducers on drug glucuronidation have been reviewed by Kiang et al. (2005).

In summary, eupatilin was metabolized by multiple CYP-mediated *O*-demethylation and UGT-mediated glucuronidation pathways. CYP1A2 plays the major role in *O*-demethylation of eupatilin to 4-*O*-desmethyleupatilin with a minor role of CYP2C8,

and the glucuronidation of eupatilin is catalysed by UGT1A1, UGT1A3, UGT1A7, UGT1A8, UGT1A9, and UGT1A10. The inter-individual variability in the pharmacokinetics of eupatilin seems to be observed due to the involvement of polymorphic drug metabolic enzymes in the metabolism of eupatilin.

Acknowledgement

This study was supported by a grant of Korea Research Foundation (No. J03203).

References

Baldwin SJ, Bloomer JC, Smith GJ, Ayrton AD, Clarke SE, Chenery RJ. 1995. Ketoconazole and sulphaphenazole as the respective selective inhibitors of P450 3A and 2C9. Xenobiotica 25:261–270.

Cheng Z, Radominska-Pandya A, Tephly TR. 1998. Cloning and expression of human UDP-glucuronosyltransferse (UGT) 1A8. Archives of Biochemistry and Biophysics 356:301–305.

Galijatovic A, Otake Y, Walle UK, Walle T. 2001. Induction of UDP-glucuronosyltransferase UGT1A1 by the flavonoid chrysin in Caco-2 cells-potential role in Caco-2 cells-potential role in carcinogen bioinactivation. Pharmaceutical Research 18:374–379.

Guillemette C. 2003. Pharmacogenomics of human UDP-glucuronosyltransferase enzymes. Pharmacogenomics Journal 3:136–158.

Iyer L, Hall D, Das S, Mortell MA, Ramirez J, Kim S, Di Rienzo A, Ratain MJ. 1999. Phenotype–genotype correlation of in vitro SN-38 (active metabolite of irinotecan) and bilirubin glucuronidation in human liver tissue with UGT1A1 promoter polymorphism. Clinical Pharmacology and Therapeutics 65:576–582.

Jang JM, Park KJ, Kim DG, Shim HJ, Ahn BO, Kim SH, Kim WB. 2003. Pharmacokinetics of a new antigastric agent, eupatilin, an active component of Stillen®, in rats. Journal of Applied Pharmacology 11:163–168.

Ji HY, Lee HW, Shim HJ, Kim SH, Kim WB, Lee HS. 2004. Metabolism of eupatilin in rats using liquid chromatography/electrospray mass spectrometry. Biomedical Chromatography 18:173–177.

Kiang TKL, Ensom MHH, Chang TKH. 2005. UDP-glucuronosyltransferses and clinical drug–drug interactions. Pharmacology and Therapeutics 106:97–132.

Kim AR, Zou YN, Park TH, Shim KH, Kim MS, Kim ND, Kim JD, Bae SJ, Choi JS, Chung HY. 2004. Active components from Artemisia iwayomogi displaying ONOO(–) scavenging activity. Phytotherapy Research 18:1–7.

Kim MJ, Kim DH, Na HK, Oh TY, Shin CY, Surh YJ. 2005a. Eupatilin a pharmacologically active flavone derived from Artemisia plants, induces apoptosis in human gastric cancer (AGS) cells. Journal of Environmental Pathology and Toxicological Oncology 24:261–269.

Kim JY, Kwon EY, Lee YS, Kim WB, Ro JY. 2005b. Eupatilin blocks mediator release via tyrosine kinase inhibition in activated guinea pig lung mast cells. Journal of Toxicology and Environmental Health Part A 68:2063–2080.

Koshihara Y, Neichi T, Murota S, Lao A, Fujimoto Y, Tatsuno T. 1983. Selective inhibition of 5-lipoxygenase by natural compounds isolated from Chinese plants. Artemiae rubripes Nakai. FEBS Letters 1158:41–44.

Miners JO, McKinnon RA. 2000. CYP1A. In: Levy RH, Thummel KE, Trager WF, Hansten PD, Eichelbaum M, editors. Metabolic drug interactions. Philadelphia, PA: Lippincott Williams & Wilkins. pp 61–73.

Miners JO, Knight KM, Houston JB, Mackenzie PI. 2006. In vitro–in vivo correlation for drugs and other compounds eliminated by glucuronidation in humans: pitfalls and promises. Biochemical Pharmacology 71:1531–1539.

Naganuma M, Saruwatari A, Okamura S, Tamura H. 2006. Turmeric and curcumin modulate the conjugation of 1-naphtol in Caco-2 cells. Biological and Pharmaceutical Bulletin 29:1476–1479.

Newton DJ, Wang RW, Lu AY. 1995. Cytochrome P450 inhibitors. Evaluation of specificities in the in vitro metabolism of therapeutic agents by human liver microsomes. Drug Metabolism and Disposition 23:154–158.

Park SC, Yoon JH, Kim W, Gwak G-Y, Kim KM, Lee SH, Lee S-M, Lee H-S. 2006. Eupatilin attenuates bile acid-induced hepatocyte apoptosis. Journal of Gastroenterology 41:772–778.

Rae JM, Soukhova NV, Flockhart DA, Desta Z. 2002. Triethylenethiophosphamide is a specific inhibitor of cytochrome P-450 2B6: Implications for cyclophosphamide metabolism. Drug Metabolism and Disposition 30:520–530.

Schweikl H, Taylor JA, Kitareewan S, Linko P, Nagorney D, Goldstein JA. 1993. Expression of CYP1A1 and CYP1A2 genes in human liver. Pharmacogenetics 3:239–249.

Seo HJ, Surh YJ. 2001. Eupatilin, a pharmacologically active flavone derived from Artemisia plants, induces apoptosis in human promyelocytic leukemia cells. Mutation Research 496:191–198.

Sesardic D, Boobis AR, Murray BP, Murray S, Segura J, De la Torre R, Davies DS. 1990. Furafylline is a potent and selective inhibitor of cytochrome P450IA2 in man. British Journal of Clinical Pharmacology 29:651–663.

Shimada T, Yamazaki H, Inui Y, Guengerich FP. 1994. Interindividual variations in human liver cytochrome P-450 enzymes involved in the oxidation of drugs, carcinogens and toxic chemicals: Studies with liver microsomes of 30 Japanese and 30 Caucasians. Journal of Pharmacology and Experimental Therapeutics 270:414–423.

Shipkova M, Wieland E. 2005. Glucuronidation in therapeutic drug monitoring. Clinica Chimica Acta 358:2–23.

Strassburg CP, Oldhafer K, Manns MP, Tukey RH. 1997. Differential expression of the UGT1A locus in human liver, biliary and gastric tissue: Identification of UGT1A7 and UGT1A10 transcripts in extrahepatic tissues. Molecular Pharmacology 52:212–220.

Suzuki H, Kneller MB, Haining RL, Trager WF, Rettie AE. 2002. (+)-N-3-benzyl-nirvanol and (–)-N-3-benzyl-phenobarbital: New potent and selective in vitro inhibitors of CYP2C19. Drug Metabolism and Disposition 30:235–239.

Venkatakrishnan K, Von Moltke LL, Greenblatt DJ. 1998. Relative quantities of catalytically active CYP2C9 and 2C19 in human liver microsomes: Application of the relative activity factor approach. Journal of Pharmaceutical Science 87:845–853.

Walsky RL, Obach RS, Gaman EA, Gleeson JPR, Proctor WR. 2005. Selective inhibition of human cytochrome P4502C8 by montelukast. Drug Metabolism and Disposition 33:413–418.

Yun CH, Shimada T, Guengerich FP. 1991, Purification and characterization of human liver microsomal cytochrome P450 2A6. Molecular Pharmacology 40:679–685.

Zhang D, Chando TJ, Everett DW, Patten CJ, Dehal SS, Humphreys WG. 2005. In vitro inhibition of UDP-glucuronosyltransferases by atazanavir and other HIV protease inhibitors and the relationship of this property to in vivo bilirubin glucuronidation. Drug Metabolism and Disposition 33:1729–1739.

RAPID COMMUNICATIONS IN MASS SPECTROMETRY
Rapid Commun. Mass Spectrom. 2007; **21**: 1139–1149
Published online in Wiley InterScience (www.interscience.wiley.com) DOI: 10.1002/rcm.2943

RCM

Metabolism and excretion of 5-ethyl-2-{5-[4-(2-hydroxyethyl)piperazine-1-sulfonyl]-2-propoxyphenyl}-7-propyl-3,5-dihydropyrrolo[3,2-*d*]-pyrimidin-4-one (SK3530) in rats

Jaeick Lee[1†], Hye Hyun Yoo[1], Kwang Jin Rhim[2], Dong-Ryul Sohn[3] and Dong-Hyun Kim[1*]

[1]Bioanalysis and Biotransformation Research Center, Korea Institute of Science and Technology, P.O. Box 131, Chungryang, Seoul, Korea
[2]Life Science R&D Center, SK Chemicals, Suwon, Korea
[3]Department of Clinical Pharmacology, College of Medicine, Soonchunhyang University, Chonan, Korea

Received 1 January 2007; Revised 18 January 2007; Accepted 19 January 2007

The *in vitro* and *in vivo* metabolism of a novel PDE 5 inhibitor, SK3530, was investigated in rats. Bile, plasma, feces, urine and liver samples were collected and analyzed using a high-performance liquid chromatography (HPLC) system equipped with ultraviolet (UV), mass spectrometric and radioactivity detectors. After a single oral administration, the mean radiocarbon recovery was 92.32 ± 6.26%, with 91.25 ± 6.25 and 1.07 ± 0.21% in the feces and urine, respectively. The biliary excretion of radioactivity for the first 24 h period was approximately 38.82%, suggesting that SK3530 is cleared by hepatobiliary excretion. *In vitro* incubation of SK3530 with rat and human liver microsomes resulted in the formation of twelve and ten metabolites, respectively. SK3530 was extensively metabolized to twenty different metabolites, including three glucuronide and three sulfate conjugates in rats. The structures of these metabolites were elucidated based on MS^n spectral analyses. Six major metabolic pathways were identified in the rat: N-dealkylation and oxidation of the hydroxyethyl moiety; N,N-deethylation and hydroxylation of the piperazine ring; hydroxylation of the propyl group and sulfate conjugation. An additional metabolite due to aromatic hydroxylation was also identified in hepatic microsomes. Copyright © 2007 John Wiley & Sons, Ltd.

Tandem mass spectrometry (MS^n) techniques are widely used for quantitative and qualitative analysis in many area of research, and play an important role in metabolic studies, such as for the structural elucidation of drug metabolites via biotransformations.[1–4] It is important to understand the metabolic fate of drugs, because biotransformation can lead to some unwanted consequences, such as rapid clearance of the drug from the body, the formation of active metabolites, drug-drug interactions due to enzyme induction or competition, as well as the formation of reactive or other toxic metabolites. Consequently, precise mass interpretation is essential to characterize the correct structure of metabolites.

Male erectile dysfunction (MED), the persistent inability to achieve or maintain an erection for satisfactory sexual performance, is a common and important medical problem. Sildenafil is a potent and selective inhibitor of human cGMP-specific phosphodiesterase type 5 (PDE 5), the predominant isozyme responsible for the metabolism of cGMP in the corpus cavernosum of the penis.[5,6] The development of sildenafil citrate (Viagra) as an effective and orally active agent for the treatment of MED has revolutionized the treatment of this disease.[7] Despite the efficacy of sildenafil as a treatment for MED, there are some notable drawbacks associated with its use. Clinically significant adverse effects have been reported, such as headache, facial flushing, dyspepsia and visual disturbance.[8] SK3530 (5-ethyl-2-{5-[4-(2-hydroxyethyl)piperazine-1-sulfonyl]-2- propoxyphenyl}-7-propyl-3,5-dihydropyrrolo[3,2-*d*]pyrimidin-4-one), a novel PDE 5 inhibitor, was designed to alleviate the drawbacks of sildenafil. This compound, currently under clinical investigation, was found to be safe and well tolerated at doses up to 150 mg.

*Correspondence to: D.-H. Kim, Bioanalysis and Biotransformation Research Center, Institute of Science and Technology, P.O. Box 131, Chungryang, Seoul 136-791, South Korea.
E-mail: dhkim@kist.re.kr
†Present Address: Bioanalysis and Mass Spectrometry, LG Life Sciences R&D, Taejon, Korea.
Contract/grant sponsor: Korea Institute of Science and Technology and SK Chemical Co.

The purpose of the present study was to examine both the *in vitro* and *in vivo* metabolism and excretion of SK3530 in rats. In addition, the structures of SK3530 metabolites were also proposed on the basis of the product ion mass spectra obtained under low-energy collision-induced dissociation (CID).

EXPERIMENTAL

Materials

[^{14}C]-SK3530 (specific activity 93.52 μCi/mg) was synthesized at the Korea Radiochemicals Center (Suwon, Korea), with radiochemical purity ≥98%, as adjudged by high-performance liquid chromatography (HPLC) radiochromatography. Unlabeled SK3530 was provided by SK Chemical Co. (Gunpo, Korea), with chemical purity of 99%. All other chemicals were the highest grade commercially available. Polyethylene glycol (PEG, average molecular weight: 300) was obtained from Sigma Chemical Co. (St. Louis, MO, USA).

Animals

Male Sprague-Dawley rats, weighing 210–250 g, were purchased from DaeHan Laboratory Animal Research Center Co. (Taejeon, Korea), and housed in a temperature (23 ± 2°C) and moisture (55 ± 10°C) controlled room, exposed to a controlled 12 h cycle of light and darkness, and allowed free access to food and water.

Preparation of dosing solution

Appropriate quantities of [^{14}C]-SK3530 were diluted with cold SK3530 to adjust the specific activity required for dose preparation. The SK3530 was dissolved in PEG solution (50% in water) to a final concentration of 40 mg mL^{-1}.

Study design and sample collection

Biliary excretion

The bile duct was cannulated with PE10 tubing 1 h prior to dosing under pentobarbital anesthesia. The rats were orally dosed with [^{14}C]-SK3530 at 40 mg kg^{-1} (2 μCi mg^{-1}). Bile was collected at 1 h intervals for the first 6 h and pooled bile was used for metabolic profile characterization.

Excretion

Following overnight fasting, rats were orally dosed with [^{14}C]-SK3530 at 40 mg kg^{-1} (5 μCi mg^{-1}), and then individually housed in metabolic cages equipped with a urine and feces separator. Urine and feces were collected and weighed at the following intervals: predose, 0–6, 6–12, 12–24, 24–48, 48–72, 72–96, 96–120, 120–144 and 144–168 h. Urine and fecal samples were stored separately at –20°C until analysis. Aliquots of feces and urine from the first 24 h period were used for metabolic profile characterization.

Plasma and liver collection

Rats were orally dosed with ^{14}C-SK-3530 at 40 mg kg^{-1}. At 4 h after dosing, animals were lightly anaesthetized with diethyl ether, blood collected by heart puncture and then killed by cervical dislocation. The liver was rapidly dissected, washed with saline, and stored at –20°C until analysis. Plasma was obtained by centrifugation at 1000 *g* for 5 min and stored at –20°C prior to analysis.

Metabolism studies

For the *in vitro* metabolic studies, [^{14}C]-SK3530 (50 μM final concentration) was incubated with 1.0 mg protein mL^{-1} of rat or human liver microsomes at 37°C for 2 h in the presence of an NADPH-generating system, in a final incubation volume of 0.5 mL. The reaction was quenched by the addition of one volume of acetonitrile. The samples were centrifuged at 1000 *g* for 5 min, and the supernatants directly analyzed by HPLC. For the isolation and characterization of biliary, urinary, fecal, hepatic, and plasma circulating metabolites, 1 μL of each sample was loaded onto Sep-Pak C_{18} cartridges for initial cleanup, and the final methanol eluate dried under nitrogen evaporation. The residue was dissolved in HPLC initial buffer and then analyzed by HPLC. More than 90% of total radioactivity was recovered after passing through Sep-Pak C_{18} cartridges.

LC/MS analysis

The HPLC system consisted of an HP 1100 series binary pump HPLC system (Agilent, Palo Alto, CA, USA), with a diode-array detector (DAD) (Agilent), a β-RAM radioactivity flow detector (IN/US Corporation, Tampa, FL), and a LC/MSD ion-trap mass spectrometer, equipped with an electrospray ionization (ESI) source (Agilent). The chromatographic separation of SK3530 and its metabolites was achieved on a Capcell-Pak C18 column (4.6 mm × 25 cm, 5 μm, Shiseido), using a linear gradient program. The mobile phases consisted of 20 mM ammonium formate at pH 4.0 (A) and 90% acetonitrile (B), with an initial composition of 30% (B), and the programmed linearly to 65% (B) for 26 min, at a flow rate of 1.0 mL min^{-1}. The entire column eluent was directly introduced into a DAD, with 10% of the eluate then transferred to the ion-trap mass spectrometer, using a 1:10 splitter; the other 90% was transported to the β-RAM radioactivity flow detector. For mass spectrometry (MS) and tandem mass spectrometry (MS^n) analyses, 10% of the eluate was introduced into ESI interface through a 50-cm-long PEEK tubing. Nitrogen was used both as the nebulizing gas, at 30 psi, and as the drying gas at a flow rate of 8 L min^{-1} and temperature of 350°C. The mass spectrometer was operated in the positive ion mode within the *m/z* range 50–800. Helium was used as the collision gas for the MS^n experiments. Fragmentation was induced with a resonant excitation amplitude of 0.85–1.00 V, following isolation of the desired precursor ion over a selected mass window of 1 Da.

RESULTS

Excretion of total radioactivity

The excretion of total radioactivity in the urine and feces after a single oral administration of [^{14}C]-SK3530 is shown in Table 1. The urinary and fecal recoveries of total radioactivity for the first 24 h period were approximately 0.98 and 82.92% of the administered dose, respectively. The total radioactivity recovered within 7 days was 92.32 ± 6.26%, with 91.25 ± 6.25 and 1.07 ± 0.21% excreted in the feces and urine, respectively.

DOI: 10.1002/rcm

Table 1. Excretion of radioactivity in the urine and feces after a single oral administration of [^{14}C]-K3530 to rats at a dose of 40 mg kg^{-1} (n = 4)

	% Dose		
Days	Urine	Feces	Total
0.25	0.46 ± 0.13*	0.01 ± 0.01	0.47 ± 0.13
0.50	0.36 ± 0.12	12.32 ± 11.81	12.68 ± 11.72
1.00	0.16 ± 0.11	70.59 ± 12.76	70.74 ± 12.85
2.00	0.04 ± 0.01	7.65 ± 3.25	7.70 ± 3.25
3.00	0.02 ± 0.01	0.52 ± 0.17	0.54 ± 0.17
4.00	0.01 ± 0.01	0.12 ± 0.09	0.13 ± 0.09
5.00	0.01 ± 0.00	0.03 ± 0.00	0.03 ± 0.00
6.00	0.01 ± 0.01	0.01 ± 0.01	0.02 ± 0.01
7.00	0.01 ± 0.01	0.01 ± 0.00	0.01 ± 0.00
Total	1.07 ± 0.21	91.25 ± 6.25	92.32 ± 6.26

*Each value represents the percentage of the total radioactivity administered.

The radioactivity excreted in bile over 24 h was 38.82 ± 8.95% of the administered dose, suggesting that SK3530 is cleared by hepatobiliary excretion.

In vitro and *in vivo* metabolic profiles of SK3530

HPLC analysis of mixtures after *in vitro* incubation of SK3530 with rat and human liver microsomes, in the presence of a NADPH-generating system, resulted in twelve and ten metabolites, respectively, including M14 as a major metabolite (Fig. 1). Relative percentages of SK3530 metabolites in each microsome are described in Table 2. This compound was not metabolized when incubated without a NADPH-generating system, nor with heat-inactivated microsomes,

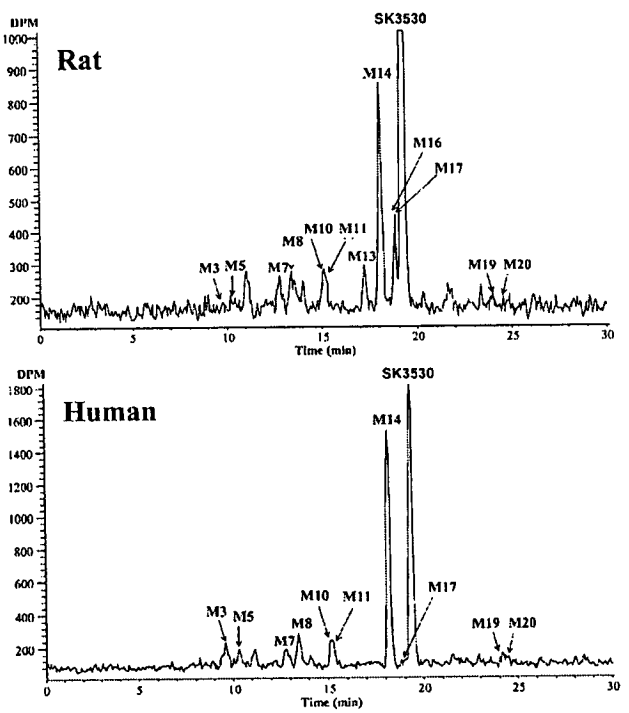

Figure 1. Representative radiochromatograms of rat and human liver microsomal incubation extracts.

Table 2. Relative percentages of SK3530 and its metabolites after *in vitro* incubation of [^{14}C]-SK3530 with rat or human liver microsomes

	Relative percentage (%)	
Metabolites	Rat	Human
SK3530	45.55	46.72
M1	—	—
M2	—	—
M3	trace	2.67
M4	—	—
M5	trace	2.11
M6	—	2.59
M7	3.36	2.22
M8	4.20	4.56
M9	—	—
M10*	4.70	3.68
M11*		
M12	—	—
M13	5.46	—
M14	27.48	38.04
M15	—	—
M16	—	—
M17	9.24	trace
M18	—	—
M19	trace	trace
M20	trace	trace

*M10 was co-eluted with M11.

suggesting that SK3530 was metabolized by cytochrome P450 enzymes.

Representative radiochromatograms of tissues and body fluids, obtained after the oral administration of [^{14}C]-SK3530, are shown in Fig. 2. SK3530 was metabolized to twenty different metabolites, including three glucuronide and three sulfate conjugates, in rats; relative percentages of SK3530 metabolites in each fluid are shown in Table 3. M18 (sulfate conjugate of SK3530) was identified as a major metabolite (approximately 70% of total radioactivity) in both feces and bile. The MH^+ ions corresponding to the peaks observed in the radiochromatograms were simultaneously identified by the mass spectra recorded using ESI ion-trap mass spectrometry.

CID of protonated SK3530

The MH^+ ion of SK3530 was observed at *m/z* 532, and the MS^2 spectrum of this ion gave rise to major product ions at *m/z* 514, 488 and 404 (Fig. 3(A)). The mechanism for the formation of these ions is proposed in Fig. 3(B). The protonated SK3530 (*m/z* 532), where the protonation occurred on the sulfonyl oxygen, could be dissociated to either the even-electron cation (EE^+) at *m/z* 404 due to heterolytic cleavage of the S–N bond involving H-transfer, or the EE^+ at *m/z* 338 due to heterolytic cleavage of the S–C_{Ar} bond.[9] The product ions at *m/z* 404 and 338 were then dissociated to the EE^+ at *m/z* 362 and 296, respectively, due to loss of C_3H_6 (42 Da). On the other hand, *ipso* protonated SK3530 (*m/z* 532) gave rise to the EE^+ at *m/z* 340 due to heterolytic cleavage involving H-transfer, and then further dissociated to a product ion at *m/z* 312 due to loss of C_2H_4 (28 Da).[9] The protonated SK3530, where the protonation occurred on the ethyl alcohol oxygen,

DOI: 10.1002/rcm

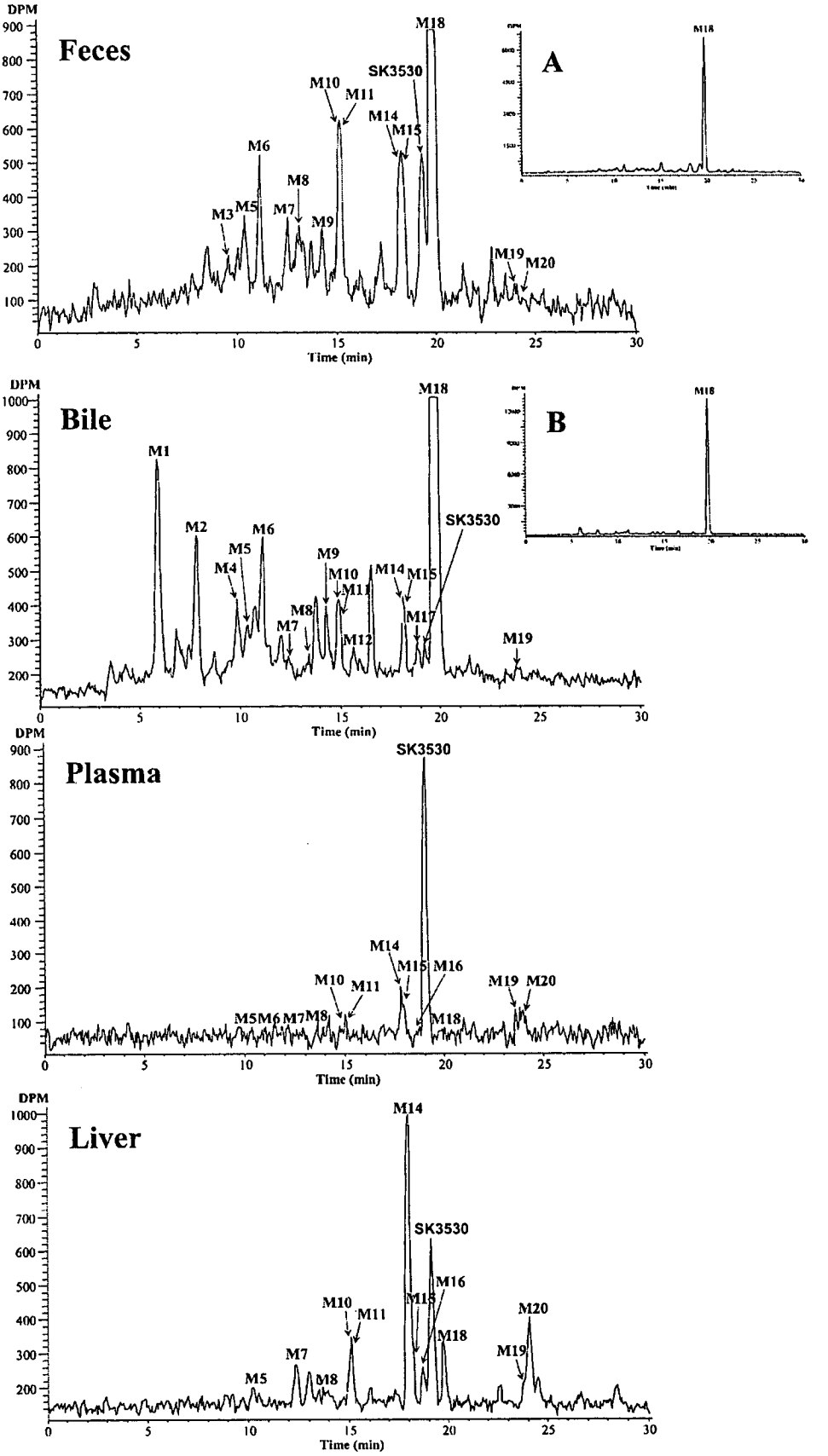

Figure 2. Representative radiochromatograms of feces, bile, plasma, liver and urine extracts obtained from rats after a single oral administration of [^{14}C]-SK3530. (A) and (B) show zoom-out chromatograms.

DOI: 10.1002/rcm

Table 3. Relative percentages of SK3530 and its metabolites

Metabolites	Relative percentage (%)				
	Feces	Bile	Plasma	Liver	Urine
SK3530	4.56	0.43	77.66	19.12	trace
M1	—	4.60	—	—	—
M2	—	2.87	—	—	—
M3	0.89	—	—	—	—
M4	—	1.58	—	—	—
M5	2.08	0.84	trace	1.41	trace
M6	3.17	2.59	trace	—	trace
M7	2.13	trace	trace	4.28	trace
M8	2.95	trace	trace	3.08	trace
M9	1.84	1.30	—	—	—
M10*	5.74	1.70	trace	7.10	trace
M11*			trace		
M12	—	trace	—	—	—
M13	—	—	—	—	—
M14*	5.69	1.37	11.22	34.31	trace
M15*					—
M16	—	—	trace	2.44	—
M17	—	0.67	—	—	trace
M18	64.96	73.05	trace	5.66	—
M19	trace	trace	trace	1.16	trace
M20	trace	—	trace	10.40	—

*M10 and M14 were co-eluted with M11 and M15, respectively.

underwent loss of H_2O (18 Da) and generated the EE^+ at *m/z* 514. The MS^3 of the product ion at *m/z* 514 gave rise to the EE^+ at *m/z* 404. The protonated SK3530, where the protonation occurred on the piperazine nitrogen, could be dissociated to the EE^+ at *m/z* 488 due to heterolytic cleavage of the N–C bond involving H-transfer.

Characterization of structure of SK3530 metabolites

Metabolites M3, M5, M13, M15 and M17

Metabolites M3, M5, M13 and M17 produced protonated molecules of *m/z* 548, indicating that these compounds were mono-hydroxylated derivatives of SK3530. M3 and M5 showed the same product ion spectrum, with characteristic ions at *m/z* 530, 512, 486, 402, 310 and 294 (Fig. 4 and Table 4). Generally, the removal of a molecule of water from an aliphatic hydroxyl group is characteristic of the dissociation of the even-electron cations (EE^+) formed by ESI.[10] The product ions at *m/z* 530 (loss of one water molecule) and 512 (loss of two water molecules) strongly indicated an alkyl chain hydroxylation. Furthermore, the product ions at *m/z* 310 and 294, which were generated by loss of C_2H_4 and C_3H_6 from their respective ions at *m/z* 338 and 336 (+16 Da from product ions at *m/z* 340 and 338 of the precursor, with subsequent loss of a water molecule), revealed that the hydroxylation occurred in the propyl chain of a pyrrolopyrimidine moiety.

M13 generated characteristic product ions at *m/z* 530, 504, 420, 378, 328 and 312, 16 Da higher than those of the corresponding product ions at *m/z* 514, 488, 404, 362, 312 and 296 of SK3530 (Fig. 4 and Table 4). These characteristic product ions, and the observed loss of a single water molecule (*m/z* 514), indicated that hydroxylation occurred on the benzene ring to which the sulfonyl is attached.

M17 gave rise to characteristic product ions at *m/z* 530, 504, 404 and 362. The product ion at *m/z* 504 (+16 Da from product ion at *m/z* 488 of precursor) indicated that the ethyl alcohol moiety attached to the piperazine ring was not modified. In addition, the product ion at *m/z* 404 strongly suggested that the benzenesulfonyl and pyrrolopyrimidine moiety were not modified. Therefore, M17 was identified as a metabolite where hydroxylation occurs on the piperazine.

Metabolite M15 produced a protonated molecule of *m/z* 546, which gained 14 Da from protonated SK3530 (*m/z* 532). M15 gave rise to characteristic product ions at *m/z* 500, 488, 404, 360, 338, 312 and 296 (Fig. 4 and Table 4). The product ions at *m/z* 488 and 404 strongly indicated that modification took place on the ethyl alcohol moiety attached to the piperazine ring. These data collectively indicated that the hydroxyethyl group attached to piperazine was oxidized to the corresponding carboxylic acid in the case of M15. This type of metabolism was also observed in tiaramide.[2,11]

Metabolites M4, M7, M10, M11, M14, M19 and M20

The MH^+ ion of M14 indicated the loss of 44 Da relative to SK3530, suggesting that the hydroxyethyl moiety was removed from the piperazine moiety (Fig. 5). This was further confirmed by the observation of characteristic product ions at *m/z* 404, 338, 312 and 296. Therefore, M14 was identified as the piperazine N-dealkylated metabolite. M20 gained 14 Da from M14. The product ions at *m/z* 485 (loss of NH_3), 460 (loss of C_3H_6), 404, 312 and 296 indicated

DOI: 10.1002/rcm

RCM

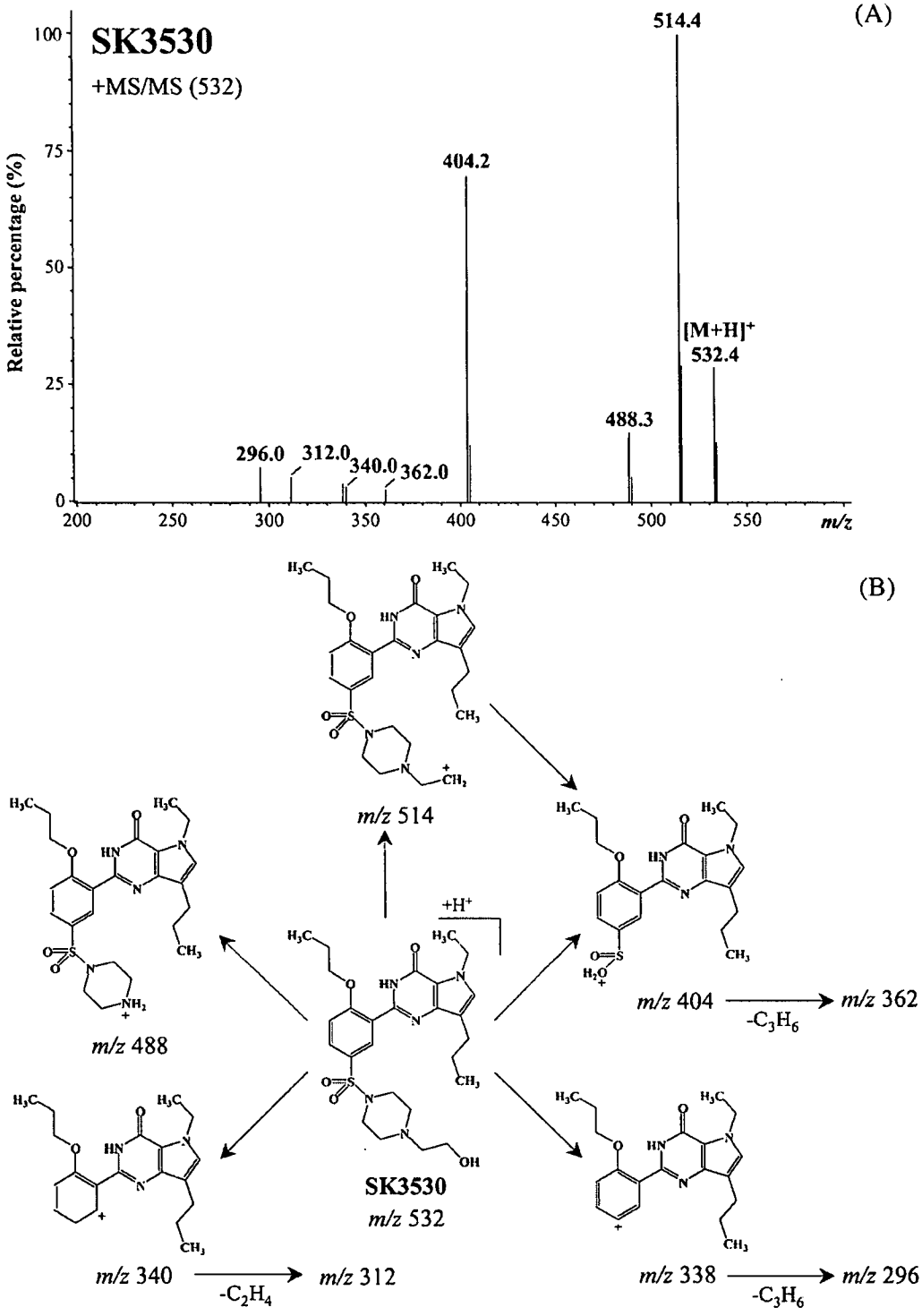

Figure 3. (A) MS/MS spectrum of the protonated SK3530 and (B) the proposed fragmentation pathways and structures of the product ions.

that carbonylation occurred in the piperazine ring of M14. Therefore, M20 could be assigned as a carbonylated metabolite in the piperazine ring of M14.

Metabolite M11 produced a protonated molecule of *m/z* 506, and gave rise to characteristic product ions at *m/z* 488, 462, 455, 404, 312 and 296. The MH^+ ion at *m/z* 506 and the product ions at *m/z* 404, 312 and 296 strongly indicated a decrease of 26 Da in the piperazine moiety. The product ion at *m/z* 462 was rationalized by the removal of a hydroxyethyl group, and the ion at *m/z* 445 by the loss of NH_3 (17 Da) from the ion at *m/z* 462. M11 was identified as a piperazine N,N-deethylated metabolite. The MH^+ ion of M10 was observed at *m/z* 462, and produced product ions at *m/z* 445, 419, 404, 312 and 296. The product ions at *m/z* 445 and 419

DOI: 10.1002/rcm

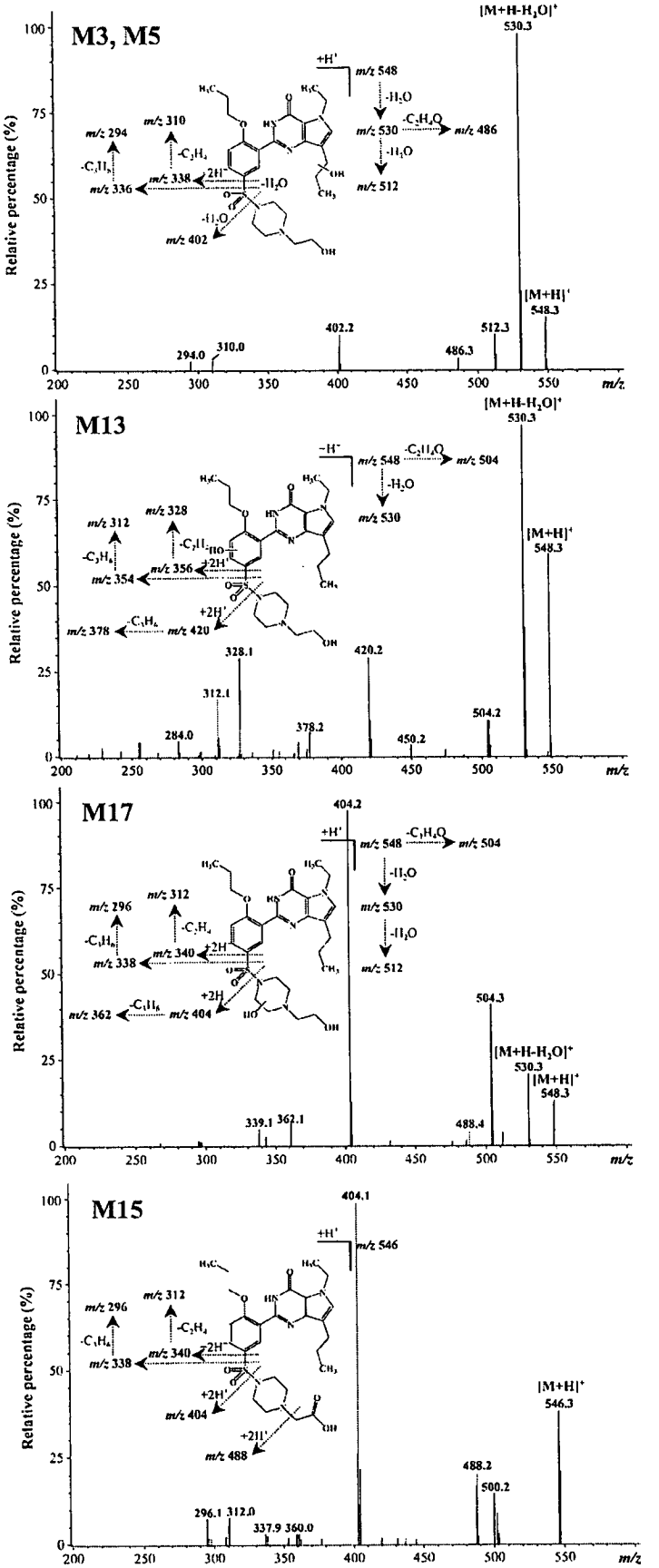

Figure 4. MS/MS spectra of the protonated molecules of SK3530 metabolites M3, M5, M13, M15 and M17.

DOI: 10.1002/rcm

Table 4. Chromatographic and mass spectrometric data of SK3530 and its metabolites

Metabolites	Rt (min)	$[M+H]^+$	MS^2 (*m/z*)
SK3530	19.0	532	514, 488, 404, 340, 338, 312, 296, 268
M1	5.7	724	548* (530, 512, 420, 312)**
M2	7.4	666	490* (472, 432, 378, 360, 312, 296, 268)**
M3	9.5	548	530, 512, 486, 402, 310, 294
M4	9.7	478	460, 404, 312, 296, 268
M5	10.2	548	530, 512, 486, 402
M6	11.1	628	548* (530, 512, 486, 402)**
M7	12.5	404	362, 344, 339, 297, 268
M8	13.5	548	530, 504, 420, 362, 312, 296, 268
M9	14.2	628	548* (530, 504, 420, 312, 296)**
M10	15.0	462	445, 419, 404, 388, 360, 338, 340, 312, 296, 269
M11	15.1	506	488, 462, 445, 419, 404, 340, 312, 296
M12	15.4	708	532* (514, 488, 404, 340, 338, 312, 296, 268)**
M13	17.2	548	530, 504, 420, 328, 312
M14	18.0	488	446, 404, 360, 338, 312, 296, 269
M15	18.1	546	500, 488, 404, 360, 338, 312, 296
M16	18.6	490	472, 432, 378, 360, 312, 296, 268
M17	18.8	548	530, 504, 488, 404, 362, 296
M18	19.7	612	532* (514, 488, 404, 340, 338, 312, 296, 268)**
M19	23.7	419	377, 360, 338, 312, 296, 268
M20	24.0	502	485, 460, 404, 362, 312, 296, 268, 235

* Major product ion of MS^2.
** Product ions of MS^2 major ion (*).

could be rationalized by the losses of NH_3 (17 Da) and ethylamine (44 Da), with H-transfer from the MH^+ ion of M10, respectively. The characteristic ions at *m/z* 404, 312 and 296 indicated that the piperazine moiety was modified. M10 was identified as a piperazine N,N-deethylated product of M14. M4 showed the MH^+ ion at *m/z* 478, suggesting M4 was the mono-hydroxylated derivative of M10. The product ions at *m/z* 404, 312 and 296, which were identical to those of SK3530 itself, indicated that the hydroxylation occurred within the ethylamine moiety of M10. The molecular weight of M19 was decreased by 43 Da relative to M10. This decrease was presumably due to the loss of the ethylamine moiety from M10 due to N-dealkylation, which was further supported by the product ions at *m/z* 338, 312 and 296 in the MS^2 spectra. For M7, the MH^+ ion was observed at *m/z* 404 and its product ion at *m/z* 362. The precursor ion at *m/z* 404 indicated the loss of 58 Da relative to M10 (*m/z* 462), and the product ion at *m/z* 362 was rationalized by the loss of C_3H_6 (42 Da) in the benzene moiety. M7 was identified as a metabolite where the piperazine moiety was removed from the parent SK3530.

Metabolites M1, M2, M6, M9, M12 and M18

M1, M2 and M12 were identified as glucuronide conjugates of M13, M16 and SK3530, and M6, M9 and M18 as sulfate conjugates of M3 (or 5), M8 and SK3530, respectively. The MH^+ ions of M1, M2 and M12 were observed at *m/z* 724, 666 and 708, respectively. These metabolites showed a neutral loss of 176 Da ($-C_6H_8O_6$) from their MH^+ ions and, thereafter, the same product ion spectra as their corresponding free forms (M13, M16 and SK3530) (Table 4). The MH^+ ions of M6, M9 and M18 were observed at *m/z* 628, 628 and 612, respectively. These metabolites showed a neutral loss of 80 Da ($-SO_3$) from their MH^+ ions and, thereafter, the same product ion spectra as their corresponding free forms (M3, M8 and SK3530) (Table 4).

DISCUSSION

The *in vitro* and *in vivo* metabolic profiles of SK3530 were evaluated to gain an understanding of the fate of this drug in rats. Using a combination of HPLC/UV and radioactivity detection, and ESI-MS, most of the metabolites were characterized. By tracking the radioactivity and MS^n spectra of SK3530 and its metabolites, both abundant molecular ions and characteristic fragment ions, the sites of metabolism of the parent drug could be assigned. The majority of radioactivity (~92% of administered dose) after a single oral administration was detected in the feces; only a small amount (~4% of administrated dose) of the parent drug SK3530 was detected. More than 38% of the administered radioactivity in bile-duct-cannulated rats was excreted into bile over 24 h (data not shown). These results indicate that SK3530 was extensively metabolized prior to its excretion into bile. The SK3530 metabolites identified in the rat were produced via five metabolic reactions (Fig. 6): (1) hydroxylation in piperazine, aliphatics or aromatic rings; (2) N-dealkylation in piperazine; (3) N,N-deethylation in piperazine; (4) carbonylation via hydroxylation in piperazine or aliphatics; and (5) deethylamination or deethyldiamination of the N,N-deethylated metabolite.

Sulfate-conjugation seems to be a characteristic of SK3530 metabolism. As shown in Table 3, a sulfate-conjugated metabolite (M18) of SK3530 was identified as a major metabolite in both the feces and bile (~65% and 73% of total radioactivity, respectively), suggesting most of the SK3530 was excreted as the sulfate-conjugated metabolite. It has been reported that no conjugated metabolites were observed in the metabolism of structural analogues of SK3530, such as sildenafil and DA-8159 (being evaluated in a phase III clinical trial), indicating that glucuronide- and sulfate-conjugations were not involved in their metabolism.[6,12,13] In the metabolism of SK3530 (Fig. 6), conjugated metabolites were especially found in the hydroxyethyl-containing molecules, indicating that the conjugation may occur in the hydroxyethyl moiety. On the other hand, M14, which is a piperazine N-dealkylated metabolite, was identified as a major metabolite in the *in vitro* system (both rat and human), but not in the *in vivo* system. This indicates that M14 undergoes the same subsequent metabolic pathway as piperazine N,N-deethylation, and is then further metabolized.

In an earlier study, sildenafil was reported to undergo the piperazine ring-opening reaction, with the subsequent

DOI: 10.1002/rcm

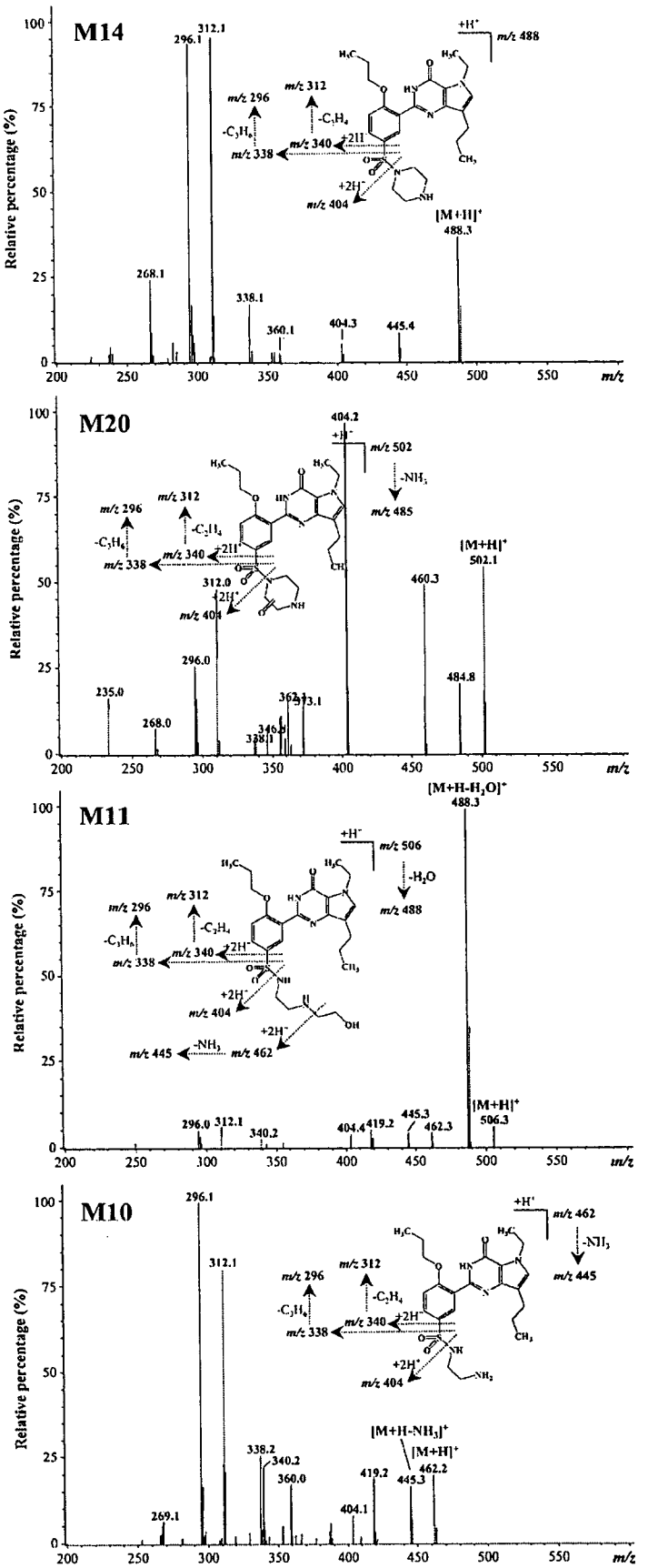

Figure 5. MS/MS spectra of the protonated molecules of SK3530 metabolites M10, M11, M14 and M20.

DOI: 10.1002/rcm

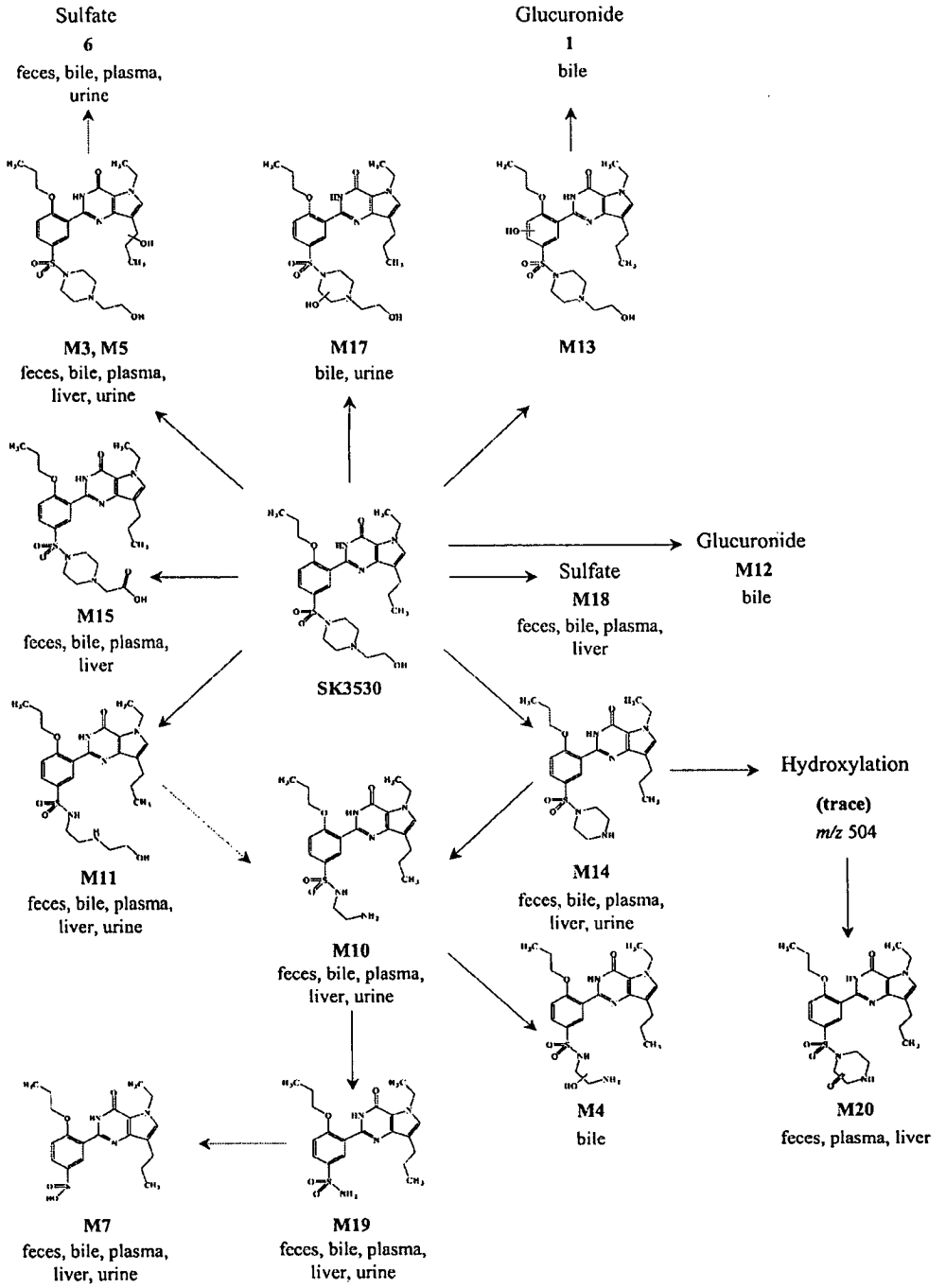

Figure 6. Postulated metabolic pathways of SK3530 in rats.

generation of piperazine N,N-deethylated metabolites (UK-331,849 and UK-150,564).[6] SK3530 also generated the piperazine ring-opened metabolites (M10, M11) and, in addition, the piperazine carbonylated metabolite (M20, lactam metabolite) was detected. The finding of piperazine carbonylated metabolite M20, together with ring-opened metabolites (M10 and M11), indicated that the α-oxidation mechanism of N-heterocyclic compounds containing a pyrrolidine, piperidine or piperazine may be involved in the formation of the ring-opened (M10 and M11) and lactam metabolites (M20).[4,14,15] These reactions were well characterized in the metabolism of nicotine, cyproheptadine, tremorine, prolitane and phencyclidine. Initial hydroxylation at the carbon adjacent to the nitrogen in piperazine ring may lead to lactam formation. The lactam metabolites can be formed from either the iminium ion or carbinolamine, but they can be converted. The iminium ions can be oxidized to lactams by aldehyde oxidase. However, it is also known that the iminium ion can undergo spontaneous hydrolysis to its corresponding carbinolamine. Furthermore, an aminoaldehyde intermediate can be produced from the ring opening of an unstable carbinolamine intermediate, and N-dealkylated metabolites, open-chain amino acids and amino alcohol metabolites can then be generated. The formation of M7,

DOI: 10.1002/rcm

M10, M11, M19 and M20 was rationalized by this mechanism, and observed as a major metabolic pathway (phase I), with the exception of the monooxidation pathway.

In conclusion, SK3530 was mainly excreted into the feces as a sulfate-conjugated form (M18) of SK3530, along with minor metabolites generated via the five previously outlined metabolic pathways. M14 (piperazine N-dealkylated metabolite) was predominant in the *in vitro* system, and was also identified as a major circulating metabolite. This metabolite was further processed to diverse metabolites (M4, M7, M10, M19 and M20) by an α-oxidation mechanism of a piperazine ring, which is initial hydroxylation at the carbon adjacent to the nitrogen in the piperazine ring. On the basis of the metabolic profiles, the *in vitro* and *in vivo* metabolic pathways of SK3530 are proposed, and are shown in Fig. 6. The identification of the urinary and biliary metabolites is important in understanding the *in vivo* metabolic fate and disposition of SK3530.

Acknowledgements

This work was supported by grants from the Korea Institute of Science and Technology and from SK Chemical Co.

REFERENCES

1. Kostiainen R, Kotiaho T, Kuuranne T, Auriola S. *J. Mass Spectrom.* 2003; **38**: 357.
2. Tozuka Z, Kaneko H, Shiraga T, Mitani Y, Beppu M, Terashita S, Kawamura A, Kagayama A. *J. Mass Spectrom.* 2003; **38**: 793.
3. Lee J, La S,Ahn BR, Jeong TC, Kim DH. *Rapid Commun. Mass Spectrom.* 2004; **18**: 1901.
4. Lee J, Son J, Chung SJ, Lee ES, Kim DH. *J. Mass Spectrom.* 2004; **39**: 1036.
5. Ballard SA, Burslem FSM, Gingell CJG, Price ME, Tang K, Turner LA, Naylor AM. *J. Urol.* 1996; **155**: 676A.
6. Walker DK, Ackland MJ, James GC, Muirhead GJ, Rance DJ, Wastall P, Wright PA. *Xenobiotica* 1999; **29**: 297.
7. Boolell M, Gepi-Attee S, Gingell JC, Allen MJ. *Br. J. Urol.* 1996; **78**: 257.
8. Boolell M, Allen MJ, Ballard SA, Gepi-Attee S, Muirhead GJ, Naylor AM, Osterloh IH, Gingell C. *Int. J. Impotence Res.* 1996; **8**: 7.
9. Lee J, Yoo HH, Kang MY, Kim DH. *Rapid Commun. Mass Spectrom.* 2005; **19**: 1767.
10. Lee SK, Lee J, Lee ES, Jahng Y, Kim DH, Jeong TC. *Rapid Commun. Mass Spectrom.* 2004; **18**: 1073.
11. Noguchi H, Okui M, Noda K, Kato R. *Xenobiotica* 1977; **7**: 491.
12. Choi SJ, Ji HY, Lee HY, Kim DS, Kim WB, Lee HS. *Biomed. Chromatogr.* 2002; **16**: 395.
13. Shim HJ, Kim YC, Lee JH, Park KJ, Kwon JW, Kim WB, Lee MG. *Biopharm. Drug Dispos.* 2005; **26**: 161.
14. Vickers S, Polsky SL. *Curr. Drug Metab.* 2000; **1**: 357.
15. Baker JK, Little TL. *J. Med. Chem.* 1985; **28**: 46.

DOI: 10.1002/rcm

Available online at www.sciencedirect.com
SCIENCE DIRECT®
European Journal of Pharmaceutical Sciences 23 (2004) 13–47
EUROPEAN JOURNAL OF PHARMACEUTICAL SCIENCES
www.elsevier.com/locate/ejps

Review

Drug permeation in biomembranes In vitro and in silico prediction and influence of physicochemical properties

Annika Mälkiä [a], Lasse Murtomäki [a,*], Arto Urtti [b], Kyösti Kontturi [a]

[a] *Laboratory of Physical Chemistry and Electrochemistry, Helsinki University of Technology, P.O. Box 6100, FIN-02015 HUT, Finland*
[b] *Department of Pharmaceutics, University of Kuopio, P.O. Box 1627, FIN-70211 Kuopio, Finland*

Received 25 November 2003; received in revised form 13 May 2004; accepted 24 May 2004

Available online 10 July 2004

Abstract

In the past decades, it has become increasingly apparent that in addition to therapeutic effect, drugs need to exhibit favourable absorption, distribution, metabolism and excretion (ADME) characteristics to produce a desirable response in vivo. As the recent progress in drug discovery technology enables rapid synthesis of vast numbers of potential drug candidates, robust methods are required for the effective screening of compounds synthesized within such programs, so that compounds with poor pharmacokinetic properties can be rejected at an early stage of drug development. Furthermore, a viable in silico method would save resources by enabling virtual screening of drug candidates already prior to synthesis. This review gives a general overview of the approaches aimed at predicting biological permeation, one of the cornerstones behind the ADME behaviour of drugs. The most important experimental and computational models are reviewed. Physicochemical factors underlying the permeation process are discussed.

Keywords: Biological permeation; Partition; Experimental models; Computational models; Physicochemical properties

1. Introduction

The recent development in drug discovery methodology, including concepts such as combinatorial chemistry and high throughput screening, is accompanied by a need to rapidly and effectively evaluate the biopharmaceutical properties of compounds synthesised within such programs in small quantities. It is recognised that the absorption, distribution, metabolism and excretion (ADME) characteristics of the drug compound are crucial for successful therapeutic activity in vivo. Accordingly, the focus in drug development has moved from aiming solely at maximum drug–receptor interactions to broader property-based design, including also pharmacokinetic and pharmaceutical properties (van de Waterbeemd et al., 2001).

One property of particular importance is the ability of drugs to cross biological membranes. The biological permeability of a drug shapes its pharmacokinetic profile in the body, affecting its absorption, distribution and elimination. Scientists from various fields including biology, chemistry, pharmacy, medicine, physics and computer science have approached the task of developing effective and accurate methods for predicting biological permeation of drugs. The importance of this work is corroborated by the findings that approximately 40% of the failures in drug development programs in clinical phase are due to problems in pharmacokinetics and drug delivery (Prentis et al., 1988; Kennedy, 1997).

The experimental approaches to study drug transport can be roughly divided into two groups: (i) transport studies through different types of biomimetic layers to model biological permeation; and (ii) two-phase partition studies where drug partitioning between water and a lipidic phase is quantified. Although effective methods to predict biological permeation are of utmost importance, two-phase parti-

* Corresponding author. Tel.: +358 9 4512575; fax: +358 9 4512580.
E-mail address: lasse.murtomaki@hut.fi (L. Murtomäki).

0928-0987/$ – see front matter © 2004 Elsevier B.V. All rights reserved.
doi:10.1016/j.ejps.2004.05.009

tion studies of drugs can provide valuable information on details and reasons behind the mechanisms of permeation, such as hydrogen bonding ability and electrostatic interactions. Furthermore, due to their longer and more standardised experimental traditions, partition coefficients measured in two-phase bulk solvent systems have so far remained the main descriptors of in vivo drug permeation.

The first calculative approaches related to biological permeation were semi-empirical models, developed to calculate two-phase partition coefficients of drugs. The increase in computer resources over the past decades has given rise to a variety of computational approaches, devoted to calculating descriptors of biological permeation. The development of a reliable theoretical method to predict biological permeation would not only save time and resources spent on experimental permeation studies, but also enable screening of drug candidates prior to synthesis.

This review discusses the methods used to study drug partition and permeation employing experimental model systems as well as computational approaches. The emphasis lies on passive transcellular drug transport, and electrochemical methods. Solubility, while an equally important ADME property, is not included in the discussion in order to limit the scope and length of the survey.

2. Basic concepts

2.1. Biological permeation

Lipid solubility and partitioning into lipid phases are crucial factors in pharmacokinetics. The transfer of drugs in the human body is determined by their ability to move across the lipid bilayer of epithelial and endothelial cell linings. Permeation across the cell membranes takes place by three main mechanisms: transcellular diffusion, paracellular diffusion and active transport (either transport into the cells or efflux out of the cells). Paracellular permeation is mainly governed by the size and the number of the pores between the cells, as well as the size and charge of the drug. Active transport processes require specific binding of the drug to the transporter protein. Diffusion across the cell membranes and transcellular permeation through the cells constitute the most important mechanisms, by which drugs cross biological membranes. The rate of transcellular diffusion affects the pharmacokinetics of the drug in the body in various ways.

Oral, transdermal, ocular and pulmonary absorption require that the drug readily passes through biological membranes, as does the distribution of the drug across the blood–brain barrier (BBB) or blood retina barrier, or its displacement to intracellular targets. Cell membrane permeation is also a prerequisite for drug elimination by the hepatocytes in the liver, but on the other hand, readily permeating drugs may also undergo reabsorption through the tubular membranes of the kidney, thereby reducing their excretion into the urine. Since the majority of drugs are administered via the oral route, the most studied form of biological permeation is human intestinal absorption (HIA). Likewise, a large number of drugs act via the central nervous system, producing either therapeutic or adverse effects. Therefore, it is important to evaluate or predict drug permeation of the blood–brain barrier.

The main properties of a drug influencing its permeation through biological membranes are lipophilicity, hydrogen-bonding capacity, charge and size (Camenisch et al., 1996). These will be discussed in the following sections together with properties of the partition or permeation medium.

2.2. Factors affecting biological permeation

Cellular membranes consist of a lipid bilayer with embedded membrane proteins and polysaccharide chains on the cell membrane surface. For passive transcellular permeation to take place, the drug must partition into the lipoid membrane. Several factors describe and influence partitioning into cell membranes.

2.2.1. log P

The lipophilicity of a drug is the most used single physicochemical property to predict its permeation in biological systems (Testa et al., 1996). Simply stated, the lipophilicity of a drug is its tendency to prefer a lipidic, or oil-like environment to an aqueous one. However, behind this property lies a net of intermolecular interactions such as hydrogen bonding and dipole effects. Thus, although lipophilicity is a property ascribed to the drug compound, it is highly dependent on the choice of lipidic environment (Kaliszan, 1992). The lipophilicity of a drug is traditionally expressed as $\log P$, the logarithm of its partition coefficient between a lipidic and an aqueous phase.

The chemical potential of a solute, μ_i, can be expressed either on the mole fraction scale or the concentration (or molality) scale:

$$\mu_i = \mu^0_{i,x} + RT\ln x_i = \mu^0_{i,c} + RT\ln(a_i/c^0) \quad (2.1)$$

where $\mu^0_{i,x/c}$ is the standard chemical potential, x_i the mole fraction and $a_i = \gamma_i c_i$ the activity of a single species of the solute; c^0 is the standard concentration, $1.0\,\mathrm{mol\,dm^{-3}}$. The mole fraction scale refers to Henry's law, which is always valid for the solvent, and for the solute at infinite dilution. The most significant problem when applying Henry's law to the solute is that the standard state is odd, $x_i = 1$, i.e. there is no solvent. The standard state of the concentration scale is also a bit hypothetical: $1.0\,\mathrm{mol\,dm^{-3}}$, with the activity coefficient γ_i equal to one, but at least achievable in principle.

The thermodynamic partition coefficient P_i is defined as the ratio of the activity of a single species of solute in two immiscible phases at equilibrium, by convention placing the

aqueous phase activity in the denominator (Reymond, 2001):

$$P_i = \frac{a_i^o}{a_i^w} = \frac{\gamma_i^o c_i^o}{\gamma_i^w c_i^w} = \exp\left(-\frac{\mu_{i,c}^{o,0} - \mu_{i,c}^{w,0}}{RT}\right)$$
$$= \exp\left(-\frac{\Delta_w^o G_i^0}{RT}\right) \quad (2.2)$$

A larger P or more positive $\log P$ thus corresponds to a higher lipophilicity. On basis of Eq. (2.1) the partition coefficient can also be defined as the ratio of the mole fractions:

$$P_{i,x} = \frac{x_i^o}{x_i^w} \quad (2.3)$$

As the ratio of the activity coefficients approaches unity rather fast with decreasing concentration, it is easy to show that the relation between these two quantities simply is:

$$\log P_{i,c} = \log P_{i,x} + \log\left(\frac{\bar{V}_w}{\bar{V}_o}\right) \quad (2.4)$$

where $\bar{V}_{w/o}$ is the molar volume of the water or the oil phase. For example, in the *n*-octanol/water system the last term is −0.94 and hence not insignificant. Furthermore, the partition coefficient has been calculated as the ratio of amount of solute in the respective phases—it should be noted that this methodology only yields comparable $\log P$ values if the volumes of the phases are equal. In the following, the partition coefficient refers to the one defined in Eq. (2.2).

2.2.2. Hydrogen bonding

Ordered lipid layers provide a finite amount of hydrogen bonding groups. These groups, the majority of which are hydrogen bond acceptors, are located exclusively in the head group region of the lipids. In order to partition into the hydrocarbon region of the bilayer, the solute must be lipophilic enough to overcome the energy losses that occur in breaking the hydrogen bonds with water or the lipid head groups. This step can thus present a considerable energy barrier for solutes, which exhibit strong hydrogen bonding (donor) tendencies. Accordingly, biological permeation can be expected to markedly depend on the hydrogen bonding capacity of the solute (El Tayar et al., 1991; Conradi et al., 1991).

Octanol, which is the most commonly used lipophilic phase in two-phase partition experiments, can provide a good hydrogen bonding environment for solutes. A solute, which makes strong hydrogen bonds with water will be able to make similar bonds in octanol. The energy required in the desolvation step of the transfer from water to octanol is thus small, and hydrogen bonding will consequently be of little effect to the octanol–water partition coefficient (Conradi et al., 1991). An example of the effect of hydrogen bonding on biological partition is seen in Fig. 1. Peptide mimetic compounds of similar octanol–water partition coefficients show variable transcellular permeation through Caco-2 monolayers in accordance with a difference in their hydrogen bonding ability. Compounds in the upper group,

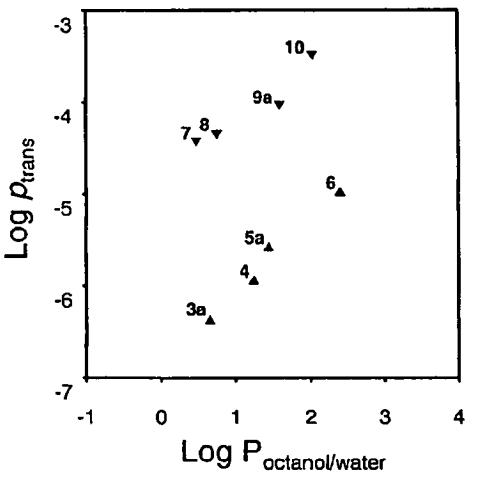

Fig. 1. Transcellular permeation through Caco-2 cell monolayers as a function of octanol–water partition coefficients for a set of dipeptide mimetic compounds. The division of the data points into two groups is in accordance with the different hydrogen bonding ability of the peptides. Compound names are given in the Appendix. Reproduced from Goodwin et al. (2001) with permission from the American Chemical Society.

numbers 7, 8, 9a and 10 are able to form four hydrogen bonds (two donors and two acceptors) while the compounds with numbers 3a, 4, 5a and 6 are able to form six (three donors and three acceptors). Hence, higher hydrogen bonding capacity has a negative effect on permeation.

The hydrogen bonding capacity of a solute can be expressed as the difference between its partition coefficient into octanol and a solvent devoid of forming hydrogen bonds, typically an alkane. Young et al. (1988) compared blood–brain partition data of histamine H_2 receptor antagonists to their octanol–water partition coefficients and found no correlation. The blood–brain partitioning was, however, successfully predicted by $\Delta\log P_{octanol/alkane}$, defined as $\log P$ (1-octanol/water) − $\log P$ (cyclohexane/water).

In a study by El Tayar et al. (1991), the solvatochromic approach was employed to analyse two-phase partition data of a variety of solutes in five solvent systems. The solvatochromic methodology (Taft et al., 1985a; Kamlet et al., 1983), also called the linear solvation energy relationship approach (LSER), states that solubility of a solute in a given solvent system can be related to solute–solvent interactions through the linear combinations of three types of terms: the cavity formation term expressed by the intrinsic molecular volume of the solute (V), the solute polarity/polarisability term (π^*) and the terms indicating the hydrogen bond acceptor (β_H) and donor (α_H) strength of the solute. The solvatochromic equation has also successfully been applied to predict oil–water partition coefficients:

$$\log P = a\left(\frac{V}{100}\right) + b\pi^* + c\beta_H + d\alpha_H + e \quad (2.5)$$

El Tayar et al. (1991) correlated the partition coefficients of 121 solutes with their solvatochromic parameters in five water–oil solvent systems (1-octanol, *n*-heptane,

chloroform, diethyl ether and *n*-butyl acetate) in order to evaluate the relative contribution of the parameters and to establish the information content of the descriptor $\Delta\log P$. They found that the solute hydrogen bond donor ability (α_H) was significant only in the *n*-heptane–water and chloroform–water systems, meaning that in the other three systems the organic solvents were as good hydrogen bond acceptors as water. This led the authors to suggest the difference between the partition coefficients measured in octanol–water and *n*-heptane–water ($\Delta\log P_{\text{octanol/heptane}}$) or chloroform–water ($\Delta\log P_{\text{octanol/chloroform}}$), as parameters to describe the hydrogen bond donor capacity of the solutes.

It has been pointed out by Leo (2000) that caution should be taken in the calculation of $\Delta\log P$ as the difference between the partition coefficients in two solvent systems to estimate solute hydrogen bond donor capacity. For example, the contribution of the cavity term in Eq. (2.4) has been found to vary between the octanol–water and the chloroform–water systems (Taft et al., 1996) and should be taken into account. Furthermore, even if the remaining solvatochromic parameters may appear insignificant in a correlation equation, this may result from an opposite effect of the polarity/polarisability term (π^*) and the solute hydrogen bond acceptor term (β_H). In addition, Leo suggested the inclusion of a parameter for excess alkane affinity (XAA) to account for the ability of the alkane chain of, e.g. octanol to accommodate large alkane portions of a solute, which he found capable of explaining outliers in earlier calculations of solute hydrogen bond donor strength (Leo, 2000). Naturally, the simplicity of the $\Delta\log P$ calculation will suffer from any additional parameter that has to be included.

Goodwin et al. (2001) compared the Caco-2 monolayer permeation of a series of dipeptide mimetics to their bulk partition coefficients. Neither the octanol–water partition coefficient (see Fig. 1) nor $\Delta\log P_{\text{octanol/}n\text{-heptane}}$ was successful in predicting biological permeation alone. A qualitatively better correlation was obtained with $\Delta\log P_{n\text{-heptane/glycol}}$. Solvatochromic analysis showed that this partition coefficient is a hybrid of the other two, consisting of contributions from both hydrogen bond donor and acceptor potential, as well as a volume term. An improved correlation was obtained with a linear combination of $\log P_{\text{octanol/water}}$ and $\Delta\log P_{\text{octanol/}n\text{-heptane}}$, suggesting that a more specific relationship of solute volume and hydrogen bonding capacity is required to properly describe biological permeation.

Lipid-containing partition systems have been considered to model the hydrogen bonding ability of biological membranes better than bulk solvents. Indeed, it was found by Vaes et al. (1998) that differences in octanol–water and liposome–water partition coefficients of neutral compounds were almost exclusively explained by hydrogen bonding. Disappearance of solute from the aqueous bulk phase in liposome–water partition studies does, however, not necessarily indicate partition into the bilayer core. Jacobs and White (1989) studied the partition of small hydrophobic peptides into liposomes and found that the binding of the peptides at the liposome–water interface was mainly driven by the hydrophobic effect, while insertion into the bilayer interior was strongly dependent on the interfacial hydrogen-bonding.

2.2.3. Solute charge

Most drugs are weak acids or weak bases and exist in solution at equilibrium between their neutral and ionised forms. When studying two-phase partition of ionisable drugs, one has to distinguish between the partition coefficient and the distribution coefficient (also called the apparent partition coefficient), the latter of which is defined as the ratio of the total drug concentrations (both neutral and ionised species) in the lipidic and aqueous phases at a certain pH:

$$\log D_i = \log \frac{a_{i,\text{tot}}^{\text{o}}}{a_{i,\text{tot}}^{\text{w}}} \tag{2.6}$$

An assumption that has been widely stated in association with biological permeation is the pH partition hypothesis, according to which only neutral and non-polar compounds are able to cross biological membranes. Accordingly, transmembrane permeation of charged and hydrophilic drugs has generally been assumed to take place through paracellular space. However, the surface area of the cell membranes is by several orders of magnitude larger than that of the paracellular channels, which outweighs the lower permeation of the transmembrane route, and due to this some of the transport of such compounds may in reality take place through transcellular diffusion (Artursson et al., 2001).

Observations of transmembrane diffusion of ionic species were initially explained by the formation of neutral ion pairs (Scherrer, 1984; Neubert, 1989; Takács-Novák and Szász, 1999). While not counteracting the ion pair theory, it has lately been shown that lipophilic ions may partition into membrane phases on their own account (Kürschner et al., 2000). In addition, it has been pointed out that even if the passive membrane transport of ions may be much slower than that of neutral compounds, the abundance of the ionised species can make it significant (Palm et al., 1999). Furthermore, a too lipophilic neutral solute may accumulate in the membrane interior instead of passing trough it. In such cases, ionisation could enhance permeation (Suhonen et al., 1998).

Other studies propose that permeating compounds enter the membrane in their neutral form despite being ionised in the bulk aqueous phase, due to a shift in the pK_a at the membrane surface caused by the change in polarity and the local electrostatic surface potential (Miyazaki et al., 1992; Beschiaschvili and Seelig, 1992). This explanation is supported by observations that compounds that carry at least one stable charge, i.e. acids with pK_a <4 or bases with pK_a >10 do not readily cross the blood–brain barrier. On the other hand, compounds possessing tertiary ammonium moieties with a pK_a of ~8 exhibit higher BB permeation than expected on basis of the fraction of unionised drug (Fischer et al., 1998).

Yet another explanation for ion permeation is the existence of an aqueous diffusion layer at the membrane interface to which the ionised species diffuses from the bulk aqueous phase much faster than the neutral species, whereas the latter enters the membrane much more readily than the ionised species. To maintain equilibrium, an interfacial dissociation reaction takes place in the diffusion layer where the neutral species is recovered due to the dissociation equilibrium (Bouchard et al., 2002). Furthermore, it has been shown that ion transport can be increased by a transmembrane potential (see next section, Mayer et al., 1985) and that the observed increase of ion partition in presence of counter ions may in fact be caused by an interfacial potential difference instead of ion pair partition (Bouchard et al., 2001a). At present, however, the effect of charge on biological permeation is not well understood and more and comprehensive studies on the subject are required.

The reason for the poor permeability of lipid bilayers towards ions is desolvation. Ions transferring through a lipid bilayer must first partition into the interfacial region and then diffuse through the non-polar hydrocarbon core. Before entering the hydrocarbon region, most ions will give up some of their hydration water. This process is energetically unfavourable and the main reason for the low diffusive permeation of ions in lipid bilayers (Cevc, 1990). The situation is traditionally appreciated in electrostatic terms by considering the energy cost of transferring an ionic charge from water, with a high dielectric constant, to the membrane interior with a low dielectric constant. The electrostatic contribution to this energy can be estimated from theoretical models, such as the modified Born equations put forth by Parsegian (1969) (2.7) and Abraham and Liszi (1978) (2.8):

$$\Delta_w^o G_{i,es}^0 = \frac{N_A z_i^2 e^2}{4\pi\varepsilon_0}\left[\frac{1}{2r_i}\left(\frac{1}{\varepsilon^o}-\frac{1}{\varepsilon^w}\right)-\frac{1}{\varepsilon^o d^o}\ln\frac{2\varepsilon^w}{\varepsilon^w+\varepsilon^o}\right] \quad (2.7)$$

$$\Delta_w^o G_{i,es}^0 = \frac{N_A z_i^2 e^2}{8\pi\varepsilon_0}\left[\left(\frac{1}{\varepsilon^o}-\frac{1}{\varepsilon_1}\right)\frac{1}{b_i^o}-\left(\frac{1}{\varepsilon^w}-\frac{1}{\varepsilon_1}\right)\frac{1}{b_i^w}\right] \quad (2.8)$$

where ε^w and ε^o are the relative permittivities of the aqueous and lipidic phases, respectively, ε_0 is the permittivity of vacuum and r_i is the ionic radius. In Eq. (2.7), the second term in the square brackets corrects the Born model for finite thickness d^o of the lipidic phase. The correction term remains insignificant so long as $r_i \ll d^o$. In the Abraham–Liszi approach in Eq. (2.8), the ion is surrounded by a local solvent layer of thickness $(b_i - r_i)$ with the relative permittivity of ε_1, as shown in Fig. 2; ε_b is the relative permittivity of the bulk solution.

The traditional estimates above, Eq. (2.7) and (2.8), apply in a dielectric continuum with an appropriate relative permittivity, which is, of course, an oversimplification of the lipid bilayer. For example, the permeability of Na^+ calculated from Eq. (2.7) is of the order of 10^{-29} cm s^{-1},

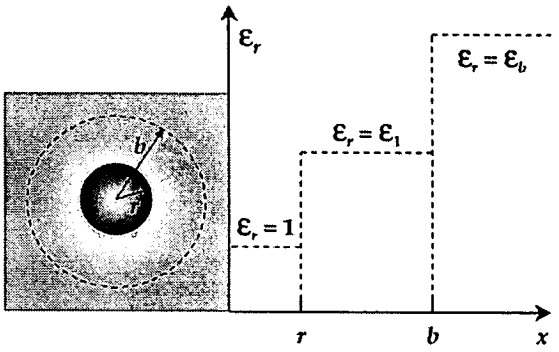

Fig. 2. Schematic representation of the Abraham–Liszi model.

while measured permeabilities are ca. 14–17 orders of magnitude higher (Wilson and Pohorille, 1996). Therefore, molecular dynamic simulations of the transport of Na^+ and Cl^- across a glycerol 1-monooleate (GMO) bilayer were carried out, and it was found that when the ion approached the polar heads of the bilayer, the bilayer withdrew inwards, forming a cavity filled with water and making the bilayer thinner at the crossing site. Accordingly, when the ion left the bilayer on the opposite side, a similar disruption was observed. The loss of hydration water in the centre of the bilayer was compensated for with solvation by the oxygen atoms of the GMO headgroups, keeping the total solvation number of the ion practically constant during the crossing. With these simulations, the authors (Wilson and Pohorille, 1996) achieved permeabilities, which were in accordance with the measured values.

As solvation increases with charge, bilayers are almost impermeable to polyions, except for certain divalent cations, which are able to cross membranes by forming neutral complexes with membrane components of opposite charge (Cevc, 1993). The zwitterions, however, form an exception to this. Pagliara et al. (1997) point out in their thorough review on the subject that the apparent lipophilicity of zwitterions is often higher than expected from their charged nature due to two reasons: (i) the presence of a significant portion of the neutral tautomer of the zwitterions (see Fig. 3); or (ii) the partial intramolecular neutralisation

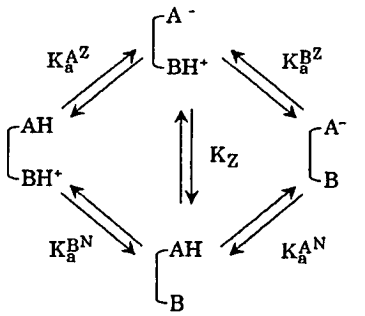

Fig. 3. Dissociation scheme of a zwitterion. K_Z is the tautomeric constant describing the equilibrium between the globally neutral, zwitterionic species and its uncharged tautomer. Reproduced from Bouchard et al. (2002) with permission from Kluwer.

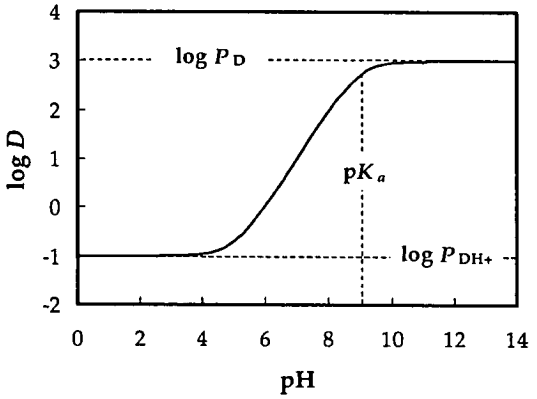

Fig. 4. Theoretical distribution profile of the monobase D with $\log P_D = 3$, $\log P_{DH+} = -1$ and aqueous $pK_a = 9$.

of the two opposite charges. As discussed by the authors, zwitterions can provide several benefits over compounds carrying a single ionisable group: (i) they exhibit a practically constant value of lipophilicity around the isoelectric pH (typically overlapping with the physiologically relevant pH region); and (ii) zwitterions in which the neutral tautomer is present to a notable extent may exhibit significant transcellular permeation.

Conclusively, taking into account the possibility of ion partition, the relationship between pH and partition for a monoprotic compound can be expressed by the following Eq. (2.9) (Reymond, 2001) and Fig. 4:

$$\log D_{D/DH} = \log(P_D + P_{DH} \times 10^{pK_a^w - pH}) - \log(1 + 10^{pK_a^w - pH}) \quad (2.9)$$

where D refers to the neutral base or deprotonated acid, and DH stands for the protonated base or neutral acid, respectively.

2.2.4. Electrostatics of lipid bilayers

The majority of membrane lipids are comprised of a head group region with one or more charged units. Since charged lipids are commonly either zwitterionic or anionic, the net charge of membrane surfaces is negative. The transverse structure of the bilayer causes the charged and dipolar lipid groups to be relatively fixed with respect to their orientation and location from the bilayer centre. Consequently, these charges and dipoles are only partially compensated by water dipoles and solution electrolytes, and a complex electric profile is generated over the membrane. This profile is composed of two components: the surface, or double-layer potential, and the dipole potential.

The surface potential arises from charged lipid headgroups at the membrane surface. These fixed charges attract counterions from the bulk aqueous solution to the interface, giving rise to a so-called electrical double layer, and an electric potential profile is established at the surface. The surface potential is not likely to have a considerable effect on the partition of neutral species into the bilayer, but increases the surface concentration, and thus the probability of permeation, of cations, whereas the probability of anion permeation should decrease.

The membrane dipole potential establishes itself in the region between the aqueous phase and the hydrocarbon interior of the membrane. The origin of the dipole potential is not well understood, but the orientation of the lipid head groups and the polarised water associated with the membrane interface are believed to provide an important contribution (Brockman, 1994; Gawrisch et al., 1992). The dipole potential of lipid bilayers is estimated to be hundreds of millivolts positive in direction of the membrane interior (Brockman, 1994), thereby making the bilayer interior more accessible to anions than cations and counteracting the effect of the surface potential.

Meijer et al. (1999) employed a self-consistent anisotropic field approach to model a phospholipid bilayer. They found that the plane tilting of the dimyristoyl phosphatidylcholine (DMPC) headgroups generated an electrostatic potential profile over the membrane, which, albeit an order of magnitude smaller than the estimated dipole potential in real bilayers, caused anions and cations to distribute unevenly over the bilayer. Both positively and negatively charged ions had difficulties penetrating the hydrocarbon interior of the bilayer, but due to the potential profile it was more accessible to anions (Fig. 5).

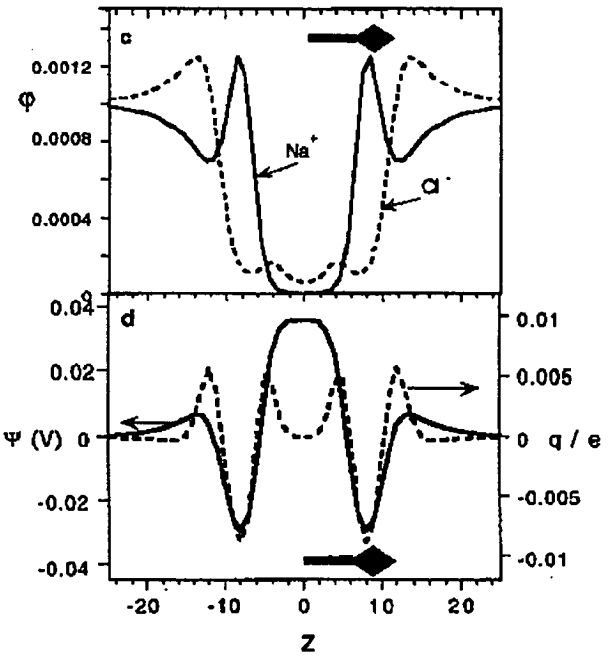

Fig. 5. The volume fraction φ, charge distribution q and electrostatic potential ψ profiles through a cross section of a free-standing liquid crystalline DMPC membrane. The director shown in the diagrams is perpendicular to the membrane surface, indicating the hydrophobic core with its tail and the head group area with its head. The volume fraction of salt solution in the bulk is 0.002. The centre of the membrane is at $z = 0$. Reproduced from Meijer et al. (1999) with permission from the American Institute of Physics.

An additional feature of cellular membranes that is absent in bulk partitioning systems, is the potential difference over the membrane. This so-called transmembrane potential of approximately −100 mV (interior to exterior) is maintained by active transporter proteins, which move ions across the membrane against their concentration gradient. Mayer et al. (1985) studied the effect of a transmembrane potential difference on cation partitioning into lipid vesicles. They found that the partition of the positively charged anaesthetic dibucaine was greatly enhanced in the presence of a potential gradient of −170 mV compared to the situation where no potential gradient was present.

The picture presented in this section only concerns the electric properties of a lipid bilayer. In biological membranes further contributions arise from the variety of proteins associated with the bilayer as well as the negatively charged glycocalix surrounding the outer leaflet of the cellular plasma membrane (Langner and Kubica, 1999).

2.2.5. Solute size and order of the partition phase

The effect of solute size on two-phase partition depends significantly on the structure and nature of the lipidic phase. Upon partitioning, in addition to the energy of cavity formation, the energy of reorganization of the solvent molecules around the solute needs to be taken into account. When partition takes place into a bulk phase, the size effect mainly depends on the polarity of the solvent compared to that of water (Spencer et al., 1979). However, in lipid membranes size effects may be more complex due to steric hindrance. Since an increase in solute size usually induces changes in other properties related to partition, an experimental evaluation of the size effect is not straightforward.

Various studies have focused on mapping the structure of a membrane bilayer. Hubbell and McConnell (1971) used electron paramagnetic resonance to show that the hydrocarbon chains of membrane phospholipids are highly ordered in the vicinity of the polar head groups, but that there exists a gradient of chain disorder from the membrane surface toward midbilayer. Similar results have been reported on basis of deuterium magnetic resonance (Seelig and Seelig, 1974) and computational studies (Tu et al., 1995; Meijer et al., 1999).

Marrink and Berendsen (1996) studied the transport of small molecules across a phospholipid membrane using molecular dynamics simulations. They described the lipid bilayer with a four-region model: region 1 is characterised by loosely bound water molecules that are attached to the choline headgroups; in region 2 the headgroup density is high and the water molecules are strongly bound, the major part of the glycerol backbones also reside in this region; region 3 contains the more ordered parts of the lipid tails and resembles a soft polymer; and region 4 comprises of the major parts of the lipid chains, in this region the chains are disordered and their density is low. According to their simulations the largest resistance for solute permeation occurs in region 3, especially for hydrophilic penetrants. Only for very hydrophobic solutes may diffusion in the water layer (regions 1 and 2) become rate-limiting. Region 4, i.e. the bilayer centre, is characterised by lower resistance to penetration than region 3 due to its more disordered nature. However, for highly hydrophobic solutes, which exhibit small electrostatic interactions, this region may act as a trap due to its favourable solution environment. An increasing size of the solute is expected to further emphasise the rate-limiting effect of region 3 for polar solutes. The anisotropic structure of the region is furthermore likely to favour permeation of non-spherical molecules over spherical ones.

An experimental study supports the importance of phase structure on permeation and partition. Benzene partition into phospholipid monolayers was found to depend significantly on the surface density of the lipids (De Young and Dill, 1988). Increasing the surface density led to solute exclusion: benzene partitioning decreased by an order of magnitude as the surface density increased from 50 to 90% of its maximum value, a range readily accessible in bilayers and biomembranes under physiological conditions. The effect of surface density was attributed to an ordering of the lipid chains, as a similar effect could be observed regardless of the method used to alter the surface density: cholesterol addition, as well as alteration of temperature and phospholipid chain length were examined.

Due to its polar hydroxyl groups, octanol is thought to form inverted micellar aggregates, particularly in its water-saturated form (Franks et al., 1993; DeBolt and Kollman, 1995), as shown by the molecular dynamics simulation image in Fig. 6. This would suggest that the octanol phase is not an isotropic bulk phase, but that it contains structures similar to those formed by lipids in biological systems. Furthermore, both experimental (Cramb and Wallace, 1997) and theoretical (Michael and Benjamin, 1995) studies indicate that at the octanol–water interface the octanol molecules are ordered with their polar groups towards the aqueous phase. These findings present a probable explanation for the success of the octanol–water partition coefficient as a lipophilicity descriptor of biopermeation. However, the structural organisation of the interfacial octanol layer is not equivalent of the order in lipid bilayers, and thus partition into octanol will not reflect steric hindrance properly.

2.2.6. Conclusions

Octanol–water partition coefficients can be expected to model the affinity of the drug for the membrane interface and hydrocarbon chains, and will successfully predict passive permeation in biomembranes only when hydrogen-bonding and electrostatic effects are not rate-limiting. Lipid partition phases provide a more biomimetic environment, but being an overall value, the lipid–water partition coefficient does not specify whether partition takes place into the bilayer interior or to the lipid–water interface. Biological permeation of charged species has received relatively little attention, however thorough studies of the topic would be warranted due to the charged nature of many drugs.

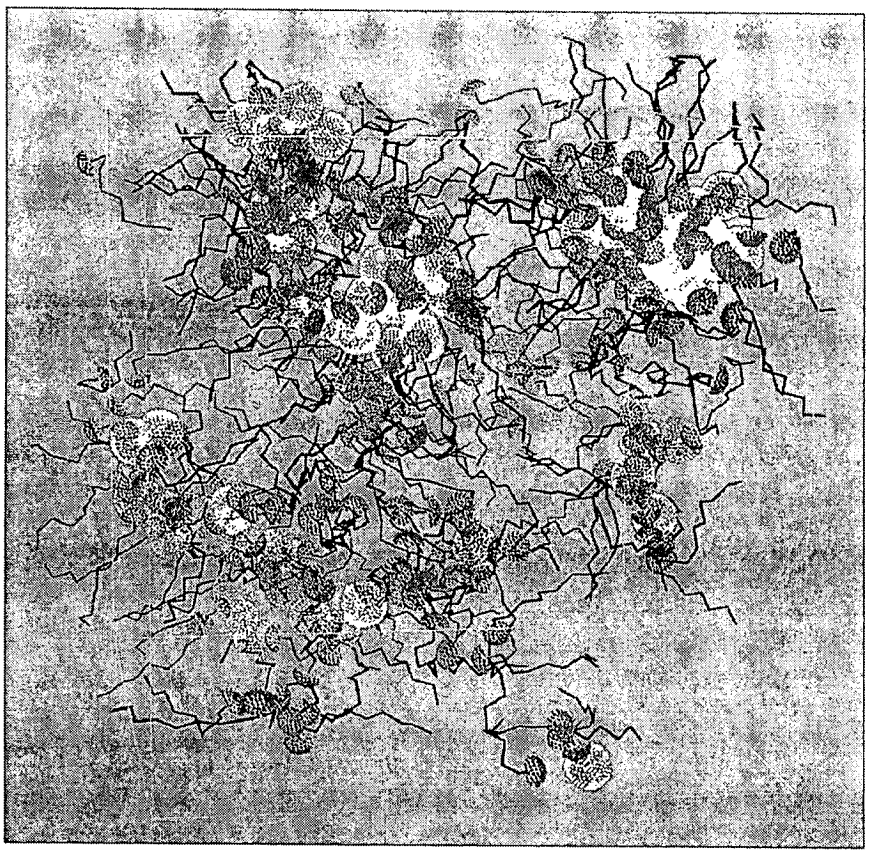

Fig. 6. Molecular dynamics simulation of water-saturated 1-octanol. Yellow van der Waals radii represent water oxygens, red represents octanol hydroxyl hydrogens, and hydrocarbon tails are shown as black chains. Reproduced from DeBolt and Kollman (1995) with permission from the American Chemical Society.

3. Experimental approaches

3.1. Octanol

The octanol–water partition coefficient is by far the most extensively used descriptor of the lipophilic character of drugs. The partition coefficient is traditionally measured by stirring or shaking an octanol–water mixture in the presence of the solute, followed by analysis of the equilibrium concentration of solute in one or both phases (Leo et al., 1971). In principle the procedure is very simple, but in reality conventional shake-flask measurements are time-consuming and tedious to make, and require relatively large amounts of solute. Recent literature presents solutions to these problems in the form of microscaling (Morgan et al., 1998) and an automated parallel plate assay (Hitzel et al., 2000). A pH-metric technique based on potentiometric titration has been developed for rapid determination of partition coefficients for ionisable drugs (Avdeef, 1993).

Correlations between octanol–water distribution coefficients and biological permeation have in some cases been reasonably good (Palm et al., 1996; Krämer, 1999; Wils et al., 1994; Zhao et al., 2002), suggesting the existence of a bell-shaped (or sigmoidal) relationship with maximum absorption around $\log D_{7.4} = 2$–3 (see Fig. 7). However, many studies also report poor or nonexistent correlations (Figs. 1 and 12b; Balon et al., 1999b; Palm et al., 1997; Conradi et al., 1991; Zhu et al., 2002), thus no definite relationship has been established. However, in combination with other de-

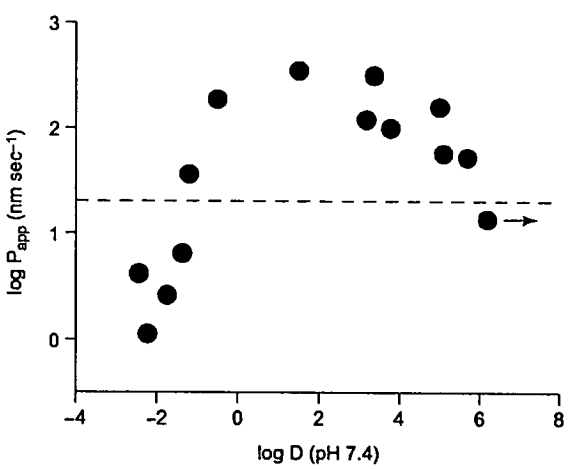

Fig. 7. Logarithm of apparent permeation across Caco-2 cell monolayers (P_{app}/nm s^{-1}) and log D at pH 7.4. Compounds above the dotted line are assumed to be well absorbed. The arrow indicates uncertainty of the result owing to analytical limit of the determination. Reprinted from Krämer (1999) with permission from Elsevier.

scriptors, octanol–water partition coefficients have in many cases resulted in good correlations, as discussed in Section 5.

3.2. Liposomes

After the realisation that lipids spontaneously form closed bilayer membranes in aqueous surroundings, these so-called liposomes were introduced as models for cellular membranes in 1965 (Bangham et al., 1965; Bangham, 1993). Owing to their superior biomimetic properties, liposomes have also been proposed as alternatives to octanol in drug partition studies.

The abundance of available lipids and preparation techniques has resulted in a variety of liposome types being employed as partition phases. Balon et al. (1999a) undertook a study in which they compared partition data obtained with different liposomes. They found only small differences between small and large unilamellar liposomes, and between small unilamellar liposomes generated by sonication and equilibrium dialysis. The authors suggested the use of sonicated small unilamellar vesicles (S-SUV) as a standard system due to the simple preparation procedure and large surface area, which enables shorter equilibrium times and higher lipid to drug ratios. Liposomes have furthermore been used in association with chromatography, as discussed in the following section.

Studies on the effect of lipid composition have indicated that the presence of cholesterol generally decreases solute partition (Balon et al., 1999a; Betageri and Rogers, 1988). Lipid charge has been found to influence partition of ionisable solutes (Betageri and Rogers, 1988; Krämer and Wunderli-Allenspach, 1996; Surewicz and Leyko, 1981). In a study by Krämer et al. (1998), partition into negatively charged liposomes was in fact larger for the cationic species than for the neutral solute. However, it has been pointed out that partition measured in the liposome–water system may not always reflect transmembrane permeation (Palm et al., 1998) as solutes may also associate with the membrane interface without entering the bilayer interior (Jacobs and White, 1989). This may also be the reason behind the observed charge-induced increase in partition. Likewise, this is a possible explanation for the significantly higher ionic partition coefficients obtained in liposomes compared to the octanol–water system (Avdeef et al., 1998; Balon et al., 1999b). Contrasting reports on correlations between the octanol and the liposome systems for neutral solutes (Gobas et al., 1988; Avdeef et al., 1998; Balon et al., 1999b) suggest that a general similarity between the two systems cannot be assumed, even if correlations can be found for structurally similar compounds. If partition is driven mainly by hydrophobic interactions, correlations between the two systems can be expected, but if electrostatics or hydrogen bonding play a significant part in the process, correlations are likely to be weak.

Relatively few studies report on correlations between liposome partition and biological permeation. Lohmann et al. (2002) reported on neither liposome–water nor octanol–water partition being able to successfully predict blood–brain barrier permeation of drugs. Balon et al. (1999b) found no correlation between liposome distribution coefficients and human intestinal absorption. A so-called absorption potential descriptor was subsequently calculated from the liposomal distribution coefficient, solubility, dose and intestinal volume, and a sigmoidal correlation to HIA could be established. This suggested that the dataset included compounds for which passive transcellular diffusion was not (a) the transport mechanism or (b) the rate-limiting factor in absorption, but active transport was taking place. Absorption potentials based on octanol–water distribution coefficients did, however, not yield significant correlations with HIA.

Liposomes have been captured on biosensor chips for the determination of drug–membrane interactions (Danelian et al., 2000). The detection method employed was surface plasmon resonance, which detects the change in the refractive index at the sensor surface caused by the interaction, and thus does not require the compounds to be radiolabelled or contain chromophores. The majority of drugs with high transcellular absorption could be identified on basis of the binding assay, however it was pointed out that the binding observed by the sensor may not always be related to transcellular transport.

In conclusion, despite offering a more biological partition environment than octanol, the liposome system suffers from similar drawbacks in terms of time and effort. To increase experimental efficacy, a fast pH-metric titration method has been developed (Avdeef et al., 1998; Balon et al., 1999a). A high-throughput development of the conventional liposome/water system for drug screening does, however, seem unlikely. The partition coefficients measured in the liposome system may not always reflect biological permeation, but drug interactions with the membrane surface. Nevertheless, information of such interactions could have implications for drug-induced membrane effects (Grinius et al., 2002).

3.3. Chromatographic membrane phases

Reverse phase liquid chromatography (RPLC) was initially introduced to improve the static octanol–water method, with advantages such as increased speed of determination, ease of automation, small sample amount and insensitivity towards impurities (Pagliara et al., 1995; Kaliszan et al., 1993). The partition coefficient is easily calculated from the retention time of the solute in the RPLC column. In RPLC, drug partition has mainly been studied using silica-bound alkylsilanes (typically octadecylsilica, ODS) as stationary phases. The stationary phase offers a more ordered organic phase than the octanol–water method, but lacks a polar region and retention is thus expected to reflect only hydrophobic interactions. Solvatochromic analysis of capacity factors have confirmed the similarity of the RPLC C_{18} retention with octanol–water partition (Abraham et al., 1997).

The main drawback of the RPLC technique is the variability of commercial columns and sensitivity towards experimental conditions, which have prevented the establishment of a universal log P scale. Other shortcomings are a low chain density found in many commercial columns and the limited pH operating range of silica-bonded phases. In addition, despite end-capping, silica-based chromatographic surfaces still contain free silanol groups that may affect solute retention. The use of polymer-based stationary phases has been considered, but their influence on the retention time is not clear and furthermore they are expected to show less stability towards hydrodynamic pressure (Law et al., 1992; Dorsey and Khaledi, 1993).

In recent years, with efforts to improve the biological predictivity of the octanol–water system, chromatography has approached the problem by introducing immobilised artificial membrane (IAM) surfaces (for reviews on the technique see Taillardat-Bertschinger et al., 2003; Stewart and Chan, 1998; Yang et al., 1996). IAMs are constructed of phospholipid analogues, which are covalently bound by one of their alkyl chains to silica particles at high molecular surface densities, thereby mimicking fluid phase phospholipid bilayers (see Figs. 8 and 9). In comparison with fluid liposomes, the density of the lipid headgroups is smaller in IAM surfaces (Ong et al., 1996) and the hydrocarbon chains are more ordered due to immobilisation. Molecular dynamics simulations (Sheng et al., 1995) have indicated that the polar interfacial region of the IAM surface mimics closely that of fluid membranes, which has further supported the use of IAMs as substitutes for liposomes in drug partition studies. The main problems associated with IAM chromatography are similar to RPLC: column variability, the instability as well as the silanophilic interactions of the silica support, and the limited pH-range (Kaliszan et al., 1993; Caldwell et al., 1998; Ottiger and Wunderli-Allenspach, 1999). Guidelines have been proposed for carrying out proper measurements of capacity factors on IAM phases (Taillardat-Bertschinger et al., 2002a).

For relatively lipophilic compounds, the use of purely aqueous mobile phases results in long retention times. It is therefore common to add an organic modifier to the mobile phase in order to accelerate elution. The most popular co-solvents are methanol and acetonitrile. Methanol is thought to be a more recommendable co-solvent due to its more water-like solvent properties. In addition, the presence of acetonitrile at concentrations above 30 wt.% disrupts the structure of water (Marcus and Migron, 1991). However, stationary phases end-capped with methyl glycolate are liable to methanolysis when methanol is used in the mobile phase (Rhee et al., 1994). In order to yield comparable partition coefficients, the capacity factors obtained in the presence of an organic modifier has to be extrapolated to 100% aqueous mobile phase. In this process, it should be kept in mind that the presence of the modifier affects the pH and ionic strength of the solution as well as the apparent pK_a of the solute. (Taillardat-Bertschinger et al., 2002a, 2003).

Results from IAM chromatography have been compared with octanol–water (Kaliszan et al., 1994; Ong et al., 1996; Barbato et al., 1997; Amato et al., 2000; Valko et al., 2000) and liposome–water partition (Ong et al., 1996; Ottiger and Wunderli-Allenspach, 1999; Taillardat-Bertschinger et al., 2002b) for various solutes. Contradictions in the comparisons suggest that the balance between the various molecular interactions that affect partition differs in the three systems. Studies on the thermodynamics of partition support this conclusion (Ong and Pidgeon, 1995; Betageri and Rogers, 1987). Structurally-related solutes, which partition mainly as a result of hydrophobic interactions, typically yield comparable results in the above mentioned partition systems. When polar (hydrogen-bonding) and electrostatic

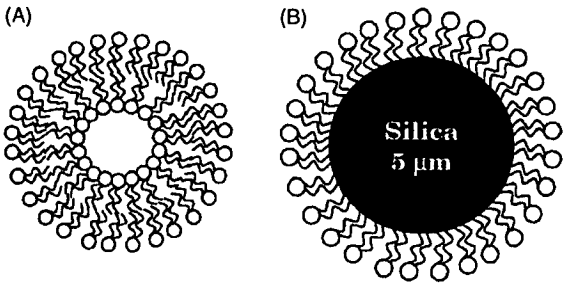

Fig. 8. Schematic structure of (A) a unilamellar liposome and (B) an IAM particle, in which a phospholipid monolayer is covalently bound to a silica particle. Reproduced from Taillardat-Bertschinger et al. (2003) with permission from the American Chemical Society.

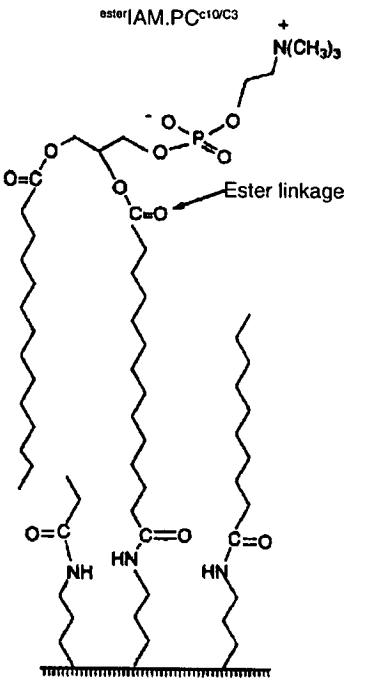

Fig. 9. Schematic of an IAM phospholipid (^{ester}IAM.PC$^{C10/C3}$). Reproduced from Ong and Pidgeon (1995) with permission from the American Chemical Society.

interactions intervene, correlations tend to break down. Partition of charged and hydrogen-bonding solutes is typically larger into liposomes than IAM phases, which is likely to result from the higher density and mobility of the polar head groups in liposomes (Taillardat-Bertschinger et al., 2002b). It is, however, not clear whether partition actually takes place into the hydrocarbon region or only to the interfacial region of the lipid head groups. In the latter case, this would explain the lower partition of charged and hydrogen-bonding solutes into octanol than liposomes and IAM, as the hydrocarbon interior of lipid mono- and bilayers should not offer a more superior environment for charged species, and less hydrogen-bonding sites than octanol. However, if partition into the lipid-containing phases actually takes place into the acyl chain region, a plausible explanation could be found in the concentrating effect of the headgroup–solute interactions, and, in the case of liposomes, a withdrawal effect of the lipid bilayer, as described in Section 2.2.3, and subsequent transfer to the liposome interior.

IAM capacity factors have also been compared with Caco-2 cell monolayer permeation, yielding only weak correlations ($n = 11$, $r^2 = 0.58$, Ong et al., 1996; $n = 9$, $r^2 = 0.32$, Stewart et al., 1998). In the latter case, correlations improved significantly when a molecular weight and a hydrogen-bonding term were included in the linear regression. Comparison between rat intestinal absorption and IAM resulted in correlations of $r^2 = 0.63$ ($n = 12$; Ong et al., 1996) and $r^2 = 0.77$ ($n = 12$; Genty et al., 2001). Again, correlations improved with the addition of a molar volume term.

IAM chromatography has furthermore been evaluated for prediction of drug permeation across the blood–brain barrier. One group found that BBB partitioning of a set of structurally and electrically diverse drugs was only weakly correlated with IAM retention or octanol–water partition coefficients, correlations were improved when size and ionisation was taken into account (Salminen et al., 1997). In another study, IAM chromatography was found to be superior over octanol–water partition and ODS chromatography in predicting BBB partition of polar and ionisable compounds (Reichel and Begley, 1998).

Recently a novel method to construct IAM stationary phases has been introduced. Krause et al. (1999) report on the use of noncovalent IAM surfaces, which are constructed by dynamic coating of a reversed-phase C_{18} column with phospholipids, thereby resulting in a bilayer structure. Improvements in comparison with the covalent IAM phases include a wide selection of lipid matrices and a more biomimetic partition phase. Column stability was found to be sufficient for multiple column runs in the presence of reasonable eluent concentrations. Excellent correlations ($n = 13$, $r^2 = 0.92$) were found between peptide binding to phospholipids vesicles and noncovalent IAM retention times.

A similar approach was taken by Loidl-Stahlhofen et al. (2001). Their study employed solid-supported lipid membranes (SSLM) composed of lipid bilayers noncovalently immobilised on silica beads. The membrane particles were incubated with the solutes of interest on microtiter plates for 2 min. Subsequently, the particles were separated by filtration and the solute concentration in the aqueous phase was analysed with HPLC. Good correlations between the obtained membrane affinity (MA) coefficients and octanol–water partition coefficients were observed for neutral compounds, whereas membrane affinity of charged solutes was found to correlate well with liposome–water distribution coefficients. The technique was found to be highly reproducible and automatisable.

The work by Beigi and co-workers (Beigi et al., 1995, 1998; Lundahl and Beigi, 1997) combines the IAM approach with liposome partition to immobilised liposome and biomembrane chromatography (ILC and IBC) wherein vesicles are immobilised in gel beads. The approach avoids the stability problems of silica-bonded lipid phases and the use of organic, non-physiological solvents as eluents. In addition, the membrane structure is more biomimetic compared to IAM lipid phases and allows for the incorporation of proteins.

Apparent (both ionised and neutral species) specific capacity factors K_s obtained with immobilised egg PC liposome chromatography were found to exhibit good linear correlations with octanol–water distribution coefficients (Beigi et al., 1995; Palm et al., 1998). K_s is defined as

$$K_s = \frac{t_r - t_0}{t_0} \tag{3.1}$$

where t_r = retention time; t_0 = column dead time. Sigmoidal correlations between IC capacity factors and human intestinal absorption were established (Beigi et al., 1995; Liu et al., 2002) allowing for qualitative identification of drugs with favourable absorption properties, as shown in Fig. 10a. In a study by Palm et al. (1998), the presence of a large and flexible compound significantly weakened the correlation between apparent capacity factors and Caco-2 cell monolayer permeation (Fig. 10b). It was pointed out that the ILC retention time results from a combination of partition into the liposome interior, partition into the lipid bilayer and electrostatic solute–lipid surface interactions, and that retention may therefore not always reflect transmembrane diffusion.

Conclusively, IAM and IL chromatography offer an automatisable system for rapid screening of drug compounds, although not really in HTS scale. However, similarly to the liposome system, the capacity factors obtained from these may in some cases not reflect biological permeation, but drug interactions with the membrane surface. Perhaps as a result of this, correlations of IAM indices with biological permeation have often improved in combination with other descriptors. A proper validation of the IAM approach would require testing with a large number of compounds. Often, only a limited number of drugs within a fairly narrow structural range are studied. Recent studies suggest that chromatographic capacity factors may find use in membrane activity studies of drugs (Ollila et al., 2002; Krause et al., 1999).

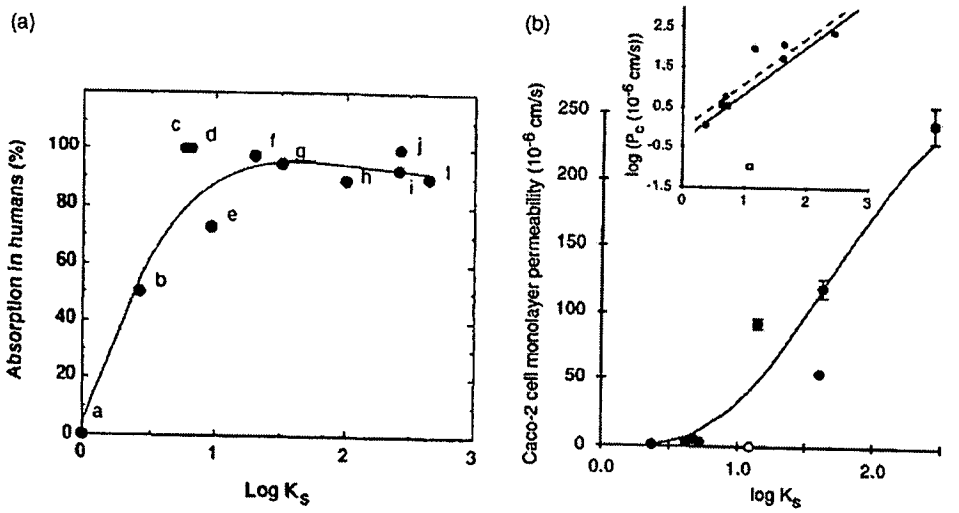

Fig. 10. Apparent (includes both ionised and neutral species) specific capacity factors from immobilised liposome chromatography vs. (a) human intestinal absorption. Compound list in Appendix. Reproduced from Beigi et al. (1995) with permission from Elsevier. (b) Caco-2 cell monolayer permeability. Reproduced from Palm et al. (1998) with permission from the American Chemical Society.

3.4. Cell culture monolayers

In recent years, the use of cell cultures to predict drug permeation in biomembranes, such as intestine (Artursson et al., 2001), skin (Suhonen et al., 2003) and cornea (Toropainen et al., 2003) has gained popularity. The most frequently used cell cultures for studies of passive drug transport are the Caco-2 cell cultures, which are derived from human colon cancer cells (human adenocarcinoma colon cells). The Caco-2 cells can be cultivated to spontaneously differentiate to form monolayers of polarised cells, with functions similar to intestinal enterocytes. The monolayers are grown on filter supports and drug passage from the donor to the acceptor compartment is measured. Transport studies through the Caco-2 monolayers can provide information on permeability coefficients, transport mechanisms and pathways, and metabolism of drug compounds (Audus et al., 1990). Another advantage of studying biological permeation with cell monolayers is that they measure the transport of the drug across the cell membrane, instead of just its interaction with the lipid bilayer.

Despite their undeniable benefits as model membranes, also the approach of using cultured cell monolayers comes with certain limitations. The method is rather laborious and time-consuming as cells have to be cultured for approximately 3 weeks prior to use and during the experiments samples are collected at time intervals of hours. To increase experimental efficacy alternative cell lines have been introduced, requiring less than a week of culture (Irvine et al., 1999; Tavelin et al., 2003a), and an automatic liquid handling system has been reported to increase capacity and significantly decrease the need for manpower during experiments (Garberg et al., 1999).

Despite the ability of Caco-2 cell cultures to predict the oral drug absorption, in particular for well absorbed compounds, the comparisons of Caco-2 data from different laboratories has revealed discrepancies, which arise from differences in cell culturing methods, experimental conditions (such as temperature, pH-gradient and hydrodynamics of the system) as well as the source of Caco-2 cells (Yee, 1997; Artursson et al., 2001; Walter and Kissel, 1995). An example of this is seen in Fig. 11, where Caco-2 permeation data from different laboratories is plotted against absorbed fraction in humans. Although a qualitatively similar correlation is observed in all cases, the assumption of one common Caco-2 permeation scale could lead to misunderstandings. To correct for intra- as well as interlaboratory variability, the cell monolayers can be characterised with respect to their electrical resistance as well as permeation of reference compounds (Larger et al., 2002).

In addition to the interlaboratory variability in Caco-2 permeability, it is also known that the expression of both the paracellular and active transport routes, as well as efflux systems, is different in Caco-2 cell lines compared to the human intestine (Artursson et al., 2001). Despite differing levels in transporter expression, Caco-2 cell cultures can be used in the identification of the role of transporters in the permeation of drug candidates. Caco-2 cell permeation has also gained regulatory acceptance as part of the biowaivers based on the Biopharmaceutical Classification System (BCS) (Lobenberg and Amidon, 2000).

Alternative cell lines that better mimic the human small intestine are continuously under development. One recently introduced cell line is 2/4/A1, which exhibits similar passive (paracellular and transcellular) absorption characteristics as the human jejunum (Tavelin et al., 2003a,b). Due to its lack of functional expression of active transport and efflux systems, the 2/4/A1 cell line holds promise for characterisation of the passive absorption of drugs.

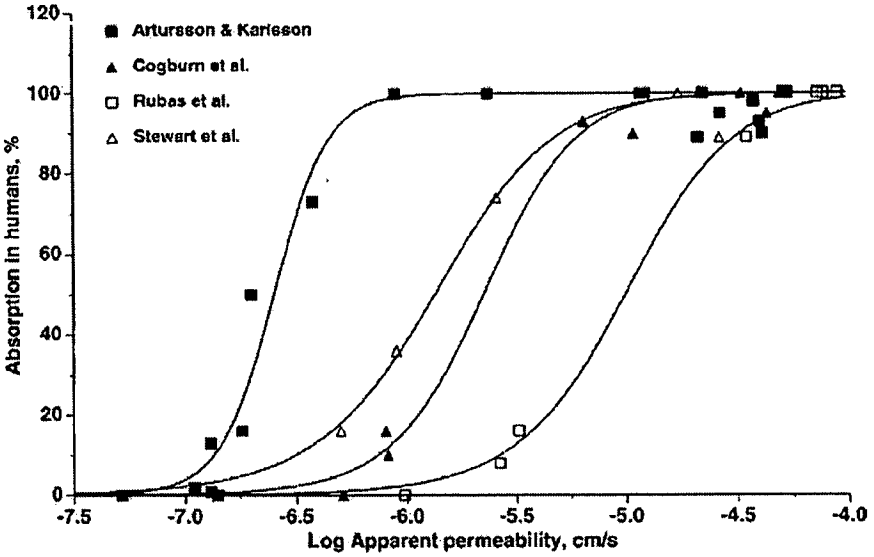

Fig. 11. Fraction absorbed (FA) in humans as a function of Caco-2 permeation data from different laboratories. The fitted lines represent the equation $FA = (0-100)/(1+(\log P_{app}/a)^b)+100$, where $a = \log P_{app}$ at FA = 50%. Reproduced from Artursson et al. (2001) with permission from Elsevier.

In a commentary, Artursson and Borchardt (1997) list several technical improvements that are required for cell culture monolayers to become an integral part of drug screening. These include miniaturisation of the cell culture apparatus; automation of the transport experiments; adaptation of the assays to handle poorly soluble compounds and complex formulations; and connecting them to effective and sensitive analytical detection apparatus. In addition, the authors stress the importance of developing standardised methods for quantification, analysis, storage and retrieval of the data accumulated in the experiments.

3.5. Artificial membranes

Kansy et al. (1998) have proposed the use of a parallel artificial membrane permeation assay (PAMPA) as a high-throughput alternative to Caco-2 monolayers for the prediction of passive drug absorption. In the PAMPA approach, the aqueous donor and acceptor compartments (96-well microtiter plate) are separated by a hydrophobic permeability filter (96-well microtiter filterplate). The filter is impregnated with an organic solution of lipid, which forms bilayer structures in the filter pores. The solute concentrations in the acceptor well are determined in parallel by UV spectrophotometry using a 96-well microplate photometer. The authors found that the PAMPA flux could be successfully used to classify compounds of low, intermediate and high human intestinal absorption.

Avdeef et al. (2001) automated the PAMPA approach further into a filter-immobilised artificial membrane (filter-IAM) assay. In this approach both acceptor and donor well concentrations were analysed at $t = 0$ and t = permeation time with UV spectrophotometry to determine membrane retention of the drugs.

In a study by Zhu et al. (2002), an artificial membrane permeability (AMP) assay was constructed on a hydrophilic membrane support, thereby shortening the permeation times to 2 h. The artificial membrane permeabilities were compared with human intestinal absorption as well as with both theoretical and experimental models thereof. The comparison with AMP and human intestinal absorption for a set of 93 commercial drugs (Fig. 12a) suggested that the artificial membrane system could be used in classifying drugs into different absorption categories. Correlating $\log P$ and $\log D_{7.4}$ with human intestinal absorption for the same set of drugs resulted in a much more scattered plot than for AMP (Fig. 12b). Even if the correlation between the AMP and the Caco-2 monolayer assays was only reasonable ($n = 49$, $r^2 = 0.67$), the systems were found to be highly comparable in absorption classification.

The structure and repeatability of the filter-immobilised lipid–solvent membranes in the above-described assays have been questioned (Wohnsland and Faller, 2001). Indeed, electrochemical studies of such filter systems have shown a time-dependent thinning of the micromembranes to occur (Ikematsu et al., 1996). In the high-throughput assay proposed by Wohnsland and Faller (2001) the acceptor and donor compartments of the 96-well titer plate are separated by a liquid hexadecane layer immobilised by a filter of 9–10 μm thickness. The liquid alkane was chosen for its ability to model the essential properties for biological permeation, i.e. lipophilicity and hydrogen bonding potential. The concentrations of the acceptor compartments were analysed with UV detection after a 5 h permeation time. Human gastrointestinal absorption was significantly better predicted by the liquid membrane permeation than by octanol–water distribution coefficients. The permeation assay was also used to construct pH-permeation profiles of

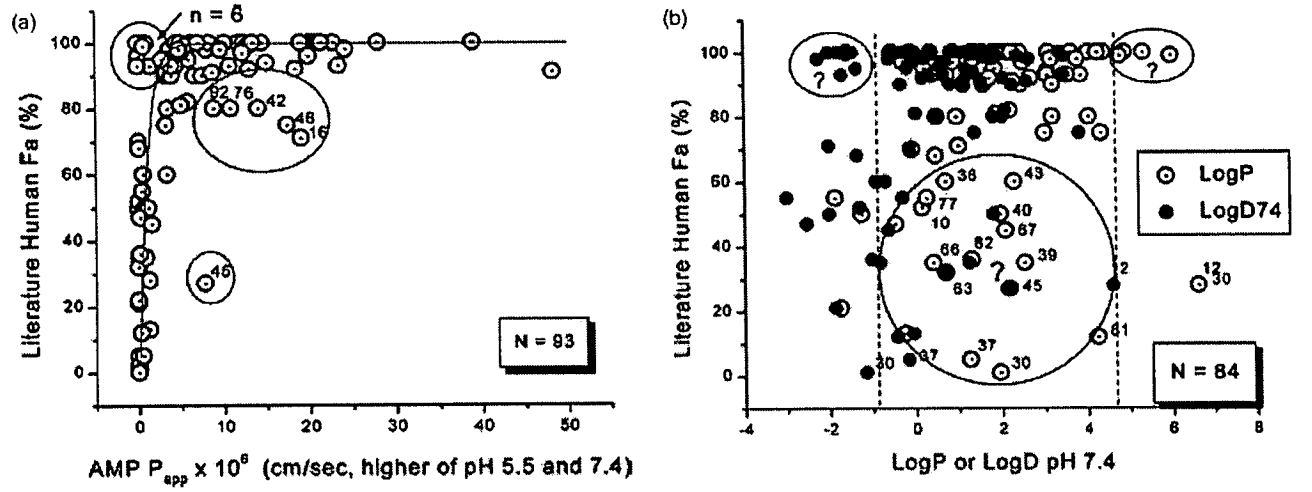

Fig. 12. (a) Artificial membrane permeation (AMP P_{app}) vs. fraction absorbed in humans for 93 commercial drugs. (b) log P and log $D_{7.4}$ vs. fraction absorbed in humans for 86 commercial drugs. Circled compound groups are outliers. Reproduced from Zhu et al. (2002) with permission from Elsevier.

the ionisable compounds, which could in turn be employed to calculate alkane–water partition coefficients and account for the unstirred water layer effect in the permeation coefficients for the highly permeable solutes.

In conclusion, the filter-immobilised membrane approach provides certain benefits over the Caco-system in terms of access to a wider pH-range, ease of automation, high throughput and lower cost. Although the lack of paracellular and active transport mechanisms found in Caco-2 monolayers may be considered a drawback, this, on the other hand, enables studies of exclusively passive transcellular diffusion without intervening processes. Further studies of immobilised membrane permeation are required before definite conclusions can be drawn concerning its applicability in drug screening.

4. Ion partition—a task for electrochemistry?

4.1. Principles

Partition and permeation of ionic drugs has received relatively little attention. In 1992, we presented the use of liquid–liquid electrochemistry as a fast, convenient and accurate means to determine ionic partition coefficients (Kontturi and Murtomäki, 1992) (for more detailed information on liquid–liquid electrochemistry, see for instance Girault and Schiffrin, 1989; Senda et al., 1991; Vanýsek, 1995). The basic equation is the Nernst equation that relates the activity of a charged species i in water and oil phase to the potential difference across a phase boundary, $\Delta_o^w\phi$:

$$\Delta_o^w\phi = \Delta_o^w\phi_i^0 + \frac{RT}{z_iF}\ln\frac{a_i^o}{a_i^w} \tag{4.1}$$

z_i is the charge number of i and $\Delta_o^w\phi_i^0$ its standard transfer potential between the phases, which is related to the standard Gibbs free energy of transfer, $\Delta_w^o G_i^{0,I}$, and therefore to the partition coefficient:

$$\log P_i^I = -\frac{\Delta_w^o G_i^{0,I}}{2.303\,RT} = -\frac{zF\Delta_o^w\phi_i^0}{2.303\,RT} \tag{4.2}$$

Since it is not possible to experimentally determine ionic free energies of transfer, or any thermodynamic ionic quantities, one commonly uses the so-called TATB assumption, which states that due to similar structure and electrostatics, the standard free energies of transfer of the tetraphenylarsonium cation ($TPAs^+$) and the tetraphenylborate anion (TPB^-) are equal (Parker, 1969):

$$\Delta_o^w G^0_{TPAs^+} = \Delta_o^w G^0_{TPB^-} = \tfrac{1}{2}\Delta_o^w G^0_{TPAsTPB} \tag{4.3}$$

Based on the TATB assumption, a Galvani potential scale can be established, and a database of standard transfer potentials of electrolytes is available on the internet (http://dcwww.epfl.ch/cgi-bin/LE/DB/InterrDB.pl). A polarisable liquid–liquid interface is formed by placing an organic solvent containing a hydrophobic electrolyte in contact with an aqueous solution of a hydrophilic electrolyte. The solvents should be only sparingly mutually soluble and the electrolytes hydrophobic and hydrophilic enough so that a potential region, where no ion transfer occurs, is obtained (Kontturi and Murtomäki, 1992). As *n*-octanol does not dissolve electrolytes, other solvents must be used; the most common choices are 1,2-dichloroethane (DCE), nitrobenzene and *o*-nitrophenyl octyl ether. The choice of solvents will be discussed later on.

Upon addition of the drug of interest into the aqueous phase, the potential difference across the interface is scanned. The drug is now transferred from the aqueous to the organic phase, which is seen as electric current. During the reverse scan, the drug returns back to the aqueous phase. A voltammogram is obtained (Fig. 13) from which the half wave potential, $\Delta_o^w\phi^0_{1/2}$, is determined approximately as

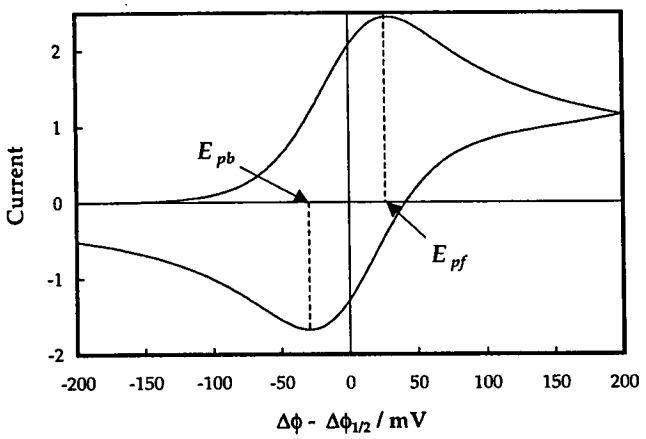

Fig. 13. A cyclic voltammogram and the half wave potential.

the midpoint of the forward (E_{pf}) and backward (E_{pb}) scan peak potentials. The standard transfer potential of ion i is then obtained as (Samec et al., 1996):

$$\Delta_o^w\phi_i^0 = \Delta_o^w\phi_{1/2} - \frac{RT}{z_iF}\ln\frac{\gamma_i^o}{\gamma_i^w} - \frac{RT}{2z_iF}\ln\frac{D_i^w}{D_i^o} - \frac{RT}{z_iF} \times \ln\left[1 + K_a\alpha^o c^o(\gamma^o)^2\left(\frac{D_{ip}}{D_i^o}\right)^{1/2}\right] \quad (4.4)$$

where γ_i and D_i are the activity and diffusion coefficient of i in the aqueous or oil phase. The expression within the brackets refers to ion association between the transferring ion and the counter ion in the oil phase: K_a is the ion pair association constant, α^o is the degree of association of the oil phase base electrolyte, c^o and γ^o are its concentration and activity coefficient, and D_{ip} is the diffusion coefficient of the ion pair in the oil phase. Association in the oil phase is often found to be negligible so that the last term can be ignored. The activity coefficient and diffusion coefficient terms are also rather small (~5 mV) and can usually be ignored.

A typical experimental setup in a liquid–liquid electrochemical measurement is:

Scheme 1. Experimental setup for liquid-liquid electrochemistry.				
Reference electrode	*Reference phase* w'	*Organic phase* o	*Aqueous phase* w	*Reference electrode*
Ag|AgCl	X^+ Cl^-	X^+ Y^-	M^+ Cl^- $drug^+$	AgCl | Ag

where XCl, XY and MCl are the base electrolytes in the reference, organic and aqueous phases, respectively. The double line between the aqueous and the organic phases indicates the polarisable interface under study. Due to the lack of suitable reference electrodes for the organic phase, a separate reference phase (w') is often used. The Galvani potential across the polarisable interface, $\Delta_o^w\phi$, is obtained subtracting the potential of the reference phase from the measured cell potential, E, as described in the literature (Girault and Schiffrin, 1989).

4.2. Ionic versus neutral partition coefficients

In the electrochemical method, the partition coefficient of an ionised species is measured, and the question arises how it is related to the partition coefficient of an electrically neutral drug. The free energy of an ion consists of an electrostatic part and a neutral part; the former part is naturally zero for a non-charged molecule. Assuming that charging a molecule by, for instance, protonation, leaves the molecular structure practically intact, subtraction of the electrostatic part, $\Delta_w^o G_{i,es}^0$, from the ionic free energy of transfer yields the free energy of transfer of the neutral molecule, $\Delta_w^o G_i^{0,N}$:

$$\Delta_w^o G_i^{0,N} = \Delta_w^o G_i^{0,I} - \Delta_w^o G_{i,es}^0 \quad (4.5)$$

One approach to estimate the contribution of electrostatics is to use theoretical solvation models, such as the ones based on the Born equation, presented in (2.7) and (2.8). As opposed to these models, where the electrostatic term of the transfer energy describes long-range ion–solvent interactions, Osakai et al. (Osakai and Ebina, 1998; Osakai et al., 1997) proposed a semi-empirical theory, where it is governed by specific short-range interactions such as donor–acceptor effects or hydrogen bonds. It was concluded that the electrostatic part of the Gibbs free energy of transfer could be described by a quadratic function of the surface electric field strength E:

$$\frac{\Delta_w^o G_{i,es}^0}{4\pi r_i^2} = \Delta A' + \Delta B' E + \Delta C' E^2 \quad (4.6)$$

where

$$E = \frac{z_i e}{4\pi\varepsilon_0 r_i^2} \quad (4.7)$$

The coefficients of Eq. (4.6) were determined by regression analysis of the $\Delta_w^o G_{i,es}^0$ values, which were calculated from Eq. (4.5) using experimental Gibbs energies of transfer and the Uhlig Eq. (4.8) for the cavity formation energy. As ionic radii needed in Eqs. (4.6) and (4.7) depend on the extent of hydration, different data sets were used for nonhydrated and hydrated cations and anions as well as polyanions.

$$\Delta_w^o G_i^{0,N} = -4\pi N_A r_i^2 \gamma \quad (4.8)$$

where γ is the interfacial tension between the aqueous and the organic phase.

The second order polynomial fits of $\Delta_w^o G_{i,es}^0$ as a function of E yielded excellent correlation coefficients between 0.931 and 0.999. Osakai and Ebina (1998) concluded that ignoring long-range electrostatic ion–solvent interactions may

be justifiable if one realises that the Gibbs free energy of transfer from one phase to another is the difference in the solvation energies between the two phases. It is thus probable that the electrostatic solvation energies in the respective phases are for the most part cancelled out in $\Delta_w^o G_{i,es}^0$, whereas short-range interactions remain. The fits presented by Osakai et al. are, of course, only valid for transfer between the solvents used in their study, namely water and nitrobenzene. For any other solvents, new fits have to be carried out, which makes the approach a bit tedious unless data is already available.

In our previous work (Kontturi and Murtomäki, 1992), we studied protonated drugs, DH^+, and calculated the partition coefficient of the neutral drug by subtracting the contribution of the proton. A slightly corrected analysis based on the complete thermodynamic cycle was presented recently (Murtomäki and Kontturi, 2002). Conclusively, the Gibbs free energy of transfer of the neutral drug can be written as:

$$\Delta_w^o G_D^0 = \Delta_w^o G_{DH^+}^0 - \Delta_w^o G_{H^+}^0 - 2.303 \times RT \times (pK_a^w - pK_a^o) \quad (4.9)$$

where the last correction term includes the pK_a values of the drug in water and oil; values for the free energy of transfer of the proton, $\Delta_w^o G_{H^+}^0$, are available in literature (http://dcwww.epfl.ch/cgi-bin/LE/DB/InterrDB.pl).

4.3. Potential–pH diagrams

Two co-operating research groups in Lausanne combined liquid–liquid electrochemistry with conventional bulk partition methods and constructed complete potential–pH diagrams at liquid–liquid interfaces for a number of ionisable drugs (Reymond et al., 1996a, 1999a; Gobry et al., 2000). These diagrams, which resemble the ones developed by Pourbaix to study corrosion of metals, give the complete picture of the effect of both the pH and an interfacial potential difference on drug partition.

The diagram is constructed on the basis of the thermodynamic cycle of the drug in a biphasic system. All of the species appearing in the cycle are bound together by three different types of equations, which are used to define the boundary lines between the predominance of each species in their respective phases. These equations are: the Nernst Eq. (4.1), which describes the partition of an ionic species between the organic and aqueous phase; Eq. (2.2), which defines the partition coefficient of a neutral species and its relation to the Gibbs energy of transfer; and equations which describe acid–base equilibria, such as the Henderson–Hasselbalch equation.

We have recently studied a series of aminoacridine derivatives with varying lipophilicity (Malkia et al., 2003). The half wave potentials in the water–nitrophenyl octyl ether system were measured with cyclic voltammetry as a function of pH of the aqueous phase. As an example, the potential–pH diagram of the topical antiseptic agent aminacrine (9-aminoacridine) is presented in Fig. 14. The pK_a of aminacrine is 9.99, thus below pH 10 its dominant form in water is protonated, and above pH 10 electrically neutral.

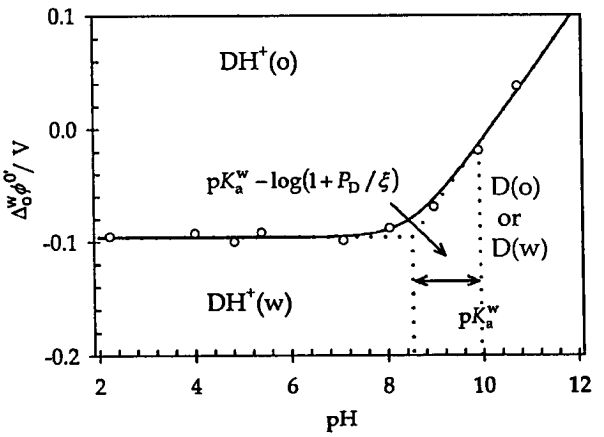

Fig. 14. Ion partition diagram of aminacrine showing the variation in the formal transfer potential with aqueous pH. The circles indicate experimental values, and the solid line represents the fitted equiconcentration lines between the dominant forms of the drug D.

At low pH, the protonated form DH^+ is in equilibrium between the phases, and the horizontal line represents their equiconcentration in the two phases. At high pH, the neutral form D is in equilibrium between the phases, but as the partition of the neutral species is independent of potential and pH, only the neutral species in one of the phases can appear in the diagram. Typically, the phase for which the compound expresses the higher affinity is chosen. The rising line 60 mV/pH unit corresponds to the proton transfer across the phase boundary:

$$D(o) + H^+(w) \leftrightarrow DH^+(o)$$

Similar assisted proton transfer by the anti-ischemic drug trimetazidine (Reymond et al., 1999b), the antihistamine cetirizine (Bouchard et al., 2001b) and piroxicam (Reymond et al., 1996b) has been reported in literature.

The pH-potential diagram can be used to measure the $\log P$ of the neutral species, as indicated in Fig. 14. The cross point of the extrapolated horizontal and rising lines differs from the aqueous pK_a^w value by the quantity $\log(1 + P_D/\xi)$ where $\xi = (D^w/D^o)^{1/2}$, the square root of the diffusion coefficient ratio in the two phases. For aminacrine, $\log(P_{D,NPOE}) = 2.37$ as measured from Fig. 14, while the calculated value from the Born model gives 2.56 (Malkia et al., 2003). The measured value in the water–octanol system is $\log(P_{D,oct}) = 2.74$ (Drayton, 1990).

Recently (Gobry et al., 2001), potential–pH diagrams were generalized to apply to an arbitrary phase volume ratio, $r = V^o/V^w$, using rather than equiconcentration lines, lines with an equal number of moles in the adjacent phases. For very lipophilic solutes the ratio r should be large, and for very hydrophilic solutes small. This way, the applicability of voltammetry can be expanded significantly. The Nernst

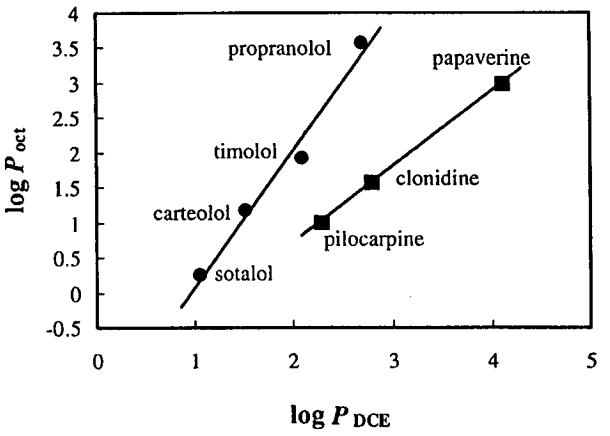

Fig. 15. The relation of $\log P_{octanol}$ and $\log P_{DCE}$. Data from Kontturi and Murtomäki (1992).

Eq. (4.1) also implies that the interfacial potential difference can be adjusted by adding salt with a common ion into the water and oil phase. The Lausanne groups (Bouchard et al., 2001a) demonstrated that the apparent increased partition of ionised drugs due to addition of lipophilic salt is not due to the formation of lipophilic ion-pairs, but the shift of the Galvani potential difference caused by the added electrolytes. The electrochemical pH–potential approach was also found to be a useful tool to study the partition behaviour of zwitterionic drugs (Bouchard et al., 2002; see Section 2.2.3).

4.4. Solvent problem

In bulk partition systems, *n*-octanol has the status of a standard. Unfortunately, electrochemistry is very troublesome in *n*-octanol, as it does not dissolve electrolytes and thus its conductivity is practically zero. The only report known to us is by Gulaboski et al. (2002) who attached a decamethyl ferrocene (DmFc) containg droplet of *n*-octanol on the graphite electrode and immersed it in an aqueous solution. Upon oxidation of DmFc on graphite, anions were transferred into *n*-octanol at the graphite-oil–water three-phase junction to maintain electroneutrality. In the electrochemical literature, there are signs of this approach becoming more common.

In our previous work (Kontturi and Murtomäki, 1992), the partition coefficients obtained at the water-1,2-dichloroethane interface were plotted against the water–*n*-octanol ones (see Fig. 15). It appeared that the drugs fell in two categories, depending on their hydrogen bonding ability. Molecules able to form hydrogen bonds, viz. β-blockers in Fig. 15, fell on their own line, while the three others without hydrogen bonding capacity formed another straight line. Taking this factor into account, the order of lipophilicity expressed as $\log P_{octanol}$ was retained in DCE for this set of drugs.

The Lausanne groups (Caron et al., 1999) investigated the effect of solvent properties on the partition of a series of β-adrenergic receptor agents (β-blockers) in both their neutral and ionised forms. The obtained $\Delta \log P$ values for the different solvents were found to mainly reflect differences in hydrogen bonding. The majority of the neutral β-blockers expressed poor hydrogen bond donor character in 1,2-dichloroethane, which was attributed to the formation of an internal hydrogen bond in these compounds. In both dibutyl ether (DBE) and *n*-octanol, internal hydrogen bonding was not favoured among the neutral species of the drugs, whereas cationic β-blockers bearing an *ortho*-O atom were observed to form internal H-bonds also in the octanol–water system.

The difference between partition coefficients of neutral and charged species in each solvent, diff($\log P^{N-I}$), was introduced to describe the effects of charge localisation on ion partition. Thus, the significantly larger diff-values obtained in the dichloroethane–water system compared to the octanol–water system, were suggested to reflect the localised charge of these monocations, which causes the ions to retain more water molecules when transferring into octanol than to DCE. This, on the other hand, indicates the greater water solubilisation and hydrogen bonding capacity of octanol compared to DCE (Caron et al., 1999). In another study (Steyaert et al., 1997), a solvatochromic analysis of a set of 44 solutes was carried out, and it was suggested that DCE could actually be a better solvent than *n*-octanol to predict biodistribution of solutes.

4.5. Biomimetic liquid–liquid interfaces

In our recent work (Liljeroth et al., 2000; Mälkiä et al., 2001a,b; Malkia et al., 2003), we introduced a novel approach for using liquid–liquid electrochemistry to study membrane activity of ionised drugs. We employed the Langmuir–Blodgett technique (Petty, 1996; Petty and Barlow, 1990) to deposit a lipid monolayer at the interface between an aqueous solution and a NPOE–PVC gel, thus improving the biomimetic properties of the conventional liquid–liquid interface. Although the presence of a monolayer was not found to inhibit ion transfer, a distinct effect could be seen in the apparent standard rate constant upon introducing the monolayer. Furthermore, combining the experimental results with a theoretical model, it was possible to estimate the strength and site of ion adsorption on the monolayer. Differences in adsorption behaviour were found even between structurally similar drugs (Malkia et al., 2003), which was attributed to small variabilities in their hydrogen bonding ability.

4.6. Conclusions

Liquid–liquid electrochemistry presents an important advantage compared to conventional bulk experiments in the possibility to study the effect of a potential difference on ion transfer, thereby mimicking the situation in biological systems. In addition, liquid–liquid electrochemistry can be

employed to investigate the effect of charge on lipophilicity and to determine the hydrogen bonding characteristics of the compounds under study. An additional benefit of the methodology is the ability to distinguish between the transfer of differently charged species of the same compound (Reymond et al., 1996a). Furthermore, it is possible to modify the liquid–liquid interface to resemble one half of a lipid bilayer and conduct transport studies through this model membrane.

An obvious disadvantage is that electrochemistry is not a very widely known discipline and, therefore, the threshold to take it into use might be difficult to overcome. A practical problem is the need for reasonable conductivity in both phases which requires the addition of supporting electrolytes. The effect of these supporting electrolytes needs to be subtracted in the analysis. Furthermore, electric current is an integral value over the contributions of all the transferring species, i.e. there is also a selectivity problem to be taken care of. For screening purposes, the method should be expandable for the parallel measurement of thousands of candidates, which may require rather a complicated instrumentation.

5. Computational approaches

In addition to the experimental approaches discussed above, an increasing number of studies focus on predicting membrane permeation of drugs from calculated molecular properties. The aim of the computational approaches is to save resources by enabling virtual screening of drug candidates and the identification of drug candidates with possible absorption problems at an early stage of drug development. In addition to saving time and effort, this can also help reduce the amount of animals used in testing. The main factor enabling the rapid growth of computational approaches has been the development in computer resources and calculation algorithms.

The basis of computational prediction of drug partition or permeation lies in quantitative structure–property relationships (QSPR). The concept of QSPR is to transform the chemical intuition and experience used in the search for compounds with desired properties into a mathematically quantified and computerised form. In other words, QSPR methods for predicting biological permeation seek to transform the chemical structure of a compound into a set of numerical descriptors of the properties relevant to its permeation, and to establish the quantitative relationship between these descriptors and the permeation of the compound. Once a correlation between structure and property is found, this knowledge can be used to screen other compounds, including ones not yet synthesised, on the computer in order to select structures with the desired properties for further trials (Karelson, 2000).

To obtain a significant correlation, it is essential to use appropriate data in building and testing the model. As discussed by Egan and Lauri (2002), many existing models are built with data that suffers from one or several of the following problems: too small sample size; bias of data towards highly permeable compounds; use of data on actively transported compounds when modelling passive transport; use of data for which other factors such as solubility, and not passive transmembrane diffusion, is the absorption rate-limiting step; and a general lack of data quality, meaning poorly repeatable experimental results and large standard errors. Furthermore, as discussed in Section 3.4 in relation with Caco-2 cell cultures: owing to variable experimental conditions, procedures and materials, some interlaboratory variability will always be present in experimental data. This should be kept in mind when building QSPR models, particularly when compiling datasets from widely different sources.

Furthermore, when constructing the model, it is important that appropriate descriptors are employed, whether theoretical or experimental (Livingstone, 2000). For drug design purposes, it is desirable that the descriptors reflect simple molecular properties and provide easily interpreted information. When a compound is flagged by a computational screen as likely to exhibit poor intestinal absorption, this will save the time and effort of synthesising and experimentally examining that compound. But in order to provide feedback for the drug design chemists, the important question to address is "what structural properties caused the compound to have poor intestinal absorption?"

Further attention needs to be given to the obtained model: a low standard error, a restricted number of descriptors, compatibility with common scientific knowledge, and the ability to correctly predict properties of compounds that were not employed in the construction of the model, are some of the qualities of a proper QSPR model (Nirmalakhandan and Speece, 1988). Several approaches exist to ensure model stability and predictive ability, including cross-validation and variable selection schemes (Wold, 1979; Norinder et al., 1997).

The first part of the section reviews some of the approaches to calculate the octanol–water partition coefficient (a thorough review can be found by Leo, 1993), whereas the second part looks into models of biological permeation.

5.1. Calculating log P from molecular structures

5.1.1. Background and development

The oil–water partition coefficient was introduced by Hansch and co-workers in the 1960s (Hansch et al., 1963; Hansch and Fujita, 1964; Fujita et al., 1964) and it is still the most popular descriptor linking drug structure to biological permeation. In relation to the partition coefficient, Hansch et al. (1963) defined the π-parameter, which allows for quantitative estimates of partition coefficients on basis of well-characterised "parent" compounds. The π_x-parameter represents the difference in $\log P$ between an x-substituted and an unsubstituted compound:

$$\log P_x = \log P_H + \pi_x \quad (5.1)$$

The fragment method was introduced by Rekker and co-workers (Nys and Rekker, 1973). Instead of using parent compounds, they divided the compounds into simple, additive fragments as shown in Eq. (5.2). The fragment contributions were determined on basis of statistical analysis of a large library of experimental log P values.

$$\log P = \sum a_n f_n + \sum b_m F_m \quad (5.2)$$

where a_n is the number of occurrences of fragment f of type n, and b_m is the number of occurrences of correction factor F of type m. The major corrections are related to whether a polar fragment is connected to an aliphatic or aromatic carbon atom, and to the effect of two polar fragments situated at close proximity.

A more general approach to predict the oil–water partition coefficient is the solvatochromic methodology (Taft et al., 1985a; Kamlet et al., 1983), also called the linear solvation energy relationship approach, which states that solubility can be related to solute–solvent interactions through the linear combinations of three types of terms: the cavity formation term V, the solute polarity/polarisability term π^* and the terms indicating the hydrogen bond acceptor (β_H) and donor (α_H) strength of the solute.

$$\log P = aV + b\pi^* + c\beta_H + d\alpha_H + e \quad (5.3)$$

The solvatochromic approach has proved successful in correlations and predictions of various physicochemical properties that involve solute–solvent interactions (Kamlet et al., 1986; Taft et al., 1985b) and the parameters contain physical meaning that can be directly related to the molecular structure. The inconvenience of the method is the need to assign fragment values to all the parameters and account for intramolecular fragment interactions, even if tabulated parameter values and rules to calculate them exist (Kamlet et al., 1983, 1988).

The above methods generally perform well for small, rigid molecules, but for larger and flexible compounds intramolecular interactions such as shielding and folding are often not properly accounted for. The concept of molecular lipophilicity potential (MLP) was first introduced in the late 1980s (Audry et al., 1986; Furet et al., 1988). The MLP is a structure–property descriptor that visualises the lipophilic properties of the molecule on its three-dimensional (3D) surface. The most commonly used MLP methodology today is the one developed by Gaillard et al. (1994). In their approach, the MLP is generated on the solvent-accessible surface (SAS) of the molecule and calculated on basis of a fragmental description of lipophilicity and a distance function:

$$\mathrm{MLP}_k = \sum_{i=1}^{N} f_i \mathrm{fct}(d_{ik}) \quad (5.4)$$

where k is the index of a given point in space, i the index of a molecular fragment, N the total number of fragments in the molecule, f_i the lipophilic constant of fragment i, fct is a distance function and d_{ik} is the distance between fragment i and point k.

The MLP calculation begins with the generation of the three-dimensional structure of the molecule. Selection of several low energy conformations for the calculations can thus shed light on the relationship between conformation and lipophilicity. Such information may be particularly useful when modelling ligand–receptor interactions. To this end, the MLP has been successfully implemented in Comparative Molecular Field Analysis (CoMFA) (Gaillard et al., 1996; Testa et al., 1996). A back-calculation to the one-dimensional log P value is also possible. After obtaining the MLP value at each point on the SAS of a molecule, a numerical integration over this space is performed. The integration yields two quantities: the total of positive MLP values, representing the lipophilic part of the molecule; and the total of negative MPL values, standing for the polar part of the molecule. These quantities are then used as independent parameters in multilinear regression for a set of compounds with known experimental log P values in order to establish the relationship between MLP and log P. This training set equation can subsequently be employed for compounds with unknown partition coefficients.

5.1.2. log P programs

The first, and still most popular commercial computer program to calculate octanol–water partition coefficients from molecular structure is Clog P, developed by the Pomona MedChem Project (Chou and Jurs, 1979; Leo and Hoekman, 2000; available from Daylight Corp., CA, USA and BioByte Corp., Claremont, CA, USA). The method follows the Rekker Eq. (5.2), but the approach used to derive the constants is different. Whereas Rekker used a 'reductionist' approach and derived the fragment values from statistical treatment of log P data without really specifying what constitutes a fragment, Clog P is based on a 'constructionist' approach. The fragments were first defined and then evaluated from as simple structures as possible, such as hydrogen gas, methane and ethane, to minimise obscuring interactions. In cases where the use of these fragment constants was incapable of yielding the measured log P value, the difference was defined in terms of universal correction factors. Many improvements have been made to Clog P since its introduction, the most significant being the ability to estimate an unknown polar fragment value which has not appeared in a solute for which a measured log P(oct) exists.

Many computerised algorithms for calculating partition coefficients have been developed since the introduction of Clog P, most of which are discussed in the recent reviews by Carrupt et al. (1997) and Mannhold and van de Waterbeemd (2001). The methodologies can roughly be divided into (i) fragmental approaches such as Clog P, log K_{ow} (Meylan and Howard, 1995; available from Syracuse Research Corporation, Syracuse, NY, USA), ACD/log P DB (Spessard,

1998; available from Advanced Chemistry Development, Toronto, Canada) and Klog*P* (Klopman et al., 1994); (ii) atom contribution approaches, such as Alog*P*98 (Ghose et al., 1998; available from Accelrys Ltd., Cambridge, UK); (iii) topological approaches such as Mlog*P* (Moriguchi et al., 1992), Vlog*P* (Gombar and Enslein, 1996; available from Accelrys Ltd.); and (iv) a neural network study (Huuskonen et al., 2000).

An essential prerequisite for the use of computerised log*P* calculators is the existence of a simple yet unambiguous way to feed the structural information into the programs. The SMILES notation (Weininger, 1988) is accepted by many log*P* programs. SMILES strings are easily written directly from knowledge of chemical structure. In addition, certain chemical structure drawing programs are able to create SMILES notations on basis of drawn structures. Another popular input format is the MDL mol-file, described more thoroughly by Dalby et al. (1992) and used by a variety of other computational applications in chemistry.

5.2. Computational approaches to predict biological permeation

Although the octanol–water partition coefficient has been found to correlate fairly well with the biological permeation of many drug compounds (Palm et al., 1996; Krämer, 1999) several studies also report on its failure (Young et al., 1988; Conradi et al., 1991; Palm et al., 1997). Good correlations are generally obtained for homologous series of solutes, but when comparing structurally diverse compounds, variable contributions of hydrogen bonding and electrostatics disrupt the trend (Artursson and Karlsson, 1991; Goodwin et al., 2001). In an attempt to improve correlations, several physicochemical descriptors have been incorporated into one model using multiple linear regression (MLR) analysis (Sugawara et al., 1998). Lobell et al. (2003) recently reported on a 34-descriptor model for the prediction of logBB, which compared favourably with other corresponding models (n_{train} = 48, r^2_{train} = 0.84, q^2_{train} = 0.79, s_{train} = 0.19, n_{test} = 17, r^2_{test} = 0.68; where n = number of compounds, r^2 = correlation coefficient, q^2 = cross-validated correlation coefficient, s = standard deviation). However, caution needs to be taken in the choice of variables, since correlations often improve when the number of descriptors grows. Furthermore, many physicochemical properties are interrelated, which makes them unsuitable for multiple linear regression analysis (Artursson et al., 2001).

One approach to circumvent the problem of collinearity of the descriptors has been the use of partial least-squares methods (PLS). Luco (1999) employed the PLS approach to model the blood–brain concentration ratio of 58 drugs using topological and constitutional descriptors calculated from the molecular structures of the compounds. A three-component model comprising 18 descriptors was able to successfully describe the blood–brain concentration ratio of the training set (n = 58, r^2 = 0.85, q^2 = 0.75, s = 0.318). The most important descriptors reflected molecular polarity, size and hydrogen bonding potential.

Another approach to build multidescriptor models is the use of neural networks. Wessel et al. (1998) employed a neural network routine in combination with a genetic algorithm to find the best descriptor subsets and subsequently to build a nonlinear 6-descriptor model for the prediction of human intestinal absorption (n_{train} = 67, $RMSE_{train}$ = 9.4% HIA; n_{cv} = 9, $RMSE_{cv}$ = 19.7% HIA; n_{test} = 10, $RMSE_{test}$ = 16.0% HIA). Although a functioning tool in model construction, the authors admitted that the neural network approach suffers from difficulties in result interpretation in that it is difficult to assess the individual contribution of each descriptor.

Computational studies have focused on developing improved descriptors of biological permeation. The approaches have emphasised variable things, such as accuracy of correlation with in vivo results, speed of calculation, low number of descriptors or to keep descriptors simple and informative in order to enable feedback to drug design. A brief review of the most common methods follows below. For each approach, a few representative example studies are discussed with the purpose of eliciting some aspects of the method in question. However, these should not be taken as a comprehensive coverage of all the studies carried out with that particular method. More detailed descriptions of computational studies on biological permeation can be found in the reviews by Norinder and Haeberlein (2002), Egan and Lauri (2002) and Clark and Grootenhuis (2003).

5.2.1. Univariate approaches

Several mnemonics for rapid and preliminary identification of drugs with permeation problems have been developed on basis of analysis of vast databases of druglike compounds. The "rule of 5" developed by Lipinski et al. (1997) is a popular atom count method for rapid and approximate identification of drugs with potential absorption problems. The rule states that if a compound satisfies any *two* of the following rules, it is likely to exhibit poor intestinal absorption: (1) MW > 500; (2) the number of hydrogen bond donors > 5 (O–H or N–H groups); (3) the number of hydrogen bond acceptors > 10 (any N or O atom, including donors); (4) CLOGP > 5.0 (or Mlog*P* (Moriguchi et al., 1992) > 4.15). The authors emphasised that the alert is primarily designed to weed out compounds with absorption and permeation problems at an early stage of drug development – compounds that pass the "rule of 5" without alert may still prove troublesome in later trials. A similar model proposes a three-dimensional box, composed of lipophilicity, hydrogen-bonding potential and size, to identify well-absorbed drugs (van de Waterbeemd, 2000).

A 2-rule model has been proposed for blood–brain partitioning by Norinder and Haeberlein (2002). It states that (1) if N + O (the sum of the number of nitrogen and oxygen atoms) in a molecule is less than or equal to five, the

molecule has a good chance of entering the brain; and (2) if $\log P - (N + O)$ is positive, then log BB is positive.

The main reasons for the approximate results obtained with univariate approaches is that they are unable to deal with interactions between the properties. Furthermore, conformational effects are unaccounted for when hydrogen bonding atoms are counted. However, due to their simple and rapid format, such methods can be effective in preliminary drug screening and their readily interpretable rules provide guidelines for future drug design (Lipinski et al., 1997).

5.2.2. Fragment count methods

5.2.2.1. The Abraham descriptors. The Abraham group has recently developed models of biological permeation with particular attention on the size and quality of their datasets. In 2001, they undertook an extensive study in which they evaluated the human intestinal absorption data of 241 drugs (Zhao et al., 2001). Reliable and diffusion rate-limited data was found for 169 compounds. A model was then constructed based on the general linear solvation energy equation:

$$\%\text{Abs} = c + eE + sS + aA + bB + vV \quad (5.5)$$

where E is the excess molar refraction, S the dipolarity/dipolarisability, A and B the hydrogen bond acidity and basicity, respectively, and V is the McGowan characteristic volume. The equation was initially applied using experimentally derived parameter values (Abraham et al., 1999, 1995, 1994; Abraham and McGowan, 1987) but recently, a fragment-based method was developed enabling calculation directly from structure (Platts et al., 1999, 2000; Abraham and Platts, 2001). The lower-case coefficients are obtained by multiple linear regression analysis. Two models were constructed on basis of training set data, and were subsequently employed to predict the absorption of test set compounds. The better model gave statistics of ($n = 38$, $r^2 = 0.83$, $q^2 = 0.75$, RMSE = 14) and ($n = 131$, RMSE = 14) for the training set and the test set, respectively. Step-wise regression was carried out to identify the most significant descriptors. Hydrogen bond acidity and basicity were found to dominate absorption, both with a negative impact, but also the volume-term was found to be a significant descriptor (positive impact). The effect of charge was investigated by inclusion of an additional parameter I in the equation, but a negligible effect was found.

In a subsequent publication (Zhao et al., 2002), the solvation-energy approach was refined. Instead of a linear relationship, the intestinal absorption was taken to depend on a linear combination of the descriptors through first order kinetics, which led to improved correlations. Removal of 20 compounds, which contained both an acid and a base group, further improved correlations. No explanation for the negative impact of these compounds on the predictability was presented. The majority of them were well-absorbed, while their charged nature at the measurement pH was not established in the study. The importance of identifying and removing dissolution rate-limited drugs from datasets when studying diffusion rate-limited absorption was emphasised.

In another study, the Abraham group (Platts et al., 2001) compiled log BB data and corresponding descriptor values for 157 compounds. After removal of nine outliers, and the inclusion of a carboxylic acid indicator, I_1, the following model was obtained (Fig. 16):

$$\log \text{BB} = 0.021 + 0.463\,E - 0.864\,S - 0.564\,A - 0.731\,B + 0.933\,V - 0.567\,I_1 \quad (5.6)$$

$$n = 148, \quad r^2 = 0.745, \quad q^2 = 0.711, \quad s = 0.343$$

The predictivity of the model was assessed by splitting the full set of compounds into training and test sets of variable size and composition. Subsequently, equations of the type of (5.6) were developed from the training sets to pre-

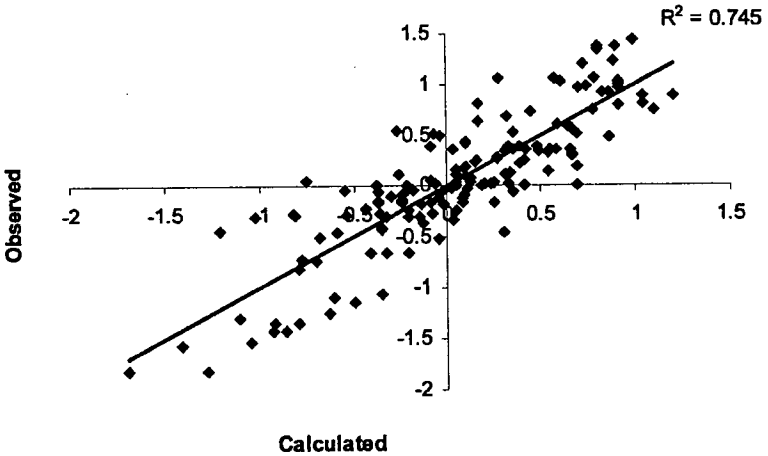

Fig. 16. Observed vs. calculated log BB using Eq. (5.6) for the complete set of compounds ($n = 148$). The corresponding statistics are given in the text and in Table 1, method 12. Reproduced from Platts et al. (2001) with permission from Elsevier.

dict the test sets. The soundness of the method was confirmed by that the statistics of the different test sets varied between $0.643 < r^2 < 0.775$ and $0.319 < s < 0.418$. Larger size was found to enhance brain uptake whereas polarity/polarisability, hydrogen bond acidity and basicity, and the presence of carboxylic acid groups had an inhibiting effect.

The approach of using linear solvation energy relationship descriptors has been successful in prediction of various physicochemical properties related to solute–solvent interactions (Kamlet et al., 1986; Taft et al., 1985b; Abraham et al., 1999). Furthermore, the Abraham descriptors contain physical meaning that can be directly related to the structure of the compounds. The initial problem of obtaining experimentally derived values for all the descriptors and ensure that intra-molecular interactions between the fragments are accounted for has been solved, which renders the method available for rapid screening. The use of linear regression schemes to adjust the model parameters, however, raises the question of descriptor interrelations.

5.2.2.2. The electrotopological state. One set of molecular structure descriptors to have gained popularity in prediction of biological permeation are the electrotopological state indices (E-state) (Kier and Hall, 1999). The E-state indices are numerical values, which contain information about the topological and electronic environment of each atom in a molecule. Several E-state formalisms have been developed. The atom level E-state index, $S(i)$, is calculated for each skeletal atom or hydride group i in a molecule as the sum of the intrinsic state of that atom, I_i, and the perturbations from all the other skeletal atoms/hydride groups in the molecule, ΔI_{ij}:

$$S(i) = I_i + \sum_j \Delta I_{ij} \qquad (j \neq i) \tag{5.7}$$

where the intrinsic state value for an atom is obtained from its valence state electronegativity and its local topology, and the perturbation term is calculated as the difference between the intrinsic state values of the atoms divided by their distance squared.

While the atom level E-state indices may be useful when comparing structurally similar compounds, that is, when atom-by-atom superposition is possible, they are not very feasible in themselves when studying structurally diverse compounds. For quantitative structure–property relationship of molecules with no similarly located atoms, the atom type E-state indices have proven more useful. The atom type E-state index is defined as the sum of the individual atom level E-state values for a particular atom type (such as –OH, =O or –NH-) in the molecule (Hall and Kier, 1995). In parallel with the atom level and atom type E-state indices, algorithms for calculating E-state indices for hydrogen atoms have been developed. Accordingly, the hydrogen atom type E-state index is defined as the sum of the individual atom level hydrogen E-state values for all atoms of a particular atom type (Rose et al., 2002) Hydrogen bond acceptor and donor E-state indices have furthermore been developed by summing the atom level hydrogen E-state values for all atom types classified as hydrogen bond donors/acceptors.

Norinder and Österberg (2001) investigated the use of electrotopological state indices in combination with calculated molecular refractivity and octanol–water partition coefficients for predicting human intestinal absorption, Caco-2 cell permeation, blood–brain partition and IAM chromatography data. Principal component analysis and partial least squares methodology were employed in building the models, and the importance of the variables was assessed with a leave-one-out approach. The E-state descriptors used in the models were Sum_N (the sum of all atom-level E-state indices of nitrogen atoms), Sum_O, Sum_H (the sum of all hydrogen E-state indices for hydrogen atoms attached to oxygen, nitrogen or sulphur atoms) and SHother (sum or all hydrogen E-state indices for remaining hydrogen atoms). The authors pointed out that more detailed atom type E-state indices led to models with degraded predictivity due to absence of these substructures from part of the compounds.

All models showed good statistics (r^2: 0.75–0.93, q^2: 0.70–0.89) and predictivity when used on test set compounds. Permeation/partition was favoured by positive contributions from the octanol–water partition coefficient as well as polarisability as described by SHother. The models contained negative contributions from the descriptors Sum_O, Sum_N and Sum_H indicating the effect of hydrogen bonding.

In a recent study, Rose et al. (2002) employed E-state, molecular connectivity and shape indices to model blood–brain partitioning of 106 compounds. The variables for the model were selected by eliminating intercorrelations and subsequently by ranking the remaining descriptors by statistical analysis. Three descriptors were selected for the final model: the hydrogen bond donor E-state index $HS^T(HBd)$, the aromatic hydrogen E-state index squared $[HS^T(arom)]^2$ and the second order difference valence molecular connectivity index squared $[d^2\chi^v]^2$. After some preliminary validation a final model was developed ($n = 102$, $r^2 = 0.66$, $q^2 = 0.62$, MAE = 0.38). On basis of the model, blood–brain partition was found to be higher for compounds with aromatic CH groups, less branching and fewer or weaker hydrogen bond donor groups. The model was also used to predict blood–brain partition of a large set of 20,039 drugs and druglike compounds. As no experimental data was available for these compounds, the predictivity of the model on external data was not established.

The use of electrotopological state indices holds potential for rapid screening of large virtual structure libraries, the model of Rose et al. (2002) was reported to compute 5000–6000 molecules per minute. However, due to the abundance of available E-state descriptors, care needs to be taken when selecting variables.

5.2.3. Polar surface area

The polar surface area (PSA) is commonly computed as the van der Waals surface area of all nitrogen and oxygen atoms, plus the area of the hydrogen atoms attached to these. van de Waterbeemd and Kansy (1992) were the first to correlate biological permeation with polar surface area. They found a strong correlation between brain uptake and the hydrophilic part of the van der Waals surface calculated for single drug conformations for a small dataset of six compounds ($n = 6$, $r^2 = 0.945$, $s = 0.294$). A poorer correlation was obtained with a larger set of 20 compounds ($n = 20$, $r^2 = 0.610$).

Palm et al. (1996) argued that as many molecules can adopt several low-energy conformations, the dynamic polar surface area (PSA_d) should be a more appropriate predictor. In the dynamic polar surface area approach, all three-dimensional conformations of the compounds are first constructed using molecular mechanics calculations. The dynamic surface area of a molecule is then obtained as the Boltzmann-weighted average of the van der Waal's surface areas calculated for all low-energy conformations of a compound. Excellent correlations were obtained between the dynamic polar surface areas of six β-adrenoreceptor antagonists and their permeation in the Caco-2 monolayer and rat ileum models. The permeation could also be reasonably well predicted by the calculated octanol–water distribution coefficients ($\log D_{oct,7.4}$) of the drugs, but unlike PSA_d, this descriptor failed to rank the permeation of the compounds in the correct order.

In a subsequent study, Palm et al. (1997) demonstrated that the dynamic polar surface area descriptor is also capable of predicting human intestinal absorption of structurally more diverse solutes. A strong sigmoidal relationship between PSA_d and fraction absorbed (FA) was observed for the twenty drugs under study ($n = 20$, $r^2 = 0.94$, RMSE = 9.2%). Drugs with a dynamic polar surface area ≤ 60 Å^2 were completely absorbed (FA > 90%) whereas drugs with a $PSA_d \geq 140$ Å^2 exhibited poor intestinal absorption (FA < 10%). A weaker sigmoidal correlation was observed between FA and the total number of hydrogen bonds ($r^2 = 0.87$, RMSE = 13.9%) and a poor result was obtained when correlating Clog P to FA ($r^2 = 0.34$, RMSE = 31.6%).

Clark (1999a) used the same 20-compound data set as Palm et al. (1997) and showed that the polar molecular surface areas calculated from a single conformation (PSA) were as successful in predicting intestinal absorption as the Boltzmann-averaged areas ($n = 20$, $r^2 = 0.94$, RMSE = 9.1%). A similar result was reached by Stenberg et al. (2001) for a set of 27 structurally diverse drugs. It was concluded that although the use of dynamic PSA may be more exact for large, flexible molecules, the computationally much faster single-conformation PSA suffices for rapid drug screening purposes.

The effect of varying the simulated solvation environment has also been investigated (Palm et al., 1998; Stenberg et al., 1999, 2001). The influence on PSA of the simulated solvent was small for relatively small and rigid solute molecules. For larger and more flexible compounds, the conformational searches in simulated water yielded more open conformations with larger PSA values than in vacuum. However, in most cases, the correlation between PSA and biological permeation was not weakened by the lack of solvent, and therefore it was postulated that for rapid screening, solvent-free simulations could be used (Stenberg et al., 2001).

A downside of the polar surface area descriptor is its inability to distinguish between nonpolar compounds or account for nonpolar atom groups, thereby failing to discriminate between molecules with identical polar surface area but different size and lipophilicity. Thus, the polar surface area will reflect the ability of the solutes to leave the hydrogen bonding environment provided by the aqueous phase and the polar head group region of the lipids, but not the affinity of the molecules for the membrane interior or size-related effects. Consequently, the PSA has been combined with other descriptors.

Stenberg et al. (1999) studied the correlation between Caco-2 monolayer permeation and surface area properties in oligopeptide derivatives. The dynamic polar surface area descriptor area was able to distinguish between compounds of variable hydrogen bonding ability, but compounds with similar hydrogen bonding characteristics and variable size or lipophilicity were poorly described. However, a linear combination of polar and nonpolar dynamic surface area yielded a strong sigmoidal relationship with Caco-2 monolayer permeation. Other descriptors that have successfully been used in combination with polar surface area to predict biological permeation include molar volume (van de Waterbeemd and Kansy, 1992), the octanol–water partition/distribution coefficient (Clark, 1999b; Egan et al., 2000; Winiwarter et al., 1998) and number of hydrogen bond donors (Winiwarter et al., 1998).

In another study by Stenberg et al. (2001), the polar surface area was reasonably correlated with intestinal absorption ($n = 21$, $r^2 = 0.81$), but poorer correlations were found for Caco-2 permeation ($n = 27$, $r^2 = 0.63$), as shown in Fig. 17a and b. The weaker correlations compared to those of Palm et al. (1997) were believed to result from the greater structural diversity of the data (peptide derivatives, highly lipophilic drugs). Combination with nonpolar surface area resulted in only slightly improved correlations. This led the authors to introduce a so-called partitioned total surface area (PTSA) model in which the total molecular surface area was fragmented into atom type areas. PLS and principal components analysis was employed to build a model from various surface area descriptors. A significant improvement in explanatory power was achieved with this model ($r^2 = 0.95$, Fig. 17c), whereas external predictivity was somewhat poorer. PSA remained the most important descriptor of the 9-descriptor model. The high interpretability of the PTSA approach was considered an additional benefit. Recently PTSA models were successfully employed in rapid construction of absorption profiles of drugs, taking into

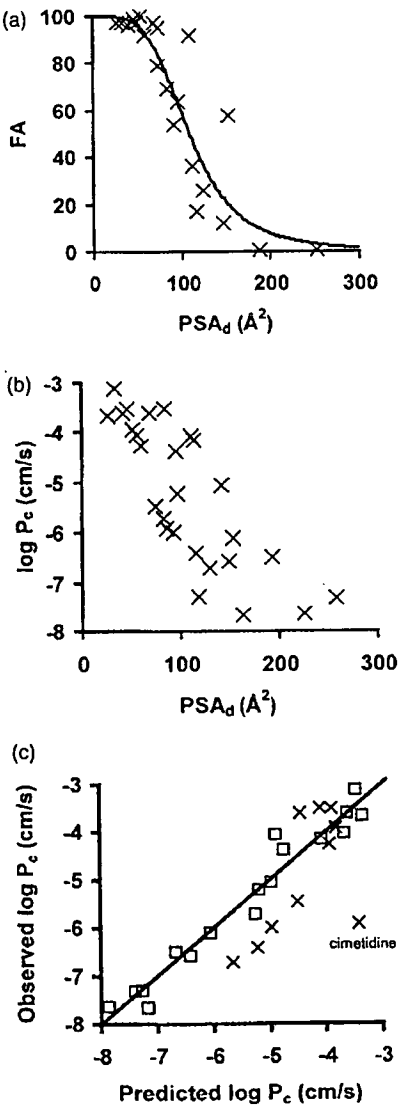

Fig. 17. Relationship between dynamic polar surface area (PSA_d) and (a) fraction absorbed after oral drug administration to humans; (b) Caco-2 cell monolayer permeability coefficient. (c) Observed Caco-2 cell monolayer permeabilities vs. calculated permeabilities from partitioned molecular surface properties (PSTA). Squares and crosses denote training and test set compounds, respectively. Statistics can be found in Table 1, method 6. All figures are from Stenberg et al. (2001), with permission from the American Chemical Society.

account both solubility and permeation (Bergström et al., 2003).

While it is obvious that hydrogen bonding is one of the properties that lie behind the polar surface area, a closer examination of this descriptor is desirable for two reasons: (i) to facilitate its interpretation so that it can be used as feedback in drug design; (ii) to investigate whether it is possible to calculate the PSA in a simplified and faster manner. Stenberg et al. (2001) undertook a study in which the PSA (single conformation) of 128 structurally diverse compounds was deconvoluted into various easily interpreted physicochemical properties using PLS methodology and principal components analysis. It was found that the number, rather than the strength of hydrogen bonding atoms constituted the main property behind PSA and that three descriptors, corresponding to the number of hydrogen bond donors, hydrogen bond acceptor oxygens and hydrogen bond acceptor nitrogens accounted for 93% of the variance in PSA.

Even if PSA can be reliably computed from a single conformation and without simulated solvent, simpler and faster methods are continuously sought. Pickett et al. (2000) reported having speeded up the calculation process employed by Clark (1999a) by omitting the optimisation step, which led to calculation times of over 10 compounds per second while retaining good correlations to human intestinal absorption. In a study by Ertl et al. (2000), the polar surface areas of 34,810 drug-like molecules were used to derive fragment contributions for a variety of polar fragments using least-squares fitting. Topological polar surface areas (TPSA) were then computed by simple summation of the obtained fragment values. Results were compared to three-dimensional PSA values for several test sets and excellent correlations ($r^2 = 0.94$) were established. Thus, the method was proposed as a replacement of the conventional PSA in rapid screening of drug molecules, having a capacity of processing over 8000 molecules per minute on a standard 450 MHz PC.

An even simpler approach correlates PSA with atom type hydrogen bond counts. Österberg and Norinder (2000) found excellent correlations between PSA and a PLS model consisting of hydrogen bond count descriptors. Prediction of various types of biological permeation (Fig. 18) using a combination of hydrogen bond descriptors and the calculated octanol–water partition coefficient varied from moderate ($r^2 = 0.65$) to good ($r^2 = 0.92$). Cheng et al. (2002) likewise found a strong correlation between PSA and a least squares regression model consisting of 18 E-state atom type count descriptors for oxygen and nitrogen atoms ($n = 438$, $r^2 = 0.992$). However, Stenberg et al. (2001) report on calculation times of the order of milliseconds for generation of static PSA and PTSA descriptors, which is not inferior to the above-presented 2D methods and retains the 3D nature of the approach. When large and flexible compounds which exhibit significant internal hydrogen-bonding are modelled, the dynamic polar surface area is expected to provide superior accuracy to the static, and especially the 2D, PSA.

In conclusion, several studies have proved the polar surface area a useful descriptor of biological permeation. Drugs with a PSA greater than 140 Å^2 have been found to exhibit poor intestinal absorption (Palm et al., 1997; Clark, 1999a; Kelder et al., 1999; Veber et al., 2002), whereas an upper limit of 60–90 Å^2 has been found for blood–brain partition (van de Waterbeemd et al., 1998; Kelder et al., 1999). Recent development has focused on the fast estimation of PSA for rapid drug screening as well as on the use of PTSA models for combined assessment of drug permeation and solubility.

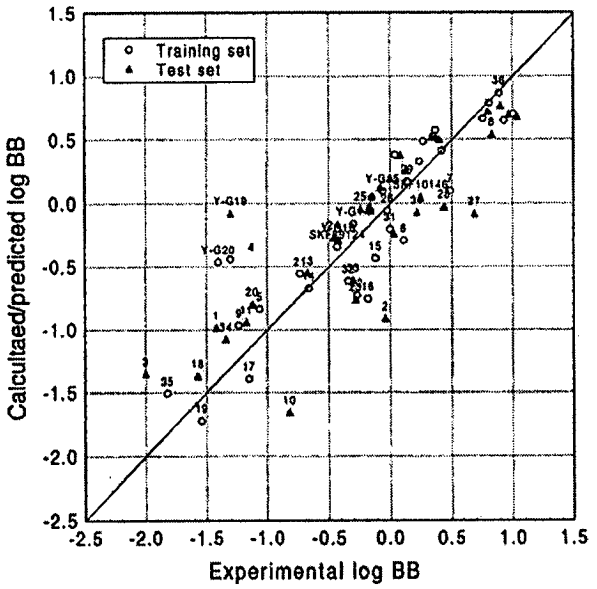

Fig. 18. Experimental log BB vs. log BB calculated (training set) and predicted (test set) using hydrogen bond count descriptors and the octanol–water partition coefficient. Statistic parameters can be found in Table 1, method 17. Compound structures are available in Clark (1999b). Fig. reproduced from Österberg and Norinder (2000) with permission from the American Chemical Society.

5.2.4. 3D molecular field models

Another approach that relates three-dimensional molecular structure with physicochemical properties of relevance to biological permeation is the use of 3D molecular fields. These fields are three-dimensional maps of the repulsive/attractive energies between a molecule and an interacting substance. The molecular electrostatic potential (MEP), describing the interaction energy between a point charge or dipole and the molecule, has found significant use in studies of ligand–receptor interactions (e.g. Boer et al., 2001). The molecular lipophilicity potential (MLP, Section 5.1.1) was developed to determine the dependence of lipophilicity on conformation and has found use in the calculation of $\log P$ and characterisation of ligand–receptor interactions (Gaillard et al., 1994, 1996). Recently, the same group reported on their version of the molecular hydrogen-bonding potential (MHBP) and its use in structure–permeation relationships (Rey et al., 2001).

The GRID program (available from Molecular Discovery Ltd., Middlesex, UK) is a commonly used tool in computational modelling of molecular surfaces (Goodford, 1985; Boobbyer et al., 1989). Its energy function is based on the sum of three interaction potentials between the target molecule and a probe (atom or group): the Lennard–Jones, the electrostatic and the hydrogen bonding potentials. GRID has been applied successfully in structure-based drug design (von Itzstein et al., 1993) and as descriptor input for quantitative structure–activity relationship (QSAR) models (Cruciani and Watson, 1994). Comparative molecular field analysis (CoMFA) is one of the most frequently employed procedures in 3D-QSAR (Kim et al., 1998). CoMFA, like GRID, uses probes to construct a three-dimensional map of the interaction energies of the target molecule. Whereas the GRID approach simply calculates the interaction fields that can subsequently be visualised using a molecular graphics program, an integral part of the CoMFA procedure is the construction of a PLS model on basis of the correlation between biological response and the computed interaction energies (Livingstone, 2000).

Despite giving rise to QSAR models with good predictivity (e.g. Cruciani and Watson, 1994), the information contained in the above-described 3D field maps can be cumbersome to interpret for drug design purposes. The problem becomes critical when the aim is quantification and comparison of a set of molecules. To this end, specialised tools for the transformation of 3D molecular interaction fields into easily interpretable descriptors are required. The VolSurf procedure (available from Molecular Discovery Ltd.) was developed by Cruciani et al. (2000). The basic concept of VolSurf is to convert the information present in 3D molecular field maps into a limited number of quantitative numerical descriptors. Molecular recognition is achieved with image analysis software, while its conversion into descriptors involves the use of external chemical knowledge. Once the descriptors have been calculated, they are correlated with the desired experimental property using chemometric tools, and turned into a model. The procedure is completely automatic once the 3D structures of the compounds have been generated, and reportedly takes approximately 2 min for 100 compounds at low resolution (Crivori et al., 2000).

Several models have been built employing VolSurf technology. Crivori et al. (2000) report on the use of VolSurf for qualitative (±) prediction of blood–brain barrier permeation. Subjecting a total of 229 compounds and 72 VolSurf descriptors to PLS discriminant analysis they arrived at a model that assigned a correct BBB permeation profile to over 90% of the compounds. The score plots for the discriminant PLS model are shown in Fig. 19. The most important descriptors affecting BBB permeation were the polarity descriptors, which, as expected, were inversely correlated with permeation. Overall, it appeared that permeation was governed by the balance of all descriptors, rather than a single descriptor type.

Ekins et al. (2001) compared different 3D-based quantitative structure–permeation relationship models, including CoMFA and VolSurf (using GRID), in the prediction of Caco-2 permeability of 2-aminobenzimidazoles. Ninteen compounds were used as a training set to construct the model. Both approaches yielded a three-component model with the statistics: (CoMFA: $n = 19$, $r^2 = 0.96$, $q^2 = 0.30$; VolSurf: $n = 19$, $r^2 = 0.76$, $q^2 = 0.54$). Despite the superior correlation coefficient of the CoMFA model for the training set compounds, both models gave similar statistics for a test set of nine compounds: (CoMFA: $n = 9$, $r^2 = 0.84$, VolSurf: $n = 9$, $r^2 = 0.83$). The best test set statistics were obtained

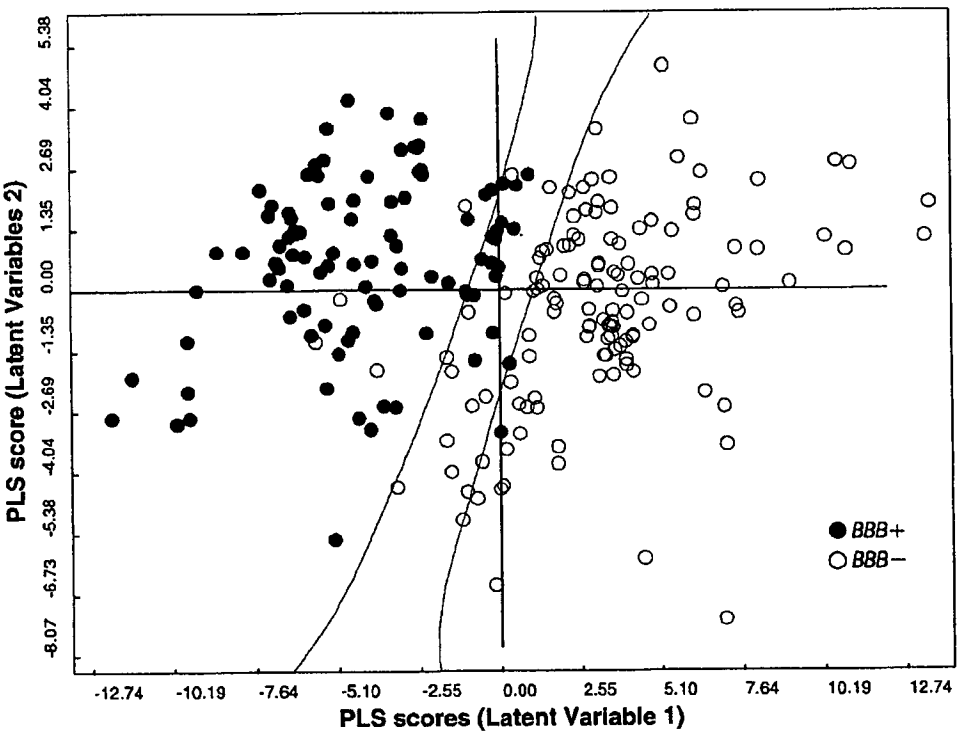

Fig. 19. The score plot for the two significant latent variables of the discriminant PLS model based on 229 compounds and 72 VolSurf descriptors. A correct BBB profile was assigned to over 90% of the compounds. Based on the 0.6 unit prediction error of the discriminant PLS, a confidence interval was drawn between the BBB+ and BBB− regions where prediction can be doubtful. Reproduced from Crivori et al. (2000) with permission from the American Chemical Society.

with the pharmacophore generation program Catalyst (Accelrys): ($n = 9$, $r^2 = 0.94$).

5.2.5. Quantum chemical approaches

Recent progress in computational hardware and algorithms has also assisted the development of molecular quantum-mechanical calculations. In addition to molecular geometry, quantum mechanics approaches take into account electronic effects, such as charge distribution, which are not inherently incorporated into molecular mechanics calculations. The main benefit of quantum-chemical descriptors is their accuracy and that they can be derived solely from the theoretical structure of a molecule (Karelson et al., 1996).

Along with many benefits, the quantum-chemical approach does contain certain downsides. Despite the continuous improvement of computational resources, quantum chemical calculations are very time-consuming. As a result, the extremely computer costly ab initio methods have often been replaced by more rapid, semiempirical quantum chemical models. An additional drawback of the quantum chemical approach is that the calculations are performed for a single structure at an unrealistic energetic minimum, corresponding to the hypothetical physical state of the gas at 0 K and infinitely low pressure. Thus, when studying flexible molecules some type of averaging over the lowest energy conformations may be required. Quantum chemical approaches are also not suitable for modelling solute–solvent interactions. When studying specific effects such as hydrogen bonding, the supermolecule approach has been adopted, where the solute molecule is modelled together with its first solvent coordination shell. Solvent bulk effects are commonly accounted for with dielectric reaction field models (Karelson et al., 1996).

In a recent study, Norinder et al. (1997, 1999) investigated the use of MolSurf (available from Qemist AB, Karlskoga, Sweden) technology in combination with multivariate statistics to predict biological permeation. The computational protocol involves performing a conformational analysis of each compound using molecular mechanics, followed by a semi-empirical geometry optimisation of the lowest energy conformation. The wave function from an ab initio calculation of this conformation is then used by the MolSurf program to compute various properties related to the valence region of the molecule. These descriptors include basicity/acidity, lipophilicity, hydrogen bonding, polarity, polarisability and charge-transfer characteristics. A partial least squares method is used to determine the relationships between the calculated MolSurf descriptors and the biological permeation of a selected training set of compounds. As not all calculated descriptors will be of importance to the model, a leave-one-out procedure is carried out, wherein the importance of each variable for the predictivity of the model is assessed. Descriptors, which decrease the predictivity are permanently deleted. Subsequently, the obtained

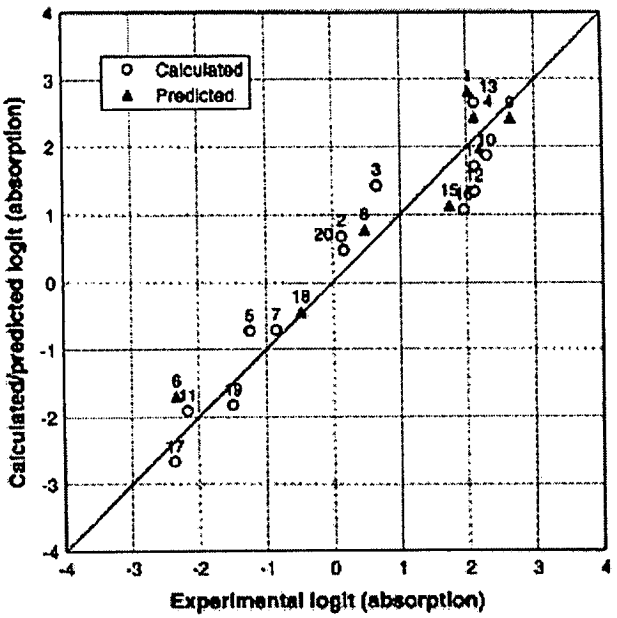

Fig. 20. Experimental human intestinal absorption vs. computed HIA using MolSurf parametrisation. Calculated = training set; Predicted = test set. Statistics can be found in Table 1, method 3. Chemical names of compounds are given in the Appendix. Reproduced from Norinder et al. (1999) with permission from Elsevier.

model can be used to predict permeation of test compounds on basis of their MolSurf parameters.

When relating the computed MolSurf descriptors of a set of compounds to their Caco-2 permeation (Norinder et al., 1997) and human intestinal absorption (Norinder et al., 1999), good correlations were obtained both in the training set and the test set ($r^2 = 0.90$, $q^2 = 0.69$, Fig. 20). The most important factors affecting the intestinal absorption of the drugs proved to be related to hydrogen bonding, which had a negative impact on permeation. The number of possible hydrogen bonding atoms was found to have a greater effect on permeation than the actual strength of the bonds. Curiously, hydrogen bond acceptor characteristics related to nitrogen atoms appeared to exert a stronger (negative) effect on intestinal absorption than those related to oxygen (Norinder et al., 1999). This was suggested to be due to the tendency of nitrogen atoms to be ionised at physiological pH. Assuming that the drugs need to be neutral in order to transfer through the membrane, the PLS modelling will thus incorporate in the MolSurf descriptors of the nitrogen atoms also the effects of deprotonation and desolvation. In both studies (Norinder et al., 1997, 1999), high polarisability and charge-transfer characteristics were factors that promoted permeation.

Quantum-chemical descriptors have also found use in originally empirical models. As mentioned earlier, the linear solvation energy relationship approach (see Sections 5.1.1 and 5.2.2) suffers from difficulties in encountering values for the various descriptors. Wilson and Famini (1991) developed a similar approach based on computationally-derived descriptors, called theoretical linear solvation energy relationships (TLSER), where the parameters are calculated from semi-empirical quantum chemistry methods.

5.3. Conclusions

Comparison of the various models developed to predict biological permeation reveals that relatively few descriptors seem to be significant for biological permeation. Accordingly, the combination of a hydrogen bond donor descriptor, a general hydrogen bonding descriptor and a lipophilicity descriptor have been found to be a working recipe for prediction of human intestinal absorption (Winiwarter et al., 2003).

When comparing the various computational methods to predict biological permeation of drugs, one should keep in mind the target application of the method. Preliminary screening of large libraries of drug candidates requires a rapid and simple method. However, for detailed and accurate studies of the mechanisms relating structure to property, the use of computationally more demanding approaches may be founded. For most applications high interpretability of results is desirable, i.e. a direct and comprehensible relation between descriptors and compound structure.

The statistics of the models discussed in this section are compiled in Table 1. As a direct comparison between the models is not feasible due to the variable size and composition (differences in structural diversity) of the datasets they are based on, the table is intended more as a summary. One thing that becomes evident upon examining the table is that while there exists an abundance of computational approaches to model biological permeation, most of them share the same problem: they are constructed/validated on too small data sets to allow for any real conclusions to be drawn. Many datasets are furthermore biased towards highly permeable compounds and contain drugs that are transported by other pathways than the passive transcellular route. As pointed out by several researchers (Bergström et al., 2003; Clark, 2003; Egan and Lauri, 2002), large and well-balanced datasets of reliable and structurally diverse data are a prerequisite for the development of computational models that can be implemented as routine screens in the drug development process.

As most of the computational approaches developed are aimed at enabling high-throughput virtual screening of vast compound libraries, the recent trend has shifted towards faster methods and more easily interpreted descriptors. Furthermore, recent studies report on combined computational screening of drug permeation and other biopharmaceutical properties, such as solubility (Bergström et al., 2003) and activity (Egan and Lauri, 2002; Pickett et al., 2000).

6. Overall conclusions

The emphasis in passive drug permeation modelling is shifting from experimental to computational methods. How-

Table 1
Summary of computational approaches to predict biological permeation

	Method	Predicted quantity	n_{train}	r^2_{train}	q^2_{train}	s_{train}	n_{test}	Test set statistics	Reference
1	Abraham	% Abs	38	0.83	0.75	14[a]	131	RMSE = 14, MAE = 11	Zhao et al. (2001)
2	E-state	Logit (Abs)	13	0.90	0.82	0.63	7	RMSE = 0.413	Norinder and Österberg (2001)
3	MolSurf	Logit (Abs)	13	0.90	0.69	0.63	7	RMSE = 0.49, Fig. 20	Norinder et al. (1999)
4	E-state	log ($P_{appCaco-2}$)	9	0.93	0.79	0.37	8	RMSE = 0.41	Norinder and Österberg (2001)
5	E-state, Clog P	log (P_{Caco-2})	17	0.71	0.67	0.84[a]	10	RMSE = 0.86	Stenberg et al. (2001)
6	PSTA	log (P_{Caco-2})	17	0.95	0.86	0.33[a]	10	RMSE = 1.15	Stenberg et al. (2001)
7	MolSurf	log (P_{Caco-2})	17	0.87	0.78	0.56[a]	10	RMSE = 0.83	Stenberg et al. (2001)
8	MolSurf	log ($P_{appCaco-2}$)	9	0.94	0.85	0.33	8	RMSE = 0.41	Norinder et al. (1997)
9	CoMFA	log ($P_{appCaco-2}$)	19	0.96	0.30	0.08[b]	9	r^2 = 0.84	Ekins et al. (2001)
10	VolSurf	log ($P_{appCaco-2}$)	19	0.76	0.54	–	9	r^2 = 0.83	Ekins et al. (2001)
11	Various molecular properties	log (BB)	48	0.84	0.79	0.19	17	r^2 = 0.68, MAE = 0.41	Lobell et al. (2003)
12	Abraham	log (BB)	148	0.75	0.71	0.34	–	Fig. 16	Platts et al. (2001)
13	Abraham	log (BB)	74	0.77/0.76	–	0.33/0.34	74	r^2 = 0.74/0.70, newline s = 0.38/0.39	Platts et al. (2001)
14	E-state	log (BB)	28	0.75	0.70	0.39	31	RMSE = 0.44	Norinder and Österberg (2001)
15	E-state	log (BB)	102	0.66	0.62	0.45	–	–	Rose et al. (2002)
16	H-bonds	log (BB)	35	0.71	0.68	0.42[a]	34	RMSE = 0.37	Österberg and Norinder (2000)
17	H-bonds	log (BB)	23	0.72	0.68	0.52[a]	22	RMSE = 0.50, Fig. 18	Österberg and Norinder (2000)

n_{train}: number of compounds in the training set; r^2_{train} and q^2_{train}: the r^2 value and the leave one out cross-validated r^2 value of the training set; s_{train}: standard deviation of the training set. Exceptions, values marked with letters *a* are RMSE, and *b* are standard error of the estimate, n_{test}: number of compounds in the test set, RMSE: root mean square error; MAE: mean absolute error.

ever, this by no means diminishes the importance of experimental approaches. More than ever, large amounts of high quality data on biological permeation are needed for the construction of reliable models, which can be applied to a wide region in chemical space. One aspect that remains unclear, is the effect of charge on permeation. Most experimental and computational methods do not properly account for solute charge, nor do there exist comprehensive studies on the subject. Liquid–liquid electrochemistry provides a system for exclusive characterisation of properties contributing to biological permeation of charged species. However, well-characterised reference data on ion permeation is needed for correlations.

Acknowledgements

A.M. thanks the Academy of Finland for financial support.

Appendix A. Explanations to figure legends

Figure	Legend	Chemical name of compound	Reference
1	3a	*N*-Acetyl-D-valyl-D-phenylalanine *N*-methylamide	Goodwin et al. (2001)
	4	*N*-Acetyl-D-leucyl-D-phenylalanine *N*-methylamide	
	5a	*N*-Acetyl-D-phenylalanyl-D-phenylalanine *N*-methylamide	
	6	*N*-Acetyl-D-cyclohexylalanyl-D-phenylalanine *N*-methylamide	
	7	*N*-Acetylglycine phenethylamide	
	8	*N*-Acetyl-D-alanine phenethylamide	
	9a	*N*-Acetyl-D-valine phenethylamide	
	10	*N*-Acetyl-D-leucine phenethylamide	
10(a)	a	Peg (polyethylene glycol)	Beigi et al. (1995)
	b	Atenolol	
	c	Salicylic acid	
	d	Aspirin	
	e	Terbutaline	
	f	Warfarin	
	g	Metoprolol	
	h	Hydrocortisone	
	i	Alprenolol	

Appendix A (*Continued*)

Figure	Legend	Chemical name of compound	Reference
	j	Corticosterone	
	k	Chlorpromazine	
	l	DL-Propranolol	
20	1	Alprenolol	Norinder et al. (1999).
	2	Atenolol	
	3	Ciprofloxacin	
	4	Diazepam	
	5	Foscarnet	
	6	Lactulose	
	7	Mannitol	
	8	Metolazone	
	9	Metoprolol	
	10	Nordiazepam	
	11	Olsalazine	
	12	Oxazepam	
	13	Oxprenolol	
	14	Phenazone	
	15	Pindolol	
	16	Practolol	
	17	Raffinose	
	18	Sulpiride	
	19	Sulphasalazine	
	20	Tranexamic acid	

References

Abraham, M.H., Liszi, J., 1978. Calculations on ionic solvation. Part I. Free energies of solvation of gaseous univalent ions using a one-layer continuum model. J. Chem. Soc., Faraday Trans. I 74, 1604–1614.

Abraham, M.H., McGowan, J.C., 1987. The use of characteristic volumes to measure cavity terms in reversed phase liquid chromatography. Chromatographia 23, 243–246.

Abraham, M.H., Platts, J.A., 2001. Hydrogen bond structural group constants. J. Org. Chem. 66, 3484–3491.

Abraham, M.H., Martins, F., Mitchell, R.C., Salter, C.J., 1999. Hydrogen bonding. 47. Characterization of the ethylene glycol–heptane partition system: hydrogen bond acidity and basicity of peptides. J. Pharm. Sci. 88, 241–247.

Abraham, M.H., Chadha, H.S., Leitao, R.A.E., Mitchell, R.C., Lambert, W.J., Kaliszan, R., Nasal, A., Haber, P., 1997. Determination of solute lipophilicity, as log *P*(octanol) and log *P*(alkane) using poly(styrene–divinylbenzene) and immobilised artificial membrane stationary phases in reversed-phase high-performance liquid chromatography. J. Chromatogr. A 766, 35–47.

Abraham, M.H., Chadha, H.S., Mitchell, R.C., 1995. The factors that influence skin penetration of solutes. J. Pharm. Pharmacol. 47, 8–16.

Abraham, M.H., Chadha, H.S., Mitchell, R.C., 1994. Hydrogen-bonding. 33. Factors that influence the distribution of solutes between blood and brain. J. Pharm. Sci. 83, 1257–1268.

Amato, M., Barbato, F., Morrica, P., Quaglia, F., La Rotonda, M.I., 2000. Interactions between amines and phospholipids: a chromatographic study on immobilised artificial membrana (IAM) stationary phases at various pH values. Helv. Chim. Acta 83, 2836–2847.

Artursson, P., Borchardt, R.T., 1997. Intestinal drug absorption and metabolism in cell cultures: Caco-2 and beyond. Pharm. Res. 14, 1655–1658.

Artursson, P., Karlsson, J., 1991. Correlation between oral drug absorption in humans and apparent drug permeability coefficients in human intestinal epithelial (Caco-2) cells. Biochem. Biophys. Res. Commun. 175, 880–885.

Artursson, P., Palm, K., Luthman, K., 2001. Caco-2 monolayers in experimental and theoretical predictions of drug transport. Adv. Drug Deliv. Rev. 46, 27–43.

Audry, E., Dubost, J.-P., Colleter, J.-C., Dallet, P., 1986. A new approach to structure–activity relations: the molecular lipophilicity potential. Eur. J. Med. Chem. 21, 71–72.

Audus, K.L., Bartel, R.L., Hidalgo, I.J., Borchardt, R.T., 1990. The use of cultured epithelial and endothelial cells for drug transport and metabolism studies. Pharm. Res. 7, 435–451.

Avdeef, A., 1993. pH-metric log-P. 2. Refinement of partition-coefficients and ionization-constants of multiprotic substances. J. Pharm. Sci. 82, 183–190.

Avdeef, A., Strafford, M., Block, E., Balogh, M.P., Chambliss, W., Khan, I., 2001. Drug absorption in vitro model: filter immobilized artificial membranes. 2. Studies of the permeability properties of lactones in *Piper methysticum*. Forst. Eur. J. Pharm. Sci. 14, 271–280.

Avdeef, A., Box, K.J., Comer, J.E.A., Hibbert, C., Tam, K.Y., 1998. pH-metric log *P* 10. Determination of liposomal membrane-water partition coefficients of ionizable drugs. Pharm. Res. 15, 209–215.

Balon, K., Riebesehl, B.U., Müller, B.W., 1999a. Determination of liposome partitioning of ionisable drugs by titration. J. Pharm. Sci. 88, 802–806.

Balon, K., Riebesehl, B.U., Müller, B.W., 1999b. Drug liposome partitioning as a tool for the prediction of human passive intestinal absorption. Pharm. Res. 16, 882–888.

Bangham, A.D., 1993. Liposomes: the Babraham connection. Chem. Phys. Lipids 64, 275–285.

Bangham, A.D., Standish, M.M., Watkins, J.C., 1965. Diffusion of univalent ions across the lamellae of swollen phospholipids. J. Mol. Biol. 13, 238–252.

Barbato, F., La Rotonda, M.I., Quaglia, F., 1997. Interactions of nonsteroidal anti-inflammatory drugs with phospholipids: comparison between octanol/buffer partition coefficients and chromatographic indexes on immobilized artificial membranes. J. Pharm. Sci. 86, 225–229.

Beigi, F., Gottschalk, I., Lagerquist Hägglund, C., Haneskog, L., Brekkan, E., Zhang, Y., Österberg, T., Lundahl, P., 1998. Immobilized liposome and biomembrane partitioning chromatography of drugs for prediction of drug transport. Int. J. Pharm. 164, 129–137.

Beigi, F., Yang, Q., Lundahl, P., 1995. Immobilized-liposome chromatographic analysis of drug partitioning into lipid bilayers. J. Chromatogr. A 704, 315–321.

Bergström, C.A.S., Strafford, M., Lazorova, L., Avdeef, A., Luthman, K., Artursson, P., 2003. Absorption classification of oral drugs based on molecular surface properties. J. Med. Chem. 46, 558–570.

Beschiaschvili, G., Seelig, J., 1992. Peptide binding to lipid bilayers. Nonclassical hydrophobic effect and membrane-induced p*K* shifts. Biochemistry 31, 10044–10053.

Betageri, G.V., Rogers, J.A., 1988. The liposome as a distribution model in QSAR studies. Int. J. Pharm. 46, 95–102.

Betageri, G.V., Rogers, J.A., 1987. Thermodynamics of partitioning of *b*-blockers in the *n*-octanol-buffer and liposome systems. Int. J. Pharm. 36, 165–173.

Boer, D.R., Kooijman, H., van der Louw, J., Groen, M., Kelder, J., Kroon, J., 2001. Relation between the molecular electrostatic potential and activity of some FF-MAS related sterol compounds. Bioorg. Med. Chem. 9, 2653–2659.

Boobbyer, D.N.A., Goodford, P.J., McWhinnie, P.M., Wade, R.C., 1989. New hydrogen-bond potentials for use in determining energetically favorable binding sites on molecules of known structure. J. Med. Chem. 32, 1083–1094.

Bouchard, G., Pagliara, A., Carrupt, P.-A., Testa, B., Gobry, V., Girault, H.H., 2002. Theoretical and experimental exploration of the lipophilicity of zwitterionic drugs in the 1,2-dichloroethane/water system. Pharm. Res. 19, 1150–1159.

Bouchard, G., Carrupt, P.-A., Testa, B., Gobry, V., Girault, H.H., 2001a. The apparent lipophilicity of quaternary ammonium ions is influenced by Galvani potential difference, not ion-pairing: a cyclic voltammetry study. Pharm. Res. 18, 702–708.

Bouchard, G., Pagliara, A., van Palen, G.P., Carrupt, P.-A., Testa, B., Gobry, V., Girault, H.H., Caron, G., Ermondi, G., Fruttero, R., 2001b. Ionic partition diagram of the zwitterionic antihistamine Cetirizine. Helv. Chim. Acta 84, 375–387.

Brockman, H., 1994. Dipole potential of lipid membranes. Chem. Phys. Lipids 73, 57–79.

Caldwell, G.W., Masucci, J.A., Evangelisto, M., White, R., 1998. Evaluation of the immobilized artificial membrane phosphatidylcholine. Drug discovery column for high-performance liquid chromatographic screening of drug–membrane interactions. J. Chromatogr. A 800, 161–169.

Camenisch, G., Folkers, G., van de Waterbeemd, H., 1996. Review of theoretical passive drug absorption models: historical background, recent developments and limitations. Pharm. Acta Helv. 71, 309–327.

Caron, G., Steyaert, G., Pagliara, A., Reymond, F., Crivori, P., Gaillard, P., Carrupt, P.-A., Avdeef, A., Comer, J., Box, K.J., Girault, H.H., Testa, B., 1999. Structure-lipophilicity relationships of neutral and protonated b-blockers. Part I. Intra- and intermolecular effects in isotropic solvent systems. Helv. Chim. Acta 82, 1211–1222.

Carrupt, P.-A., Testa, B., Gaillard, P., 1997. Computational approaches to lipophilicity: methods and applications. In: Lipkowitz, K.B., Boyd, D.B. (Eds.), Reviews in Computational Chemistry. Wiley, New York, vol. 11, Chapter 5, pp. 241–315.

Cevc, G., 1993. Solute transport across bilayers. In: Cevc, G. (Ed.), Phospholipids Handbook. Marcel Decker, New York, pp. 639–661.

Cevc, G., 1990. The molecular mechanism of interaction between monovalent ions and polar surfaces, such as lipid bilayer membranes. Chem. Phys. Lett. 170, 283–288.

Cheng, A., Diller, D.J., Dixon, S.L., Egan, W.J., Lauri, G., Merz Jr., K.M., 2002. Computation of the physio-chemical properties and data mining of large molecular collections. J. Comput. Chem. 23, 172–183.

Chou, J.T., Jurs, P.C., 1979. Computer-assisted computation of partition coefficients from molecular structures using fragment constants. J. Chem. Inf. Comput. Sci. 19, 172–178.

Clark, D.E., 2003. In silico prediction of blood–brain barrier permeation. Drug Discov. Today 8, 927–933.

Clark, D.E., 1999a. Rapid calculation of polar molecular surface area and its application to the prediction of transport phenomena. 1. Prediction of intestinal absorption. J. Pharm. Sci. 88, 807–814.

Clark, D.E., 1999b. Rapid calculation of polar molecular surface area and its application to the prediction of transport phenomena. 2. Prediction of blood–brain barrier penetration. J. Pharm. Sci. 88, 815–821.

Clark, D.E., Grootenhuis, P.D.J., 2003. Predicting passive transport in silico: history, hype, hope. Curr. Top. Med. Chem. 3, 1193–1203.

Conradi, R.A., Hilgers, A.R., Ho, N.F.H., Burton, P.S., 1991. The influence of peptide structure on transport across Caco-2 cells. Pharm. Res. 8, 1453–1460.

Cramb, D.T., Wallace, S.C., 1997. Structure and biomembrane mimetic behavior of the water–octanol interface. J. Phys. Chem. B 101, 2741–2744.

Crivori, P., Cruciani, G., Carrupt, P.-A., Testa, B., 2000. Predicting blood–brain barrier permeation from three-dimensional molecular structure. J. Med. Chem. 43, 2204–2216.

Cruciani, G., Watson, K.A., 1994. Comparative molecular field analysis using GRID force-field and GOLPE variable selection methods in a study of inhibitors of glycogen phosphorylase *b*. J. Med. Chem. 37, 2589–2601.

Cruciani, G., Crivori, P., Carrupt, P.-A., Testa, B., 2000. Molecular fields in quantitative structure–permeation relationships: the VolSurf approach. J. Mol. Struct. (Theochem.) 503, 17–30.

Dalby, A., Nourse, J.G., Hounshell, W.D., Gushurst, A.K.I., Grier, D.L., Lealand, B.A., Laufer, J., 1992. Description of several chemical structure file formats used by computer programs developed at molecular design limited. J. Chem. Inf. Comput. Sci. 32, 244–255.

Danelian, E., Karlén, A., Karlsson, R., Winiwarter, S., Hansson, A., Löfås, S., Lennernäs, H., Hämäläinen, M.D., 2000. SPR biosensor studies of the direct interaction between 27 drugs and a liposome surface: correlation with fraction absorbed in humans. J. Med. Chem. 43, 2083–2086.

DeBolt, S.E., Kollman, P.A., 1995. Investigation of structure, dynamics, and solvation in 1-octanol and its water-saturated solution: molecular dynamics and free-energy perturbation studies. J. Am. Chem. Soc. 117, 5316–5340.

De Young, L.R., Dill, K.A., 1988. Solute partitioning into lipid bilayer membranes. Biochemistry 27, 5281–5289.

Dorsey, J.G., Khaledi, M.G., 1993. Review: hydrophobicity estimations by reversed-phase liquid chromatography–implications for biological partitioning processes. J. Chromatogr. A 656, 485–499.

Drayton, C.J., 1990. Cumulative subject index and drug compendium. In: Hansch, C., Sammes, P.G., Taylor J.B. (Eds.), Comprehensive Medicinal Chemistry, vol. 6. Pergamon Press, Oxford.

Egan, W.J., Lauri, G., 2002. Prediction of intestinal permeability. Adv. Drug Deliv. Rev. 54, 273–289.

Egan, W.J., Merz Jr., K.M., Baldwin, J.J., 2000. Prediction of drug absorption using multivariate statistics. J. Med. Chem. 43, 3867–3877.

Ekins, S., Durst, G.L., Stratford, R.E., Thorner, D.A., Lewis, R., Loncharich, R.J., Wikel, J.H., 2001. Three-dimensional quantitative structure-permeability relationship analysis for a series of inhibitors of rhinovirus replication. J. Chem. Inf. Comput. Sci. 41, 1578–1586.

El Tayar, N., Tsai, R.-S., Testa, B., Carrupt, P.-A., Leo, A., 1991. Partitioning of solutes in different solvent systems: the contribution of hydrogen bonding capacity and polarity. J. Pharm. Sci. 80, 590–598.

Ertl, P., Rohde, B., Selzer, P., 2000. Fast calculation of molecular polar surface area as a sum of fragment-based contributions and its appli-

cations to the prediction of drug transport properties. J. Med. Chem. 43, 3714–3717.

Fischer, H., Gottschlich, R., Seelig, A., 1998. Blood–brain barrier permeation: molecular parameters governing passive diffusion. J. Membr. Biol. 165, 201–211.

Franks, N.P., Abraham, M.H., Lieb, W.R., 1993. Molecular organization of liquid *n*-octanol: an X-ray diffraction analysis. J. Pharm. Sci. 82, 466–470.

Fujita, T., Iwasa, J., Hansch, C., 1964. A new substituent constant π derived from partition coefficients. J. Am. Chem. Soc. 86, 5175–5180.

Furet, P., Sele, A., Cohen, N.C., 1988. 3D molecular lipophilicity potential profiles: a new tool in molecular modeling. J. Mol. Graph. 6, 182–189.

Gaillard, P., Carrupt, P.-A., Testa, B., Schambel, P., 1996. Binding of arylpiperazines, (aryloxy)propanolamines, and tetrahydropyridylindoles to the 5-HT1A receptor: contribution of the molecular lipophilicity potential to three-dimensional quantitative structure-affinity relationship models. J. Med. Chem. 39, 126–134.

Gaillard, P., Carrupt, P.-A., Testa, B., Boudon, A., 1994. Molecular lipophilicity potential, a tool in 3D QSAR: method and applications. J. Comput. Aided Mol. Des. 8, 83–96.

Garberg, P., Eriksson, P., Schipper, N., Sjöström, B., 1999. Automated absorption assessment using Caco-2 cells cultured on both sides of polycarbonate membranes. Pharm. Res. 16, 441–445.

Gawrisch, K., Ruston, D., Zimmerberg, J., Parsegian, V.A., Rand, R.P., Fuller, N., 1992. Membrane dipole potentials, hydration forces, and the ordering of water at membrane surfaces. Biophys. J. 61, 1213–1223.

Genty, M., González, G., Clere, C., Desangle-Gouty, V., Legendre, J.-Y., 2001. Determination of the passive absorption through the rat intestine using chromatographic indices and molar volume. Eur. J. Pharm. Sci. 12, 223–229.

Ghose, A.K., Viswanadhan, V.N., Wendoloski, J.J., 1998. Prediction of hydrophobic (lipophilic) properties of small organic molecules using fragmental methods: an analysis of ALOGP and CLOGP methods. J. Phys. Chem. A 102, 3762–3772.

Girault, H.H.J., Schiffrin, D.J., 1989. Electrochemistry of liquid–liquid interfaces. In: Bard, A.J. (Ed.), Electroanalytical Chemistry, vol. 15. Marcel Dekker, New York, pp. 1–141.

Gobas, F.A.P.C., Lahittete, J.M., Garofalo, G., Shiu, W.Y., MacKay, D., 1988. A novel method for measuring membrane-water partition coefficients of hydrophobic organic chemicals: comparison with 1-octanol–water partitioning. J. Pharm. Sci. 77, 265–272.

Gobry, V., Ulmenau, S., Reymond, F., Bouchard, G., Carrupt, P.-A., Testa, B., Girault, H.H., 2001. Generalization of ionic partition diagrams to lipophilic componds and to biphasic systems with variable phase volume ratios. J. Am. Chem. Soc. 123, 10684–10690.

Gobry, V., Bouchard, G., Carrupt, P.-A., Testa, B., Girault, H.H., 2000. Physicochemical characterization of Sildenafil: ionisation, lipophilicity behaviour, and ionic-partition diagram studied by two-phase titration and electrochemistry. Helv. Chim. Acta 83, 1465–1474.

Gombar, V.K., Enslein, K., 1996. Assessment of *n*-octanol/water partition coefficient: when is the assessment reliable? J. Chem. Inf. Comput. Sci. 36, 1127–1134.

Goodford, P.J., 1985. A computational procedure for determining energetically favorable binding sites on biologically important macromolecules. J. Med. Chem. 28, 849–857.

Goodwin, J.T., Conradi, R.A., Ho, N.F.H., Burton, P.S., 2001. Physicochemical determinants of passive membrane permeability: role of solute hydrogen-bonding potential and volume. J. Med. Chem. 44, 3721–3729.

Grinius, L., Stanton, D.T., Morris, C.M., Howard, J.M., Curnow, A.W., 2002. Profiling of drugs for membrane activity using liposomes as an in vitro model system. Drug Dev. Ind. Pharm. 28, 193–202.

Gulaboski, R., Mirèeski, V., Scholz, F., 2002. An electrochemical method for determination of the standard Gibbs energy of anion transfer between water and *n*-octanol. Electrochem. Comm. 4, 277–283.

Hall, L.H., Kier, L.B., 1995. Electrotopological state indices for atom types: a novel combination of electronic, topological, and valence state information. J. Chem. Inf. Comput. Sci. 35, 1039–1045.

Hansch, C., Fujita, T., 1964. r-s-p analysis. A method for the correlation of biological activity and chemical structure. J. Am. Chem. Soc. 86, 1616–1626.

Hansch, C., Muir, R.M., Fujita, T., Maloney, P.P., Geiger, F., Streich, M., 1963. The correlation of biological activity of plant growth regulators and chloromycetin derivatives with Hammett constants and partition coefficients. J. Am. Chem. Soc. 85, 2817–2824.

Hitzel, L., Watt, A.P., Locker, K.L., 2000. An increased throughput method for the determination of partition coefficients. Pharm. Res. 17, 1389–1395.

Hubbell, W.L., McConnell, H.M., 1971. Molecular motion in spin-labeled phospholipids and membranes. J. Am. Chem. Soc. 93, 314–326.

Huuskonen, J.J., Livingstone, D.J., Tetko, I.V., 2000. Neural network modeling for estimation of partition coefficient based on atom-type electrotopological state indices. J. Chem. Inf. Comput. Sci. 40, 947–955.

Ikematsu, M., Iseki, M., Sugiyama, Y., Mizukami, A., 1996. Lipid bilayer formation in a microporous membrane filter monitored by ac impedance analysis and purple membrane photoresponses. J. Electroanal. Chem. 403, 61–68.

Irvine, J.D., Takahashi, L., Lockhart, K., Cheong, J., Tolan, J.W., Selick, H.E., Grove, J.R., 1999. MDCK (Madin–Darby Canine Kidney) cells: a tool for membrane permeability screening. J. Pharm. Sci. 88, 28–33.

Jacobs, R.E., White, S.H., 1989. The nature of the hydrophobic binding of small peptides at the bilayer interface: implications for the insertion of transbilayer helices. Biochemistry 28, 3421–3437.

Kaliszan, R., 1992. Quantitative structure–retention relationships. Anal. Chem. 64, 619A–631A.

Kaliszan, R., Nasal, A., Bucinski, A., 1994. Chromatographic hydrophobicity parameter determined on an immobilized artificial membrane column: relationships to standard measures of hydrophobicity and bioactivity. Eur. J. Med. Chem. 29, 163–170.

Kaliszan, R., Kaliszan, A., Wainer, I.W., 1993. Deactivated hydrocarbonaceous silica and immobilized artificial membrane stationary phases in high-performance liquid chromatographic determination of hydrophobicities of organic bases: relationship to log *P* and CLOGP. J. Pharm. Biomed. Anal. 11, 505–511.

Kamlet, M.J., Doherty, R.M., Carr, P.W., Mackay, D., Abraham, M.H., Taft, R.W., 1988. Linear solvation energy relationships. 44. Parameter estimation rules that allow accurate prediction of octanol/water partition coefficients and other solubility and toxicity properties of polychlorinated biphenyls and polycyclic aromatic hydrocarbons. Environ. Sci. Technol. 22, 503–509.

Kamlet, M.J., Abraham, D.J., Doherty, R.M., Taft, R.W., Abraham, M.H., 1986. Solubility properties in polymers and biological media. 6. An equation for correlation and prediction of solubilities of liquid organic nonelectrolytes in blood. J. Pharm. Sci. 75, 350–355.

Kamlet, M.J., Abboud, J.L.M., Abraham, M.H., Taft, R.W., 1983. Linear solvation energy relationships. 23. A comprehensive collection of the solvatochromic parameters, π, α, and β, and some methods for simplifying the generalized solvatochromic equation. J. Org. Chem. 48, 2877–2887.

Karelson, M., 2000. Molecular Descriptors in QSAR/QSPR. Wiley, New York.

Karelson, M., Lobanov, V.S., Katritzky, A.R., 1996. Quantum-chemical descriptors in QSAR/QSPR studies. Chem. Rev. 96, 1027–1043.

Kelder, J., Grootenhuis, P.D.J., Bayada, D.M., Delbressine, L.P.C., Ploemen, J.-P., 1999. Polar molecular surface as a dominating determinant for oral absorption and brain penetration of drugs. Pharm. Res. 16, 1514–1519.

Kennedy, T., 1997. Managing the drug discovery/development interface. Drug Discov. Today 2, 436–444.

Kier, L.B., Hall, L.H., 1999. Molecular Structure Description: The Electrotopological State. Academic Press, San Diego.

Kim, K.H., Greco, G., Novellino, E., 1998. A critical review of recent CoMFA applications. In: Kubinyi, H., Folkers, G., Martin, Y.C. (Eds.), 3D QSAR in Drug Design. Kluwer Academic, Doldrecht, The Netherlands, pp. 257–316.

Klopman, G., Li, J.-Y., Wang, S., Dimayuga, M., 1994. Computer automated log P calculations based on an extended group contribution approach. J. Chem. Inf. Comput. Sci. 34, 752–781.

Kontturi, K., Murtomäki, L., 1992. Electrochemical determination of partition coefficients of drugs. J. Pharm. Sci. 81, 970–975.

Krause, E., Dathe, M., Wieprecht, T., Bienert, M., 1999. Noncovalent immobilized artificial membrane chromatography, and improved method for describing peptide-lipid bilayer interactions. J. Chromatogr. A 849, 125–133.

Krämer, S.D., 1999. Absorption prediction from physicochemical parameters. Pharm. Sci. Technol. Today 2, 373–380.

Krämer, S.D., Wunderli-Allenspach, H., 1996. The pH-dependence in the partitioning behaviour of (RS)-[^{3}H] propranolol between MDCK cell lipid vesicles and buffer. Pharm. Res. 13, 1851–1855.

Krämer, S.D., Braun, A., Jakits-Deiser, C., Wunderli-Allenspach, H., 1998. Towards the predictability of drug-lipid membrane interactions: the pH-dependent affinity of propranolol to phosphatidylionsitol containing liposomes. Pharm. Res. 15, 739–744.

Kürschner, M., Nielsen, K., von Langen, J.R.G., Schenk, W.A., Zimmermann, U., Sukhorukov, V.L., 2000. Effect of fluorine substitution on the interaction of lipophilic ions with the plasma membrane of mammalian cells. Biophys. J. 79, 1490–1497.

Langner, M., Kubica, K., 1999. The electrostatics of lipid surfaces. Chem. Phys. Lipids 101, 3–35.

Larger, P., Altamura, M., Catalioto, R.-M., Giuliani, S., Maggi, C.A., Valenti, C., Triolo, A., 2002. Simultaneous LC-MS/MS determination of reference pharmaceuticals as a method for the characterization of the Caco-2 cell monolayer absorption properties. Anal. Chem. 74, 5273–5281.

Law, B., Weir, S., Ward, N.A., 1992. Fundamental studies in reversed-phase liquid–solid extraction of basic drugs I: ionic interactions. J. Pharm. Biomed. Anal. 10, 167–179.

Leo, A.J., 2000. Evaluating hydrogen-bond donor strength. J. Pharm. Sci. 89, 1567–1578.

Leo, A.J., 1993. Calculating log P_{oct} from structures. Chem. Rev. 93, 1281–1306.

Leo, A.J., Hoekman, D., 2000. Calculating log P(oct) with no missing fragments the problem of estimating new interaction parameters. Perspect. Drug Discov. Des. 18, 19–38.

Leo, A., Hansch, C., Elkins, D., 1971. Partition coefficients and their uses. Chem. Rev. 71, 525–616.

Liljeroth, P., Mälkiä, A., Cunnane, V.J., Kontturi, A.-K., Kontturi, K., 2000. Langmuir–Blodgett monolayers at a liquid–liquid interface. Langmuir 16, 6667–6673.

Lipinski, C.A., Lombardo, F., Dominy, B.W., Feeney, P.J., 1997. Experimental and computational approaches to estimate solubility and permeability in drug discovery and development settings. Adv. Drug Deliv. Rev. 23, 3–25.

Liu, X.-Y., Nakamura, C., Yang, Q., Kamo, N., Miyake, J., 2002. Immobilized liposome chromatography to study drug–membrane interactions. Correlation with drug absorption in humans. J. Chromatogr. A 961, 113–118.

Livingstone, D.J., 2000. The characterization of chemical structures using molecular properties. A survey. J. Chem. Inf. Comput. Sci. 40, 195–209.

Lobenberg, R., Amidon, G.L., 2000. Modern bioavailability, bioequivalence and biopharmaceutics classification system. New scientific approaches to international regulatory standards. Eur. J. Pharm. Biopharm. 50, 3–12.

Lobell, M., Molnár, L., Keserü, G.M., 2003. Recent advances in the prediction of blood–brain partitioning from molecular structure. J. Pharm. Sci. 92, 360–370.

Lohmann, C., Huwel, S., Galla, H.J., 2002. Predicting blood–brain barrier permeability of drugs: evaluation of different in vitro assays. J. Drug Target 10, 263–276.

Loidl-Stahlhofen, A., Eckert, A., Hartmann, T., Schöttner, M., 2001. Solid-supported lipid membranes as a tool for determination of membrane affinity: high-throughput screening of a physicochemical parameter. J. Pharm. Sci. 90, 599–606.

Luco, J.M., 1999. Prediction of the brain–blood distribution of a large set of drugs from structurally derived descriptors using partial least-squares (PLS) modeling. J. Chem. Inf. Comput. Sci. 39, 396–404.

Lundahl, P., Beigi, F., 1997. Immobilized liposome chromatography of drugs for model analysis of drug–membrane interactions. Adv. Drug Deliv. Rev. 23, 221–227.

Malkia, A., Liljeroth, P., Kontturi, K., 2003. Membrane activity of ionisable drugs: a task for liquid–liquid electrochemistry? Electrochem. Commun. 5, 473–479.

Mannhold, R., van de Waterbeemd, H., 2001. Substructure and whole molecule approaches for calculating log P. J. Comput. Aided Mol. Des. 15, 337–354.

Marcus, Y., Migron, Y., 1991. Polarity, hydrogen bonding, and structure of mixtures of water and cyanomethane. J. Phys. Chem. 95, 400–406.

Marrink, S.J., Berendsen, H.J.C., 1996. Permeation process of small molecules across lipid membranes studied by molecular dynamics simulations. J. Phys. Chem. 100, 16729–16738.

Mayer, L.D., Bally, M.B., Hope, M.J., Cullis, P.R., 1985. Uptake of dibucaine into large unilamellar vesicles in response to a membrane potential. J. Biol. Chem. 260, 802–808.

Meijer, L.A., Leermakers, F.A.M., Lyklema, J., 1999. Self-consistent-field modelling of complex molecules with united atom detail in inhomogenous systems. Cyclic and branched foreign molecules in dimyristoylphosphatidylcholine membranes. J. Chem. Phys. 110, 6560–6579.

Meylan, W.M., Howard, P.H., 1995. Atom/fragment contribution method for estimating octanol–water partition coefficients. J. Pharm. Sci. 84, 83–92.

Michael, D., Benjamin, I., 1995. Proposed experimental probe of the liquid/liquid interface structure: molecular dynamics of charge transfer at the water/octanol interface. J. Phys. Chem. 99, 16810–16813.

Miyazaki, J., Hideg, K., Marsh, D., 1992. Interfacial ionization and partitioning of membrane-bound local anaesthetics. Biochim. Biophys. Acta 1103, 62–68.

Morgan, M.E., Liu, K., Anderson, B.D., 1998. Microscale titrimetric and spectrophotometric methods for determination of ionization constants and partition coefficients of new drug candidates. J. Pharm. Sci. 87, 238–245.

Moriguchi, I., Hirono, S., Liu, Q., Nakagome, I., Matsushita, Y., 1992. Simple method of calculating octanol/water partition coefficient. Chem. Pharm. Bull. 40, 127–130.

Murtomäki, L., Kontturi, K., 2002. Correction to electrochemical determination of partition coefficients of drugs. J Pharm. Sci. 91, 900–901 [J. Pharm Sci 81 (1992) 970–974].

Mälkiä, A., Liljeroth, P., Kontturi, A.-K., Kontturi, K., 2001a. Electrochemistry at lipid monolayer-modified liquid–liquid interfaces as an improvement to drug partitioning studies. J. Phys. Chem. B 105, 10884–10892.

Mälkiä, A., Liljeroth, P., Kontturi, K., 2001b. Drug transfer through biomimetic Langmuir–Blodgett monolayers at a liquid–liquid interface. Anal. Sci. 17 (Suppl.), i345–i348.

Neubert, R., 1989. Ion-pair transport across membranes. Pharm. Res. 6, 743–747.

Nirmalakhandan, N., Speece, R.E., 1988. Structure–activity relationships. Quantitative techniques for predicting the behaviour of chemicals in the ecosystem. Environ. Sci. Technol. 22, 606–615.

Norinder, U., Haeberlein, M., 2002. Computational approaches to the prediction of the blood–brain distribution. Adv. Drug Deliv. Rev. 54, 291–313.

Norinder, U., Österberg, T., 2001. Theoretical calculation and prediction of drug transport processes using simple parameters and partial least

squares projections to latent structures (PLS) statistics. The use of electrotopological state indices. J. Pharm. Sci. 90, 1076–1085.

Norinder, U., Österberg, T., Artursson, P., 1999. Theoretical calculation and prediction of intestinal absorption of drugs in humans using MolSurf parametrization and PLS statistics. Eur. J. Pharm. Sci. 8, 49–56.

Norinder, U., Österberg, T., Artursson, P., 1997. Theoretical calculation and prediction of Caco-2 cell permeability using MolSurf parametrization and PLS statistics. Pharm. Res. 14, 1786–1791.

Nys, G.G., Rekker, R.F., 1973. Statistical analysis of a series of partition coefficients with special reference to the predictability of folding of drug molecules. Introduction of hydrophobic fragmental constants (f values). Chim. Ther. 8, 521–535.

Ollila, F., Halling, K., Vuorela, P., Vuorela, H., Slotte, J.P., 2002. Characterization of flavonoid-biomembrane interactions. Arch. Biochem. Biophys. 399, 103–108.

Österberg, T., Norinder, U., 2000. Prediction of polar surface area and drug transport processes using simple parameters and PLS statistics. J. Chem. Inf. Comput. Sci. 40, 1408–1411.

Ong, S., Pidgeon, C., 1995. Thermodynamics of solute partitioning into immobilized artificial membranes. Anal. Chem. 67, 2119–2128.

Ong, S., Liu, H., Pidgeon, C., 1996. Immobilized-artificial-membrane chromatography: measurements of membrane partition coefficient and predicting drug membrane permeability. J. Chromatogr. A 728, 113–128.

Osakai, T., Ebina, K., 1998. Non-Bornian theory of the Gibbs energy of ion transfer between two immiscible liquids. J. Phys. Chem. B 102, 5691–5698.

Osakai, T., Ogata, A., Ebina, K., 1997. Hydration of ions in organic solvent and its significance in the Gibbs energy of ion transfer between two immiscible liquids. J. Phys. Chem. B 101, 8341–8348.

Ottiger, C., Wunderli-Allenspach, H., 1999. Immobilized artificial membrane (IAM)-HPLC for partition studies of neutral and ionised acids and bases in comparison with the liposomal partition system. Pharm. Res. 16, 643–650.

Pagliara, A., Carrupt, P.-A., Caron, G., Gaillard, P., Testa, B., 1997. Lipophilicity profiles of ampholytes. Chem. Rev. 97, 3385–3400.

Pagliara, A., Khamis, E., Trinh, A., Carrupt, P.-A., Tsai, R.-S., Testa, B., 1995. Structural properties governing retention mechanisms on RP-HPLC stationary phases used for lipophilicity measurements. J. Liq. Chromatogr. 18, 1721–1745.

Palm, K., Luthman, K., Ros, J., Gråsjö, J., Artursson, P., 1999. Effect of molecular charge on intestinal epithelial drug transport: pH-dependent transport of cationic drugs. J. Pharmacol. Exp. Ther. 291, 435–443.

Palm, K., Luthman, K., Ungell, A.-L., Strandlund, G., Beigi, F., Lundahl, P., Artursson, P., 1998. Evaluation of dynamic polar molecular surface area as predictor of drug absorption: comparison with other computational and experimental predictors. J. Med. Chem. 41, 5382–5392.

Palm, K., Stenberg, P., Luthman, K., Artursson, P., 1997. Polar molecular surface properties predict the intenstinal absorption of drugs in humans. Pharm. Res. 14, 568–571.

Palm, K., Luthman, K., Ungell, A.-L., Strandlund, G., Artursson, P., 1996. Correlation of drug absorption with molecular surface properties. J. Pharm. Sci. 85, 32–39.

Parker, A.J., 1969. Protic-dipolar aprotic solvent effects on rates of bimolecular reactions. Chem. Rev. 69, 1–32.

Parsegian, A., 1969. Energy of an ion crossing a low dielectric membrane: solutions to four relevant electrostatic problems. Nature 221, 844–846.

Petty, M.C., 1996. Langmuir–Blodgett Films: An Introduction. University Press, Cambridge, p. 234.

Petty, M.C., Barlow, W.A., 1990. Film deposition. In: Roberts, G.G. (Ed.), Langmuir–Blodgett Films. Plenum Press, New York, pp. 93–132.

Pickett, S.D., McLay, I.M., Clark, D.E., 2000. Enhancing the hit-to-lead properties of lead optimization libraries. J. Chem. Inf. Comput. Sci. 40, 263–272.

Platts, J.A., Abraham, M.H., Zhao, Y.H., Hersey, A., Ijaz, L., Butina, D., 2001. Correlation and prediction of a large blood—brain distribution data set—an LFER study. Eur. J. Med. Chem. 36, 719–730.

Platts, J.A., Abraham, M.H., Butina, D., Hersey, A., 2000. Estimation of molecular linear free energy relationship descriptors by a group contribution approach. 2. Prediction of partition coefficients. J. Chem. Inf. Comput. Sci. 40, 71–80.

Platts, J.A., Butina, D., Abraham, M.H., Hersey, A., 1999. Estimation of molecular linear free energy relation descriptors using a group contribution approach. J. Chem. Inf. Comput. Sci. 39, 835–845.

Prentis, R.A., Lis, Y., Walker, S.R., 1988. Pharmaceutical innovation by the seven UK-owned pharmaceutical companies (1964–1985). Br. J. Clin. Pharmacol. 25, 387–396.

Reichel, A., Begley, D.J., 1998. Potential of immobilized artificial membranes for predicting drug penetration across the blood–brain barrier. Pharm. Res. 15, 1270–1274.

Rey, S., Caron, G., Ermondi, G., Gaillard, P., Pagliara, A., Carrupt, P.-A., Testa, B., 2001. Development of molecular hydrogen-bonding potentials (MHBPs) and their application to structure–permeation relations. J. Mol. Graph. Model. 19, 521–535.

Reymond, F., 2001. Transfer mechanisms and lipophilicity of ionizable drugs. In: Volkov, A.G. (Ed.), Liquid Interfaces in Chemical, Biological, and Pharmaceutical Applications. Marcel Dekker, New York, pp. 729–773.

Reymond, F., Chopineaux-Courtois, V., Steyaert, G., Bouchard, G., Carrupt, P-A., Testa, B., Girault, H.H., 1999a. Ionic partition diagrams of ionisable drugs: pH-lipophilicity profiles, transfer mechanisms and charge effects on solvation. J. Electroanal. Chem. 462, 235–250.

Reymond, F., Steyaert, G., Carrupt, P.-A., Morin, D., Tillement, J.-P., Girault, H.H., Testa, B., 1999b. The pH-partition profile of the anti-ischemic drug trimetazidine may explain its reduction of intracellular acidosis. Pharm. Res. 16, 616–624.

Reymond, F., Steyaert, G., Carrupt, P.-A., Testa, B., Girault, H., 1996a. Ionic partition diagrams: a potential–pH representation. J. Am. Chem. Soc. 118, 11951–11957.

Reymond, F., Steyaert, G., Pagliara, A., Carrupt, P.-A., Testa, B., Girault, H.H., 1996b. Transfer mechanism of ionic drugs: piroxicam as an agent facilitating proton transfer. Helv. Chim. Acta 79, 1651–1669.

Rhee, D., Markovich, R., Chae, W.G., Qiu, X., Pidgeon, C., 1994. Chromatographic surfaces prepared from lyso phosphatidylcholine ligands. Anal. Chim. Acta 297, 377–386.

Rose, K., Hall, L.H., Kier, L.B., 2002. Modeling blood–brain barrier partitioning using the electrotopological state. J. Chem. Inf. Comput. Sci. 42, 651–666.

Salminen, T., Pulli, A., Taskinen, J., 1997. Relationship between immobilized artificial membrane chromatographic retention and the brain penetration of structurally diverse drugs. J. Pharm. Biomed. Anal. 15, 469–477.

Samec, Z., Langmaier, J., Trojánek, A., 1996. Polarization phenomena at the water-nitrophenyl octyl ether interface. Part 1. Evaluation of the standard Gibbs energies of ion transfer from the solubility and voltammetric measurements. J. Electroanal. Chem. 409, 1–7.

Scherrer, R.A., 1984. The treatment of ionizable compounds in quantitative structure-activity studies with special consideration to ion partitioning. ACS Symp. Ser. 255 (Pestic. Synth. Ration. Approaches), 225–246.

Seelig, A., Seelig, J., 1974. The dynamic structure of fatty acyl chains in a phospholipid bilayer measured by deuterium magnetic resonance. Biochemistry 13, 4839–4845.

Senda, M., Kakiuchi, T., Osakai, T., 1991. Electrochemistry at the interface between two immiscible electrolyte solutions. Electrochim. Acta 36, 253–262.

Sheng, Q., Schulten, K., Pidgeon, C., 1995. Molecular dynamics simulation of immobilized artificial membranes. J. Phys. Chem. 99, 11018–11027.

Spencer, J.N., Gleim, J.E., Blevins, C.H., Garrett, R.C., Mayer, F.J., 1979. Enthalpies of solution and transfer enthalpies. An analysis of the pure

base calorimetric method for the determination of hydrogen bond enthalpies. J. Phys. Chem. 83, 1249–1255.

Spessard, G.O., 1998. ACD Labs/LogP dB 3.5 and ChemSketch 3.5. J. Chem. Inf. Comput. Sci. 38, 1250–1253.

Stenberg, P., Norinder, U., Luthman, K., Artursson, P., 2001. Experimental and computational screening models for the prediction of intestinal drug absorption. J. Med. Chem. 44, 1927–1937.

Stenberg, P., Luthman, K., Artursson, P., 1999. Prediction of membrane permeability to peptides from calculated dynamic molecular surface properties. Pharm. Res. 16, 205–212.

Stewart, B.H., Chan, O.H., 1998. Use of immobilized artificial membrane chromatography for drug transport applications. J. Pharm. Sci. 87, 1471–1478.

Stewart, B.H., Chung, F.Y., Tait, B., John, C., Chan, O.H., 1998. Hydrophobicity of HIV protease inhibitors by immobilized artificial membrane chromatography: applications and significance to drug transport. Pharm. Res. 15, 1401–1406.

Steyaert, G., Lisa, G., Gaillard, P., Boss, G., Reymond, F., Girault, H.H., Carrupt, P.-A., Testa, B., 1997. Intermolecular forces expressed in 1,2-dichloroethane-water partition coefficients. A solvatochromic analysis. J. Chem. Soc., Faraday Trans. 93, 401–406.

Sugawara, M., Takekuma, Y., Yamada, H., Kobayashi, M., Iseki, K., Miyazaki, K., 1998. A general approach for the prediction of the intestinal absorption of drugs: regression analysis using the physicochemical properties and drug–membrane electrostatic interaction. J. Pharm. Sci. 87, 960–966.

Suhonen, T.M., Pasonen-Seppänen, S., Kirjavainen, M., Tammi, M., Tammi, R., Urtti, A., 2003. The permeability barrier in organotypic culture model derived from rat epidermal keratinocytes. Eur. J. Pharm. Sci. 20, 107–113.

Suhonen, P., Järvinen, T., Koivisto, S., Urtti, A., 1998. Different effects of pH on the permeation of pilocarpine and pilocarpine prodrugs across the isolated rabbit cornea. Eur. J. Pharm. Sci. 6, 169–176.

Surewicz, W.K., Leyko, W., 1981. Interaction of propranolol with model phospholipid membranes. Monolayer, spin label and fluorescence spectroscopy studies. Biochim. Biophys. Acta 643, 387–397.

Syracuse Research Corporation, 301 Plainfield Road, Suite 350, Syracuse, New York 13212-2510, http://www.syrres.com/.

Taft, R.W., Berthelot, M., Laurence, C., Leo, A., 1996. Hydrogen bonds and molecular structure, CHEMTECH, 20–29 July.

Taft, R.W., Abraham, M.H., Famini, G.R., Doherty, R.M., Abboud, J.L., Kamlet, M.J., 1985a. Solubility properties in polymers and biological media 5: an analysis of the physicochemical properties which influence octanol–water partition coefficients of aliphatic and aromatic solutes. J. Pharm. Sci. 74, 807–814.

Taft, R.W., Abraham, M.H., Doherty, R.M., Kamlet, M.J., 1985b. Linear solvation energy relationships. 29. Solution properties of some tetraalkylammonium halide ion pairs and dissociated ions. J. Am. Chem. Soc. 107, 3105–3110.

Taillardat-Bertschinger, A., Carrupt, P.-A., Barbato, F., Testa, B., 2003. Immobilized artificial membrane HPLC in drug research. J. Med. Chem. 46, 655–665.

Taillardat-Bertschinger, A., Galland, A., Carrupt, P.-A., Testa, B., 2002a. Immobilized artificial membrane liquid chromatography: proposed guidelines for technical optimization of retention measurements. J. Chromatogr. A 953, 39–53.

Taillardat-Bertschinger, A., Marca Martinet, C.A., Carrupt, P.-A., Reist, M., Caron, G., Fruttero, R., Testa, B., 2002b. Molecular factors influencing retention on immobilized artificial membranes (IAM) compared to partitioning in liposomes and *n*-octanol. Pharm. Res. 19, 729–737.

Takács-Novák, K., Szász, G., 1999. Ion-pair partition of quaternary ammonium drugs: the influence of counter ions of different lipophilicity, size and flexibility. Pharm. Res. 16, 1633–1638.

Tavelin, S., Taipalensuu, J., Hallböök, F., Vellonen, K.-S., Moore, V., Artursson, P., 2003a. An improved cell culture model based on 2/4/A1 cell monolayers for studies of intestinal drug transport: characterization of transport routes. Pharm. Res. 20, 373–381.

Tavelin, S., Taipalensuu, J., Söderberg, L., Morrison, R., Chong, S., Artursson, P., 2003b. Prediction of the oral absorption of low-permeability drugs using small intestine-like 2/4/A1 cell monolayers. Pharm. Res. 20, 397–405.

Testa, B., Carrupt, P.-A., Gaillard, P., Billois, F., Weber, P., 1996. Lipophilicity in molecular modelling. Pharm. Res. 13, 335–343.

Toropainen, E., Ranta, V.P., Palmgren, J., Vellonen, K.S., Talvitie, A., Suhonen, P., Hämäläinen, K.M., Auriola, S., Urtti, A., 2003. Paracellular and transcellular permeability in human corneal epithelial cell culture model. Eur. J. Pharm. Sci. 20, 99–106.

Tu, K., Tobias, D.J., Klein, M.L., 1995. Constant pressure and temperature molecular dynamics simulation of a fully hydrated liquid crystal phase dipalmitoylphosphatidylcholine bilayer. Biophys. J. 69, 2558–2562.

Vaes, W.H.J., Urrestarazu Ramos, E., Verhaar, H.J.M., Cramer, C.J., Hermens, J.L.M., 1998. Understanding and estimating membrane/water partition coefficients: approaches to derive quantitative structure property relationships. Chem. Res. Toxicol. 11, 847–854.

Valko, K., Du, C.M., Bevan, C.D., Reynolds, D.P., Abraham, M.H., 2000. Rapid-gradient HPLC method for measuring drug interactions with immobilized artificial membrane: comparison with other lipophilicity measures. J. Pharm. Sci. 89, 1085–1096.

van de Waterbeemd, H., 2000. Intestinal permeability: prediction from theory. Drugs Pharm. Sci. 106, 31–49.

van de Waterbeemd, H., Kansy, M., 1992. Hydrogen-bonding capacity and brain penetration. Chimia 46, 299–303.

van de Waterbeemd, H., Smith, D.A., Beaumont, K., Walker, D.K., 2001. Property-based design: optimization of drug absorption and pharmacokinetics. J. Med. Chem. 44, 1313–1333.

van de Waterbeemd, H., Camenisch, G., Folkers, G., Chretien, J.R., Raevsky, O.A., 1998. Estimation of blood–brain barrier crossing of drugs using molecular size and shape, and H-bonding descriptors. J. Drug Target. 6, 151–165.

Vanýsek, P., 1995. Charge transfer processes on liquid/liquid interfaces: the first century. Electrochim. Acta 40, 2841–2847.

Veber, D.F., Johnson, S.R., Cheng, H.-Y., Smith, B.R., Ward, K.W., Kopple, K.D., 2002. Molecular properties that influence the oral bioavailability of drug candidates. J. Med. Chem. 45, 2615–2623.

von Itzstein, M., Wu, W.-Y., Kok, G.B., Pegg, M.S., Dyason, J.C., Jin, B., Phan, T.V., Smythe, M.L., White, H.F., Oliver, S.W., Colman, P.M., Varghese, J.N., Ryan, D.M., Woods, J.M., Bethell, R.C., Hotham, V.J., Cameron, J.M., Penn, C.R., 1993. Rational design of potent sialidase-based inhibitors of influenza virus replication. Nature 363, 418–423.

Walter, E., Kissel, T., 1995. Heterogeneity in the human intestinal cell line Caco-2 leads to differences in transepithelial transport. Eur. J. Pharm. Sci. 3, 215–230.

Weininger, D., 1988. SMILES, a chemical language and information system. 1. Introduction to methodology and encoding rules. J. Chem. Inf. Comput. Sci. 28, 31–36.

Wessel, M.D., Jurs, P.C., Tolan, J.W., Muskal, S.M., 1998. Prediction of human intestinal absorption of drug compounds from molecular structure. J. Chem. Inf. Comput. Sci. 38, 726–735.

Wils, P., Warnery, A., Phung-ba, V., Legrain, S., Scherman, D., 1994. High lipophilicity decreases drug transport across intestinal epithelial cells. J. Pharmacol. Exp. Ther. 269, 654–658.

Wilson, L.Y., Famini, G.R., 1991. Using theoretical descriptors in quantitative structure-activity relationships: some toxicological indices. J. Med. Chem. 34, 1668–1674.

Wilson, M.A., Pohorille, A., 1996. Mechanism of unassisted ion transport across membrane bilayers. J. Am. Chem. Soc. 118, 6580–6587.

Winiwarter, S., Ax, F., Lennernäs, H., Hallberg, A., Pettersson, C., Karlén, A., 2003. Hydrogen bonding descriptors in the prediction of human in vivo intestinal permeability. J. Mol. Graph. Model. 21, 273–287.

Winiwarter, S., Bonham, N.M., Ax, F., Hallberg, A., Lennernäs, H., Karlén, A., 1998. Correlation of human jejunal permeability (in vivo) of drugs with experimentally and theoretically derived parameters. A multivariate data analysis approach. J. Med. Chem. 41, 4939–4949.

Wohnsland, F., Faller, B., 2001. High-throughput permeability pH profile and high-throughput alkane/water log P with artificial membranes. J. Med. Chem. 44, 923–930.

Wold, S., 1979. Cross-validatory estimation of the number of components in factor and principal components models. Technometrics 20, 379–405.

Yang, C.Y., Cai, S.J., Liu, H., Pidgeon, C., 1996. Immobilized artificial membranes: screens for drug membrane interactions. Adv. Drug Deliv. Rev. 23, 229–256.

Yee, S., 1997. In vitro permeability across Caco-2 cells (colonic) can predict in vivo (small intestinal) absorption in man: fact or myth. Pharm. Res. 14, 763–766.

Young, R.C., Mitchell, R.C., Brown, T.H., Ganellin, C.R., Griffiths, R., Jones, M., Rana, K.K., Saunders, D., Smith, I.R., Sore, N.E., Wilks, T.J., 1988. Development of a new physicochemical model for brain penetration and its application to the design of centrally acting H2 receptor histamine antagonists. J. Med. Chem. 31, 656–671.

Zhao, Y.H., Abraham, M.H., Le, J., Hersey, A., Luscombe, C.N., Beck, G., Sherborne, B., Cooper, I., 2002. Rate-limited steps of human oral absorption and QSAR studies. Pharm. Res. 19, 1446–1457.

Zhao, Y.H., Le, J., Abraham, M.H., Hersey, A., Eddershaw, P.J., Luscombe, C.N., Boutina, D., Beck, G., Sherborne, B., Cooper, I., Platts, J.A., 2001. Evaluation of human intestinal absorption data and subsequent derivation of a quantitative structure-activity relationship (QSAR) with the Abraham descriptors. J. Pharm. Sci. 90, 749–784.

Zhu, C., Jiang, L., Chen, T.-M., Hwang, K.-K., 2002. A comparative study of artificial membrane permeability assay for high throughput profiling of drug absorption potential. Eur. J. Med. Chem. 37, 399–407.

0090-9556/04/3205-566–571$20.00
DRUG METABOLISM AND DISPOSITION
Copyright © 2004 by The American Society for Pharmacology and Experimental Therapeutics
DMD 32:566–571, 2004

Vol. 32, No. 5
1347/1149053
Printed in U.S.A.

PHARMACOKINETICS AND METABOLISM OF LUMIRACOXIB IN HEALTHY MALE SUBJECTS

James B. Mangold, Helen Gu, Lolita C. Rodriguez, Johanne Bonner, Janet Dickson, and Christiane Rordorf

Preclinical Safety–ADME, Novartis Pharmaceuticals Corporation, East Hanover, New Jersey (J.B.M., H.G., L.C.R.); Clinical Pharmacology, Novartis Pharmaceuticals Research Centre, Horsham, United Kingdom (J.B.); Inveresk Research, Tranent, Scotland (J.D.); and Novartis Pharma AG, Basel, Switzerland (C.R.)

Received December 1, 2003; accepted February 11, 2004

This article is available online at http://dmd.aspetjournals.org

ABSTRACT:

Lumiracoxib (Prexige; 2-[(2-fluoro-6-chlorophenyl)amino]-5-methyl-benzeneacetic acid) is a novel, chemically distinct cyclooxygenase-2 selective inhibitor, which has been developed for the treatment of osteoarthritis, rheumatoid arthritis, and acute pain. The absorption, metabolism, disposition, and mass balance of [^{14}C]lumiracoxib were investigated in four healthy male subjects after a single 400-mg oral dose. Serial blood and complete urine and feces were collected for 168 h postdose. Lumiracoxib was rapidly absorbed, achieving mean plasma concentrations >1 μg/ml within 1 h of dosing. Unchanged drug in plasma accounted for 81 to 91% of radioactivity up to 2.5 h postdose, suggesting a modest first-pass effect; unchanged drug was the major circulating component in plasma, accounting for ~43% of the $AUC_{0\ to\ 24h}$. The terminal half-life of lumiracoxib in plasma was 6.5 h. Major plasma metabolites were the 5-carboxy, 4′-hydroxy, and 4′-hydroxy-5-carboxy derivatives. Excretion involved both renal (54.1%) and fecal (42.7%) routes, and dose recovery was almost complete (96.8%). Lumiracoxib was extensively metabolized before excretion, with little unchanged drug in urine (3.3% of dose) or feces (2.0% of dose). The major metabolic pathways of lumiracoxib were oxidation of the 5-methyl group and hydroxylation of the dihaloaromatic ring. Glucuronic acid conjugates of lumiracoxib metabolites (and to a minor extent lumiracoxib itself) were identified, although there was no evidence of cysteine, mercapturic acid, or glutathione conjugates. In summary, orally administered lumiracoxib is rapidly absorbed and undergoes extensive metabolism before excretion via urine and feces, with no evidence of formation of potentially reactive metabolites.

Traditional nonselective nonsteroidal anti-inflammatory drugs (NSAIDs[1]) are the mainstay of therapy for osteoarthritis, rheumatoid arthritis, and acute pain, although their long-term use is associated with gastrointestinal (GI) ulceration and serious GI complications such as perforation and bleeding (Hernandez-Diaz and Garcia-Rodriguez, 2001). This is thought to be due to local inhibition of the cyclooxygenase (COX)-1 enzyme, which generates prostaglandins that are normally cytoprotective in the GI tract (Crofford, 1997; Warner et al., 1999). The identification of a second isoform, COX-2, which is up-regulated as a result of inflammation (Fu et al., 1990), provided the impetus for the development of COX-2 selective inhibitors (Flower, 2003). Subsequently, the COX-2 selective inhibitors have been shown to have efficacy comparable with NSAIDs but a superior GI safety profile during long-term use (Bombardier et al., 2000; Goldstein et al., 2001).

Lumiracoxib (Prexige; 2-[(2-fluoro-6-chlorophenyl)amino]-5-methyl-benzeneacetic acid) is a COX-2 selective inhibitor (Marshall et al., 2002), which has been developed for the treatment of osteoarthritis, rheumatoid arthritis, and acute pain. Lumiracoxib is chemically distinct from other COX-2 selective inhibitors in that it has a carboxylic acid group that confers weakly acidic properties (pK_a 4.7; Fig. 1). This structure may be the reason for its distinct pharmacokinetic and pharmacodynamic profile. For example, lumiracoxib is characterized by rapid absorption (t_{max} 2 h) and sustained higher concentrations in synovial fluid versus plasma (2- to 3-fold from 12 to 24 h postdose) in patients with rheumatoid arthritis (Reynolds et al., 2003), the latter being a characteristic typically associated with the acidic nature of traditional NSAIDs (Rainsford et al., 1981; Bruno et al., 1988; Day et al., 1999).

Lumiracoxib has been shown to demonstrate dose-proportional and time-independent pharmacokinetics in single- and multiple-dose studies in healthy subjects and patients with osteoarthritis, at doses up to 800 mg once daily (Rordorf et al., 2002; Scott et al., 2002a,b, 2003a). In addition, near dose-proportional pharmacokinetics have been observed in patients with rheumatoid arthritis at doses up to 1200 mg once daily, with no accumulation and maintenance of COX-2 selectivity (Scott et al., 2003b). Lumiracoxib also demonstrates good oral bioavailability of 74% (Hartmann et al., 2003) and is rapidly and

[1] Abbreviations used are: NSAID, nonsteroidal anti-inflammatory drug; GI, gastrointestinal; COX, cyclooxygenase; HPLC, high performance liquid chromatography; LSC, liquid scintillation counting; MS, mass spectrometry; $AUC_{0-\infty}$, area under the concentration-time curve from time zero to infinity; AUC_{0-24h}, area under the concentration-time curve from time zero to 24 h; t_{max}, time to maximum concentration; CL/F, apparent plasma clearance.

Address correspondence to: Dr. James B. Mangold, Preclinical Safety–ADME, Novartis Pharmaceuticals Corporation, East Hanover; NJ 07936. E-mail: james.mangold@pharma.novartis.com

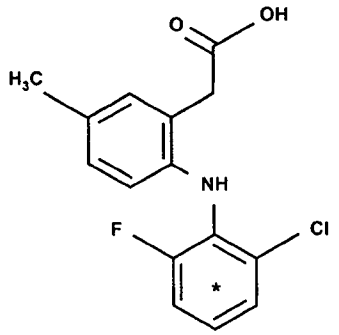

FIG. 1. *Structure of [^{14}C]lumiracoxib (* indicates uniform distribution of ^{14}C-label).*

efficiently absorbed from all regions of the GI tract (Wilding et al., 2004). In vitro, lumiracoxib is extensively metabolized by the hepatic cytochrome P450 isozyme CYP2C9 (Novartis data on file). In vivo, lumiracoxib showed no significant pharmacokinetic interaction with *R*- or *S*-warfarin, a particularly sensitive CYP2C9 substrate (Bonner et al., 2003), and fluconazole, a potent CYP2C9 inhibitor, had no clinically significant effect on the pharmacokinetics of lumiracoxib (Yih et al., 2003). The present study was conducted to characterize the absorption, metabolism, disposition, and mass balance of a single 400-mg oral dose of [^{14}C]lumiracoxib in healthy male subjects.

Materials and Methods

Study. Four healthy male, nonsmoking subjects, aged 39 to 51 years, participated in this open-label study. The study was conducted in accordance with Good Clinical Practice guidelines and the Declaration of Helsinki (1964 and subsequent revisions), and all subjects gave written informed consent before participation. Subjects were genotyped with regard to hepatic cytochrome P450 2C9, with genotypes corresponding to "poor metabolizer" status excluded from the study. Subjects were admitted to the study site at least 20 h before dosing. Blood was collected by either direct venipuncture or an indwelling cannula into lithium heparin tubes predose and at 0.5, 1, 1.5, 2, 2.5, 3, 4, 6, 8, 12, 24, 36, 48, 72, 96, 120, 144, and 168 h postdose. Plasma was prepared within 30 min of sampling by centrifugation between 3°C and 5°C for 15 min at approximately 800*g*. Urine was collected predose and at 0 to 8, 8 to 24, 24 to 48, 48 to 72, 72 to 96, 96 to 120, 120 to 144, and 144 to 168 h postdose. Fecal samples were collected predose and thereafter up to study completion. Blood, plasma, urine, and feces were stored at ≤−20°C until analysis.

Study Medication. All subjects received a single 400-mg oral dose of [^{14}C]lumiracoxib (prepared by the Isotope Laboratory, Novartis Pharmaceuticals Corporation, East Hanover, NJ), containing a mean dose of radioactivity of 87.2 μCi, in the form of two capsules. The ^{14}C label was uniformly distributed in the dihaloaromatic ring, as shown in Fig. 1. The radioactive label had a specific activity of 0.21 μCi/mg and a radiochemical purity of 98%. No medication other than study drug was allowed from 14 days before lumiracoxib dosing until all study completion evaluations were complete.

Analysis of Unchanged Lumiracoxib. Plasma concentrations of unchanged lumiracoxib were measured using a validated HPLC assay (range, 10–5000 ng/ml). Acidified plasma (0.5 ml) was extracted using pentane/methyl chloride (2:1, v/v). The organic layer was dried and reconstituted in 200 μl of water/methanol (80:20, v/v). Chromatographic separation was achieved at 40°C on a 5-μm fluoro SEP RP octyl HPLC column (3.2 mm × 150 mm). A linear elution gradient (24–80% acetonitrile in 0.05% phosphoric acid) was run over 15 min at 1.0 ml/min, and the analytes were monitored using UV detection at 270 nm. A derivative of lumiracoxib was used as an internal standard. Noncompartmental pharmacokinetic parameters were derived using standard methods.

Total Radioactivity Measurement and Sample Preparation for Characterization of Lumiracoxib Metabolites. For blood, plasma, urine, and feces, levels of total radioactivity were determined in aliquots of each sample by liquid scintillation counting (LSC). LSC for plasma, urine, and other clear samples used Quickszint 1 liquid (Zinsser Analytic GmbH, Frankfurt, Germany) or Flo-Scint II (PerkinElmer Life and Analytical Sciences, Boston, MA) scintillation fluid. Whole blood and fecal samples were combusted before LSC (Packard Tri-Carb 306 sample oxidizer, Carbo-Sorb CO_2 absorbing fluid, and Permafluor E+ scintillation fluid). For extracts, extraction efficiency was calculated based on the total radioactivity in the original aliquot and the resulting extract.

Plasma. For metabolite profiles, equal volumes of plasma from each subject per time point were pooled and extracted twice with acetonitrile (6 ml and 3 ml, respectively). The combined extracts were evaporated to dryness with a stream of nitrogen at 37°C (Turbo-vap LV; Caliper Life Sciences, Hopkintown, MA), reconstituted with water/methanol/acetonitrile (8:1:1, v/v, 150 μl), vortex-mixed, and centrifuged. An aliquot of 20 μl was used to determine total radioactivity using a Packard 2550TR liquid scintillation counter, and 100 to 120 μl was analyzed by HPLC to obtain the metabolite profile.

Urine. Frozen urine samples were thawed at room temperature and filtered through a 0.45-μm nylon filter. Aliquots of 200 μl were assayed in duplicate for total radioactivity using the Packard 2550TR liquid scintillation counter. An aliquot of 5 ml (from 0- to 8-h and 8- to 24-h samples) and 10 ml (24- to 48-h samples) from each subject was lyophilized in a FLEXI-DRY freeze-dryer (FTS/Kinetics Thermal Systems, Stone Ridge, NY). The residue was reconstituted with methanol/water (2:8, v/v, 1 ml), vortex-mixed, and centrifuged at approximately 2000*g* at 18°C for 5 min. A 120-μl aliquot was analyzed by HPLC to obtain the metabolite profile.

Feces. For metabolite profiles, aliquots of dried fecal samples for each subject were pooled to encompass ≥95% of the total fecal radioactivity excretion. Each pooled sample was then extracted with methanol (three times, ~150 ml) by shaking vigorously for 5 min. Each sample was centrifuged between extractions, and the extract was separated from the post-extract solid by decanting. The methanol extracts were combined and partitioned with an equal volume of hexane to remove fatty material. Duplicate aliquots of the methanol layer were then analyzed for total radioactivity using the Packard 2550TR liquid scintillation counter. Each methanol extract was then evaporated to dryness and then reconstituted with ~8 ml of methanol, transferred to plastic centrifuge tubes, vortex-mixed, and sonicated for ~3 min. One milliliter of the suspension was transferred to a clean tube, assayed in duplicate for radioactivity, and then centrifuged at ~2000*g* at 18°C for 5 min. An aliquot of the supernatant was then analyzed by HPLC to obtain the metabolite profile.

Metabolite Analysis by HPLC. Metabolites in plasma, urine, and fecal extract samples were resolved using a Waters Alliance HPLC System, model 2690, with Millenium32 software (Waters, Milford, MA) . The HPLC system incorporated an Inertsil ODS-2 (4.6 × 250 mm × 5 μm column; GL Sciences, Inc., Tokyo, Japan); mobile phases, A = 0.02 M ammonium acetate (pH ~6), B = acetonitrile; flow rate, 1.0 ml/min; ultraviolet detector wavelength, 280 nm. The HPLC apparatus was connected in series to a Waters photodiode array detector (model 996) and an IN/US βRAM radioactivity detector (IN/US Systems, Tampa, FL) or a Gilson fraction collector (model FC204; Gilson, Inc., Middleton, WI). The gradient elution program was as follows (all gradient steps were linear): 0 to 2 min, 0% solvent B; 2 to 5 min, 0 to 15% solvent B; 5 to 10 min, 15% solvent B; 10 to 25 min, 15 to 30% solvent B; 25 to 40 min, 30 to 50% solvent B; 40 to 45 min, 50 to 100% solvent B; 45 to 55 min, 100% solvent B. Total HPLC flow was divided (1:1) into the MS electrospray ionization source and radioactivity detector after diversion of the first 2 min to waste.

After the injection of plasma or urinary extracts, column eluent was sampled at 0.2 min/well intervals using the fraction collector directly into 96-Deep Well LumaPlates (PerkinElmer Life and Analytical Sciences). The plates were dried in a SPE DRY-96 (Argonaut, Foster City, CA) at 45°C using a stream of nitrogen. Each plate was assayed for radioactivity at 10 min/well in a Packard TopCount radioactivity detector (model NXT). Fecal extracts were analyzed using HPLC with online radioactivity detection. The column effluent (1 ml/min) was mixed with liquid scintillant at a flow rate of 3 ml/min (Flo-Scint II; PerkinElmer Life and Analytical Sciences).

Metabolite Identification by Liquid Chromatography/MS and NMR. Metabolites were identified in pooled human urine, feces, and plasma samples using either a Waters Alliance HPLC 2690 equipped with a Finnigan LCQ (ion trap) MS and an IN/US βRAM radioactivity detector or a Shimadzu HPLC equipped with a Sciex API-3000 (triple quadrupole) MS (PerkinElmerSciex

TABLE 1

Pharmacokinetic parameters for lumiracoxib in plasma and total radioactivity concentrations in blood and plasma

Values are mean ± S.D., except for t_{max}, which are median (range).

	Plasma Lumiracoxib[a]	Blood Radioactivity[b]	Plasma Radioactivity
C_{max} (μg Eq/ml)	7.28 ± 1.39	6.88 ± 0.57	12.0 ± 1.58
t_{max} (h)	4.0 (2.5–4.0)	4.0 (4.0–6.0)	4.0 (4.0–6.0)
AUC_{0-168h} (μg Eq · h/ml)	48.4 ± 6.15	85.6 ± 10.6	187 ± 29.7
$AUC_{0-\infty}$ (μg Eq · h/ml)	48.4 ± 6.12	89.6 ± 11.0	240 ± 30.5
$t_{1/2,z}$ (h)	6.54 ± 1.43	8.59 ± 1.25	186 ± 43
CL/F (l/h)	8.36 ± 1.04		

[a] C_{max} and AUC values for plasma lumiracoxib are expressed as μg/ml or μg · h/ml, respectively.
[b] C_{max} and AUC values for blood are expressed as μg Eq/g or μg Eq · h/g, respectively.

Instruments, Boston, MA). The chromatographic separation was the same as that used for generating the metabolite profiles.

The LCQ-MS was operated in negative ion mode with capillary temperature at 225°C, spray needle voltage at −4.0 kV, and sheath gas pressure and auxiliary gas flow at 80 and 30 arbitrary units, respectively. The Sciex API-3000 MS was operated in the positive ion mode with a Turbo Ion Spray probe temperature of 380°C; ionization voltage, 5 kV; nitrogen curtain and nebulizer gas setting, 11; collision energy, 15~25 eV; declustering and focusing potentials, 80 and 260 V, respectively. Metabolites associated with peaks in the chromatogram were identified based on their observed mass and fragmentation behavior. Additionally, the presence of the expected chlorine isotope pattern provided further verification of suspected drug-related metabolites. In cases where synthetic reference standards were available, chromatographic retention times and MS results were used to further support the structural assignment.

Confirmatory identification of 4′-hydroxy (4′-OH) metabolites (M5 and M23) in selected lyophilized plasma, urine, and feces samples was performed using HPLC coupled to ^{19}F NMR and proton NMR (^{1}H NMR). The HPLC system used for ^{19}F NMR consisted of a Bruker LC22C pump, a Bischoff UV detector, and a Bruker Peak Sampling Unit; the ^{19}F NMR analysis of lumiracoxib samples and reference lumiracoxib analogs was accomplished using a Bruker DMX500 spectrometer equipped with a 4-mm inverse triple (^{1}H, ^{13}C, ^{31}P) flow probe with a shielded Z-axis gradient coil. Proton spectra were acquired using a composite pulse presaturation experiment. The spectral width was set for 12,000 Hz, and ^{1}H 90° pulse was 8.75 μs at a power level of 7 dB. For ^{19}F data collection, the ^{1}H channel of the probe was tuned for the observation of ^{19}F. The spectral width was set for 37,593 Hz, the ^{19}F 90° pulse was 5 μs at 4 dB, and 32K data points were collected using 3-s recycle delay.

An evaluation of lumiracoxib metabolites was performed using a Discovery RP-Amide C16 analytical column (4.6 × 150 mm, 5 μm; Supelco, Bellefonte, PA). The mobile phases were: A = 0.1% trifluoroacetic acid in deuterium oxide, B = 0.1% trifluoroacetic acid in deuterated acetonitrile (1.0 ml/min) with UV detection at 260 nm. The gradient elution program was as follows (all gradient steps were linear): 0 to 35 min, 25 to 75% solvent B; 35 to 40 min, 75 to 95% solvent B; 40 to 45 min, 95% solvent B. The HPLC separation was interrupted every 30 s (time-slicing technique) to acquire ^{19}F data. Identification of metabolites was based on the evaluation of the ^{19}F and ^{1}H data collected by this technique. Reference standards of lumiracoxib analogs were analyzed in the same way to facilitate the interpretation of the ^{19}F and ^{1}H metabolite spectra.

Results

Four male subjects took part in this study with a mean age of 46 ± 6 years (range 39–51 years) and a mean weight of 78.6 ± 8.8 kg (range 71–87.6 kg). All subjects were of the CYP2C9 *1/*1 genotype. No adverse events or clinically significant changes in vital signs, clinical chemistry, hematology, or urinalysis were observed during the course of the study.

Blood and Plasma Concentrations of Radioactivity. Mean blood and plasma concentrations of radioactivity and key pharmacokinetic parameters are summarized in Table 1 and Fig. 2. The mean $AUC_{0-\infty}$ of blood and plasma radioactivity was 89.6 μg Eq · h/g and 240 μg Eq · h/ml, respectively. The mean C_{max} (at ~4 h postdose) of radioactivity in blood and plasma was 6.88 μg Eq/g and 12.0 μg Eq/ml, respectively. The apparent terminal half-life of the mean total radioactivity in blood and plasma ranged from 7.1 to 9.8 h in blood and 136 to 240 h in plasma. Extraction recovery of radioactivity in plasma, urine, and feces was 68 to 98%, 82 to 100%, and 74 to 83%, respectively.

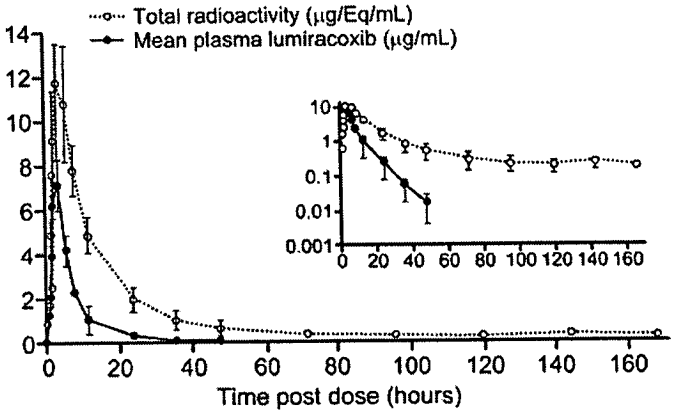

FIG. 2. *Plasma lumiracoxib and radioactivity concentrations (mean ± S.D.) after a single 400-mg oral dose of [^{14}C]lumiracoxib (n = 4).*

Y-axis of inset is semilog scale.

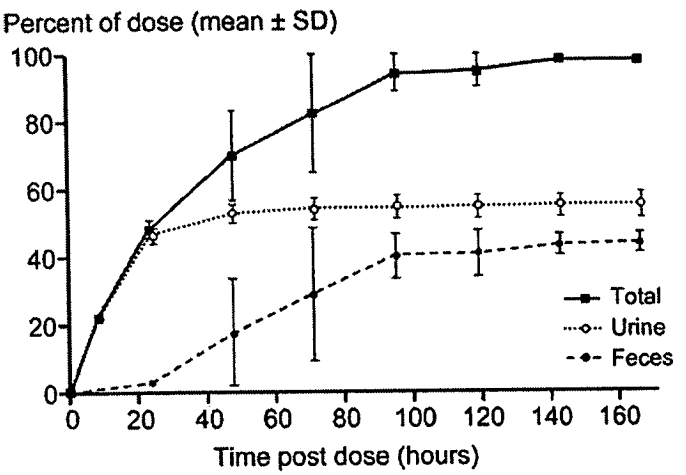

FIG. 3. *Cumulative excretion of radioactivity in human urine and feces (n = 4, mean ± S.D.).*

Plasma Lumiracoxib Concentrations. These data show that a single oral dose of [^{14}C]lumiracoxib (400 mg) is rapidly absorbed, achieving mean plasma concentrations >1 μg/ml within 1 h postdose and a mean peak plasma concentration (C_{max}) of 7.28 μg/ml by a median of 4 h (range 2.5–4.0 h) postdose (Table 1). Unchanged lumiracoxib was the major drug-related circulating component in plasma, accounting for 81 to 91% of the radioactivity up to 2.5 h postdose, and approximately 43% of total plasma radioactivity $AUC_{0\text{ to }24h}$, 38% of $AUC_{0\text{ to }48h}$, and 26% of the $AUC_{0\text{ to }168h}$. The apparent plasma clearance (CL/F) for lumiracoxib was 8.36 l/h, and the mean $AUC_{0-\infty}$ value for plasma lumiracoxib was 48.4 ± 6.12 μg · h/ml. Using radiolabeled lumiracoxib in capsule form, the terminal plasma half-life of lumiracoxib ranged from 5.4 to 8.6 h (mean 6.5 h). Lumiracoxib pharmacokinetics in blood paralleled that of plasma; the blood/plasma radioactivity ratio was approximately 0.53.

Excretion and Mass Balance in Urine and Feces. Approximately

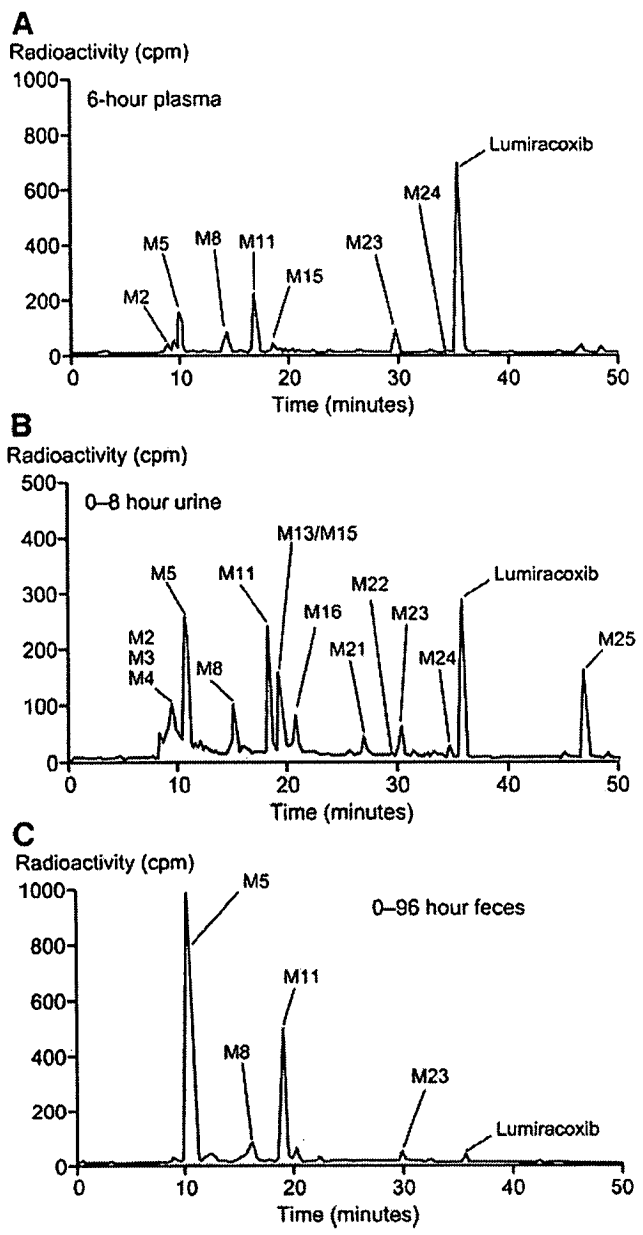

FIG. 4. *Lumiracoxib and metabolites in pooled human plasma 6 h after a single 400-mg oral dose of [^{14}C]lumiracoxib (n = 4) (A), in human urine after a single 400-mg oral dose of [^{14}C]lumiracoxib (0–8 h) (subject 5104) (B), and in human feces after a single 400-mg oral dose of [^{14}C]lumiracoxib (0–96 h) (subject 5101) (C).*

equal proportions of radioactivity were recovered in urine (mean recovery 54.1% of initial dose) and feces (mean recovery 42.7% of initial dose) in all four subjects (Fig. 3). The majority of urinary excretion (~85%) occurred during the first 24 h postdose and overall dose recovery was almost complete (96.8 ± 0.8%) within the 168-h collection period. Only a small percentage of the dose was excreted as unchanged drug in urine (3.3%, range 2.5–4.4%) and feces (1.9%, range 0.5–4.1%).

Metabolism of Lumiracoxib. A number of glucuronic acid conjugates of lumiracoxib metabolites (and to a minor extent, lumiracoxib, itself) were identified, but there was no evidence of glutathione-derived metabolites (glutathione, cysteine, or mercapturic acid conjugates) in either plasma or excreta. In plasma, lumiracoxib was the major circulating component with three major metabolites (M5, 4′-hydroxy-5-carboxy; M11, 5-carboxy; and M23, 4′-hydroxy) and at least two minor metabolites (M8 and M15) (Fig. 4A). The characteristics and structure of the main metabolites are shown in Table 2. Relative plasma exposure was highest for the M11 and M5 metabolites. In urine, at least 20 metabolites were identified, with most accounting for <2% of the dose. Metabolites M5 and M11 were the most prominent, representing 7.8% and 6.3% of the dose, respectively (Fig. 4B). Metabolite profiles in feces were less complex than in urine, although metabolites M5 and M11 were the major components, accounting for 20.5% and 8.28% of the dose, respectively (Fig. 4C).

TABLE 2

Characteristics and structure of the five main metabolites

Metabolite	[M-H]$^-$ (mol. wt.)	Relative Plasma Exposure (%)[a]	Structure
		μg Eq · h/ml	
M5 (4′-OH-5-COOH)	338 (339)	12.5 (8.2)	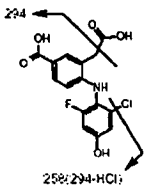
M11 (5-COOH)	322 (323)	16.6 (10.8)	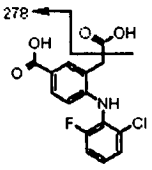
M23 (4′-OH)	308 (309)	8.8 (5.8)	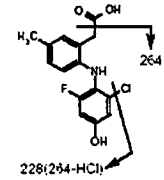
M8 (4′OH-5-COOH lactam)	320 (321)	4.1 (2.7)	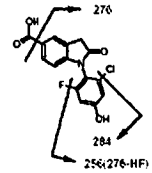
M15 (5-COOH lactam)	304 (305)	5.9 (3.9)	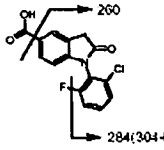

[M-H]$^-$ = molecular weight of negative ion following loss of a proton.
[a] AUC_{0-48h} relative to a total of 153 μg Eq · h/ml.

MS identification of metabolites derived through 4′-hydroxylation was confirmed by ^{19}F NMR and ^{1}H NMR as illustrated in Fig. 5 and comparison to an available reference standard. The metabolic pathway of lumiracoxib in humans is shown in Fig. 6.

Discussion

After administration of a single oral dose of [^{14}C]lumiracoxib, lumiracoxib was rapidly absorbed, with peak plasma concentrations of both unchanged lumiracoxib and radioactivity being reached around 4 h postdose. The concentration of unchanged lumiracoxib in plasma up to 2.5 h postdose was equivalent to 81 to 91% of the radioactive dose, with the level of unchanged lumiracoxib demonstrating an

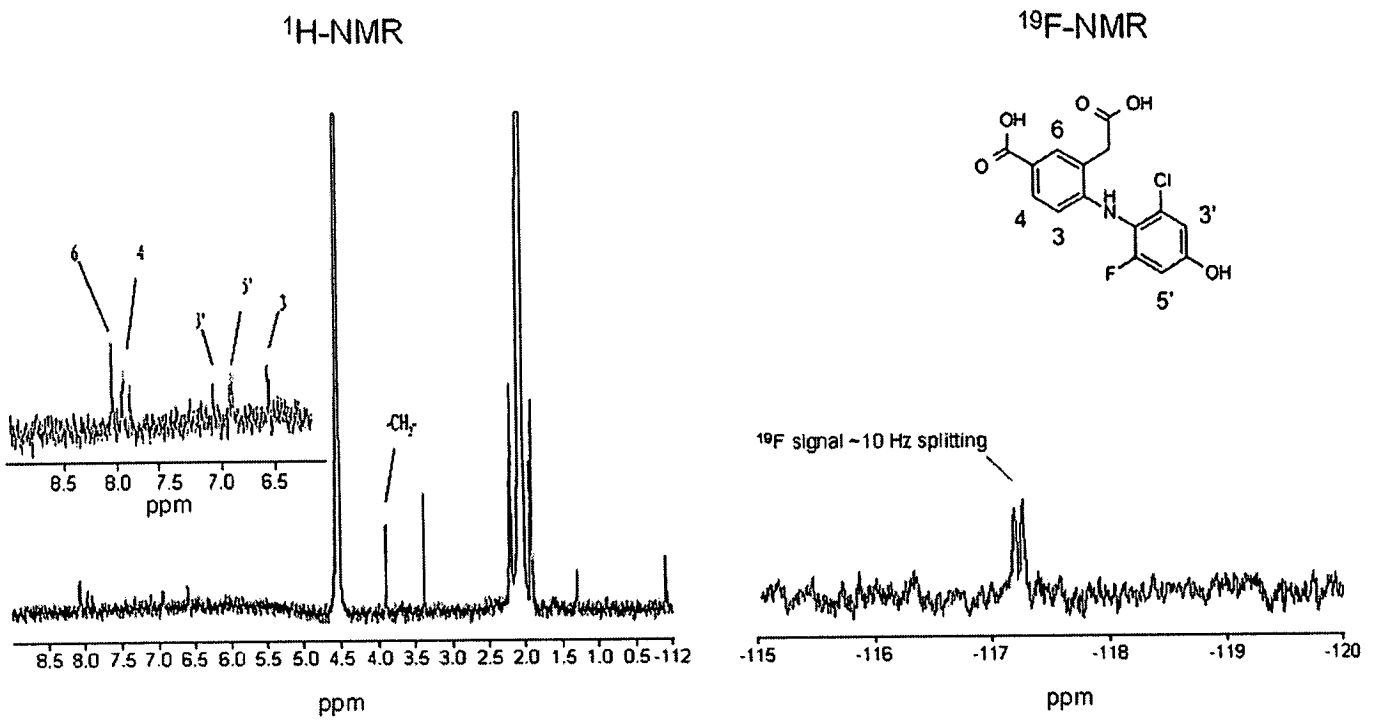

FIG. 5. *^{19}F NMR and ^{1}H NMR spectra of metabolite M5.*

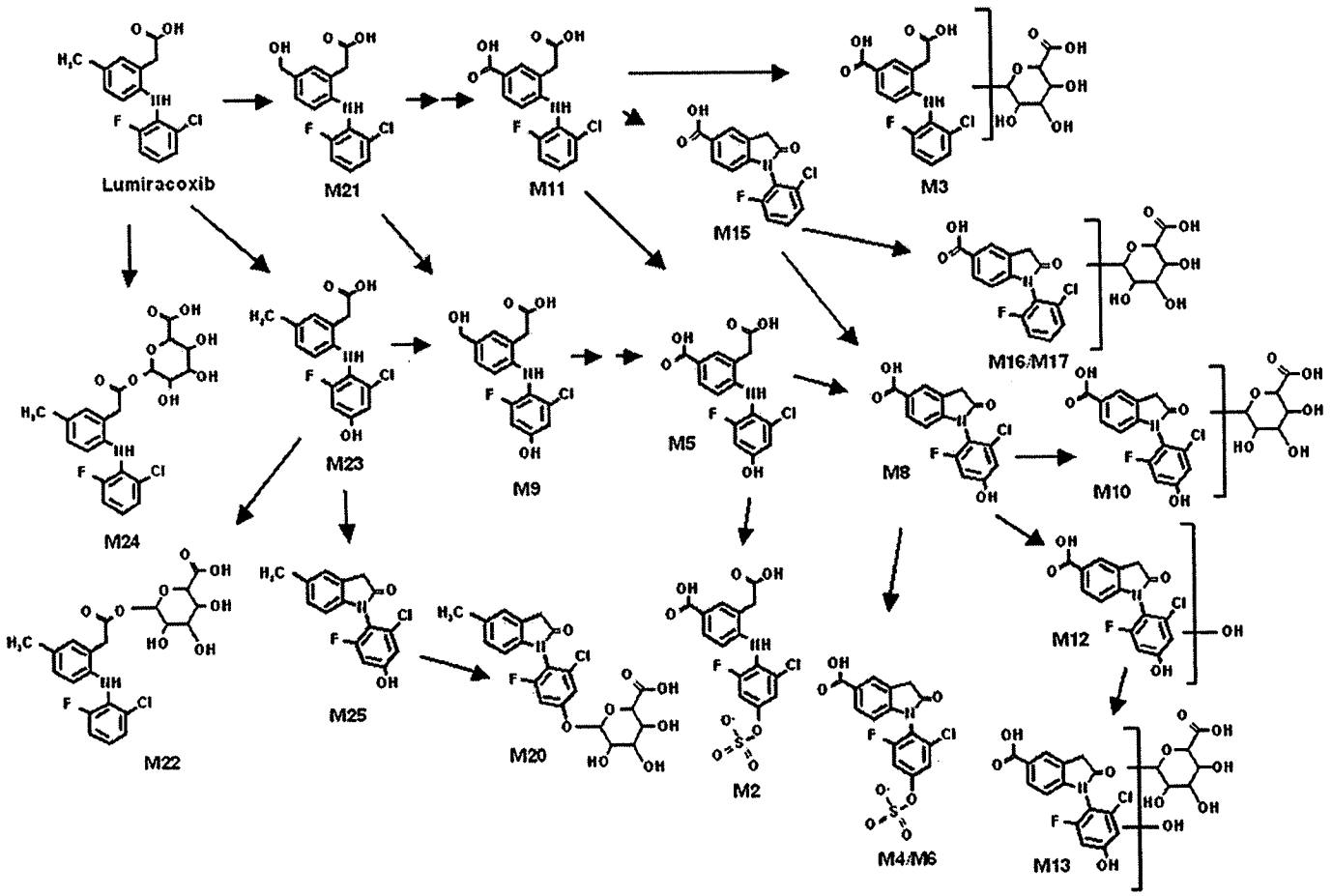

FIG. 6. *Metabolism of lumiracoxib in humans.*

apparent mean plasma terminal half-life of around 6.5 h. This suggests that lumiracoxib was well absorbed and subject to only a modest first-pass effect. In addition, orally administered single-dose [^{14}C]lumiracoxib was well tolerated.

Lumiracoxib (radioactivity) was primarily excreted in the urine (54.1%) and feces (42.7%). The majority of urinary excretion occurred during the first 24 h postdose, and overall dose recovery was complete (96.8%) within 168 h of dosing. The observation that more than 54% of lumiracoxib radioactivity was excreted via urine lends further support to [^{14}C]lumiracoxib being well absorbed. Moreover, the fact that urinary and fecal excretion of unchanged lumiracoxib accounted for only a small proportion of total radioactivity (3.3% and 2.0% of the dose, respectively) suggests that [^{14}C]lumiracoxib is extensively metabolized before excretion, assuming that metabolism in feces by gut flora is minimal. This contention was firmly supported by the lumiracoxib metabolite profile, in which a broad spectrum of metabolites was identified. This metabolite profile illustrated that lumiracoxib is metabolized mainly via oxidative metabolism of the 5-methyl group and hydroxylation of the dihaloaromatic ring (a process confirmed by ^{19}F NMR).

Although a number of glucuronic acid conjugates of lumiracoxib metabolites (and to a minor extent, lumiracoxib, itself) were identified, the lack of any evidence of cysteine, mercapturic acid, or glutathione conjugates in plasma, urine, or feces may prove advantageous given that formation of these derivatives frequently reflects bioactivation (Hinson and Forkert, 1995). Conjugates of this type could be envisioned as being derived from oxidative processes or, as more recently reported, from acyl glucuronidation-related mechanisms (Grillo and Hua, 2003; Grillo et al., 2003). The major metabolites of lumiracoxib were, in fact, the 4′-hydroxy-5-carboxy (M5), 5-carboxy (M11), and 4′-hydroxy (M23) derivatives of lumiracoxib. Only the 4′-hydroxy metabolite has been shown to be active, having similar potency and COX-2 selectivity to the parent molecule (Novartis, data on file). Plasma exposure to 4′-hydroxy-lumiracoxib in this study was around 10% that of the parent molecule, a finding consistent with previously reported levels (Reynolds et al., 2003), suggesting that this metabolite is unlikely to contribute significantly to efficacy. Further phase II conjugation of metabolites (and to a minor extent, lumiracoxib) was observed. Cyclization to the corresponding lactam occurred with several metabolites, whereas direct glucuronic acid conjugation of lumiracoxib (acyl glucuronide formation) was a relatively minor metabolic pathway, accounting for approximately 2.5% of the dose.

Given the extensive metabolism of lumiracoxib by the hepatic cytochrome P450 isozyme CYP2C9, the potential exists for hepatic dysfunction, or the coadministration of other drugs metabolized by the same enzyme system, to adversely affect lumiracoxib pharmacokinetics. However, studies show that lumiracoxib pharmacokinetics remain unchanged in patients with moderate hepatic impairment (Kalbag et al., 2002), and no clinically significant pharmacokinetic interactions have been found between lumiracoxib and the sensitive CYP2C9 substrate, warfarin (Bonner et al., 2003) or the potent CYP2C9 inhibitor, fluconazole (Yih et al., 2003). These findings may suggest that compensatory pathways for metabolism exist.

In summary, orally administered lumiracoxib was well tolerated and rapidly absorbed, with unchanged lumiracoxib accounting for the majority of drug present in plasma. Lumiracoxib undergoes extensive metabolism before excretion via urine and feces, with no evidence of formation of potentially reactive metabolites.

Acknowledgments. We thank Dr. Graham Scott, Dr. Nigel McCracken, and Dawn Keirs and coworkers (Inveresk) for their efforts in the clinical development, conduct, and sample collection aspects of this study. We also thank Drs. Alban Allentoff and Grazyna Ciszewska for providing the radiolabeled drug substance and Dr. Michael Shapiro and Jefferson Chin for NMR analyses and interpretation.

References

Bombardier C, Laine L, Reicin A, Shapiro D, Burgos-Vargas R, Davis B, Day R, Ferraz MB, Hawkey CJ, Hochberg MC, et al.; VIGOR Study Group (2000) Comparison of upper gastrointestinal toxicity of rofecoxib and naproxen in patients with rheumatoid arthritis. VIGOR Study Group. *N Engl J Med* **343**:1520–1528.

Bonner J, Branson J, Milosavljev S, Rordorf C, and Scott G (2003) Co-administration of lumiracoxib and warfarin does not alter the pharmacokinetic profile of *R*- or *S*-warfarin. *Ann Rheum Dis* **62 (Suppl. 1)**:264 (Abstract FRI0225).

Bruno R, Iliadis A, Jullien I, Guego M, Pinhas H, Cunci S, and Cano JP (1988) Naproxen kinetics in synovial fluid of patients with osteoarthritis. *Br J Clin Pharmacol* **26**:41–44.

Crofford LJ (1997) COX-1 and COX-2 tissue expression: implications and predictions. *J Rheumatol* **24 (Suppl. 49)**:15–19.

Day RO, McLachlan AJ, Graham GG, and Williams KM (1999) Pharmacokinetics of nonsteroidal anti-inflammatory drugs in synovial fluid. *Clin Pharmacokinet* **36**:191–210.

Flower RJ (2003) The development of COX2 inhibitors. *Nat Rev Drug Discov* **2**:179–191.

Fu JY, Masferrer JL, Seibert K, Raz A, and Needleman P (1990) The induction and suppression of prostaglandin H2 synthase (cyclooxygenase) in human monocytes. *J Biol Chem* **265**:16737–16740.

Goldstein JL, Correa P, Zhao WW, Burr AM, Hubbard RC, Verburg KM, and Geis GS (2001) Reduced incidence of gastroduodenal ulcers with celecoxib, a novel cyclooxygenase-2 inhibitor, compared to naproxen in patients with arthritis. *Am J Gastroenterol* **96**:1019–1027.

Grillo MP and Hua F (2003) Identification of zomepirac-S-acyl-glutathione in vitro in incubations with rat hepatocytes and in vivo in rat bile. *Drug Metab Dispos* **31**:1429–1436.

Grillo MP, Knutson CG, Sanders PE, Waldon DJ, Hua F, and Ware JA (2003) Studies on the chemical reactivity of diclofenac acyl glucuronide with glutathione: identification of diclofenac-S-acyl-glutathione in rat bile. *Drug Metab Dispos* **31**:1327–1336.

Hartmann S, Scott G, Rordorf C, Campestrini J, Branson J, and Keller U (2003) Lumiracoxib demonstrates high absolute bioavailability in healthy subjects, in *European Collaboration: Towards Drug Development and Rational Drug Therapy. Proceedings of the Sixth Congress of the European Association for Clinical Pharmacology and Therapeutics* 2003 June-24–28; Istanbul (Tulunay FC and Orme M, eds) p. 124 (Abstract P-199) , Springer-Verlag, Berlin.

Hernandez-Diaz S and Garcia-Rodriguez LA (2001) Epidemiologic assessment of the safety of conventional nonsteroidal anti-inflammatory drugs. *Am J Med* **110 (Suppl. 3A)**:20S–27S.

Hinson JA and Forkert PG (1995) Phase II enzymes and bioactivation. *Can J Physiol Pharmacol* **73**:1407–1413.

Kalbag J, Scott G, Yeh C-M, Gurrieric P, Milosavljev S, and Rordorf C (2002) Lumiracoxib pharmacokinetics remain unchanged between subjects with a moderate degree of hepatic impairment and healthy subjects. *J Clin Pharmacol* **42**:1051–1071 (Abstract 17).

Marshall PJ, Berry JC, Wasvary J, van Duzer J, Du Z, Scott G, Rordorf C, Milosavljev S, and Fujimoto RA (2002) The in vitro and in vivo selectivity of COX189, a new and highly selective inhibitor of COX-2. *Ann Rheum Dis* **61 (Suppl. 1)**:259 (Abstract SAT0013).

Rainsford KD, Schweitzer A, and Brune K (1981) Autoradiographic and biochemical observations on the distribution of non-steroid anti-inflammatory drugs. *Arch Int Pharmacodyn Ther* **250**:180–194.

Reynolds C, Scott G, Looby M, Milosavljev S, Huff JP, Ruff DA, and Rordorf C (2003) Pharmacokinetics of lumiracoxib in synovial fluid and plasma of patients with rheumatoid arthritis, in *European Collaboration: Towards Drug Development and Rational Drug Therapy. Proceedings of the Sixth Congress of the European Association for Clinical Pharmacology and Therapeutics*; 2003 June-24–28; Istanbul (Tulunay FC and Orme M, eds) p. 123 (Abstract P-195), Springer-Verlag, Berlin.

Rordorf C, Scott G, Milosavljev S, Blood P, Branson J, and Greig G (2002) Steady state pharmacokinetics, pharmacodynamics, safety and tolerability of COX189 in healthy subjects. *Ann Rheum Dis* **61 (Suppl. 1)**:420 (Abstract AB0284).

Scott G, Branson J, Milosavljev S, Rordorf C, Haraoui B, Ouellet J-P, and Schell E (2003a) Lumiracoxib demonstrates dose-proportional and time-independent pharmacokinetics in patients with osteoarthritis of the knee. Ann Rheum Dis **62 (Suppl. 1)**:267 (Abstract FRI0235).

Scott G, Rordorf C, Blood P, Branson J, Milosavljev S, and Greig G (2002a) Dose escalation study to assess the safety, tolerability, pharmacokinetics and pharmacodynamics of COX189 in healthy subjects. *Ann Rheum Dis* **61 (Suppl. 1)**:242 (Abstract FRI0300).

Scott G, Rordorf C, Milosavljev S, Chase W, Fleischmann R, and Kivitz A (2003b) Multiple-dose lumiracoxib shows rapid absorption and COX-2 selectivity without accumulation in patients with rheumatoid arthritis, in *European Collaboration: Towards Drug Development and Rational Drug Therapy. Proceedings of the Sixth Congress of the European Association for Clinical Pharmacology and Therapeutics*; 2003 June-24–28; Istanbul (Tulunay FC and Orme M eds), p. 124 (Abstract P-197). Springer-Verlag, Berlin.

Scott G, Rordorf C, Milosavljev S, and Ferber G (2002b) Pharmacokinetics and pharmacodynamics of COX189 in patients with knee or hip primary osteoarthritis *Ann Rheum Dis* **61 (Suppl. 1)**:128 (Abstract THU0233).

Warner TD, Giuliano F, Vojnovic I, Bukasa A, Mitchell JA, and Vane JR (1999) Nonsteroid drug selectivities for cyclo-oxygenase-1 rather than cyclo-oxygenase-2 are associated with human gastrointestinal toxicity: a full in vitro analysis. *Proc Natl Acad Sci USA* **9**:7563–7568.

Wilding IR, Connor AL, Carpenter P, Rordorf C, Branson J, Milosavljev S, and Scott G (2004) Lumiracoxib shows similar bioavailability at different sites in the gastrointestinal tract. *Pharm Res (NY)* **21**:443–446.

Yih L, Scott G, Yeh C-M, Milosavljev S, Laurent A, and Rordorf C (2003) Fluconazole does not affect lumiracoxib pharmacokinetics in healthy subjects: a two-stage, open-label, randomized, crossover study, in European Collaboration: Towards Drug Development and Rational Drug Therapy. Proceedings of the Sixth Congress of the European Association for Clinical *Pharmacology and Therapeutics*. (Tulunay FC and Orme M eds) Berlin: Springer-Verlag; p. 123 (Abstract P-194).

JOURNAL OF AGRICULTURAL AND FOOD CHEMISTRY

Absorption and Bioavailability of Artepillin C in Rats after Oral Administration

YUTAKA KONISHI,*,† YOSHITAKA HITOMI,† MICHIKO YOSHIDA,‡ AND EIJI YOSHIOKA§

Central Laboratories for Frontier Technology, Kirin Brewery Co., Ltd., 1-13-5, Fukuura, Kanazawa-ku, Yokohama-shi, Kanagawa 236-0004, Japan, R&D Laboratory, Functional Food Division, Kirin Brewery Co., Ltd., 3 Miyaharacho, Takasaki-shi, Gunma 370-1295, Japan, and Pharmaceutical Development Laboratories, Pharmaceutical Division, Kirin Brewery Co., Ltd., 2–2 Souja-machi 1 chome, Maebashi-shi, Gunma 371-0853, Japan

Artepillin C (AC), an active ingredient of Brazilian propolis, permeates intact across Caco-2 cells by transcellular passive diffusion. The permeation of AC across Caco-2 cells is as efficient as that of phenolic acids and the microbial metabolites of poorly absorbed polyphenols, which are actively absorbed by the monocarboxylic acid transporter (MCT) (*Biochim. Biophys. Acta* **2005**, *1713*, 138–144). Here, the absorption of orally administered AC in rats has been studied to evaluate its pharmacokinetics and bioavailability in vivo in comparison with those of *p*-coumaric acid (CA), a substrate of MCT. Rats were given 100 μmol/kg of body weight of AC or CA, and blood was subsequently collected from the portal vein and abdominal artery. AC, CA, and their metabolites were quantified by coulometric detection using HPLC–ECD. The serum concentration of intact AC and CA in the portal vein peaked at 5–10 min after administration, with a C_{max} of 19.7 μmol/L for AC and 74.8 μmol/L for CA. The area under the curve (AUC) for intact AC and CA in the portal vein was calculated from the serum concentration as 182.6 and 3057.3 μmol·min·L^{-1}, respectively. The absorption efficiency of CA was about 17-fold higher than that of AC. Furthermore, the bioavailability of CA was about 278-fold higher than that of AC, and the ratio of AUC in the abdominal artery to AUC in the portal vein was 0.04 and 0.70, for AC and CA, respectively. Thus, AC is likely to be more susceptible to hepatic elimination than is CA. The bioactive compound of AC in vivo should be investigated further.

KEYWORDS: Artepillin C; p-coumaric acid; monocarboxylic acid transporter; intestinal absorption; rat

INTRODUCTION

Artepillin C (AC; 3,5-diprenyl-4-hydroxycinnamic acid) is one of the principal phenolic acids present in propolis extract and has been ascribed to various biological activities of the extract, such as its antibacterial, antiviral, and anticarcinogenic properties (*1*–*5*). However, there are very few reports in the literature concerning the absorption, distribution, and excretion of AC. Recently, it was reported that intact AC was readily absorbed by the intestine and gave protection against oxidative stress in vitro, suggesting that AC is the principal bioactive compound in propolis (*6*). As it is considered timely to reevaluate the biological activity and health effects of polyphenols in terms of their bioavailability (*7*), it would be desirable to determine the absorption characteristics and bioavailability of AC in detail.

We have recently elucidated the absorption characteristics of many phenolic acids (i.e. ferulic, *p*-coumaric, gallic, caffeic acids) and related compounds (i.e. chlorogenic, rosmarinic acids) in terms of their affinity for the monocarboxylic acid transporter (MCT) and have demonstrated the diverse nature of the absorption of phenolic compounds in Caco-2 cells (i.e. MCT-mediated absorption, partial MCT-mediated absorption, paracellular diffusion) (*8*–*11*). It has been also shown that the absorption characteristics of these compounds in Caco-2 cells in vitro correlates well with their absorption efficiencies and bioavailabilities in vivo (*12*, *13*). Furthermore, the physiological significance of the microbial metabolites of poorly absorbed parent polyphenols has now been firmly established (*7*); these metabolites are also thought to be absorbed and distributed by MCT, similar to phenolic acids (*14*, *15*). These observations highlight the physiological impact of MCT-mediated absorption and distribution in humans, which involves specific transport systems that act not only for phenolic acids but also for "metabonutrients", that is, microbial metabolites of poorly absorbed polyphenols or dietary fibers having biological activities (*14*, *15*).

The key features of a substrate for MCT are thought to be a monoanionic carboxylic acid group and a nonpolar side chain or aromatic hydrophobic moiety (*16*). Because AC seems to

* To whom correspondence should be addressed. (Tel: +81–45–788–7588; Fax: +81–45–788–4047; E-mail: konishiy@kirin.co.jp).
† Central Laboratories for Frontier Technology.
‡ R&D Laboratory.
§ Pharmaceutical Development Laboratories.

10.1021/jf051962y CCC: $30.25
Published on Web 12/06/2005

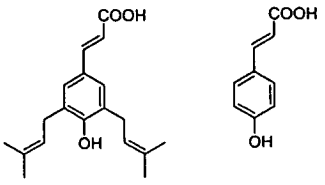

Artepillin C p-Coumaric acid

Figure 1. Chemical structures of AC and CA.

fulfill the structural criteria for a MCT substrate (**Figure 1**), we have previously examined whether AC is transported by MCT and have shown that it mainly permeates intact across Caco-2 cells by transcellular passive diffusion with a permeation efficiency as high as those of MCT substrates (*17*). It is generally considered, however, that the first hepatic elimination of hydrophobic compounds that are absorbed by transcellular passive diffusion is high and that their bioavailability is necessarily low. The current study was designed to examine the intestinal absorption efficiency and bioavailability of AC in vivo by means of pharmacokinetics and to compare them with those of the MCT substrate CA.

MATERIALS AND METHODS

Materials. AC, CA, and sulfatase type H-5 were purchased from Sigma-Aldrich, Inc. (St. Louis, MO). The other chemicals used in this study were of analytical grade.

Animals and Diets. Male Wistar rats (7 weeks old, Charles River Japan, Yokohama, Japan) were housed in an air-conditioned room (22 ± 1 °C) under 12-h dark/12-light cycles, with free access to tap water and a commercial nonpurified CE-2 diet (CLEA Japan, Inc., Tokyo, Japan). Three rats to be administered AC or CA were assigned to each time point of each experimental group. This study was approved by the Ethics Committee of Kirin Brewery Co., Ltd.

Sample Preparation. Rats were fasted for 20 h and their body weight was measured (182−213 g). They were given AC or CA (100 μmol/kg in 50% propyleneglycol) by gastric intubation. Blood was withdrawn from the portal vein and abdominal artery at each time point (5, 10, 20, 30, 60, and 90 min) after the administration of AC or CA. Serum was obtained by centrifugation and was stored at −80 °C until analysis.

HPLC−ECD Analysis. An HPLC−ECD fitted with a coulometric detection system was used to measure the amount of AC, CA, and their conjugates in serum samples according to a previously described method (*14*, *15*). In brief, to 25 μL of serum was added 25 μL of 0.1 mol/L sodium acetate buffer (pH 5.0), and 100 μL of 0.83 mol/L acetic acid in methanol. The mixture was vortexed, sonicated, and centrifuged (at 8500*g* for 5 min at 4 °C), and the supernatant was injected onto an HPLC C18 column (ODS150, MC Medical, Inc., Tokyo, Japan). For AC, mobile phase A (solvent A) was 50 mM sodium acetate containing 40% acetonitrile and 20% methanol (pH 3.0), and mobile phase B (solvent B) was 50 mM sodium acetate containing 80% methanol (pH 3.5). The elution profile (0.6 mL/min) was as follows: 0−28.5 min, linear gradient from 85% solvent A/15% solvent B to 0% solvent A/100% solvent B; 28.5−32 min, isocratic elution 0% solvent A/100% solvent B; 32−35 min, isocratic elution 85% solvent A/15% solvent B. Eight electrode detector potentials (from 200 to 760 mV in increments of 80 mV) were used. For CA, mobile phase A (solvent A) was 50 mM sodium acetate containing 5% methanol (pH 3.0), and mobile phase B (solvent B) was 50 mM sodium acetate containing 40% acetonitrile and 20% methanol (pH 3.5). The elution profile (0.6 mL/min) was as follows: 0−28.5 min, linear gradient from 85% solvent A/15% solvent B to 20% solvent A/80% solvent B; 28.5−31 min, isocratic elution 0% solvent A/100% solvent B; 31−35 min, isocratic elution 85% solvent A/15% solvent B. Eight electrode detector potentials (from 0 to 700 mV in increments of 100 mV) were used. The quantitative determination of AC and CA was performed by using an external standard method, which verified that the detector response was linear for concentrations of up to 400 μmol/L for AC and 600 μmol/L for CA.

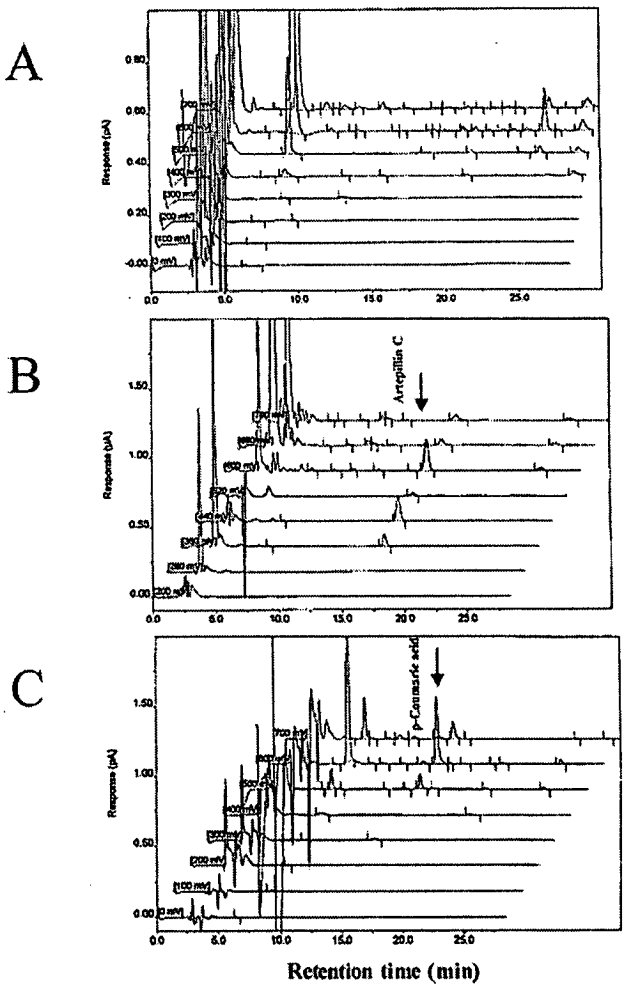

Figure 2. Chromatograms obtained by HPLC–ECD analysis of rat serum before (**A**) and after the administration of AC (**B**) or CA (**C**).

Enzymatic Hydrolysis and Determination of AC or CA Conjugates. Serum (25 μL) was mixed with 25 μL of sulfatase type H-5 solution in 0.1 mol/L acetate buffer (pH 5.0) containing both 12.5 units of sulfatase and about 270 units of β-glucuronidase activity. The mixture was incubated at 37 °C for 45 min. The difference in AC or CA content before and after sulfatase treatment was assumed to be due the amount of the respective sulfate and glucuronide conjugates in the sample.

Data Analysis. Noncompartmental pharmacokinetic parameters were calculated from the serum concentration−time data by using WinNonlin. The measured values were used to determine the maximum serum concentration, C_{max}, and the time, t_{max}, taken to reach C_{max}. The results of C_{max} are expressed as the mean ± SEM of three determinations. The area under the curve (AUC) for the serum concentration−time data from zero to the final sampling time at 1.5 h ($AUC_{0-1.5h}$) was calculated by using the linear/log trapezoidal rule. The elimination half-life ($t_{1/2}$) was calculated from a log−linear regression of the terminal phase of the serum concentration−time profile. AUC and $t_{1/2}$ were calculated by using the mean concentration value at each time point.

RESULTS

Determination of AC and CA in Serum Samples. Figure 2 shows representative HPLC profiles of serum from a control rat (A), and serum from rats given AC (B) and CA (C). On the basis of a comparison in two dimensions (i.e. chromatographic and voltammetric), the identity of the AC or CA peak was

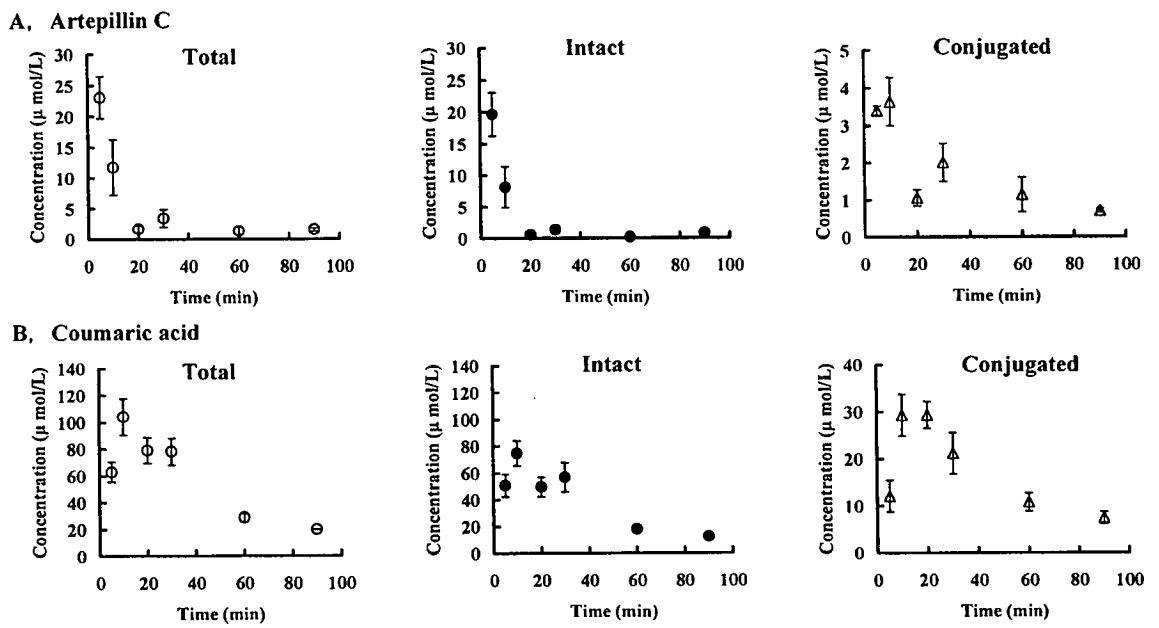

Figure 3. Serum concentration of phenolic acid in the portal vein as a function of time after the administration of AC (A) or CA (B). Each point is expressed as the mean ± SEM, $n = 3$.

determined by evaluating the peak area ratio for the oxidation channels (lower or upper) adjacent to the dominant oxidation channel. An accuracy in the ratio of more than 70% was considered to support peak purity (*18*). The retention time (t_R) and dominant oxidation potential were, respectively, 16.3 min and 440 mV for AC and 14.9 min and 600 mV for CA. Experiments with AC- or CA-spiked serum showed that this procedure gave more than 97% recovery for both compounds throughout the detection range.

Quantitative Changes in AC, CA, and Their Metabolites in Rat Serum. The mean serum concentrations of AC, CA, and their metabolites of sulfate and glucuronide in the portal vein as a function of time after administration are shown in **Figure 3**. The concentrations of total and intact AC and CA were measured after and before deconjugation with sulfatase treatment, and the results of the noncompartmental pharmacokinetics analysis are given in **Table 1**. The intestinal absorption of intact AC and CA was fast: the first and second peak levels were 5 min (19.67 μmol/L) and 30 min (1.39 μmol/L) for AC and 10 min (74.75 μmol/L) and 30 min (56.94 μmol/L) for CA. There was a difference in the AUC in the portal vein (AUC_{portal}) calculated for intact AC and CA. The absorption efficiency of CA was estimated to be 17-fold greater than that of AC. This finding shows that the intestinal absorption efficiency of CA is much higher than that of AC (**Table 1**).

Furthermore, the concentration of AC, CA, and their metabolites in the abdominal artery was investigated as a function of time after administration to clarify hepatic elimination (**Figure 4**), and the results of the noncompartmental pharmacokinetics analysis are also given in **Table 1**. At all time points after administration, there was much less intact AC in the abdominal artery than in the portal vein. In contrast, a large amount of intact CA was detected in the abdominal artery at all time points after administration, and the concentration of CA in the abdominal artery showed the same trend over time as that in the portal vein. Intriguingly, the AUC in the abdominal artery ($AUC_{abdominal}$) for CA was about 278-fold greater than that for AC (**Table 1**).

Table 1. Pharmacokinetic Parameters of Intact AC and CA in the Portal Vein and Abdominal Artery after the Administration of a Single Oral Dose of 100 μmol/kg AC or CA[a]

	AC	CA
Portal Vein		
C_{max},[b] μmol/L	19.67 ± 3.43	74.75 ± 9.27
t_{max}, min	5	10
$AUC_{0-1.5h}$, μmol·min·L^{-1}	182.6	3057.3
$t_{1/2}$, min	86.6	27.5
relative absorption efficiency	16.7	
Abdominal Artery		
C_{max}, μmol/L	0.55 ± 0.12	47.36 ± 9.54
t_{max}, min	5	10
$AUC_{0-1.5h}$, μmol·min·L^{-1}	7.72	2143.0
$t_{1/2}$, min	23.2	27.5
relative bioavailability	277.6	

[a] Abbreviations: AC, artepillin C; CA, *p*-coumaric acid; C_{max}, maximum serum concentration; t_{max}, time to reach the C_{max}; AUC, area under the serum concentration–time curve; $t_{1/2}$, elimination half-life. Relative absorption efficiency was calculated as follows: AUC_{portal} of CA/AUC_{portal} of AC. Relative bioavailability was calculated as follows: $AUC_{abdominal}$ of CA/$AUC_{abdominal}$ of AC. [b] Values of C_{max} are the mean ± SEM, $n = 3$.

The concentration of conjugated AC in the abdominal artery was also much lower than that in the portal vein, although the concentration of conjugated AC in the abdominal artery exhibited the same trend over time as that in the portal vein (**Figures 3** and **4**). In contrast, the concentration profile of conjugated CA in the abdominal artery was nearly the same as that in the portal vein. The noncompartmental pharmacokinetics analysis of conjugated AC and CA is shown in **Table 2**. The AUC and C_{max} of conjugated CA in the portal vein were nearly the same as the corresponding values in the abdominal artery, whereas the values of AUC and C_{max} of conjugated AC were much lower in the abdominal artery than those in the portal vein (**Table 2**).

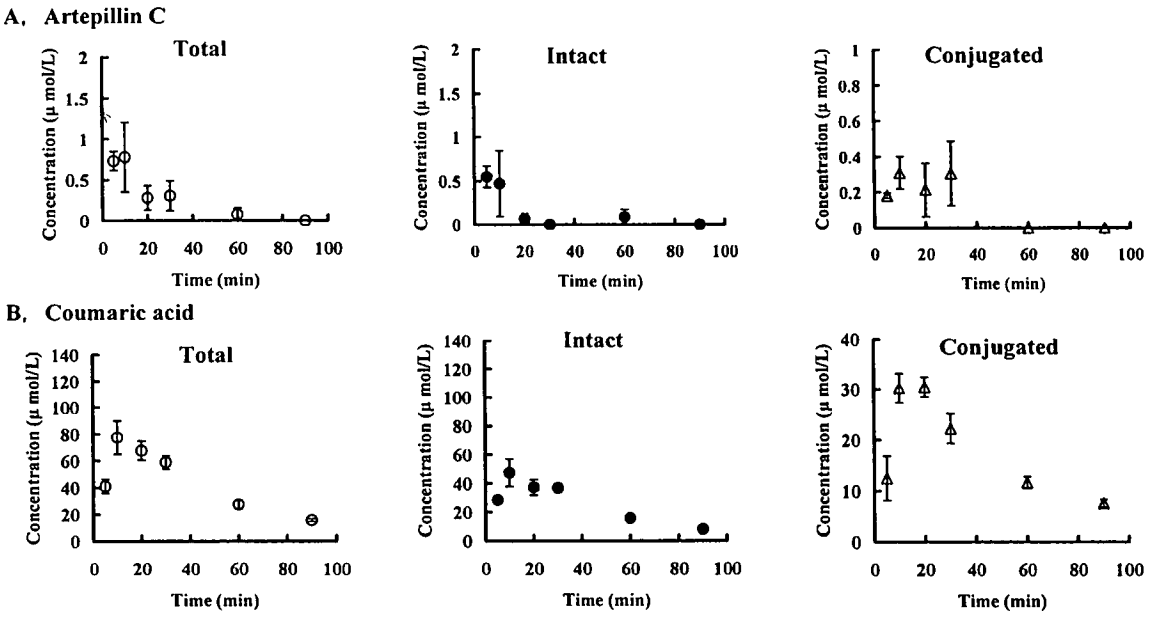

Figure 4. Serum concentration of phenolic acid in the abdominal artery as a function of time after the administration of AC (A) or CA (B). Each point is expressed as the mean ± SEM, $n = 3$.

Table 2. Pharmacokinetic Parameters of AC and CA Conjugates in the Portal Vein and Abdominal Artery after the Administration of a Single Oral Dose of 100 μmol/kg AC or CA[a]

	AC	CA
	Portal Vein	
C_{max},[b] μmol/L	3.64 ± 0.64	29.36 ± 2.83
t_{max},min	10	20
$AUC_{0-1.5h}$, μmol·min·L^{-1}	135.4	1410.7
$t_{1/2}$, min	40.0	39.8
	Abdominal Artery	
C_{max}, μmol/L	0.31 ± 0.09	30.43 ± 1.94
t_{max},min	10	20
$AUC_{0-1.5h}$, μmol·min·L^{-1}	6.8	1477.8
$t_{1/2}$, min	nc	38.6

[a] Abbreviation: AC, artepillin C; CA, *p*-coumaric acid; C_{max}, maximum serum concentration; t_{max}, time to reach the C_{max}; AUC, area under the serum concentration–time curve; nc, not calculated. [b] Values of C_{max} are the mean ± SEM, $n = 3$; $t_{1/2}$, elimination half-life.

DISCUSSION

In this study, we have demonstrated that the in vivo absorption efficiency of intact AC is lower than that of intact CA, indicating that there is a specific difference in the absorption characteristics of these two phenolic acids in vivo. Indeed, the absorption characteristics of AC are different from those of CA in Caco-2 cells (i.e. transcellular passive diffusion for AC versus MCT-mediated active transport for CA) (*9*, *17*). However, the absorption efficiency of intact AC and CA in vivo is apparently different from that observed in the in vitro Caco-2 cell system, because the absorption efficiency of AC was found to be as high as that of an MCT substrate such as CA in Caco-2 cells (*17*), in contrast to the lower absorption efficiency of rosmarinic and gallic acids, which are absorbed by paracellular diffusion (*9*, *11*). It is possible that this discrepancy in absorption efficiency between in vivo and in vitro studies might originate from such differences as an unstirred water layer, a mucin layer, or some other feature of the evaluation method employed. Further, the difference of absorption efficiency in stomach between CA and AC might cause this discrepancy. Indeed, it was reported that MCT expression was detected in mouse stomach (*19*) and that both transport systems for ferulic acid via transcellular passive diffusion and MCT-mediated absorption might operate (*20*), but at present the exact reason is unknown.

For gut absorption of dietary polyphenols, it is generally considered that the partition coefficient seems to govern their permeation across epithelial cells, because only passive diffusion appears to be involved (*21*). Indeed, it was reported that the lipophilicity of flavonoids and their affinity for liposomal membranes were well-correlated with their absorptivity into Caco-2 cells (*22*). Quercetin, one of the most typical and prevalent flavonoids in the human diet, and its glucosides were taken up into Caco-2 cells according to their own liphophilicity and were further conjugated across the epithelium (*23*). It was also reported that quercetin glucosides might be taken up intracellularly by SGLT1 (*24*) and transported by efflux into the intestinal lumen by MRP2 (*25*), indicating that the absorption and metabolism of quercetin and its glucosides are complex. Nevertheless, it is reasonable to assume that quercetin permeates across epithelial cells by transcellular passive diffusion (*22*), although a precise analysis of its absorption characteristics has not been performed, as it has in the case of AC (*17*). The same mechanism appears to govern the transport of isoflavonoids such as genistein and diazein, although isoflavones are transported as intact aglycons more efficiently than as flavonoids owing to their steric structure (*26*). In contrast to the deduced absorption characteristics in vitro, the absorption efficiency of quercetin or daizein in vivo is low in human or rat (*27*–*29*), which is in keeping with our findings for AC in this study. It is possible that an unknown but specific elimination mechanism might be involved in the low absorption efficiency in vivo to preserve homeostasis, because it would be harmful to living things if a xenobiotic compound with affinity for biomembranes could permeate across the epithelium easily and enter into enterocytes.

Furthermore, we also have demonstrated that the in vivo bioavailability of intact AC is much lower than that of intact CA. We found that the ratio of $AUC_{abdominal}$ to AUC_{portal} for intact AC and CA was 0.04 and 0.70, respectively, which suggests that intact AC is much more susceptible than intact

Table 3. Absorption Characteristics, Absorption Efficiency, and Bioavailability of Phenolics[a]

	CA[b]	CFA[c]	GA or RA[d]	AC[e]
phenolic characteristics	MCT-mediated active transport	paracellular diffusion[f]	paracellular diffusion	transcellular diffusion
efficiency	high	low	low	low
bioavailability	high	low	low	low

[a] Abbreviation: CA, p-coumaric acid; CFA, caffeic acid; GA, gallic acid; RA, rosmarinic acid; AC, artepillin C. [b] From refs *9*, *12*. [c] From refs *10*, *13*. [d] From refs *9*, *11–13*. [e] From ref *17*. [f] MCT-mediated active transport, in part.

CA to hepatic elimination. It is likely that a mechanism for eliminating AC in vivo might be involved, as mentioned above.

Considerable amounts of AC and CA conjugates were observed in the portal vein (**Figure 3**), although no AC and CA conjugates were transported in Caco-2 cells (*9*, *17*). This finding indicates that conjugation of AC and CA occurs during their permeation across the rat epithelium, consistent with results obtained in our previous in vivo studies (*12*, *13*). The discrepancy in conjugate formation between the in vivo and the in vitro Caco-2 cell system also might originate from differences in the evaluation method, as discussed above for the absorption efficiency or bioavailability. The $AUC_{abdominal}$ of conjugated AC was much lower than the AUC_{portal} of conjugated AC (ratio 0.05), and similar results were obtained for intact AC. This finding also suggests that AC may be eliminated by a specific mechanism. In contrast, because the AUC_{portal} of conjugated CA was nearly the same as the $AUC_{abdominal}$ of conjugated CA (**Table 2**), it is possible that CA is conjugated mainly during the absorption process and that further conjugation does not occur in the liver.

In this study, apart from the propyleneglycol concentration of the vehicle, which was 50% due to the lipophilicity of AC, the other experimental conditions were exactly the same as those used in previous in vivo studies (propyleneglycol concentration 10%). It has been reported that the vehicle used for oral administration can affect the absorption efficiency of flavonoids (*30*). Indeed, there are differences in the C_{max} values and concentration profiles of CA between this study and previous in vivo studies (*12*), but the AUC and t_{max} values were almost constant, indicating the high absorption efficiency and bioavailability of CA, similar to the results of the previous in vivo study. These results, together with a series of our previous works (*9–13*, *17*), have been used to summarize the diversity of absorption characteristics, absorption efficiency, and bioavailability of dietary phenolic compounds in **Table 3**, highlighting the unique physiological significance of the MCT-mediated transport system. We have focused on the physiological impact of MCT-mediated absorption and distribution in humans, which involves specific transport systems that act not only for phenolic acids but also for microbial metabolites of poorly absorbed polyphenols or dietary fibers (*14*, *15*). It is highly desirable to assess in full the health effects of phenolic acids and "metabo-nutrients", in other words, microbial metabolites with the biological activities of polyphenols or dietary fibers (*15*).

In conclusion, we have demonstrated that the absorption efficiency and bioavailability of AC are extremely low in vivo, in comparison to those of CA, which is absorbed and distributed by the MCT-mediated transport system. To evaluate the health effect of AC or propolis, further identification and characterization of its bioactive compounds in vivo are required.

ABBREVIATIONS USED

MCT, monocarboxylic acid transporter; AC, artepillin C; CA, *p*-coumaric acid; ECD, electrochemical detector.

ACKNOWLEDGMENT

We thank Mrs. K. Hagiwara for support during this work.

LITERATURE CITED

(1) Aga, H.; Shibuya, T.; Sugimoto, T.; Kurimoto, M.; Nakajima, S. Isolation and identification of anti-microbial compounds in Brazilian propolis, *Biosci., Biotechnol., Biochem.* **1994**, *58*, 945–946.

(2) Kimoto, T.; Arai, S.; Kohguchi, M.; Aga, M.; Nomura, Y.; Micallef, M. J.; Kurimoto, M.; Mito, K. 1998 Apoptosis and suppression of tumor growth by Artepillin C extracted from Brazilian propolis. *Cancer Detect. Prev.* **1998**, *22*, 506–515.

(3) Sugimoto, Y.; Iba, Y.; Kayasuga, R.; Kirino, Y.; Nishiga, M.; Alejandra Hossen, M.; Okihara, K.; Sugimoto, H.; Yamada, H.; Kamei, C. Inhibitory effects of propolis granular APC on 4-(methylnitrosamino)–(3-pyridyl)-1-butanone-induced lung tumorigenesis in A/J mice. *Cancer Lett.* **2003**, *193*, 155–159.

(4) Khayyal, M. T.; el-Ghazaly, M. A.; el-Khatib, A. S. Mechanisms involved in the antiinflammatory effect of propolis extract. *Drugs Exp. Clin. Res.* **1993**, *19*, 197–203.

(5) Dimov, V.; Ivanovska, N.; Bankova, V.; Popov, S. Immunomodulatory action of propolis. Prophylatic activity against gram-negative infections and adjuvant effect of the water-soluble derivative. *Vaccine* **1992**, *10*, 817–823.

(6) Shimizu, K.; Ashida, H.; Matsuura, Y.; Kanazawa, K. Antioxidative bioavailability of artepillin C in Brazilian propolis. *Arch. Biochem. Biophys.* **2004**, *424*, 181–188.

(7) Scalbert, A.; Johnson, I. T.; Saltmarsh, M. Polyphenols: Antioxidants and beyond. *Am. J. Clin. Nutr.* **2005**, *81*, 215S–217S.

(8) Konishi, Y.; Shimizu, M. Transepithelial transport of ferulic acid by monocarboxylic acid transporter in Caco-2 cell monolayers. *Biosci. Biotechnol. Biochem.* **2003**, *67*, 856–862.

(9) Konishi, Y.; Kobayashi, S.; Shimizu, M. Transepithelial transport of *p*-coumaric acid and gallic acid by monocarboxylic acid transporter in Caco-2 cell monolayers. *Biosci. Biotechnol. Biochem.* **2003**, *67*, 2317–2324.

(10) Konishi, Y.; Kobayashi, S. Transepithelial transport of chlorogenic acid, caffeic acid, and their colonic metabolites in intestinal Caco-2 cell monolayers. *J. Agric. Food Chem.* **2004**, *52*, 2518–2526.

(11) Konishi, Y.; Kobayashi, S. Transepithelial transport of rosmarinic acid in intestinal Caco-2 cell monolayers. *Biosci. Biotechnol. Biochem.* **2005**, *69*, 583–591.

(12) Konishi, Y.; Hitomi, Y.; Yoshioka, E. Intestinal absorption of p-coumaric and gallic acids in rats after oral administration. *J. Agric. Food Chem.* **2004**, *52*, 2527–2532.

(13) Konishi, Y.; Hitomi, Y.; Yoshida, M.; Yoshioka, E. Pharmacokinetic study of caffeic and rosmarinic acids in rats after oral administration. *J. Agric. Food Chem.* **2005**, *53*, 4740–4746.

(14) Konishi, Y.; Kobayashi, S. Microbial metabolites of ingested caffeic acid are absorbed by the monocarboxylic acid transporter (MCT) in intestinal Caco-2 cell monolayers. *J. Agric. Food Chem.* **2004**, *52*, 6418–6424.

(15) Konishi, Y. Transepithelial transport of microbial metabolites of quercetin in intestinal Caco-2 cell monolayers. *J. Agric. Food Chem.* **2005**, *53*, 601–607.

(16) Rahman, B.; Schneider, H. P.; Broer, A.; Deitmer, J. W.; Broer, S. Helix 8 and Helix 10 are involved in substrate recognition in the rat monocarboxylate transporter MCT1. *Biochemistry* **1999**, *38*, 11577–11584.

(17) Konishi, Y. Transepithelial transport of artepillin C in intestinal Caco-2 cell monolayers. *Biochim. Biophys. Acta* **2005**, *1713*, 138–144.

(18) Guo, C.; Cao, G.; Sofic, E.; Prior, R. L. High-performance liquid chromatography coupled with coulometric array detection of electroactive components in fruits and vegetables: Relationship to oxygen radical absorbance capacity. *J. Agric. Food Chem.* **1997**, *45*, 1787−1796.

(19) Koehler-Stec, E. M.; Simpson, I. A.; Vannucci, S. J.; Landschulz, K. T.; Landschulz, W. H. Monocarboxylate transporter expression in mouse brain. *Am. J. Physiol.* **1998**, *275*, E516-E524.

(20) Zhao, Z.; Egashira, Y.; Sanada, H. Ferulic acid is quickly absorbed from rat stomach as the free form and then conjugated mainly in liver. *J. Nutr.* **2004**, *134*, 3083−3088.

(21) Scalbert, A.; Williamson, G. Dietary intake and bioavailability of polyphenols. *J. Nutr.* **2000**, *130*, 2073S−2085S.

(22) Murota, K.; Terao, J. Antioxidative flavonoid quercetin: Implication of its intestinal absorption and metabolism. *Arch. Biochem. Biophys.* **2003**, *417*, 12−17.

(23) Murota, K.; Shimizu, S.; Chujo, H.; Moon, J. H.; Terao, J. Efficiency of absorption and metabolic conversion of quercetin and its glucosides in human intestinal cell line Caco-2. *Arch. Biochem. Biophys.* **2000**, *384*, 391−397.

(24) Walgren, R. A.; Lin, J. T.; Kinne, R. K. H.; Walle, T. Cellular uptake of dietary flavonoids quercetin 4′-beta-glucoside by sodium-dependent glucose transporter SGLT1. *J. Pharmacol. Exp. Ther.* **2000**, *294*, 837−843.

(25) Walgren, R. A.; Karnky, K. J. J.; Lindenmayer, G. E. Walle, T. Efflux of dietary flavonoids quercetin 4′-beta-glucoside across human intestinal Caco-2 cell monolayers by apical multidrug resistance-associated protein-2. *J. Pharmacol. Exp. Ther.* **2000**, *294*, 830−836.

(26) Murota, K.; Shimizu, S.; Miyamoto, S.; Izumi, T.; Obata, A.; Kikuchi, M.; Terao, J. Unique uptake and transport of isoflavone aglycones by human intestinal Caco-2 cells: Comparison of isoflavonoids and flavonoids. *J. Nutr.* **2002**, *132*, 1956−1961.

(27) Shimoi, K.; Yoshizumi, K.; Kido, T.; Usui, Y.; Yumoto, T. Absorption and urinary excretion of quercetin, rutin, and αG-rutin, a water soluble flavonoid, in rats. *J. Agric. Food Chem.* **2003**, *51*, 2785−2789.

(28) Scalbert, A.; Morand, C.; Manach, C.; Remesy, C. Absorption and metabolism of polyphenols in the gut and impact on health. *Biomed. Pharmacother.* **2002**, *56*, 276−282.

(29) Bloedon, L. T.; Jeffcoat, A. R.; Lopaczynski, W.; Schell, M. J.; Black, T. M.; Dix, K. J.; Thomas, B. F.; Albright, C.; Busby, M. G.; Crowell, J. A.; Zeisel, S. H. Safety and pharmacokinetics of purified soy isoflavones: Single dose administration to postmenopausal women. *Am. J. Clin. Nutr.* **2002**, *76*, 1126−1137.

(30) Piskula, M. K.; Terao, J. Quercetin's solubility affects its accumulation in rat plasma after oral administration. *J. Agric. Food Chem.* **1998**, *46*, 4313−4317.

Received for review August 10, 2005. Revised manuscript received October 16, 2005. Accepted October 19, 2005.

JF051962Y

Published in final edited form as:
J Drug Target. 2005 December ; 13(10): 573–583.

Oral delivery of low-molecular-weight heparin using sodium caprate as absorption enhancer reaches therapeutic levels

NUSRAT A. MOTLEKAR[1], **KALKUNTE S. SRIVENUGOPAL**[1], **MITCHELL S. WACHTEL**[2], and **BI-BOTTI C. YOUAN**[1]

1 Department of Pharmaceutical Sciences, School of Pharmacy, Texas Tech University Health Sciences Center, Amarillo, Texas, USA, and

2 Department of Pathology, Divisions of Anatomic Pathology and Research, Texas Tech University Health Sciences Center, Lubbock, Texas, USA

Abstract

The primary objective of this study was to evaluate sodium caprate as an oral penetration enhancer for low molecular weight heparin (LMWH), ardeparin. *In vitro* studies using Caco-2 cell monolayer indicated that 0.0625% of sodium caprate gave approximately 2-fold enhancement of ardeparin compared to negative control with almost 100% cell survival as evaluated by MTT cytotoxicity assay. *In vivo* studies in rats with ardeparin (1200 IU/kg) and sodium caprate (100 mg/kg) led to a relative bioavailability of 27% with plasma anti-factor Xa levels within the therapeutic range (> 0.2 IU/ml). Moreover, under these conditions, histological examination provided evidence that there was no damage to the gastrointestinal wall. Regional permeability studies using rat intestine indicated the colon as the region of maximum permeation. These results suggest that, at the dose administered, sodium caprate acts as a relatively safe and efficient absorption enhancer in the quest for alternatives for the oral delivery of LMWH.

Keywords

Sodium caprate; low molecular weight heparin; Caco-2 cell monolayer; absorption enhancer; ardeparin; oral absorption

Introduction

The transport of molecules across the intestinal epithelium occurs mainly by passive diffusion through transcellular or paracellular routes, and through carrier-mediated active or facilitated transport (Ward et al. 2000). Among these, the paracellular route is a dominant pathway for the passive transepithelial transport of hydrophilic molecules in the small intestine. Many hydrophilic drugs such as low molecular weight heparins (LMWHs) are not absorbed by the intestinal epithelium because of the presence of junctional complexes (Lutz and Siahaan 1997) and limitations due to their physicochemical characteristics such as hydrophilicity and molecular weight. Among approaches used to increase the intestinal absorption of hydrophilic drugs, the use of absorption enhancers (Aungst 2000), offers a promising one for developing oral formulations of macromolecules. Several permeation enhancer systems are now available to facilitate the absorption of poorly permeable compounds across the intestinal mucosa. Research has tended to focus on fatty acids such as sodium caprate, perhaps because of their natural presence in foodstuffs and dairy products (Muranishi 1990,Aungst 2000). A wide range of studies in cell culture systems and animal species have shown that sodium caprate has

Correspondence: B. C. Youan, Texas Tech University Health Sciences Center, 1300 Coulter Drive, Amarillo, Texas 79106, USA. Tel: 806 356 4015. Ext. 236. Fax: 806 354 4034. E-mail: bibotti.youan@ttuhsc.edu

significantly enhanced the transport of drugs across intestinal mucosa (Anderberg et al. 1993,Takahashi et al. 1994,Tomita et al. 1995,Chao et al. 1999,Aungst 2000). There appears to be broad agreement in the literature in relation to the mechanism of action of sodium caprate. Sodium caprate is a sodium salt of medium chain fatty acid (caprate C10) which has been shown to enhance the paracellular permeability of hydrophilic compounds. It has been studied extensively and has been included in a marketed product for human use in the form of a suppository product Doctacillin™ used in Sweden, Denmark and Japan (Kazuhiko Kitao 1984,Makoto Tanaka et al. 2000,Cano-Cebrian et al. 2005).

Heparin and LMWHs are the agents of choice in the management of deep vein thrombosis. However, their use is limited as they are currently administered via injection. The development of an oral formulation would increase patient compliance and lead to a reduction in healthcare costs. LMWH is a glycosaminoglycan composed of an alternating sequence of sulfated and/or unsulfated residues of D-glucuronic and *N*-acetyl-D-galactosamine linked by β (1?) and β (1?) bonds. LMWH has been used for the prevention and treatment of venous thrombo-embolism (VTE) (Boneu 2000) and to replace unfractionated heparin (UFH), due primarily to its longer half-life and lower incidence of adverse reactions. A major problem in the successful clinical use of LMWH is its poor oral bioavailability due to its high molecular weight, charge density, hydrophilicity, (Ross and Toth 2005) and instability under acidic conditions of the stomach. The main disadvantage of LMWH is that currently available treatment is in the form of painful once or twice daily injections. The availability of oral LMWH formulations may result in shortened hospital stay, improvement of patient compliance, and reduction in healthcare expenses related to VTE.

Various strategies are under investigation to improve oral bioavailability of LMWH. For example, the carrier compound, sodium *N*-decanoate (SNAD) was found to increase the enteral absorption of LMWH in experimental animals (Salartash et al. 2000). Intestinal absorption of LMWH has previously been reported with rectal administration of absorption enhancers such as sodium cholate in rats and human subjects (Nissan et al. 2000), the duodenal administration of Carbopol 934P in rats and pigs and the intestinal administration of chitosan derivatives or mono-*N*-carboxymethyl chitosan in rats (Thanou et al. 2001b). Other alternative routes such as nasal (Arnold et al. 2002) and transdermal (Mitragotri and Kost 2001) have and are also being investigated. However, several reports have shown that oral administration is the most preferred route for drug delivery (Lobenberg et al. 2000). Therefore, the enhancement of oral bioavailability of LMWH remains a pharmaceutical challenge and would be clinically advantageous if successful. In the present manuscript, sodium caprate was tested for its absorption enhancing effect along with a LMWH, namely ardeparin, in rats. In addition, the absorption enhancing efficacy, region of maximal permeation and the cytotoxicity of the enhancer was evaluated in rats and in the Caco-2 cell culture model.

Materials and methods

LMWH, typically Ardeparin (68 units/mg, anti-factor Xa activity) was obtained from Celcus Laboratories Inc. (Cincinnati, OH, USA). Sodium caprate was obtained from Sigma Chemicals Co. (St Louis, MO, USA). Caco-2 cells (C2BBe1 clone), Dulbecco段modified eagle medium (DMEM), fetal bovine serum (FBS), penicillin, streptomycin, phosphate buffered saline (PBS), and Trypsin嗯DTA were obtained from American Tissue Culture Collection (ATCC, Rockville, MD, USA). Human transferrin was purchased from Gibco SRL (Los Angeles, CA, USA). MTT reagent was purchased from Sigma Chemicals Co. Sodium dodecyl sulfate (SDS) was purchased from Bio-Rad Laboratories (Hercules, CA, USA). Radioactive ^{14}C mannitol and ^{3}H ardeparin were obtained from American Radiolabeled Chemicals Inc. (St Louis, MO, USA).

Size exclusion chromatography (SEC) of ardeparin

The SEC method used for the characterization was adapted from Bertini et al. (2005). The equipment consisted of a Viscotek system GPCmax™ equipped with an integrated degasser/ pump/autosampler unit. The detector system used in this study was a Viscotek Triple Detector Array (TDA™). The light scattering (LS) detector was the primary technique used in this chromatography experiment for absolute determination of molecular weight of the sample. The LS detector had the following technical specifications: a 90? (right angle) and 7? (low angle) geometry for maximum signal-to-noise ratio and to obtain the most accurate values for large molecules; cell volume of 18 μl; maximum back pressure on cell of 15 psi; maximum signal of 2.5 V; a 670 nm wavelength laser light source. A Deflection Refractive Index (RI) detector was employed as the primary concentration detector with the following technical specifications: cell volume of 12 μl; maximum back pressure on cell of 5 psi; maximum signal of 2.5 V; a light emitting diode (LED) at 660 nm wavelength. SEC Viscosity (VIS) detector was employed to determine the intrinsic viscosity [η] of the sample solution. It is characterized by four capillaries with a differential Wheatstone bridge configuration. The samples were run at 30蚓 in 0.1M sodium nitrate at 1 ml/min flow-rate. Samples were prepared with approximately 0.3? % concentrations and were injected in triplicate at 100 μl injection volume. Two G3000-PWXL columns were employed to achieve the desired separation.

Caco-2 cell culture

Human colon adenocarcinoma Caco-2 cells (C2BBe1 clone), were maintained in culture medium (DMEM supplemented with 10% FBS, 100 U/ml penicillin, 100 μg/ml streptomycin, and 10 μg/ml human Transferrin) at 37蚓 in 5% CO_2 and at 90% relative humidity. The medium was changed every other day until the flasks reached 90% confluence which was determined by microscopy in the case of 96-well plates and transepithelial electrical resistance (TEER) in the case of transwells. The cells were harvested with trypsin喀DTA, resuspended in culture medium, and seeded at a density of 2000 cells/well in flat bottom 96-well micro-titer tissue culture plates and 200,000 cells/well for transwells and allowed to grow in a humidified 37蚓 incubator (5% CO_2). Culture medium was changed every 48 h.

Transport studies across Caco-2 cell monolayers

Human colon adenocarcinoma (Caco-2) cells were seeded at a density of 200,000 cells/well onto collagen treated polycarbonate Transwell® inserts (0.4 μm pore size, 0.33 cm^2 area) and allowed to grow at 37蚓. Culture medium was changed every 48 h. Cell monolayer integrity was evaluated by monitoring TEER using a EVOM™ voltohmmeter (World Precision Instruments, Sarasota, FL, USA). TEER values of < 500 Ω cm^2 in representative cell monolayers were indicative of monolayer integrity. Prior to each experiment, membranes were rinsed twice with warm PBS solution. The inserts were then immersed into transport buffer. After equilibrium in the incubator for 30 min, measurements of the TEER values of the inserts were performed. For the transport studies, ^3H ardeparin or ^{14}C mannitol with or without enhancer was added to the apical chamber. The amount of ardeparin and mannitol used was 0.045 μCi in each chamber. The concentrations of sodium caprate used were 0.0625, 0.125 and 0.25%. Samples were withdrawn from the basolateral chamber at predetermined time intervals. The amount of ^3H ardeparin and ^{14}C mannitol transported across the cell monolayer was determined by scintillation counting using a Beckman LS 6500 liquid scintillation counter (Beckman instruments, Inc., Fullerton, CA, USA). At the end of the experiment, TEER values were measured to establish the effect of enhancer on monolayer integrity.

In vitro *cytotoxicity studies*

Caco-2 cells were plated at a density of 4.0 ? 10^3 cells/well in 96-well flat-bottomed microtiter plates, incubated for 48 h. After washing with PBS, the cells were incubated with 200 μl of

test sample and controls. DMEM media alone was used as negative control and SDS (0.1%) as positive control. The permeation enhancer, sodium caprate in DMEM media was incubated with Caco-2 monolayer in 96-well plates at various concentrations (0.01, 0.03, 0.06, 0.12, 0.25, 0.5 and 1%). These concentrations were chosen based on the currently used concentrations investigated to formulate dosage form of macromolecules in general. The cells were exposed to the compounds for 6 and 12 h. After specified periods of incubation (5% CO_2, 37蚓) with the test compounds, the cell viability was assessed with the colorimetric MTT (3-(4,5-dimethylthiazol-2-yl)-2,5-diphenyltetrazolium bromide) assay (Ouyang et al. 2002,Mossman 1983,Scudiero et al. 1988) and the absorbance was measured at 570 nm with a microplate reader (Tecan Spectra Flour Plus, Hayward, CA, USA). This assay is based on the reduction of MTT tetrazolium by the mitochondrial dehydrogenase in viable cells to colored formazan dye. The cell viability was expressed as the percentage absorbance of test compounds relative to positive control.

Gastrointestinal permeability studies

Gastrointestinal (GI) permeability of ardeparin and sodium caprate was examined in a modified Ussing chamber (surface area 0.7 cm^2) using rat intestine for 3 h. Male Sprague啤 awley rats (Charles River Laboratories, Charlotte, NC, USA), weighing 250? 00 g, were used. The rats were anaesthetized and the GI tract tissues were isolated using a previously reported method (Asada et al. 1995). The duodenal and ileal segments were removed from top and bottom (13 cm on either side) and the residual small intestine was designated as jejunum. In the present study, the central part of the jejunum was used. Colon region was removed following the caecum and was used for the permeability experiments as well. The experimental segments were obtained and the underlying muscularis was removed before mounting onto a modified Ussing chamber. PBS was added to the serosal side. The tissues were exposed to ardeparin either alone or in the presence of enhancer at a concentration of 6%. Mixing was performed by means of a magnetic stirrer and by bubbling with 95% O_2, 5% CO_2 gas. The solution was maintained at 37蚓 by means of water-jacketed reservoirs connected to a constant-temperature circulating pump. At predetermined time intervals up to 180 min, samples of 100 μls were taken from the serosal side and replaced with an equal volume of fresh transport medium. Ardeparin appearing in the receiver compartment was analyzed by colorimetric detection (Teien et al. 1976).

The apparent permeability coefficients (P_{app}) were calculated by the relationship:

$$P_{app} = \frac{dM}{dt}\frac{1}{AC_0}\frac{1}{60} \quad (1)$$

where, dM/dt is the flux across the tissue, A is the surface area of the membrane and C_0 is the initial drug concentration. The results of experiments performed at least in triplicate are presented as mean ? SD. Transport enhancement ratios were calculated from P_{app} values according to the following equation: $R = P_{app}$ (sample)/P_{app} (control) (Thanou et al. 2001a). The viability of intestinal membrane during the test period was monitored by measuring the transport of trypan blue dye. There was no transport of dye during the incubation, confirming that the viability of the intestinal tissue was maintained during the transport experiment.

All studies were approved by the Animal Care and Use Committee and were conducted in accordance with the NIH Guide for the Care and Use of Laboratory Animals.

In vivo *studies in rat*

Male Sprague啤 awley rats (Charles River laboratories), 250? 50 g, were used for the *in vivo* absorption experiments (three否x rats in each group). The animals were fasted for at least

12 h prior to the experiment, with free access to water. Prior to the experiment, the rats were anaesthetized by an intramuscular injection of an anaesthetic cocktail containing xylazine (10 mg/kg) and ketamine (100 mg/kg) in order to obtain the control blood sample from the tail vein at zero time point. Anaesthesia was maintained with additional intramuscular injections of anaesthetic solution as needed throughout the experiments. The rats then received one of the following treatments: (a) oral ardeparin (600 IU/kg) in 400 μl of $NaHCO_3$ solution (1.5 g/ 100 cc, pH 8.2) so as to neutralize the gastric acidity, (b) oral ardeparin (600, 1200, 2400 and 4800 IU/kg) plus sodium caprate (100 mg/kg) in 400 μl of $NaHCO_3$ solution, (c) oral sodium caprate (100 mg/kg) in 400 μl of $NaHCO_3$ solution, (d) parenteral (i.v. and s.c.) ardeparin, and (e) oral $NaHCO_3$ solution 400 μl. The formulations were orally administered to the animals by placing the feeding tube deeply into the throat to initiate the swallow reflex. The gavage tube was made of stainless steel with a blunt end so as to avoid causing lesions on the tissue surface. Serial blood samples were collected from the tip of the anaesthetized rat tail at 0, 30, 60, 90, 120, 240, 360 and 480 min in citrated micro-centrifuge tubes and plasma was harvested by centrifugation (1600 ? g for 5 min) and stored at −20蚓 for further analysis. Ardeparin absorption was determined by measuring plasma anti-factor Xa levels using a colorimetric assay kit (Teien et al. 1976) (Chromogenix Coatest Heparin Kit; Diapharma Group Inc., West Chester, OH, USA).

Pharmacokinetic analysis

Standard non-compartmental analysis (Kinetica, Version 4.0; Innaphase Corp., Philadelphia, PA, USA) was performed for ardeparin absorption profiles. The area under the plasma concentration versus time curve ($AUC_{0?\ 80}$) was calculated by the trapezoidal method. Absolute and relative bioavailability (F absolute and F relative) was estimated by comparing $AUC_{0?\ 80}$ for orally administered ardeparin with that of intravenously and subcutaneously administered ardeparin, respectively.

Statistical analysis

Pharmacokinetic parameters of different formulations were compared by analysis of variance. When the differences in the means were significant, post hoc pair-wise comparisons were conducted using Newman? euls multiple comparison (GraphPad Prism, version 4.0; GraphPad Software, San Diego, CA, USA). Differences in p values < 0.05 were considered statistically significant.

Histological evaluation of gastrointestinal tissues from rats

Formulations were administered to rats by oral gavage as described above. The GI tissues before administration of formulation were prepared as control samples. At the end of the *in vivo* experiment, gastric and intestinal tissues were isolated from the rats and fixed in neutral buffered formalin for processing. The tissue specimens were washed with alcohol to remove any tissue water. Specimens were embedded in paraffin and cut into sections with a thickness of approximately 5 microns by a microtome at −20蚓. The sections were stained with haematoxylin and eosin (H&E) and examined under an optical microscope (Olympus, Melville, NY, USA).

Results and discussion

Size exclusion chromatography for ardeparin

Since one of the parameters affecting the biological activity of heparin is the molecular weight, accurate determination of its value is particularly important (Nieduszynski 1989). The high degree of polydispersity of chain length, together with the overall sulfation pattern and conformational differences, represents the main challenge in the characterization. In the present

work, we focused on ardeparin, with the aim of obtaining the molecular weights and their distributions by High Performance-Size Exclusion Chromatography (HP-SEC) technique by combining three primary detectors connected in series: refractometer, viscometer and right angle laser LS. One of the advantages of a TDA assembly is that chromatographic calibrations are not necessary (Bertini et al. 2005). The viscometer detector is also useful for determining the size of molecules in solution. The weight average molecular weight (Mw), number average molecular weight (Mn), z average molecular weight (Mz), polydispersity index, and intrinsic viscosity values obtained were 7544, 5616, 9583 Da, 1.34 and 0.0694 dl/g, respectively. These values were comparable to data in the literature (Nieduszynski 1989).

The hydrodynamic radius for the molecule, ardeparin was ~19蚊 (or 1.9 nm). The calculated pore radius of the tight junctions in Caco-2 cells is reported to be 4.5蚊 (Watson et al. 2001). These data clearly showed that the relatively large size of ardeparin as compared to the pore size of the tight junctions in Caco-2 cells, necessitates the use of a penetration enhancer such as sodium caprate used in the present study. It has been suggested that sodium caprate increases the number of functional pores, both small and large, through which molecules larger than 4□ A may permeate (Watson et al. 2001).

Transport studies across Caco-2 cell monolayers

The transport of ardeparin was evaluated in the presence of increasing concentrations of sodium caprate (0, 0.0625, 0.125 and 0.25%). The permeation of mannitol across the monolayer was also assessed concomitantly in order to confirm the integrity of the cell monolayer. The P_{app} values of ardeparin across Caco-2 monolayers were calculated using Equation 1 and are listed in Table I. A significant difference was observed in the fluxes of the drug with and without enhancer from the apical side to the basolateral side. An enhancer dose-dependant increase in the transport of ardeparin was observed (Table I). The higher P_{app} values of ardeparin in the presence of enhancer indicate that the enhancer modulated the permeability barrier of the cells leading to increased transport of the drug across the cells. Addition of increasing concentrations of sodium caprate resulted in similar dose-dependant increases in mannitol transport (Table I). The hydrodynamic radius of mannitol is 4.1蚊 (Kaskel et al. 1987,Knipp et al. 1997) while that of ardeparin that we have determined was 19蚊. Since the tight junction permeability is size selective, it allows passage of small molecules with radius similar to that of the tight junctional pathway in Caco-2 cells (Watson et al. 2001) (4.5蚊) such as mannitol and not of larger molecules such as ardeparin. Compared to control, sodium caprate 0.0625, 0.125 and 0.25% gave an enhancement ratio of 1.97, 6.36 and 7.34, respectively, as shown in Table I. The enhancement of paracellular transport of sodium caprate across Caco-2 cell monolayers has been previously studied for heparin disaccharide (Cho et al. 2002). In this case, the permeability enhancement ratio was found to be 2.3 with 0.2% of sodium caprate which is lower than that observed in our studies. This difference may be attributed to the difference in the cell culture methods, the heparin molecule used, and the protocols used for the transport studies. The mechanism of action for this enhancer has been well studied. Sodium caprate exerts its enhancing effects mainly via the paracellular route, inducing dilatations of the tight junctions (Sawada et al. 1991,Anderberg et al. 1993) The proposed mechanism of action is an increase in the intracellular calcium levels through the activation of phospholipase C in the plasma membrane (Lindmark et al. 1995,1998). The increase in calcium levels is considered to induce the contraction of calmodulin-dependant actin microfilaments, resulting in increased paracellular permeability (Madara et al. 1986). Sodium caprate has been reported to have an absorption-enhancing effect on hydrophilic compounds by opening the tight junction as well as by perturbing the fluidity of the brush border membrane, thereby leading to an increase in absorption through the paracellular pathway (Shimazaki et al. 1998).

TEER data suggests that sodium caprate enhances the transport of ardeparin by loosening the tight junctions and increasing paracellular transport. Since TEER is believed to be well correlated with changes in paracellular permeability of cell monolayers (Madara et al. 1988), the effects of sodium caprate on the TEER values across Caco-2 monolayers were also monitored. As shown in Table I, in the presence of 0.25, 0.125 and 0.0625%, the TEER values decreased to 63, 48 and 27% of the control (media alone), respectively, and were found to recover slightly.

In vitro *cytotoxicity studies*

Caco-2 cells were exposed to sodium caprate at concentrations of 0.01, 0.03, 0.06, 0.12, 0.25, 0.5 and 1% for 6 or 12 h following which cell viability was assessed using the MTTassay. Duration of 6 and 12 h was selected because scintigraphic gastric transit studies in humans suggest that they are physiologically relevant average and maximum exposure times, respectively, in the GI tract (Sethia and Squillante 2004). Figure 1 shows the percent cell viability with respect to the control upon exposure to various concentrations of sodium caprate. Significant decrease in cell viability was seen only at or above 0.25 and 0.125% sodium caprate for 6 and 12 h exposure, respectively. No significant decrease in cell viability was seen until 0.0625% concentration of sodium caprate. These results suggest that the ability of sodium caprate to increase permeability across cells as seen above is not a direct result of its toxicity.

In general, cell culture models are often found to be more sensitive to the cytotoxic effects of permeation enhancers than intact intestinal membrane (Chao et al. 1999,Aungst 2000). Some enhancers have been clearly cytotoxic in Caco-2 studies but caused relatively little damage when administered to animals at doses effective for absorption enhancement. This is clearly the case with sodium caprate. According to the results, sodium caprate at a concentration of 0.125% was found to be toxic to the cells after 12 h incubation. However, no perceptible evidence of mucosal irritation or damage was obtained when the oral formulation containing 100 mg/kg sodium caprate was delivered to the rat *in vivo* as evidenced by histological studies. This discrepancy could be partly explained by assuming that the enhancer is diluted *in vivo* to concentrations tolerable to the intestinal mucosa. In addition, the intact tissue produces a protective mucous layer not found in Caco-2 monolayers and the *in vivo* intestinal tissue possesses mechanisms allowing recovery from trauma over time which may not be present in cell cultures.

Gastrointestinal permeability studies

The effects of sodium caprate across the intact rat GI tissues were examined by an *in vitro* Ussing chamber method. Figure 2 shows the effect of sodium caprate on the permeability of ardeparin across the stomach, duodenal, jejunal and ileal tissue. The enhancer significantly increased the permeability of ardeparin across the duodenal, jejunal, ileal and colonic tissue. At pH 7.4, P_{app} values for the enhancer in the various intestinal sites exhibited marked and significant differences. The P_{app} values for ardeparin were significantly lower in the stomach than in the duodenum, jejunum, ileum, or colon both in the absence and presence of enhancer. However, no significant difference was observed between duodenum, jejunum and ileum. The absorption enhancing effect of sodium caprate was greater across the colon than in the other regions, suggesting regional differences in the absorption promoting effect of sodium caprate. From Figure 2, we obtained the enhancement ratios for ardeparin in the presence of sodium caprate. These ratios were 1.08, 1.31, 1.33 and 1.26 for stomach, duodenum, jejunum and ileum, respectively, the ratio being highest for colon at 1.60. The results obtained were consistent with other studies conducted with sodium caprate (Shimazaki et al. 1990). Jejunal absorption was enhanced to a smaller extent than colonic absorption in rats due to the differences in its effects on the paracellular pathway. Similarly, a slight increase in rectal absorption was observed when sodium caprate was transported into the rectal tissue (Lennernas

et al. 2002). Thus, our findings are consistent with previously reported results pertaining to enhancing effects of sodium caprate. Furthermore, it has also been proposed that the paracellular pore in rat colon is accessible to molecules with a radius < 11蚊 (Bertini et al. 2005). Thus, the pore may be accessible to ardeparin with a radius of 19蚊. This is supported by the low level of anti-factor Xa obtained without any penetration enhancer in our *in vivo* studies (Figure 2).

In vivo *studies*

The anti-factor Xa activity versus time profiles for the formulations (dose 600? 800 IU/kg) are depicted in Figure 3. Oral administration of ardeparin using all these doses with no enhancer yielded extremely low plasma anti-factor Xa activity levels which were in the sub-therapeutic range indicating its restricted intestinal absorption by the barrier function of the intestinal epithelium. For clarity purposes, because the profiles were similar of all these doses without enhancer, only the profile of the group with the dose of 600 IU/kg with no enhancer is shown along with other groups (Figure 3). It has been previously reported that the plasma anti-factor Xa activity required for obtaining 50% of anti-thrombotic effect is 0.12 IU/ml, and that in male Sprague噢 awley rats, a plasma anti-factor Xa level of 0.2 IU/ml or higher results in evident anti-thrombotic effects (Bianchini et al. 1995). Sodium caprate at the dose of 100 mg/kg was chosen for subsequent experiments based on successful studies with antisense oligonucleotides (Raoof et al. 2002). Upon co-administration of 600 IU/kg of ardeparin with sodium caprate (100 mg/kg), a significant increase in drug levels was observed for ardeparin. However, therapeutic levels were not obtained. In contrast, concomitant administration of 1200 IU/kg ardeparin, with sodium caprate at the same dose, rapidly increased the intestinal absorption of ardeparin in rats. The plasma antifactor-Xa activity was increased with a maximum value of 0.2 IU/ml, 30 min after administration. The activity gradually decreased and was sustained up to 480 min. With further increase in the dose of ardeparin to 2400 and 4800 IU/kg, there was an increase in the anti-factor Xa value as shown in Figure 3. Thus, it was shown that sodium caprate, having a medium length saturated fatty acid carbon chain facilitated the transport of ardeparin through the intestinal mucosal barrier in a dose-dependant manner. As mentioned earlier, sodium caprate has a carbon chain length of C10. Two 2-hydroxybenzoyl derivatives, SNAC having eight carbon chain lengths and SNAD having 10 carbon chain lengths, have been developed as delivery agents for UFH (Salartash et al. 2000) and LMWH, (Uchiyama et al. 1999) respectively. In these two cases, C8晶 10 was the optimum carbon chain length for enhancing the absorption of UFH (Leone-Bay et al. 1998). Hence, the carbon chain length in the case of sodium caprate may partly explain the enhancement observed. Adequate anti-thrombotic activity would be obtained by the administration of ardeparin (600? 800 IU/kg) with sodium caprate (100 mg/kg) as the plasma anti-factor Xa activities were maintained at greater than 0.2 IU/ml (Bianchini et al. 1995). The pharmacokinetic parameters presented in Table II indicate that formulations containing the enhancer achieved significantly higher bioavailability compared to drug alone. There is a difference between the T_{max} of these two doses suggesting that the duration of action of the formulation with drug dose of 4800 IU/kg is relatively longer (60 min) than that of 2400 IU/kg dose (30 min). However, there is no significant difference between the absolute and relative bioavailabilities between the formulations with ardeparin dose between 1200 and 4800 IU/kg. Since the dose of sodium caprate in each case was constant, it may be possible that the enhancer allowed passage of only a certain number of macromolecules through the tight junctions after which a saturation point is reached which is not favorable for further transport on a time-dependant fashion. This argument may be supported by recent studies which showed that sodium caprate had no effect on pore radius but increased permeability of a macromolecule via a mechanism involving increased number of functional pores both small and large through which molecules can permeate (Watson et al. 2001).

Histological evaluation of gastrointestinal tissues

The local toxicity of sodium caprate in the small intestine is one of the major concerns in relation to the use of this fatty acid in pharmaceutical products. Ampicillin suppositories containing 5% of sodium caprate caused non-specific damage to the rectal mucosa according to the results obtained in a study conducted in humans (Lindmark et al. 1997). However, the damage was reversible and was attributed not only to caprate but also to the triglyceride suppository base. The toxicity of sodium caprate has been studied *in vitro* at various concentrations and durations of exposure. A close examination of the data reported suggests that sodium caprate at effective concentrations in the vicinity of its critical micelle concentration (13 mM) (Cano-Cebrian et al. 2005) *in vitro* does not affect epithelial viability (Soderholm et al. 1998) and does not cause serious cytotoxicity笈 ts effects moreover being reversible (Yamamoto et al. 1997,Quan et al. 1998, Chao et al. 1999,Uchiyama et al. 1999). This is in agreement with our current investigations.

Upon single oral administration of formulation, the histological change in the GI wall was evaluated by H&E staining. For the formulation used in these experiments, the dose of sodium caprate was 100 mg/kg. As shown in Figure 4, evidence of damage to the GI wall, such as villi fusion, occasional epithelial cell shedding, and congestion of mucosal capillary with blood and focal trauma, were not found in parts of the stomach, duodenum, jejunum, ileum and colon. These results suggest that increased absorption of the LMWH, ardeparin was not caused by damage to the GI epithelium after the oral administration of sodium caprate at the dose administered. The formulation was therefore well tolerated by the animals in this operating condition. It is important to point out that based on the pharmacokinetic profiles observed with oral administration of one dose of the enhancer (100 mg/kg) with the LMWH, it is unlikely that the colon or even the ileum were exposed to levels of sodium caprate sufficient to cause damage to the epithelium. Thus, further dose dependent studies of the enhancer on different intestinal tissues would be required to provide more insight on the toxicology assessment.

Conclusions

Sodium caprate increased absorption of LMWH, ardeparin both *in vitro* and *in vivo*. Its cytotoxicity in Caco-2 cells was not found to be severe. Colonic permeation of ardeparin was found to increase considerably upon addition of sodium caprate. The plasma anti-factor Xa activity obtained with 100 mg/kg dose of caprate and 1200? 800 IU/kg of ardeparin was above therapeutic level and sustained for about 480 min. Furthermore, histological evaluation of GI tissues from animals exposed to the investigated dose of sodium caprate, resulted in no abnormal histopathological findings indicating that it did not cause any tissue damage. In conclusion, our results suggest that the use of sodium caprate as an absorption enhancer, represents an attractive strategy to enhance the oral delivery of LMWH.

Acknowledgements

This study was supported by grants from Texas Tech University Health Sciences Center School of Pharmacy and National Institutes of Health (GM 069397-01A2). The authors are also grateful to: Viscotek Co. (Houston, TX) for their assistance with Triple Array Detection SEC, Dr Thomas Abbruscato for kindly providing assistance with Ussing chamber experiments and Dr Surendra Gupta (American Radiolabeled Chemicals, Inc) for his generous contribution with the radiolabeled ardeparin. Helpful discussions during the redaction of this manuscript with Dr. Michael A. Veronin (Assistant Professor of Pharmaceutical Sciences at TTUHSC SOP) are appreciated.

References

Anderberg EK, Lindmark T, Artursson P. Sodium caprate elicits dilatations in human intestinal tight junctions and enhances drug absorption by the paracellular route. Pharm Res 1993;10:857? 64. [PubMed: 8321854]

Arnold J, Ahsan F, Meezan E, Pillion DJ. Nasal administration of low molecular weight heparin. J Pharm Sci 2002;91:1707? 714. [PubMed: 12115833]

Asada H, Douen T, Waki M, Adachi S, Fujita T, Yamamoto A, Muranishi S. Absorption characteristics of chemically modified-insulin derivatives with various fatty acids in the small and large intestine. J Pharm Sci 1995;84:682? 87. [PubMed: 7562404]

Aungst BJ. Intestinal permeation enhancers. J Pharm Sci 2000;89:429? 42. [PubMed: 10737905]

Bertini S, Bisio A, Torri G, Bensi D, Terbojevich M. Molecular weight determination of heparin and dermatan sulfate by size exclusion chromatography with a triple detector array. Biomacromolecules 2005;6:168? 73. [PubMed: 15638517]

Bianchini P, Bergonzini GL, Parma B, Osima B. Relationship between plasma antifactor Xa activity and the antithrombotic activity of heparins of different molecular mass. Haemostasis 1995;25:288? 98. [PubMed: 8586320]

Boneu B. Low molecular weight heparins: Are they superior to unfractionated heparins to prevent and to treat deep vein thrombosis? Thromb Res 2000;100:V113娞120. [PubMed: 11053624]

Cano-Cebrian MJ, Zornoza T, Granero L, Polache A. Intestinal absorption enhancement via the paracellular route by fatty acids, chitosans and others: A target for drug delivery. Current Drug Delivery 2005;2:9? 2. [PubMed: 16305404]

Chao AC, Nguyen JV, Broughall M, Griffin A, Fix JA, Daddona PE. *In vitro* and *in vivo* evaluation of effects of sodium caprate on enteral peptide absorption and on mucosal morphology. Int J Pharm 1999;191:15? 4. [PubMed: 10556736]

Cho SY, Kim JS, Li H, Shim C, Linhardt RJ, Kim YS. Enhancement of paracellular transport of heparin disaccharide across Caco-2 cell monolayers. Arch Pharm Res 2002;25:86? 2. [PubMed: 11885699]

Kaskel FJ, Kumar AM, Lockhart EA, Evan A, Spitzer A. Factors affecting proximal tubular reabsorption during development. Am J Physiol 1987;252(1 Pt 2):F188鈥197. [PubMed: 3101512]

Kazuhiko Kitao K-iN. 1984. Adjuvant for promoting absorption of pharmacologically active substances through the rectum, Kyoto Yakuhin Kogyo Kabushiki Kaisha, assignee. USA. Patent 4485033.

Knipp GT, Ho NF, Barsuhn CL, Borchardt RT. Paracellular diffusion in Caco-2 cell monolayers: Effect of perturbation on the transport of hydrophilic compounds that vary in charge and size. J Pharm Sci 1997;86:1105? 110. [PubMed: 9344165]

Lennernas H, Gjellan K, Hallgren R, Graffner C. The influence of caprate on rectal absorption of phenoxymethyl-penicillin: Experience from an *in vivo* perfusion in humans. J Pharm Pharmacol 2002;54:499? 08. [PubMed: 11999127]

Leone-Bay A, Paton DR, Freeman J, Lercara C, O京oole D, Gschneidner D, Wang E, Harris E, Rosado C, Rivera T, et al. Synthesis and evaluation of compounds that facilitate the gastrointestinal absorption of heparin. J Med Chem 1998;41:1163? 171. [PubMed: 9544216]

Lindmark T, Nikkila T, Artursson P. Mechanisms of absorption enhancement by medium chain fatty acids in intestinal epithelial Caco-2 cell monolayers. J Pharmacol Exp Ther 1995;275:958? 64. [PubMed: 7473188]

Lindmark T, Schipper N, Lazorova L, de Boer AG, Artursson P. Absorption enhancement in intestinal epithelial Caco-2 monolayers by sodium caprate: Assessment of molecular weight dependence and demonstration of transport routes. J Drug Target 1998;5:215? 23. [PubMed: 9606011]

Lindmark T, Soderholm JD, Olaison G, Alvan G, Ocklind G, Artursson P. Mechanism of absorption enhancement in humans after rectal administration of ampicillin in suppositories containing sodium caprate. Pharm Res 1997;14:930? 35. [PubMed: 9244152]

Lobenberg, R.; Amidon, GL.; Vieira, M. Solubility as a limiting factor to drug absorption. In: Dressman, JB.; Lennernas, H., editors. Oral drug absorption. New York: Marcel Dekker; 2000. p. 137-142.

Lutz KL, Siahaan TJ. Molecular structure of the apical junction complex and its contribution to the paracellular barrier. J Pharm Sci 1997;86:977? 84. [PubMed: 9294808]

Madara JL, Barenberg D, Carlson S. Effects of cytochalasin D on occluding junctions of intestinal absorptive cells: Further evidence that the cytoskeleton may influence paracellular permeability and junctional charge selectivity. J Cell Biol 1986;102:2125? 136. [PubMed: 3711143]

Madara JL, Stafford J, Barenberg D, Carlson S. Functional coupling of tight junctions and microfilaments in T84 monolayers. Am J Physiol 1988;254(3 Pt 1):G416埪423. [PubMed: 3279816]

Makoto, Tanaka T.; Etsuhisa, K.; Kanagawa-ken; Norimitsu, T.; Hachioji. Bristol-Myers Squibb Company, assignee. JM216 Formulations; USA: 2000.

Mitragotri S, Kost J. Transdermal delivery of heparin and low-molecular weight heparin using low-frequency ultrasound. Pharm Res 2001;18:1151? 156. [PubMed: 11587487]

Mosmann T. Rapid colorimetric assay for cellular growth and survival: Application to proliferation and cytotoxicity assays. J Immunol Methods 1983;65:55? 3. [PubMed: 6606682]

Muranishi S. Absorption enhancers. Crit Rev Ther Drug Carrier Syst 1990;7:1? 3. [PubMed: 2257635]

Nieduszynski, I. General physical properties of heparin. In: Lane, DA.; Lindahl, U., editors. Heparin: Chemical and biological properties. Clinical applications. London: Arnold Edward; 1989. p. 51-63.

Nissan A, Ziv E, Kidron M, Bar-On H, Friedman G, Hyam E, Eldor A. Intestinal absorption of low molecular weight heparin in animals and human subjects. Haemostasis 2000;30:225? 32. [PubMed: 11251329]

Ouyang H, Morris-Natschke SL, Ishaq KS, Ward P, Liu D, Leonard S, Thakker D. Structure-activity relationships for enhancement of paracellular permeability across caco-2 cell monolayers by 3-alkylamido-2-alkoxypropylphosphocholines. J Med Chem 2002;45:2857? 866. [PubMed: 12061888]

Quan YS, Hattori K, Lundborg E, Fujita T, Murakami M, Muranishi S, Yamamato A. Effectiveness and toxicity screening of various absorption enhancers using Caco-2 cell monolayers. Biol Pharm Bull 1998;21:615? 20. [PubMed: 9657048]

Raoof AA, Ramtoola Z, McKenna B, Yu RZ, Hardee G, Geary RS. Effect of sodium caprate on the intestinal absorption of two modified antisense oligonucleotides in pigs. Eur J Pharm Sci 2002;17:131? 38. [PubMed: 12393140]

Ross BP, Toth I. Gastrointestinal absorption of heparin by lipidization or coadministration with penetration enhancers. Current Drug Delivery 2005;2:277? 87. [PubMed: 16305430]

Salartash K, Lepore M, Gonze MD, Leone-Bay A, Baughman R, Sternbergh WC 3rd, Bower JC, Money SR. Treatment of experimentally induced caval thrombosis with oral low molecular weight heparin and delivery agent in a porcine model of deep venous thrombosis. Ann Surg 2000;231:789? 94. [PubMed: 10816621]

Sawada T, Ogawa T, Tomita M, Hayashi M, Awazu S. Role of paracellular pathway in nonelectrolyte permeation across rat colon epithelium enhanced by sodium caprate and sodium caprylate. Pharm Res 1991;8:1365? 371. [PubMed: 1798671]

Scudiero DA, Shoemaker RH, Paull KD, Monks A, Tierney S. Evaluation of a soluble tetrazolium/formazan assay for cell growth and drug sensitivity in culture using human and other tumor cell lines. Cancer Res 1988;48:4827? 833. [PubMed: 3409223]

Sethia S, Squillante E. *In vitro—in vivo* evaluation of supercritical processed solid dispersions: Permeability and viability assessment in Caco-2 cells. J Pharm Sci 2004;93:2985? 993. [PubMed: 15468328]

Shimazaki T, Tomita M, Sadahiro S, Hayashi M, Awazu S. Absorption-enhancing effects of sodium caprate and palmitoyl carnitine in rat and human colons. Dig Dis Sci 1990;43:641? 45. [PubMed: 9539662]

Soderholm JD, Oman H, Blomquist L, Veen J, Lindmark T, Olaison G. Reversible increase in tight junction permeability to macromolecules in rat ileal mucosa *in vitro* by sodium caprate, a constituent of milk fat. Dig Dis Sci 1998;43:1547? 552. [PubMed: 9690393]

Takahashi K, Murakami T, Yumoto R, Hattori T, Higashi Y, Yata N. Decanoic acid induced enhancement of rectal absorption of hydrophilic compounds in rats. Pharm Res 1994;11:1401? 404. [PubMed: 7855042]

Teien AN, Lie M, Abildgaard U. Assay of heparin in plasma using a chromogenic substrate for activated factor X. Thromb Res 1976;8:413? 16. [PubMed: 1265712]

Thanou M, Nihot MT, Jansen M, Verhoef JC, Junginger HE. Mono-N-carboxymethyl chitosan (MCC), a polyampholytic chitosan derivative, enhances the intestinal absorption of low molecular weight heparin across intestinal epithelia *in vitro* and *in vivo*. J Pharm Sci 2001a;90:38? 6. [PubMed: 11064377]

Thanou M, Verhoef JC, Junginger HE. Oral drug absorption enhancement by chitosan and its derivatives. Adv Drug Deliv Rev 2001b;52:117? 26. [PubMed: 11718935]

Tomita M, Hayashi M, Awazu S. Absorption-enhancing mechanism of sodium caprate and decanoylcarnitine in Caco-2 cells. J Pharmacol Exp Ther 1995;272:739? 43. [PubMed: 7853188]

Uchiyama T, Sugiyama T, Quan YS, Kotani A, Okada N, Fujita T, Muranishi S, Yamamoto A. Enhanced permeability of insulin across the rat intestinal membrane by various absorption enhancers: Their intestinal mucosal toxicity and absorption-enhancing mechanism of n-lauryl-β-D-maltopyranoside. J Pharm Pharmacol 1999;51:1241? 250. [PubMed: 10632081]

Ward PD, Tippin TK, Thakker DR. Enhancing paracellular permeability by modulating epithelial tight junctions. Pharm Sci Technol Today 2000;3:346? 58. [PubMed: 11050459]

Watson CJ, Rowland M, Warhurst G. Functional modeling of tight junctions in intestinal cell monolayers using polyethylene glycol oligomers. Am J Physiol Cell Physiol 2001;281:C388昌397. [PubMed: 11443038]

Yamamoto A, Okagawa T, Kotani A, Uchiyama T, Shimura T, Tabata S, Kondo S, Muranishi S. Effects of different absorption enhancers on the permeation of ebiratide, an ACTH analogue, across intestinal membranes. J Pharm Pharmacol 1997;49:1057? 061. [PubMed: 9401937]

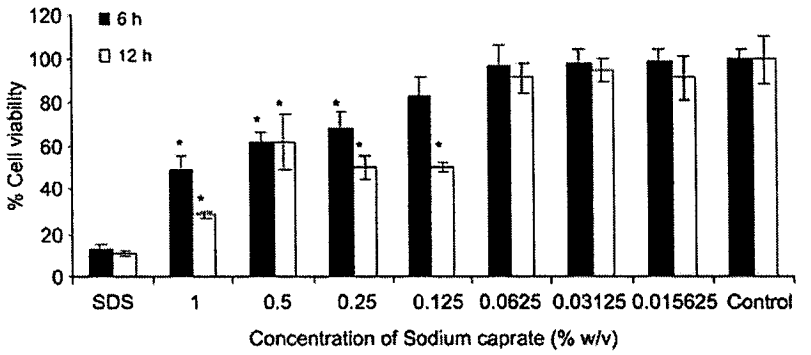

Figure 1.
Caco-2 cell viability after exposure to various concentrations of sodium caprate for 6 and 12 h. The values are means of three independent experiments. *Significantly different compared with control ($p < 0.05$).

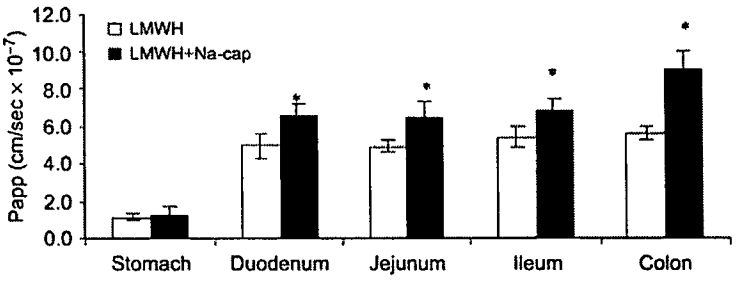

Figure 2.
Regional permeability of ardeparin across rat GI tissues. *Significantly different as compared to control. Data are shown as the mean concentration and error bars represent the SEM (n = 3).

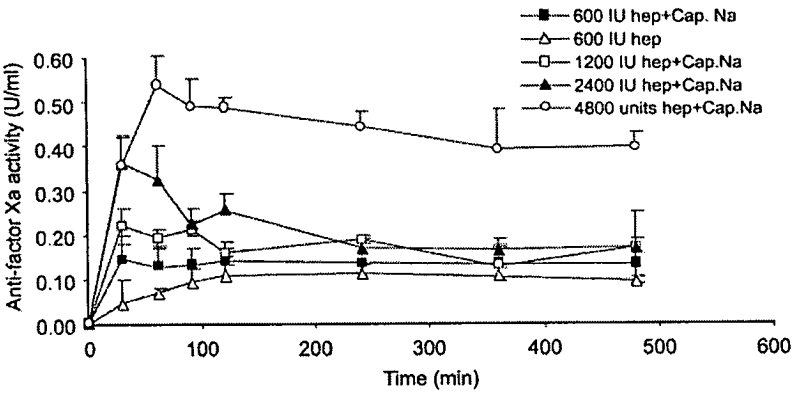

Figure 3.
Anti-factor Xa activity-time profiles of ardeparin in rats after oral administration of various formulations. Data are shown as the mean concentration, and error bars represent the SEM ($n = 4$?).

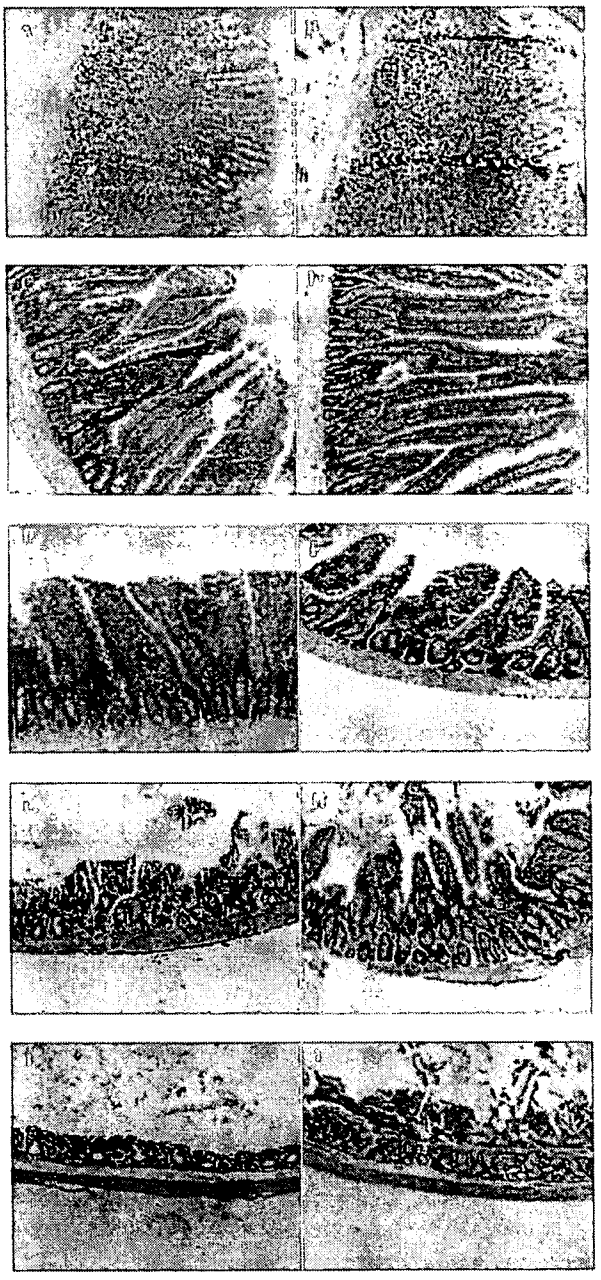

Figure 4.

H&E photomicrographs of gastric and intestinal tissue sections after oral administration of sodium caprate (100 mg/kg and LMWH 1200 IU/kg). All panels represent cross-sections of gastric and intestinal tissues. The original magnification was 100 ? for all panels. A, stomach (control); B, stomach (test); C, duodenum (control); D, duodenum (test); E, jejunum (control); F, jejunum (test); G, ileum (control); H, ileum (test); I, colon (control); J, colon (test).

Table I

Effect of sodium caprate on TEER and ^{3}H ardeparin and ^{14}C mannitol fluxes across Caco-2 cell monolayer.

Sodium caprate (%)	TEER (% decrease from control)	^{3}H ardeparin ($\times 10^{-7}$cm/s)	^{14}C mannitol ($\times 10^{-7}$cm/s)	Enhancemen ratio (ER)
0	100	2.83 ± 0.62	7.5 ± 3.1	1
0.0625	27	5.6 ± 0.8 *	44 ± 14.9 *	1.97
0.125	48	18 ± 5.7 *	46.9 ± 3.3 *	6.36
0.25	63	20.8 ± 2.4 *	68.5 ± 4.3 *	7.34

* Significantly different compared to control.

Table II

Pharmacokinetic parameters following oral administration of ardeparin in rats.

Formulation (dose/kg)	C_{max}(IU/ml)	T_{max} (min)	$F_{absolute}$ (%)	$F_{relative}$ (%)
600 IU ard	0.19 ± 0.031	240 ± 147.98	3.37 ± 0.71	11.17 ± 2.81
600 IU ard + Cap.Na	0.142 ± 0.026 *	30 ± 15.29 *	4.75 ± 0.16 *	15.72 ± 1.99 *
1200 IU ard + Cap.Na	0.220 ± 0.053 *	30 ± 18.23 *	8.17 ± 2.98 *	27.06 ± 2.29 *
2400 IU ard + Cap.Na	0.358 ± 0.055 *	30 ± 7.34 *	9.16 ± 2.2 *	30.34 ± 4.15 *
4800 IU ard + Cap.Na	0.541 ± 0.036 *	60 ± 20.00 *	7.67 ± 1.02 *	5.40 ± 6.89 *

* Significantly different compared to 600 IU ardeparin (ard) alone ($p < 0.05$).

EUROPEAN JOURNAL OF PHARMACEUTICAL SCIENCES 32 (2007) 271–277

available at www.sciencedirect.com

ScienceDirect

journal homepage: www.elsevier.com/locate/ejps

Pharmacokinetics and excretion balance of OR-1896, a pharmacologically active metabolite of levosimendan, in healthy men

Jaakko Puttonen[a,b,*], *Tarmo Laine*[c], *Meri Ramela*[c], *Sari Häkkinen*[c], *Wenhui Zhang*[d], *Rajendra Pradhan*[d], *Pertti Pentikäinen*[e], *Mikko Koskinen*[c]

[a] *Research and Development, Orion Pharma, P.O. Box 1780, FIN-70701 Kuopio, Finland*
[b] *Department of Pharmaceutics, University of Kuopio, Finland*
[c] *Research and Development, Orion Pharma, P.O. Box 65, 02101 Espoo, Finland*
[d] *Abbott Laboratories, Abbott Park, Chicago, IL 60064, USA*
[e] *Helsinki University Central Hospital, Department of Internal Medicine, P.O. Box 340, 00029 Helsinki, Finland*

ARTICLE INFO

Article history:
Received 5 April 2007
Received in revised form
3 August 2007
Accepted 4 August 2007
Published on line 10 August 2007

Keywords:
Pharmacokinetics
OR-1896
OR-1855
Levosimendan
Mass balance

ABSTRACT

Objective: To investigate the pharmacokinetics and excretion balance of [^{14}C]-OR-1896, a pharmacologically active metabolite of levosimendan, in six healthy male subjects. In addition, pharmacokinetic parameters of total radiocarbon and the deacetylated congener, OR-1855, were determined.

Methods: OR-1896 was administered as a single intravenous infusion of 200 μg of [^{14}C]-OR-1896 (specific activity 8.6 MBq/mg) over 10 min. The pharmacokinetic parameters were calculated by three-compartmental methods.

Results: During the 14-day collection of urine and faeces, excretion (±S.D.) averaged 94.2 ± 1.4% of the [^{14}C]-OR-1896 dose. Mean recovery of radiocarbon in urine was 86.8 ± 1.9% and in faeces 7.4 ± 1.5%. Mean terminal elimination half-life of OR-1896 ($t_{1/2}$) was 70.0 ± 44.9 h. Maximum concentrations of OR-1855 were approximately 30% to that of OR-1896. Total clearance and the volume of distribution of OR-1896 were 2.0 ± 0.4 l/h and 175.6 ± 74.5 l, respectively. Renal clearances of OR-1896 and OR-1855 were 0.9 ± 0.4 l/h and (5.4 ± 2.3) × 10^{-4} l/h, respectively.

Conclusions: This study provides data to demonstrate that nearly one half of OR-1896 is eliminated unchanged into urine and that the active metabolites metabolite of levosimendan remain in the body longer than levosimendan. The remaining half of OR-1896 dose is eliminated through other metabolic routes, partially through interconversion back to OR-1855 with further metabolism of OR-1855. Given the fact that the pharmacological activity and potency of OR-1896 is similar to levosimendan, these results emphasize the clinical significance of OR-1896 and its contribution to the long-lasting effects of levosimendan.

* *Corresponding author at:* Quintiles OY, Metsänneidonkuja 10, FI-02130 Espoo, Finland. Tel.: +358 40 343 3019; fax: +358 9 6133 3009.
E-mail address: jaakko.puttonen@quintiles.com (J. Puttonen).

0928-0987/$ – see front matter
doi:10.1016/j.ejps.2007.08.003

1. Introduction

Levosimendan (Simdax®, Orion Pharma, Espoo, Finland) is an intravenous drug used for the treatment of congestive heart failure. It is an opener of ATP-dependent potassium channels in vascular smooth muscle that induces vasodilatation of arterial, venous, and coronary vessels (Yokoshiki et al., 1997) and in cardiac myocytes where it has antistunning effects (Sonntag et al., 2004). It has inotropic effects in the myocardium through enhancing the myofilament sensitivity to calcium by binding to troponin C (Innes and Wagstaff, 2003; Hasenfuss et al., 1998; Pollesello et al., 1994).

The elimination half-life of i.v. levosimendan is about 1 h in both healthy volunteers and patients with heart failure (Sandell et al., 1995; Sundberg et al., 1998). It is extensively metabolised by conjugation with glutathione to cysteine and cysteinylglycine conjugates and eliminated by the renal and faecal routes. As a minor pathway, the *N–N* bond of levosimendan is reduced in the intestine by bacteria to an inactive amine metabolite, OR-1855 which is reabsorbed and further metabolised to an *N*-acetylated conjugate OR-1896 (Fig. 1) (Antila et al., 1999). This pathway accounts for approximately 5% of the total metabolism of levosimendan (Antila et al., 2004a). The enzyme responsible for the acetylation of OR-1855 to OR-1896, N-acetyltransferase 2 (NAT2), is polymorphically expressed in Caucasian population (Meyer and Zanger, 1997) and the acetylation capacity of an individual has a marked effect on the plasma levels of OR-1896. It has been shown that the exposure of OR-1896 may be up to 3.5 times higher in rapid acetylators compared with slow acetylators (Antila et al., 2004a,b).

OR-1896 is formed slowly after levosimendan administration, the peak concentration in plasma is observed approximately 60 h after start of the infusion in healthy subjects and 70–80 h in patients with heart failure (Kivikko et al., 2002a,b; Antila et al., 2004a,b). The effects of levosimendan last much longer than expected on the basis of the pharmacokinetics of the parent drug and it has been shown that OR-1896 has haemodynamic properties similar to levosimendan (Kristof et al., 1998; Takahashi et al., 2000a,b). Therefore, the slow formation and elimination of OR-1896 likely account for the long-lasting haemodynamic effects seen after levosimendan administration (Follath et al., 2002; Kivikko et al., 2003).

Previous studies have shown that the steady-state concentrations of levosimendan in plasma during a 24-h infusion with infusion rates 0.1 and 0.2 μg/(kg min) are approximately 30–40 and 60–70 ng/ml, respectively (Kivikko et al., 2002a,b). Correspondingly, concentrations of OR-1896 were approximately 3–5 and 5–7 ng/ml. About 40% of OR-1896 is bound to plasma proteins, whereas the parent drug is approximately 97% protein bound (Antila et al., 2004a,b). Since the free fraction of OR-1896 in plasma is much higher than that of the parent compound, there is a greater possibility for OR-1896 to interact with target receptors. As OR-1896 is pharmacologically as potent as levosimendan itself, has a long half-life, and has a high free fraction, it has an important role in the overall haemodynamic responses to levosimendan administration.

Due to the long-acting pharmacological effect of OR-1896, it is important to characterise its pharmacokinetic properties. Since only a small portion of levosimendan dose is converted to OR-1896 it is very difficult to characterise the mass balance of this metabolite after administration of levosimendan in man by usual chemical methods. In this study, radiolabelled metabolite OR-1896 was given to healthy volunteers in order to study its pharmacokinetics and excretion properties.

2. Materials and methods

2.1. Study design and subjects

This open-label, non-randomised, single dose study was conducted at SGS Biopharma Research Unit, Stuivenberg, Antwerp, Belgium. Six healthy male subjects with mean

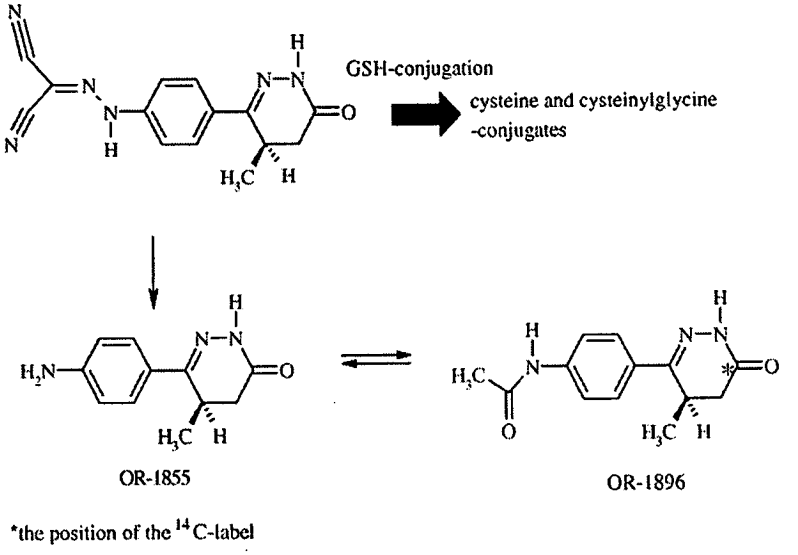

Fig. 1 – Formation of OR-1896 from levosimendan.

(±S.D.) age of 37 ± 10 years (range 25–50 years) and average weight 74 ± 12 kg (range 58–86 kg) were enrolled. All subjects were in a good physical condition with normal mental status as determined by the medical history and the general clinical examination. No concomitant medications were used by the subjects.

The radiolabelled test compound was synthesized in the Department of Medicinal Chemistry, Orion Pharma, Espoo, Finland. The dose of OR-1896 was 200 μg, administered as a [^{14}C]-OR-1896 0.01 mg/ml solution intravenous infusion over 10 min. The specific radioactivity of the solution was 86.45 kBq/ml and the total radioactivity of the dose was 1.7 MBq.

The study was conducted according to good clinical practice (ICH/135/95) guidelines of the European Community and the Declaration of Helsinki (last amended in Somerset West, South Africa, 1996). The study protocol, the subject information text and informed consent were approved prior to the initiation of the study by the Medical Ethics Committee registered by the National Order of Physicians of Belgium.

2.2. *Sampling of blood, breath, urine and faeces*

Blood samples were collected by venipuncture just prior to the study drug administration, and 5, 10, 15, 20, 30, 40 and 50 min as well as 1, 1.25, 1.5, 2, 2.5, 3, 4, 6, 8, 10, 12, 24, 36 and 48 h after the start of the drug administration. Thereafter, blood samples were taken every 24 h until 312 h after the study drug administration. Samples of expired carbon dioxide were obtained 2, 4, 6, 7, 24 and 30 h after the start of the infusion by requesting the study subjects to blow through a glass straw into a vial containing a suitable base to trap 1 mmol of carbon dioxide (CO_2). The endpoint was reached when the phenolphthalein indicator was consistently bleached. All voided urine from each subject was collected into separate vials for 14 days following the infusion of the study drug. The volume and time were recorded. Faeces were collected for 14 days following study drug administration. Each stool was weighed and time was recorded. Stool samples were homogenized with water and aliquots were combusted to CO_2 for radioactivity determination.

2.3. *Analytical methods*

Radioactivity in plasma, urine and faeces was determined by liquid scintillation counting (LSC) at SGS Biopharma, Antwerp, Belgium. The amount of radiocarbon in plasma, urine and faeces was calculated, and excretion rate and half-life of radiocarbon in urine was reported. The lower limits of quantitation (LLOQ) were 0.22, 0.11 and 0.22 Bq/g for plasma, urine and faeces, respectively.

Validated methods were used to determine the concentrations of OR-1896 and OR-1855 in plasma, urine and faeces for the pharmacokinetic analysis. The method involved liquid–liquid extraction followed by HPLC analysis and MS/MS detection of [^{14}C]-OR-1896 and [^{14}C]-OR-1855. Internal standards [$^{13}C_6$]OR-1896 and [$^{13}C_6$]OR-1539 were added to 0.5 ml of plasma, 0.5 ml of urine and 1 g of faeces in methanol and the samples were extracted with 5 ml of ethyl acetate–hexane (80:20; plasma, 40:60; urine and faeces) and concentrated to almost dryness at +40 °C using a TurboVap evaporator. An aliquot of 125 μl of 2 mM ammonium acetate, pH 6.0 was added. After centrifuging, the supernatant was transferred into an unused conical autosampler vial for the liquid chromatographic–tandem mass spectrometric analysis. An aliquot of 70 μl of the extract was injected into the liquid chromatographic column. The liquid chromatographic system consisted of an HP 1100 series high-performance liquid chromatographic system (Hewlett Packard, Waldbronn, Germany). A Chromolith RP-18e reversed phase column (100 mm × 4.6 mm i.d., E. Merck) was used with a Chromolith RP-18e pre-column Chromolith RP-18e (5 mm × 4.6 mm i.d., E. Merck). The mobile phase consisted of 2 mM ammonium acetate, pH 6.0 and methanol–acetonitrile (80:20, v/v) in the mixture of buffer and organic of 59:41 (v/v). The flow-rate was 1.0 ml/min.

The column effluent was directed to a PE Sciex API 2000 (plasma) or API 4000 (urine and faeces) triple quadruple mass spectrometer (Perkin-Elmer Sciex Instruments, Foster City, CA, USA) equipped with a standard atmospheric pressure chemical ionisation source. The effluent was introduced through a heated nebulizer interface.

[^{14}C]-OR-1855 and [^{14}C]-OR-1896 were quantitated using linear regression analysis. The calibration curves were constructed after analysing the OR-1855 and OR-1896. The calibration curves were obtained by plotting the peak area ratios against the concentrations by using 1/x-weighed weighted (plasma) or $1/x^2$-weighed weighted (urine, faeces) linear regression model for OR-1855 and OR-1896. The calibration curves were characterised by back-calculated values for the calibration standards. The concentrations of the validation samples and the quality control samples were calculated from the measured peak area ratios using the equation of the appropriate calibration curve. Finally, the results were multiplied with the value 1.0989 (=1/0.91, the atom% of [^{14}C]-OR-1896 is 91%) to obtain the total concentration (both labelled and unlabelled) of OR-1896 and OR-1855 in samples.

LLOQ:s were 0.5 and 0.75 ng/ml in plasma and urine, respectively. LLOQ:s for OR-1855 and OR-1896 in faeces were 0.25 and 0.3 ng/g, respectively. Bioanalytical validation, including calibration ranges, accuracy and precision are presented in Table 1.

Table 1 – Summary of the validation performance of the LC–MS/MS bioanalytical methods used for the analysis of [^{14}C]-OR-1896 and [^{14}C]-OR-1855

	Plasma	Urine	Faeces
Calibration range (ng/ml)			
^{14}C-OR-1896	0.5–40.0	0.75–40.0	0.02–20.0
^{14}C-OR-1855	0.5–40.0	0.75–40.0	0.02–20.0
Accuracy (bias%)			
^{14}C-OR-1896	−3.0 to 1.6	−3.9 to 5.5	−0.7 to 6.4
^{14}C-OR-1855	−5.6 to 1.5	6.6–9.0	3.9–13.4
Precision (R.S.D.%)			
^{14}C-OR-1896	3.6–7.1	4.6–6.9	3.2–9.2
^{14}C-OR-1855	2.9–8.5	4.4–4.9	0.8–9.0

2.4. Assessment of pharmacokinetics

2.4.1. Radiocarbon

Total radioactivity (Bq/g) was converted to nanogram equivalent of OR-1896 per gram (ng equiv./g). The specific activity of 86.45 kBq/g of solution corresponds to 8.645 MBq/mg of drug, and 1 Bq corresponds to 0.114 ng equiv. of OR-1896. Radioactivity of expired carbon dioxide in breath samples was also measured. Pharmacokinetic parameters of total radiocarbon in plasma (nanogram equivalent of OR-1896 per gram, ng equiv./g) were calculated by non-compartmental methods at SGS Biopharma using WinNonlin Professional (version 3.2) (Pharsight Corporation, Mountain View, CA, USA).

2.4.2. OR-1896 and OR-1855

The amount of OR-1896 and OR-1855 excreted daily into urine and into faeces was calculated as was the cumulative excretion of each. Excretion rate and excretion half-life for OR-1896 and OR-1855 were also determined. Excretion rate for each collection interval (amount eliminated per unit of time) of OR-1896 and OR-1855 was calculated according to the formula:

$$\frac{\text{concentration} \times \text{volume}}{\text{end time} - \text{start time}}$$

Pharmacokinetic parameters for OR-1896 in plasma were estimated using a three-compartmental model. The model was chosen based on visual evaluation of the residual plots, correlation between observed and predicted concentration values and on the Schwarz and Akaike criteria for model fitting (Ludden et al., 1994). Non-compartmental methods were used in pharmacokinetic calculations of OR-1855 since the dose of OR-1855 was not known. For determination of terminal elimination half-life of OR-1896, a weighing weighting factor $1/y^2$ (reciprocal of the square of the concentration) was used. Urine and faeces pharmacokinetics were assessed with non-compartmental methods. Renal clearance of OR-1896 and OR-1855 was calculated according to the formula:

$$Cl_r = \frac{Ae\,(\text{amount of unchanged drug excreted into urine})}{AUC_{0-t}}$$

Calculations were made with WinNonlin 4.0 Professional computer program. Values of 0 were included in the calculations.

2.5. Statistical methods

Descriptive statistics (mean ± S.D.) were used to describe the pharmacokinetics and excretion of total radiocarbon, OR-1896 and OR-1855. All statistical calculations of pharmacokinetic parameters derived from OR-1896 and OR-1855 were performed using SAS 8.2 for Windows (SAS Inc., Cary, NC, USA). All statistical calculations of pharmacokinetic parameters derived from radiocarbon data were performed at SGS Biopharma.

3. Results

In this study, six subjects were given a dose of 200 μg of [^{14}C]-OR-1896 as an intravenous infusion over 10 min. The dose was well tolerated, and the maximum OR-1896 levels in plasma were similar to those seen after 24-h infusion of levosimendan, with infusion rate of 0.2 μg/(kg min) (Kivikko et al., 2002b). All six subjects completed the study.

3.1. Mass balance of [^{14}C]-OR-1896

Fourteen days after administration of [^{14}C]-OR-1896 the subjects had excreted 92–96% of the radioactive dose (Table 2). For two of the six subjects overall excretion of over 95% of the dose was reached. Excretion to urine was fastest during the first 4–5 days after intake, and excretion rate declined with a half-life of 32.6 ± 16.0 h (Fig. 2a). The cumulative recovery of radiocarbon in urine was 86.8 ± 1.9% of the radioactive dose within 14 days (Table 2 and Fig. 2b). Mean recovery of radiocarbon in faeces was 7.4 ± 1.5% of the radioactive dose within 14 days. No quantifiable excretion of radiocarbon was found in expired carbon dioxide measured up to 30 h post-dose.

3.2. Pharmacokinetics of the total radiocarbon, OR-1896 and OR-1855

Mean total radiocarbon peak concentration was 5.59 ± 2.16 ng equiv./g (range 3.32–8.75 ng equiv./g) and was reached immediately after the end of the study drug infusion (10–15 min after the start of the infusion). The mean AUC_{0-t} (calculated until 312 h) was 228 ± 40.3 h ng equiv./g. The pharmacokinetic parameters of total radiocarbon are summarized in Table 3.

The pharmacokinetic parameters of OR-1896 were determined with a three-compartmental model. The mean peak concentration of OR-1896 in plasma was 5.0 ± 2.4 ng/ml (Table 4 and Fig. 3). The concentrations of OR-1896 declined tri-exponentially, with rapid distribution phase half-life ($t_{1/2\alpha}$) of 1.0 ± 1.5 h, slow distribution half-life ($t_{1/2\beta}$) of 6.9 ± 8.8 h and a terminal elimination half-life of 70.0 ± 44.9 h (Table 4 and Fig. 3). In one subject, terminal elimination was approximately 144 h, which mainly caused the large variation. Last measurable concentrations in plasma were observed at a mean of 32 h (range 12–48 h) after starting the infusion. Total clearance and the volume of distribution of OR-1896 at steady state were

Table 2 – Total cumulative recovery of radiocarbon (% of the dose, mean ± S.D., n = 6)

	Day 1	Day 3	Day 7	Day 14	Range (day 14)
Urine	24.9 ± 4.3	56.4 ± 6.3	80.0 ± 3.5	86.8 ± 1.9	[84.1, 89.7]
Faeces	0.3 ± 0.2[a]	1.9 ± 0.9	5.9 ± 1.1	7.4 ± 1.5	[5.8, 9.1]
Total recovery	25.4 ± 4.2	58.3 ± 6.1	86.0 ± 3.0	94.2 ± 1.4	[92.2, 95.9]

[a] n = 3.

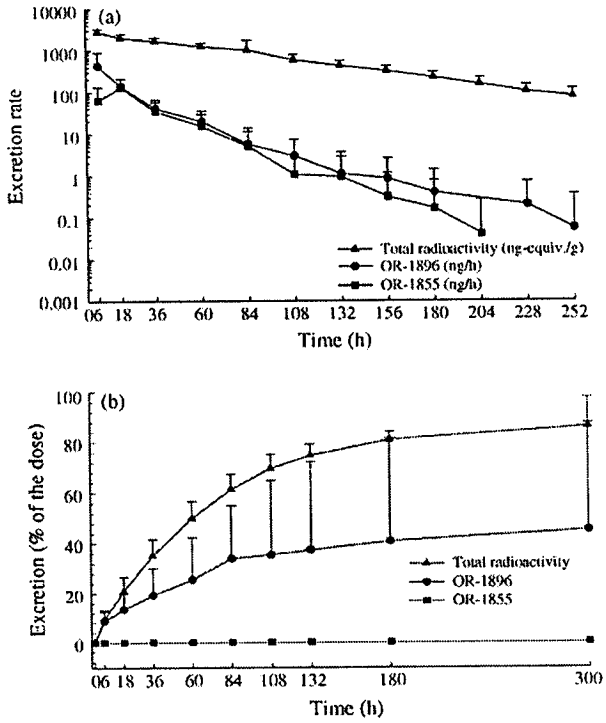

Fig. 2 – (a) Excretion rate of total radioactivity, OR-1896 and OR-1855 to urine (mean + S.D., n = 6). (b) Cumulative excretion of total radioactivity, OR-1896 and OR-1855 to urine (mean + S.D., n = 6).

Table 3 – Pharmacokinetics of total radiocarbon in plasma

Parameter	Mean ± S.D.	Range
C_{max} (ng equiv./g)	5.59 ± 2.16	[3.32, 8.75]
t_{max} (h)	0.18 ± 0.03	[0.17, 0.25]
AUC_{0-t} (h ng equiv./g)	228 ± 40.3	[166, 279]
AUC_{∞} (h ng equiv./g)	231 ± 41.4	[167, 284]
$t_{1/2}$ (h)	47.8 ± 7.47	[36.8, 59.7]

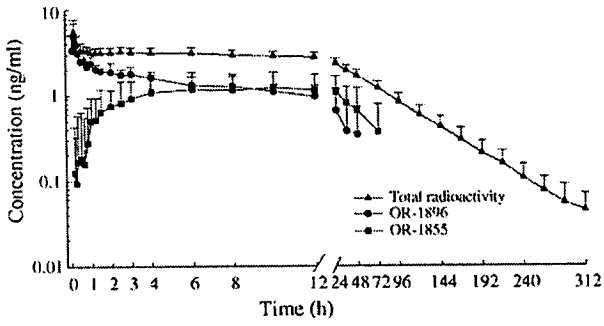

Fig. 3 – Mean concentrations of total radioactivity, [^{14}C]-OR-1896 and [^{14}C]-OR-1855 in plasma after a 10-min intravenous infusion of 200 μg of [^{14}C]-labelled OR-1896 in healthy male volunteers (mean + S.D., n = 6).

2.0 ± 0.4 l/h and 175.6 ± 74.5 l, respectively. Renal clearance of OR-1896 was 0.9 ± 0.4 l/h.

The mean peak concentration of the deacetylated metabolite OR-1855 in plasma was 1.5 ± 0.4 ng/ml, observed approximately 8 h after starting the infusion. The AUC_{0-t} of OR-1855 was approximately 35% smaller than corresponding value of OR-1896 (Table 4). Elimination half-life of OR-1855 was slightly shorter than that of OR-1896. Last detectable concentrations of OR-1855 in plasma were observed from 36 to 72 h after the start of the infusion. Renal clearance of OR-1855 was negligible, being $(5.4 \pm 2.3) \times 10^{-4}$ l/h. The volume of distribution for OR-1855 could not be determined since its dose was not known.

One subject was not included in the pharmacokinetic analysis of OR-1896 since the data could not be fitted according to the three-compartmental model. In addition, one subject was excluded in the pharmacokinetic analysis of OR-1855 since he did not have concentrations in plasma above the detection limit.

The main pharmacokinetic parameters for OR-1896 and OR-1855 are summarized in Table 4, and the mean concentrations in plasma are presented in Fig. 3.

Table 4 – Pharmacokinetic parameters (mean ± S.D.) of OR-1896 and OR-1855 in plasma after an intravenous infusion of 200 μg of [^{14}C]-OR-1896 for 10 min in healthy male volunteers

	OR-1896 (n = 5)	95% CI	OR-1855[a] (n = 5)	95% CI
AUC_{0-t} (h ng equiv./ml)	102.1 ± 21.0	[78.3, 108.6]	66.3 ± 26.6	[33.3, 99.3]
C_{max} (ng/ml)	5.0 ± 2.4	[1.8, 6.5]	1.5 ± 0.4	[1.1, 2.0]
t_{max} (h)	0.2 ± 0.04	[0.17, 0.25]	7.6 ± 2.6	[4.4, 10.8]
$t_{1/2\alpha}$ (h)	1.0 ± 1.5	[0, 2.8]	N.D.	N.D.
$t_{1/2\beta}$ (h)	6.9 ± 8.8	[0, 17.8]	N.D.	N.D.
$t_{1/2\gamma}$ (h)	70.0 ± 44.9	[14.3, 125.7]	54.5 ± 17.8	[35.3, 66.7]
CL_{tot} (l/h)	2.0 ± 0.4	[1.6, 2.5]	N.D.	N.D.
CL_r (l/h)	0.9 ± 0.4	[0.7, 2.0]	$(5.4 \pm 2.3) \times 10^{-4}$	$[2.5 \times 10^{-4}, 8.2 \times 10^{-4}]$
V_{ss} (l)	176 ± 75	[83.1, 268.0]	N.D.	N.D.

AUC_{0-t} = area under the curve to the last measurable concentration; C_{max} = peak concentration in plasma; t_{max} = time to peak concentration; $t_{1/2\alpha}$ = elimination half-life of the rapid distribution phase; $t_{1/2\beta}$ = elimination half-life in the slow distribution phase; $t_{1/2\gamma}$ = terminal elimination half-life; CL_{tot} = total plasma clearance; CL_r = renal clearance; V_{ss} = volume of distribution at steady state; N.D. = not determined.

[a] Parameters determined by non-compartmental methods.

Table 5 – Pharmacokinetic parameters (mean ± S.D.) of OR-1896 and OR-1855 in urine and faeces after an intravenous infusion of 200 μg of [^{14}C]-OR-1896 for 10 min in healthy male volunteers

	OR-1896 [95% CI]		OR-1855 [95% CI]	
	Urine	Faeces	Urine	Faeces
Cumulative excretion (%)	45.2 ± 35.5 [8.0, 82.4]	0.003 ± 0.002 [0.000, 0.005]	0.03 ± 0.01 [0.02, 0.04]	0.004 ± 0.002 [0.002, 0.005]
Cumulative amount recovered (μg)	90.5 ± 70.9 [16.0, 164.9]	5.0 ± 4.6 [0.2, 9.9]	0.054 ± 0.020 [0.034, 0.075]	7.0 ± 3.3 [3.6, 10.4]
Elimination half-life (h)	74.6 ± 62.2 [9.3, 139.9]	N.D.	48.0 ± 17.2 [30.0, 66.0]	N.D.
Maximum observed excretion rate (ng/h)	1.17 ± 0.16 [1.00, 1.34]	0.04 ± 0.02 [0.02, 0.05]	0.67 ± 0.30 [0.36, 0.98]	0.04 ± 0.02 [0.03, 0.06]

N.D. = not determined.

3.3. *Excretion of OR-1896 and OR-1855*

Cumulative mean renal excretion of OR-1896 within 14 days was 45.2 ± 35.5% of the dose (Table 5). For all subjects, urine samples contained OR-1896 as the predominant compound. The mean half-life of elimination into urine based on the excretion rate of OR-1896 was 74.6 ± 62.2 h. The recovery of OR-1855 in urine was 0.03 ± 0.01% of the dose and $t_{1/2}$ was 48.0 ± 17.2 h.

Only very small amounts of metabolites were recovered in faeces within 14 days. OR-1855 was excreted in faeces slightly faster than OR-1896 but the cumulative amount of OR-1855 recovered was similar to OR-1896. The amount of OR-1896 and OR-1855 recovered in faeces was 0.003 ± 0.002 and 0.004 ± 0.002% of the dose, respectively.

4. Discussion

In this study, elimination of OR-1896 occurred slower and the exposure was larger than that of OR-1855. OR-1855 appeared slowly into plasma, most likely as a result of deacetylation of OR-1896. There was some variation between the subjects and it has been observed earlier that the acetylation capacity of an individual has a marked effect on the plasma levels and exposure of both OR-1896 and OR-1855 (Antila et al., 2004a,b).

Approximately 94% of the radioactive [^{14}C]-OR-1896 dose was recovered in 2 weeks. Forty-five percent of the OR-1896 dose was excreted unchanged in the urine and 0.03% as OR-1855 within 14 days. The rest of radioactivity (about 55%) is excreted into urine mainly in the form of further metabolites of OR-1855 and OR-1896. Since this study was a mass balance study focusing on the excretion of the radioactive label, identification of the further metabolites was not performed in this context. However, identification of these metabolites is ongoing and the results will be presented in detail in a subsequent study and published separately. Given that OR-1855 is metabolised further, negligible amounts of OR-1855 are found in the urine. Only very small amounts of radioactivity were recovered in faeces within the 2-week collection period. The recovery of unchanged OR-1855 in urine and faeces was negligible.

Based on the exposure (AUC) of total radioactivity (228 h ng equiv./ml), OR-1896 and OR-1855 accounted for approximately 75% of radioactivity in plasma (102 and 66 h ng equiv./ml, respectively).

Although haemodialysis clearance of approximately 100 ml/min for OR-1896 has been determined in patients with renal failure (Puttonen et al., 2007), this study was the first to determine the renal clearance of the pharmacologically active metabolite of levosimendan, OR-1896 in healthy volunteers. Renal clearance of OR-1896 represented approximately 45% of the total clearance. The total clearance of [^{13}C]-OR-1896 has been observed to be 0.034 l/(h kg), which is approximately 2.4 l/h in a person weighing 70 kg (Antila et al., 2004a,b). This is in accordance with the result obtained in the present study.

In conclusion, this study provides data to demonstrate that nearly one half of OR-1896 is eliminated unchanged into urine and that the active metabolites metabolite of levosimendan remain in the body longer than levosimendan the parent drug itself. The remaining half of OR-1896 dose is also eliminated through other metabolic routes, partially through interconversion back to OR-1855 with further metabolism of OR-1855. It has been demonstrated in previous studies that the haemodynamic effects of levosimendan last longer than expected on the basis of the pharmacokinetics of the parent drug (Kivikko et al., 2002b). Given the fact that the pharmacological activity and potency of OR-1896 is similar to levosimendan, these results emphasize the clinical significance of OR-1896 and its contribution to the long-lasting effects of levosimendan.

Acknowledgements

The study was supported by Orion Pharma, Espoo, Finland. The authors want to thank SGS Biopharma, Antwerp, Belgium for the radioactivity analyses. Ms. Tuula Filén is acknowledged for drawing the figures.

REFERENCES

Antila, S., Huuskonen, H., Nevalainen, T., Kanerva, H., Vanninen, P., Lehtonen, L., 1999. Site dependent bioavailability and metabolism of levosimendan in dogs. Eur. J. Pharm. Sci. 9, 85–91.

Antila, S., Pesonen, U., Lehtonen, L., Tapanainen, P., Nikkanen, H., Vaahtera, K., Scheinin, H., 2004a. Pharmacokinetics of levosimendan and its active metabolite OR-1896 in rapid and slow acetylators. Eur. J. Pharm. Sci. 23, 213–222.

Antila, S., Kivikko, M., Lehtonen, L., Eha, J., Heikkilä, A., Pohjanjousi, P., Pentikäinen, P.J., 2004b. Pharmacokinetics of levosimendan and its circulating metabolites in patients with heart failure after an extended continuous infusion of levosimendan. Br. J. Clin. Pharmacol. 57, 412–415.

Follath, F., Cleland, J.G., Just, H., Papp, J.G., Scholz, H., Peuhkurinen, K., Harjola, V.P., Mitrovic, V., Abdalla, M., Sandell, E.P., Lehtonen, L., 2002. Efficacy and safety of intravenous levosimendan compared with dobutamine in severe low-output heart failure (the LIDO study): a randomised double-blind trial. Lancet 360, 196–202.

Hasenfuss, G., Pieske, B., Castell, M., Kretschman, B., Maier, L., Hanjörg, J., 1998. Influence on novel inotropic agent levosimendan on isometric tension and calcium cycling in failing human myocardium. Circulation 98, 2141–2147.

Innes, C.A., Wagstaff, A.J., 2003. Levosimendan. A review of its use in the management of acute decompensated heart failure. Drugs 63, 2651–2671.

Kivikko, M., Antila, S., Eha, J., Lehtonen, L., Pentikäinen, P.J., 2002a. Pharmacodynamics and safety of a new calcium sensitizer, levosimendan, and its metabolites during an extended infusion in patients with severe heart failure. J. Clin. Pharmacol. 42, 43–51.

Kivikko, M., Antila, S., Eha, J., Lehtonen, L., Pentikäinen, P.J., 2002b. Pharmacokinetics of levosimendan and its metabolites during and after a 24-hour continuous infusion in patients with severe heart failure. Int. J. Clin. Pharm. Ther. 40, 465–471.

Kivikko, M., Lehtonen, L., Colucci, W.S., on Behalf of the Study Investigators, 2003. Sustained hemodynamic effects of intravenous levosimendan. Circulation 107, 81–86.

Kristof, E., Szigeti, G., Papp, Z., Bodi, A., Facsko, A., Kovacs, L., Papp, J.G., Kranias, E.G., Edes, I., 1998. Cardiac responses to calcium sensitizers and isoproterenol in intact guinea pig hearts. Effects on cyclic AMP levels, protein phosphorylation, myoplasmic calcium concentration and left ventricular function. Ann. N.Y. Acad. Sci. 853, 316–319.

Ludden, T.M., Beal, S.L., Sheiner, L.B., 1994. Comparison of the Akaike Information Criterion, the Schwarz criterion and the F test as guides to model selection. J. Pharmacokinet. Biopharm. 22, 431–435.

Meyer, U.A., Zanger, U.M., 1997. Molecular mechanisms of genetic polymorphisms of drug metabolism. Annu. Rev. Pharmacol. Toxicol. 37, 269–296.

Pollesello, P., Ovaska, M., Kaivola, J., Tilgmann, C., Lundström, K., Kalkkinen, N., Ulmanen, I., Nissinen, E., Taskinen, J., 1994. Binding of a new Ca^{2+}-sensitizer, levosimendan, to recombinant human cardiac troponin C. J. Biol. Chem. 269, 28584–28590.

Puttonen, J., Kantele, S., Kivikko, M., Häkkinen, S., Harjola, V.-P., Koskinen, P., Pentikäinen, P.J., 2007. Effect of severe renal failure and haemodialysis on the pharmacokinetics of levosimendan and its metabolites. Clin. Pharmacokinet. 46, 235–246.

Sandell, E.P., Häyhä, M., Antila, S., Heikkinen, P., Ottoila, P., Lehtonen, L., Pentikäinen, P.J., 1995. Pharmacokinetics of levosimendan in healthy volunteers and patients with congestive heart failure. J. Cardiovasc. Pharmacol. 26 (Suppl. 1), S57–S62.

Sonntag, S., Sundberg, S., Lehtonen, L., Kleber, F., 2004. The calcium sensitizer levosimendan improves the function of stunned myocardium after percutaneous transluminal coronary angioplasty in acute myocardial ischemia. J. Am. Coll. Cardiol. 43, 2177–2182.

Sundberg, S., Antila, S., Scheinin, H., Häyhä, M., Virtanen, M., Lehtonen, L., 1998. Integrated pharmacokinetics and pharmacodynamics of the novel calcium sensitizer levosimendan as assessed by systolic time intervals. Int. J. Clin. Pharmacol. Ther. 36, 629–635.

Takahashi, R., Talukder, M.A.H., Endoh, M., 2000a. Effects of OR-1896, an active metabolite of levosimendan on contractile force and aequorin light transients in intact rabbit ventricular myocardium. J. Cardiovasc. Pharmacol. 36, 118–125.

Takahashi, R., Talukder, M.A.H., Endoh, M., 2000b. Inotropic effects of OR-1896, an active metabolite of levosimendan, on canine ventricular myocardium. Eur. J. Pharmacol. 400, 103–112.

Yokoshiki, H., Katsube, Y., Sunagawa, M., Sperelakis, N., 1997. The novel calcium sensitizer levosimendan activates the ATP-sensitive K^+ channel in rat ventricular cells. J. Pharmacol. Exp. Ther. 283, 375–383.

PERGAMON

Food and Chemical Toxicology 38 (2000) 1043–1051

www.elsevier.com/locate/foodchemtox

Research Section

Absorption, distribution, metabolism and excretion of intravenously and dermally administered triethanolamine in mice*

W. T. STOTT†, J. M. WAECHTER, Jr, D. L. RICK and A. L. MENDRALA

Toxicology & Environmental Research, Bldg 1803, The Dow Chemical Company, Midland, MI 48674, USA

(Accepted 6 June 2000)

Abstract—Triethanolamine (TEA) is an amino alcohol having widespread applications in consumer goods and as an industrial chemical. A number of relatively high-dose dermal toxicity studies have been conducted in rats and mice reflecting the principal route of human exposure to TEA. The absorption, distribution, metabolism and excretion (ADME) of ^{14}C-TEA derived radioactivity were determined in male C3H/HeJ mice following dermal application of 2000 mg/kg (neat) or, to characterize blood kinetics, intravenous (iv) injection of 1 mg/kg ^{14}C-TEA. Balance and excretion data were also collected in mice utilizing several dermal dosing scenarios (1000 mg/kg in acetone, 2000 mg/kg neat, 2000 mg/kg in water) and, for comparative purposes, in male Fischer 344 rats dosed dermally with 1000 mg/kg neat ^{14}C-TEA. Urine, feces, expired CO_2 (iv) and, where appropriate, blood were collected over a 24- or 48-hour period post-dosing. The half-life for dermal absorption of radioactivity was estimated to be 1.3 hours. Intravenously administered radioactivity was eliminated in a biphasic manner with a prominent initial phase (half-life of 0.3 hr) followed by a slower terminal phase (half-life of 10 hr). Radioactivity was excreted primarily via the urine (49–69%) as unmetabolized TEA, regardless of dosage, route or vehicle used. Fecal excretion of radioactivity comprised 16–28% of dose administered. The body burden at sacrifice (sum of liver, kidney, carcass and non-application site skin) ranged from 3 to 6% of the dose. It was concluded that TEA is absorbed extensively following dermal application to mice at dosages relevant to toxicity testing and that acetone or water vehicles do not appear to significantly alter *total* uptake. Significantly, the blood kinetics and ADME of TEA in mice and/or rats differs from that of a related chemical, diethanolamine, which appears to be more toxic to rodents than TEA.

Keywords: triethanolamine; alkanolamines; pharmacokinetics; metabolism.

Abbreviations: ADME = absorption, distribution, metabolism and excretion; DEA = diethanolamine; GC = gas chromatography; LSC = liquid scintillation spectroscopy; MEA = monoethanolamine; NDELA = *N*-nitrosodiethanolamine; TEA = triethanolamine.

INTRODUCTION

Triethanolamine (TEA) is an amino alcohol having widespread applications in consumer goods and as an industrial chemical (Knaak *et al.*, 1997). Based on its usage and relatively low vapor pressure (< 0.01 mm Hg), exposure to humans occurs principally via the dermal route. For this reason, the toxicity of TEA has often been studied in laboratory animals dosed via skin application, typically to the dorsal, shaved, surfaces of mice as acetone solutions at lower doses or neat at higher doses.

TEA is relatively non-toxic to laboratory animals. The oral and dermal LD_{50} in rats is reported to be 5400–11,000 mg/kg in rats and greater than 20,000

*This work was supported by the Alkanolamines Panel of the Chemical Manufacturers Association.

†Corresponding author: e-mail: wstott@dow.com

0278-6915/00/$ - see front matter
PII: S0278-6915(00)00095-8

mg/kg in rabbits (reviewed by Knaak *et al.*, 1997). Subacute dermal application of up to 3000 mg/kg/day to B6C3F$_1$ mice (Melnick *et al.*, 1988) or subchronic dermal application of up to 2250 mg/kg/day TEA to C3H/HeJ mice (DePass *et al.*, 1995), have failed to identify evidence of significant systemic and only minimal localized skin effects. Chronic dermal application of up to 2000 mg/kg/day in male B6C3F$_1$ mice reportedly caused slight acanthosis following 18, but not 24, months (Hejtmancik *et al.*, 1995). No skin effects were noted in female mice administered 1000 mg/kg/day nor were treatment-related non-neoplastic systemic effects reported in either sex. The evaluation of liver pathology in the chronic study was, however, confounded by infection with *Helicobacter hepaticus* (Fox *et al.*, 1998) resulting in the invalidation of the mouse bioassay (NTP, 1999). Rats administered TEA over subacute or chronic periods by similar means displayed localized skin irritation at 2000 mg/kg/day (Melnick *et al.*, 1988) and at 63 mg/kg/day (males) and 250 mg/kg/day (females) (NTP, 1999), but no clear-cut systemic toxicity. In contrast, subchronic feeding and drinking water studies in rats and/or guinea pigs ingesting more than 85–200 mg/kg/day (Kindsvatter, 1940; Smyth *et al.*, 1951; reviewed by Knaak *et al.*, 1997) and a chronic drinking water study in rats at doses greater than 500–1000 mg/kg/day (Maekawa *et al.*, 1986) have indicated that the kidneys and/or liver may be target organs of ingested TEA.

The lack of identifiable systemic toxicity in high-dose mouse TEA toxicity studies and the route-dependency of TEA toxicity in rat studies suggested that dermal absorption of TEA might be limited. However, no comprehensive data are available on the absorption, distribution, metabolism and excretion (ADME) of TEA in animals. Kohri *et al.* (1982) reported that approximately 53% and 20% of orally administered TEA was excreted in rats via the urine and feces, respectively, within 24 hr post-dosing, but no blood kinetic nor distribution data were presented. The purpose of this study, therefore, was to provide ADME data for ^{14}C-TEA in a test animal that has been used in the toxicity testing of TEA, the C3H/HeJ mouse. Excretion and distribution data were also obtained in F344 rats for comparative purposes.

MATERIALS AND METHODS

Test material

^{14}C-UL-Triethanolamine (sp. act. 34.7 mCi/mmol) was purchased from Amersham Corporation (Arlington Heights, IL, USA). A radiochemical purity of 98.6% was established by liquid chromatography. Non-radiolabeled TEA with a purity of 99.6% was obtained from Texaco Chemical Company (Austin, TX, USA).

Animals

Male C3H/HeJ mice were obtained from Jackson Laboratories (Bar Harbor, ME, USA). This species and strain was chosen because of its previous use in dermal toxicity studies with TEA (DePass *et al.*, 1995). The weight of mice used in these studies ranged from 20 to 30 g. Male F344 rats were obtained from Charles River Laboratories (Kingston, NY, USA) and weighed from 231 to 247 g. Mice and rats were examined for health status by a veterinarian on arrival and were acclimated to the laboratory for at least 7 days prior to use. The animals were weighed, randomly assigned to study groups using a computerized randomization procedure, and identified by uniquely numbered metal ear tags.

Animals were singly housed in suspended wire-mesh bottomed, stainless-steel cages in environmentally-controlled animal rooms. Animals from which excreta were collected were subsequently housed in glass Roth-style metabolism cages. The latter animals were acclimated to the cages for 1–2 days prior to dosing. Purina® Certified Lab Diet #5002 and tap water were available to all animals *ad lib.* throughout the course of the study.

Intravenous administration

In order to provide accurate blood kinetics and appropriate reference ADME data for subsequent dermal application of TEA, mice were administered ^{14}C-TEA via iv injection. A 1 mg/kg dose of ^{14}C-TEA as an aqueous solution (0.5 mg/ml) was administered via tail vein injection to 27 male mice. The dosing volume administered was 2 ml/kg body weight and the average amount of radioactivity injected per mouse was 1.7 μCi. Immediately following dosing, mice were returned to their cages, with the animals designated for excreta collection and euthanasia at 24 hr post-dosing placed in Roth-type metabolism cages. All mice were euthanized under methoxyflurane anesthesia by cervical dislocation. Blood samples were collected via orbital sinus puncture from groups of three mice at 0.083, 0.167, 0.5, 1, 2, 4, 6, 12 and 24 hr post-dosing. Kinetic parameters in the blood were calculated using PK Solutions 2.0 (Summit Research Services, Ashland, OH, USA).

Urine, feces and expired CO_2 were collected at 12 and 24 hr from the 24-hr group of mice housed in metabolism cages. Urine and feces were collected in containers cooled on dry ice. Expired CO_2 was trapped in a solution of monoethanolamine/ethylene glycol monomethyl ether (3:7). Subsequent dermal experiments did not include trapping expired $^{14}CO_2$ as none was excreted via this route following iv administration. Following euthanization of this group, tails were removed, the animals were skinned, and the liver and kidneys were excised. Roth cages were washed with a solution of acetone and water to recover urine adhering to the sides. Radioactivity in the excreta, CO_2 trapping solutions, cage-wash

solutions, liver, kidneys, skin and remaining carcass was determined as described below.

Dermal application

The blood kinetics and ADME of ^{14}C-TEA-derived radioactivity were determined following dermal application of 2000 mg/kg of neat ^{14}C-TEA without occlusion of the application site (i.e. available to grooming activity). Balance and excretion data only were also collected from mice dosed with TEA utilizing several other dosing scenarios: (1) 1000 mg/kg in acetone (unoccluded); (2) 2000 mg/kg neat (occluded–see below); (3) 2000 mg/kg neutralized in water (occluded). Neat TEA and TEA in an acetone vehicle have been employed in dermal toxicity assays of TEA while aqueous-based materials more typically reflect human contact with TEA in consumer and industrial products.

The application site was prepared by clipping an area approximately 2 × 3 cm on the anterior dorsal side of all test animals, roughly between the scapulae, approximately 15 hr prior to dosing. Care was taken to avoid nicking the skin. Specific groups of mice were prevented from grooming the application site via use of an occlusive device. In these latter instances, mice were anesthetized with methoxyfluorane immediately following clipping and a small glass ring (1.5 cm diameter × 0.5 cm high) was fixed to their backs using a cyanoacrylate adhesive. The same procedure was used to dose rats. On application of TEA to the enclosed skin, a polyethylene screen was glued to the top of the ring. A dosing volume of approximately 1.5 and 6 ml/kg (40–60 and 200 µl/mouse) for neat and diluted dosing solutions, respectively, was spread over an approximately 2 cm^2 area of application site skin or within the 1.8 cm^2 area enclosed by an attached ring. Rats were administered approximately 200 µl within an attached occlusive device. All test materials were applied using a microlitre syringe equipped with a blunt feeding-type needle. Individual animals within an experiment received the same average total radioactivity (1.8–8 µCi). All animals were euthanized under methoxyflurane anesthesia by cervical dislocation.

The absorption kinetics of dermally applied radioactivity was determined in mice administered 2000 mg/kg of neat ^{14}C-TEA (unoccluded) using the modelling program noted above. The elimination of radioactivity from the blood of these mice was monitored over a 48-hr period; however, only absorption kinetics is reported. Excretion kinetics from these animals may have been confounded by the variable nature of dermal absorption related to grooming activity altering the surface area dosed and ingestion of some of the dosing solution.

No vehicle (2000 mg/kg)

24 mice were dosed dermally with 2000 mg/kg of undiluted (neat) ^{14}C-TEA and allowed access to the application site. Blood samples were collected from groups of three mice via orbital sinus puncture at 0.25, 0.5, 1, 3, 6, 12, 24 and 48 hr post-dosing. Three additional mice were administered 2000 mg/kg of undiluted (neat) ^{14}C-TEA by application of the dose solution to skin encased in a glass and nylon occlusive device (see above) preventing access to the application site. Immediately following dosing, these latter mice plus mice scheduled for euthanasia at 48 hr post-dosing were placed in Roth-type metabolism cages for the separation of urine and feces. Urine and feces were collected at 6 and 12 hr post-dosing (if available) and every 12 hrs thereafter. Several tissues were collected from animals at 48 hr post-dosing from both groups to determine distribution of radioactivity; liver, kidney, application site skin, skin remote from the application site, and the remaining carcass homogenate. Where appropriate, occlusive devices used to restrict access to the dosed site were removed and washed with water to recover any residual radioactivity. Radioactivity in excreta, cage wash solution, occlusive device wash solution, liver, kidneys, skin and remaining carcass was determined.

No vehicle (1000 mg/kg)—rats

In addition to mice, three rats were administered 1000 mg/kg of undiluted (neat) ^{14}C-TEA by application of a dose solution to skin encased in a glass and nylon occlusive device (described above), preventing access to the application site. Immediately following dosing, rats were returned to their metabolism cages for the separation of urine and feces. Collection of urine, feces and tissue samples following euthanasia were the same as with the mice.

Acetone vehicle (1000 mg/kg)

Three mice were dosed dermally with 1000 mg/kg ^{14}C-TEA in an acetone vehicle. Immediately following dosing, the animals were returned to their Roth-type metabolism cages for collection of excreta over the next 24 hr. Urine and feces were collected at 6-hr intervals. Following euthanasia, animals were skinned, liver and kidneys excised, and cages were washed with a solution of acetone and water to ensure complete collection of urine. Radioactivity in excreta, cage wash solution, livers, kidneys, skin and remaining carcass were determined as noted below.

Water vehicle (2000 mg/kg)

Three mice were dosed dermally with 2000 mg/kg ^{14}C-TEA in aqueous solution in which the pH was adjusted to neutrality with HCl. Test material was applied within a glass ring (as described above) to restrict access to the dose site and to aid in containing the larger dosing volume, approximately 200 µl/animal. Immediately following dosing, the animals were returned to their Roth-type metabolism cages for collection of excreta over the next 24 hr. Following euthanasia of the latter animals, the skin from the dose site and remaining skin was removed, liver and kidneys excised, and each Roth cage washed

with a solution of acetone and water. The glass ring from each animal used to restrict access to the dosed site was removed from the skin and washed with water to recover any residual radioactivity. Radioactivity in excreta, cage wash solution, ring wash solution, liver, kidneys, skin and remaining carcass was measured as described below.

Radioactivity analyses

Aliquots of urine, cage wash, and ring wash were added directly to ACS® liquid scintillation cocktail (Amersham Corporation, Arlington Heights, IL, USA) and the radioactivity quantified by liquid scintillation spectroscopy. Aqueous homogenates (33–50%) of feces, liver and carcass and rat kidneys were prepared using a Polytron® homogenizer (Brinkmann Co., Lucerne, Switzerland). Aliquots of these homogenates, blood, and whole kidneys from mice were combusted in a Biological Materials Oxidizer (R.J. Harvey Instruments Corp., Hillsdale, NJ, USA) and the $^{14}CO_2$ generated during combustion trapped in toluene-based liquid scintillation cocktail (Spectrofluor®) and counted directly by liquid scintillation spectroscopy (LSC). Skin radioactivity was determined in a representative sample either by combustion in a Biological Materials Oxidizer as described above or by pulverizing it to a fine powder by hammermilling at −180°C in a Spex® freezer mill (Cat. #6700, Spex Industries Inc., Metuchen, NJ, USA) and suspending it in a xylene-based liquid scintillation cocktail (ACS) water gel . Radioactivity in all samples was then determined by LSC.

Urinalysis

Selected urine samples from mice dosed iv or dermally with ^{14}C-TEA were analyzed using ion-exchange chromatography. The urine was injected directly onto a Corasil Type II® (37–50 μm) (Waters Associates Inc., Milford, MA, USA) precolumn. The analytical column was a 55 mm glass (12 mm i.d.) packed with Aminex® 50WX4 (30–35 μm) cation ion exchange resin (Bio-Rad Laboratories, Richmond, CA, USA). Samples were eluted with isocratic 0.2 M K_2HPO_4 (pH 8) at a flow rate of 1.2 ml/min using a model 6000A chromatography pump (Waters Associates). Eluent was monitored using a Tri-Carb RAM 7500 radioactivity monitor (Packard Instrument Co., Inc., Downers Grove, IL, USA) either alone or in tandem with a LC-55 UV spectrophotometer (Perkin Elmer, Oak Brook, IL, USA) at a wavelength of 210 nm. Selected fractions of eluent collected during liquid chromatography, were freeze-dried to remove the aqueous portion of the eluent and reconstituted in methanol for analysis by mass spectroscopy. Aliquots of the reconstituted fractions were transferred to a glass cup for direct probe positive-ion mass spectroscopic analysis. A Finnigan 4610/INCOS data system was employed using the following conditions: probe heat, applied at scan #50 from ambient to 250°C at rate 6; temperature of electron impact source, 150°C; electron multiplier voltage, 1250 volts; pre-amplifier sensitivity, 10^{-7} amps/volt; electron energy, 72.9 eV; and mass range, 29 m/z to 300 m/z scanned at 3 sec/scan.

In addition, selected fractions of the eluent collected during liquid chromatography were analyzed by gas chromatography (GC) with a mass selective detector (GC/MSD). A Hewlett Packard 5890 with a 5970B mass selective detector was used. GC separation of (MEA), diethanolamine (DEA) and TEA standards was achieved using a Quadrex 007 (5/95 phenyl/methyl silicone) column (1 m × 0.32 mm.; film thickness, 5 μ) with oven temperature held for 2 min at 60°C then raised at a rate of 40°C/min to 200°C where it was held for 3 min. The carrier gas was helium at 2 psig column headpressure with other conditions as follows:injection port temperature was 250°C; transfer line temperature was 280°C; electron multiplier voltage was 2400 volts; split injection at a split ratio of approximately 10:1 and the solvent divert valve open at 0.1 min and closed at 1.5 min. The ions monitored in the selected ion monitoring mode (SIM) were m/z 30 amu for MEA, m/z 74 amu for DEA, m/z 118 amu for TEA, and m/z 59 amu for butanediol which was used as an internal standard. The detection limits for MEA, DEA and TEA were 10, 50 and 50 μg/ml, respectively.

RESULTS

Blood kinetics

Fig. 1(A) displays the elimination of ^{14}C-TEA derived radioactivity from blood of mice following a 1 mg/kg iv dose of ^{14}C-TEA. Radioactivity in blood declined in a bi-exponential manner through 24 hr post-dosing and was well described using a two-phase analysis. A relatively rapid initial phase of ^{14}C elimination ($t_{1/2\alpha}$=0.3 hr, k_α=2.414 hr^{-1}) was followed by a slower terminal phase ($t_{1/2\beta}$=10 hr, k_β=0.068 hr^{-1}). Clearance of radioactivity from blood was calculated to be approximately 1.5 ml hr^{-1} kg^{-1} and the apparent volume of distribution was estimated to be approximately 11 ml. Radioactivity remained detectable through 24 hr post-dosing, at which time the animals were euthanized. The blood ^{14}C concentration–time course curve (AUC) values calculated through 24 hr and by extrapolating the ^{14}C concentration–time course curve to infinity, are 0.617 μg-eq hr $ml^{-1}$and 0.684 μg-eq hr ml^{-1}, respectively.

The absorption and elimination of radioactivity from the blood of mice following dermal application of 2000 ml/kg neat ^{14}C-TEA are shown in Fig. 1(B). These data were also well described using two-phase analysis. Mean radioactivity in blood approached or reached peak levels of approximately 97 μg-eq ml^{-1} by 3 hr post-dosing, with a half-life of absorption of 0.7 hr. After the peak concentration was achieved, the absorbed radioactivity was eliminated from the

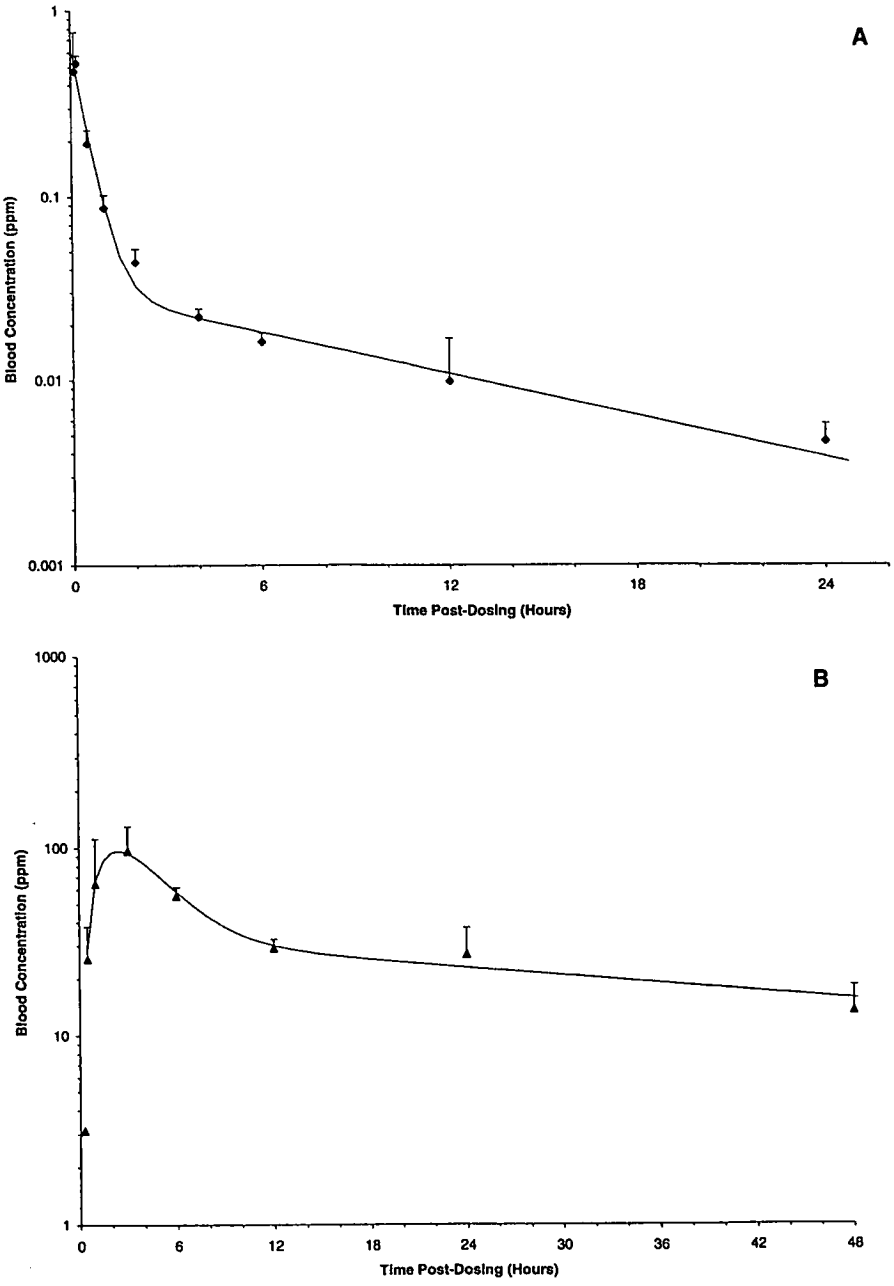

Fig. 1. Radioactivity (TEA equivalents) in the blood of male C3H/HeJ mice administered ^{14}C-triethanolamine via (A) iv injection (1 mg/kg) or (B) dermal application (2000 mg/kg; neat—unoccluded). Average and standard deviation of three mice/time point (symbols). Lines are estimates derived when observed values were fitted (PK Solution, Summit Research Services, Ashland, OH, USA)

blood in a bi-exponential manner. An initial phase of ^{14}C elimination ($t_{1/2\alpha}=1.9$ hr, $k_\alpha=0.366$ hr^{-1}) was followed by a slower terminal phase ($t_{1/2\beta}=31$ hr, $k_\beta=0.022$ hr^{-1}). Clearance of radioactivity from the blood of the 2000 mg/kg dermally-dosed animals was calculated to be approximately 955 ml hr^{-1} kg^{-1}. Radioactivity remained detectable through 48 hr post-dosing, at which time the animals were euthanized. The blood ^{14}C concentration–time course curve (AUC) value, calculated through a similar interval as the 1 mg/kg iv dose, 0–24 hr, is 1002 μg-eq hr ml^{-1}. By extrapolating the ^{14}C concentration–time course curve to infinity an AUC of 2093 μg-eq hr ml^{-1} was calculated.

Excretion and distribution data

Excretion and distribution of radioactivity following iv or dermal application of ^{14}C-TEA to mice are presented in Fig. 2(A). Urine was the primary route for elimination of radioactivity (49–69% of total dose; 58–79% of absorbed dose) followed by feces (16–28% of total dose; 19–32% of absorbed dose) regardless of dose, route or vehicle used. For calculation purposes, radioactivity recovered from application site skin and, where appropriate, occlusive device wash solution was not considered to have been "absorbed". Data for mice administered 2000 mg/kg (neat unoccluded, neat occluded, and water vehicle occluded) are for 48 hr post-dosing, however, greater than 90% of the total urinary radioactivity had been excreted by 24 hr post-dosing from all dosed animals supporting the use of these data for comparative purposes. The average amount of administered radioactivity remaining in the body at sacrifice (sum of liver, kidney, carcass and non-application site skin) was 3.1% for iv-dosed animals and 3.3%, 5.7% and 6.1% for dermally-dosed mice at 1000 mg/kg in acetone, 2000 mg/kg neat (unoccluded) and 2000 mg/kg neat (occluded), respectively. The average amount of the administered dose found in the skin at the application site of dermally-dosed mice with access to the application site ranged from 1.2 to 2.1%, while approximately 6–11% was present at this site in mice having restricted access (occluded) (Fig. 2A). The distribution of radioactivity in the internal organs and tissues followed the same pattern regardless of dose, route or vehicle used: carcass > liver > kidney. Distribution and excretion of ^{14}C-TEA derived radioactivity in F344 rats is shown in Fig. 2(B). The primary route of excretion was the urine (54% of the dose). Approximately 9.6% of the applied dose was found at the site of application in rats (application site skin plus occlusive device washes). A higher amount, 17%, was present in the rest of the pelt. The distribution of radioactivity in the remaining organs and tissues was as follows: carcass > liver > kidney.

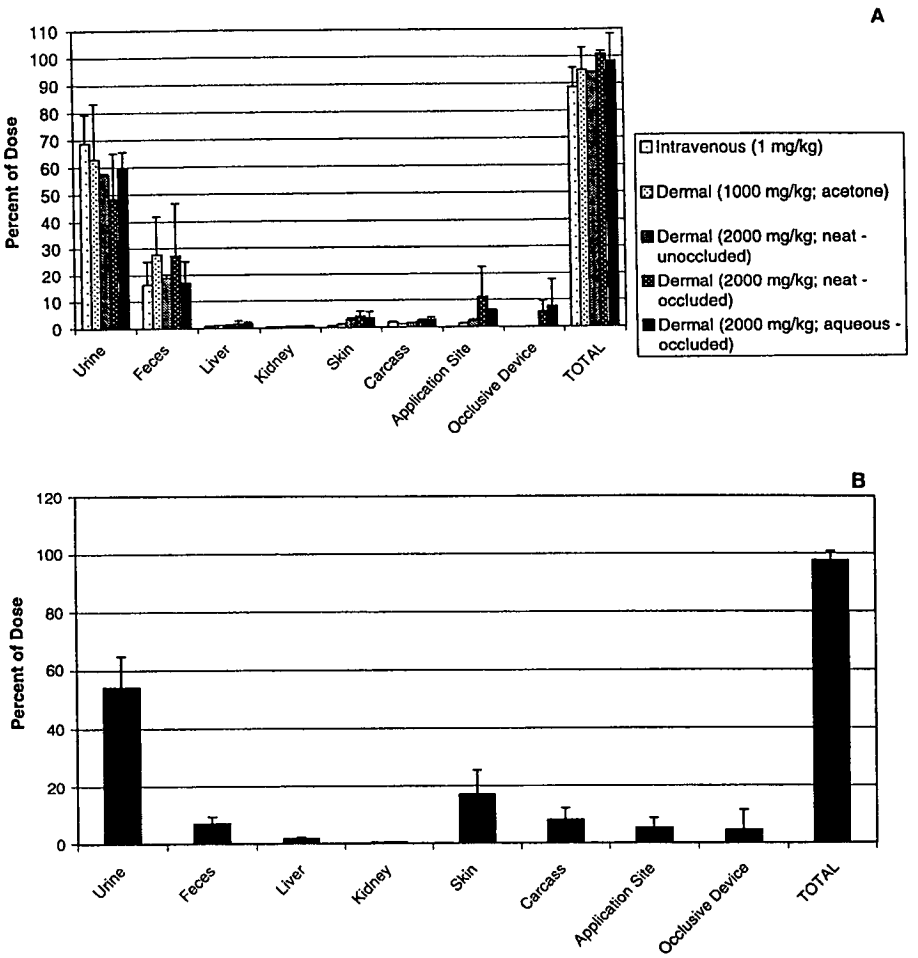

Fig. 2. Distribution and excretion data for ^{14}C-triethanolamine-derived radioactivity obtained from (A) male C3H/HeJ mice or (B) male F344 rats administered ^{14}C-triethanolamine via iv injection or dermal application under several dosing scenarios. Values are the average and standard deviations for three animals/time point at 24 or 48 hr post-dosing (see text for discussion).

Urinalysis

Figure 3(A) shows a representative radiochromatogram of the urine from mice dosed iv or dermally with ^{14}C-TEA when analyzed by ion-exchange liquid chromatography. The radioactivity in the urine was eluted as one peak at 14 min, and co-eluted with authentic standards of TEA. Recovery of injected radioactivity was 100% in all cases. The very small peak eluting at 4 min was also found in approximately the same relative quantity in the radiolabeled test material. Mass spectral analysis of freeze-dried fractions of the eluent collected at 14 min produced a spectrum which was virtually identical with that of an authentic TEA standard (Fig. 3B). Analysis by GC/MSD of selected radiolabeled fractions of eluent collected during liquid chromatography produced peaks eluting at the retention time of TEA (with a characteristic fragment ion of m/z = 118) but no peaks eluted at the retention times of MEA or DEA verifying that no *N*-dealkylation occurred (data not shown).

DISCUSSION

TEA was extensively and relatively rapidly absorbed by an apparent first-order process following a single application of 2000 ml/kg neat ^{14}C-TEA to the denuded skin of C3H/HeJ mice (Fig. 1B). This dose reflects those utilized in a number of assays of TEA toxicity in mice (see Introduction). A maximum blood concentration of approximately 100 μg-eq TEA/ml was approached within 1 hr post-application of 2000 ml/kg neat ^{14}C-TEA and maintained up to 3 hr post-dosing. A comparison of the AUC values from 0 to 24 hr across the route/dose levels suggests some dose-proportionality in blood clearance of ^{14}C-TEA-derived radioactivity. The AUC for the 1 mg/kg iv-dosed animals, calculated from 0 to 24 hr post-dosing is 0.617 μg-eq hr ml^{-1}, while the AUC for the 2000 mg/kg dermally-dosed animals over the same time period is 1002 μg-eq hr ml^{-1}. Assuming 92% of the dermal dose was absorbed (amount excreted plus that remaining in the body minus that found at the dose site), the approximately

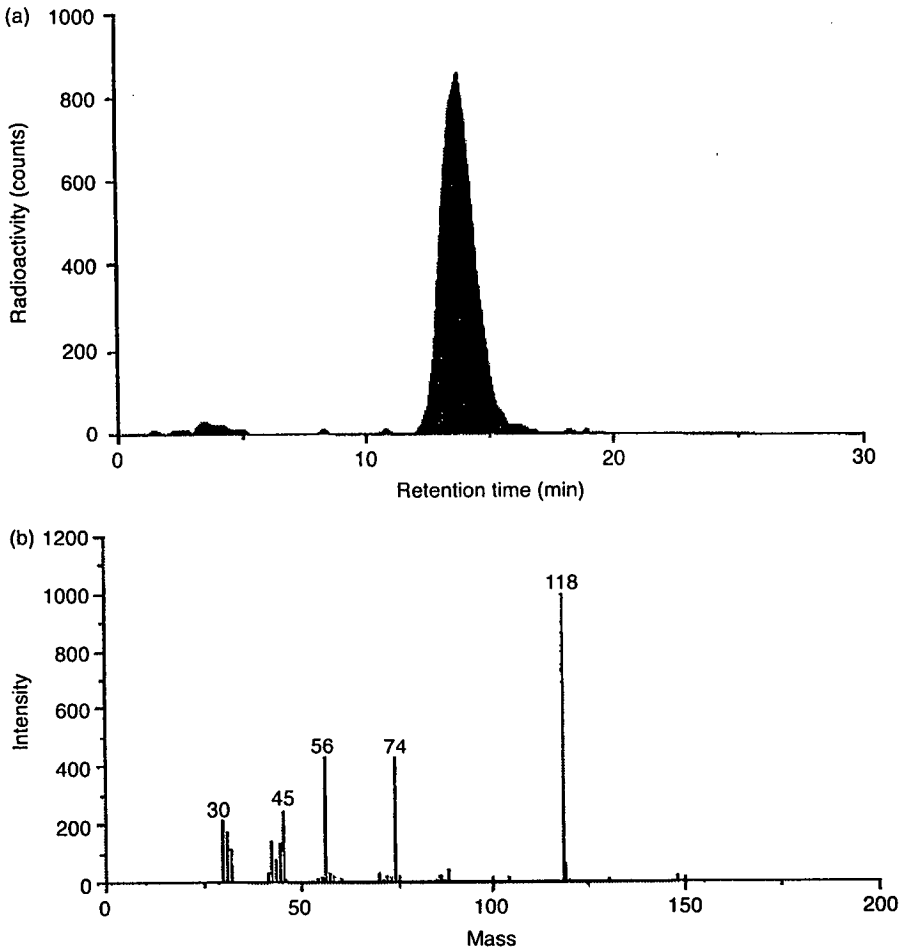

Fig. 3. Analysis of urine from male C3H/HeJ mice administered ^{14}C-triethanolamine via iv injection (1 mg/kg) or dermal application (2000 mg/kg; neat—unoccluded); (A) representative radiochromatogram and (B) mass spectrum of peak recovered from freeze-dried urine eluting at retention time of TEA.

1800-fold increase in dose is reasonably proportional to the approximately 1600-fold increase in AUC. The large increase in dose was accompanied by a decrease in the clearance of radioactivity from the whole blood, suggesting that blood clearance of ^{14}C-TEA may be a saturable process. However, the comparison of elimination kinetics in the dermal-dosed animals *vs* iv-dosed animals should be viewed with caution. Kinetics in the former may have been influenced by grooming of the application site which was not occluded, consistent with toxicity testing practices, and by the non-bolus, dynamic, nature of dermal dosing.

Excluding radioactivity remaining on/in the skin at the application site and, where appropriate, occlusive devices, greater than 82% of administered doses of ^{14}C-TEA were absorbed by mice within 24–48 hr post-dosing (Fig. 2A). A similar level of absorption, 88%, was noted to occur in rats administered 1000 mg/kg neat ^{14}C-TEA; however, it is noteworthy that this includes the nearly 17% of the dose that was found in/on skin distant from the site of administration. The relatively high skin value for rats was attributed to leakage of the occlusive devices used and subsequent grooming activity by 48 hr post application. The highest level of absorption observed, 94%, was in mice administered 1000 mg/kg ^{14}C-TEA in an acetone vehicle (unoccluded site). These results demonstrate the relatively high systemic exposure of mice administered TEA by repeated dermal application in a number of skin-painting assays including up to 2300 mg/kg/day TEA as neat chemical or an acetone vehicle by DePass *et al.* (1995) and 2000 mg/kg/day by Hejtmancik *et al.* (1995). As in the present study, skin painting animal studies did not prevent access to the dosing site, a portion of the systemic dose may result from the ingestion of test material during grooming activity. Once absorbed, ^{14}C-TEA-derived radioactivity was eliminated from the blood of dosed mice in a biphasic manner which readily fits a two-compartment distribution model. As demonstrated using iv-administered test material (Fig. 1A), a pronounced decrease occurred during the initial phase (calculated half-life of 0.3 hr), with radioactivity dropping an order of magnitude within 2 hr of dosing. This initial phase was followed by a slower phase of elimination with a calculated half-life of approximately 8.0 hr. A similar, albeit not so pronounced, biphasic elimination was observed in mice administered ^{14}C-TEA via dermal application (Fig. 1B), despite the slower internalization of the administered dose. The elimination kinetics in the latter mice may also have been influenced by ingestion of some of the dosing solution applied to the skin as the application site was not occluded and susceptible to grooming. The distribution and excretion of ^{14}C-TEA-derived radioactivity in mice did not appear to be markedly dose, route or vehicle dependent (Fig. 2A). Urine was the primary route of excretion for iv- or dermally-administered radioactivity accounting for 58–79% of the *absorbed* dose, excluding application site skin and, where appropriate, occlusive device residual radioactivity from the total dose. A smaller proportion of the absorbed dose was excreted via the feces (19–32%) and only minor amounts remained in the two major internal organs examined, liver (0.8–1.8%) and kidneys (0.2–0.5%) at 48 hr post-dosing. The remaining carcass and non-application site skin contained only 1–3% and 0.5–5% of the dose, respectively. Similar values were obtained in dermally-dosed rats (Fig. 2B). These results are consistent with that of Kohri *et al.* (1982), who reported that 53% of oral 2–3-mg/kg doses of TEA were excreted unchanged in the urine of Wistar rats.

Analysis of urinary radioactivity in the present study also revealed primarily unmetabolized TEA. A minor compound found in the urine co-eluted with an impurity found in approximately the same relative quantity in the radiolabeled test material. The lack of urinary metabolites, especially DEA, even at relatively large doses of TEA is particularly significant, since it has been suggested by Lijinsky *et al.* (1972) that TEA may be dealkylated and subsequently nitrosated *in vivo* to form the carcinogenic nitrosamine *N*-nitrosodiethanolamine (NDELA). Any extensive dealkylation or nitrosation of TEA would have been detected, since both DEA and NDELA are excreted in the urine (ECETOC, 1990; Mathews *et al.*, 1995, 1997; J. Waechter, unpublished data).

It is worthy of note that just as the toxicity of TEA differs substantially with the toxicity of DEA in rats and mice so too does the blood kinetics and ADME of these two ethanolamines differ. As noted, apart from renal toxicity on chronic administration of high oral doses, TEA displays little systemic toxicity. In contrast, DEA has been shown to affect a relatively wide spectrum of tissues including liver, kidneys and erythron in rats and/or mice (Knaak *et al.*, 1997; Melnick *et al.*, 1988, 1994a,b). Unlike TEA, DEA has been shown to be metabolically incorporated into hepatic phosholipids (Barbee and Hartung, 1979; Mathews *et al.*, 1995) and accumulates in the liver of treated rats and mice. Mathews *et al.* (1997) reported that livers of rats administered 7 mg/kg ^{14}C-DEA via iv injection or oral dosing retained approximately 27% of the radioactivity at 48 hr post-dosing. Mice administered from 8 and 81 mg/kg ^{14}C-DEA via dermal application or 15 mg/kg via iv injection retained 13–37% and 54%, respectively, of the administered dose at 48 hr post-dosing. Furthermore, DEA has been found to have a terminal half-life in the blood of rats administered 10 mg/kg via iv injection of approximately 195 hr (reviewed by Knaak *et al.*, 1997), nearly 20-fold that for ^{14}C-TEA derived radioactivity. Further, a steady increase in red blood cell radioactivity occurred in ^{14}C-DEA-treated rats for at least 7 days post iv dosing, consistent with metabolic incorporation of DEA into membrane lipids.

In conclusion, TEA appears to be absorbed extensively following dermal application to mice at doses relevant to toxicity testing. Use of an acetone or water vehicle did not appear to alter total uptake to any great extent over a 24–48-hr period. Thus, the general lack of systemic toxicity in dermal studies is not due to a lack of systemically available TEA. However, once absorbed, TEA has a relatively short half-life in the blood of mice and is excreted primarily via the urine unmetabolized, much as it appears to be in rats. Significantly, the blood kinetics and ADME of TEA in mice and/or rats differ significantly from that of a related ethanolamine, DEA, consistent with their differing toxicity profiles in these species.

Acknowledgements—The authors express their appreciation to M. Heinert, J. Pitt and M. Dryzga for their technical support and to Drs J. Y. Domoradzki, H-W. Leung (Union Carbide) and R. Rossbacher (BASF), and Mr R. Papciak (Huntsman Corp.) for their review of the manuscript.

REFERENCES

Barbee S. J. and Hartung R. (1979) The effect of diethanolamine on hepatic and renal phospholipid metabolism in the rat. *Toxicology and Applied Pharmacology* **47**, 421–430.

DePass L. R., Fowler E. H. and Leung H-W (1995) Subchronic toxicity study of triethanolamine in C3H/HeJ mice. *Food and Chemical Toxicology* **33**, 675–680.

ECETOC (1990) *Human Exposure to N-Nitrosamines, Their Effects, and a Risk Assessment for N-Nitrosodiethanolamine in Personal Care Products.* ECETOC Technical Report No. 41, pp. 20–26. European Chemical Industry Ecology & Toxicology Centre, Brussels.

Fox J. G., MacGregor J. A., Shen Z., Li X., Lewis R. and Dangler C. A. (1998) Comparison of methods of identifying Helicobacter hepaticus in B6C3F1 mice used in a carcinogenesis bioassay. *Journal of Clinical Microbiology* **36**, 1382–1387.

Hejtmancik M., Toft J. D., Persing and Melnick R. L. (1995) Two-year dermal study of triethanolamine in F344 rats and B6C3F1 mice. *Toxicologist* 15, Abstr. No. 202.

Kinsvatter V. H. (1940) Acute and chronic toxicity of triethanolamine. *Journal of Industrial Hygiene and Toxicology* **22**, 206–212.

Knaak J. B., Leung H-W, Stott W. T., Busch J. and Bilsky J. (1997) Toxicology of mono- di-, and triethanolamine. *Review of Environmental Contamination and Toxicology* **149**, 1–86.

Kohri N., Matsuda T., Umeniwa K., Miyazaki K. and Arita T. (1982) Development of assay method in biological fluids and biological fate of triethanolamine. *Yakuzaigaku* **42**, 342–348.

Lijinsky W., Keefer L., Conrad E. and Van de Bogart R. (1972) Nitrosation of tertiary amines and some biologic implications. *Journal of the National Cancer Institute* **49**, 1239–1249.

Maekawa A., Onodera H., Tanigawa H., Furuta K., Kanno J., Matsuoka C., Ogiu T. and Hayashi Y. (1986) Lack of carcinogenicity of triethanolamine in F344 rats. *Journal of Toxicology and Environmental Health* **19**, 345–357.

Mathews J. M., Garner C. E., Black S. L. and Mathews H. B. (1997) Diethanolamine absorption, metabolism and disposition in rat and mouse following oral, intravenous and dermal administration. *Xenobiotica* **27**, 733–746.

Mathews J. M., Garner C. E. and Mathews H. B. (1995) Metabolism, bioaccumulation, and incorporation of diethanolamine into phospholipids. *Chemical Research in Toxicology* **8**, 625–633.

Melnick R., Hejtmancik M., Mezza L., Ryan M., Persing R., & Peters A. (1988). Comparative effects of triethanolamine (TEA) and diethanolamine (DEA) in short-term dermal studies. *Toxicologist* **8**, Abstr No. 505.

Melnick R. L., Mahler J., Bucher J. R., Hejtmancik M., Singer A. and Persing R. L. (1994a) Toxicity of diethanolamine. 2. Drinking water and topical application exposures in B6C3F1 mice. *Journal of Applied Toxicology* **14**, 11–19.

Melnick R. L., Mahler J., Bucher J. R., Thompson M., Hejtmancik M., Ryan M. J. and Mezza L. E. (1994b) Toxicity of diethanolamine. 1. Drinking water and topical application exposures in F344 Rats. *Journal of Applied Toxicology* **14**, 1–9.

NTP (1999) Toxicology and Carcinogenesis Studies of Triethanolamine in F344/N Rats and B6C3F1 Mice. National Toxicology Program. TRP TR #449, NIH Pub. No. 00-3365.

Smyth H. F., Carpenter C. P. and Weil C. S. (1951) Range-finding toxicity data: List IV. *American Medical Association Archives of Industrial Hygiene and Occupational Medicine* **4**, 119–122.

Pharmacokinetics and Metabolism of an α,β-Blocker, Amosulalol Hydrochloride, in Mice: Biliary Excretion of Carbamoyl Glucuronide

Katsuhiro SUZUKI and Hidetaka KAMIMURA*

Drug Metabolism Research Laboratories, Drug Discovery Research, Astellas Pharma Inc.; 1–1–8 Azusawa, Itabashi-ku, Tokyo 174–8511, Japan. Received March 8, 2007; accepted May 2, 2007

The pharmacokinetics and metabolism of an α,β-blocker, amosulalol hydrochloride, were investigated in mice. After intravenous administration (10 mg/kg), the plasma concentration of the unchanged drug declined biphasically, with a terminal half-life of 1.1 h. The maximum plasma concentrations were reached at 0.25 h after oral administration, and then declined with apparent half-lives of 0.8—1.3 h. The systemic bioavailability of a 10-mg/kg dose was 38.7%. The area under the plasma concentration curve increased more than proportionally to the dose, which suggests metabolic saturation. After oral and intravenous administrations of ^{14}C-labelled amosulalol hydrochloride, 64.7% and 81.0% of the radioactivity were recovered, respectively, in the urine within 48 h. HPLC-UV and LC/MS analyses demonstrated that the major urinary metabolite was the glucuronide of M-2 (desmethyl metabolite at the *o*-methoxyphenoxy group) followed by M-5, the M-3 glucuronide, and the M-4 glucuronide, in that order. In the bile sample, amosulalol carbamoyl glucuronide was found as a new metabolite of this drug.

Key words amosulalol; pharmacokinetics; carbamoyl glucuronide; metabolism; mouse

Amosulalol hydrochloride is a combined α- and β-blocker that was selected from a series of sulphonamide-substituted phenylethylamines. It blocks both postsynaptic α_1- and β_1-adrenoceptors to almost the same extent. When administered to conscious, spontaneously hypertensive rats, it reduces blood pressure *via* its α_1-blocking activity without causing reflex tachycardia because of its β_1-blocking action.[1] This drug exhibited dose-dependent hypotensive effects in healthy volunteers,[2] and is used for the treatment of essential hypertension.[3] In contrast to a structurally related α- and β-blocker, labetalol,[4] amosulalol's first-pass metabolism was almost negligible in humans.[2] However, this drug was extensively metabolized in laboratory animals[5] yielding an order of total body clearance as follows: rats>dogs>monkeys>humans.[2,6] The metabolites found in these animals were derived through the hydroxylation (M-1, M-3, M-4), demethylation (M-2), and oxidative cleavage of the C-N bond (M-5). Some of them were subsequently conjugated to their glucuronides or sulfates. In humans, only the sulfate of M-3 was quantified as the urinary metabolite.[7] In the present study, pharmacokinetic and metabolic studies of amosulalol hydrochloride in mice were undertaken, with amosulalol carbamoyl glucuronide being reported as a new amosulalol metabolite found in bile.

MATERIALS AND METHODS

Chemicals Amosulalol hydrochloride and its metabolites, M-1, M-2, M-3, M-4 and M-6 (desmethyl metabolite at *o*-methoxyphenoxy group of M-1), were supplied by the Chemistry Laboratories of Astellas Pharma Inc. (Ibaraki, Japan). M-5 (*o*-methoxyphenoxy acetic acid) was purchased from Tokyo Kasei (Tokyo, Japan). ^{14}C-Amosulalol hydrochloride, labelled at both of the carbons in the ethyl group of the *o*-methoxyphenoxy ethyl moiety, was synthesized in our laboratories.[8] All other reagents were of analytical grade.

Animal Studies Male ICR mice (4—7 weeks) were purchased from Charles River Laboratories Japan or CLEA Japan, and used after a one-week period of acclimatization. Amosulalol hydrochloride was administered intravenously as a solution in saline and orally as an aqueous solution. Mice were fasted overnight before oral administration, and fed 4 h after dosing. Blood samples were taken from the inferior *vena cava* with heparinized syringes under diethyl ether anesthesia, and each animal was sacrificed at each sampling point. For urine and fecal sample collection, animals were kept in glass metabolic cages for 24 or 48 h after dosing. For the metabolite identification, bile samples were obtained from bile duct-cannulated mice during hours 0 and 24 after dosing. This research was conducted in accordance with the "Principles of Laboratory Animal Care" (NIH publication #85-23, revised 1985).

Determination of Radioactivity The urine collected was diluted 10-fold with distilled water. Aquaol-2 (10 ml, New England Nuclear) was then added to a 0.1-ml aliquot of the diluted sample. In addition, about 100 mg of dried feces was combusted in a sample oxidizer (Packard, Model 306). The resulting $^{14}CO_2$ was absorbed in 7 ml of Oxisorb-CO_2 (New England Nuclear), after which it was mixed with 11 ml of Oxiprep-2 (New England Nuclear). The radioactivity was counted with a liquid-scintillation spectrometer (Packard, Model 3255), with quench corrected by the external standard.

Quantification of Amosulalol The concentration of the unchanged drug in plasma and urine was determined using HPLC with fluorescence detection[9] and gas chromatography with nitrogen-sensitive detection,[10] respectively.

Pharmacokinetic Analyses Four animals were used at each sampling point, and the mean plasma concentration–time curves obtained were used for pharmacokinetic analysis. The concentration curve obtained after intravenous administration was fitted to a two-compartment open model using the equation $Cp=Ae^{-\alpha t}+Be^{-\beta t}$ ($\alpha>\beta$), where A and B are ordinate axis intercepts, and α and β are the composite rate constants for the distribution and elimination phases. The area under the plasma concentration curve ($AUC_{i.v.}$), elimination half-life ($t_{1/2}\beta$), and total body clearance (CL_{tot}) were calculated using the nonlinear least-square program

* To whom correspondence should be addressed. e-mail: hidetaka.kamimura@jp.astellas.com

NONLIN[11] according to the following equations:

$$AUC_{i.v.} = A/\alpha + B/\beta, \quad t_{1/2}\beta = 0.693/\beta, \quad CL_{tot} = Dose/AUC_{i.v.}$$

The *AUC* after oral administration was estimated using the following equation:

$$AUC_{p.o.} = AUC_{p.o.(0-t)} + Cp(t)/\beta$$

where $AUC_{p.o.(0-t)}$ is the *AUC* from zero to the last time (t) at which a measurable concentration was observed, by the trapezoidal method, and $Cp(t)$ is the plasma concentration at time t. Systemic availability (F) was calculated using the following equation:

$$F = (AUC_{p.o.}/AUC_{i.v.}) \cdot 100$$

Identification and Quantification of Metabolites After oral administration of 100 mg/kg amosulalol hydrochloride, the urine and bile samples were collected and then pooled. A 0.5-ml portion of the sample was diluted with 100 mM ammonium acetate (1 ml for urine, 1.5 ml for bile) and applied to an Oasis HLB cartridge (1 cc/30 mg, Waters, MA, U.S.A.) that was preconditioned with 1 ml of methanol followed by 1 ml of water. The cartridge was washed with water and eluted with 2 ml of methanol containing 0.1% acetic acid. The eluate obtained was successively concentrated under reduced pressure. The residue was dissolved in methanol (0.5 ml) and 100 mM ammonium acetate (0.5 ml) and injected into a LC/MS for metabolite identification.

The basic metabolites, M-1, M-2, M-3, M-4, and M-6, and their conjugates in urine were quantified using HPLC-UV methods monitored at 271 nm both before and after either enzymatic or acid hydrolysis.[7] The acidic metabolite, M-5, was converted to its methyl ester using ethereal diazomethane, and analyzed using GC-MS.[7]

Purification of an Unknown Biliary Metabolite The bile sample (3.5 ml) was diluted with 100 mM ammonium acetate (14 ml) and loaded onto an Oasis HLB cartridge (20 cc/1 g) that had been conditioned with 20 ml of methanol followed by 20 ml of water. The cartridge was washed with water and then eluted stepwise with 20-ml aliquots of solutions of ammonium acetate–methanol–water–formic acid with the following compositions and in the following order, A (100 : 250 : 650 : 1), B (100 : 500 : 500 : 1), C (100 : 750 : 250 : 1), and D (100 : 900 : 0 : 1). The B and C eluates were concentrated and applied to a preparative HPLC fitted with an Inertsil ODS-3 250 mm×10 mm I.D. particle size 5-μm column (Shimadzu LC-10A systems, Kyoto, Japan) maintained at 40 °C. The column was eluted with mixtures of ammonium acetate–methanol–water–formic acid of compositions A (100 : 100 : 800 : 1) and B (100 : 800 : 100 : 1) at a constant flow rate (4.6 ml/min). The metabolite was detected by UV absorption at 248 nm. The solvent gradient program went from 5% B at the beginning up to minute 5, followed by a linear increase to 100% B at 60 min. Eluates were collected from the beginning at the rate of 0.5 min per fraction. The fraction (2.3 ml) eluted from 28.5 to 29 min was diluted and subjected to a solid phase extraction with Oasis HLB to yield a metabolite (0.6 mg).

LC/MS LC/MS was performed using a HP1100-series HPLC system (Agilent Technologies, Inc., Waldbronn, Germany), equipped with a Surveyor photodiode array detector (ThermoElectron, CA, U.S.A.), ion trap mass spectrometer LCQ^{Deca} equipped with an electro-spray interface (ESI) (ThermoElectron), and a Capcell Pak C_{18} UG120 column (250 mm×2.0 mm I.D. particle size 5-μm: Shiseido Fine Chemicals, Tokyo, Japan). The column was maintained at 40 °C for all HPLC experiments. The mobile phases consisted of 10 mM ammonium acetate (pH 9.0)–methanol (19 : 1) (A) and 10 mm ammonium acetate (pH 9.0)–methanol–acetonitrile (2 : 19 : 19) (B). The linear gradient solvent program began with 0% B, which increased to 30% B at 10 min, 35% at 20 min, and 80% B at 30 min, with a constant flow rate of 0.21 ml/min. The metabolite was detected at 271 nm. All eluates were introduced to the ESI interface for ionization and scanned at m/z 150—1000 between 5 and 35 min in positive ion mode. The divert valve was set to "waste" for minutes 0 to 4, then to "source" for minutes 4 to 35. The heated capillary temperature was set at 300 °C, and the spray voltage was set at 3.5 kV for all scans. Comprehensive characterization of the metabolites in the urine and bile samples was conducted by subtracting the raw mass data obtained from the respective blank samples using Metabolite ID® 2.0 (ThermoElectron).

Mass Spectrometer The total ion scan and product ion scan of the purified unknown metabolite from mouse bile were obtained using TSQ7000 (ThermoElectron) with an ESI interface using flow injection analysis (FIA). Elution for FIA was subjected to a mixture of 0.1% formic acid–acetonitrile (7 : 3) as the mobile phase at the rate of 1.0 ml/min. The heated capillary temperature was set at 300 °C, and the spray voltage was set at 4.5 kV. Nitrogen was used as the sheath gas (60 psi), and no auxiliary gas was employed. The total ion scan was conducted from m/z 200 to 900 in positive ion mode. The product ion scan was conducted as follows: parent ion at m/z 618.10 $[M+NH_4]^+$, collision energy −15 eV, scan range from m/z 10 to 630, and argon gas for collision set at 1.5 kgf/cm^2.

NMR Spectrometer The NMR spectra of amosulalol hydrochloride and its metabolite were recorded on a JNM-ALPHA500 (500 MHz; JEOL Ltd., Tokyo, Japan). The sample was dissolved in methanol-d_4, and chemical shifts downfield from tetramethylsilane were reported in ppm (δ). The coupling constants were given in Hz.

RESULTS

Pharmacokinetics After intravenous administration of 10 mg/kg amosulalol hydrochloride, the plasma concentration of the unchanged drug declined in a biphasic manner, and the values for $t_{1/2}\beta$, $AUC_{i.v.}$, and CL_{tot} were 1.1 h, 0.93 μg·h/ml, and 10.7 l/h/kg, respectively (Fig. 1). After oral administration (10—100 mg/kg), the maximum plasma concentrations were obtained at 0.25 h, after which they declined with apparent half-lives of 0.8—1.3 h. The $AUC_{p.o.}$ increased at a rate more than proportional to the dose (0.36, 1.54 and 7.94 μg·h/ml at 10, 30 and 100 mg/kg, respectively). The maximum plasma concentration obtained after 10-mg/kg dosing (0.31 μg/ml) was similar to that found in humans after a therapeutic dose of this drug (12.5 mg/man).[2] The systemic bioavailability at 10 mg/kg was 38.7%.

Excretion of Radioactivity into Urine and Feces Within 48 h after oral administration of the ^{14}C-labelled compound, 64.7±2.0% of the radioactivity was excreted in the

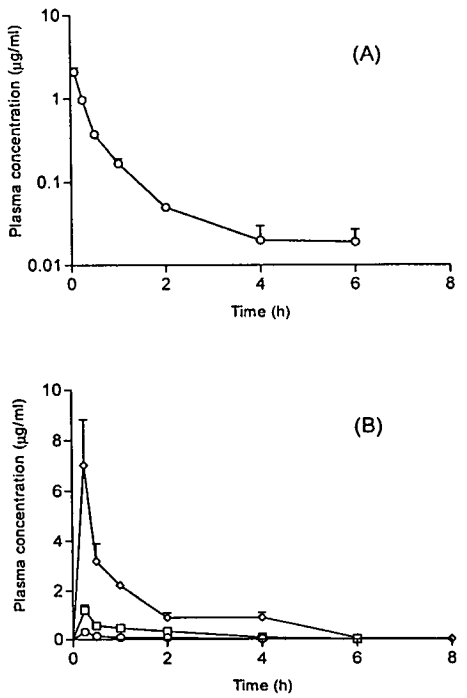

Fig. 1. Plasma Concentration–Time Profiles of the Unchanged Drug after Intravenous and Oral Administration of Amosulalol Hydrochloride to Mice

(A) i.v., 10 mg/kg; (B) *p.o.*, ○ 10 mg/kg, □ 30 mg/kg, ◇ 100 mg/kg. Each point represents the mean+S.E.M. of four animals.

urine, and 29.3±0.6% in the feces. The respective recoveries after intravenous administration reached 81.0±3.0% and 17.8±0.2% within 48 h, most of which was excreted within the first 24 h.

Excretion of Amosulalol and Its Metabolites into Urine and Bile After intravenous administration of amosulalol hydrochloride, urinary excretion of the unchanged drug was 16.6±3.1% (0—24 h). Renal clearance (CL_{renal}) was calculated to be 1.8 l/h/kg, which was much less than the CL_{tot} of 10.7 l/h/kg. Following oral administration of the drug, 7.6± 1.6% of the dose was recovered as the unchanged form.

Figure 2 shows the HPLC-UV chromatograms of the urine and bile samples. Several peaks corresponding to metabolites previously reported to be present in rats, dogs, and monkeys were found.[6] Quantification of the metabolites revealed that M-2 glucuronide was the major metabolite in the urine, accounting for 22.1% of the dose (Table 1). The second major metabolite was M-5, followed by M-3 glucuronide and M-4 glucuronide. The total of the quantified urinary metabolites (53.8%) was about 10% less than that measured by radioactive counting (64.7%), which may suggest the presence of other unknown metabolites in the urine. The LC/MS analyses of the bile with reconstruction of the total ion mass chromatograms from *m/z* 350 to 650 revealed that one large unknown peak was present at the retention time of approximately 21 min (data not shown).

Identification of an Unknown Biliary Metabolite The MS spectrum of the unknown peak was present at *m/z* 618 and 623, which corresponded to the adduct ions of [M+

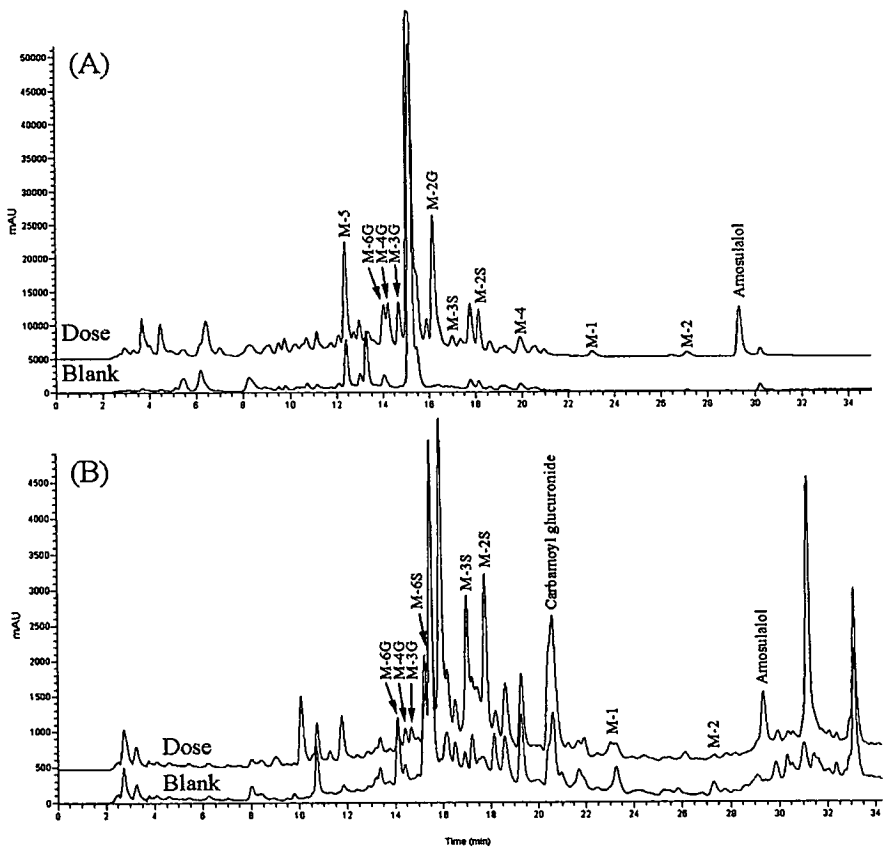

Fig. 2. HPLC/UV Chromatograms of the Urine and Bile Samples after Oral Administration of 100 mg/kg Amosulalol Hydrochloride to Mice

(A) Urine sample; (B) bile sample.

Table 1. Quantification of Amosulalol and Its Metabolites in Mouse Urine (0—24 h)

	Urinary excretion (mol/mol% of dose)
Amosulalol	7.6±1.6
M-1	1.7±0.3
M-2	0.9±0.1
M-2 glucuronide	22.1±3.5
M-2 sulfate	0.2±0.1
M-3 glucuronide	5.8±0.6
M-3 sulfate	1.4±0.5
M-4 glucuronide	4.7±0.8
M-5	7.0±1.3
M-6 glucuronide	2.3±0.2
Total	53.8±8.6

Mice were given 100 mg/kg of amosulalol hydrochloride orally. Values are expressed as the mean±S.E.M. of three animals.

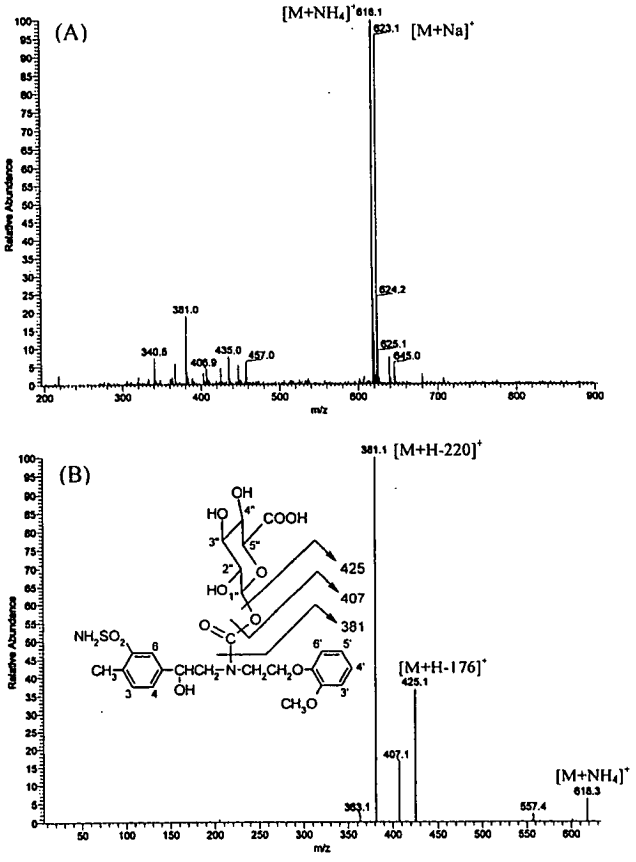

Fig. 3. MS Spectra of Amosulalol Carbamoyl Glucuronide Purified from Mouse Bile

(A) Total ion scan; (B) product ion scan at *m/z* 618.

$NH_4]^+$ and $[M+Na]^+$, respectively (Fig. 3A). The molecular ion of the unknown metabolite was considered to be *m/z* 600, which was 44 u (CO_2) and 176 u (glucuronosyl moiety) greater than that of the parent drug. Product ions observed at *m/z* 381 (M+H−220) as aglycone and *m/z* 425 (M+H−176) as *N*-carboxy amosulalol in the product ion scan at *m/z* 618 supported the assertion that an additional functional group was present (Fig. 3B). A fragment ion at *m/z* 407 caused by the elimination of glucuronic acid was also observed. Subsequent ^{1}H-NMR and TOCSY experiments were conducted on

Table 2. ^{1}H-NMR Data for Amosulalol Hydrochloride and Amosulalol Carbamoyl Glucuronide

Position	Chemical shift value (ppm)	
	Amosulalol hydrochloride	Amosulalol carbamoyl glucuronide
1,2,5-Trisubstituted benzene ring		
3	7.41	7.34
4	7.56	7.50
6	8.08	8.04
Ar–CH_3	2.67	2.65
Ar–HO–C<u>H</u>–	5.06	5.05, 5.15
–C<u>H</u>$_2$–NH–	3.27, 3.43	3.55—3.7
–NH–C<u>H</u>$_2$–	3.52	3.7—3.8
–CH_2–O–	4.30	4.1—4.22
1,2-Disubstituted benzene ring		
3′	6.94	6.7—7.0
4′	7.04	6.7—7.0
5′	7.04	6.7—7.0
6′	7.04	6.7—7.0
CH_3O–Ar	3.85	3.75
Glucuronic acid		
1″	—	5.43, 5.45
2″—5″	—	3.4—3.7

The position of the structure is tentatively numbered as shown in Fig. 3.

the metabolite in order to elucidate its structure by comparing it with that of the unchanged drug. The NMR data are listed in Table 2. A couple of anomeric proton doublet signals were observed in the spectrum at δ 5.43 and 5.45 [0.5H (J=7.8 Hz), each]. The anomeric proton signal values exhibited a significant downfield chemical shift compared to those of the typical carbinol glucuronides. This shift seemed to result from the deshielding of the glucuronosyl anomeric proton by the carbonyl group. The proton signals of the aglycone moiety exhibited almost the same chemical shift values as those of amosulalol, except for those adjacent to the nitrogen atom. This suggests that the carbonyl group was attached at the secondary amino moiety. The large coupling constant value of the anomeric proton signal indicated that the glucuronide was a β-anomer.[12] The anomeric proton signal split suggested the presence of two conformational isomers of the carbamoyl glucuronide in methanol-d_4. This is probably due to the slow rotation of the carbonyl glucuronic acid moiety at the C–N bond of the carbamate.[13] An overview of the postulated metabolic pathways of this drug in mice is shown in Fig. 4.

DISCUSSION

Labetalol, an α and β-blocker that is structurally related to amosulalol hydrochloride, possesses a phenolic hydroxy group, the glucuronidation of which is one of the main elimination routes.[4] Labetalol exhibited non-linear pharmacokinetics in humans, which lead to considerable variations in bioavailability in clinical practice.[14,15] In contrast to labetalol, amosulalol hydrochloride does not possess any phenolic hydroxy moiety, and thus exhibited linear pharmacokinetics in humans[2] as well as rats, dogs, and monkeys.[6] The effect of first-pass metabolism is almost negligible in humans. However, the systemic bioavailability of this drug in rats, dogs, and monkeys was 22—31%, 51—59%, and 57—66%, respectively.[6] Since ^{14}C-amosulalol was almost com-

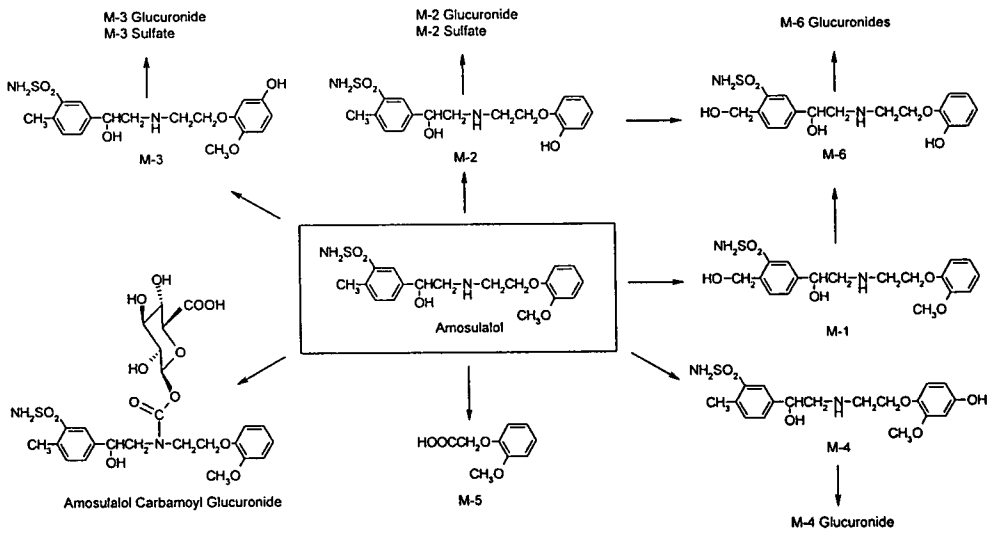

Fig. 4. Postulated Metabolic Pathways of Amosulalol Hydrochloride in Mice

pletely absorbed in the gastrointestinal tract of rats and dogs,[5] the reduced bioavailability for these animals could possibly be due to first-pass metabolism. The mice in this study showed a systemic bioavailability of 38.7% at the dose of 10 mg/kg, and the urinary excretion of radioactivity did not differ greatly between intravenous and oral administration. These findings suggest that this drug is well-absorbed in the gastrointestinal tract and undergoes first-pass metabolism in mice in a manner similar to that reported for rats. Unlike the rats or any of the other species tested, the mice exhibited non-linear pharmacokinetics after oral administration.

The CL_{renal} value obtained after intravenous administration to mice was relatively small compared to the CL_{tot} value, which also suggested that the main route of elimination was metabolism. After oral administration, 7.6% of the dose was found in the urine as the unchanged drug, together with a large number of metabolites. The primary urinary metabolites in rats, dogs, monkeys, and humans were reported to be M-6 sulphate, M-5, M-5, and M-3 sulphate, respectively.[7] Unlike these species, 22.1% of the dose in mice was excreted into the urine as M-2 glucuronide. This metabolite, characteristic to mice, was derived through demethylation at the *o*-methoxyphenoxy group, and subsequent conjugation with glucuronide. The second major metabolite was M-5, which is derived through oxidative C–N cleavage, followed by M-3 glucuronide and M-4 glucuronide. M-3 sulfate was the only metabolite quantified in human urine (12.7% of the dose).[7] Urinary excretion of this metabolite in mice, however, remained at 1.4%.

Amosulalol has a secondary aliphatic amine in its molecule. Some secondary amines, as well as some primary and tertiary amines, can be metabolized by direct conjugation with glucuronic acid. The conjugated form of amosulalol found in mouse bile, however, yielded a molecular ion 44 u greater than that of amosulalol plus the glucuronosyl moiety. The extreme downfield chemical shift of the anomeric proton signal observed in NMR analysis implies that the parent drug was conjugated with carbonyl glucuronic acid. The chemical shift of the protons adjacent to the nitrogen atom of the secondary aliphatic amine group suggested that this metabolite was amosulalol carbamoyl glucuronide.

The antiarrythmic agent, tocainide, was first reported to form a carbamoyl glucuronide in humans.[16] Subsequently, reports on the formation of various carbamoyl glucuronides by primary and secondary amines were published (recently reviewed by Schaefer).[17] It has been proposed that the mechanism that generates these glucuronides starts by forming carbamic acid as an intermediate under physiological conditions in the liver through a reversible reaction with CO_2 dissolved in the environmental fluid.[13,18—22] UDP-glucuronyl transferase (UGT) then causes the immediate conjugation of this carbamic acid with glucuronic acid by utilizing UDP-glucuronic acid as a cofactor. Recent studies using recombinant human enzymes suggest that UGT2B7, UGT1A3, UGT2B4, and UGT1A6 may be the UGT isozymes responsible for the formation of sertraline carbamoyl glucuronide,[21] and UGT2B7 for the formation of varenicline carbamoyl glucuronide.[22] The mechanism of amosulalol carbamoyl glucuronide formation is not known. However, this metabolite found in the bile may also be derived through the series of reactions described above in the mouse liver.

In conclusion, amosulalol hydrochloride was extensively metabolized with non-linear pharmacokinetics in mice. The major metabolite in urine was M-2 glucuronite. Carbamoyl glucuronide of amosulalol was isolated and characterized from bile samples.

Acknowledgements We wish to thank Ms. K. Tashiro, Mr. Y. Enjoji and Mr. H. Sasaki of the former Yamanouchi Pharmaceutical Co. Ltd., for generating the pharmacokinetic data, and Ms. T. Yokoi and Ms. M. Funatsu of Astellas Pharma Inc. for the NMR and mass analyses.

REFERENCES

1) Inagaki O., Sudoh K., Shibasaki M., Nakagawa C., Honda K., *J. Cardiovasc. Pharmacol.*, **24**, 794—802 (1994).
2) Nakashima M., Asano M., Ohguchi S., Hashimoto H., Seki T., Miyazaki M., Takenaka T., *Clin. Pharmacol. Ther.*, **36**, 436—443 (1984).
3) Ando K., Noda H., Ogata E., Fujita T., *J. Cardiovasc. Pharmacol.*, **20**,

7—10 (1992).
4) Martin L. E., Hopkins R., Bland R., *Br. J. Clin. Pharmac.*, **1976** (Suppl.), 695—710 (1976).
5) Sasaki H., Kamimura H., Kaniwa H., Kawamura S., Takaichi M., Yokoshima T., *Xenobiotica*, **14**, 621—631 (1984).
6) Kamimura H., Sasaki H., Kawamura S., *Xenobiotica*, **14**, 613—620 (1984).
7) Kamimura H., Sasaki H., Kawamura S., *Xenobiotica*, **15**, 413—420 (1985).
8) Arima H., Tamazawa K., *J. Label. Compounds Radiopharm.*, **XX**, 803—811 (1983).
9) Kamimura H., Sasaki H., Kawamura S., *J. Chromatogr. A*, **225**, 115—121 (1981).
10) Kamimura H., Sasaki H., Kawamura S., Shimizu M., Matsumoto H., Kobayashi Y., *J. Chromatogr. A*, **275**, 81—87 (1983).
11) Metzler C. M., Elfring G. K., McEwen A. J., *Biometrics*, **30**, 562—563 (1974).
12) Oatis J. E., Jr., Baker J. P., McCarthy J. R., Knapp D. R., *J. Med. Chem.*, **26**, 1687—1691 (1983).
13) Shaffer C. L., Gunduz M., O'Connell T. N., Obach R. S., Yee S., *Drug Metab. Dispos.*, **33**, 1688—1699 (2005).
14) Homeida M., Jackson L., Roberts C. J., *Br. Med. J.*, **2**, 1048—1050 (1978).
15) McNeil J. J., Anderson A. E., Louis W. J., Morgan D. J., *Br. J. Clin. Pharmac.*, **8**, 157—161 (1979).
16) Elvin A. T., Keenaghan J. B., Byrnes E. W., Tenthorey P. A., McMaster P. D., Takman B. H., Lalka D., Meyer M. B., Ronfield R. A., *J. Pharm. Sci.*, **69**, 47—49 (1980).
17) Schaefer W. H., *Curr. Drug Metab.*, **7**, 873—881 (2006).
18) Schaefer W. H., *Drug Metab. Dispos.*, **20**, 130—133 (1992).
19) Beconi M. G., Mao A., Liu D. Q., Kochansky C., Pereira T., Raab C., Pearson P., Chiu S.-H. L., *Drug Metab. Dispos.*, **31**, 1269—1277 (2003).
20) Edlund P. O., Baranczewski P., *J. Pharm. Biomed. Anal.*, **34**, 1079—1090 (2004).
21) Obach R. S., Cox L. M., Tremaine L. M., *Drug Metab. Dispos.*, **33**, 262—270 (2005).
22) Obach R. S., Reed-Hagen A. E., Krueger S. S., Obach B. J., O'Connell T. N., Zandi K. S., Miller S., Coe J. W., *Drug Metab. Dispos.*, **34**, 121—130 (2006).

Permeability enhancing effects of the alkylglycoside, octylglucoside, on insulin permeation across epithelial membrane in vitro.

Phani Prasanth Tirumalasetty, John G. Eley

Corium International, Inc., Redwood City, California, USA
Department of Pharmaceutical Sciences, College of Pharmacy, Idaho State University, Pocatello, Idaho, USA

Received 19 September 2005, Revised 17 January 2006, Accepted 18 January 2006, Published 2 February 2006

Abstract: PURPOSE: To evaluate the permeability enhancing effects of octylglucoside (OG) for molecules with poor absorption such as insulin by in vitro cell models. **METHODS**: Transepithelial electrical resistance (TEER) was monitored to ensure monolayer integrity. Permeability was ascertained using paracellular markers. Markers and insulin were dissolved in Hanks balanced salt solution and placed on the apical side of the cells in Transwell® plates and allowed to diffuse under sink conditions. **RESULTS**: The effect of OG on the permeability of molecules across both monolayers was concentration and time dependent. Enhanced transport of the three molecules was observed across both monolayers treated with OG as compared to untreated monolayers. The effects of OG were reversible at low concentrations but there was permanent damage to cells at higher concentrations. Absorption enhancement was greater across T-84 monolayers compared to Caco-2 monolayers. **CONCLUSIONS**: The results indicate OG has potential as a permeability enhancer for poorly absorbed drugs with no significant damage to monolayers at low concentrations. Immediate attenuation in TEER upon exposure to OG indicates that permeability enhancing effects were likely to be associated with modulation of tight junctions suggesting the involvement of paracellular transport.

INTRODUCTION

Latest developments in biotechnology have led to the synthesis of a diverse array of peptide drugs (1). A major hindrance to deliver therapeutically effective doses of these macromolecules is their poor absorption through biological membranes leaving the parenteral route as the only choice for delivery. Because of the potent pharmacological effects and expected low toxicity of such drugs research is being directed to develop non-invasive routes of delivery (2).

These include transdermal, nasal, pulmonary, buccal and ocular (3). These routes are attractive because of the circumvention of first-pass metabolism and consequent route via endothelial membranes allowing rapid exchange of fluids and dissolved substances (4). However, these routes have limitations such as enzymatic breakdown and epithelial barriers, in view of which, several approaches have been investigated to improve bioavailability. One such approach is coadministration of transport enhancers and protease inhibitors (5, 6).

Absorption enhancers such as bile salts, surfactants, and phospholipids have been employed to improve bioavailability (7, 8). Although this approach has shown improved bioavailability, their mucosal toxicity has been a drawback, highlighting a requirement for non toxic permeation enhancers (9, 10).

Surfactants form a major group of paracellular permeability enhancers (PPEs) which enhance the permeation of molecules across biological barriers. Alkylglycosides are a class of water-soluble nonionic surfactants consisting of a series of compounds with alkyl chain lengths of between 5 and 13 carbons glycosidically linked to a mono- or disaccharide. Orally administered alkylglycosides are rapidly hydrolyzed to sugars and fatty alcohols. (11). Octylglucoside (OG), an alkylglycoside, containing the monosaccharide maltose ring, glycosidically linked to an 8-carbon alkyl chain has been successful in improving absorption of drugs (12). A significant increase in the rectal absorption of carboxyfluorescein in the presence of alkylglycosides having carbon chain length of 8-12 carbons was observed concluding OG improved rectal absorption (13). It has been reported that among the alkylglycosides studied, dodecylmaltoside and OG were effective in lowering the resistance of human carcinoma cell lines by opening tight junctions and allowing efficient cell recovery (14).

The aim of this investigation was to evaluate the absorption enhancing effects of OG on the permeability of insulin across human carcinoma monolayers. The toxicity of OG was assessed by measuring the reversibility of transepithelial electrical resistance (TEER). Paracellular permeation

Corresponding Author: John G. Eley, Department of Pharmaceutical Sciences, College of Pharmacy, Idaho State University, Campus Box 8334, Pocatello, ID. 83209. johneley@otc.isu.edu

effects of OG were characterized by studying the permeation of lucifer yellow and ^{3}[H]-mannitol used as paracellular transport markers.

MATERIALS AND METHODS

Hank's balanced salt solution (HBSS), Dulbecco's Modified Eagle Medium (DME)/High glucose, heat inactivated fetal bovine serum (FBS), trypsin /EDTA solution and sodium bicarbonate were obtained from HyClone (Logan, UT). Caco-2 and T-84 cells were purchased from American Type Culture Collection (Rockville, MD). Insulin, lucifer yellow and ^{3}[H]-mannitol were acquired from Sigma (St Louis, MO). Cell flasks, pipettes, and general cell consumables were purchased from Fisher Scientific (Atlanta, GA). Transwell® permeable support (cell culture inserts, clear polyester membranes) were purchased from Corning Scientific Products (Acton, MA). All other chemicals and materials of analytical grade were obtained from Fisher Scientific (Atlanta, GA).

Cell maintenance

Caco-2 and T-84 cells were employed to evaluate the effects of OG. These cells originate from human adenocarcinoma and exhibit characteristics of intestinal epithelium such as microvilli, intercellular tight junctions, enzymes, nutrient and efflux transporters and are appropriate models for evaluating the permeability of drug molecules (15, 16, 17).

Cells were seeded at $1x10^4$ cells/ml in 75cm^2 flasks until confluent. Caco-2 and T-84 cells were maintained in DMEM/High glucose and DME/F-12, 1:1 respectively supplemented with heat inactivated FBS (20%), penicillin-streptomycin solution (0.01%), pH adjusted to 7.35 using sodium bicarbonate (7.5%). Cells were maintained at 37° C in an atmosphere of 5% CO_2. Cells in flasks were first washed with Ca^{+2}/Mg^{+2} free HBSS, and then treated with trypsin/EDTA solution (0.05%). Trypsin was removed and cells were incubated at 37°C for 20 minutes. Cell suspension in HBSS was made up to 50ml with HBSS and centrifuged to remove traces of trypsin. Cells were counted with a haemocytometer and resuspended in respective culture medium to seed. Cells were seeded at a density of $7.5x10^4$ cells/cm^2 on to clear permeable polyester treated Transwells® inserts (surface area 1 or 4.71 cm^2).

Measurement of transepithelial electrical resistance (TEER)

Resistance (Ohms.cm^2) across cell monolayers was measured using a voltohmmeter at 24 hours intervals until and after cells attained confluence. Instrumentation consisted of an Evom Epithelial voltohmmeter and an Endohm tissue resistance measurement chamber (World Precision Instruments, Sarasota, FL). Blank wells were used to determine background resistance. High resistance readings indicate that cells were closely packed and forming tight junctions. Caco-2 cells were used at resistance readings between 220-300 Ohm.cm^2 and 1200-1500 Ohm.cm^2 for T-84 cells. Cells were maintained in serum-free medium 24 hours prior to transport studies. Resistance was recorded and taken as control prior to the apical application of OG. Cells were exposed to OG and change in resistance was recorded as a function of time, OG was removed and cells washed with HBSS. After washing, wells containing cells were placed in respective culture medium and resistance was recorded every hour for 12 hours in order to study the reversibility of resistance and assess cell recovery.

Preparation of solutions

Compounds were dissolved in HBSS at pH 7.4 except insulin, which was dissolved in 0.1N HCL (pH 2.3) then made up to the required quantity with HBSS to maintain physiological conditions (pH 7.4) during transport studies.

Transport studies

Transport studies were conducted using Transwell® plates at room temperature from the apical to basolateral side. ^{3}[H]-mannitol, lucifer yellow and insulin were placed on the apical side at the following concentrations 0.1μCi/ml, 0.025%w/v and 0.067% w/v respectively with and without OG at concentrations of 0.2% - 0.5% w/v in HBSS and HBSS (1.5 ml) was placed in the receiver compartment. Inserts from Transwells® were moved to wells containing fresh HBSS at predetermined intervals up to 6hr to maintain sink conditions. Samples collected from basolateral compartments were analyzed for Lucifer yellow and insulin by reversed phase high-pressure liquid chromatography (RP-HPLC). ^{3}[H]-mannitol was determined by a scintillation counting using a Beckman LS 5000 TD and a LS 5000 TA series liquid scintillation system (Fullerton, CA).

HPLC Analysis

The HPLC system (Varian, CA) consisted of a Prostar 210/215 solvent delivery module connected to Prostar 320 UV/VIS detector and Prostar 400 Autosampler.

Chromatographic conditions for Lucifer Yellow:

A C-18 column (150 x 4.6 mm) with 5μm particles of 100 Å pore size (Microsorb, Varian, CA) was used in

conjunction with a mixture of water/methanol (70:30) with paired ion chromatography (PIC) 'A' reagent as mobile phase. At room temperature, flow rate 1ml/min and at λ_{max} 280 nm LY was eluted after 6 minutes.

Chromatographic conditions for Insulin:

A C-8 column (150x4.6mm) with 5µm particles of 100 Å pore size (Phenomenex, CA) was used. The mobile phase consisted of solvent A (0.1% trifloroacetic acid in water) and solvent B (95:5 Acetonitrile and water with 0.085% trifloroacetic acid). The gradient consisted of solvent B from 30% – 40 % in 12minutes. At room temperature, flow rate 1ml/min at λ_{max} of 218nm insulin was eluted after 6 minutes.

Scintillation counting:

Concentration of ^{3}[H]-mannitol transported to the basolateral side was detected by mixing 500µl aliquot of sample with 2 ml of Scintiverse® and counted for 2 minutes.

Recovery studies

Transwells® plates containing cells treated with OG were rinsed twice with HBSS. Both apical and basolateral chambers were replenished with fresh media and replaced in the incubator. TEER values were recorded every hour for 12 hours from the point of incubation to observe increase in TEER indicating cell recovery.

Data Analysis

TEER was measured prior to each experiment to ensure the confluency of the monolayers and also during transport studies to observe the effect of transport enhancer at each sample point. The apparent permeability coefficient (P_{eff}) was calculated using the following equation.

$$P_{eff} = (dQ/dt)*(1/A)*(1/C_0).$$

Where dQ/dt (cumulative amount transported, µg/sec) is the flux of the marker/drug compound across Caco-2 cell monolayers and is measured as the slope of the regression line describing the cumulative amount versus time. A (cm^2) represents the diffusional area of the inserts, and C_o (µg/mL) denotes the initial concentration of marker/drug compound in the donor compartment. (20, 21). All measurements and $P_{(eff)}$ were in triplicate (n=3) and expressed as mean (±) SD values.

RESULTS AND DISCUSSION

Effect of OG on TEER of Caco-2 and T-84 monolayers

Previously thirteen alkylglycosides were evaluated for potential use as permeability enhancers using epithelial cells of which OG was found to be a promising candidate (14). In this present study, Caco-2 and T-84 monolayers were used to further evaluate the penetration enhancing effects of OG. To assess the effect of short term exposure both monolayers were treated with OG at 0.1% to 1% for 1 hour (data not shown). There was an immediate decrease in TEER compared to controls at these concentrations after 1 minute. At 0.1% after the initial fall, an increase in TEER was observed which could be due to low lipid to surfactant ratio resulting in surfactant binding to cell membrane causing stabilization (18). At higher concentrations, after an immediate fall, TEER continued to decrease over the exposure period. TEER was restored to its original value after removal of OG demonstrating a reversible effect when applied at 0.1% - 0.5% indicating optimum concentration range for this exposure time. The effect of OG also depends on time of exposure. The results using both monolayers exposed to OG for 6 hours are shown in figures 1 and 2. A concentration-dependent effect is evident on resistance across both monolayers showing an immediate fall followed by prolonged reduction.

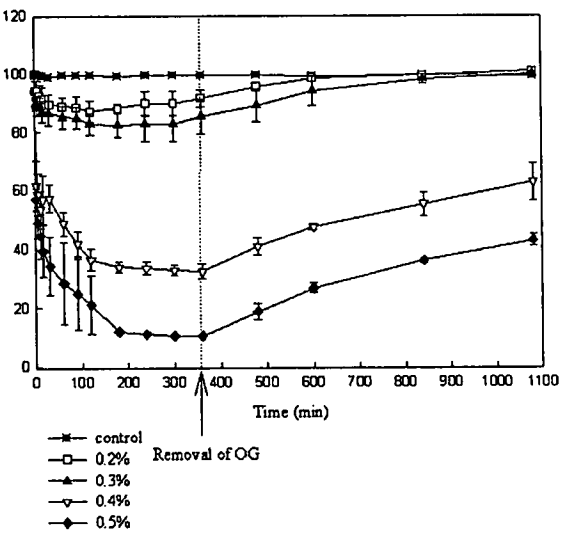

Figure 1. Effect of OG on TEER of Caco-2 monolayers for long exposure periods. *TEER (%) vs. Time (mins)*

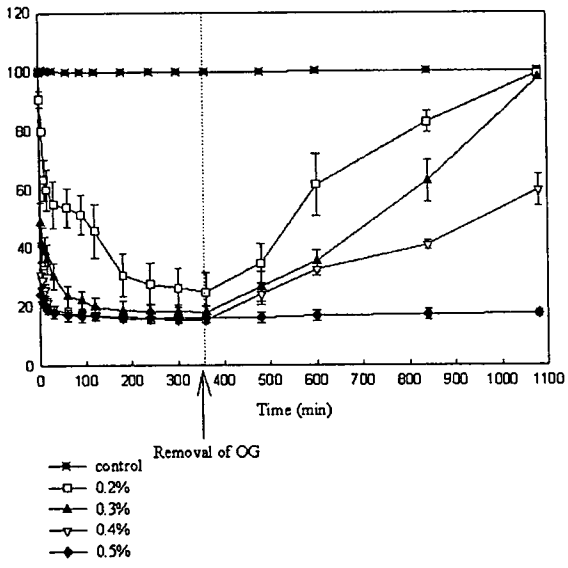

Figure 2. Effect of OG on TEER of T-84 monolayers for long exposure periods. *TEER (%) vs. Time (mins)*

Both figures indicate that after a sharp fall, resistance continued to decrease over the six hour exposure period. The lower concentrations of 0.2% and 0.3% OG had less effect on Caco-2 cells than on T-84 cells. Higher concentrations exceeding 0.5% showed similar effects on both cells lines decreasing resistance by around eighty percent.

Figures 1 and 2 also illustrate the recovery of cells after removal of OG after 6 hours. Recovery is observed only when cells are incubated in culture medium containing serum indicating requirement of proteins for their repair and taking place over a period of 12 hours. Full recovery occurred in cells exposed to 0.2% and 0.3% OG and only partial or negative recovery for cells treated with higher concentrations. Lack of recovery indicates possible solubilization of tight junction associated proteins (TJAP's) or ATP depletion which alters the phosphorylation state of TJAP's thereby resulting in the inactivation of kinases (19). This was ascertained by microscopic studies revealing intercellular gaps between the cells and also detachment of cells from the monolayers exposed to concentrations ≥ 0.5% w/v. OG could possibly be affecting signaling pathways responsible for changing phosphorylation states of TJAP's or myosin light chain components. The effect of OG was greater in T-84 than Caco-2 cells. This could be attributed to the well-developed junctional network in T-84 monolayers compared to discontinuous and poorly developed tight junctions in Caco-2 monolayers. This is evident from 4-5 times greater TEER values across T-84 monolayers. The minimum effective concentration of OG required to attenuate TEER over a period of 6 hours allowing recovery was found to be 0.2 -0.3% w/v. Higher concentrations disallow recovery. It is apparent that the effectiveness of OG in reducing resistance immediately upon exposure and allowing complete recovery after removal suggests a possible mode of action by the modulation of tight junctions associated proteins.

Effect of OG on the paracellular permeability

To determine if OG induced attenuation in TEER is accompanied by an increase in paracellular permeability, transport experiments were conducted using paracellular markers.

Effect of OG on permeability of paracellular markers

OG was applied in conjunction with paracellular markers to qualify its effect on paracellular permeability. In the absence of OG a low baseline permeability was observed with negligible amounts of both markers. The P_{eff} values of markers across Caco-2 monolayers in controls was found to be in the same range as that observed by other investigators (20, 21). No significant difference in permeability of markers was observed at concentrations below 0.1% w/v compared to control. At concentrations ≥ 0.1%w/v, a noticeable improvement in the permeability of the marker was observed.

Tables 1 and 2 illustrate the cumulative amounts and permeability coefficient (P_{eff}) of ^{3}[H]-mannitol and lucifer yellow transported at 0.2%, 0.3%, 0.4% and 0.5% w/v concentrations of OG across Caco-2 and T-84 monolayers. The enhancing effect of OG on the transport of markers across both the cell lines is concentration dependent. The permeability of ^{3}[H]-mannitol was greater compared to lucifer yellow across both monolayers attributed to the different physico-chemical properties of the markers such as the lower molecular weight of ^{3}[H]-mannitol. The permeability of both markers was greater across T-84 than Caco-2 monolayers due to the more organized junctional complex in T-84. It has been proposed that resistance across monolayers is proportional to the number of strands found within tight junctions. Since OG is thought to affect tight junction proteins and T-84 cells contain more protein strands than Caco-2 cells, this results in higher permeability (22). Permeability of these markers indicates that OG induced decrease in TEER is associated with increased permeability across both monolayers.

Table 1. Effect of OG on cumulative amount (CA) transported and permeability coefficient (P_{eff}) of molecules across Caco-2 monolayers.

	^{3}[H]-mannitol		Lucifer yellow		Insulin	
OG (%w/v)	CA(滑 i)	P_{eff} (cm/s)	CA(痢)	P_{eff} (cm/s)	CA(痢)	P_{eff} (cm/s)
Control	0.009	1.0×10^{-6}	1.0	3.9×10^{-7}	4.50	5.6×10^{-8}
0.2	0.011	1.0×10^{-6}	3.63	1.4×10^{-6}	4.53	6.0×10^{-8}
0.3	0.022	2.4×10^{-6}	3.93	1.5×10^{-6}	9.0	3.0×10^{-7}
0.4	0.052	5.5×10^{-6}	9.56	4.5×10^{-6}	32.3	5.8×10^{-7}
0.5	0.063	1.0×10^{-5}	15.37	8.1×10^{-6}	68.4	8.4×10^{-7}

Table 2. Effect of OG on cumulative amount (CA) transported and permeability coefficient (P_{eff}) of molecules across T-84 monolayers.

	^{3}[H]-mannitol		Lucifer yellow		Insulin	
OG (%w/v)	CA(滑 i)	P_{eff} (cm/s)	CA(痢)	P_{eff} (cm/s)	CA(痢)	P_{eff} (cm/s)
Control	0.007	6.6×10^{-7}	1.0	3.1×10^{-7}	0.77	6.9×10^{-9}
0.2	0.013	1.9×10^{-6}	6.21	3.0×10^{-6}	0.82	1.0×10^{-8}
0.3	0.139	1.9×10^{-5}	12.83	8.7×10^{-6}	6.50	1.4×10^{-7}
0.4	0.140	2.2×10^{-5}	16.43	8.9×10^{-6}	23.7	1.6×10^{-7}
0.5	0.174	2.3×10^{-5}	17.21	9.8×10^{-6}	42.5	6.7×10^{-7}

Effect of OG on transport of insulin across Caco-2 and T-84 monolayers

Transport across Caco-2 and T-84 monolayers was determined following addition of insulin in the apical side of Transwell® plates with 0.2%, 0.3%, 0.4% and 0.5% OG and in the absence of OG. The decrease in TEER caused by OG was in accordance with increased permeability of insulin across both the monolayers.

Permeability profiles of insulin across both monolayers at each concentrations of OG are illustrated in figures 3 and 4.

The P_{eff} and cumulative amount transported for insulin across Caco-2 and T-84 monolayers in the presence of OG are summarized in Tables 1 and 2. A concentration dependent effect of OG is evident on enhanced permeability of insulin. There was no significant enhancement in the permeability of insulin across both monolayers treated with 0.2% and 0.3% OG compared to controls.

Even though 0.2% and 0.3% OG decreased TEER (figures 1 and 2) being due in part to the relative high molecular weight of insulin. When 0.4% and 0.5% OG was applied together with insulin a noticeable improvement in insulin permeability of between 40-70 percent was observed across T-84 and Caco-2 cells respectively. At 0.2 and 0.3% OG cells remained unaffected by the surfactant for up to 6hr allowing a moderate amount of insulin to be transported. However, at 0.4% and higher OG an irregular pattern of accumulation of insulin occurred after 4hr owing to the denudation and permanent damage to cells so disrupting the formed monolayer. Therefore a steady-state was not observed and further data after this time would have been unqualified. Even though the decrease in TEER was more significant across T-84 monolayers compared to Caco-2, the permeability of insulin was elevated in Caco-2 monolayers compared to T-84 at all concentrations of OG. This paradoxical situation is probably due to the poorly developed junctional complexes in Caco-2 cells accompanied by the spatial occupation and molecular weight of insulin.

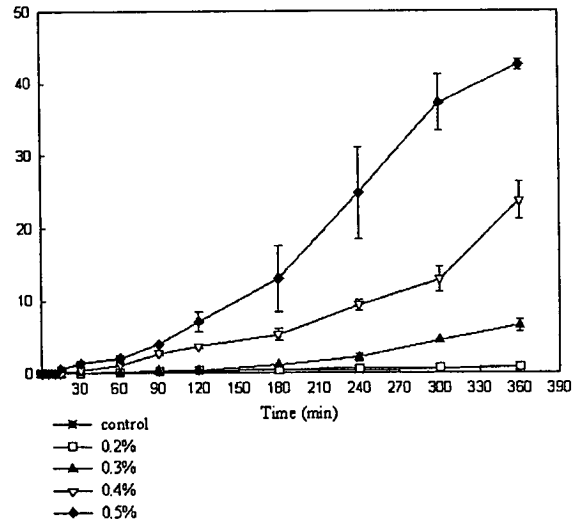

Figure 3. Transport of insulin across T-84 monolayers in the presence of OG. *Cumulative amount transported (μg) vs. Time (mins)*

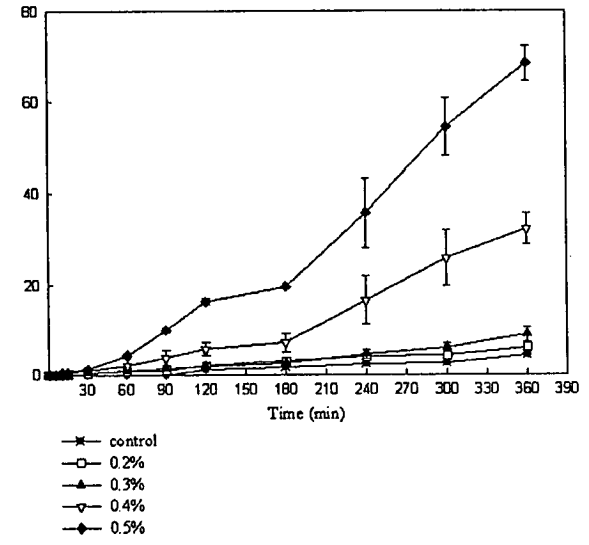

Figure 4. Transport of insulin across Caco-2 monolayers in the presence of OG. *Cumulative amount transported (μg) vs. Time (mins)*

The decrease in TEER was immediate but did not result in instant transport of marker or insulin molecules showing an asymptotic relationship between solute flux and TEER (23). The lag time observed indicates the time required for marker or insulin to diffuse from the apical side through membranes and intercellular spaces of cells and the polyester well support before reaching the basolateral side.

OG concentrations 0.4 % and 0.5% showed a significant enhancement in insulin transport but the problem remains that at these concentrations only partial recovery is possible. From HPLC analysis of insulin, it is evident that there is no insulin degradation as no degradation product peaks were evident. This could also be attributed to insulin being permeated via the paracellular route which is considered to be low on proteolytic activity (24).

In figures 5 and 6, effective permeability(P_{eff}), was plotted against molecular weight of ^{3}[H]-mannitol, lucifer yellow and insulin illustrating a molecular weight dependent transport of molecules at each concentration of OG across Caco-2 and T-84 monolayers. Results observed in the study showed that permeation is mainly via the paracellular route. Permeation via this route is limited to the pore size between the cells and also the molecular weight and radius of the permeate (25). The permeability coefficient decreased as the molecular weight of the molecule increased showing an inverse proportionality.

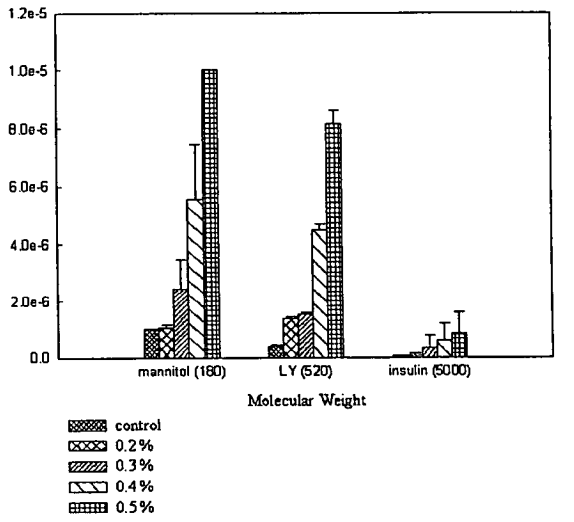

Figure 5. Correlation between molecular weight of the molecules and their P_{eff} across Caco-2 monolayers at each concentration of OG. *Permeability Coefficient (cm/sec) vs. Molecular Weight*

There is a correlation between Peff and the size of the various molecules transported. Figures 5 and 6 show this clearly and table i and ii confirm the relationship. Insulin is about 10 x larger than lucifer yellow and 30 x larger than mannitol (given that insulin has a MW around 5,700). Assuming a paracellular transport, even if tight junctions are not completely rigid larger molecules are probably going

to have a more restricted passage than smaller ones. Peff is less the larger the molecule and is also dependent on the concentration of OG (the higher concentration of OG the higher the Peff).This confirms that in general smaller molecules are transported across monolayers at a higher rate than larger molecules.

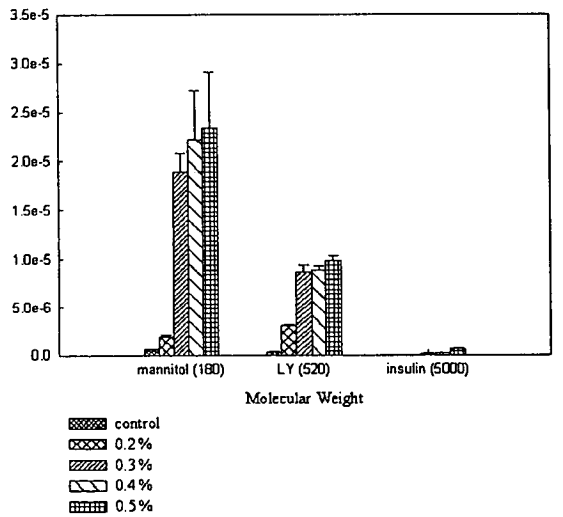

Figure 6. Correlation between molecular weight of the molecules and their P_{eff} across T-84 monolayers at each concentration of OG. *Permeability Coefficient (cm/sec) vs. Molecular Weight*

SUMMARY AND CONCLUSIONS

It is a requirement that absorption enhancers have the ability to loosen tight junctions in a reversible and timely manner. Complete recovery of cells is highly desirable to avoid cell damage due to repeated application.

OG at low concentrations has the ability to lower resistance across cell monolayers, and allow their recovery, probably by loosening tight junctions. However, higher concentrations are required to enhance the actual transport of molecules which do not allow complete recovery of cells.

Concentrations of 0.5% w/v and above of OG may not be advisable for practical use in formulation even though they exhibited maximum attenuation in TEER and transport of molecules. OG did enhance the passage of insulin in viable amounts accompanied with partial recovery of cells. Therefore OG, although not an ideal enhancing agent for insulin, may be appropriate for other proteins, peptides or poorly soluble agents. The potential use of OG could be an important contribution towards the formulation and development of selective and efficient delivery systems.

REFERENCES

[1] Pauletti, GM., Gangwar, S, Knipp, T., Nerurkar,MM, Franklin W. Okumu, FW., Tamura, K., Siahaan, TJ. and Borchardt, R.T. Structural requirement for absorption of peptide drugs. Journal of controlled release, 41: 3-17, 1996.

[2] Verhoef JC. Bodde HE. de Boer AG. Bouwstra JA. Junginger HE. Merkus FW. Breimer DD. Transport of peptide and protein drugs across biological membranes. [Review][95 refs] European Journal of Drug Metabolism & Pharmacokinetics. 15(2):83-93, 1990 Apr-Jun.

[3] Heinemann, L., Pf zner, A. and Heise, T. Alternative routes of administration as an approach to improve insulin therapy: Update on dermal, oral, nasal and pulmonary insulin delivery 7 (14): 1327-1351, 2001Sept.

[4] Chein, YW. and Banga, AK. Potential developments in systemic delivery of insulin. Drug Dev. Ind. Pharm., 15: 1601-1617, 1989.

[5] Houston, JB. and Wood, SG. Gastrointestinal absorption of drugs and other xenobiotics. in progress in drug metabolism, Vol. 4, Bridges, J.W. and Chasseaud, L.F., Eds., John Whiley and Sons, New York, 1980, Chapter 2.

[6] Hoener, B., and Benet, LZ. Factors influencing drug absorption and drug availability. In: Modern Pharmaceutics, Banker, G.S. and Rodes, C.T., Eds., 1979, Chapter 4.

[7] Hinchcliffe, M and Illum, L. Intranasal insulin delivery and therapy. Advanced Drug Delivery, 35: 199-234, 1999.

[8] Gizurarson, S., and Bechgaard, E. Intranasal administration of insulin to humans. Diabetes Research Clinical Pract., 12 (2): 71-84, 1991 May.

[9] Drejer, K. Pharmacokinetics of intranasally administered insulin with phospholipids as absorption enhancers. Diabetologia, 53(suppl. 1): A61, 1990.

[10] Moses, AC., Gordon, GS., Carey MC. and Flier JS. Insulin administered intranasally as an insulin –bile salt aerosol – effectiveness and reproducibility in normal and diabetic subjects. Diabetes, 32 (11): 1040-1041, 1983 Nov.

[11] Weber, N., and Bening, H. Metabolism of orally administered alkyl β-glucosides in the mouse. J. Nutr., 114 (2): 247-254, 1984 Feb.

[12] Humphrey, MJ. The oral bioavailability of peptides and related drugs. In: Davis, S.S., Illum, L., and Tomlinson, E., eds., Delivery Systems for peptide drugs, New York, Plenum Press, 139-151.

[13] Murakami, M., Kusanoi, Y., Takada, K and Muranishi, S. Assessment of enhancing ability of

medium-chain alkyl saccharides as new absorption enhancers in rat rectum. International Journal of Pharmaceutics, 79:159-169, 1992 Feb.

[14] Eley, J. and Tirumalasetty, P. In vitro assessment of alkylglycosides as permeability enhancers. AAPS PharmSciTech., 2(3):1-7 (article 12), 2001.

[15] Verhoef, J., and Witter, A. In vivo fate of a behaviorally active ACTH 4-9 analog in rats after systemic administration. Pharmac. Biochem. Behav., 4 95): 583-590, 1976 May.

[16] Shinkai, H., Toi, K., Kumashiro, I., Seto, Y., Fukuma, M., Dan, K.and Toyoshima,S. N-Acylphenylalanines and related compounds. A new class of oral hypoglycemic agents. Journal of Med. Chem., 31: 2092-2097, 1988.

[17] MacFadyen, RJ., Meredith, PA. and Elliott, HL. Enalapril clinical pharmacokinetics and pharmacokinetic-pharmacodynamic relationships: an overview. Clinical pharmacokinetics, 25 (4): 274-282, 1993 Oct.

[18] Gullikson, GW., Cline, WS., Lorenzsonn ,V., Benz, L., Olsen, WA. and Bass P. Effect of anionic surfactants on hamster small intestinal membrane structure and function: relationship to surface activity. Gasteroenterology, 73 (3): 501-511, 1977 Sep.

[19] Tsukamoto, T. and Nigam, SK. Role of tyrosine phosphorylation in the reassembly of occludine and other tight junction proteins. American Journal of Physiology, 276: F737-F750, 1999 May.

[20] Shiyin, Y. Invitro permeability across Caco-2 cells can predict invivo absorption in man- fact or myth. Pharmaceutical research, 14(6): 763-766, 1997 June.

[21] Delie, F. and Rubas, W. A human colonic cell line sharing similarities with enterocytes as a model to examine oral absorption: advantages and limitations of the Caco-2 model. Critical Reviews in Therapeutic Drug Carrier Systems, 14(3): 221-286, 1997.

[22] Claude, P. and Goodenough, D. Fracture faces of zonalae occludens from tight and leaky epithelia. Journal of Cell Biology, 58 (2): 390-400, 1973 Aug.

[23] Madara, JL., Barenberg, D., Carlson, S., Effect of cytochalasin-D on occluding junctions of intestinal absorptive cells: further evidence that the cytoskeleton may influence paracellular pathway and junction charge selectivity. Journal of Cell Biology, 102(6): 2125- 2136, 1986 June.

[24] Lee, VHL., Yamamoto, A and Bhaskar, U. Mucosal penetration enhancers for facilitation of peptide and protein drug absorption. Critical reviews in therapeutic drug carrier system, 8(2): 91-192, 1991.

[25] Knipp, GT., Ho, NFH., Barsuhn, CL., and Borchardt, RT. Paracellular diffusion in Caco-2 monolayers: Effect of perturbation on the transport of hydrophilic compounds that vary in charge and size. Journal of Pharmaceutical Sciences. 86(10): 1105-1110, 1997 Oct.

© Basic & Clinical Pharmacology & Toxicology 2005, 96, 162–166.
Printed in Denmark . All rights reserved

Basic & Clinical Pharmacology & Toxicology
Copyright ©
ISSN 1742-7835

MiniReview

Which *in vitro* Screens Guide the Prediction of Oral Absorption and Volume of Distribution?

Han van de Waterbeemd

Pfizer Global Research and Development, PDM, Sandwich Laboratories, IPC 664, Ramsgate Road, Sandwich, Kent CT13 9NJ, U.K.

(Received July 12, 2004; Accepted October 6, 2004)

Abstract: The development of medium to high-throughput *in vitro* screening of ADME (Absorption, Distribution, Metabolism, Excretion) properties has been the reply to higher demands on drug metabolism scientists to cope with progress in chemistry and biology. Two areas will be discussed here, namely screens for oral absorption and for volume of distribution. The prediction of these human pharmacokinetic parameters can be based on proper combination of simple physicochemical measurements. In the future *in vitro* screens most likely will be combined with *in silico* assessments of various ADME properties leading to the concept of *in combo* screening in drug discovery.

Oral absorption

In this chapter we will discuss current *in vitro* systems for predicting oral absorption/permeability. These include cell-based systems such as Caco-2, MDCK, and non-cell based systems such as PAMPA. Since oral absorption can be influenced by transporters and CYP3A4 metabolism, the increasing interest in appropriate screens for these factors will be briefly considered. With some modifications many of these screens can also be used as a blood-brain barrier model to estimate uptake in the brain.

Since the oral route is often preferred for drug administration, an early estimate of the absorption potential is highly desirable. The methods (table 1) used to assess permeability are a compromise between high throughput and high predictability. Combinations of various screens discussed below, and including also appropriate solubility assays, may give the best possible estimate for oral absorption (Van de Waterbeemd *et al.* 2003; Van de Waterbeemd 2004).

Cell lines – Caco-2, MDCK and beyond

Several cell-based assays have been developed to screen the permeability/absorption potential (Ungell & Karlson 2003). Initially the 24-well format was used, but now most of these cell-based assays exist in 96-well format. Most of these systems are intended to screen for oral absorption, others have been developed more specifically to mimic the transport through the blood-brain barrier. Such cell lines include Caco-2, MDCK and 2/4/A1 (Tavelin *et al.* 2003) cells. There is an approximate sigmoidal relationship between flux through such cells and human intestinal absorption. Predictions on the steep part of the sigmoid curve are often not reliable.

Some transporters are expressed in these cell lines albeit

Table 1.

In vitro models for membrane permeability and oral absorption [2].

Non-cell based systems
Octanol/water distribution
Cyclohexane/water distribution, dodecane/water distribution
Phospholipid vesicles
Liposome partitioning
Immobilised artificial membranes (IAM)
Immobilised liposome chromatography (ILC)
Micellar electrokinetic chromatography (MEKC)
Biopartitioning micellar chromatography (BMC)
Impregnated (or artificial) membranes
PAMPA
Filter IAM
Hexadecane-coated polycarbonate filters
Transil™ particles
SPR biosensor
Surface activity
Cell-based systems
Original cell lines Transfected cell lines
Caco-2 MDCK-MDR1
MDCK MDCK-MRP2-OATP2
TC7 LLC-PK1
HT29
2/4/A1

Author for correspondence: Han van de Waterbeemd, PDM, Pfizer Global Research and Development, IPC 331, Sandwich, Kent CT13 9 NJ, U.K. (fax +44 1304 652937, e-mail han_waterbeemd@sandwich.pfizer.com).

to different levels depending on the cell line. MDCK cells grow faster than Caco-2, and 2/4/A1 have the advantage to have very low levels of expressed transporter and are thus suitable to study passive diffusion (fig. 1).

MDCK cells are also suitable to transfect one or more transporters to study their specific effect, such as MDCK-MDR1 cells to study the role of P-gp or MDCK-MRP2-OATP2 for more complex transporter effects.

These assays are quite costly and not always predictive for the *in vivo* situation. There is therefore an interest in establishing a "pure" non-biological permeability model, such as PAMPA, as discussed below.

Role of transporters in absorption

The role of transporter proteins in drug disposition is still far from fully understood. These transporters are expressed in most organs involved in uptake and excretion such as gut wall, blood-brain barrier, hepatocytes, and kidney. Examples of clinical relevance of transporter-mediated effects have been reported (Ayrton & Morgan 2001). It is also believed that some drug-drug interactions are based on the competition for a particular transporter. Most studied so far is the ABC transporter P-glycoprotein (P-gp, product of the *MDR1* or *ABCB1* gene), although other transporters are increasingly investigated. Efforts to predict whether a compound is a substrate or an inhibitor have focussed so far mainly on P-gp. One of the drivers to work on P-gp first is that it has been shown to be involved in multidrug resistance as well as to limit the oral uptake of drugs and the brain access. It is sometimes observed that a good correlation is obtained only when subsets of closely related structures are considered (Dearden *et al.* 2003). This may be due to the existence of two or more binding sites on P-gp. Seelig & Gatlik-Landwojtowicz (2004) found that P-gp affinity increases with increasing lipophilicity and with increasing hydrogen-bonding capacity. Since these are rather unspecific criteria, the same group also suggested structural features typically associated with P-gp recognition.

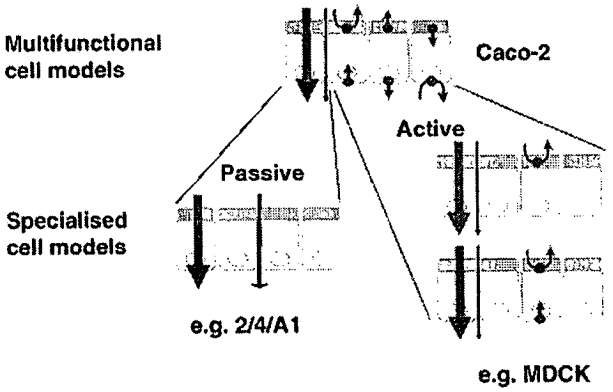

Fig. 1. Studies of transport mechanism using different cell-based assays. Caco-2 data may be too complex and can be decomposed in simpler mixed active/passive models such as MDCK, as well as models for passive transport only such as the 2/4/A1 cell line (Tavelin *et al.* 2003).

The P-gp efflux transporter is expressed in Caco-2 cell lines. By measuring the bi-directional transport ratio, this assay is therefore often used to flag potential P-gp-related absorption problems. However, such data should be handled with care. In a recent study it was shown that although the blood-brain barrier expresses P-gp there is no relationship between the P-gp efflux ratio as measured with Caco-2 cells and limited brain penetration (Faassen *et al.* 2003).

Several P-gp assays are in use. A monolayer efflux assay using the MDCK2-MDR1 cell line can identify substrates. The calcein-AM and ATPase assays identify P-gp inhibitors and modulators, which may or may not be substrates.

Artificial membranes – parallel artificial membrane permeation assay (PAMPA)

When screening for absorption by passive membrane permeability, artificial membranes have the advantage of offering a highly reproducible and high-throughput system. Artificial membranes have been compared to Caco-2 cells (Camenisch *et al.* 1997), and for passive diffusion found to behave very similar. This was the basis for the development of a parallel artificial membrane permeation assay (PAMPA) for rapid prediction of transcellular absorption potential (Kansy *et al.* 1998). In this system, permeability is assessed through a membrane formed by a mixture of lecithin and an inert organic solvent on a hydrophobic filter support. Whilst not completely predictive for human oral absorption, PAMPA data show definite trends in the ability of molecules to permeate membranes by passive diffusion, which may be valuable in screening large compound libraries. This system is commercially available or can easily be implemented. Recently a PAMPA-blood-brain barrier system has been developed (Di *et al.* 2003). Further optimisations of the experimental conditions have been investigated (Avdeef 2003). Predictability increases when a pH of 6.5 or 5.5 is used on the donor side. It was also demonstrated that the effect of a co-solvent such as DMSO can have a marked effect depending on the basic or acidic nature of the compound. PAMPA results can be made more relevant by stirring, adjusted such that the unstirred water layer thickness matches the 30–100 μm range estimated in the human gut wall (Bermejo *et al.* 2004). A further development is called Double-Sink™ PAMPA, using a pH gradient and a chemical scavenger at the receiver site to mimic *in vivo* sink conditions and the presence of plasma proteins. The use of hydrophilic filters increases the rate of permeation and reduces transport time to 2 hr compared to over 10 hr using a hydrophobic membrane (Zhu *et al.* 2002).

A similar system has been reported based on polycarbonate filters coated with hexadecane (Wohnsland & Faller 2001). This system consists in a 9–10 μm hexadecane liquid layer immobilised between two aqueous compartments. It was observed that in this set up, diffusion through the un-

stirred water layer becomes the rate-limiting step for lipophilic compounds. To mimic the *in vivo* environment, permeability measurements were repeated at different pH values in the range 4–8, and the highest transport value used for correlation with the percentage absorbed in human. This gives a sigmoidal dependence, which is better than taking values measured at a single pH, e.g. 6.8.

Models based on PAMPA data have been constructed using QSAR and VolSurf tools. These studies show that PAMPA and log D_{oct} data differ only by a hydrogen-bonding descriptor. This highlights that PAMPA is just another lipophilicity scale. It was recently also shown that a linear relationship exists between PAMPA data and dodecane/water partitioning. In summary, the PAMPA approach is believed to yield results comparable to Caco-2 studies. However, this seems a contradiction with the fact that PAMPA is only measuring passive diffusion and should be simpler in data interpretation than Caco-2 in which various transporters are expressed. PAMPA is however easier to automate and cheaper than the Caco-2 assay.

Artificial membranes – immobilised artificial membranes, immobilised liposome chromatography, micellar electrokinetic chromatography and bipartitioning micellar chromatography

Immobilised artificial membranes are another means of measuring the lipophilic characteristics of drug candidates and other chemicals. Immobilized artificial membrane columns may better mimic membrane interactions than the isotropic octanol/water or other solvent/solvent partitioning system. These chromatographic indices appear to be a significant predictor of passive absorption through the rat intestine (Genty *et al.* 2001).

A related alternative is called immobilised liposome chromatography (ILC). Compounds with the same octanol/water log P were shown to have very different degrees of membrane partitioning on immobilized liposome chromatography depending on the charge of the compound.

Another relatively new lipophilicity scale proposed for use in ADME prediction is based on micellar electrokinetic chromatography (MEKC). A further variant is called bipartitioning micellar chromatography (BMC) and uses mobile phases of Brij35 [polyoxyethylene(23)lauryl ether]. Similarly, the retention factors of 16 β-blockers obtained with micellar chromatography with sodium dodecyl sulfate as micelle-forming agent correlates well with permeability coefficients in Caco-2 monolayers and apparent permeability coefficients in rat intestinal segments. Each of these scales produce a lipophilicity index related but not identical to octanol/water partitioning.

Liposome partitioning and biosensors

Liposomes, which are lipid bilayer vesicles prepared from mixtures of lipids, also provide a useful tool for studying passive permeability of molecules through lipid. This system has e.g. been used to demonstrate the passive nature of the absorption mechanism of monocarboxylic acids. Liposome partitioning of ionizable drugs can be determined by titration and has been correlated with human absorption (Balon *et al.* 1999). A further partition system based on the use of liposomes, and commercialised under the name Transil™ (Loidl-Stahlhofen *et al.* 2001) has been investigated. It appears that such lipophilicity values are very useful in physiologically-based pharmacokinetic modelling, such as in the program PK-Sim (Willmann *et al.* 2003).

Liposomes have been attached to a biosensor surface. The interactions between drugs and the liposomes can be monitored directly using surface plasmon resonance technology, which measures changes in refractive index at the sensor surface caused by changes in mass. Drug-liposome interactions have been measured for 27 drugs and compared to fraction absorbed in humans (Danelian *et al.* 2000). A reasonable correlation was obtained, but most likely this method in its present form represents just another way of measuring "lipophilicity".

Surface activity measurements

By the pioneering work of Seelig *et al.* (1994) it has been shown that surface activity and amphiphilicity of compounds correlate to several *in vivo* processes, including blood-brain barrier penetration, gastrointestinal absorption, and development of phospholipidosis. A commercial instrument is now available (Suomalainen *et al.* 2004).

Volume of distribution

The volume of distribution in man is traditionally predicted from *in vivo* data in preclinical animals with appropriate scaling to man (Smith *et al.* 2001). This can be based on allometric scaling using the body weight (BW) of the species

$$Vd = a \cdot BW^b \quad (1)$$

where and b are regression coefficients, and b is ca 0.9–1.0. This approach is illustrated in fig. 2 for fluconazole (Smith *et al.* 2001).

In cases where plasma protein binding varies across the species, allometric scaling should be based upon the volume of distribution of unbound drug. The considerably lower free fraction (10 to 20 times) of zamifenacin in human compared to animal plasma results in decreased volume (weight normalised) of total drug, although the volume of unbound drug remains constant. This is a major factor in the markedly higher C_{max} (of total drug) after oral dosing in man compared to animal species (Beaumont *et al.* 1996). This is not always the case for acidic drugs, which are restricted to the blood compartment (typically with a volume of distribution of less than 0.1 l/kg) as changes in protein binding will not alter the volume of distribution of total drug.

An extensive retrospective analysis (Obach *et al.* 1997) examined various scaling approaches to the prediction of clinical pharmacokinetic parameters. In this analysis the

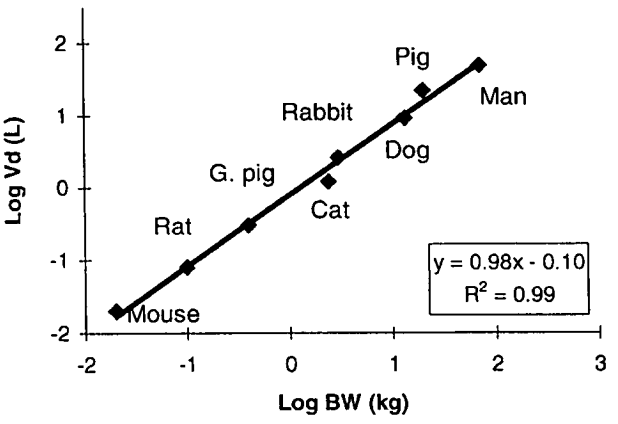

Fig. 2. Allometric relationship between body weight (BW) and volume of distribution (Vd) for anti-fungal fluconazole (Smith *et al.* 2001).

most successful predictions of volume of distribution were achieved by calculating unbound fraction in tissues (f_{ut}) of animals and assuming this would be similar in man. Volume of distribution was then calculated using measured plasma protein binding values and standard values for physiological parameters such as extracellular fluid and plasma volumes. The equation used was as follows:

$$V_{d(human)}=V_p+(f_{u(human)}.V_e)+(f_{b(human)} \cdot R \cdot V_p) + V_r \cdot (f_{u(human)}/f_{ut}) \quad (2)$$

This incorporates volumes of the various fluid compartments, plasma (V_p), extracellular fluid (V_e), and remainder (V_r) in addition to extracellular protein bound drug determined by the ratio of binding proteins in extracellular fluid relative to plasma (R). The predicted volume of distribution calculated by this method had an average-fold error of 1.56, with 88% of compounds (n=16) predicted within two times the actual value. This method was slightly more reliable than allometric scaling of the volume of distribution of unbound drug which provided an average-fold error of 1.83, with 77% of compounds (n=13) predicted within two times the actual value. Both methods were significantly better than allometric scaled values without consideration of protein binding differences which only predicted 53% of compounds (n=15) within two times the actual value (average-fold error=2.78).

A new approach defined as fractal volume of distribution, which scales the numerical values of volume of distribution proportionally to the body mass was introduced and found the give better results than interspecies allometric scaling (Karalis *et al.* 2001; Karalis & Macheras 2002).

More recently new approaches have been explored using the Oie-Tozer equation or a physiological/mechanistical model and the measurement of simple physicochemical properties (Lombardo *et al.* 2002 & 2004; Keldenich *et al.* 2004; Poulin & Theil 2002). The Oie-Tozer equation gives a relationship between the volume of distribution at steady state and the fraction unbound in tissues (f_{ut}). The latter can be estimated from the following equation

$$f_{ut}=0.23 \log D-0.93 f_{i(7.4)}+0.89 \log f_u \quad (3)$$

where log D is the distribution coefficient in octanol/water at pH 7.4, $f_{i(7.4)}$ is the fraction of drug ionised at pH 7.4 and f_u is the fraction of drug unbound the plasma proteins. In other words, by measuring *in vitro* the log D, pKa and plasma protein binding a good estimate of the *in vivo* volume of distribution is obtained yielding approximately a two-fold mean accuracy (Lombardo *et al.* 2002 & 2004). Other approaches have recently been presented using a physiological model and measurement of membrane affinity and albumin binding (using the Transil™ technology) (Keldenich *et al.* 2004) or a combination of plasma protein binding and octanol/water as well as olive oil/water partitioning (Poulin & Theil, 2002).

Outlook

A range of *in vitro* screens can be used to estimate human oral absorption and volume of distribution. With increasing experience in each of these further improvements can be expected. In particular it is often from a combination of such assays and the use of an *in silico* approach that best results are obtained.

The development of *in silico* ADME models is however not straightforward and there are various reasons why models may fail (Stouch *et al.* 2003). These are related to original data quality, expectations of the user and proper usage. Some endpoints are complex and this adds to the difficulty to develop a useful model. Models for oral absorption and volume of distribution are among the promising ones (Bergström 2005). Further development of robust *in silico* tools, in combination with high-throughput *in vitro* screening, will lead to an *in combo* approach towards the estimation of oral absorption and volume of distribution and other key ADME properties in drug discovery (Dickins & Van de Waterbeemd, 2004).

References

Avdeef, A.: *Absorption and drug development.* Wiley, Hoboken, USA, 2003.

Ayrton, A. & P. Morgan: Role of transport proteins in drug absorption, distribution and excretion. *Xenobiotica* 2001, **31**, 469–497.

Balon, K., B. U. Riebesehl & B. W. Muller: Drug liposome partitioning as a tool for the prediction of human passive intestinal absorption. *Pharm. Res.* 1999, **16**, 882–888.

Beaumont, K. C., A.G. Causey, P. E. Coates & D.A. Smith: Pharmacokinetics and metabolism of zamifenacin in mouse, rat, dog and man. *Xenobiotica* 1996, **26**, 459–471.

Bermejo, M., A. Avdeef, A. Ruiz, R. Nalda, J. A. Ruell, O. Tsinman, I. Gonzalez, C. Fernandez, G. Sanchez, T. M. Garrigues & V. Merino: PAMPA – a drug absorption in vitro model 7. Comparing rat in situ, Caco-2, and PAMPA permeability of fluoroquinolones. *Eur. J. Pharm. Sci.* 2004, **21**, 429–441.

Bergström, C. A. S.: *In silico* predictions of drug solubility and permeability: Two rate-limiting barriers to oral drug absorption. *Basic & Clinical Pharmacology & Toxicology* 2005, **96**, 156–161.

Camenisch, G., G. Folkers & H. Van de Waterbeemd: Comparison of passive drug transport through Caco-2 cells and artificial membranes. *Int. J. Pharmaceut.* 1997, **147**, 61–70.

Danelian, E., A. Karlén, R. Karlsson, S. Winiwarter, A. Hansson, S. Löfås, H. Lennernäs & D. Hämäläinen: SPR biosensor studies of the direct interaction between 27 drugs and a liposome surface: Correlation with fraction absorbed in humans. *J. Med. Chem.* 2000, **43**, 2083–2086.

Dearden, J. C., A. Al-Noobi, A. C. Scott & S. A. Thomson: QSAR studies on P-glycoprotein-regulated multidrug resistance and on its reversal by phenothiazines. *SAR QSAR Environ. Res.* 2003, **14**, 447–454.

Di, L., E. H. Kerns, K. Fan, O. J. McConnell & G. T. Carter: High throughput artificial membrane permeability assay for blood-brain barrier. *Eur. J. Med. Chem.* 2003, **38**, 223–232.

Dickins, M. & Van de Waterbeemd, H.: Simulation models for drug disposition and drug interactions. *BioSilico* 2004, **2**, 38–45.

Faassen, F., G. Vogel, H. Spanings & H. Vromans: Caco-2 permeability, P-glycoprotein transport ratios and brain penetration of heterocyclic drugs. *Int. J. Pharmaceut.* 2003, **263**,113–122.

Genty, M., G. Gonzalez, C. Clere, V. Desangle-Gouty & J.-Y. Legendre: Determination of the passive absorption through the rat intestine using chromatographic indices and molar volume. *Eur. J. Pharm. Sci.* 2001, **12**, 223–229.

Kansy, M., F. Senner & K. Gubernator: Physicochemical high throughput screening: Parallel artificial membrane permeation assay in the description of passive absorption processes. *J. Med. Chem.* 1998, **41**, 1007–1010.

Karalis, V., L. Claret, A. Iliadis & P. Macheras: Fractal volume of distribution: it scales proportionally to the body mass. *Pharm. Res.* 2001, **18**, 1056–1060.

Karalis, V. & P. Macheras: Drug disposition viewed in terms of the fractal volume of distribution, *Pharm. Res.* 2002, **19**, 697–704.

Keldenich, J., W. Schmitt & S. Willmann,: A physiological model for predicting organ/plasma partitioning and volume of distribution. In: *Biological and physicochemical profiling in drug research.* Eds.: B. Testa, S.D. Krämer, H. Wunderli-Allensbach & G. Folkers, VHCA, Zurich, and Wiley-VCH, Weinheim, 2004, in press.

Loidl-Stahlhofen, A., A. Eckrt, T. Hartmann & M. Schottner: Solid-supported lipid membranes as a tool for determination of membrane affinity: high-throughput screening of a physicochemical parameter. *J. Pharm. Sci.* 2001, **90**, 599–606.

Lombardo, F., R. S. Obach, M. Y. Shalaeva & F. Gao: Prediction of volume of distribution values in humans for neutral and basic drugs using physicochemical measurements and plasma protein binding data. *J. Med. Chem.* 2002, **45**, 2867–2876.

Lombardo, F., R. S. Obach, M. Y. Shalaeva & F. Gao: Prediction of human volume of distribution values for neutral and basic drugs. 2. Extended data set and leave-class-out statistics. *J. Med. Chem.* 2004, **47**, 1242–1250.

Obach, R. S., J. G. Baxter, T. E. Liston, M. Silber, B. C. Jones, F. MacIntyre, D. J. Rance & P. Wastall: The prediction of human pharmacokinetic parameters from preclinical and in vitro metabolism data. *J. Pharm. Exp. Therap.* 1997, **283**, 48–58.

Poulin, P. & Theil, F.-P.: Prediction of pharmacokinetics prior to in vivo studies. 1. Mechanism-based prediction of volume of distribution. *J. Pharm. Sci.* 2002, **91**, 129–156.

Seelig, A. & E. Gatlik-Landwojtowicz: Biophysical characterization of inhibitors of multidrug efflux transporters – their membrane and protein interactions. *Mini-Revs. Med. Chem.* 2004, in press.

Seelig, A., R. Gottschlich & R. M. Devant: A method to determine the ability of drugs to diffuse through the blood-brain barrier. *Proc. Natl. Acad. Sci. USA* 1994, **91**, 68–72.

Smith, D.A., H. Van de Waterbeemd & D. K. Walker: *Pharmacokinetics and metabolism in drug design.* Wiley-VCH, Weinheim, Germany, 2001, pp. 123–132.

Stouch, T. R., J. R. Kenyon, S. R. Johnson, X.-Q. Chen, A. Doweyko & Y. Li: In silico ADME/tox: why models fail. *J. Comput. Aid. Mol. Des.* 2003, **17**, 83–92.

Suomalainen, P., C. Johans, T. Söderlund & P. K. J. Kinnunen: Surface activity profiling of drugs applied to the prediction of blood-brain barrier permeability. *J. Med. Chem.* 2004, **47**, 1783–1788.

Tavelin, S., J. Taipalensuu, I. Söderberg, R. Morrison, S. Chong & P. Artursson: Prediction of the oral absorption of low permeability drugs using small intestinal-like 2/4/A1 cell monolayers. *Pharm. Res.* 2003, **20**, 397–405.

Ungell, A.-L. & J. Karlson: Cell cultures in drug discovery: An industrial perspective. In: *Drug bioavailability.* Eds. H. Van de Waterbeemd, H. Lennernas & P. Artursson. Wiley-VCH, Weinheim, Germany, 2003, pp. 90–131.

Van de Waterbeemd, H., H. Lennernäs & P. Artursson (Eds.): *Drug bioavailability.* Wiley-VCH, Weinheim, Germany, 2003.

Van de Waterbeemd, H.: Property-based lead optimisation. In: *Biological and physicochemical profiling in drug research.* Eds.: B. Testa, S. D. Krämer, H. Wunderli-Allensbach & G. Folkers. VHCA, Zürich, and Wiley-VCH, Weinheim, 2004, in press.

Willmann, S., Lippert, J., Severstre, M., J. Solodenk & W. Schmitt: PK-Sim: a physiologically based pharmacokinetic "whole-body" model. *BioSilico* 2003, **1**, 121–124.

Wohnsland, F. & B. Faller: High-throughput permeability pH profile and high-throughput alkane/water log P with artificial membranes. *J. Med. Chem.* 2001, **44**, 923–930.

Zhu, C., L. Jiang, T.-M. Chen & K.-K. Hwang: A comparative study of artificial membrane permeability assay for high throughput profiling of drug absorption potential. *Eur. J. Med. Chem.* 2002, **37**, 399–407.

Effects of Capsaicin on Cellular Damage and Monolayer Permeability in Human Intestinal Caco-2 Cells

Yuri TSUKURA,[a] Maya MORI,[a] Yoshihiko HIROTANI,[a,b] Kenji IKEDA,[b] Fumio AMANO,[c] Ryuji KATO,[a] Yoshio IJIRI,[a] and Kazuhiko TANAKA*,[a]

[a] *Laboratory of Clinical Pharmacy & Clinical Pharmacokinetics, Osaka University of Pharmaceutical Sciences;* [c] *Laboratory of Biodefense and Regulation, Osaka University of Pharmaceutical Sciences; 4–20–1 Nasahara, Takatsuki, Osaka 569–1094, Japan: and* [b] *Laboratory of Clinical Pharmaceutics, Faculty of Pharmacy, Osaka Ohatani University; 3–11–1 Nishikiorikita, Tondabayashi, Osaka 584–8540, Japan.*

Received March 26, 2007; accepted August 1, 2007; published online August 6, 2007

Recent studies suggest that capsaicin (Cap), a major constituent of hot pepper, may affect the function and permeability of the intestinal mucosa *in vitro*. However, the relationships between the dose of Cap and the barrier and/or transporter functions on intestinal epithelial cells are unknown. The aim of this study was to investigate whether Cap initiates cellular injury and alter epithelial permeability in Caco-2 cells. Cellular toxicity, as measured using a lactate dehydrogenase release assay, was not observed at high concentrations of Cap (up to 300 μM). When cell viability was measured by a WST-1 assay (tetrazolium salt-based assay), damage to Caco-2 monolayers was observed at doses of 200 and 300 μM of Cap. The barrier function of tight junctions was assessed by measuring transepithelial electrical resistance (TEER) in Caco-2 cells. Treatment of Caco-2 cells with Cap at doses above 100 μM significantly decreased the TEER compared to treatment with buffer alone for 2 h ($p<0.05$). We next examined the effects of Cap on the activity of P-glycoprotein (P-gp) found on transcellular transporters. At doses of 100 and 200 μM, Cap inhibited the transport of rhodamine 123 by P-gp-mediated efflux in Caco-2 cells. Cap thus exhibited inhibitory effects on P-gp. The results of this study indicate that Cap, a dietary phytochemical, causes functional and structural changes in Caco-2 cell monolayers at noncytotoxic doses (less than 100 μM of Cap). The concomitant administration of Cap with drugs that are substrates of P-gp might increase the plasma concentrations of such drugs.

Key words capsaicin; Caco-2; P-glycoprotein; tight junction; food–drug interaction

Some dietary constituents and phytochemicals have recently been identified as important factors affecting drug disposition. The effects of these factors on drug absorption are thought to vary depending on the epithelial barrier functions and transporters. Ingestion of many types of herbal supplements results in interactions with drugs administered concomitantly.

The intestinal mucosal epithelium constitutes the major barrier (including tight junctions (TJ) and efflux transporters) to the absorption of drugs that are administrated orally. A TJ forms a paracellular barrier on the lateral membranes of adjacent cells and acts as a structural barrier to the paracellular passage of water-soluble molecules and bacteria.[1,2] Disruption of the TJ barrier allows paracellular penetration of toxic luminal substances such as anticancer drugs and nonsteroidal anti-inflammatory drugs (NSAIDs),[3,4] which promote gastrointestinal mucosal injury.

During absorption, dietary supplements can interact with the efflux transporters present in enterocytes, and marked interaction may occur with drugs administered concomitantly. A role has been suggested for P-glycoprotein (P-gp) in the intestinal absorption and prehepatic elimination of numerous xenobiotics, including drugs.[5] Both its location on the apical membrane of enterocytes and its function as an efflux pump suggest an important role for the intestinal P-gp in modulating permeability to drugs.

Capsaicin (Cap) is a major component of hot pepper, a widely consumed spice in Southeast Asian countries. Cap has previously been shown to be a substrate of P-gp[6] and to inhibit P-gp.[7,8] Cap also has chemopreventive and chemoprotective properties[9,10] and has been found to affect the permeability of human colon carcinoma cell line (HCT-8) in intestinal epithelial monolayers.[11] Although high doses of Cap cause mucosal damage through direct cytotoxic effects, the effects of various doses of Cap on the gastrointestinal TJ barrier and P-gp are unknown.

In the present study, we examined the effects of Cap on the intestinal epithelial TJ barrier and P-gp using a filter-grown Caco-2 intestinal epithelial monolayer. Caco-2 cells grown on permeable inserts form TJ and attain many of the morphological and functional characteristics of small intestinal enterocytes[12] and are widely used as an *in vitro* model in drug-absorption studies. This cellular model system can be used to determine the effects of Cap on paracellular and transcellular permeability.

MATERIALS AND METHODS

Materials Dulbecco's modified Eagle's medium (DMEM), trypsin, penicillin, streptomycin, and Hank's balanced salt solution (HBSS) were purchased from Invitrogen Corp. (CA, U.S.A.). Fetal bovine serum (FBS) was purchased from BioSource International Inc. (CA, U.S.A.). Millicell-PCF 3.0 μM permeable filters (12 mm) were purchased from Millipore Corp. (MA, U.S.A.). Rhodamine 123 (Rh123) was purchased from Sigma-Aldrich Inc. (MO, U.S.A.). Cap was kindly provided by Maruishi Pharmaceutical Co., Ltd. (Osaka, Japan). MTX "LDH" kit was purchased from Kyokuto Pharmaceutical Industrial Co. (Tokyo, Japan). Cell Counting Kit was purchased from DOJINDO Laboratories (Kumamoto, Japan). All other chemicals were of reagent grade.

* To whom correspondence should be addressed. e-mail: pico@gly.oups.ac.jp

Cell Cultures Caco-2 cells (passage 52—60), from a human colonic carcinoma, were grown in a culture medium composed of DMEM with 4.5 mg/ml glucose, 50 U/ml streptomycin, 50 U/ml penicillin, 4 mmol/l glutamine, and 10% FBS in 25-cm^2 tissue culture flasks (Becton-Dickinson Ind., NJ, U.S.A.). The cells were maintained at 37 °C in an atmosphere of 5% CO_2/95% air in a CO_2 incubator (NAPCO Inc., NC, U.S.A.) until they reached 80—90% confluence, usually in 5—7 d. The cells were subcultured by partial digestion with 0.25% trypsin and 1 mmol/l EDTA in Ca^{2+}- and Mg^{2+}-free phosphate-buffered saline (PBS) solution. The Caco-2 cells were then detached from the stock cultures by trypsin digestion, washed once by centrifugation, resuspended, and subcultured in 10 ml of medium in culture flasks at a concentration of 1×10^5 cells/ml. The cultures were observed on a regular basis under an inverted light microscope to monitor growth and contamination. For growth on filters, high-density Caco-2 cells (2.0×10^5 cells/ml) were plated on nitrocellulose-based Millicell-HA filters. The Caco-2 cells were fed with culture medium every alternate day and then daily for 18 or 25 d by replacing 0.4 ml of the medium in the apical chamber and 0.6 ml of the medium in the basolateral chamber. They were monitored regularly for confluence by measuring transepithelial electrical resistance (TEER).

Cellular Toxicity Test Lactate Dehydrogenase (LDH) Release Assay: LDH activity was measured in Ca^{2+}- and Mg^{2+}-free PBS solution. The assay is based on the oxidation of NADH in the presence of pyruvate. Briefly, Caco-2 cells (5×10^3 cells/well) were plated on a 96-well multiplate (SUMITOMO BAKELITE Co., Ltd., Tokyo, Japan) and treated with Cap for 72 h. The LDH reagent was added to each well. Following 2-h incubation at 37 °C, the stop solution was added and absorbance at 560 nm was determined by a Multiskan JX microplate reader (Thermo LabSystems, MA, U.S.A.). Results are expressed as percentages of absorbance of 0.1% Tween 20 (100% LDH release) and HBSS (0% LDH release).

Cell Viability Assay: The viability of Caco-2 cells was determined by a cell proliferation assay using WST-1 reagent. WST-1 is a water-soluble sulfonated tetrazolium salt that is cleaved by cellular succinate dehydrogenases in living cells, yielding dark blue formazan. Damaged or dead cells exhibit reduced dehydrogenase activity. Briefly, Caco-2 cells (5×10^3 cells/well) were plated on a 96-well multiplate and treated with Cap for 2 h. WST-1 solution/culture medium (5 mmol/l, 1 : 9) was added to each well. Following 3-h incubation at 37 °C, absorbance at 450 nm (reference at 630 nm) was measured by a Multiskan JX microplate reader. Percentage cell viability was calculated based on the absorbance measured relative that of cells exposed to culture medium alone.

Determination of Epithelial Monolayer Resistance and Permeability Experiment The permeabilities of Rh123 through Caco-2 cell monolayers were determined in both the apical-to-basolateral (A→B) and basolateral-to-apical (B→A) directions at pH 7.4. Cap was added to both sides at the same concentrations. Before the permeability experiments, the cell monolayers were washed twice with PBS (pH 7.4). After washing, the cells were allowed to reach equilibrium in transport buffer for 60 min. TEER was measured using a Millicell-ERS voltohmmeter (Millipore Corp., Bedford, MA, U.S.A.). Cell monolayers with TEER values below 300 $\Omega\cdot cm^{-2}$ were not used. The apical or basolateral solution was changed to 5% ethanol/HBSS containing Rh123 (loading dose of 5 μM) with or without Cap. Samples were obtained after 120 min by moving the cell monolayer to a new receiver well containing fresh HBSS. The samples were diluted with 500 μl HBSS, and fluorescence was determined at 485/546 nm (excitation/emission) on a fluorometer (HITACHI, F-3000, Tokyo, Japan). All the transport experiments were performed in triplicate. The TEER values were measured after each experiment.

Cap dissolved in 5% ethanol was diluted with 5% ethanol in HBSS to prepare samples with 0—300 μM of Cap. Control samples included 5% ethanol in HBSS. Apparent permeability coefficient (P_{app}) was determined according to the following equation: $P_{app}=(dQ/dt)/(AC_0)$ (cm/s). dQ/dt (nmol/s) is the flux rate, A (cm^2) is the effective surface area of the cell monolayer, and C_0 (nmol/ml) is the initial drug concentration (5000 nmol/ml) in the donor chamber.

Data Analysis Results are expressed as means±S.D. Statistical analyses were performed using Student's unpaired t-test and Tukey multiple comparison test, and differences were regarded as significant at the $p<0.05$ level.

RESULTS

Cellular Damage by Cap LDH Method The cytotoxic effects of ethanol, which was used to enhance the solubility of Cap, were determined by measuring LDH release in Caco-2 cells. Ethanol slightly increased the LDH release by Caco-2 cells at various concentrations (2.5%, 5.0%, and 10% in HBSS) compared with the control (HBSS) (Fig. 1). Cap at various concentrations (0—300 μM), including that dissolved in 5% ethanol/HBSS, did not increase LDH release (Fig. 1).

WST-1 Method There was a marked decrease in cell viability at 200 and 300 μM Cap compared with the decreases observed when the medium and Cap concentrations below 100 μM were used. Percentage cell viability was 32% and

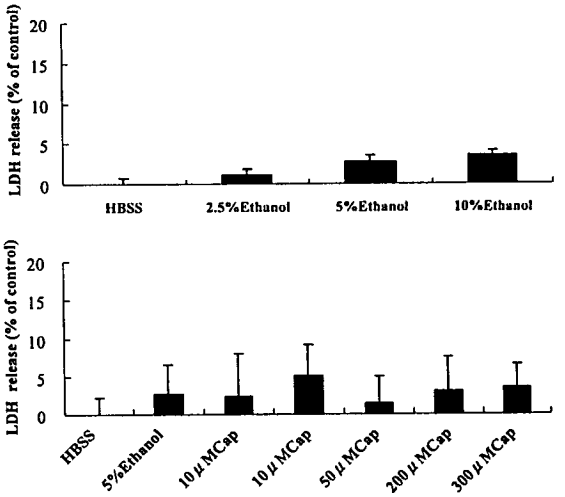

Fig. 1. Effects of Ethanol and Cap on LDH Release (%) as Measured by LDH Release Assay

Values are mean±S.D. (n=8). LDH release (%) were relative values calculated as 0% in HBSS and 100% in 0.1% Tween 20. LDH, lactate dehydrogenase; HBSS, Hank's balanced salt solution; Cap, capsaicin.

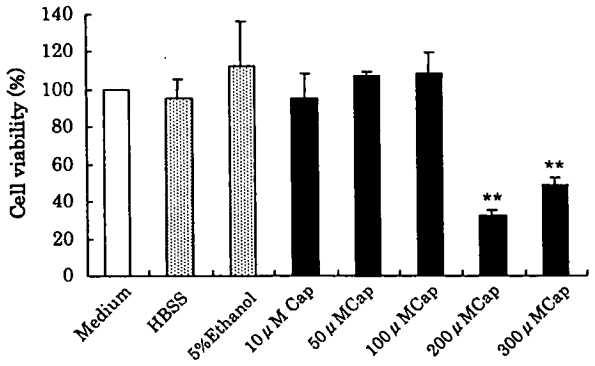

Fig. 2. Effects of Cap on Caco-2 Cell Viability as Measured by WST-1 Assay after 2 h Exposure

Values are mean±S.D. (n=8). Cell viability (%) was calculated as 100% in medium. **p<0.01, compared with medium. Medium, DMEM including 10% fetal bovine serum and penicillin–streptomycin; HBSS, Hank's balanced salt solution; Cap, capsaicin.

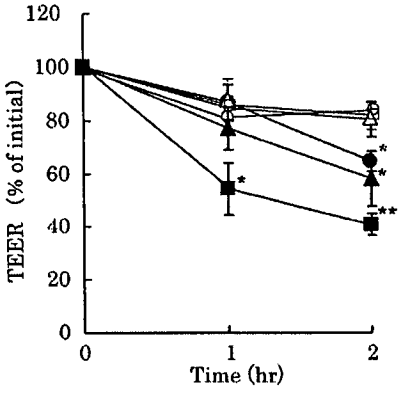

Fig. 3. Effects of Cap on TEER of Caco-2 Cells

Caco-2 monolayers were treated with Cap for 2 h. Values are mean±S.D. (n=3—4). Experiments were repeated in triplicate to ensure reproducibility. ○, Cap 0 μM; △, Cap 10 μM; □, 50 μM; ●, 100 μM; ▲, 200 μM; ■, 300 μM. *p<0.05, **p<0.01, compared with the control (5% ethanol/HBSS). Cap, capsaicin; TEER, transepithelial electrical resistance.

49% of that of the medium with culture in 200 and 300 μM Cap, respectively (Fig. 2). Cap produced marked damage at higher concentrations (200, 300 μM).

Effects of Cap on the TJ Barrier of Caco-2 Cells The effects of Cap on TJ barrier function of Caco-2 cell monolayers were evaluated by measuring TEER. After 1-h treatment, TEER was significantly decreased at 300 μM of Cap; similarly, at 2 h, it was significantly decreased at 100, 200, and 300 μM of Cap compared with the control (5% ethanol/HBSS) (Fig. 3).

Effects of Cap on Rh123 Transport P-gp function was evaluated by measuring the transepithelial transport of Rh123 across Caco-2 cell monolayers. A→B transport of Rh123, a substrate for P-gp, was significantly increased in the presence of 100 and 200 μM Cap at 2 h and 300 μM Cap at 1 and 2 h compared with the control (5% ethanol/HBSS) (Table 1). The P_{app} of Rh123 following loading with 300 μM Cap at 1 and 2 h increased approximately three- and six-fold, respectively. These findings indicate that Cap produces the functional and morphological opening of intestinal epithelial TJ barrier of Caco-2 cells. B→A transport of Rh123 was significantly decreased in the presence of 100 μM Cap at 1 and 2 h and 200 μM Cap at 1 h (Table 1). In the presence of 100 μM Cap at 2 h, A→B transport of Rh123 was enhanced, while transport in the B→A direction was inhibited.

Table 1. Apparent Permeability Coefficients (P_{app}×10^{-6} cm/s) of Rh123 Transport across Caco-2 Cell Monolayers

Sample		P_{app} (×10^{-6} cm/s)	
		A→B	B→A
5% Ethanol	1 h	0.128±0.030	1.33±0.21
	2 h	0.116±0.019	1.42±0.16
10 μM Cap	1 h	0.120±0.024	1.43±0.18
	2 h	0.157±0.097	1.35±0.05
50 μM Cap	1 h	0.117±0.003	1.27±0.19
	2 h	0.176±0.046	1.30±0.13
100 μM Cap	1 h	0.139±0.057	1.00±0.23*
	2 h	0.155±0.011*	1.08±0.20*
200 μM Cap	1 h	0.160±0.012	1.03±0.08**
	2 h	0.175±0.014**	1.44±0.12
300 μM Cap	1 h	0.333±0.009**	1.11±0.19
	2 h	0.691±0.073**	1.36±0.12

Values are means±S.D. (n=4—6). Experiments were repeated in triplicate to ensure reproducibility. *p<0.05, **p<0.01, compared with 5% ethanol. A→B (left), apical to basolateral chamber; B→A (right), basolateral to apical chamber; Rh123, rhodamine123; Cap, capsaicin.

DISCUSSION

One important function of the intestinal epithelia is to protect against mucosal penetration of toxic compounds, bacteria, and bacterial byproducts as well as dietetic additives present in the intestinal lumen. The intestinal epithelium has barrier functions against and performs efflux transport of these substances. The TJ acts as a structural barrier against paracellular permeation of luminal compounds.[1,2] Disruption of the TJ barrier causes increased epithelial penetration by toxic luminal substances that may promote mucosal injury. P-gp is an active efflux transporter and is abundantly expressed in the intestinal epithelium as one of many important epithelial barriers. Intestinal P-gp also plays a significant role in absorption and presystemic elimination of many peroral xenobiotics, including drugs. The study of the factors regulating these barrier functions is thus important from the perspective of both pharmacology and toxicology.

The efficiencies of the absorption of orally administered drugs can be affected by foods, including supplements. Healthy foods contain multiple nutrients, nonnutrients, and phytochemicals. The pharmacological effects of Cap, which include protection of the gastric mucosa[13] and vasodilation in rats[14] have been previously investigated, and recent research on Cap receptors[15,16] has suggested its potential function as an analgesic. Besides these neuronal and vascular effects of Cap, direct interactions of Cap with gastrointestinal epithelia are likely to occur. However, such direct interactions have not yet been clearly determined.

We first examined the effects of ethanol, used as a solvent, on Caco-2 cell monolayers. No toxic effects were observed with ethanol at concentrations less than 10% with LDH release method (Fig. 1). At the doses used (≤300 μM), Cap did not significantly increase the LDH release by Caco-2 cells (Fig. 1). However, Cap at concentrations of 200 and 300 μM markedly decreased cell viability in the WST-1 method, sug-

gesting that cell damage might be observed with exposure to higher concentrations of Cap (Fig. 2). At concentrations of up to 100 μM, Cap did not exhibit cell damage after 2-h incubation. The WST-1 assay is used for measuring the proliferation and viability of cells, and LDH release assay for monitoring cell death due to cell membrane destruction. For these reasons, we consider the WST-1 assay more sensitive in determining cell damage than the LDH release assay.

We next examined the effects of Cap on the barrier function of monolayers of Caco-2 cells *in vitro*. Paracellular permeability has been correlated with decrease in intestinal epithelial resistance.[17] The use of TEER as a measure of the integrity of membrane barriers has also been reported in studies evaluating the damage caused by drugs such as fenadine·HCl or indomethacin.[18,19] In addition, TEER measurements have been reported to indicate the permeablity of cell monolayers and their barrier properties.[20,21] Therefore, we used TEER values to monitor the damage induced by Cap in Caco-2 cells. The confluent Caco-2 cell monolayers cultured for approximately 20 d and used in the experiments were subjected to 0—300 μM Cap in 5% EtOH/HBSS for 2 h. Significant damage with decrease in TEER was induced in these Caco-2 cell monolayers by treatment with 100, 200, and 300 μM Cap for 2 h (Fig. 3). These experiments thus demonstrated the possibility of direct damage to Caco-2 cells *in vitro* at high concentrations of Cap. In the Caco-2 monolayer experiments, when 300 μM Cap was added, Caco-2 cells were disrupted (Table 1). In the present study, we demonstrated that high doses of Cap had direct cytotoxic effects on epithelial cells at the gastrointestinal surface, with resultant rupture of epithelial layers and formation of large open wounds on the epithelial surface. Thus, the Cap-induced increase in TJ permeability was due to an irreversible change in the TJ barrier, and may have been caused by cell death or the formation of large open wounds on the epithelial surface.

Recent studies have suggested that altered intestinal epithelial TJ permeability may be a significant risk factor for many diseases such as Crohn's disease,[3] NSAID-associated enteritis,[22] and diarrheal syndromes.[23] It has been reported that in these disorders, increase in intestinal epithelial TJ permeability allows paracellular penetration of toxic luminal substances, aggravating intestinal inflammation and mucosal injury.[3,22,23] Consumption of Cap in these clinical conditions may enhance increase in TJ permeability, resulting in greater mucosal penetration of luminal substances and further worsening of intestinal inflammation.

In the present study, we also evaluated the effects of Cap exposure on P-gp function in Caco-2 cell monolayers. We measured the permeability of Rh123 as a substrate of P-gp. The fluorescent dye Rh123 is frequently used as a P-gp index substrate. A good correlation between Rh123 transport and P-gp expression has been found.[24] We observed that Cap was capable of inhibiting P-gp efflux activity at a concentration of 100 μM, a noncytotoxic concentration, with incubation for 2 h (Table 1). We confirmed that verapamil (100 μM), a P-gp inhibitor, also inhibited the B→A transport of Rh123 across Caco-2 cells (data not shown). In addition, we found that Cap may inhibit P-gp function without decreasing TEER at 100 μM in 1 h (Table 1). It is possible that dietary Cap affects the bioavailability of co-administered drugs by inhibiting intestinal P-gp function. We reported that the bioavailability of digoxin which is a substrate of P-gp increased by oral co-administration of Cap.[25] Cap may also simultaneously cause opening of TJ. In this study, Cap induced TJ opening and inhibition of P-gp in a dose-dependent and exposure-time-dependent manner. However, Cap might not inhibit P-gp function at concentrations that induced opening of the Caco-2 TJ barrier, with the exception of exposure to 100 μM Cap for 2 h.

The apicolaterally located TJ forms a paracellular seal or barrier between the lateral membranes of the adjacent cells and acts as structural barrier against the paracellular penetration.[26] In this study, the disruption of the TJ barrier by cell damage or cytotoxicity at high doses of Cap allows an increase in epithelial penetration (A→B). And also, Cap at high levels may have a direct effect on the protein structure including TJ-related proteins. Caco-2 monolayers may lost the efflux function of P-gp protein located basolateral side of Caco-2 monolayers connected with the results of a marked decrease in cell viability by treatment with high doses of Cap (Fig. 2). Although the mechanisms leading to the barrier disruption remain unknown, current thinking suggests that both the apical and basolateral membranes of Caco-2 monolayers can respond to the cytotoxic action of Cap.

In conclusion, the results of this study indicate that Cap inhibits P-gp function in the intestinal epithelium at low noncytotoxic doses and causes the opening of the intestinal epithelial TJ barrier at high doses. Since ingestion of Cap can be expected to markedly alter the permeabilities of drugs, the use of Cap during drug administration should be evaluated.

Acknowledgements We would like to express our graduate to Maruishi Company for the generous supply of Cap.

REFERENCES

1) Anderson J. M., Van Itallie C. M., *Am. J. Physiol.*, **269**, G467—G475 (1995).
2) Madara J. L., *J. Clin. Invest.*, **83**, 1089—1094 (1989).
3) Hollander D., *Gut*, **29**, 1621—1624 (1988).
4) Tang A. S., Chikhale P. J., Shah P. K., Borchardt R. T., *Pharm. Res.*, **10**, 1620—1626 (1993).
5) Juliano R. L., Ling V., *Biochim. Biophys. Acta*, **455**, 152—162 (1976).
6) Loo T. W., Clarke D. M., *J. Biol. Chem.*, **272**, 709—712 (1997).
7) Nabekura T., Kamiyama S., Kitagawa S., *Biochem. Biophys. Res. Commun.*, **327**, 866—870 (2005).
8) Han Y., Tan T. M., Lim L.-Y., *Biochem. Pharmacol.*, **71**, 1727—1734 (2006).
9) Shimeda Y., Hirotani Y., Akimoto Y., Shindou K., Ijiri Y., Nishihori T., Tanaka K., *Biol. Pharm. Bull.*, **28**, 1635—1638 (2005).
10) Han S. S., Keum Y. S., Seo H. J., Chun K. S., Lee S. S., Surh Y. J., *Cancer Lett.*, **164**, 119—126 (2001).
11) Jensen-Jarolim E., Gajdzik L., Haberl I., Kraft D., Scheiner O., Graf J., *J. Nutr.*, **128**, 577—581 (1988).
12) Artursson P., Karlsson J., *Biochem. Biophys. Res. Commun.*, **175**, 880—885 (1991).
13) Holzer P., Pabst M. A., Lippe I. T., *Gastroenterology*, **96**, 1425—1433 (1989).
14) Lippe I. T., Sametz W., Sabin K., Holzer P., *Am. J. Physiol.*, **265**, H1864—H1868 (1993).
15) Caterina M. J., Schumacher M. A., Tominaga M., Rosen T. A., Levine J. D., Julius D., *Nature* (London), **389**, 816—824 (1997).
16) Caterina M. J., Leffler A., Malmberg A. B., Martin W. J., Trafton J., Petersen-Zeitz K. R., Koltzenburg M., Basbaum A. I., Julius D., *Science*, **288**, 306—313 (2000).
17) Madara J. L., Dharmsathaphorn K., *J. Cell Biol.*, **101**, 2124—2133 (1985).

18) Lin H., Gebhardt M., Bian S., Kwon K. A., Shim C. K., Chung S. J., Kim D. D., *Int. J. Pharm.*, **330**, 23—31 (2007).
19) Albert S. T., Prashant J., Praful K. S., Ronald T. B., *Pharm. Res.*, **10**, 1620—1626 (1993).
20) Hidalgo I. J., Raub T. J., Borchardt R. T., *Gastroenterology*, **96**, 736—749 (1989).
21) Grasset E., Pinto M., Dussaulx E., Zweibaum A., Desjeux J. F., *Am. J. Physiol.*, **247**, C260—C267 (1984).
22) Bjarnason I., Williams P., Smethurst P., Peters T. J., Levi A. J., *Gut*, **27**, 1292—1297 (1986).
23) Spitz J., Yuhan R., Koutsouri A., Blatt C., Alverdy J., Hecth G., *Am. J. Physiol.*, **268**, G374—G379 (1995).
24) Lee J. S., Paull K., Alvarez M., Hose C., Monks A., Grever M., Fojo A. T., Bates S. E., *Mol. Pharmacol.*, **46**, 627—638 (1994).
25) Hirotani Y., Yamamoto K., Tomishi H., Nishihori T., Umeda T., Tanaka K., *Jpn. J. TDM*, **24**, 23—28 (2007).
26) Thomas Y. M., Don N., Vuong B., Hanh N., Neil H., *Am. J. Physiol.*, **276**, G965—G974 (1999).

Cancer Chemother Pharmacol (2001) 47: 106–112
DOI 10.1007/s002800000213

ORIGINAL ARTICLE

Kenichi Yasoshima · Takashi Kuwabara · Eiichi Fuse
Tomoko Kuramitu · Noriaki Kurata
Hiroyoshi Nishiie · Takayoshi Oishi
Hiroyuki Kobayashi · Satoshi Kobayashi

Pharmacokinetics, distribution, metabolism and excretion of [^{3}H]UCN-01 in rats and dogs after intravenous administration

Received: 4 February 2000 / Accepted: 31 August 2000 / Published online: 30 November 2000

Abstract *Purpose*: To evaluate the metabolic fate of UCN-01, a signal transduction inhibitor, blood and plasma concentrations, distribution, metabolism and excretion were investigated in rats and dogs after intravenous administration of [^{3}H]UCN-01. *Methods*: The radioactivity in plasma, blood and tissues was measured after intravenous administration of UCN-01. In addition, the radioactivity excreted in bile, urine and feces was also determined. *Results*: The radioactivity in rat and dog plasma disappeared triphasically with terminal half-lives of 21.3 and 27.2 h, respectively. The ratios of the blood-to-plasma concentrations ranged from 0.82 to 1.13 in rats and 0.81 to 1.73 in dogs. From 0.5 to 4 h after giving [^{3}H]UCN-01 to rats, the radioactivity in all tissues except the brain and testes was higher than in plasma. The highest concentration was observed in the lungs followed by the liver and kidneys. The radioactivity was mainly excreted in feces, reaching 96.0% of the radioactivity dose in rats and 78.4% in dogs up to 168 h after injection. Since the biliary excreted radioactivity was 67.2% over 48 h in bile duct-cannulated rats, most of the radioactivity excreted in feces was from biliary radioactivity. There were several metabolites in bile samples, but little UCN-01. *Conclusions*: UCN-01 is mainly eliminated by the liver, and there are high concentrations of radioactivity derived from [^{3}H]UCN-01 in all tissues except the brain and testes.

Key words 7-Hydroxystaurosporine (UCN-01) · Protein kinase inhibitor · Metabolism · Excretion · Pharmacokinetics

K. Yasoshima · T. Kuwabara (✉) · E. Fuse · T. Kuramitu
N. Kurata · H. Nishiie · T. Oishi · H. Kobayashi · S. Kobayashi
Drug Development Research Laboratories,
Pharmaceutical Research Institute,
Kyowa Hakko Kogyo Co., Ltd., 1188,
Shimotogari, Nagaizumi-Cho,
Sunto-Gun, Shizuoka 411-8731, Japan
e-mail: takashi.kuwabara@kyowa.co.jp
Tel.: +81-559-892021; Fax: +81-559-892073

Introduction

UCN-01 (7-hydroxystaurosporine; Fig. 1) was originally reported as a selective protein kinase C inhibitor. It exhibits potent antitumor activity in both in vitro and in vivo models [1, 2, 5]. Recent studies have revealed that UCN-01 induces G1 phase accumulation in several human tumor cells [4, 10, 15] and this effect is associated with dephosphorylation of the retinoblastoma protein and its regulatory factors including cyclin-dependent kinase 2 (CDK2) and CDK inhibitors $p21^{Cip1/WAF1}$ and $p27^{Kip1}$ [4]. UCN-01 also induces apoptosis in leukemia and colon carcinoma cell lines [9, 17, 20]. Furthermore, UCN-01 synergistically enhances the antitumor activity of cytotoxic chemotherapeutic agents such as mitomycin C, cisplatin and 5-fluorouracil with G2 abrogation [3, 12, 16]. Currently, UCN-01 is being evaluated as a new type of anticancer drug in patients with refractory neoplasms in the United States and Japan [6, 13].

We have previously reported the plasma concentration-time profiles of UCN-01 measured by HPLC in experimental animals and patients [6, 11, 13]. UCN-01 in plasma after intravenous administration disappears biphasically in mice and rats, and triphasically in dogs with elimination half-lives of about 4 h in mice and rats and 12 h in dogs. The systemic clearance (CL_{tot}) values in mice, rats and dogs are relatively high (1.93–2.64, 2.82–3.86 and 0.616 l/h per kg, respectively). The distribution volumes at steady-state (Vd_{ss}) in mice, rats and dogs are also high (7.89–8.42, 13.0–16.9 and 6.09 l/kg, respectively). No saturation in pharmacokinetics was observed in these animals [11]. On the other hand, the elimination half-lives of UCN-01 in patients is extremely long (253–1660 h) and the Vd_{ss} and CL_{tot} are very low (0.0796–0.158 l/kg and 0.0407–0.252 ml/h per kg, respectively) [6].

Protein binding studies have revealed that this marked species difference in pharmacokinetics is due, at least in part, to specifically high binding of UCN-01 to human α_1-acid glycoprotein [6, 7]. The binding affinity of

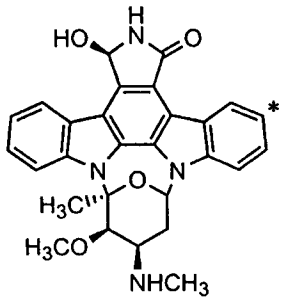

Fig. 1 Chemical structure of [^{3}H]UCN-01. The *asterisk* represents the tritium labeling position

UCN-01 to rat and dog α_1-acid glycoprotein is much weaker than to human α_1-acid glycoprotein [6, 7]. However, it would still be very useful to investigate the disposition of [^{3}H]UCN-01 in experimental animals in order to evaluate the metabolic fate of UCN-01 in the body. Because of weak protein binding, the disposition of UCN-01 in rats and dogs may reflect the disposition of "free UCN-01" in humans. Therefore, we conducted studies on the blood and plasma concentrations, distribution, metabolism and excretion of [^{3}H]UCN-01 in rats and dogs.

Materials and methods

Chemicals

UCN-01 (7-hydroxystaurosporine) was produced by fermentation in our institute as described previously [18]. [^{3}H]UCN-01 (Fig. 1) was synthesized by Amersham International (Little Chalfont, UK) with a specific activity of 548 GBq/mmol (TRQ 6529) or 307 GBq/mmol (TRQ7253). [^{3}H]UCN-01 was purified by HPLC to a radiochemical purity of more than 96% just before use. Acetonitrile (HPLC grade) was purchased from Kanto Chemical (Tokyo, Japan). Other reagents used were of analytical grade obtained commercially.

Preparation of dosing solutions

Purified [^{3}H]UCN-01 was dried under nitrogen and dissolved together with unlabeled UCN-01 in 1.2 mg/ml citric acid hydrate with disodium hydrogenphosphate dodecahydrate (5.6 mg/ml) and sodium chloride (6.0 mg/ml). Solutions of [^{3}H]UCN-01 at concentrations of 1.75 mg/ml (1.05–5.95 MBq/ml) were prepared for rats, and 1.0 mg/ml (0.98 MBq/ml) for dogs. The solutions were administered at doses of 2 ml/kg (rats) and 0.5 ml/kg (dogs).

Animals

Male Sprague Dawley rats were obtained at 6 weeks of age from Nihon SLC (Shizuoka, Japan), and used at 7 weeks of age when they weighed 200–270 g. Male beagle dogs were obtained from HRP (Kalamazoo, Mich.), and used at 3 years of age when they weighed 10 to 11 kg. All animals were accustomed to a 12-h light/dark cycle under controlled temperature and humidity conditions, with free access to standard laboratory chow and water before the start of the experiments. Food and water were given ad libitum starting 6 h after dosing. In the bile excretion study, saline including 5% sucrose was given instead of water. All experiments were approved by the Welfare Committee for Experimental Animals of our institute.

Blood and plasma concentration and excretion in rats

For the kinetic studies, [^{3}H]UCN-01 at 3.5 mg/kg was administered to four male rats via the femoral vein. Blood samples (0.2–0.3 ml) were serially collected from the tail vein at 0.05, 0.1, 0.25, 0.5, 1, 2, 4, 8, 12, 24, 48 and 72 h after dosing into heparinized capillary tubes (Drummond Scientific, Broomall, Pa.). A portion of each blood sample was used for the measurement of radioactivity directly, and plasma samples were obtained by centrifugation of the remainder (11,000 *g*, 10 min, 4 °C). For the excretion studies, after intravenous administration of [^{3}H]UCN-01 to another five male rats, the rats were retained in metabolic cages. Urine and feces samples were collected during the following periods up to 168 h after dosing: 0–4, 4–8, 8–12, 12–24 and every 24 h for urine, and 0–12, 12–24 and every 24 h for feces. The feces samples were homogenized with water. After sampling, the rats were killed with diethylether. The carcasses were placed in 750 ml of 0.5 *N* sodium hydroxide solution at 50 °C for a few days and then homogenized. The interiors of the cages were washed with 50% methanol and the radioactivity in the washings was also determined.

Blood and plasma concentration and excretion in dogs

[^{3}H]UCN-01 was administered at a dose of 0.5 mg/kg to two male dogs via the foreleg vein. Blood samples (5 ml) were collected from the contralateral foreleg vein using a heparinized syringe at 0.083, 0.25, 0.5, 1, 2, 4, 6, 8, 12, 24, 48, 72, 96, 120, 144 and 168 h after dosing. A portion of each blood sample was used for the measurement of the radioactivity directly. Also, an aliquot of blood was used to measure the hematocrit. Plasma samples were obtained by centrifugation of the remainder (2000 *g*, 10 min, room temperature). The dogs were housed in metabolic cages and the spontaneously excreted urine and feces were collected up to 168 h during the following periods: 0–6, 6–12, 12–24 and every 24 h for urine, and every 24 h for feces. At 6 and 12 h, urine in the bladder was also collected using a catheter. The cages were washed with 50% methanol and the washings collected after the experiment. The feces samples were homogenized with water.

Biliary excretion in rats

Under light anesthesia with diethylether, the bile ducts of male rats were cannulated with a PE-10 polyethylene tube (Becton Dickinson, Parsippany, N.J.). After recovery from the anesthesia, [^{3}H]UCN-01 at a dose of 3.5 mg/kg was administered to four male rats via the femoral vein. The rats were kept in restraining cages and bile, urine and feces were collected during the following periods: 0–2, 2–4, 4–6, 6–8, 8–12, 12–24 and 24–48 h for bile, 0–12, 12–24 and 24–48 h for urine, and 0–24 and 24–48 h for feces. After sampling, the rats were killed with diethylether and the carcasses were treated as described above. The feces samples were homogenized with water.

Metabolites in rat plasma, bile and urine

In order to investigate the metabolism of [^{3}H]UCN-01, rat plasma, bile and urine samples were subjected to HPLC analysis. Plasma samples were deproteinized with an equal volume of ice-cold acetonitrile and, after centrifugation, the supernatants were subjected to HPLC. The bile samples were diluted with mobile phase (A), described below, before HPLC. The HPLC system consisted of a solvent module 126 pump and a 171 radioisotope detector (Beckman, Fullerton, Calif.) equipped with an AM-312 ODS column (150 × 6.0 mm i.d.; YMC, Kyoto, Japan). The mobile phases were 0.05 *M* phosphate buffer containing 1% triethylamine (pH

7.3) and acetonitrile at a ratio of 9:1 (A) or 4:6 (B). The fraction of mobile phase (B) was increased linearly from 0 to 100% over 20 min and held there for the following 10 min. The total flow rate was set at 1 ml/min. The radioactivity in the eluate was measured with a radioisotope detector after mixing with Scintisol EX-H (Wako Pure Chemical, Osaka, Japan) at a flow rate of 4 ml/min.

Tissue distribution in rat

To determine the tissue radioactivity, rats were killed by bleeding from the femoral artery 0.5, 1, 4, 8 and 24 h after administration of [^{3}H]UCN-01 via the contralateral femoral vein at a dose of 3.5 mg/kg. Three rats were used for each time-point. Blood was collected into heparinized tubes and the plasma was obtained as described above. An aliquot of blood was also used to measure the hematocrit. The tissues indicated in the Table 4 were removed and the wet weight was measured. The brain, kidneys, spleen, pancreas, testes, stomach, small intestine and large intestine were homogenized with an appropriate volume of saline. The radioactivity in these tissues and tissue homogenates was determined.

Determination of radioactivity in the samples

Total and nonvolatile radioactivity were measured in the blood, plasma, urine, bile, feces homogenate, carcass homogenate and cage washings. The volatile radioactivity was also calculated by subtracting nonvolatile radioactivity from total radioactivity. The total radioactivity in the plasma, urine, bile and cage washings was determined after emulsifying with liquid scintillator (Scintisol EX-H or Ultima Gold; Packard, Meriden, Ct.). The blood, feces homogenate and carcass homogenates were dissolved in tissue dissolver (Solvable; Daiichi Pure Chemicals, Tokyo, Japan), treated overnight with hydrogen peroxide, and then mixed with liquid scintillator (Hionic Fluor, Packard). For the determination of nonvolatile radioactivity, the samples were dried in a freeze-dryer to remove the volatile radioactivity, and then treated as described above. The tissues and tissue homogenates were dried in a freeze-dryer, dissolved in Solvable at 50 °C for 3 h, and then mixed with Hionic Fluor. For all samples, radioactivity was measured using a liquid scintillation counter (LSC4530 or Tri-Carb 300 or 2200, Packard, LS6500; Beckman).

The counting efficiency was automatically corrected using an external standard. Samples from control animals treated by the same methods were used to obtain the background counts. The radioactivity detection limit was defined as twice the value of the corresponding background count. The radioactive concentration in blood, plasma and tissue samples was calculated as the equivalent concentration of [^{3}H]UCN-01 from the specific radioactivity of each dosing solution. The excreted radioactivity in bile, urine and feces was expressed as a percentage of the dosed radioactivity. The ratio of the radioactivity in erythrocytes to that in blood (RBC) was calculated from the following equation:

$$RBC(\%) = (1 - (1 - Ht)/Rb) \times 100$$

where Ht is the hematocrit and Rb is the ratio of the blood to the plasma concentration.

In this report, since the volatile radioactivity can be considered to originate from tritiated water, to avoid confusion, 'radioactivity' indicates 'nonvolatile radioactivity', unless otherwise specified.

Pharmacokinetic analysis

Individual pharmacokinetic parameters were analyzed using model-independent methods [8, 21]. The concentrations of radioactivity in plasma and blood were converted to logarithms and plotted against time. The slope of the terminal phase (elimination rate constant of the β phase) was determined by log-linear regression analysis, and those of the second and first phases (elimination rate constant of the α and π phase) were determined by the method of residuals. In this study, the time-points of the β phase were designated at and after 24 h and those of the α phase at and after 2 h. The elimination half-lives ($t_{1/2}\pi$, $t_{1/2}\alpha$ and $t_{1/2}\beta$) were calculated by dividing 0.693 by the elimination rate constant of the respective phase. The area under the concentration-time curve ($AUC_{0-\infty}$) was calculated by the trapezoidal rule, and extrapolated to infinity. The systemic clearance (CL_{tot}) was calculated as dose/$AUC_{0-\infty}$.

Results

Blood and plasma radioactivity concentration-time profiles

Figure 2 shows the radioactive concentration-time profiles in plasma and blood after intravenous administration of UCN-01. After intravenous administration of [^{3}H]UCN-01 at 3.5 mg/kg to rats, the blood concentration of radioactivity was 0.975 ± 0.213 μg equivalents/ml (mean ± SD of four rats) at 0.05 h, and then disappeared biphasically to below the detection limit after 48 h. No

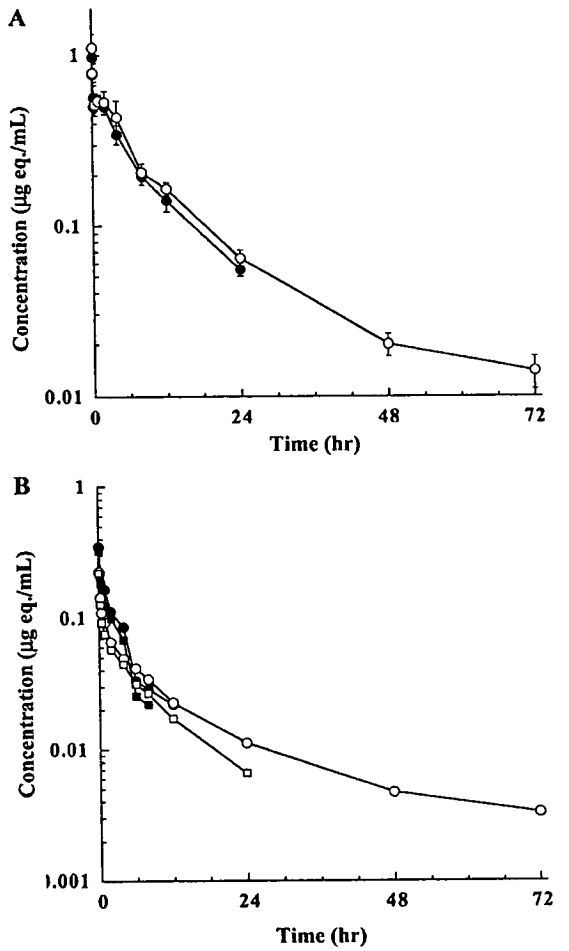

Fig. 2 A Blood (●) and plasma (○) radioactive concentration time-profiles after intravenous administration of [^{3}H]UCN-01 at a dose of 3.5 mg/kg to rats. Each point represents the mean ± SD from four rats. B Individual blood (●, ■) and plasma (○, □) radioactive concentration time-profiles after intravenous administration of [^{3}H]UCN-01 at a dose of 0.5 mg/kg to two dogs

Table 1 Pharmacokinetic parameters of [^{3}H]UCN-01 in blood and plasma after intravenous administration of [^{3}H]UCN-01 at doses of 3.5 mg/kg to rats and 0.5 mg/kg to dogs. For rats each value is the mean ± SD (n = 4); for dogs each blood value is a mean (n = 2), and each plasma value is an individual value

	$t_{1/2}\pi$ (h)	$t_{1/2}\alpha$ (h)	$t_{1/2}\beta$ (h)	$AUC_{0-\infty}$ (μg equivalents · h/ml)	CL_{tot} (l/h/kg)
Rat					
Blood	0.37 ± 0.21	7.17 ± 0.17	–[a]	5.40 ± 0.45	0.652 ± 0.056
Plasma	0.02 ± 0.02	4.08 ± 0.68	21.3 ± 2.3	7.53 ± 0.68	0.468 ± 0.042
Dog					
Blood	0.33	3.29	–[a]	0.804	0.635
Plasma					
No. 1	0.33	4.18	27.2	1.21	0.412
No. 2	0.33	7.20	–[a]	0.71	0.703

[a] Could not be calculated

terminal elimination phase (β phase) was observed in contrast to plasma (Fig. 2A). The plasma radioactivity at 0.05 h (1.10 ± 0.22 μg equivalents/ml) was very similar to the level in blood (Fig. 2A), and disappeared triphasically to 0.014 ± 0.003 μg equivalents/ml at 72 h with a terminal half-life of 21.3 ± 2.3 h (Table 1). The AUC values for blood and plasma were 5.40 and 7.53 μg equivalents · h/ml, respectively. The blood to plasma concentration ratios (Rb) were almost constant, ranging from 0.82 to 1.13, and were independent of the time after injection. Calculated RBC values were 31.6% to 52.9%.

After intravenous administration of [^{3}H]UCN-01 at 0.5 mg/kg to dogs, the blood radioactivity was 0.337 μg equivalents/ml (mean of two dogs) at 0.083 h and disappeared biphasically. At 12 h after dosing, the radioactivity in one dog was 0.022 μg equivalents/ml and that in the other was below the detection limit (Fig. 2B). No terminal elimination phase (β phase) was observed in either dog. The plasma radioactivity in one dog was 0.225 μg equivalents/ml at 0.083 h and disappeared triphasically to 0.0033 μg equivalents/ml at 72 h with a terminal half-life of 27.2 h, which was comparable with that in rats (Table 1). In the other dog, the plasma radioactivity was 0.220 μg equivalents/ml at 0.083 h, and then disappeared biphasically to below the detection limit after 24 h. The distribution of radioactivity into erythrocytes (RBC) in dogs was higher than in rats. That is, Rb values up to 4 h after dosing were 1.51–1.73, and then decreased to 0.81–0.97 at later time-points. RBC values were about 65% up to 4 h. In both rats and dogs, significant levels of volatile radioactivity were found in blood and plasma samples at time-points in the elimination phase (data not shown).

Table 2 Cumulative excretion of nonvolatile radioactivity in urine and feces after an intravenous administration of [^{3}H]UCN-01 to rats (3.5 mg/kg) and to dogs (0.5 mg/kg). Values are percent of dose. For rats each value is the mean ± SD (n = 5), and for dogs each value is the mean (n = 2)

Time period (h)	Rat		Dog	
	Urine	Feces	Urine	Feces
0–4	0.5 ± 0.1	–[a]	–[a]	–[a]
0–8	1.1 ± 0.0	–[a]	0.3[b]	–[a]
0–12	1.5 ± 0.1	2.8 ± 3.3	0.5	–[a]
0–24	1.8 ± 0.2	57.3 ± 14.6	0.6	50.9
0–48	1.9 ± 0.2	91.6 ± 4.8	0.8	67.0
0–72	2.0 ± 0.2	94.9 ± 3.3	0.8	73.1
0–96	2.0 ± 0.3	95.5 ± 3.2	0.9	76.6
0–120	2.0 ± 0.3	95.8 ± 3.2	0.9	77.5
0–144	2.1 ± 0.3	95.9 ± 3.1	0.9	78.1
0–168	2.1 ± 0.3	96.0 ± 3.1	0.9	78.4

[a] Not collected
[b] 0–6 h

Urinary and fecal excretion of radioactivity

The urinary and fecal excretion of radioactivity in rats and dogs after intravenous administration of [^{3}H]UCN-01 are shown in Table 2. In rats, the radioactivity was mainly excreted in feces, that is 57.3 ± 14.6% (mean ± SD, n = 5) of the injected radioactivity was excreted over the initial 24 h, and 96.0 ± 3.1% over 168 h. The urinary excretion was very low, only 2.1% up to 168 h. The radioactivity remaining in the carcass was 1.4%. Total recovery of volatile and nonvolatile radioactivity was 102.2%, comprising 4.0% excreted in the urine, 94.8% excreted in the feces and 3.3% remaining in the carcass. The volatile radioactivity accounted for approximately half the total radioactivity in the urine and carcass, but there was little in the feces.

In dogs, the excreted radioactivity in the urine and feces was 0.6% and 50.9% (mean of two dogs) over the first 24 h after injection and 0.9% and 78.4% over 168 h, respectively. Fecal excretion was also the main route, as in rats. The excretion of total radioactivity (volatile and nonvolatile) in the urine and feces was 1.3% and 77.3%, respectively. The volatile radioactivity was about 0.4% in the urine and there was little in the feces.

Biliary excretion in rats

Table 3 shows the cumulative biliary excretion of radioactivity after intravenous administration of [^{3}H]UCN-01 to rats. The biliary excretion of radioactivity was 49.7 ± 5.1% (mean ± SD, n = 4) over the first 12 h and 67.2 ± 2.9% over 48 h. Urinary and fecal excretion of radioactivity was 4.0 ± 1.3% and 9.1 ± 5.4%, respectively. Total recovery of volatile and nonvolatile radioactivity was 104.3%, comprising 70.5% in the bile, 5.9% excreted in the urine, 9.1% excreted in the feces

Table 3 Cumulative excretion of nonvolatile radioactivity of [^{3}H]UCN-01 in bile, urine and feces after intravenous administration of [^{3}H]UCN-01 at a dose of 3.5 mg/kg to rats following cannulation of the bile duct. Values are percent of dose. Each value is the mean ± SD ($n = 4$)

Time period (h)	Bile	Urine	Feces
0–2	15.0 ± 3.8	–[a]	–[a]
0–4	28.8 ± 4.6	–[a]	–[a]
0–6	36.8 ± 5.1	–[a]	–[a]
0–8	42.5 ± 5.3	–[a]	–[a]
0–12	49.7 ± 5.1	2.0 ± 0.6	–[a]
0–24	61.5 ± 5.6	2.7 ± 0.7	3.5 ± 2.7
0–48	67.2 ± 2.9	4.0 ± 1.3	9.1 ± 5.4

[a] Not collected

and 18.9% remaining in the carcass. The volatile radioactivity in the bile was only 3.3%.

Metabolites in rat plasma, bile and urine

The rat plasma, bile and urine samples obtained from the above studies were analyzed by HPLC to elucidate the metabolism of UCN-01. Figure 3 shows typical chromatograms of a plasma sample at 15 min after dosing (A), a bile sample over the first 6 h (B) and a urine sample over the first 12 h (C). In the plasma, there were three minor unidentified peaks besides UCN-01. The ratio of UCN-01 radioactivity to total radioactivity in the sample was 58.2% at 15 min decreasing to 17.7% at 4 h (data not shown). In bile, there was no radioactivity at the UCN-01 position and several polar metabolites were observed. In urine, there were two peaks: a minor peak due to UCN-01 and a major peak ahead of it.

Tissue distribution in rats

The concentration of radioactivity in tissues after intravenous administration of [^{3}H]UCN-01 to rats is shown in Table 4. All the tissues except brain and testis showed a higher concentration of radioactivity than plasma at 0.5 to 4 h after dosing. Most tissues showed their highest concentration at 0.5 or 1 h, indicating rapid tissue distribution of UCN-01. At 0.5 h after administration, in comparison with the plasma concentration (0.468 μg equivalents/ml), the distribution to endocrinal and reticuloendothelial tissues was relatively high. The highest concentration of radioactivity was observed in the lungs (37.6 μg equivalents/g), followed by the liver (16.2 μg equivalents/g), kidneys (13.5 μg equivalents/g), thyroid gland (12.4 μg equivalents/g), pituitary gland (11.7 μg equivalents/g), adrenal gland (11.5 μg equivalents/g) and pancreas (10.6 μg equivalents/g). At 1 h after administration, the tissue concentrations of radioactivity were comparable with those at 0.5 h with a similar distribution pattern. At 4 h and thereafter, in parallel with the decrease in plasma radioactivity, the radioactivity in most tissues also decreased. At 24 h after

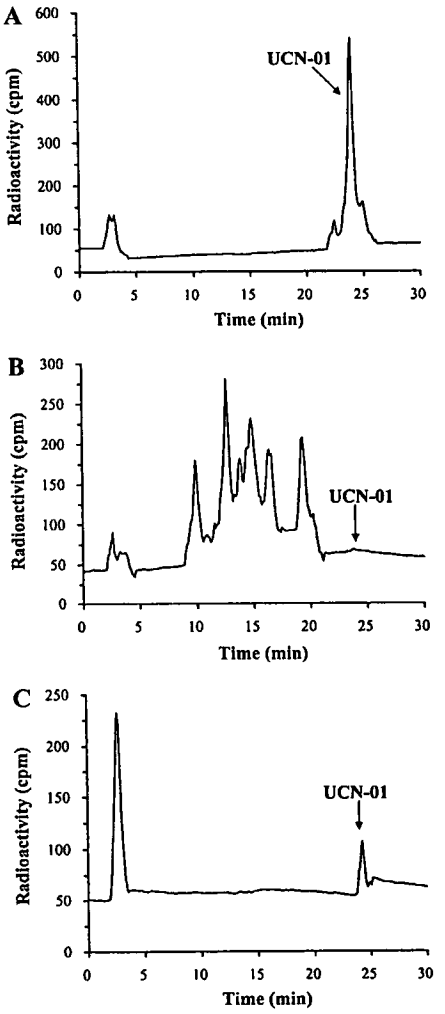

Fig. 3A–C Typical HPLC radiochromatograms of plasma at 15 min (A), bile over the first 6 h (B) and urine over the first 12 h (C). These samples were obtained from rats given 3.5 mg/kg [^{3}H]UCN-01

administration, the plasma concentration had fallen to 0.15 times that at 0.5 h. The ratios of tissue concentrations at 24 h to those at 0.5 h were 0.05 in the lungs, 0.08 in the liver, 0.07 in the kidneys and 0.04 in the thyroid grand. Also, the concentrations in bone marrow, in which UCN-01 exhibits dose-limiting toxicity in rats [13], decreased from 5.62 μg equivalents/g at 0.5 h to 0.590 μg equivalents/g at 24 h. However, the decrease in concentration in several tissues such as Harderian gland, testes, skin and intestinal tract were relatively slow. The slow decrease in the intestinal tract may partially have been due to biliary excretion of [^{3}H]UCN-01.

Discussion

We investigated the metabolic fate of UCN-01 after intravenous administration in rats and dogs using radiolabeled drug. [^{3}H]UCN-01 disappeared triexponentially

Table 4 Tissue distribution of radioactivity after intravenous administration of [^{3}H]UCN-01 at a dose of 3.5 mg/kg to rats. Values are concentrations (μg equivalents per ml or g tissue) of UCN-01 (means ± SD, $n = 3$)

Tissue	0.5 h	1 h	4 h	8 h	24 h
Plasma	0.468 ± 0.066	0.463 ± 0.026	0.355 ± 0.031	0.215 ± 0.034	0.0682 ± 0.0551
Blood	0.577 ± 0.039	0.542 ± 0.011	0.350 ± 0.007	0.195 ± 0.031	0.0600 ± 0.0465
Brain	0.245 ± 0.058	0.344 ± 0.068	0.153 ± 0.005	0.147 ± 0.012	0.0798 ± 0.0278
Pituitary gland	11.7 ± 0.2	11.0 ± 2.3	7.24 ± 2.60	5.48 ± 2.43	1.85 ± 1.07
Eye balls	0.862 ± 0.162	0.881 ± 0.098	0.510 ± 0.101	0.297 ± 0.063	0.119 ± 0.066
Harderian gland	3.51 ± 0.45	4.42 ± 0.27	5.85 ± 0.62	5.53 ± 0.50	3.76 ± 1.11
Submaxillary gland	8.63 ± 0.85	8.66 ± 0.60	6.64 ± 1.13	3.84 ± 0.69	0.661 ± 0.576
Submaxillaric lymph node	4.38 ± 0.38	4.70 ± 0.16	4.47 ± 0.54	3.55 ± 0.60	0.668 ± 0.479
Thyroid gland	12.4 ± 3.5	7.22 ± 0.78	4.29 ± 0.43	2.37 ± 0.70	0.516 ± 0.356
Thymus	3.21 ± 0.25	3.79 ± 0.31	3.80 ± 0.31	2.90 ± 0.56	0.680 ± 0.489
Heart	5.05 ± 0.22	3.94 ± 0.39	2.24 ± 0.14	1.09 ± 0.27	0.278 ± 0.230
Lungs	37.6 ± 2.0	35.2 ± 6.3	19.3 ± 4.1	10.2 ± 2.2	2.05 ± 1.76
Liver	16.2 ± 1.7	16.3 ± 1.1	10.7 ± 0.4	5.13 ± 0.78	1.24 ± 0.76
Kidneys	13.5 ± 1.1	11.2 ± 0.2	7.34 ± 0.89	3.57 ± 0.74	0.992 ± 0.581
Adrenal gland	11.5 ± 0.3	8.45 ± 1.45	5.55 ± 0.73	3.05 ± 0.63	0.815 ± 0.556
Spleen	7.93 ± 0.30	6.84 ± 2.32	6.06 ± 1.07	3.78 ± 0.86	1.00 ± 0.84
Pancreas	10.6 ± 1.2	8.56 ± 0.59	7.24 ± 1.46	4.95 ± 1.06	0.815 ± 0.653
Perirenal fat	1.04 ± 0.08	1.02 ± 0.09	0.776 ± 0.034	0.468 ± 0.068	0.137 ± 0.095
Brown fat	5.27 ± 0.31	4.34 ± 0.46	2.39 ± 0.20	1.65 ± 0.42	0.649 ± 0.554
Mesenteric lymph node	4.92 ± 0.23	4.89 ± 0.28	4.45 ± 0.85	3.16 ± 0.65	0.730 ± 0.477
Muscle	3.37 ± 0.31	2.69 ± 0.23	1.79 ± 0.19	0.935 ± 0.174	0.186 ± 0.145
Skin	1.60 ± 0.08	1.73 ± 0.17	2.16 ± 0.21	1.72 ± 0.25	0.431 ± 0.359
Bone marrow	5.62 ± 0.31	5.90 ± 0.37	4.81 ± 0.30	2.55 ± 0.71	0.590 ± 0.434
Testes	0.326 ± 0.059	0.353 ± 0.111	0.342 ± 0.067	0.293 ± 0.069	0.225 ± 0.036
Seminal vesicle	1.40 ± 0.10	2.01 ± 0.29	1.73 ± 0.30	1.20 ± 0.39	0.385 ± 0.339
Prostate	3.12 ± 0.26	3.73 ± 0.23	2.75 ± 0.09	1.49 ± 0.18	0.380 ± 0.284
Urinary bladder	1.94 ± 0.16	1.72 ± 0.24	1.43 ± 0.18	0.695 ± 0.106	0.212 ± 0.141
Stomach	7.72 ± 1.08	7.01 ± 1.39	3.01 ± 1.20	1.77 ± 0.28	0.937 ± 0.429
Small intestine	6.19 ± 0.84	7.07 ± 0.61	9.70 ± 0.58	5.13 ± 1.06	1.10 ± 1.11
Large intestine	3.18 ± 0.22	3.17 ± 0.42	2.37 ± 0.36	3.99 ± 0.29	2.76 ± 1.76

from plasma, was highly distributed to tissues, extensively metabolized in the liver and finally excreted into the feces via the bile. Since [^{3}H]UCN-01 was used in the present study, the nonvolatile radioactivity was mainly estimated to avoid the effect of the ^3H_2O which is easily produced. The ratios of volatile to total radioactivity were low in plasma and feces. Although this ratio was 50% in urine, the urinary excretion was low. The contribution of ^3H_2O to the total metabolic fate was thought to be minimal.

The elimination half-life of plasma radioactivity in rats and dogs was 21.3 h and 27.2 h, respectively, much longer than previously reported values (4.46 h for rats and 11.6 h for dogs) [11]. Also, the AUC of the radioactivity in rats was seven times higher than that of UCN-01. Since the concentrations of radioactivity during the elimination phase in rats were more than ten times higher than the concentrations of UCN-01 determined by HPLC (about 0.003 μg/ml at 24 h after dosing [11]), the differences in the half-lives could be accounted for by the presence of metabolites in the plasma. Indeed, several metabolites were found in the plasma samples (Fig. 3A).

In both rats and dogs the main route of excretion was fecal. The urinary excretion of UCN-01 was minimal (Fig. 3C). This supports a previous finding that the hepatic clearance of UCN-01 makes a major contribution to its systemic clearance [11]. Studies with bile duct-cannulated rats have shown that most of the excreted [^{3}H]UCN-01 in the feces is via the bile, although a smaller fraction is apparently excreted by direct secretion into the gastrointestinal tract. This was supported by finding a significant level of radioactivity in the stomach (i.e. 7.72 μg equivalents/g at 0.5 h, Table 4) and in the stomach contents (data not shown). The radioactivity in the stomach and its contents was calculated to be approximately 1% of the injected dose. Most of the radioactivity in the bile was due to the metabolites (Fig. 3B). Therefore, the elimination of UCN-01 in rats was expected to be mainly due to metabolism in the liver. It is very important to determine the structures of these metabolites and the metabolic enzyme(s) involved in order to predict drug-drug interactions in clinical situations. Although the structures of these metabolites have not been elucidated, judging from their hydrophilicity in comparison with UCN-01, the metabolism could be catalyzed by cytochrome P450. Further studies are ongoing.

It has been shown that the strong protein binding of UCN-01 is specific to human α_1-acid glycoprotein but not to rat or dog α_1-acid glycoprotein [6, 7]. Considering this species difference, the results of this study cannot be directly extrapolated to predict the metabolic fate of UCN-01 in humans. Recent UCN-01 phase I studies have revealed that the peak plasma concentrations of UCN-01 (C_{max}) after infusion tend to be saturated at

higher dose levels. This nonlinear pharmacokinetics might be due to saturation of the strong binding of UCN-01 to human α_1-acid glycoprotein. At these dose levels, significant levels of "free UCN-01" are observed [14, 19]. If it is assumed that there are no species differences in tissue transfer of "free drug", "free UCN-01" would behave as it did in rats. Therefore, it is expected that "free UCN-01" from α_1-acid glycoprotein in humans may be finally metabolized in the liver and excreted into the bile in humans. Very little excretion of UCN-01 into patients' urine [19] may support this speculation.

Acknowledgements We wish to thank Ms. Yoko Hasegawa-Yoda and Fumiko Oiji-Tamai for their excellent technical assistance.

References

1. Akinaga S, Gomi K, Morimoto M, Tamaoki T, Okabe M (1991) Antitumor activity of UCN-01, a selective inhibitor of protein kinase C, in murine and human tumor models. Cancer Res 51: 4888
2. Akinaga S, Nomura K, Gomi K, Okabe M (1993) Enhancement of antitumor activity of mitomycin C in vitro and in vivo by UCN-01, a selective inhibitor of protein kinase C. Cancer Chemother Pharmacol 32: 183
3. Akinaga S, Nomura K, Gomi K, Okabe M (1993) Synergistic antitumor effect of UCN-01, a protein kinase (C) inhibitor, combined with various anti-cancer agents. Proc Am Assoc Cancer Res 33: 3072
4. Akiyama T, Yoshida T, Tsujita T, Shimizu M, Mizukami T, Okabe M, Akinaga S (1997) G1 phase accumulation induced by UCN-01 is associated with dephosphorylation of Rb and CDK2 proteins as well as induction of CDK inhibitor p21/Cip1/WAF1/Sdi1 in p53-mutated human epidermoid carcinoma A431 cells. Cancer Res 57: 1495
5. Bunch RT, Eastman A (1996) Enhancement of cisplatin-induced cytotoxicity by 7-hydroxystaurosporine (UCN-01), a new G2-checkpoint inhibitor. Clin Cancer Res 2: 791
6. Fuse E, Tanii H, Kurata N, Kobayashi H, Shimada Y, Tamura T, Sasaki Y, Tanigawara Y, Lush RD, Headlee D, Figg WD, Arbuck SG, Senderowicz AM, Sausville EA, Akinaga S, Kuwabara T, Kobayashi S (1998) Unpredicted clinical pharmacology of UCN-01 caused by specific binding to human α_1-acid glycoprotein. Cancer Res 58: 3248
7. Fuse E, Tanii H, Takai K, Asanome K, Kurata N, Kobayashi H, Kuwabara T, Kobayashi S, Sugiyama Y (1999) Altered pharmacokinetics of a novel anticancer drug, UCN-01, caused by specific high affinity binding to α_1-acid glycoprotein in humans. Cancer Res 59: 1054
8. Gibaldi M, Perrier D (1982) Noncompartmental analysis based on statistical moment theory. In: Gibaldi M, Perrier D (eds) Pharmacokinetics. Marcel Dekker, New York, p 409
9. Harkin ST, Cohen GM, Gescher A (1998) Modulation of apoptosis in rat thymocytes by analogs of staurosporine: lack of direct association with inhibition of protein kinase C. Mol Pharmacol 54: 663
10. Kawakami K, Futami H, Takahara J, Yamaguchi K (1996) UCN-01, 7-hydroxyl-staurosporine, inhibits kinase activity of cyclin-dependent kinases and reduces the phosphorylation of the retinoblastoma susceptibility gene product in A549 human lung cancer cell line. Biochem Biophys Res Commun 219: 778
11. Kurata N, Kuwabara T, Tanii H, Fuse E, Akiyama T, Akinaga S, Kobayashi H, Yamaguchi K, Kobayashi S (1999) Pharmacokinetics and pharmacodynamics of a novel protein kinase inhibitor, UCN-01. Cancer Chemother Pharmacol 44: 12
12. Pollack IF, Kawecki S, Lazo JS (1996) Blocking of glioma proliferation in in vitro and in vivo and potentiating the effects of BCNU and cisplatin: UCN-01, a selective protein kinase C inhibitor. J Neurosurg 84: 1024
13. Sausville EA, Lush RD, Headlee D, Smith AC, Figg WD, Arbuck SG, Senderowicz AM, Fuse E, Tanii H, Kuwabara T, Kobayashi S (1998) Clinical pharmacology of UCN-01: initial observations and comparison to preclinical models. Cancer Chemother Pharmacol 42: S54
14. Senderowicz AM, Headlee D, Lush R, Arbuck S, Bauer K, Figg WD, Murgo A, Inoue K, Kobayashi S, Kuwabara T, Sausville EA (1999) Phase I trial of infusional UCN-01, a novel protein kinase inhibitor, in patients with refractory neoplasms. Proc Am Soc Clin Oncol 18: 159a
15. Seynaeve CM, Stetler-Stevenson M, Sebers S, Kaur G, Sausville EA, Worland PJ (1993) Cell cycle arrest and growth inhibition by the protein kinase antagonist UCN-01 in human breast carcinoma cells. Cancer Res 53: 2081
16. Shao RG, Cao CX, Shimizu T, O'Connor PM, Kohn KW, Pommier Y (1997) Abrogation of an S-phase checkpoint and potentiation of camptothecin cytotoxicity by 7-hydroxystaurosporine (UCN-01) in human cancer cell lines, possibly influenced by p53 function. Cancer Res 57: 4029
17. Shao RG, Shimizu T, Pommier Y (1997) 7-Hydroxystaurosporine (UCN-01) induces apoptosis in human colon carcinoma and leukemia cells independently of p53. Exp Cell Res 234: 388
18. Takahashi I, Kobayashi E, Asano K, Yoshida M, Nakano H (1987) UCN-01, a selective inhibitor of protein kinase C from *Streptomyces*. J Antibiot 40: 1782
19. Tamura T, Sasaski Y, Minami H, Fujii K, Ito K, Igarashi T, Kamiya Y, Kurata T, Ohtsu T, Onozawa Y, Yamamoto N, Yamanoto Y, Watanabe Y, Tanigawara Y, Fuse E, Kuwabara T, Kobayashi S, Shimada Y (1999) Phase I study of UCN-01 by 3-hour infusion. Proc Am Soc Clin Oncol 18: 159a
20. Wang Q, Worland PJ, Clark JL, Carlson BA, Sausville EA (1995) Apoptosis in 7-hydroxystaurosporine-treated T lymphoblasts correlates with activation of cyclin-dependent kinases 1 and 2. Cell Growth Differ 6: 927
21. Watari N, Benet LZ (1989) Determination of mean input time, mean residence time, and steady-state volume of distribution with multiple drug inputs. J Pharmacokinet Biopharm 17: 593

Pharmaceutical Research, Vol. 19, No. 12, December 2002 (© 2002)

Research Paper

Human, Rat, and Mouse Metabolism of Resveratrol

Chongwoo Yu,[1,2] Young Geun Shin,[1] Anita Chow,[3] Yongmei Li,[1] Jerome W. Kosmeder,[1] Yong Sup Lee,[4] Wendy H. Hirschelman,[2] John M. Pezzuto,[1,3] Rajendra G. Mehta,[3] and Richard B. van Breemen[1,5]

Received September 3, 2002; accepted September 9, 2002

Purpose. Resveratrol, a phenolic phytoalexin occurring in grapes, wine, peanuts, and cranberries, has been reported to have anticarcinogenic, antioxidative, phytoestrogenic, and cardioprotective activities. Because little is known about the metabolism of this potentially important compound, the *in vitro* and *in vivo* metabolism of *trans*-resveratrol were investigated.

Methods. The *in vitro* experiments included incubation with human liver microsomes, human hepatocytes, and rat hepatocytes and the *in vivo* studies included oral or intraperitoneal administration of resveratrol to rats and mice. Methanol extracts of rat urine, mouse serum, human hepatocytes, rat hepatocytes, and human liver microsomes were analyzed for resveratrol metabolites using reversed-phase high-performance liquid chromatography with on-line ultraviolet-photodiode array detection and mass spectrometric detection (LC-DAD-MS and LC-UV-MS-MS). UV-photodiode array analysis facilitated the identification of *cis*- and *trans*-isomers of resveratrol and its metabolites. Negative ion electrospray mass spectrometric analysis provided molecular weight confirmation of resveratrol metabolites and tandem mass spectrometry allowed structural information to be obtained.

Results. No resveratrol metabolites were detected in the microsomal incubations, and no phase I metabolites, such as oxidations, reductions, or hydrolyzes, were observed in any samples. However, abundant *trans*-resveratrol-3-*O*-glucuronide and *trans*-resveratrol-3-sulfate were identified in rat urine, mouse serum, and incubations with rat and human hepatocytes. Incubation with β-glucuronidase and sulfatase to release free resveratrol was used to confirm the structures of these conjugates. Only trace amounts of *cis*-resveratrol were detected, indicating that isomerization was not an important factor in the metabolism and elimination of resveratrol.

Conclusion. Our results indicate that *trans*-resveratrol-3-*O*-glucuronide and *trans*-resveratrol-3-sulfate are the most abundant metabolites of resveratrol. Virtually no unconjugated resveratrol was detected in urine or serum samples, which might have implications regarding the significance of *in vitro* studies that used only unconjugated resveratrol.

KEY WORDS: *trans*-resveratrol; metabolism; LC-MS-MS; glucuronides; sulfates.

[1] Department of Medicinal Chemistry and Pharmacognosy, University of Illinois at Chicago, 833 South Wood St., Chicago, Illinois 60612.

[2] Department of Chemistry, University of Illinois at Chicago, Chicago, Illinois 60607.

[3] Department of Surgical Oncology, University of Illinois at Chicago, Chicago, Illinois 60612.

[4] Medicinal Chemistry, Research Center, Korea Institute of Science and Technology, Seoul, 130-650, Korea.

[5] To whom correspondence should be addressed. (e-mail address: Breemen@uic.edu)

INTRODUCTION

Cancer chemoprevention may be regarded as the ingestion of nontoxic quantities of dietary or pharmaceutical agents that are capable of preventing, inhibiting or reversing the process of carcinogenesis (1,2). One dietary compound under investigation as a chemoprevention agent is *trans*-resveratrol (*trans*-3,5,4'-trihydroxystilbene) (Fig. 1) (3,4), which is a naturally occurring phytoalexin produced by plants in response to fungal infection or abiotic stresses, such as heavy metal ions or ultraviolet light (UV) (5). Resveratrol has attracted considerable attention because of its presence in dietary sources, such as grapes, wine, peanuts, and cranberries (6). In addition to cancer chemoprevention (3,4), other properties of resveratrol include antioxidative (7–9), antiplatelet (10–12), antifungal (13), phytoestrogenic (14,15), and cardioprotective activities (10,16,17).

The efficacy of orally administrated resveratrol will depend on its absorption, metabolism, and tissue distribution. Although many studies have implicated a role of resveratrol in disease prevention, only a few studies have addressed the bioavailability and metabolism of resveratrol (18–23). However, none of these has provided a conclusive metabolic profile for resveratrol including its metabolite structures.

Human liver-derived experimental systems have been used extensively for the evaluation of drug metabolism, including the use of intact cell systems, such as hepatocytes, and cell-free systems, such as microsomes, or recombinant enzymes, like specific cytochrome P-450 isozymes. Intact hepatocytes with full complements of enzymes and cofactors at physiologic levels and natural orientations should be more representative of the liver than cell-free systems with disrupted membranes, incomplete cofactors, and enzymes (24). *In vivo* studies provide an overall indication of drug metabolism resulting from all organ systems. In the present study, cryopreserved human and rat hepatocytes were compared with human liver microsomes in the evaluation of resveratrol metabolism (24,25). In addition, resveratrol metabolites were identified in rat urine and mouse serum. All metabolites were characterized using high-performance liquid chromatography (HPLC) with diode array detector (DAD) UV detection, connected on-line with electrospray mass spectrometry or tandem mass spectrometry (LC-DAD-MS and LC-UV-MS-MS).

MATERIALS AND METHODS

Materials

trans-Resveratrol, NADPH, β-glucuronidase (type B-10 from boving liver), and sulfatase (type IV: from *Aerobacter aerogenes*, partially purified) were purchased from Sigma Chemical (St. Louis, MO, USA). Formic acid (88%) was obtained from J. T. Baker (Phillipsburg, NJ, USA) and was diluted to the desired concentration using deionized distilled water. HPLC-grade methanol, water, dimethyl sulfoxide (DMSO), and acetonitrile were purchased from Fisher (Fair Lawn, NJ, USA). Naringenin was purchased from Indofine Chemical (Somerville, NJ, USA). Human liver microsomes, cryopreserved human and rat hepatocytes, Krebs-Henseleit

0724-8741/02/1200-1907/0 © 2002 Plenum Publishing Corporation

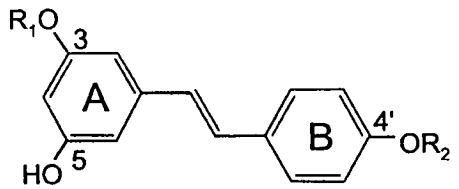

(a) R_1 = H, R_2 = H
(b) R_1 = glucuronic acid, R_2 = H
(c) R_1 = H, R_2 = glucuronic acid
(d) R_1 = SO_3H, R_2 = H
(e) R_1 = H, R_2 = SO_3H

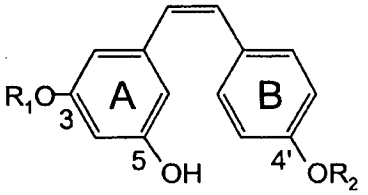

(f) R_1 = H, R_2 = H
(g) R_1 = glucuronic acid, R_2 = H

Fig. 1. Structures of resveratrol and resveratrol conjugates. (a) *trans*-resveratrol; (b) *trans*-resveratrol-3-*O*-glucuronide; (c) *trans*-resveratrol-4'-*O*-glucuronide; (d) *trans*-resveratrol-3-sulfate; (e) *trans*-resveratrol-4'-sulfate; (f) *cis*-resveratrol; and (g) *cis*-resveratrol-3-*O*-glucuronide.

buffer, and minimum essential media (MEM) were obtained from In Vitro Technologies (Baltimore, MD, USA).

To convert *trans*-resveratrol into *cis*-resveratrol, 0.7 mL of a 0.01 mg/mL *trans*-resveratrol solution in methanol was exposed to UV light (λ = 254 nm) for 10 min.

Methods

Incubation of Resveratrol in Human Liver Microsomes

Human liver microsomes (1 mg protein/mL) were incubated in 50 mM phosphate buffer (pH 7.4) with 5 mM resveratrol in the presence of 1 mM NADPH for 0, 15, 30, and 60 min. After incubation, two volumes of acetonitrile were added to the reaction mixture, vortexed for 30 s, and then centrifuged for 3 min at 10,000 g. The supernatant was collected and evaporated to dryness, and the residue was redissolved in 200 μL of methanol for analysis.

Incubation of Resveratrol with Hepatocytes

A cryopreserved sample of human hepatocytes was immersed in a 37°C water bath and shaken gently for 80–90 s The cell suspension was transferred to a 50-mL centrifuge tube that had been precooled in ice. Minimum essential medium (12 mL) was added to the cell suspension at the rate of 1 mL per 15 s. After each addition of 1 mL of medium, the tube was shaken gently to prevent the cells from settling. Next, the tube was centrifuged at 50 g at 4°C for 5 min. The supernatant was removed by aspiration, and the cell pellet was resuspended in 5 mL of Krebs-Henseleit buffer to provide a cell density of approximately 1×10^6 viable hepatocytes/mL. A 1-mL aliquot of the human hepatocytes suspension was transferred to a well of a 12-well plate, and 0.1 mL of 0.1 mM *trans*-resveratrol in 10% DMSO was added. The 12-well plate was incubated at 37°C for 4 h. During the incubation, 0.35-mL aliquots of the cell suspension (one aliquot per well) containing *trans*-resveratrol metabolites were removed at 1, 2, and 4 h and transferred to Eppendorf tubes. After the addition of 0.35 mL of cold methanol for deactivation, each tube was vortex-mixed for 30 s A control experiment was performed using the same procedures except that the hepatocytes were deactivated by the addition of cold methanol before incubation with resveratrol. After centrifuging at 10,000 g for 3 min, the supernatant was transferred to another 1.5-mL Eppendorf tube and evaporated to dryness *in vacuo*. The residue was redissolved in 0.2 mL of methanol and centrifuged at 10,000 g for 3 min. The supernatant was collected and mixed with 0.4 mL of water. Rat hepatocyte samples were prepared in the same manner as the human hepatocyte samples.

Preparation of Rat Urine Samples

Resveratrol (20 mg/kg, dissolved in 6.5% ethanol in neobee oil) was administered intraperitoneally (IP) to three Sprague–Dawley female rats (75 days old, average weight = 228 g), and urine was collected in metabolic cages for 2 h. Also, control urine samples from two rats receiving no resveratrol were obtained. A 100-μL aliquot of each urine sample was mixed with 250 μL of acetonitrile and centrifuged at 10,000 g for 3 min at 4°C. The supernatant was collected for analysis. The research using rats and mouse adhered to the "Principles of Laboratory Animal Care" (NIH publication #85-23, revised in 1985).

Preparation of Mouse Serum Samples

Resveratrol was dissolved in a minimum volume of ethanol and then mixed with corn oil as a vehicle for drug delivery. The final concentration of ethanol in the corn oil was 5.4%. In one experiment, resveratrol at 20 mg/kg was administrated via IP injection to 12 Balb/c female mice (4 weeks old, average body weight 19.5 g). In another experiment, resveratrol at 20 mg/kg was administered via gavage to 12 Balb/c female mice (4 weeks old, average weight 19.3 g). Control mice that did not receive resveratrol were used for both the IP injection and gavage experiments.

Blood samples (100–400 μL) were obtained by heart puncture at 0.25, 0.5, 1, 2, 4, and 6 h, after treatment with resveratrol. After clotting, the blood samples were centrifuged at 100 g for 20 min, and serum was collected from each sample and stored at −70°C until analysis. A 25-μL aliquot of each mouse serum sample was mixed with 75 μL of acetonitrile and centrifuged at 10,000 g at 4°C for 3 min. Supernatants were collected for analysis.

The third experiment was conducted using gavage and the same procedures except for the following modifications. The dose of resveratrol was increased from 20 mg/kg to 60 mg/kg. Also, blood samples were obtained at 0.25, 0.5, 1, 2, and 3 h after administration of resveratrol.

Enzymatic Hydrolysis of Resveratrol Glucuronide and Resveratrol Sulfate

To confirm the presence of sulfate and glucuronide conjugates of resveratrol, enzymatic cleavage was performed ac-

cording to the method of Kuhnle *et al.* (20) and Sfakianos *et al.* (26) with the following modifications. For resveratrol sulfate, aliquots of the extracts were evaporated to dryness and reconstituted in 150 μL of 50 mM phosphate buffer (pH 7.4) containing 0.5 U (30 μL) of aryl sulfatase. After incubating at 37°C for 2.5 and 18.5 h, respectively, 100 μL of cold methanol was added into each sample vial to stop the reaction. For resveratrol glucuronide, aliquots of extracts were incubated with β-glucuronidase (final concentration = 8,000 U/mL) in 50 mM phosphate buffer (pH 5.5, 150 μL) for 1 h. The reaction was terminated by adding 150 μL of cold methanol. After centrifugation at 10,000 g for 3 min at 4°C, supernatants were collected, evaporated to dryness *in vacuo*, and reconstituted in 50 μL of 50% methanol. Control incubations were performed without addition of enzyme. All sample preparations were performed in dim light to minimize photochemical isomerization of *trans*-resveratrol to the *cis*-form.

Synthesis of Resveratrol Monosulfate Isomers

To determine the attachment site of sulfate in resveratrol sulfate, resveratrol monosulfate isomers were synthesized. Resveratrol sulfate was formed by standard reaction conditions with one equivalent of sulfur trioxide-pyridine complex in dry pyridine (27). The yield of monosulfates was approximately 30%, and the remainder was unreacted resveratrol. The ratio of 3- and 4'-monosulfates was determined to be 7:3, and the mixture was separated by preparative HPLC. Structures of the isomers were confirmed by nuclear magnetic resonance measurements. Spectra were recorded on a Bruker (Billerica, MA) 300 MHz instrument, and the following data were obtained.

Resveratrol-3-sulfate: Amorphous white solid, ^{1}H-NMR (CD_3OD) d 7.38 (d, J = 8.6 Hz, H-2',6'), 7.05 (d, J = 16.5 Hz, *trans*-vinyl), 6.99 (dd, J = 2.2 Hz, H-2), 6.87 (d, J = 16.5 Hz, *trans*-vinyl), 6.78 (d, J = 8.6 Hz, H-3',5'), 6.75 (dd, J = 2.1 Hz, H-6), 6.67 (dd, J = 2.1 Hz, H-4), HPLC retention time 13.1 min.

Resveratrol-4'-sulfate: Amorphous white solid, ^{1}H-NMR (CD_3OD) d 7.51 (d, J = 8.7 Hz, H-2',6'), 7.30 (d, J = 8.6 Hz, H-3',5'), 7.05 (d, J = 16.3 Hz, *trans*-vinyl), 6.87 (d, J = 16.5 Hz, *trans*-vinyl), 6.50 (d, J = 2.1 Hz, H-2,6), 6.20 (dd, J = 2.1 Hz, H-4), HPLC retention time 11.6 min.

Liquid Chromatography-Mass Spectrometry (LC-MS)

LC-DAD-MS analyses were performed using an Agilent (Palo Alto, CA, USA) 1100 HPLC system equipped with a photodiode array detector and interfaced to a model G1946A single quadruple electrospray mass spectrometer. UV spectra were recorded from 200–360 nm. A Micromass (Manchester, UK) Quattro II triple quadruple mass spectrometer equipped with a Waters (Milford, MA, USA) 2690 HPLC system and 2487 UV detector was used for LC-UV-MS-MS. UV chromatograms were recorded at 210 and 300 nm. HPLC separations were obtained at 25°C using a Waters XTerra MS C_{18} column (2.1 mm × 100 mm, 3.5-μm particle size).

Aliquots (10 μL) of urine or serum extracts were injected directly onto the HPLC column and eluted with a solvent system consisting of 0.1% (v/v) formic acid and acetonitrile. A 60-min linear gradient was used from 10–30% acetonitrile, and for some mouse serum samples a 30-min linear gradient was used from 10–80% acetonitrile. There was a 10-min re-equilibration period with the initial solvent mixture between analyses. The flow rate was 0.2 mL/min.

Negative ion electrospray mass spectra were obtained using the Agilent mass spectrometer with the electrospray capillary set at 4 kV. The flow rate of the nitrogen drying gas was 6.0 L/min at a temperature of 300°C. Mass spectra were recorded over the range of *m/z* 70–800. Alternatively, selected ion monitoring was used for greater sensitivity by recording signals for ions of *m/z* 227, 307, and 403 with a dwell time of 592 ms/ion. Negative ion electrospray tandem mass spectra were recorded using the Micromass triple quadruple instrument with the electrospray capillary set at 2.5 kV and a source block temperature of 100°C. Nitrogen was used as the drying and nebulizing gas at flow rates of approximately 8 L/min and 0.8 L/min, respectively. Argon at a pressure of 1.4 × 10^{-3} mbar was used as the collision gas for collision-induced dissociation (CID). UV spectra were monitored at 300 nm. Product ion scans were carried out using the deprotonated molecules of resveratrol and its metabolites as precursor ions. When greater sensitivity was required, multiple reaction monitoring was used as described in the Results and Discussion section.

For the quantitative analysis of *trans*-resveratrol, *trans*-resveratrol-3-sulfate, and *trans*-resveratrol-3-glucuronide, calibration curves were constructed by plotting the LC-MS-MS peak area ratio of *trans*-resveratrol or *trans*-resveratrol-3-sulfate to the internal standard naringenin (at 0.8 μM) against the analyte concentration. Note that no impurities and no *cis*-resveratrol were detected in the *trans*-resveratrol standard, which was used for all studies. The linear regression analyses of these standard curves showed a correlation coefficient of r^2 = 0.999. Because no resveratrol glucuronide standards were available, the concentration of *trans*-resveratrol-3-glucuronide was estimated using the *trans*-resveratrol standard curve.

RESULTS AND DISCUSSION

Human Microsomes and Hepatocytes

After incubation of *trans*-resveratrol with human liver microsomes, intact resveratrol but no metabolites were detected using LC-DAD-MS. However, resveratrol incubated with human hepatocytes for 4 h showed several new peaks with abundant deprotonated molecules of *m/z* 403 and 307. Therefore, LC-UV-MS-MS with product ion scanning (Fig. 2) and multiple reaction monitoring (Fig. 3) were performed for greater sensitivity and selectivity to confirm these peaks as metabolites of resveratrol. *trans*-Resveratrol was detected at a retention time of 30.8 min, and the corresponding product ion CID mass spectrum is shown in Fig. 2A.

Resveratrol sulfate has been reported in studies with perfused rat intestine and human liver (19,21,22). In our studies, resveratrol sulfate was detected in incubations with some human hepatocytes, as well as with rat hepatocytes and in mouse serum. For example, in the LC-UV-MS-MS analysis of a mouse serum extract (Fig. 2B), the ion of *m/z* 307 fragmented to form a product ion of *m/z* 227 that corresponded to resveratrol itself after the loss of sulfate. Furthermore, only one resveratrol monosulfate and no disulfate metabolites were

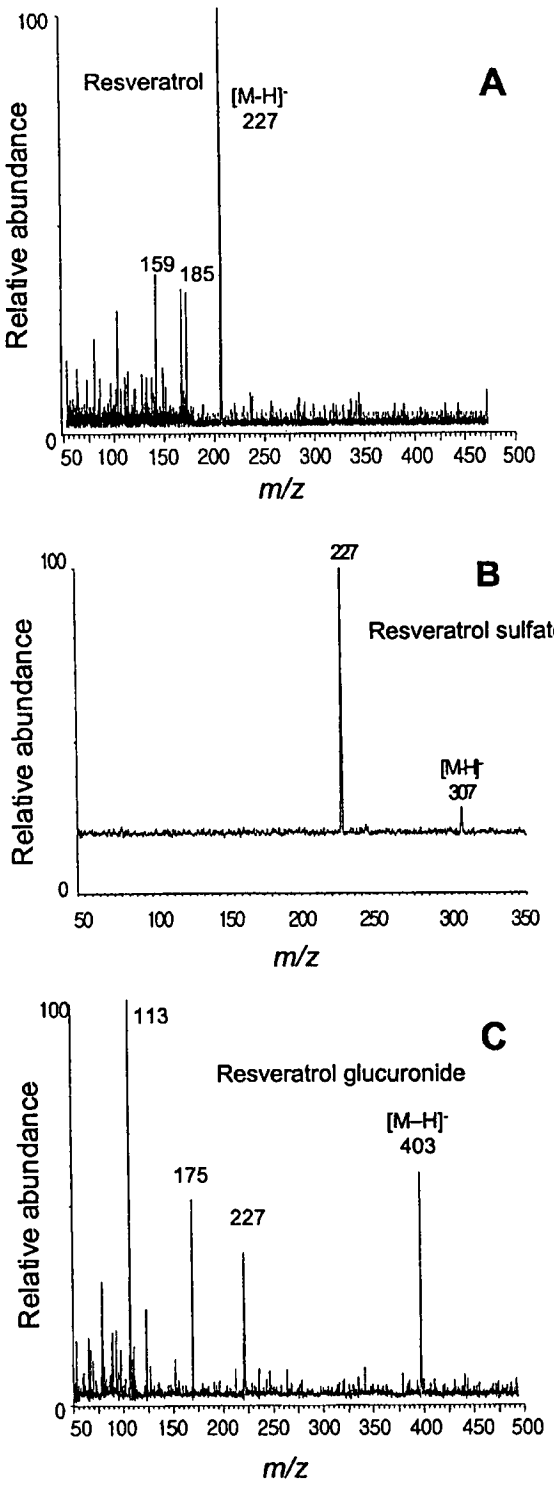

Fig. 2. LC-UV-MS-MS product ion mass spectra obtained using negative ion electrospray and CID during the analysis of resveratrol metabolites. (A) Resveratrol eluting at 30.8 min (extract of human hepatocyte incubation); (B) Resveratrol sulfate at 28.0 min retention time (mouse serum extract); (C) Resveratrol glucuronide at 18.1 min (human hepatocyte incubation)

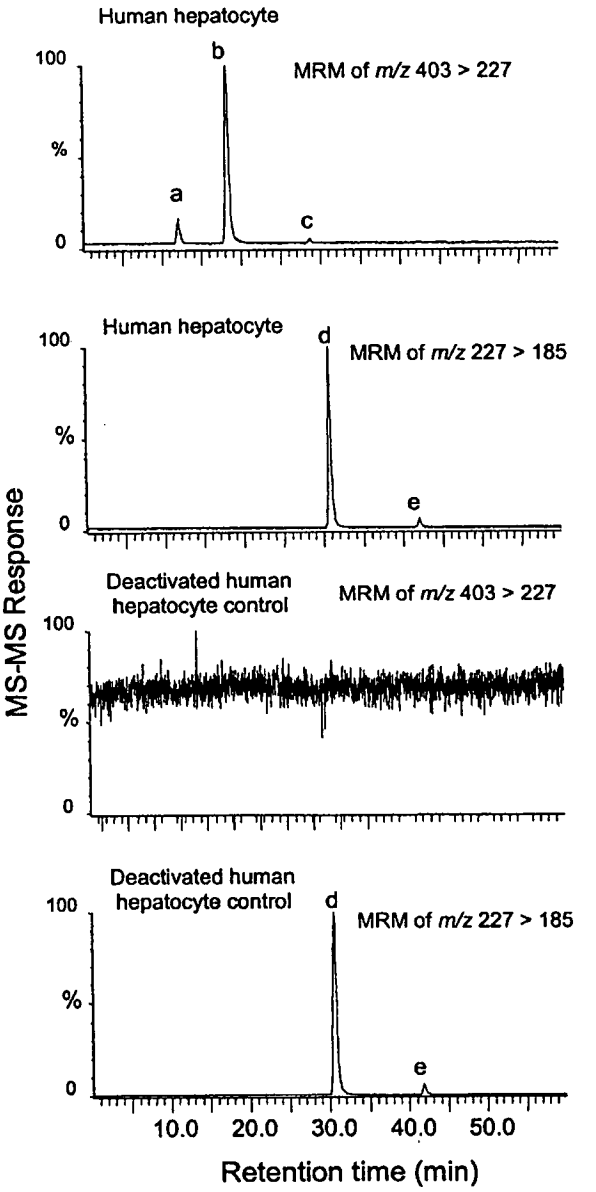

Fig. 3. Negative ion electrospray multiple reaction monitoring LC-UV-MS-MS analysis of resveratrol incubated for 4 h with human hepatocytes or deactivated human hepatocytes (control). Peaks were assigned to the following compounds. (a) *trans*-resveratrol-4'-*O*-glucuronide; (b) *trans*-resveratrol-3-*O*-glucuronide; (c) *cis*-resveratrol-3-*O*-glucuronide; (d) *trans*-resveratrol; (e) *cis*-resveratrol.

detected. This resveratrol sulfate isomer was synthesized and confirmed to be *trans*-resveratrol-3-sulfate.

LC-UV-MS-MS with multiple reaction monitoring of the transition of *m/z* 403 → 227 was performed and showed three resveratrol glucuronide peaks eluting at 12.1, 18.1, and 28.6 min (Fig. 3). LC-UV-MS-MS with MRM of an identical control containing deactivated human hepatocytes showed no signals for resveratrol glucuronide. Instead, only *trans*-resveratrol and a trace of the *cis*-isomer were detected at 30.8 and 42.0 min (Fig. 3), respectively. The ion of *m/z* 403 (Fig.

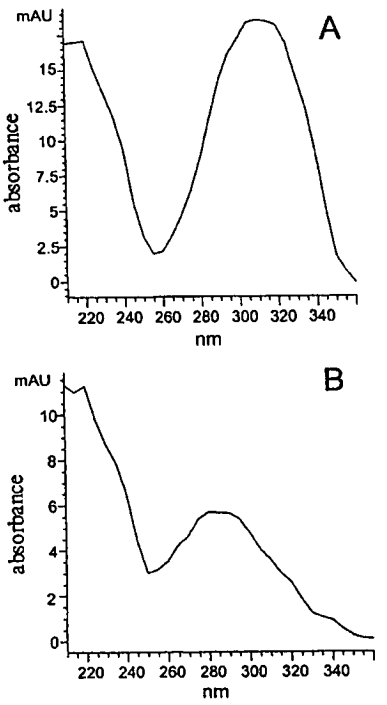

Fig. 4. UV spectra obtained during LC-DAD-MS of human hepatocytes for (A) *trans*-resveratrol conjugates, and (B) *cis*-resveratrol conjugates.

2C), which was detected at 18.1 min fragmented to form product ions of *m/z* 227 and *m/z* 175 that corresponded to resveratrol itself after the loss of glucuronic acid and dehydrated glucuronic acid, respectively. Also, a product ion of *m/z* 113 was observed, which can be considered characteristic of the presence of a glucuronic acid moiety. The ion of *m/z* 113 was formed by further dissociation of the fragment ion of *m/z* 175 and is common in the negative ion mass spectra of glucuronide metabolites (28,29). Therefore, the peak at 18.1 min was identified as resveratrol monoglucuronide. No peaks corresponding to a diglucuronide (mw = 580) were detected. For comparison, the negative ion MS-MS product ion spectrum of resveratrol (retention time 30.8 min) is shown in Fig. 2A. Note the absence of glucuronic acid ions of *m/z* 175 or 113 in the resveratrol tandem mass spectrum.

The use of a DAD in the LC-DAD-MS analysis allowed the confirmation of the identity of each chromatographic peak not only by its retention time but also by its spectrum. The UV/DAD spectra pattern obtained for *trans*-resveratrol and *cis*-resveratrol conjugates (Fig. 4) were consistent with those obtained for *trans*-resveratrol and *cis*-resveratrol standards that have been reported in other studies (30,31). It should be noted that *trans*-resveratrol produced the same UV/DAD spectrum whether conjugated at the 3- or 4'-position. Therefore, only one UV/DAD spectrum for these two glucuronides of *trans*-resveratrol is shown in Fig. 4. These spectra indicate that the conformations of the three resveratrol glucuronides detected at 12.1, 18.1, and 28.6 min in Fig. 3 are *trans*-, *trans*-, and *cis*-, respectively.

Because synthetic resveratrol-3-sulfate was retained longer than resveratrol-4'-sulfate during reversed-phase HPLC (13.1 and 11.6 min, respectively), it is probable that resveratrol-3-*O*-glucuronic acid will be retained longer than resveratrol-4'-*O*-glucuronide. The longer retention times of the conjugates at the C-3 position of the A ring are probably the result hydrogen bonding of the sulfate or glucuronic acid to the –OH group at C-5 of the A ring making the conjugate less polar than the corresponding conjugates at the C-4' position. When the sulfate group or glucuronic acid is attached at the C-4' of ring B, the two unconjugated phenolic OH groups on the A ring are fully exposed rendering the molecule more polar. As a result, resveratrol-4'-sulfate elutes earlier than resveratrol-3-sulfate. By analogy, *trans*-resveratrol-4'-*O*-glucuronide is probably the earlier eluting glucuronide peak at 12.1 min, and the glucuronide at 18.1 min is assigned as *trans*-resveratrol-3-*O*-glucuronide. The resveratrol glucuronide eluting at 28.6 min is assigned as *cis*-resveratrol-3-*O*-glucuronide by comparison of the retention times of *trans*-resveratrol, *cis*-resveratrol, and *trans*-resveratrol-3-*O*-glucuronide, respectively, and also considering steric effects. The structures of all of these compounds are shown in Fig. 1.

Because the amount of resveratrol sulfate was minor compared with the formation of the glucuronide in the incubations with human hepatocytes, resveratrol sulfate seems to be a minor human hepatic metabolite.

Table I. Summary of Resveratrol Metabolites Detected Using LC-UV-MS-MS

Experiments	Detected metabolites	Retention time
Human microsome control	None	—
Human microsome 1 h	None	—
Human hepatocytes control	None	—
Human hepatocytes 4 h	*trans*-resveratrol-4'-*O*-glucuronide	12.1 min
	trans-resveratrol-3-*O*-glucuronide	18.1 min
	cis-resveratrol-3-*O*-glucuronide	28.6 min
Rat urine control	None	—
Rat urine 2 h	*trans*-resveratrol-3-*O*-glucuronide	18.0 min
Rat hepatocytes control	None	—
Rat hepatocytes 4 h	*trans*-resveratrol-3-*O*-glucuronide	18.4 min
	trans-resveratrol-3-sulfate	32.9 min
Mouse serum control	None	—
Mouse serum gavage 15 min	*trans*-resveratrol-3-*O*-glucuronide	17.2 min
	trans-resveratrol-3-sulfate	30.1 min

Rat Urine and Hepatocytes

During LC-UV-MS-MS MRM analysis of rat urine samples, the transition *m/z* 403 → 227 was monitored for resveratrol glucuronide, *m/z* 307 → 227 for resveratrol sulfate, and *m/z* 227 → 185 for resveratrol. However, only one peak was detected at 18.0 min (data not shown) for the transition *m/z* 403 → 227. This metabolite was identified as *trans*-resveratrol-3-*O*-glucuronide and showed the same retention time as in the analysis of resveratrol metabolites from human hepatocytes. Analysis of rat hepatocytes was also performed using LC-UV-MS-MS with MRM. In this case, two major peaks were detected at 18.4 and 32.9 min (data not shown). Based on the mass chromatogram and by comparing the retention times, we have assigned these peaks as *trans*-resveratrol-3-*O*-glucuronide, and *trans*-resveratrol-3-sulfate, respectively. Resveratrol sulfate was the more abundant metabolite in rat hepatocytes. All of the resveratrol metabolites detected in these experiments are summarized in Table I.

Mouse Serum

Resveratrol was administered to mice at two different doses using IP injection or gavage, and serial blood samples were obtained various time points up to 4 h. Resveratrol glucuronide and resveratrol sulfate were detected as the only resveratrol metabolites in the mouse serum samples, and both of these metabolites were detected after IP or intragastric (IG) administration. The time courses for the appearance of resveratrol sulfate and resveratrol glucuronide in mouse serum following both routes of administration are shown in Fig. 5.

After the administration of 20 mg/kg, the maximum concentrations of both metabolites were observed in the serum samples obtained at the first time point of 15 min (Fig. 5A). In these samples, the concentration of resveratrol sulfate (13 μM) in the mouse serum was almost 3-fold greater than that of resveratrol glucuronide (5 μM). Only traces of unconjugated resveratrol were observed. Furthermore, no resveratrol or its metabolites were detected after 1 h (Fig. 5A).

To confirm the peak assigned to resveratrol sulfate and resveratrol glucuronide, aliquots of mouse serum samples were incubated with sulfatase and β-glucuronidase, respectively and then re-analyzed using LC-UV-MS-MS. As a result, the resveratrol sulfate peak disappeared whereas a resveratrol peak appeared in the sulfatase incubation (Fig. 6), and the resveratrol glucuronide peak disappeared whereas a resveratrol peak appeared in the β-glucuronidase incubation. The resveratrol peak intensity increased as the incubation time increased in both cases. Finally, these observations were confirmed using LC-DAD-MS with a UV photodiode array detector and mass spectrometric scanning in the range *m/z* 70–800. All of the UV/DAD spectra obtained were consistent with the data obtained in the studies of rat urine, rat hepatocytes, and human hepatocytes samples (Fig. 4). Furthermore, the mass spectra of these peaks were consistent with those observed in the other experiments. Resveratrol sulfate was not affected by the β-glucuronidase incubation and resveratrol glucuronide was not affected by sulfatase incubation and they were still observed eluting at approximately 30 and 17 min, respectively. Therefore, our data confirm the presence of resveratrol sulfate and resveratrol glucuronide in the mouse serum samples. Although the attachment site of glucuronide in resveratrol glucuronide is under investigation, it is reasonable to speculate that the conformations of major resveratrol metabolites in mouse serum are *trans*-resveratrol-3-sulfate and *trans*-resveratrol-3-*O*-glucuronide.

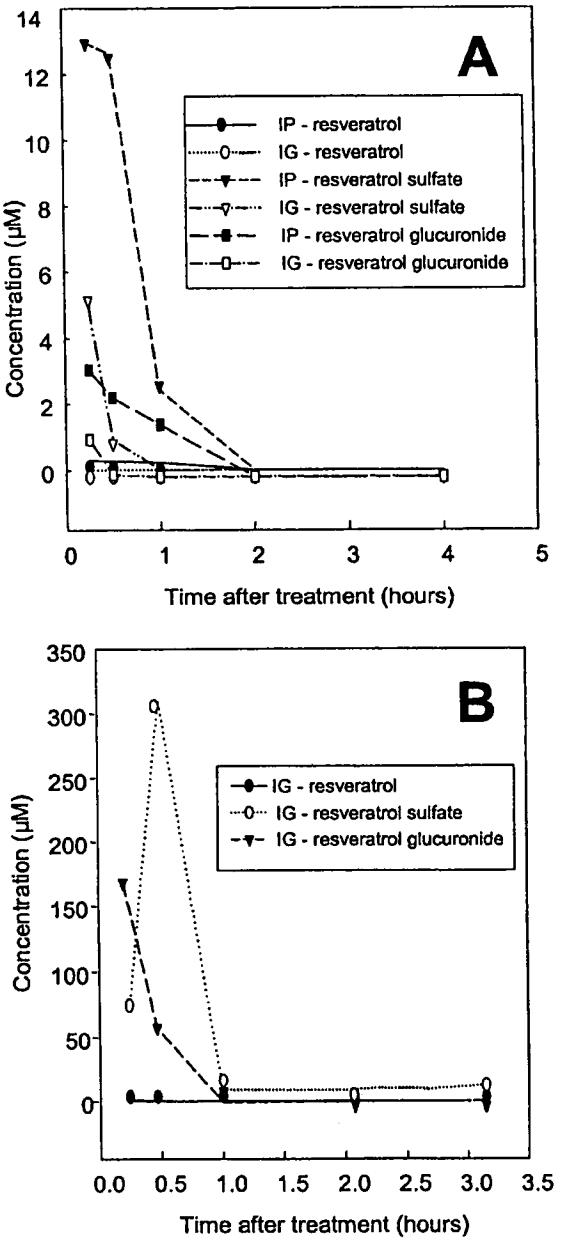

Fig. 5. Resveratrol metabolites in mouse serum following doses of (A) 20 mg/kg via IP injection or gavage (IG), and (B) 60 mg/kg via gavage (IG). Each data point represents the analysis of pooled blood samples from five control or five treated mice. Because no resveratrol or resveratrol conjugates were detected in the control serum, these data are not plotted.

In the second set of experiments, 60 mg/kg of resveratrol was given only via gavage because oral administration would be more relevant to future clinical investigations, and serum was collected serially up to 3 h. LC-DAD-MS and LC-UV-

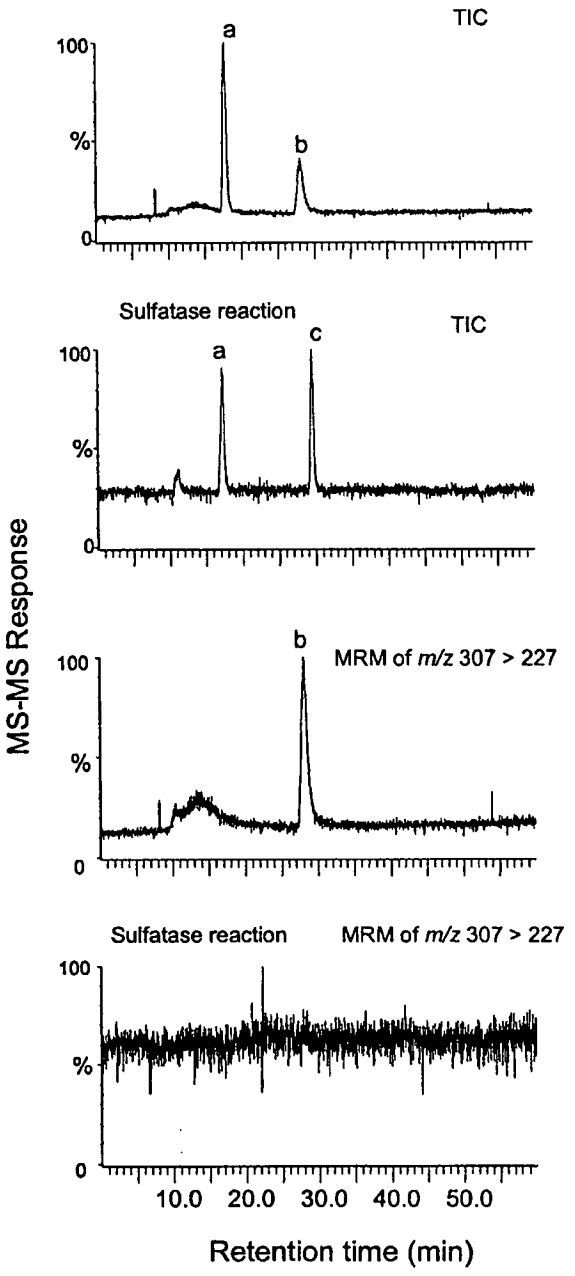

Fig. 6. LC-UV-MS-MS analysis of mouse serum collected after 15 min of administrating resveratrol via gavage and the same mouse serum sample incubated with sulfatase for 18.5 h. Peaks were assigned to the following compounds. (a) *trans*-resveratrol-3-*O*-glucuronide; (b) *trans*-resveratrol-3-sulfate; (c) *trans*-resveratrol.

MS-MS analysis were performed using the same conditions as described above. The same resveratrol sulfate and resveratrol glucuronide metabolites were detected in these analyses as were observed in the analyses of serum samples following administration of the lower dose of resveratrol. The resveratrol sulfate concentration reached a maximum value in mouse serum after 30 min instead of 15 min as observed for the lower dosage, probably because more time was required to absorb the large volume that was administered. Note that serum resveratrol disappeared after 30 min but that resveratrol sulfate and resveratrol glucuronide were still detectable 3 h after the highest dosage (Fig. 5B). The prolonged detection of low levels of resveratrol sulfate and resveratrol glucuronide in serum following the highest dose suggests that resveratrol was distributed to various tissues and was being cleared slowly. Perhaps only the highest dosage produced tissue levels that were high enough for subsequent detection of the cleared metabolites.

CONCLUSION

Although many studies have implicated a role for resveratrol in disease prevention, information on *in vivo* bioavailability and metabolism is incomplete and the structures of the resveratrol metabolites were uncertain. Our LC-DAD-MS and LC-UV-MS-MS data for the human, rat, and mouse experiments indicate that *trans*-resveratrol-3-*O*-glucuronide is the primary metabolite of resveratrol in human liver, and that *trans*-resveratrol-3-*O*-glucuronide and *trans*-resveratrol-3-sulfate are both significant metabolites in rat urine, mouse serum, and formed by rat hepatocytes. It is important to note that no phase I metabolites of resveratrol such as oxidations, reductions or hydrolyzes were detected in any of these systems. Furthermore, conjugated resveratrol and not its free form were found to predominate in the circulation. These data suggest that the potential biologic activity of resveratrol conjugates should be considered in future investigations. Furthermore, the form of resveratrol in cells and tissues after oral or IP administration should be investigated to determine the levels of conjugated and unconjugated resveratrol at these potential points of action.

ACKNOWLEDGMENT

These studies were funded by grants R24 CA83124 and P01 CA48112 awarded by the National Cancer Institute.

REFERENCES

1. M. B. Sporn, N. M. Dunlop, D. L. Newton, and J. M. Smith. Prevention of chemical carcinogenesis by vitamin A and its synthetic analogs (retinoids). *Fed. Proc.* **35**:1332–1338 (1976).
2. W. K. Hong and M. B. Sporn. Recent advances in chemoprevention of cancer. *Science* **278**:1073–1074 (1997).
3. M. Jang, L. Cai, G. O. Udeani, K. V. Slowing, C. F. Thomas, C. W. W. Beecher, H. H. S. Fong, N. R. Farnsworth, A. D. Kinghorn, R. G. Mehta, R. C. Moon, and J. M. Pezzuto. Cancer chemopreventive activity of resveratrol, a natural product derived from grapes. *Science* **275**:218–220 (1997).
4. M. Jang and J. M. Pezzuto. Cancer chemopreventive activity of resveratrol. *Drugs Exp. Clin. Res* **25**:65–77 (1999).
5. J. A. Bailey. Mechanism of phytoalexin accumulation. In *Phytoalexins*, eds. J. A. Baily and J. W. Manfield, pp. 289–318, Wiley, New York, 1982.
6. Y. Wang, F. Catana, Y. Yang, R. Roderick, and R. B. van Breemen. Analysis of resveratrol in grape products, cranberry juice and wine using liquid chromatography-mass spectrometry. *J. Agric. Food Chem.* **50**:431–435 (2002).
7. E. N. Frankel, A. L. Waterhouse, and J. E. Kinsella. Inhibition of human LDL oxidation by resveratrol. *Lancet* **341**:1103–1104 (1993).
8. N. J. Miller and C. A. Rice-Evans. Antioxidant activity of resveratrol in red wine—to the editor. *Clin. Chem.* **41**:1789 (1995).
9. B. Fuhrman, A. Lavy, and M. Aviram. Consumption of red wine with meals reduces the susceptibility of human plasma and low-density-lipoprotein to lipid-peroxidation. *Am. J. Clin. Nutr.* **42**: 549–554 (1995).

10. A. A. E. Bertelli, L. Giovannini, D. Giannesi, M. Migliori, W. Bernini, M. Fregoni, and A. Bertelli. Antiplatelet activity of synthetic and natural resveratrol in red wine. *Int. J. Tissue React.* **17**:1–3 (1995).
11. C. R. Pace-Asciak, S. E. Hahn, E. P. Diamandis, G. Soleas, and D. M. Goldberg. The red wine phenolics *trans*-resveratrol and quercetin block human platelet-aggregation and eicosanoid synthesis—Implications for protection against coronary heart-disease. *Clin. Chim. Acta* **235**:207–219 (1995).
12. Y. Kimura, H. Okuda, and S. Arichi. Effects of stilbenes on arachidonate metabolism in leukocytes. *Biochim. Biophys. Acta* **834**: 275–278 (1985).
13. S. Sotheeswaran and V. Pasupathy. Distribution of resveratrol oligomers in plants. *Phtyochemistry* **32**:1083–1092 (1993).
14. P. Kopp. Resveratrol, a phytoestrogen found in red wine. A possible explanation for the conundrum of the "French paradox"? *Eur. J. Endocrinol.* **138**:619–620 (1998).
15. R. Lu and G. Serrero. Resveratrol, a natural product derived from grape exhibits antiestrogenic activity and inhibits the growth of the human breast cancer cells. *J. Cell Physiol.* **179**:297–304 (1999).
16. D. K. Das, M. Sato, P. S. Ray, G. Maulik, R. M. Engelman. A. A. E. Bertelli, A. Bertelli. Cardioprotection of red wine: Role of polyphenolic antioxidants. *Drugs Exptl. Clin. Res.* **25**:115–120 (1999).
17. C. R. Pace-Asciak, O. Rounova, S. E. Hahn, E. P. Diamandis, and D. M. Goldberg. Wines and grape juices as modulation of platelet aggregation in healthy human subjects. *Clin. Chim. Acta.* **246**:163–182 (1996).
18. A. A. E. Bertelli, L. Giovannini, R. Stradi, S. Urien, J.-P. Tillement, and A. Bertelli. Kinetics of *trans*- and *cis*-resveratrol (3,4',5-trihydroxystilbene) after red wine oral administration in rats. *Int. J. Clin. Pharm. Res.* **16**:77–81 (1996).
19. W. Andlauer, J. Kolb, K. Siebert, and P. Fürst. Assessment of resveratrol bioavailability in the perfused small intestine of the rat. *Drugs Exptl. Clin. Res.* **26**:47–55 (2000).
20. G. Kuhnle, J. P. Spencer, G. Chowrimootoo, H. Schroeter, E. S. Debnam, S. K. S. Srai, C. Rice-Evans, and U. Hahn. Resveratrol is absorbed in the small intestine as resveratrol glucuronide. *Biochem. Biophys. Res. Commun.* **272**:212–217 (2000).
21. C. De Santi, A. Pietrabissa, R. Spisni, F. Mosca, and G. M. Pacifici. Sulphation of resveratrol, a natural product present in grapes and wine, in human liver and duodenum. *Xenobiotica* **30**:609–617 (2000).
22. C. De Santi, A. Pietrabissa, R. Spisni, F. Mosca, and G. M. Pacifici. Sulphation of resveratrol, a natural product present in wine, and its inhibition by natural flavonoids. *Xenobiotica* **30**:857–866 (2000).
23. C. De Santi, A. Pietrabissa, F. Mosca, and G. M. Pacifici. Glucuronidation of resveratrol, a natural product present in grape and wine, in the human liver. *Xenobiotica* **30**:1047–1054 (2000).
24. A. P. Li, C. Lu, J. A. Brent, C. Pham, A. Fackett, C. E. Ruegg, and P. M. Silber. Cryopreserved human hepatocytes: characterization of drug-metabolizing enzyme activities and applications in higher throughput screening assays for hepatotoxicity, metabolic stability, and drug-drug interaction potential. *Chem. Biol. Interact.* **121**:17–35 (1999).
25. A. P. Li. Overview: Hepatocytes and cryopreservation—a personal historical perspective. *Chem. Biol. Interact.* **121**:1–5 (1999).
26. J. Sfakianos, L. Coward, M. Kirk, and S. Barnes. Intestinal uptake and biliary excretion of the isoflavones genistein in rats. *J. Nutr.* **127**:1260–1268 (1997).
27. N. Kawai, Y. Fujibayashi, S. Kuwabara, K.-I. Takao, Y. Ijuin, and S. Kobayashi. Synthesis of a potential key intermediate of akaterpin, specific inhibitor of PI-PLC. *Tetrahedron* **56**:6467–6478 (2000).
28. L. Debrauwer, E. Rathahao, G. Boudry, M. Baradat, and J. P. Cravedi. Identification of major metabolites of prochloraz in rainbow trout by liquid chromatography and tandem mass spectrometry. *J. Agric. Food Chem.* **49**:3821–3826 (2001).
29. P. Manini, R. Andreoli, A. Mutti, E. Bergamaschi, I. Franchini, and W. M. A. Niessen. Determination of glucuronide molecules of toxicological interest by liquid chromatography negative-ion mass spectrometry with atmospheric pressure chemical ionization. *Chromatographia* **47**:659–666 (1998).
30. D. M. Goldberg, E. Ng, A. Karumanchiri, J. Yan, E. P. Diamandis, and G. J. Soleas. Assay of resveratrol glycosides and isomers in wine by direct-injection high-performance liquid chromatography. *J. Chromatogr. A* **708**:89–98 (1995).
31. B. C. Trela and A. L. Waterhouse. Resveratrol: Isomeric molar absorptivities and stability. *J. Agric. Food Chem.* **44**:1253–1257 (1996).